PhD in Geotechnical Engineering and Geo-Sciences

UNIVERSITAT POLITÈCNICA DE CATALUNYA
BARCELONATECH
Department of Geotechnical Engineering and Geo-Sciences

Assessment of the magnitude-frequency relationship of landslides and rockfalls: Application to hazard mapping

Guillem Domènech i Surinyach
Author

Jordi Corominas Dulcet
Supervisor

Barcelona, September 2015

This work has been supported by FPU-UPC 2009 Research Fellowship Program and the Interreg Project SUDOE IV B/DO-SMS, ref. SOE1/P2/F157
Cover designed by Eduardo Makhoul

UNIVERSITAT POLITÈCNICA DE CATALUNYA
BARCELONATECH
Escola de Doctorat

Curs acadèmic:

Acta de qualificació de tesi doctoral

Nom i cognoms
GUILLEM DOMÈNECH I SURINYACH

Programa de doctorat
DOCTORAT EN ENGINYERIA DEL TERRENY

Unitat estructural responsable del programa
DEPARTAMENT D'ENGINYERIA DEL TERRENY, CARTOGRÀFICA I GEOFÍSICA (ETCG)

Resolució del Tribunal

Reunit el Tribunal designat a l'efecte, el doctorand / la doctoranda exposa el tema de la seva tesi doctoral titulada **Assessment of the magnitude-frequency relationship of landslides and rockfalls: Application to hazard mapping**

Acabada la lectura i després de donar resposta a les qüestions formulades pels membres titulars del tribunal, aquest atorga la qualificació:

☐ NO APTE ☐ APROVAT ☐ NOTABLE ☐ EXCEL·LENT

(Nom, cognoms i signatura)	(Nom, cognoms i signatura)
President/a	Secretari/ària

(Nom, cognoms i signatura)	(Nom, cognoms i signatura)	(Nom, cognoms i signatura)
Vocal	Vocal	Vocal

_____, _____ d'/de _____ de _____

El resultat de l'escrutini dels vots emesos pels membres titulars del tribunal, efectuat per l'Escola de Doctorat, a instància de la Comissió de Doctorat de la UPC, atorga la MENCIÓ CUM LAUDE:

☐ SÍ ☐ NO

(Nom, cognoms i signatura)	(Nom, cognoms i signatura)
President de la Comissió Permanent de l'Escola de Doctorat	Secretari de la Comissió Permanent de l'Escola de Doctorat

Barcelona, _____ d'/de _____ de _____

a la Mar, en Pau i en Martí,
font d'alegria inesgotable

Resum

Degut al creixement exponencial de la població durant les últimes dècades, l'avaluació de la perillositat de colades de terra i despreniments i la seva zonificació han esdevingut eines fonamentals pel que fa a la planificació del territori, sobretot en zones muntanyoses.
La perillositat degut a fenòmens de vessant va ser definida com la probabilitat d'ocurrència d'un fenomen potencialment danyí en una determinada àrea i per un determinat període de temps. D'aquesta manera, és necessari conèixer la probabilitat d'ocurrència (o freqüència) per cada tipus d'esllavissada i magnitud.
L'objectiu d'aquesta tesis és el desenvolupament d'una metodologia objectiva, quantitativa i reproduïble que permeti l'obtenció de les relacions magnitud-freqüència per colades de terra, de mida mitja i gran i per despreniments.
Aquest procediment s'ha aplicat a la Vall de Barcedana i la Serra del Montsec per grans colades de terra i despreniments, respectivament. Les dues àrees d'estudi estan situades dins de la Conca de Tremp (Pirineu Oriental).
Pel que fa a les colades de terra, s'ha distingit entre 1) reactivacions i 2) vessants intactes. La freqüència de les reactivacions s'ha obtingut a partir de l'anàlisi d'11 grups d'ortofotos que cobreixen des del 1956 al 2013. La magnitud s'ha calculat com l'àrea de les trencades mitjançant la cartografia d'esllavissades i les ortofotos.
La relació magnitud-freqüència resultant de les reactivacions ha servit per obtenir la probabilitat de reactivació per un determinat volum. Aquesta ha estat comparada amb la probabilitat de reactivació determinada a partir dels llindars de pluja que han donat lloc a la reactivació de 4 grans esllavissades, també situades dins la Conca de Tremp. Les dates de reactivació han estat aproximades mitjançant la dendrogeomorfologia i els llindars s'han determinat mitjançant l'anàlisi ROC.
La susceptibilitat de les primeres trenades s'ha obtingut mitjançant un model determinista anomenat SINMAP. La freqüència per cada classe de susceptibilitat s'ha calculat mitjançant un inventari de primeres trencades identificades al camp i a través d'ortofotos.
S'ha desenvolupat un algoritme per tal d'obtenir l'àrea de les colades de terra més grans que la mida del píxel a través de l'agregació automàtic de píxels situats en un mateix vessant i que presenten una mateix classe de susceptibilitat. Finalment, s'ha definit la matriu magnitud-freqüència per la zonificació de la perillositat dels vessants intactes.
Pel que fa als despreniments, s'ha definit una metodologia per obtenir la distribució de volums de cicatrius de despreniments d'un penya-segat. S'ha assumit que els volums de cicatrius de despreniments poden ser una primera aproximació dels volum de despreniments. En aquest cas, la distribució de les cicatrius de despreniments s'ha calculat utilitzant un núvol de punts d'alta resolució de la paret obtingut amb un LIDAR terrestre. S'han calculat vàries distribucions de volums per tal de tenir en compte els diferents mecanismes de despreniment i el conseqüent rang de volums despresos.
Finalment, s'ha proposat una metodologia per tal de convertir la freqüència estadística (% de volums de cicatrius), calculada en el pas anterior, a freqüència temporal (número anual de volums de cicatrius). Per això, el volum total de material després s'ha calculat mitjançant el núvol de punts, mencionat anteriorment. El període de temps durant el qual s'ha després tot el volum de material s'ha estimat mitjançant la datació de la superfície inicial a partir de la qual va començar l'actual activitat de despreniments. Aquesta datació s'ha fet mitjançant l'isòtop cosmogenic, ^{36}Cl.

Abstract

Due to the exponential grown of the population within the last decades, the landslide hazard assessment of earthflows and rockfalls and their hazard mapping have become an essential tool for the territory management, mostly in mountainous areas.
The landslide hazard was defined as the probability of occurrence of a potentially damaging phenomenon in a certain area and within a given period of time. Thus, the probability of occurrence (or frequency) for each type of landslide and magnitude must be known.
The aim of this research is to develop an objective, quantitative and reproducible methodology to obtain the magnitude-frequency relations for medium and large size earthflows and rockfalls. This procedure has been set up in the Barcedana Valley and Montsec Range for large earthflows and rockfalls, respectively. Both study areas are located within the Tremp Basin (Eastern Pyrenees).
Concerning the earthflows, they have been split between 1) reactivations and 2) intact slopes. The frequency of the reactivations has been obtained by analysing 11 sets of orthophotos covering a period from 1956 to 2013. The magnitude has been calculated as the area of the landslides obtained from the landslide mapping and from the orthophotos.
The resulting magnitude-frequency relation for reactivations has been used to derive the probability of landslide reactivation for a given volume. It has been compared with probability of landslide reactivation obtained from the rainfall threshold responsible for the reactivation of 4-large landslides located within the Tremp Basin as well. The reactivation date has been estimated by means of dendrogeomorphology and the rainfall threshold has been determined by means of ROC analysis.
The susceptibility of first-time slope failures have been obtained using a deterministic model named SINMAP. The frequency for each susceptibility class has been calculated using the inventory of first-time failures identified in the field and by means of orthophotos.
An algorithm to obtain the area of the earthflows larger than the pixel size has been developed through an automatic aggregation of pixels located within the same slope and having the same susceptibility class. The obtained magnitude-frequency relation of first-time failures has been compared with the one obtained from the mapped first-time failures. Finally, the magnitude-frequency matrix for hazard mapping of intact slopes has been defined.
Concerning the rockfalls, a methodology to obtain the rockfall scar size distribution of a cliff has been defined. It has been assumed the rockfall scar volumes as proxy for the rockfall volumes. In that case, the distribution of rockfall scars has been calculated using a high resolution point cloud of the rockwall obtained by a terrestrial laser scanner and following. Several volume distributions have been calculated to take into account the different detachment mechanisms and the consequent range of detached volumes.
Finally, a procedure has been developed to convert form statistical frequency (% of scar volumes), calculated in the previous step, to temporal frequency (annual number of the scar volumes). To this, the total volume of material lost has been computed using the afore-mentioned point cloud. The elapsed time within the total volume has been removed has been estimated by dating the initial surface, from which the current rockfall activity started, by means of terrestrial cosmogenic nuclide, ^{36}Cl.

Resumen

Debido al crecimiento exponencial de la población durante las últimas décadas, la evaluación de la peligrosidad de coladas de tierra y desprendimientos i su zonificación se ha convertido en herramientas indispensables para la planificación del territorio, sobretodo en zonas montañosas.
La peligrosidad debido a fenómenos de vertiente fue definida como la probabilidad de ocurrencia de un fenómeno potencialmente dañino en una determinada área y en un determinado período de tiempo. Así, es necesario conocer la probabilidad de ocurrencia (o frecuencia) para cada tipo de deslizamiento y magnitud.
El objetivo de esta tesis es el desarrollo de una metodología objetiva, cuantitativa y reproducible que permita la obtención de las relaciones magnitud-frecuencia para coladas de tierra, de tamaño medio y grande y para desprendimientos.
Este procedimiento se ha aplicado en Valle de Barcedana y en la Sierra del Montsec para grandes coladas de tierra y desprendimientos, respectivamente. Las dos áreas de estudio están situadas dentro de la Cuenca de Tremp (Pirineo Oriental).
En cuanto a las coladas de tierra, se ha distinguido entre 1) reactivaciones y 2) vertientes intactos. La frecuencia de las reactivaciones se ha obtenido a partir del análisis de 11 grupos de ortofotos que engloban des del 1956 hasta el 2013. La magnitud se ha calculado como el área de las roturas mediante la cartografía de deslizamientos y ortofotos.
La relación magnitud-frecuencia de las reactivaciones ha permitido obtener la probabilidad de reactivación per un determinado volumen. Esta ha sido comparada con la probabilidad de reactivación determinada a partir de los umbrales de lluvia que han dado lugar a la reactivación de 4 grandes deslizamientos, también situados dentro de la Cuenca de Tremp. Las fechas de reactivación han sido aproximadas mediante la dendrogeomorfología y los umbrales se han determinado mediante el análisis ROC.
La susceptibilidad de las primeras roturas se ha obtenido mediante un modelo determinista llamado SINMAP. La frecuencia para cada clase de susceptibilidad se ha calculado mediante un inventario de primeras roturas identificadas en el campo y a través de ortofotos.
Se ha desarrollado un algoritmo para obtener el área de las coladas de tierra más grandes que el tamaño del píxel a través de la agregación automática de píxeles situados en una misma vertiente y que presentan una misma clase de susceptibilidad. Finalmente, se ha definido la matriz magnitud-frecuencia para la zonificación de la peligrosidad de las vertientes intactas.
En lo que concierne a los desprendimientos, se ha definido una metodología para obtener la distribución de volúmenes de cicatrices de desprendimientos de un acantilado. Se ha asumido que los volúmenes de cicatrices de desprendimientos pueden ser una primera aproximación de los volúmenes de desprendimientos. En este caso, la distribución de las cicatrices de desprendimientos se ha calculado utilizando una nube de puntos de alta resolución de la pared obtenida con un LIDAR terrestre. Se han calculado varias distribuciones de volúmenes para tener en cuenta los diferentes mecanismos de desprendimiento y el consecuente rango de volúmenes desprendidos.
Finalmente, se ha propuesto una metodología para transformar la frecuencia estadística (% de volúmenes de cicatrices), calculada en el paso anterior, en frecuencia temporal (número anual de volúmenes de cicatrices). Para esto, el volumen de material desprendido se ha calculado mediante la susodicha nube de puntos. El período de tiempo durante el cual se ha desprendido la totalidad del volumen de material se ha estimado mediante la datación de la superficie inicial a partir de la cual empezó la actual actividad de desprendimientos. Esta datación se ha hecho mediante el isótopo cosmogénico ^{36}Cl.

Acknowledgments

Vull donar les gràcies a la Universitat Politècnica de Catalunya (UPC) pel finançament de la beca FPU i al Projecte Interreg SUDOE IV B / DO-SMS pel finançament dels treballs sobre el camp.
D'altra banda, és clar que cap tesi és fruit del treball d'una sola persona i aquesta, no és cap excepció , ans al contrari, aquest podria ser el capítol més extens de tots. És per això que vull donar les gràcies al meu tutor, en Jordi Corominas, per haver-me donat la oportunitat d'endinsar-me en el món de les esllavissades i en el dels riscos geològics en general; pel seu suport en tots els aspectes, per la seva paciència, pels seus consells, per les seves idees, per les seves correccions, per la seva rigorositat i per tot el que he pogut aprendre d'ell.
També vull mostrar la meva gratitud cap a la Nieves Lantada, en Marcel Hürlimann, en Jose Moya i en Jean Vaunat per la seva ajuda.
Muchas gracias a la Agencia Estatal de METeorología (AEMET) por cedernos sus datos y a Manuel Gómez del Departamento de Ingeniería Hidráulica, Marítima y ambiental de la UPC por sus consejos durante el tratamiento de estos. También quiero agradecer la ayuda de Juan Remondo, de la Universidad de Cantabria, por su ayuda con el SIG y sus valiosos comentarios.
A Antonio Abellán de la Université de Lausanne y Manuel Jesús Royan, de la Universitat de Barcelona por su ayuda en la campaña con el LIDAR.
A la Maribel Ortego i en David Garcia-Sellés, per l'ajuda durant el tractament de les dades.
I also want to express my gratitude to Silke Merchel, Georg Rugel, Steffan Pavetich as well as Shavkat Akhmadaliev and the DREAMS operator team for their help and support during the stay in Dresden; to guide me within the amazing world of the Cosmogenic Nuclides.
Many thanks to Massimiliano Alvioli from the CNR-IRPI, in Perugia (Italy), for his help during the generation of the Slope Units and his advices.
Vull agrair les correccions fetes per en Guillaume G. Chevalier i l'Héctor Marín Moreno.
No em puc oblidar de tota la gent que he conegut en aquest llarg viatge: els companys del despatx de correus, els que he conegut després al Departament d'Enginyeria del Terreny, Cartogràfica i Geofísica de la UPC, it was also a pleasure to meet the guys of the LARAM school 2010 held in Salerno, e anche grazie a tutto quello che ho imparato accanto al Po.
Els companys del CNB, pels bons moments passats junts i per ajudar-me a conèixer llocs on no havia estat mai, moltes gràcies.
Els companys de pis que he tingut a llarg d'aquest anys, que no han estat pocs i dels quals n'han sortit molt bones amistats: Tomàs, Maria, Jordi, ha set genial.
A la Clàudia, l'Alba, l'Olga, l'Héctor, l'Amadeu, la Natàlia, en Victor, l'Andrés, i als de "telecos", l'Edu, en Marc, en Peppe i en Carlos. Per tots els dinars compartits i les mil i una històries que se'n derivaven.
També a tots els meus amics de Sant Joan que, tot i no ser a Harvard, a vegades hi havia molts nervis, sobretot quan venia el vent de cara.
I com no podia ser d'una altra manera, vull agrair el suport incondicional de la meva família, tiets, cosins, "nebots", de l'Avi Joan, que tot i marxar molt aviat, d'algun lloc havia de sortir la tossuderia per acabar la tesi. Als meus pares, que tot i no saber molt bé què es fa en un doctorat, sempre m'han recolzat, als meus germans i cunyats, tots plegats un regal i a les tres darreres incorporacions: la Mar, en Martí i en Pau.

Table of contents

Chapter 1

1 Introduction

1.1 Motivation

A slope failure may take place by the decay of the material strength, the increase of pore water pressures, the increase of shear stresses (i.e. earthquake shaking), among others. The progression of the material downslope after the failure is a landslide (Cruden, 1991). According to Hungr et al. (2014), several types of landslides can be defined based on the mode of motion (Baltzer, 1875), the material (Heim, 1932; Zaruba and Mencl, 1969) or the combination of failure and propagation mechanisms (Hutchinson, 1968, 1988). One of the most widely accepted classification is the one made by Varnes (1978) which has been constantly modified and updated.

Earthflows and rockfalls are two of the most common landslides in mountainous areas and may also affect populated areas. Thus, the evaluation of the landslide hazard is required.

Varnes D. J. (1984) defined the natural hazard term as "the probability of occurrence within a specific period of time and within a given area of a potentially damaging phenomenon". Results are expressed using the magnitude-frequency relationship (e.g. Guzzetti et al., 2004; Hungr et al., 2008; Van Den Eeckhaut et al., 2007). This information may be later used for the generation of the landslide hazard map which should be used by the local authorities for the land use management.

One of the main challenges when generating landslide hazard maps at small scale (< regional scale) is the definition of a standardized methodology for the quantitative evaluation of the hazard. Thus, both components involved in the hazard assessment (frequency and magnitude) must be quantified.

The degree of hazard can be represented as the combination of these two components using the M-F matrixes (Cardinali et al., 2006, 2002).

Several attempts have been carried out in different countries such as Italy, Switzerland and Australia (among others) to develop their own methodologies and technical guidelines for the landslide hazard mapping (AGS, 2007; Kranitz and Bensi, 2009; Raetzo and Loup, 2009).

Several authors agree that landslide inventories are the bases of the landslide hazard maps (Bertolini and Pizziolo, 2008; Corominas et al., 2014; Pizziolo, 1996)

This thesis aims at developing a methodology to evaluate the frequency and the magnitude of earthflows and rockfalls in a quantitative way and application to the landslide hazard maps.

1.2 Aim of the research

This work was born from the collaboration carried out with the Geological Survey of Catalonia (ICGC) for the preparation of the "Mapa per la Prevenció dels Riscos Geològics 1:25000" (Geological Risks Prevention Map 1:25000). It was identified the necessity to develop a procedure to evaluate the landslide hazard, and its integration at a regional scale mapping.

The aim of this research has been the development of a rigorous, objective and reproducible methodology to establish the magnitude-frequency relationship of earthflows and rockfalls for the latter application to the hazard mapping at regional scale. Thus, this work has been clearly differentiated into two parts: Earthflows and rockfalls.

To this end, two study sites located in the Tremp Basin (Eastern Pyrenees, Spain) have been selected and described in chapter 2: The first one is the Barcedana Valley where the methodology has been develop for earthflows. The second area of study, where the rockfall phenomenon has been analysed, is located in the south face of the Montsec Range.

Earthflows hazard has been assessed considering both the reactivation and first-time failures. In chapter 3 the lithological, morphological and landslide mapping carried out in the study area are presented as well as the analysis of the reactivated landslides. The magnitude-frequency relation has been obtained. In order to validate it, the annual probability of 4 large landslides located within the Tremp Basin has been evaluated in chapter 4. In this case, series of reactivated landslides have been reconstructed by means of dendrogeomorphology. A method to determine the possible date of landslide reactivations and the establishment of a rainfall threshold within the Tremp Basin has been proposed. The annual probability of reactivation has been calculated and compared with annual probability of reactivation calculated from the magnitude-frequency curve for reactivations obtained in the previous chapter.

Concerning the first-time failures (chapter 5), the potential of large slope failures (rotational slides and earthflows) of the intact slopes has been evaluated applying a deterministic model. The area of the potential failures may contain multiple pixels and it is used as a proxy the landslide magnitude. The magnitude-frequency matrix for the hazard mapping has been obtained.

When working with rockfall hazard, it has been assumed that the rockfall scar volumes can be a proxy of the rockfall volumes when no data of past events exist. The rockfall scar size distribution has been calculated using a TLS (chapter 6). Since the rockfall scars can be the result of one or several rockfall events, 3 different approaches have been defined considering the different typology of volumes. Finally, in order to obtain the temporal frequency of the rockfall scar size distribution, the total volume of material lost and the time necessary to generate this distribution have been calculated in chapter 7

.

Chapter 2

2 Study area

The area of study is located within the Tremp Basin (Conca de Tremp) an erosive depression located in the Eastern Pre-Pyrenees (Spain) about 170 km north-west of Barcelona. The Tremp Basin borders on the Montsec Range (Serra del Montsec) to the south and the Sant Gervàs Range (Serra de Sant Gervàs), the Peracalç Range (Serra de Peracalç) and the Boumort Range (Serra de Boumort) to the north (Figure 2-1, a).

Typical Mediterranean climatic conditions prevail in the area with intense storms at the end of spring and beginning of autumn and dry spells in January-February and early summer. The mean annual precipitation is about 600-700 mm mostly as high intensity storms (Novoa, 1984) and the mean annual temperature is 12.5º with high variations. The study area has been split in two smaller parts according to the phenomenon occurring in each one (Figure 2-1, b).

The first one is located in the Barcedana Valley (Vall de Barcedana). With an extension about 25 km^2 and an altitude ranging from 400 to 650 m asl, it is located in the southern part of the Tremp Basin. It borders on the Montsec Range to the south and the Llimiana Range (Serra Llimiana), the Obacs Range (Serra dels Obacs) and La Freixa to the north. Surrounding summits have a maximum elevation of 1,700 m asl. Three small villages with a total of 80 inhabitants are present in the area: Sant Cristòfol de la Vall, Sant Martí de Barcedana and Sant Miquel de la Vall. The territory is mostly occupied by crops and farm land. Translational landslides and earthflows may occur during the wet period (autumn) affecting the whole area and the LV-912 road in particular.

The second study area is the “Roca del Arcs” in the Montsec Range which is affected by rockfalls. Located in the south face of the Montsec Range, a 750 m long and 200 m high cliff has been selected due to the presence of large rockfall scars which are indicative of the rockfall activity. It is a well known climbing wall which reaches a maximum elevation of 1,200 m asl. Unlike the Barcedana Valley, rockfalls in Roca dels Arcs does not affect any infrastructure.

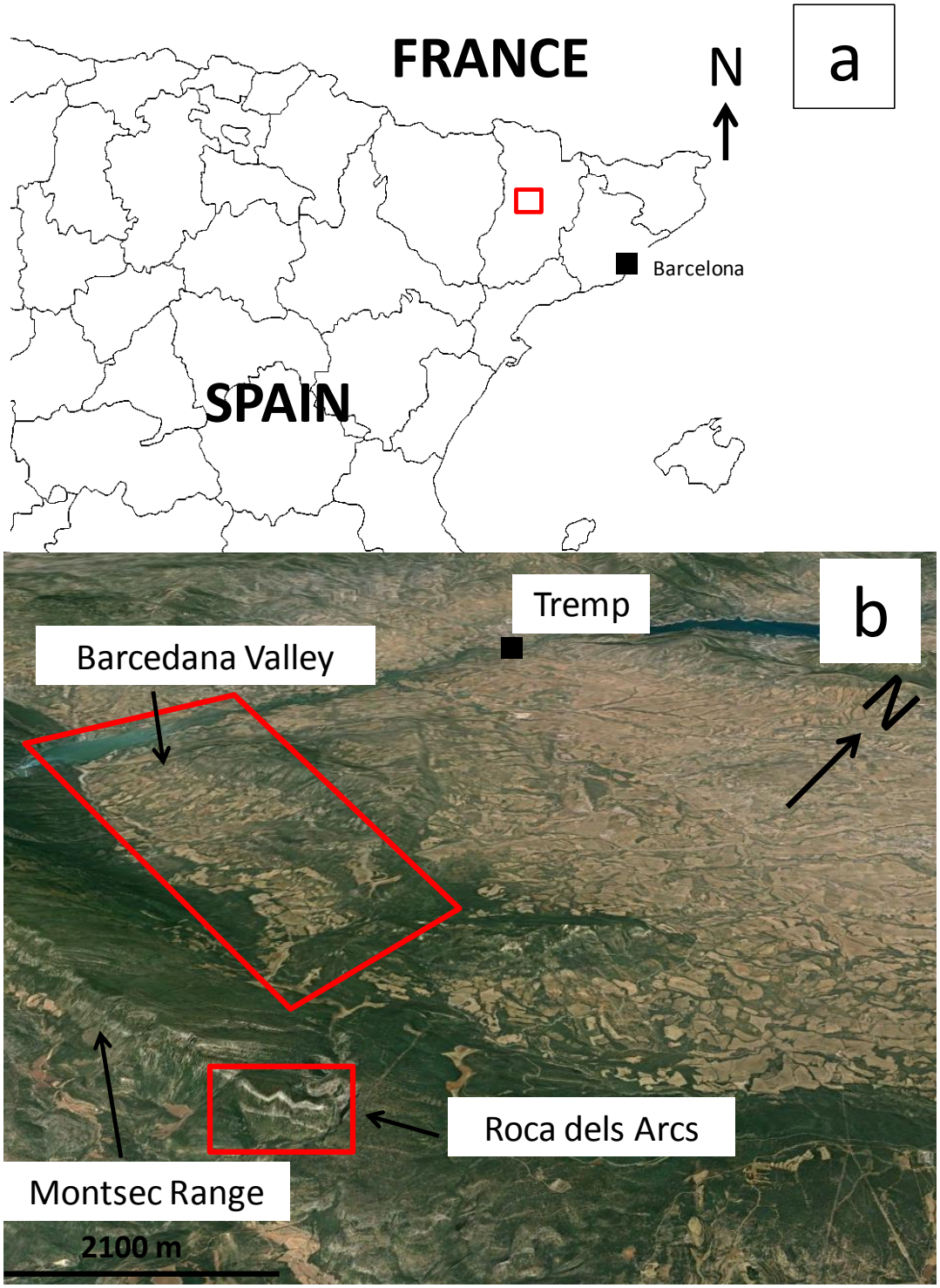

Figure 2-1: a) Location of the Tremp Basin represented with a red rectangle. b) south-east part of the Tremp Basin. Landslide and rockfall study area, located in Barcedana Valley and Montsec Range respectively, are delimited with red rectangles.

Geological framework

The Pyrenees fold-and-thrust belt was formed during the Alpine orogeny (Upper Cretaceous and Lower Tertiary) as the result of the collision between the Iberian and European plates. It produced a shortening of the Pyrenees between 100 and 150 km and a deformation of the thrust sheets being displaced to the south.

The Tremp Basin corresponds to the south-central Pyrenean Area (South Central Unit, SCU) (Seguret, 1972) (Figure 2-2, a). It includes Boixols, Montsec, and Sierras Marginales thrusts, from north to south (Figure 2-2, c).

The Montsec thrust sheet shows a syncline to the north part. It is also known as Tremp-Graus basin. Materials from the Upper Cretaceous/Paleocene (Garumnian facies) to Eocene-Oligocene conglomerates are present. To the south, in the frontal part of the Montsec thrust, where the Montsec Range is comprised, limestones and marls from the Upper Cretaceous are present (Figure 2-2, b). They have been widely studied by Caus et al. (1999).

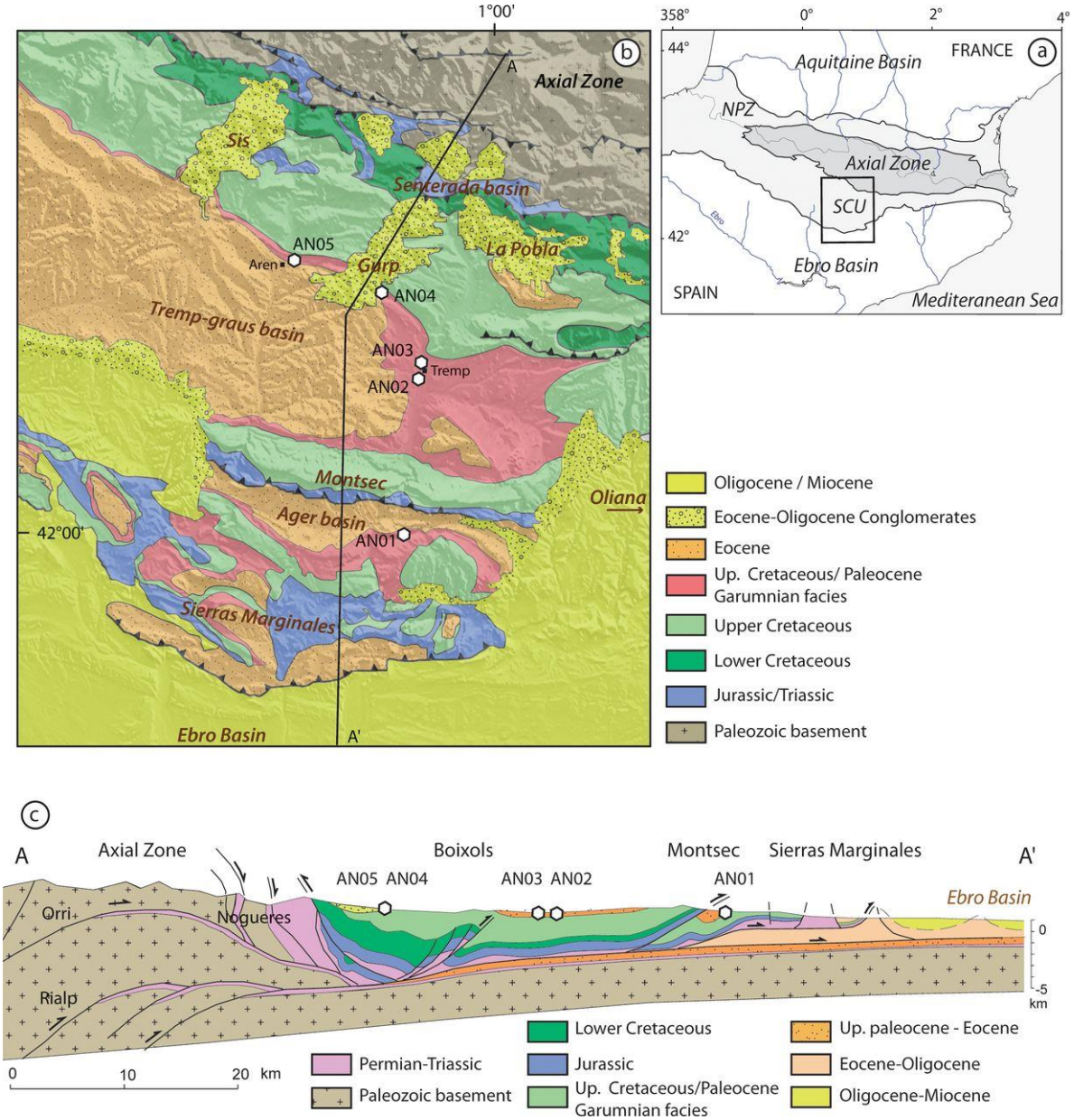

Figure 2-2: a) Geographical and geological location of the South Central Unit (SCU) (Seguret, 1972). b) Geological map of the SCU where the Tremp Basin is located. c) Geological cross-section deduced from the ECORS seismic profile (Muñoz, 1992). Boixols, Montsec and Sierras Marginales thrusts are shown (from Fillon et al., 2013).

In the Montsec and Sierras Marginales thrust sheets, materials from Garumnian (Leymerie, 1862) appear. They are mostly alluvial and fluvial materials, but also lacustrine, interbedded

with Upper Cretaceous and Lower Palaeogene marine deposits. These materials reach the maximum thickness (>800 m) in the Tremp-Graus Basin where it was named Tremp Formation (Mey et al., 1968) and later called Tremp Group (Cuevas, 1992; Cuevas et al., 1991) (Figure 2-3). It comprises Fm. Claret, Fm. Esplugafreda, Fm. Talarn, Fm. Conques and Fm. Posa. A last revision of the Tremp Group was carried out by Pujalte and Schmitz (2005).

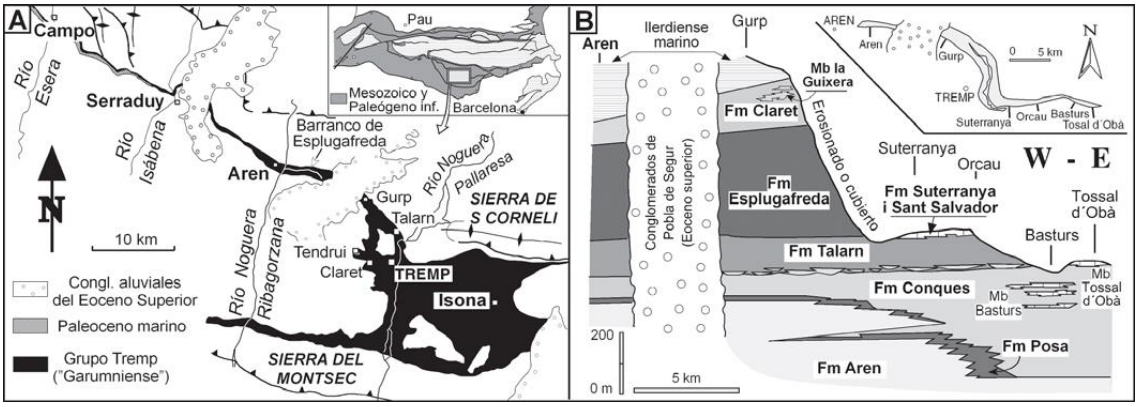

Figure 2-3: A) Outcrops of the Tremp Group B) Formation of Tremp Group according to (Cuevas, 1992; Cuevas et al., 1991) (from Pujalte and Schmitz, 2005).

Commonly, Garumnian deposits of the central Pre-Pyrenees are divided in three main parts (Rosell et al., 2001): the Lower Red Garumnian (red lutites), the Vallcebre Limestones (intermediate limestone) and the Upper Red Garumnian (red lutites). Another fourth transitional level called Grey Garumnian is added at the base (Figure 2-5):

1- Grey Garumnian (from Rosell et al., 2001): Within the Tremp Basin, it is just present in the Montsec thrust sheet. From the diagenetic point of view, it is completely different of the other typical Garumnian materials. It is made of grey lutite, lignite, sandstone and interbedded limestone layers. Located at the roof of the Arenys Sandstones (Gresos d'Arenys), it is of Maastrichtian age.

2- Lower Red Garumnian (red lutites) (from Rosell et al., 2001): It presents a maximum thickness in the Vallcebre area as well as in the Montsec thrust sheet axis (Western Isona) but becomes thinner at the basin margins until disappears. It is made of red silty materials with interbedded levels of lenticular fining upward sandstones. Between silty deposits, there exist thin layers of fine grain sandstone with cross lamination. These silty deposits are often affected by joints and present calcareous nodules. The roof of the Lower Red Garumnian level has been defined as the limit between Mesozoic and Cenozoic.

3- Vallcebre Limestones (intermediate limestone) (from Rosell et al., 2001): The name comes from the Vallcebre locality where it reaches the maximum thickness of about 50 m. In the Tremp Basin, they are considerably thinner exhibiting several micritic calcareous sections, frequently recrystallized, of Maastrichtian-Danian age.

4- Upper Red Garumnian (red lutites) (from Rosell et al., 2001): It is the most expansive level of Garumnian facies. It is of Thanetian age and may contain gypsum and anhydrite nodules. Well-developed evaporitic lentils can be found as well.

Figure 2-4: Simplified cross section of the Tremp Basin (from Rosell et al., 2001). No vertical scale. Horizontal scale: 50 km. **1)** Grey Garumnian. **2** and **3**) Lower Red Garumnian. There are expansive red clays at the bottom. The other part is affected by pedogenic processes with small channels. **4)** Vallcebre Limestones. **5, 6** and **7)** Upper Red Garumnian: Dejection cones with conglomerates and sandstones (5), marly paleosoils and lacustrine limestones (6) and evaporites (7).

According to the available material, two types of mass movements are given in the study area. In the Tremp Basin, fine materials from the Garumnian facies are responsible for earthflow occurrences (Figure 2-5 and Figure 2-6, A). In the Montsec Range, rockfalls from the Upper Cretaceous limestone cliffs are given (Figure 2-5 and Figure 2-6, B).

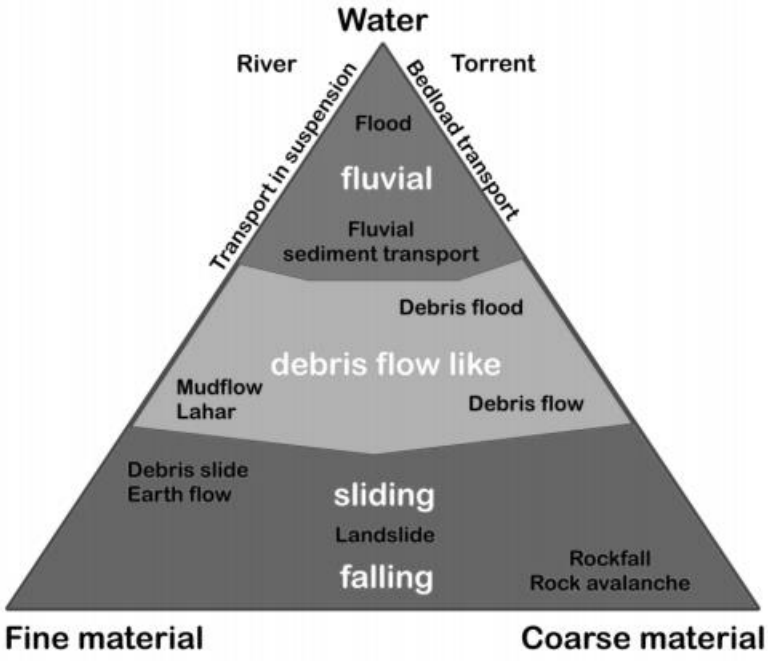

Figure 2-5: Triangular diagram of mass movements according to the water, fine and coarse material content. Modified after Phillips and Davies (1991) (from ONR-24-800, 2007).

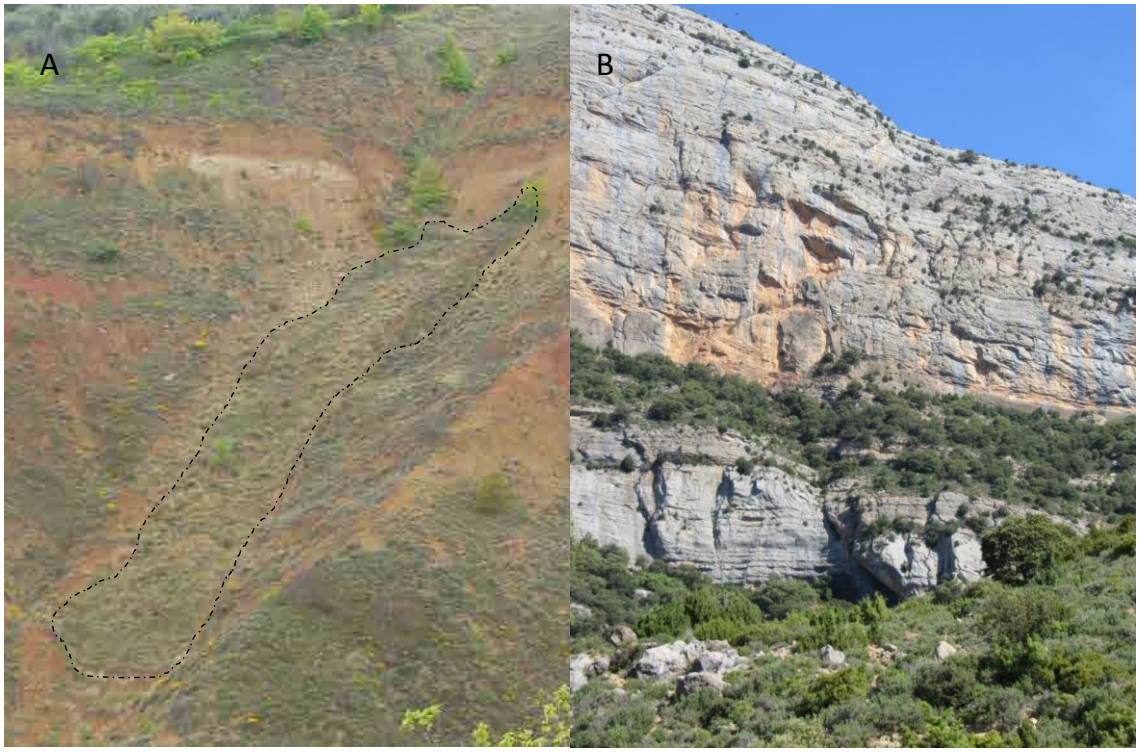

Figure 2-6: A) Earthflow at the Barcedana Valley in Garumnian materials. B) Rockfalls occurrences in the Upper Cretaceous limestones

2.1 Earthflows in Barcedana Valley

A flow is a spatially continuous movement in which surfaces of shear are short lived, closely spaced, and usually not preserved (Cruden and Varnes, 1996).

Davies et al. (2013) defined earthflows as "the slow gravitational downslope movement of water-saturated, fine-grained materials".

Recently, Hungr et al. (2014) revised the classification of landslides made by Varnes (Varnes, 1978) and defined the earthflows as a "rapid or slower, intermittent flow-like movement of plastic, clayey soil, facilitated by a combination of sliding along multiple discrete shear surfaces, and internal shear strains. Long periods of relative dormancy alternate with more rapid surges". Other published works found in the literature define the earthflows as fine-grained material (clayey or silty clay soil, sensitive clay deposits, weathered fine-grained bedrock) with a plastic or visco-plastic behavior (Mackey & Roering, 2011; Simoni et al., 2013; Can et al., 2005: Keefer and Johnson, 1983: Malet et al., 2005) with different velocities: < 4 m/yr (Mackey & Roering, 2011), 0.01 to 0.4 m/day (Can et al., 2005) or 0.5 to 5 m/yr (Delong et al., 2012). They are generally large (>500 m long) and deep seated (>5 m thick) (Mackey & Roering, 2011).

Although they are the most common hillslope mass-movements, the variability concerning the movement such as flow or slide, the type of material involved, and the range of velocities leads to confusion in classification (Davies et al., 2013).

Usually, earthflow occurrences are related to reactivations of ancient slides (Prokešová et al., 2014) with short periods of high activity followed by long periods of tiny displacements (Giordan et al., 2013)

The intermittent flow-like movement, occurred due to seasonal patterns, is maintained over long distances and periods of time (Malet et al., 2005), and is related to pore pressure fluctuations

(Malet, 2002; Picarelli, 2001) that might be controlled by precipitation (rainfall and snowmelt), groundwater and air pressure variations (Schulz et al., 2009). In low-permeability soils, periods of accumulated rainfall are needed to reduce soil suction and increase the pore-water pressures. Therefore, the response to rainfall or snowmelt of earthflows to landsliding is usually delayed (Iverson and Major, 1987)

Earthflows can exhibit several shapes like hourglass, tongue or teardrop shape in plain view (Giordan et al., 2013; Keefer and Johnson, 1983), with an ample crown scarp, upslope, presenting traction cracks that break the terrain into blocks. This upper part is called zone of depletion. Downslope, there is a narrower and elongated zone where the material is canalised to the depositional area, in which, the material flows above the intact material. Compression is given in this part of the landslide (Keefer and Johnson, 1983). Another typical feature of the earthflow is a sinusoidal longitudinal profile, concave upward in the zone of depletion and convex downward in the accumulation zone, caused by the loss of material near the head of the earthflow and its accumulation on the toe (Keefer and Johnson, 1983).

The Barcedana Valley borders on the Llimiana Range (Sierra de Llimiana) to the north and the Montsec Range (Sierra del Montsec) to the south (Figure 2-7). The Llimiana Range is formed by well cemented materials from Oligocene: Sandstones, conglomerates, reddish and grey lutites, limestones with alveolines as well as marls and lutites. To the south, the Montsec Range exhibits also well cemented materials from Garumnian Facies: Micritic limestones, calcarenites and lutites of Fm La Posa (Maastrichtian); Sandstones and calcarenites of Fm Gresos d'Areny (Maastrichtian) and limestones, calcarenites and sandstones of Campanian-Maastrichtian age (Figure 2-8).

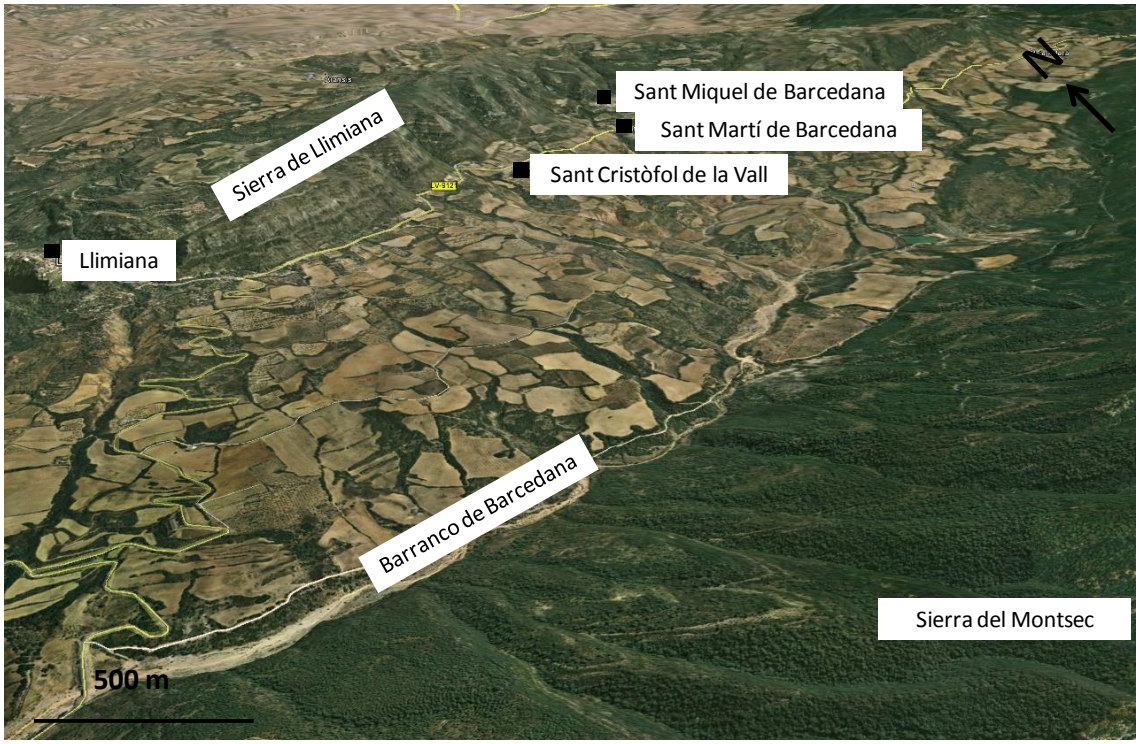

Figure 2-7: Barcedana Valley

Between both ranges, within the valley, a big extension of colluvium can be found. It is mainly composed of clays with angular sandy and silty clasts of Holocene age. Garumnian deposits are also present: Red lutites, paleosoils, sandstones and gypsum of Selandian–Thanetian age, as

well as micritic limestones, calcarenites and lutites of Fm La Posa (Maastrichtian) (Figure 2-8).
In Figure 2-9, a simplified cross section A'-A (Figure 2-8) of the Barcedana Valley is shown (Linares et al., 2002). The lithological units 4, 5, 6 and 7 correspond to the four Garumnian levels afore-described (Rosell et al., 2001). As it can be seen, Lower and Upper Garumnian levels (5 and 7) are considerably thicker than the intermediate level of limestones and sandstones. It is found at 600 m asl with a maximum thickness of about 35 m.
According to the geological map (ICGC, 2015), published works (Linares et al., 2002; Rosell et al., 2001) and field observations (more detailed in next chapter 3), the cartographic units from Garumnian facies, outcropping in the Barcedana Valley, have been classified as follows:

Table 2-1: Classification of the cartographic units (ICGC, 2015) according to Garumnian Facies (Rosell et al., 2001)

Geology (ICGC, 2015)	Garumnian Facies (Rosell et al., 2001)
PPlg	Upper Red Garumnian
-	Vallcebre Limestones
KMlg	Lower Red Garumnian
KMcp	Grey Garumnian

As it can be seen in Table 2-1, Vallcebre Limestones do not outcrop in Barcedana Valley. As afore-mentioned, they are considerably thin in the Tremp Basin (Rosell et al., 2001). Furthermore, its thickness is drastically reduced in the southern margin of the basin (Figure 2-4). Therefore, either they are covered by quaternary colluvium or they are not present in this part of the basin.
Materials from the Red Garumnian Facies (PPlg and KMlg) are the main responsible for the several numbers of earthflows occurred, especially, during rainy events where the water seems to assist the instability of some slopes. These landslides can reach magnitudes of thousands of square meters and they usually affect the road L-912.
Some studies have been carried out within the Tremp Basin (e.g. Forné, 2004; Oliveras, 2011; Montero, 2011; Canales, 2011; Abancó et al., 2009; Linares et al., 2002) as well as in Garumnian Materials close to the Tremp Basin (e.g. Pinyol et al., 2012).
From the geomechanical point of view, results of the studied landslides within basin show low plasticity clay according to the Casagrande Classification (Casagrande, 1942). Grain sizes vary from silt to silty sand according to the granulometric curve. Peak friction angle about 25º with a cohesion value of 58kPa and a residual friction angle ranging from 9º to 15º have been obtained. Stability analysis suggested landslide thickness ranging from 1.5 to 6m in steep slopes (16 to 23º) and from 7 to 12 m in more gentle slopes (7.5 to 10º).

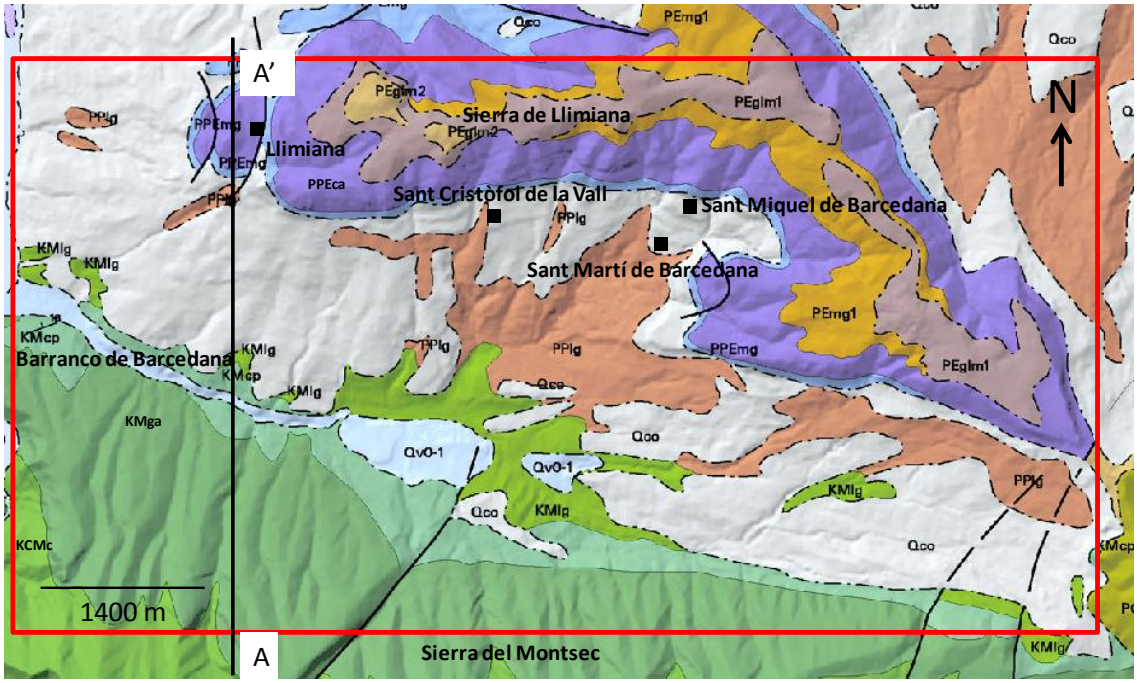

Figure 2-8: Geological map of Barcedana Valley (from ICGC, 2015). Geological cross section A'-A shown in Figure 2-9: **Qco**: Colluvial deposits. Clays with angular cobbles. Holocene. **Qv0-1**: Angular clasts, sands or silt. Holocene. **PEglm2**: Sandstones, grey and reddish lutites and conglomerates. Fm Montllobar. Lower Eocene. **PEglm1**: Sandstones, conglomerates and reddish lutites. Fm Montllobar. Lower Eocene. **PEmg1**: Sandstones within the Fm Artés. Upper Eocene. **PPEca**: Limestone with alveolines. Fm Cadí-Àger. Ilerdian. **PPEmg**: Marls and lutites. Fm Fígols. Ilerdian. **PPlg**: Red lutites, paleosoils, sandstones and gypsum. Upper part of the Tremp Group. Garumnian Facies. Selandian-Thanetian. **KMlg**: Red lutites, sandstones and paleosoils. Tremp Group. Garumnian Facies. Maastrichtian. **KMcp**: Micritic limestones, calcarenites and lutites. Fm La Posa. Garumnian Facies. Maastrichtian. **KMga**: Sandstones and calcarenites. Fm Gresos d'Areny. Maastrichtian. **KCMc**: Limestones, calcarenites and sandstones. Fm Bona. Campanian-Maastrichtian.

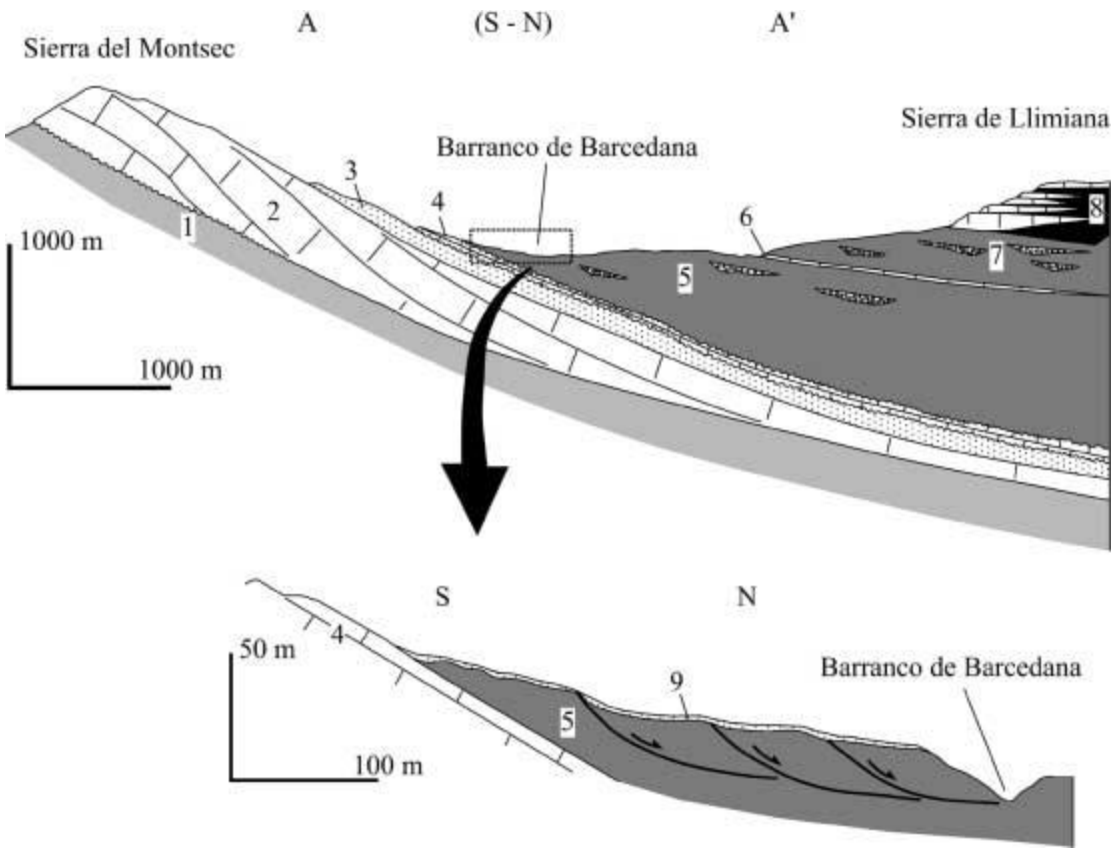

Figure 2-9: Geological cross section A-A' (Figure 2-7). From (Linares et al., 2002): **1)** Santonian marls. **2)** Campanian limestones and calcarenites. **3)** Sandstones and calcarenites. Fm Gresos d'Areny. **4)** Pelites, sandstones and limestones, Grey Garumnian, Maastrichtian. **5)** Pelites and sandstones. Lower red level, Garumnian, Maastrichtian. **6)** Limestones and sandstones. Intermediate level, Garumnian, Danian. **7)** Pelites, sandstones and evaporites. Upper level, Garumnian, Danian. **8)** Limestones and pelites. Eocene, Ilerdian. **9)** Gravel. Quaternary.

2.2 Rockfall in Montsec Range (Roca dels Arcs)

Hungr et al. (2014) defined the rockfalls as the "detachment, fall, rolling, and bouncing of rock fragments. May occur singly or in clusters, but there is little dynamic interaction between the most mobile moving fragments, which interact mainly with the substrate (path). Fragment deformation is unimportant, although fragments can break during impacts. Usually of limited volume"

Rockfall is a type of landslide or common slope process in mountainous areas that comprises the detachment of a volume of rock mass from a steep slope, its transportation by bouncing, rolling and/or sliding and deposition in the accumulation zone (Hutchinson, 1988; Varnes, 1978). Such accumulation forms talus slopes of rock fragments at base of the source area (Evans and Hungr, 1993).

The detachment of a rock mass, along discontinuities such as bedding planes, joints, cleavage, faults, etc can be given in terms of individual rigid fragments moving independently and impacting against the floor, also known as fragmental rockfall (Evans and Hungr 1993) or may involve a whole mass of material moving as a flow (rock avalanche) (Hungr et al., 2014). The detached block may remain as a single unit or break into several smaller boulders or event disintegrate as a granular mass (Bourrier et al., 2013).

According to Poisel and Preh (2011), the most common rockfall mechanisms in a small scale

are: 1-falling (Figure 2-10 a), 2-sliding (Figure 2-10 b), 3-rotation of rock blocks (Figure 2-10 g), 4-buckling (Figure 2-10 h) and 5-toppling (Figure 2-10 i and j).

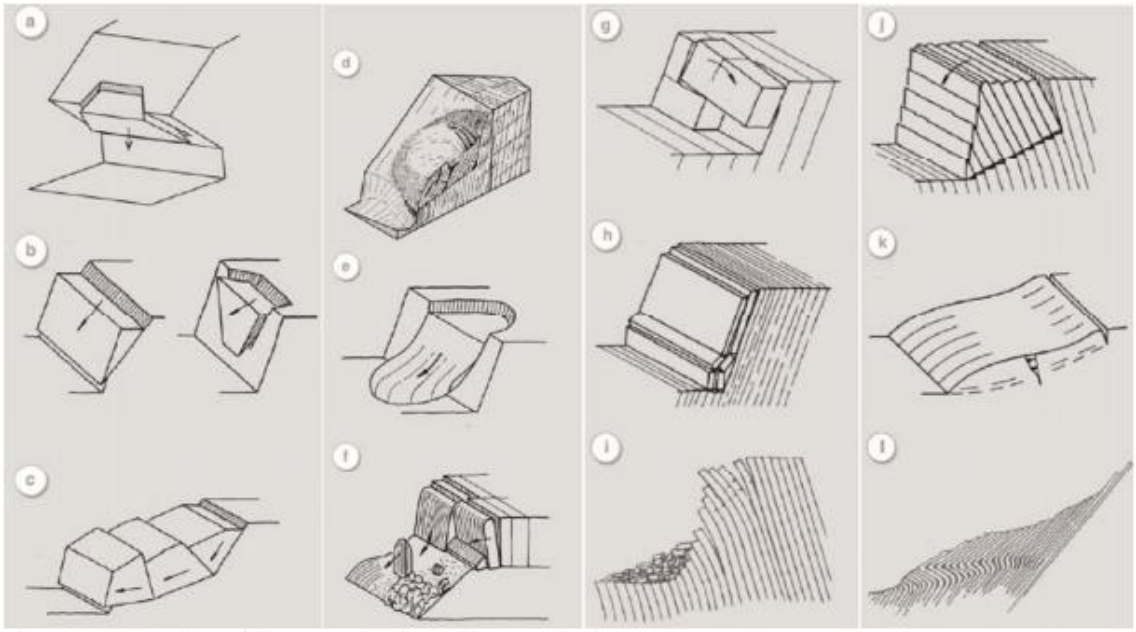

Figure 2-10: Rock slope failure mechanisms (from: Poisel and Preh, 2004)

Sometimes, there is not a clear distinction between rock avalanching and rockfall and both processes may be given at the same time: A single boulder located within a rock avalanche can roll down further, acting also as a rockfall (Bourrier et al., 2013). In such a case, the predominant process is the most dangerous one.

The Roca dels Arcs cliff (Figure 2-11) is composed of two calcareous bars of limestones, calcarenites and sandstones of Fm Bona (Campanian-Maastrichtian) (Figure 2-12). The upper part, the one studied in this thesis, is about 200 m high and 750 m long.

Although it is not very fractured, the cliff is being affected by rockfalls and consequently, several scars from detached blocks can be observed as well as fallen boulders at the bottom, mostly, covered by vegetation. This area is not affected by the human activity and no data about past rockfall events is available.

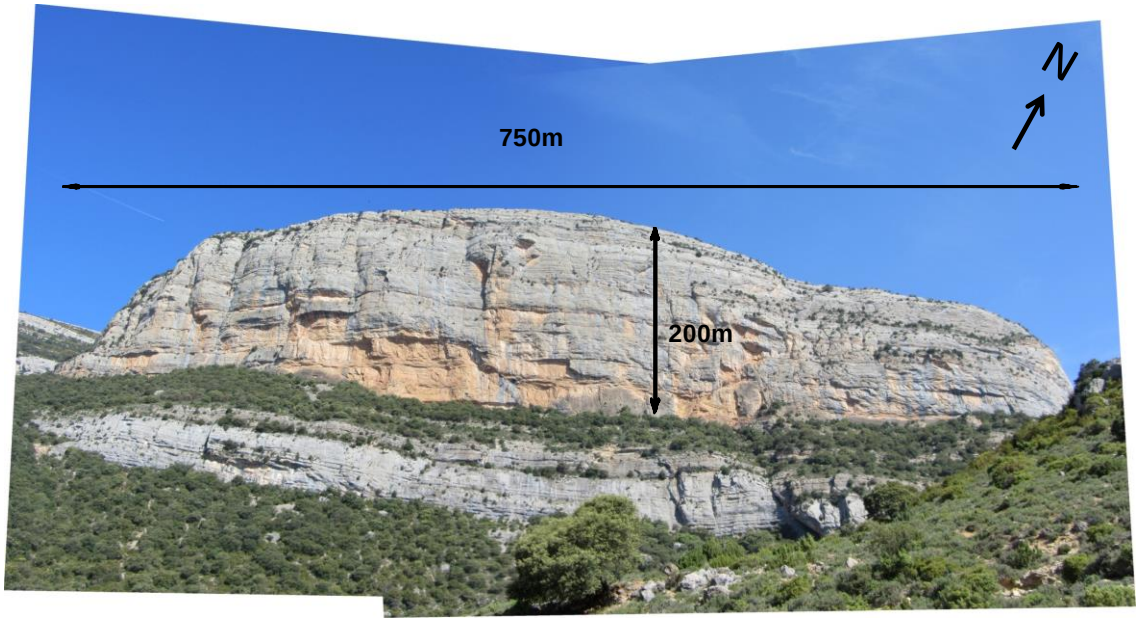

Figure 2-11: Roca dels Arcs.

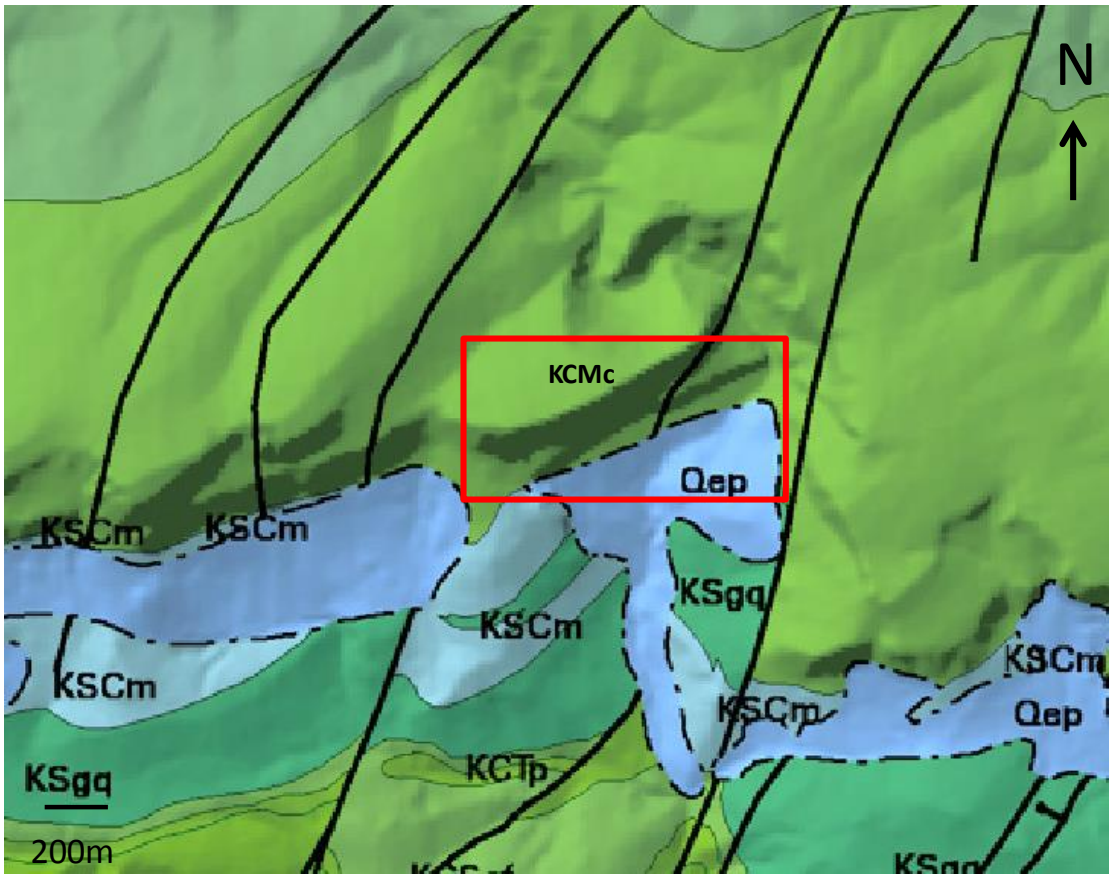

Figure 2-12: Geological map of La Roca dels Arcs area (from ICGC, 2015): **Qep**: Talus scree of Holocene age. **KCMc**: Limestones, calcarenites and sandstones. Fm Bona (Campanian-Maastrichtian).

Part I: Earthflows

Chapter 3

3 Landslide hazard assessment

Varnes D. J. (1984) defined the term "Natural hazard" as the probability of occurrence within a specific period of time and within a given area of a potentially damaging phenomenon. It includes temporal probability or frequency, spatial probability and intensity, which is usually defined as the energy or the magnitude (volume or area) of the occurrence.

It is important to notice the difference between intensity and magnitude: intensity may be described by a set of parameters such as maximum movement velocity, total displacement, differential displacement, depth of the moving mass, peak discharge per unit width or kinetic energy per unit area (Fell et al., 2008). Some authors as Cardinali et al. (2002) defined the intensity as a function of the landslide volume and of the expected velocity. On the other hand, the magnitude refers to the landslide size, i.e., the area or the volume.

The landslide hazard assessment is evaluated according to the scale of analysis. Although a common nomenclature about the scale does not exist, some examples can be found in the literature which defined different levels: Castellanos Abella (2008) divided the landslide risk assessment in Cuba in 4 levels: National (1:1,000,000), Provincial (1:100,000), Municipal (1:50,000) and Local (1:25,000). Cascini (2008) suggested 4 levels as well: 1-Small scale (<1:100,000): Used for landslides inventory in areas of at least 10,000 km^2. It should be used to inform the local authorities; 2-Medium scale (1:100,000 to 1:25,000): Applied to areas between 1000 and 10,000 km^2. Suitable for landslide inventories and first approximation hazard zoning. Used for regional zoning: 3-Large scale (1:25,000 to 1:5,000): For landslide inventory, in areas from 10 to 1,000 km^2. Used for local hazard zoning; 4-Detailed scale (>1:5,000): Applied over an area of several to tens of square kilometers. Used for local and site specific hazard zoning. He also highlighted that maps should be displayed at the appropriate scale according to the purpose and according to the resolution and quality of the available data. Fell et al., (2008) defined three levels of zoning: Regional (1:25,000 to 1:250,000), Local (1:5,000 to 1:25,000) and Site-specific (1:5,000 to 1:1,000).

For landslide hazard zoning purposes, the Magnitude Frequency (MF) matrix is typically used (Figure 3-1). The level of hazard is determined according to the magnitude and the frequency of the phenomenon. Therefore, those 2 parameters must be properly evaluated. For instance, small landslides with low magnitude but with a high frequency cannot be defined as high dangerous areas since structural damage to the buildings can occur, but they do not represent a threat to the people lives. This topic has been widely treated in countries such as Switzerland, Italy as well as Australia, among others, where they have developed their own methodologies (AGS, 2007; Kranitz and Bensi, 2009; Raetzo and Loup, 2009). Furthermore, different MF matrices have also been built up according to the phenomenon and the relevance of each input parameter (e.g. Cardinali et al. 2002; Cardinali et al., 2006; Raetzo et al., 2002; Sterlacchini et al., 2007; Adapt Alp 5.1, 2010; Strozzi et al., 2013). Nevertheless, and despite the high number of studies carried out, the definition of the level of hazard according to magnitude and the frequency has not been solved yet and further discussion is needed.

Landslide hazard can be expressed in qualitative or quantitative terms. Usually, qualitative assessment includes subjective criteria of experts and, therefore, a certain ambiguity in the interpretation of the damage. MF matrices are usually presented in qualitative terms as low, medium, high and very high. However, if frequency and intensity can be quantified, the

different degree of damages can be quantified as well.

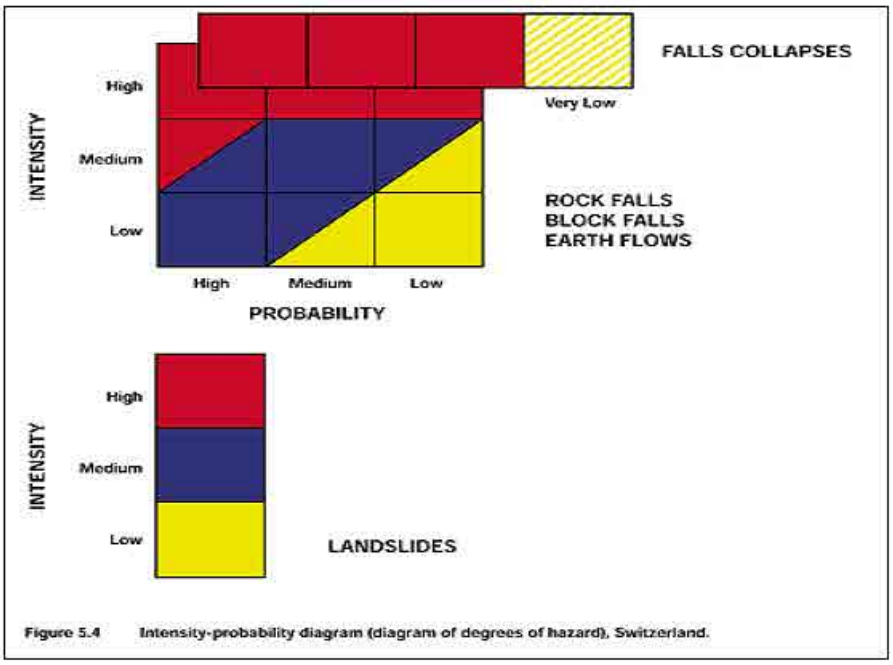

Figure 3-1: Landslide hazard matrix. Modified after Lateltin et al. (2005) (from Strozzi et al., 2013).

Currently, efforts towards quantitative assessment of landslide hazard in terms of probability or annual frequency are performed (e.g. Bell & Glade, 2004; Guzzetti et al., 2005; Jaiswal et al., 2011; Erener & Düzgün 2013; Motamedi & Liang, 2013; Lari et al., 2014; Vranken et al., 2014; Corominas et al., 2014). It allows an objective and comparable definition of the damaging potential.

Guzzetti et al. (2005) used a probabilistic approach to quantify, at the basin scale, the probability of having a landslide of a specific size within a period of time N in a specific location by combining the size, the temporal and the spatial probability as follows:

$$H_L = P_{AL} \times P_N \times S$$

Equation 3-1

in which P_{AL} is the probability of having a landslide of a size A_L, P_N is the probability of occurrence of a landslide within a period of time N, and S is the probability of having a landslide in a given location. It is assumed that the three probabilities are independent.

However, the landslide frequency is a spatially-distributed parameter. As the frequency outside the landslide source area depends on the landslide size (Stark and Hovius, 2001; Van Den Eeckhaut et al., 2007), the quantitative landslide hazard assessment at smaller scales is strongly based on the relations between magnitude and frequency of landslides (Corominas & Moya, 2008).

To this end, MF relations have been widely used in different natural hazards (floods, earthquakes). They describe the frequency of a landslide of a given magnitude.

3.1 Magnitude frequency relations

Landslide MF curves are necessary for the proper understanding and characterization of landslide hazard.
They permit to determine the relationship between landslide size and occurrence, and the frequency when introduced the temporal component (Guthrie & Evans, 2005).
They were taken from seismology since Gutenberg & Richter (1954) was the first to define the number of earthquakes (N) exceeding a given magnitude (M) using the following expression:

$$\log N = A + bM$$

Equation 3-2

in which N is the number of earthquakes with a magnitude higher than M. A and b are parameters that depend on the study area, time interval, etc.
MF relations are usually built up by means of landslide inventories. In the literature, several MF curves have been defined (e.g. Hovius et al., 1997; Guzzetti et al., 2002; Brardinoni & Church, 2004; Van Den Eeckhaut et al., 2007; Brunetti et al., 2009; Stoffel, 2010). Typically, the frequency or the probability of occurrence is given as Cumulative Frequency (CF). It is important to notice that such a frequency (or probability) can be expressed considering the time interval of the occurrences (e.g. annual) or referred to the total number of failures (Stark & Hovius, 2001). The magnitude, as afore mentioned, is given in terms of landslide size (volume or area) (Figure 3-2).
Typically, MF curves are approximated to a power law relation following a log-normal distribution (Anon, 2001; Malamud et al., 2004; Hovius et al., 1997). In many cases, a roll-over effect is produced (Figure 3-2). It is usually related with undersampling of low-magnitude events (Stark & Hovius, 2001; Guzzetti et al., 2002) i.e. some small-sized landslides have not been identified and, consequently, their probability has been underestimated. However, some authors suggest that the roll over is given in too much large occurrences to be considered as data biasing (Pelletier et al., 1997; Turcotte et al., 2002) and some physical reason must be responsible for. To account for the rollover some authors have used a Double Pareto or Inverse Gamma distribution (e.g. Malamud et al., 2004b; Malamud et al., 2004a; Guzzetti et al., 2005).
Restrictions of the MF curves will depend on the data available to build up them, i.e. information about frequency and magnitude of the phenomenon.

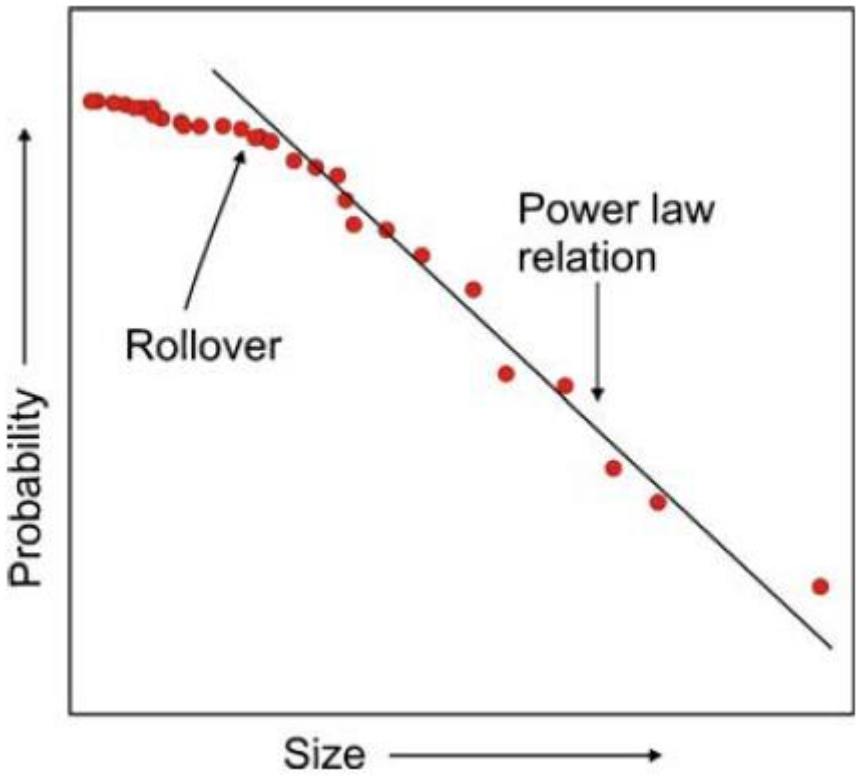

Figure 3-2: Schematic representation of the MF curves (from Guthrie et al., 2008).

3.2 Susceptibility assessment

The landslide susceptibility assessment involves the classification, volume (or area) and the spatial distribution of existing and potential landslides (Cascini, 2008). Several methods exist for the assessment of the susceptibility. According to Corominas et al. (2014), they can be divided in: 1) Knowledge driven methods 2) data driven methods and 3) Physically-based methods. It is also interesting the review done by Guzzetti et al. (2009).

The bases of all these methods are the landslide inventories (e.g. Carrara et al., 1991). They should provide information about type, volume, magnitude, date and location (Martha et al., 2013).

Knowledge driven methods, also known as heuristic methods, are performed mainly by the expert criteria. They can be the result of direct geomorphologic mapping in the field or the result of combining several factors from the terrain properties or lithology into a GIS. The importance of each factor is given by experts. Results can be later combined with frequency in order to obtain the landslide hazard. Comparison of the results with other areas is not possible due to the high degree of subjectivity introduced by the expert criteria. These methods are commonly used when no detailed information is available as well as at small scales where managing detailed data is not straightforward (e.g. Van Westen, 2000; Cardinali et al., 2002; Castellanos Abellan & Van Westen, 2007; Faraji Sabokbar et al. 2014; Günther et al., 2014).

Data driven methods also consider the importance of several factors (from the terrain and material strength) but, in this case, the importance of each factor and its combination is evaluated statistically (e.g. Luzi et al., 2000; Van Westen et al., 2003; Ayalew & Yamagishi, 2005; Greco et al., 2006; Chen & Wang, 2007).

Knowledge and data driven methods assume that conditions for instability are the same that

those responsible for past failures (Westen et al., 2005). It is not always true since when a slope slides, it reaches an equilibrium state which requires different conditions to become unstable again.

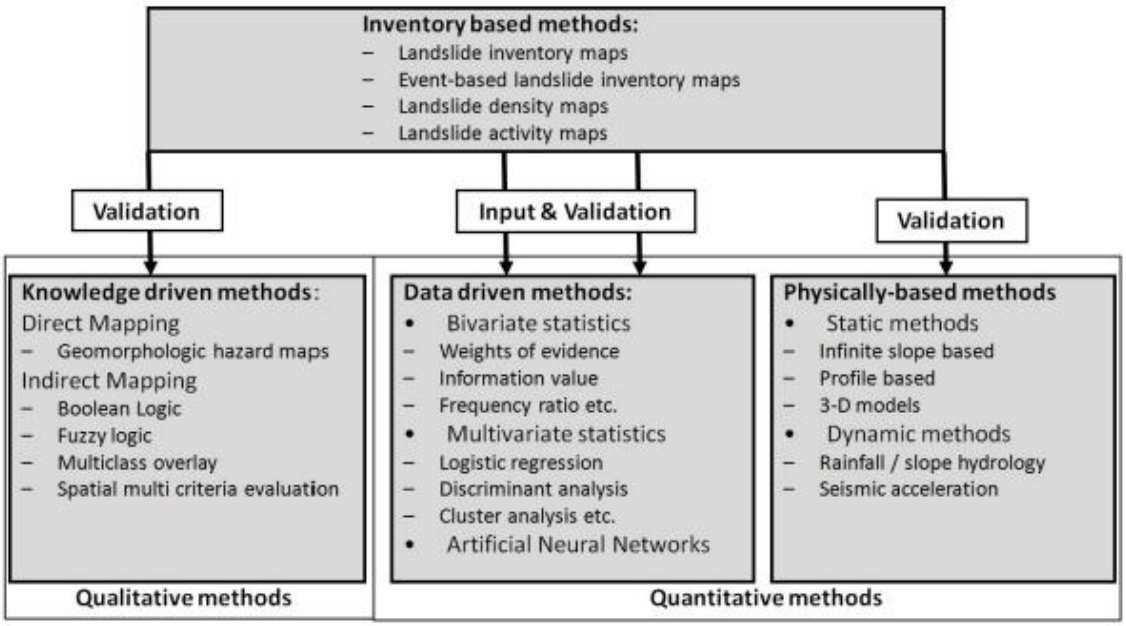

Figure 3-3: Landslide initiation susceptibility assessment methods (Corominas et al., 2014)

Finally, deterministic models, or also known as physically-based methods, are usually used in local and site-specific analyses although they are progressively incorporated to the regional analyses as well. They consist in slope stability models coupled with hydrological models and implemented on Geographical Information System (GIS) (e.g., Pack et al., 2005). The factor of safety (FS) is computed in each grid cell using the infinite slope stability analysis. Topographical properties such as the slope are obtained from a Digital Elevation Model (DEM). Terrain parameters (friction angle and cohesion) are either provided by the laboratory tests or estimated. Due to the uncertainties of the input values, some authors have introduced statistical techniques such as Montecarlo simulation or First-order second-moment (FOSM) to account for these uncertainties (formal probability and reliability analyses). Therefore, the FS is calculated as the probability of failure i.e. the probability of being less than 1 (e.g.: Frattini et al., 2004; Dahal & Hasegawa, 2008; Tarolli et al., 2011; Fuchs et al., 2014; Mergili et al., 2014).

3.3 Frequency assessment

When working with landslides, the frequency between first-time slope failures and the reactivated ones must be differentiated. Both situations are completely different. On the one hand, reactivated landslides have reached an apparent more stable state with gentle slopes and residual geomechanical properties. On the other hand, intact slopes mobilize peak strength conditions and produce steeper slope angles.

According to Corominas and Moya (2008), two approaches exist to assess the probability of occurrence of landsliding: A) The analysis of potential for slope failures, which considers the instability of slopes and the existing landslides and B) the statistical treatment of the past landslide events.

The analysis of future slope failures can be calculated by means of: 1) event tree methods, 2) slope stability analysis and numerical modelling and 3) formal probability and reliability

analysis.
Logistic tree methods describe the set of decisions necessary to predict an outcome. The outcome probability is the product of the probabilities (Pradhan, 2013) of each decision (e.g., Annaka et al. 2007; Kong, 2002). The physically-based models can be also used as a tool for assessing the landslide probability by linking the FS with the frequency of a given triggering factor (e.g. Haneberg, 2004; Wu and Abdel-Latif, 2000; Luzi et al. 2000 and Haneberg, 2006). Finally, the formal probability and reliability analysis consider the probability of the FS being less than 1.
The statistical treatment of past events can be performed by: 1) analysing the frequency of past landslide events or 2) determining the frequency of the triggering factors of past occurrences.
Frequency of past events can be analysed by using records of past landslide events from which, the failure date is known or it has been deduced from aerial photographs among others (Guzzetti et al. 1999; Guzzetti et al. 2005) or by calculating the recurrence interval of the triggering event (rainfall or earthquake) (e.g: Jaiswal and van Westen, 2009; Ko Ko et al. 2004; Finlay et al., 1997).
The frequency can be expressed as absolute or relative (Corominas & Moya, 2008), i.e., expressing the number of events in a given terrain unit or normalized to the unit area (m^2) or length (m), respectively. The frequency can also consider the temporal factor (Nº events/year or Nº events/year/km^2). In such a case, the frequency can be turned into probability using either the Poisson (Equation 3-3) or the Binomial Model (Equation 3-4) (Crovelli, 2000). Thus, the probability of having one or more landslides (or triggering events) within a specified period of time t can be calculated by:

Poisson Model

$$P\{N(t) \geq 1\} = 1 - e^{\frac{-t}{\mu}}$$

Equation 3-3

in which μ is the mean recurrence interval between successive failures or triggering events.

Binomial Model

$$P\{N(t) \geq 1\} = 1 - (1-p)^t = 1 - (1 - \frac{1}{\mu})^t$$

Equation 3-4

in which μ is the mean recurrence interval between successive failures or triggering events and p is the estimated probability of having an event in time t.

Concerning the Poisson Model, it is assumed that (Crovelli, 2000): a) The number of events which occur in disjoint time intervals are independent, b) the probability of an event occurring in a very short time is proportional to the length of the time interval c) the probability of more than one event occurring in a short time is negligible d) The probability distribution of the events remains the same for all time intervals of a fixed length and e) the mean recurrence of events will remain the same in the future as it was observed in the past.
Assumptions made in the Binomial model are: a) There are t independent trials, b) each trial results in a success (landslide) or a "failure" (no landslides), c) the probability of success p

remains the same from trial to trial and d) the mean recurrence of events will remain the same in the future as it was observed in the past.
Crovelli (2000) demonstrated that the Binomial Model is an approximation of the Poisson Model. The Binomial Model overestimates exceedance probabilities for short mean recurrence intervals (a few years) and short periods of time.

As mentioned in chapter 2, earthflows are a predominant landslide type in our study area and their hazard assessment is one of the goals of this work.

3.4 Earthflow hazard assessment: Examples

Ancient (and well known) earthflows have contributed significantly to the damage produced by landslides. Therefore, an important hazard management tool is a proper mapping (Bertolini & Pizziolo, 2008) and characterization of these movements. To this end, several works are found in the literature. For instance, a Landslide Inventory Map (LIM) was carried out by the Emilia-Romagna region (Pizziolo, 1996) which is being constantly updated. It has been considered when future activities on landslides have been planed such as urban management (Bertolini and Pizziolo, 2008).
Cardinali et al. (2002) proposed a method to evaluate the hazard and risk of earthflows (among others) in Umbria (Central Italy). It is based on the identification of existent past landslides, on the inspection of the geological and morphological factors and on the study of historical information of past landslides. They agree that one of the most valuable information source to determine the landslide hazard is the multi-temporal landslide inventory map.
It is also really interesting the review about landslide hazard and risk assessment strategies for earthflows, occurred in Emilia-Romagna Region (Italy), carried out by Bertolini et al. (2005). He concluded that one of the most effective tools for hazard and risk reduction consists in sharing the knowledge about landslides through dissemination of maps and inventories.
Revellino et al. (2010) studied the earthflows in Benevento province (Southern Italy) were several landslides affect settled areas as well as road networks. They mapped several landslides and identified the lithologies prone to failure. The spatial evolution of the earthflows was mainly controlled by the lithology and the structure which should be considered for future failures. On the other hand, reactivations were related with earthquakes and heavy and long rainfall periods.
When dealing with the earthflow hazard assessment at site-specific scale, the landslide monitoring is a key issue for the landslide temporal and spatial investigation. Malet (2002) monitored the Super-Sauze earthflow located in Alpes-de-Haute-Provence, France by means of GPS and conventional methods such as geodetic methods or wire extensometer. The relationship between the groundwater level, rainfall and landslide movements allowed them to understand the behaviour of the flow and determine pore water pressure initiation threshold.
Delong et al. (2012) inspected an active earthflow in 2003 and 2007 by means of airborne laser swath mapping (ALSM) in California in order to detect landscape changes. Furthermore, by dating the sediments using the cosmogenic nuclide ^{10}Be, they obtained earthflow velocities ranging from 0.5 to 5 m/yr.
Petley et al. (2005) also used the typical tools to measure displacements and water pressures (inclinometers, extensometers and piezometers), on an earthflow located in the NE Italy, combined with Electronic Distance Measurement (EDM) which measure the position of several reflectors located on the landslides in time intervals of 6 h. They concluded that it was composed of 4 different types of movement differentiated themselves by the different pore

pressure conditions. They also suggested that the movement starts at the toe of the landslides, retrograding upslope.

3.5 Objective

As it has been shown in the previous sections, earthflows are one of the most common and damaging phenomenon in mountainous areas. Due to their dimensions and complex behaviour, they are often analysed individually. Notwithstanding, a first landslide hazard assessment at smaller scales is necessary as a first approximation for further detailed studies, if required. Although most of occurrences are reactivations of ancient earthflows, new failures should be predicted as well. Thus, a distinction between first-time slope failures and landslide reactivations has been made as the procedure to prepare susceptibility and hazard maps for first-time slope failures and reactivations cannot be the same. As mentioned before, intact slopes mobilize peak strength conditions and produce steeper slope angles. Conversely, reactivated landslides have reached an apparent more stable state with gentle slopes and residual geomechanical properties leading to different morphometric parameters. Additionally, neither the frequency nor the magnitude may be calculated similarly: reactivations have suffered several failures and their frequency may be calculated from those past instabilities, whereas in intact slopes, information about past events is not available and other procedures must be followed.
Regarding the magnitude, it can be determined using the area of the reactivations. For the fist-time slope failures it may be calculated as the area prone to failure. Therefore, it is necessary to evaluate the susceptibility of the study area using methods such as deterministic models, among others.
The objective of this work is to evaluate the magnitude and frequency of earthflows at a large scale for a local hazard zoning (Cascini, 2008). In this chapter, the methodology to evaluate the MCF of reactivations is shown. Concerning the first-time slope failures, which have been treated in chapter 5, a brief introduction is given in the next sections.
To this end, a first data collection has been made by means of: a) cartographic sources such as topographic maps, aerial photographs, etc; b) lithological, morphological and landslide mapping (first-time slope failures and reactivations) and c) activity indicators, morphological features and other characteristics

3.6 Data collection

3.6.1 Cartographic sources

In Table 3-1, summarizes the information gathered to carry out the landslide and lithological mapping. Most of it has been obtained from the Geological Survey of Catalonia (ICGC, 2015) as well as by several field campaigns performed by Georisc S. L. (2009) and the author of this thesis. Geological map has been obtained form the Geological Survey of Catalonia (ICGC, 2015) and it contains the main lithostratigraphic units present in the study area. They have been widely described in chapter 2.
In the lithological map there are represented the units obtained from the reclassification of the geological map. It is explained in more detail in the next sections.

Table 3-1: Characteristics of the gathered information.

Documentation	Format	Year	Scale	Pixel Resolution	Source
Topographic map	Paper/Digital	2010	1:5,000	-	(ICGC, 2015)
Aerial photographs					
1957	Paper	1957	1:33,000	-	(ICGC, 2015)
1975	Paper	1975	1:18,000	-	(ICGC, 2015)
1987	Paper	1987	1:22,000	-	(ICGC, 2015)
Ortophoto					
1956	Digital	1956	1:5,000	50cm	(ICGC, 2015)
1990	Digital	1990	1:25,000	50cm	(ICGC, 2015)
1993	Digital	1993	1:25,000	50cm	(ICGC, 2015)
1997	Digital	1997	1:5,000	50cm	(ICGC, 2015)
2003	Digital	2003	1:5,000	50cm	(ICGC, 2015)
2005	Digital	2005	1:5,000	50cm	(ICGC, 2015)
2007	Digital	2007	1:5,000	50cm	(ICGC, 2015)
2008	Digital	2008	1:5,000	50cm	(ICGC, 2015)
2009	Digital	2009	1:5,000	50cm	(ICGC, 2015)
2011	Digital	2011	1:5,000	50cm	(ICGC, 2015)
2013	Digital	2013	1:5,000	50cm	(ICGC, 2015)
Geological map	Digital	After 1990	1:50,000	-	(ICGC, 2015)
Digital elevation model	Digital	-	-	5m/pixel	(ICGC, 2015)
Lithological map	Paper/Digital	2009/2013	1:5,000	-	(Georisc S. L., 2009) & and field trips performed by the author of this thesis
Landslide map	Paper/Digital	2009/2013	1:5,000	-	(Georisc S. L., 2009) & and field trips performed by the author of this thesis

3.6.2 Geomechanical properties of the Garumnian Clay

Most of the landslides given in the study are located within the Garumnian Clays, thus several studies conducted at the UPC, in the Geomechanical Laboratory, were revised to obtain the geomechanical properties of the Garumnian Clay (Table 3-2).

The studies of Forné (2004), Canales (2011), Montero (2011) and Oliveras (2011) were conducted within the Tremp basin. The soil is classified as low plasticity clay (CL) with low liquid limit (w_L=31.65-41.75%) and plastic index (PI=13.85-18.42%). Calculated void ratios (0.27-0.28) are low. They low clay content (<1%) agrees with the low plasticity having a silty clay. A wide range of residual friction angles was calculated (9.1-16º) as well as a wide range of peak friction angles (16-20º).

Concerning the study of Pinyol et al. (2012), it was conducted 20 km far from the Tremp Basin, but within the Garumnian Clays. The soil is classified as high plasticity clay (CH). It agrees with the high content of clay fraction (40%). Calculated void ratios (0.68-0.96) are high, probably due to the decompression and weathering of the outcrops of the Garumnian clay

(Pinyol et al., 2012). The tested samples show higher liquid limit (w_L= 54-57%) and plastic index (PI= 26-31%) compared with the afore-mentioned works. They calculated friction angle was 10-12º.

Table 3-2: Geomechanical properties of the Garumian Clay obtained from several studies conducted at the UPC. Samples were tested in the Geothecnical Laboratory of UPC.

Author	**Geomechanical properties**									
	Natural density [KN/m^3]	Water content [%]	Void ratio (e)	Clay content [%]	Liquid limit (w_L) [%]	Plastic Index (PI) [%]	Soil classification	Cohesion [kPa]	Peak friction angle [º]	Residual friction angle [º]
(Forné, 2004)	18	-	-	<1	41.75	18.42	CL	-	16-20	16
(Canales, 2011): sample 1	22.5-22.6	-	0.27-0.28	<1	38.51-39.57	15.6-16.7	CL	58	25.5	9.1
(Montero, 2011)	21.56	-	-	-	31.65	13.85	CL	-	-	15.6
(Oliveras, 2011)	22.96	-	-	-	35.94	13.93	CL	-	-	9.1
(Pinyol et al., 2012)	17.1-8.8	40	0.68-0.96	40	54-57	26-31	CH	-	-	10-12

3.6.3 Lithological, morphological and landslide mapping

The aim of this section is to obtain a reliable base map, from which, further analysis can be performed for a proper hazard assessment. Such a map must contain complete information about lithologies representative for the hazard analysis, landslides and activity indicators.
A first lithological, morphological and landslide mapping with activity indicators and other characteristics, related with landslides, has been performed through several field campaigns, revision of previous studies (Georisc S. L. 2009), geological information and aerial photointerpretation (ICGC, 2015) which covered a period of 57 years (from 1956 to 2013).

Six lithological units have been defined as the basis for the landslide hazard assessment (Table 3-3). They have been grouped according to the geological map (ICGC, 2015) and from the geomechanical point of view, according to the field campaigns carried out by Georisc S. L. (2009) and the author of this thesis. Materials that show the same prone to landsliding have been merged: 6 lithological classes have been obtained. A total of 119 landslides have been identified.

Table 3-3: Lithological units defined as the basis for the landslide hazard assessment. Simplified lithology used in the field campaigns.

Unit code	1	2	3	4	5	6
Name	Hard rock	Interbedded weak and hard rocks	Weak rock	Coarse colluvium	Fine colluvium	Slide material
Lithology (simplified)	Limestone, conglomerate and massive sandstones	Sandstones, limestones, conglomerates and lutites	Lutites, marls and sandstones	Granular colluvium with clayey and silty matrix	Fine colluvium with clayey and silty matrix	Fine colluvium with clayey and silty matrix

1) Hard rock:

Figure 3-4: Sandstones, calcarenites and conglomerates (Photo: Guillem Domènech).

This unit is located at the southern part of the Barcedana Valley (The Montsec north face). It is mainly composed of well cemented conglomerates and competent sandstones and limestones. During the field campaigns some large rockfalls have been advised within this unit. Presence of lutites and clayey material from Garumnian and bedding with dips about 45º may be responsible for such instabilities.

2) Interbedded weak and hard rocks:

Figure 3-5: Limestones with alveolines (Photo: Guillem Domènech).

Located at the northern of Barcedana Valley. They consist of competent limestones with alveolines (Figure 3-5) and well cemented conglomerates with interbedded sandstones and lutites. In some parts of the valley, they are quite fractured and generate rockfalls. The village of Llimiana has been built up on this unit.

3) Weak rock:

Figure 3-6: Sandstones from the Upper Red Garumnian (Photo: Guillem Domènech).

It is located in the central part of Barcedana Valley. It is mostly present in the quasi vertical gully walls. It is mostly composed of fine sand and silt size particles. Feldspar grains can be observed. In some parts of the study area it can be found as competent sandstones (Figure 3-6, small photo). In other parts of the valley, it appears as a less competent material which in some cases, it can be manually broken up. However, in both cases, when it gets wet, its geomechanical properties change completely due to their low liquid limit, plasticity index and void ratio (Table 3-2) and it becomes a high susceptible material to failure. This change may be due to their silty matrix.

4) Coarse colluvium

Figure 3-7: Coarse colluvium. Clast supported with clayey, silty and sandy matrix from Garumnian (Photo: Guillem Domènech).

It is located in the central part of the Barcedana Valley. It is mostly made of angular clasts (centimetre and decimetre in size) in a silty matrix. It is well gradated and shows a chaotic internal structure.

5) Fine colluvium

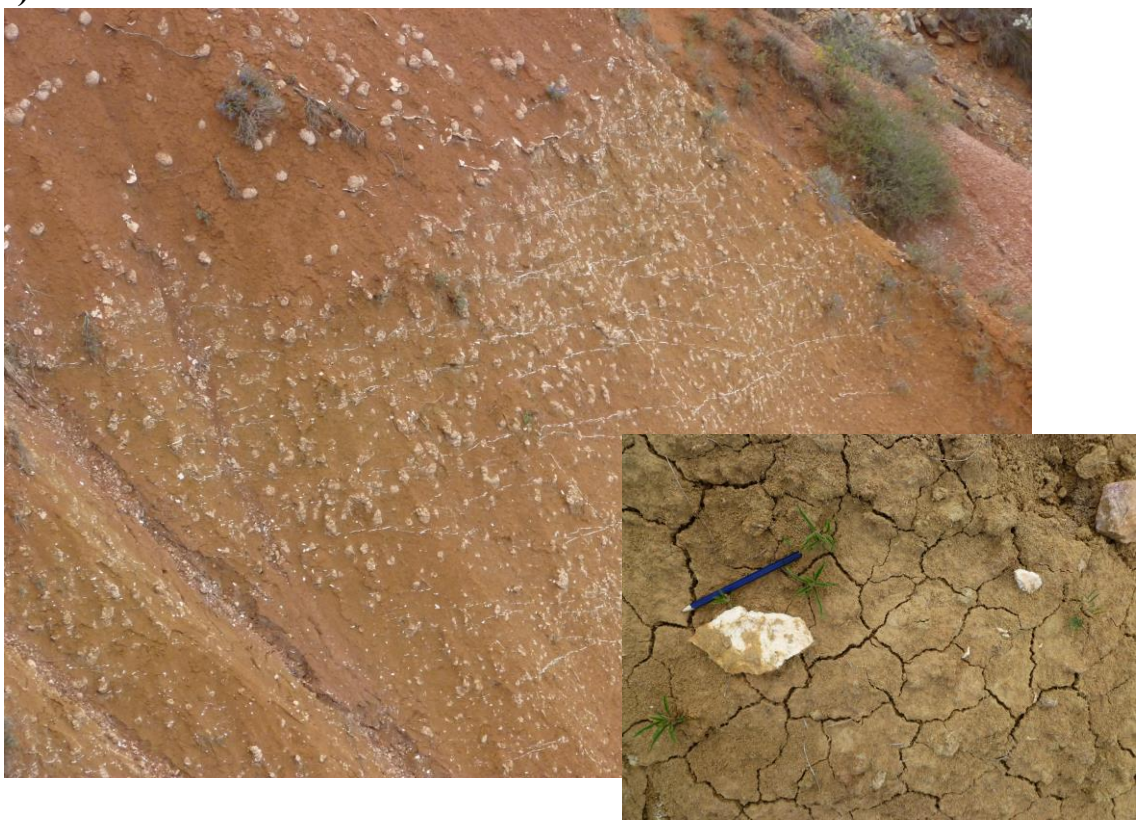

Figure 3-8: Fine colluvium from the Upper Red Garumnian with gypsum (Photo: Guillem Domènech).

It is the most extended and problematic material from the Barcedana Valley. It is low plasticity silty clay. It is responsible of a high number of instabilities. In many cases evaporites such as gypsum and anhydrite from materials of the Upper Red Garumnian are present.

6) Slide material

Figure 3-9: Slide material. Fine colluvium from the Upper Red Garumnian (Photo: Guillem Domènech).

This material is the result of instability processes (earthflows, translational slides) and therefore, it should present different properties compared with the previous ones. It is mainly composed of clayey and silty materials from Garumnian facies as well as clasts of several sizes (from centimetre to decimetre size). It is low plasticity (CL) silty clay (<1% clay content) with low liquid limit (w_L=31.65-41.75%) and low plasticity index (PI=13.85-18.42%) (Table 3-2) being able to flow, in presence of water, within very gentle slopes. It shows low residual friction angles ranging from 9 to 16º.
This material is located in the central part of the Barcedana Valley.

3.6.4 Activity indicators, morphological features and other characteristics

Several morphological features as well as activity indicators and other characteristics related to landslides have been mapped in Barcedana Valley (Table 3-4).

Table 3-4: Morphological features, activity indicators and other features mapped in Barcedana Valley

Morphological features	Activity indicators	Other features
Boulder impact marks	Disturbed trees	Fluvio-torrential erosion
Movement direction	Disturbed bedding	Blocks bigger than 100 m^3
Landslide lobe	Terrain cracks	Slopes with swollen and remoulded material
Metric scar height	Structure with slight pathologies	Discontinuity between landslides
Decametric scar height	Structure with severe pathologies	Water presence
Scar bottom	Fallen trees	Blocks from 1-10 m^3
Translational platform	Trees with impact injuries	Blocks from 10-100 m^3
Huge rock mass detached from the bedrock by means of open cracks	Intact bedding	

3.7 Methodology for the obtaining of the magnitude and frequency of reactivations

Two different procedures have been followed. The first one, which is later detailed, consists in the obtaining of the MCF of reactivations mapped in the Barcedana Valley. On the other hand, the annual temporal probability of four large-rainfall-triggered landslides, located also in the Tremp Basin, has been calculated using ROC curves. An average threshold for large landslides has been defined for that area. In that case a brief explanation about the methodology and the results can be found in the next sections. However, more details are shown in the chapter 4 of this thesis.

3.7.1 Magnitude and frequency of landslide reactivations

Landslides have been mapped using the work carried out by Georisc S. L. (2009), several field campaigns carried out by the author of this thesis and orthophoto observation (11 sets, Table 3-1). These orthophotos were used directly from the Catalan Geological Survey (ICGC) website (ICGC, 2015).

Each landslide as well as any reactivation have been identified in the different set of orthophotos. Thus, the frequency of reactivation has been calculated by dividing the total number or reactivations over the time period covered by the orthophotos. Orthophotos were also used for the later treatment of the two phenomena.

The frequency has been computed by analysing a set of aerial photographs. A reactivation has been considered between one or more sets of the available orthophotos if the landslide exhibited morphological changes and/or changes in the road, present in the study area, were observed.

The area of the several mapped landslides has been use as an approximation of their magnitude.

Finally, the magnitude-cumulative frequency relationship for landslide reactivations has been calculated.

3.7.2 Determination of rainfall thresholds to reactivate large landslides by means of ROC curves

A method to determine the possible dates of reactivations of 4 large rainfall-triggered landslides and the establishment of a rainfall threshold, within the Tremp Basin (Spain), has been proposed. Then, the temporal probability of reactivation has been computed.

Some thresholds have been analysed considering several accumulated rainfall and different intensity-duration relationships. Threshold performance has been evaluated by means of ROC analysis (Receiver Operating Characteristics) (Fawcett, 2006) that permit to classify them. Finally, the temporal probability is estimated combining the probability of the threshold being exceeded and the probability of landslide initiation given that the threshold is exceeded.

First of all, mapping of landslides and their units as well as the tree-ring analysis have been prepared from different studies conducted in the Tremp Basin (eastern Pyrenees).

Selected landslides have areas ranging from 6,020 to 800,000 m^2. They have been analysed with dendrochronology (Figure 4-16) which permits dating, within one year (dendrological), anomalies in the tree rings caused by landslides. It has been considered that a reactivation has occurred if three or more trees on the landslide show anomalies in their rings. To this, 12 years with reactivations have been calculated.

The main handicap when working with this technique is that a direct relationship with triggering events cannot be established.

Secondly, rainfall data were provided by the AEMET (Spanish meteorological Office). There are five gauges located between 1.5 and 17.5 km away from the sampled landslides (Figure 4-18) (Table 4-2). The identification of possible combinations of rainfall that could justify the occurrence of failures in the past has been made. As above mentioned, dendrogeomorphological results do not provide a specific date about landslide events. Furthermore, years with no dendrological response do not imply lack of failure or reactivation because trees might have not been affected. Thus, two types of approaches have been used: a) accumulated precipitation within a given period of time (accumulated rainfall) and b) accumulated rainfall followed by a minimum-daily-triggering precipitation (antecedent rainfall).

A great variability of thresholds have been defined in order to understand which is the best combination explaining the failures; from short periods with relatively intense events, to long periods with more gentle precipitations.

A receiver operating characteristics (ROC) analysis (Fawcett, 2006) has been conducted to evaluate the performance and reliability of different thresholds and decide which is the best that explain the failures. It uses the true positive (tp) rate or also called hit rate and the false positive (fp) rate, also called false alarm rate. Both rates are plot in a ROC graph which depicts relative tradeoffs between benefits (tp) i.e. hit rate and costs (fp) i.e. false alarm rate.

Finally, the average temporal probability of the whole Tremp basin has been evaluated considering the probability that a threshold will be exceeded and considering the probability that a landslide occurs given the exceedance. Both probabilities have been obtained using the Poison model. More details about the followed methodology can be found in chapter 4.

3.8 Magnitude and frequency of first-time slope failures

The analysis of the occurrence of first-time slope failures has been obtained by means of a slope stability model implemented on a GIS platform. A methodology has been developed to calculate the size of the potential failure when it is larger than the grid cell size.

The frequency has been calculated by linking the Stability Index (SI) (obtained with the slope stability model) and the occurrence of first-time failures in the last 50 years identified by means of aerial photointerpretation. Finally, the landslide hazard map has been obtained considering

the MF-matrix.
More details about the methodology can be found in chapter 5

3.9 Results and discussion

A total of 109 landslides (fist-time failures and reactivations) were identified. They have an area ranging from 380 m^2 to 911,900 m^2 (Figure 3-10). Usually, smaller reactivations occur in steep slopes of fine colluvium (lithological unit 5) and/or weak rocks (lithological unit 3) and larger reactivations take place in more gentle slopes within fine and coarse colluvium deposits (lithological units 5 and 4 respectively). Such large landslides are typically located at the eastern part of the Barcedana Valley. They present activity indicators such as fallen as well as disturbed trees but their limits are not easily distinguishable.
More information about mapped landslides can be found in Annex 1: Landslide characteristics.

Figure 3-10: Range of landslide size. From a few hundreds of m^2 (left) to thousands of m^2 (right)

3.9.1 Landslide reactivations

A total of 92 landslides over 109 have been identified as reactivations. It represents the 84.4% of the total. It seems to be a reasonable ratio considering that, usually, earthflow occurrences are related to reactivations of ancient slides (Prokešová et al., 2014). From the 92 failures, in 4 large earthflows any reactivation has been identified by means of the orthophotos although activity indicators and their large area suggest that they belong to ancient slides. Hence, a total of 88 earthflows (80.73%) have been used.
In Figure 3-11, the Magnitude-Cumulative Frequency (MCF) of reactivations is shown. The landslide areas range from 380 m^2 416,700 m^2, with a roll over effect around 600 m^2. Observing the MCF curve, a maximum frequency of 3 reactivations per year and a minim frequency of 1 reactivation each 14.5 years have been found.
The distribution is well fitted by an inverse power law with an exponent of -0.543. If comparing it with the values found in the literature (Table 3-6), it appears that in Barcedana Valley, the distribution presents a smaller exponent. This fact can be due to the lack of small size landslide reactivations or the presence of a great number of large size reactivations.

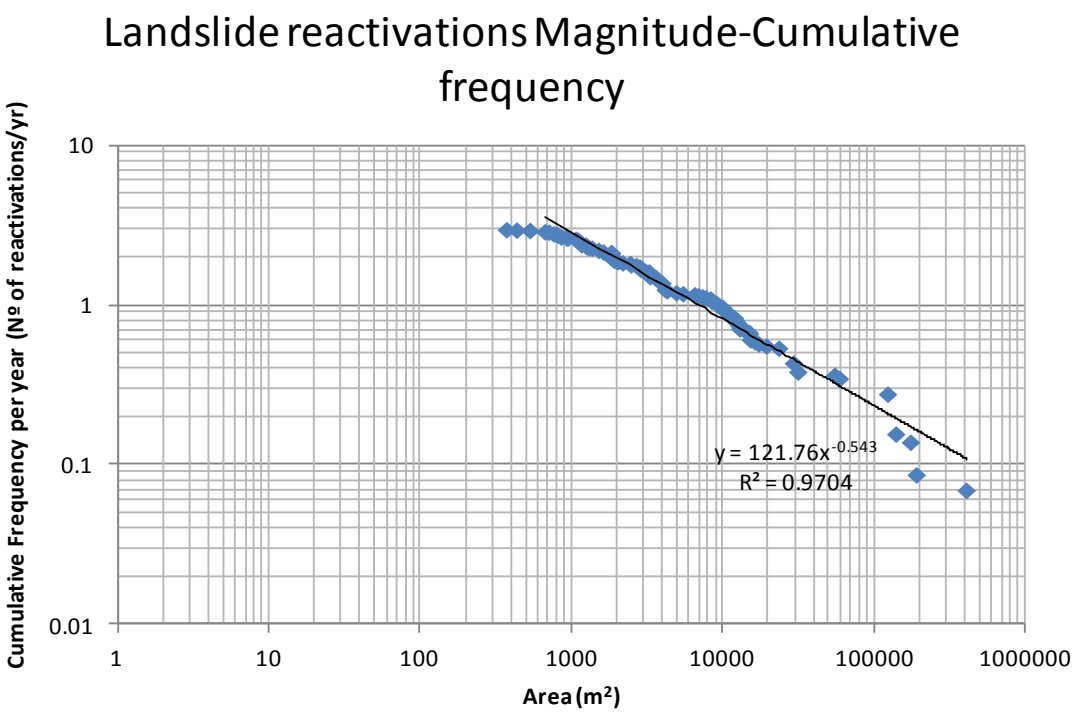

Figure 3-11: MCF for landslide reactivations.

In the dendrological analysis performed to 4 large landslides and their subunits of the Tremp Basin (chapter 4), the temporal probability of reactivation has been of 0.66. Considering that they have and area equal or greater than 6,020 m^2 (subunit 3 of Les Pales landslide) and using the afore-mentioned MCF curve for landslide reactivations (Figure 3-11), the number of expected reactivations per year is 1.08. Using the Poison model (Equation 3-3), the annual probability of having one or more landslides equal or greater than 6,020 m^2 is 0.66 (Table 3-5). This is the same probability of reactivation calculated for large landslide in chapter 4.

Table 3-5: Annual temporal probability of reactivations for landslides larger than 6,020 m^2

Landslide size (m^2)	Annual frequency (1/μ)	AEP according to the Poisson Model $[P\{N(t) \geq 1\} = 1 - e^{\frac{-t}{\mu}}]$
> 6,020	1.08	0.66

Table 3-6: Characteristics of landslide volume distributions taken from Van Den Eeckhaut et al. (2007). N: Number of landslides; b: Exponent.

Author	Site	Type of inventory	Distribution features	N	b
Pelletier et al. (1997)	Akaishi Ranges (central Japan)	Historical	Cumulative frequency distribution of landslide areas	3,424	2-3
Pelletier et al. (1997)	Eastern Cordillera (Bolivia)	Historical	Cumulative frequency distribution of landslide areas	-	1.6-2; 2.6-3
Fuji (1969 in Guzzetti et al., 2002)	Japan	Event (heavy rainfall)	Cumulative frequency distribution of landslide scar areas	800	0.96-1.6
Hovius et al. (1997)	Southern Alps (New Zealand)	Historical (<60 year old)	Annual cumulative frequency distribution of landslide scar areas	4,984	1.16-2.16
Pelletier et al. (1997)	Northridge (California, USA)	Earthquake	Cumulative frequency distribution of landslide areas	>11,000	1.6-2.6
Hovius et al. (2000)	Ma-an and Wan-li catchment (Taiwan)	Historical (<10 year old)	Annual cumulative frequency distribution of landslide scar areas	1,040	0.7-1.7

3.10 Conclusions

The following conclusions have been determined from several field observations:

-Sometimes, the distinction between coarse (unit 4) and fine (unit 5) colluvium is not easy. Some deposits may look like a granular colluvium (unit 4) due to their high content in clasts and coarse material. Nevertheless, the clayey and silty matrix may lead to poor geotechnical properties (Table 3-2) being necessary to classify this material as fine colluvium.
-Most of the colluvium (5) is part of eroded weak rock materials (3) of the Upper Red Garumnian Facies (PPlg). Therefore, in some cases, the contact between both materials is not clear and thus, the cartography between both materials is not obvious.
-Distinction between intact fine colluvium and remoulded material belonging to a landslide is not trivial due to very old movements difficult to identify as well as more recent failures that have been masked due to anthropic actions, mostly in crops.
-Materials from the Upper Red Garumnian (PPlg) show high plasticity (CH, Lambe & Whitman, 1979). It agrees with the study conducted by Pinyol et al. (2012). However, within the Tremp Basin, the outcropping materials are low plasticity silty clays (clay content<1%) and low values of void ratios (0.27-0.28) as well as liquid limit (w_L= 31.65-41.75%) and plasticity index (PI= 13.85-18.42%) Consequently, in presence of water, their behaviour change completely being able to flow in very gentle (Table 3-2) slopes.
-The presence of Upper Red Garumnian materials within the matrix of the sandstones and the paleosoils of the weak rocks (unit 3), as well as within the matrix of the granular colluvium (unit 4), leads to a high reduction of the material strength turning into a flow in presence of water due to the low plasticity index and the low void ratio.
-Regarding the geological classification (ICGC, 2015), most of the failures occur in the Upper Red Garumnian (PPlg) materials, colluvial deposits (Qco) and Lower Red Garumnian (KMlg) materials.

The following conclusions have been determined from the analysis of the landslide inventory and the orthophotos:

-Most of the earthflows identified in the Barcedana Valley have been classified as reactivations (92 over 109) what is in good agreement with other published works (Prokešová et al., 2014). The other earthflows have been considered first-time slope failures.
-Landslide areas range from 380 m^2 416,700 m^2, with a roll over effect around 600 m^2. Frequencies ranging from 3 reactivations per year to 1 reactivation each 14.5 years have been determined.
-MCF distribution has found to be well fitted by an inverse power law with an exponent equal to -0.543. It is a small value compared with the literature. It can be as a consequence of the lack of small size reactivations or the presence of a great number of large size reactivations in the Barcedana Valley.

The following conclusions have been determined by comparing the results obtained from the field inventory and orthophoto observation, and the dendrogeomorphological analysis:

-The annual exceedance probability of having one or more reactivations, calculated from the dendrogeomorphological analysis, for failures greater or equal than 6,020 m^2 (area of Les Pales landslide) is 0.66.
-The annual probability of having one or more reactivations for failures greater or equal than

6,020 m^2, using the MCF curve obtained from the landslide inventory and the orthophotos analysis and the Poisson model, is 0.66.

-Even the lack of data in both analyses (by means of dendrogeomorphological and by orthophotos), the probability of occurrence following two different approaches is the same. It leads to think that it may be a reliable probability for the Tremp Basin.

Chapter 4

4 Determination of rainfall thresholds to reactivate large landslides by means of ROC points

4.1 Introduction

Rainfall is a well known landslide triggering factor that contributes to the build up of water pressures into the ground (Campbell, 1975; Wilson, 1989) and reduction of its effective stress thus reducing the soil strength and, eventually, its failure. Groundwater conditions responsible for slope failures are related to rainfall through infiltration, soil characteristics, moisture content, and rainfall history (Wieczorek, 1996). A proper understanding of this phenomenon is necessary to predict the rainfall induced landslides.

The influence of rainfall on landslides differs substantially depending upon landslide mechanism, dimensions, kinematics, material involved, etc (Aleotti, 2004). Shallow failures are usually triggered by short intense storms (Corominas & Moya 1999; Guzzetti et al. 1992) while most deep-seated landslides are affected by long-term variation of annual rainfall which has to last several years (Bonnard and Noverraz, 2001). A threshold is the minimum or maximum level of some quantity needed for a process to take place or a state to change (White et al., 1996). A minimum threshold defines the lowest level below which a process does not occur. A maximum threshold represents the level above which a process always occurs. For rainfall-induced landslides, a threshold may define the rainfall, soil moisture, or hydrological conditions that when reached or exceeded, are likely to trigger landslides (F. Guzzetti et al., 2008). Prediction of rainfall-induced landslides in many areas has been difficult due to lack of monitoring and availability of reliable data (Sengupta et al., 2010). In such cases, the hillslope hydrological processes have to be studied in detail to reveal and explain the mechanisms that cause or reactivate landslides during rainfall (Wilson and Wieczorek, 1995). Rainfall intensity (I) and duration (D) relations are the most common type of thresholds proposed in the literature. Rainfall intensity (I) is the amount of precipitation accumulated in a period of time or the rate of precipitation in a period, most commonly measured in millimetres per hour. Caine (1980) was the first who introduced the parameter using a database of debris flow slope failures. Other thresholds were proposed by Cannon & Gartner (2005) who worked with debris flow or by Jakob & Weatherly (2003) who wanted to establish a regional threshold for shallow landslides and debris flow that could be easily implemented by the Greater Vancouver Regional District (GVRD). Some authors (Cannon and Ellen, 1985; Jibson, 1989; Wieczorek et al., 2000) refine this approach by normalizing the intensity value with the mean annual rainfall (MAP). It permits to emphasize the regionalization of the thresholds, since the calculation takes into account the climatic regimes of the study area (Aleotti, 2004). Moreover, thresholds based on the daily rainfall (R) (Campbell, 1975), rainfall event (E)-duration (D) thresholds (Cannon and Ellen, 1985), and rainfall event (E)- intensity (I) thresholds (Jibson, 1989) have also been utilised to predict rainfall-induced landslides (Sengupta et al., 2010). Local authorities can use these critical rainfall amounts to develop landslide early warning systems to implement

evacuation procedures (or improve if they already exist) (Hansen et al., 1995) while geotechnical engineers can use them in the design of man-made slopes (Anderson et al., 1987).
Two types of landslide-triggering rainfall thresholds can be established: A) Physical thresholds which are calculated by means of process-based models. They couple hydrological and stability models which compute the factor of safety for simple failure mechanisms from different infiltration scenarios (e.g. Godt et al., 2008; Iverson, 2000). The most important limitation of this models are the detailed spatial information required on hydrological, lithological, morphological and soil characteristics that control the initiation of landslides (Guzzetti et al., 2007). Various approaches have been proposed to obtain physical thresholds (Rahardjo et al., 2001). B) Empirically rainfall thresholds are based on the study of rainfall events that has produced landslides in the past. These thresholds not only take into account the event rainfall, but the antecedent conditions. As it has been said before, a short intense rainfall is usually needed to trigger shallow landslides. On the other hand, the occurrence of deep-seated landslides or failure of impervious materials needs long-lasting and continuous rainfalls (days, weeks or months).

4.2 Empirical rainfall-triggering thresholds

Triggering thresholds separate combinations of daily and antecedent rainfall or of rainfall intensity and duration that triggered landslides from those combinations that failed to trigger landslides (Terlien, 1998). The influence of antecedent rainfall is difficult to quantify as it depends on several factors, including the heterogeneity of soils (strength and permeability properties) and the regional climate (Aleotti, 2004). Landslides in slope covered with coarse colluvium having large interparticle voids, debris flows or previous soils due to the presence of preferential groundwater passageways (macropores, animal burrows, root channels) can occur without significant antecedent rainfall (Corominas and Moya, 1999; Corominas, 2000). On the contrary, in low-permeability soils antecedent rainfall can be an important factor because it reduces soil suction and increases the pore-water pressures in soils.
Terlien (1998) concluded that for shallow soil slips, antecedent soil moisture controls the required rainfall duration while the soil hydrological properties determine the minimum required rainfall intensity. Two key difficulties are the definition of the period over which to accumulate the precipitation and the exactly data of the landslide event. Empirical rainfall-triggering thresholds require accurate rainfall data and detailed information on the occurrence of slope failures. Landslide occurrence might be ascertained by compiling an inventory of slope failures immediately after the event or by mean of indirect techniques as dendrochronological analysis when no landslide data is available. The use of dendrochronology allows knowing the landslide activity of a specific area, where there is a lack of historical information, within a dendrochronological year. The main drawback relies in the impossibility to obtain the exact date for such event. Hence, a more comprehensive study must be carried out to correlate rainfall events with landslides failures (e.g. Corominas & Moya (1999). Rainfall data should be collected from a carefully designed and sufficiently dense network of recording rain gauges, of probably no less than 1 gauge for about each 50 km^2. Additionally, the temporal resolution of rainfall measurements is crucial. Daily precipitation records do not capture peak rainfall intensity, a fundamental measure where convective precipitations of short duration and high intensity trigger mass movements (Reichenbach et al. 1998).
According to Guzzetti et al. (1997), empirical thresholds for the initiation of landslides can be loosely defined as global, regional, or local. The global thresholds attempt to establish the general minimum level below which landslides do not occur. Some of this examples can be

found in Caine (1980); Innes (1983); Jibson (1989); Clarizia et al. (1996); Crosta & Frattini (2001); Cannon & Gartner (2005).
Regional thresholds are defined for areas extending from a few to several thousand square Kilometres of similar meteorological, climatic, and physiographic characteristics, and are potentially suited for landslide warning systems. Local thresholds consider the local climatic regime and geomorphological setting, and are applicable to single landslides or to a group of landslides in areas extending from a few to some hundreds of square kilometres. A limitation of regional and local ID thresholds is the fact that thresholds defined for a specific region or area cannot be easily exported to a neighbouring regions or similar areas (Crosta, 1989).

4.3 Previous works carried out so far using empirical rainfall thresholds

Most of the works carried out so far in determining the empirical rainfall thresholds are based in detailed landslide inventories and rainfall data. Caine (1980) was the first in establishing an empirical threshold for debris flows based on rainfall intensity-duration relations:

$$I = 14.82D^{-0.39}$$

Equation 4-1

in which I is the rainfall intensity (mm/hr), and D is the duration of rainfall (hr).

It allows a fairly simple definition of the rainfall necessary to provoke shallow instability on undisturbed slopes. In the Piedmont region, Aleotti (2004) used five well-known landslide events and hourly rainfall to implement a warning system for rainfall-induced shallow failures. Zêzere et al. (2005) reconstructed the dates of landslide activity from field work, archive investigation and interviews with the population living in the study area. It allows them to conclude that in the Lisbon area, the occurrence of shallow translational soil slips is related to intense rainfall periods (1 to 15 days), while deep slope movements occurred in relation to longer periods of less intense rain (30 to 90 days). Guzzetti et al. (2007) collected 853 rainfall events from the literature, including international journals, conference proceedings and reports. Each event includes its location, rainfall conditions, type and number of landslides, main rock types cropping out in the region and climate information. It permits to define new thresholds for the possible initiation of rainfall-induced landslides in the Central European Adriatic Danubian South-Eastern Space (CADSES) area, located in central and southern Europe. A summary of the Norwegian Geotechnical Institute (NGI) regarding the duration and intensity of precipitation events that may trigger debris flows and shallow landslides can be found in Nadim et al. (2009). In such a case, thresholds of different failures in Norway and Nicaragua are presented. In another work, Sengupta et al. (2010) worked with a not large rainfall data base (from 1998 to 2006) but with a well-known landslide activity of Lanta Khola landslide. Since they knew the exact date of landslide reactivation, they were able to plot the total cumulative rainfall (E) against event duration (D) in order to get the local thresholds. Jaiswal & Van Westen (2009) prepared an extensive landslide database, covering a time span of 15 years. It permits to define a threshold for each area according to the method suggested by Zêzere et al. (2005) and the subsequent assessment of temporal probability.
On the other hand, only a few works, where the exact date of landslide events is unknown, have been found in the literature. Corominas & Moya (1999) reconstructed the landslide activity in

relation to rainfall in the Eastern Pyrenees, in Spain, by means of dendrochronology. The attempt to reconstruct a complete record of the landslide activity in the region, failed because few written references exist in local archives. Hence, they had to find out the most reliable rainfall events that resulted (or did not result) in landslides within a dendrochronological year.

4.4 Estimation of temporal probability

Temporal probability of landslide initiation can be estimated either using physically-based or empirical rainfall threshold methods (Jaiswal and van Westen, 2009). Temporal probability can be analysed by evaluating the temporal probability of the rainfall events themselves combined with an analysis of the rainfall threshold. A few works exist in the literature as the one done by (Ko Ko et al., 2004). They calculated the empirical rainfall threshold along the Unanderra and Moss Vale Railway Line in the State of New South Wales, Australia using a binomial probability model. Information on the exact date of the landsliding was provided and rainfall data was available covering a period of 109 years. Temporal probability of two sites was evaluated as well as its spatial and temporal variation. Jaiswal & Van Westen (2009) estimated the temporal probability for landslide initiation using the probability of exceedance of a rainfall threshold and the probability of occurrence of landslides related to the rainfall threshold in a railway alignment and the national highway in the southern India using a Poisson probability model. Information about 14 landslides triggered during the period 1992 to 2006 was used. Finlay et al. (1997) used ninety years of historical landslide records as input to the Poisson and binomial probability distributions to predict rainfall thresholds, relate the number of landslides and rainfall, and calculate the probability of landsliding of a slope given a rain event. However, probabilistic assessments of landslide frequency and hazard that are based on historical records are difficult to perform because most landslide records cover short periods of historical time and small geographic areas.

4.5 Objective

Most of studies referenced in the scientific literature establish the triggering rainfall thresholds from detailed landslide inventories where the exact moment of the event is known as well as the rainfall amount of the rainfall recorded so far. Unfortunately, in our study area neither exact day nor approximate date are known. Alternatively, series of landslides have been reconstructed by means of dendrogeomorphology. First-time slope failures and landslide reactivations have been identified with a precision of one year. Despite being a very good accuracy is not sufficient to establish a direct relationship with triggering events.

A method to determine the possible date of landslide reactivations and the establishment of a rainfall threshold within the Tremp Basin (Spain) is proposed. Some thresholds have been analysed considering several accumulated rainfall and different intensity-duration relationships. Threshold performance has been evaluated by means of ROC analysis (Receiver Operating Characteristics) (Fawcett, 2006) that permit to classify them. Finally, the temporal probability is estimated combining the probability of the threshold being exceeded and the probability of landslide initiation given that the threshold is exceeded.

4.6 Methodology

The procedure to carry out this work has been: a) identification of landslides and their subunits by means of geomorphological mapping, b) dendrogeomorphological sampling, c) determination of years with failures, d) collection and processing of the available rainfall data, e) proposition of thresholds, f) validation and g) calculation of temporal probability of failure.

4.6.1 a) Identification of landslides and their subunits

Mapping of landslides and their units as well as the tree-ring analysis have been prepared from different studies conducted in the Tremp Basin (eastern Pyrenees). Over tens of failures, a total of four large landslides have been selected to be analysed with dendrochronology (Figure 4-1): Clot dels Oms, Les Pales, Sant Salvador, and Mas Guillem. Characteristics of each landslide are shown in Table 4-1. Although Les Pales has been treated as a single landslide, it comprises three smaller landslides.

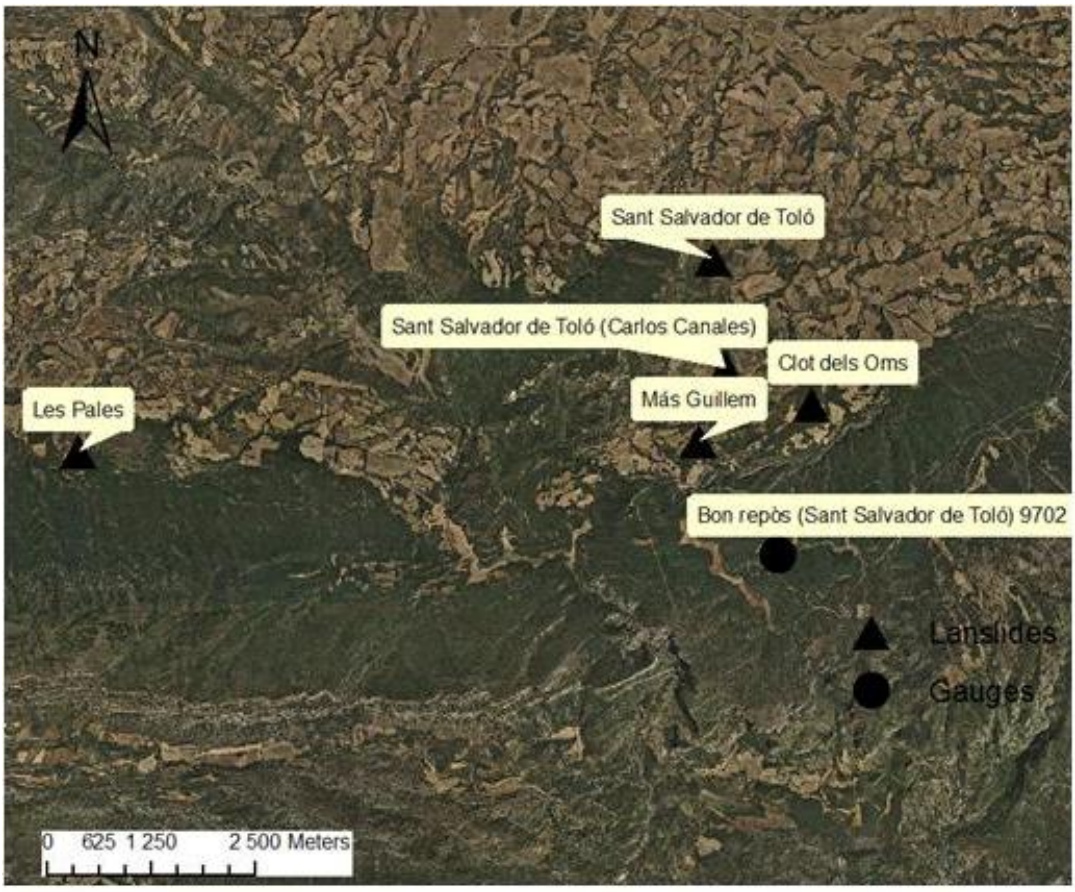

Figure 4-1: Landslide locations.

Table 4-1: Characteristics of each Landslide. Coordinates according to the European zone 31T georeferencing (Forné, 2004; Montero, 2011; Oliveras, 2011). TL: Translational Landslide; RL: Rotational Landslide; E: Earthflow.

Landslide	X UTM (m)	Y UTM (m)	Z UTM (m)	Length(m)	Width (m)	Extension (m^2)	Avergage slope (^{o})	Typology
Clot dels Oms1	338,909	4,657,644	780	370	129	47,660	11.4	E
Clot dels Oms2	338,988	4,657,957	720	260	99	25,860	11.3	E
Clot dels Oms3	338,984	4,658,044	710	71	101	7,198	13	RL
Clot dels Oms4	339,125	4,657,879	730	603	85	51,360	11	TL
Clot dels Oms5	339,040	4,657,720	760	334	93	31,140	10.9	TL
Les Pales1	330,147	4,657,052	551	340	79	26,860	10.7	E+RL
Les Pales2	330,147	4,657,052	551	290	33	9,570	13.6	E
Les Pales3	330,147	4,657,052	551	215	28	6,020	14	E
Sant Salvador	337,661	4,659,292	900	2,000	400	800,000	9.4	RL+E
Mas Guillem	337,651	4,657,141	855	500	100	50,000	11.5	TL

Table 4-2: Geotechnical parameters of each landslide (Forné, 2004; Montero, 2011; Oliveras, 2011).

Landslide	**Residual friction angle(º)**	**Soil Classification (Casagrande)**	**Granulometry**
Clot dels Oms	9	Low-medium plasticity clay	-
Les Pales	15	Low-medium plasticity clay	-
Sant Salvador	9	Low-medium plasticity clay	Silt
Mas Guillem	15	Silty or clayey fine sands with slight plasticity.	Silty Sand

.

Clot Dels Oms:

It is a large landslide located in south-eastern part of the Tremp Basin and developed in a low-medium plasticity clay with a residual friction angle of 9º (Table 4-2). A geomorphological cartography as well as the dendrological analysis have been carried out by Oliveras (2011) given a total of 5 units (Figure 4-2).

Unit 1 is a large earthflow with an extension of 47,660 m^2, a length of 370 m and width of 129 m (Table 4-1). Tension cracks and lobes are present, mostly at the bottom of the failure.

Unit 2 is another earthflow located just bellow unit 1. It has an extension of 25,860 m^2, a length of 260 m and 99 m of width (Table 4-1). Lobes and small scarps are present due to subsequent reactivations, mostly at the bottom where unit 3 is located. Such a failure is a rotational landslide with an extension of 7,198 m^2, 71 m long and a width of 101 m (Table 4-1). At the top, a scarp of 2 m high can be recognised. The bottom is delimited by the Mas Guillem gully. Torrential erosion has not been observed.

Unit 4 (Figure 4-3) is a translational landslide with an extension of 51,360 m^2, 603 m long and 85 m width (Table 4-1). It is the longest unit with a long scarp (about 70 m) in the middle of the unit and some lobes and tension cracks at the bottom which is also delimitated by the Mas Guillem gully.

Finally, unit 5 is another translational landslide with a length of 334 m, a width of 93 m and 31,140 m^2 of extension (Table 4-1). The high presence of vegetation in the whole landslide complicates the identification of the movement as well as the identification of geomorphological indicators as cracks, lobes, little scarps etc.

12 trees (Pinus Sylvestris) not affected by the failure have been selected. The have been defined as reference trees (Figure 4-2). They are used to identify possible anomalies in the tree rings due to other factors not related with the landslide movement (climatic factors). On the other hand, 24 affected trees have been sampled (Figure 4-2). 10 of them are located in the unit 5, 7 at the bottom of the unit 4, 5 in unit 2, 1 in the unit 3 and 1 of them in the area between unit 1 and 2 (Figure 4-2).

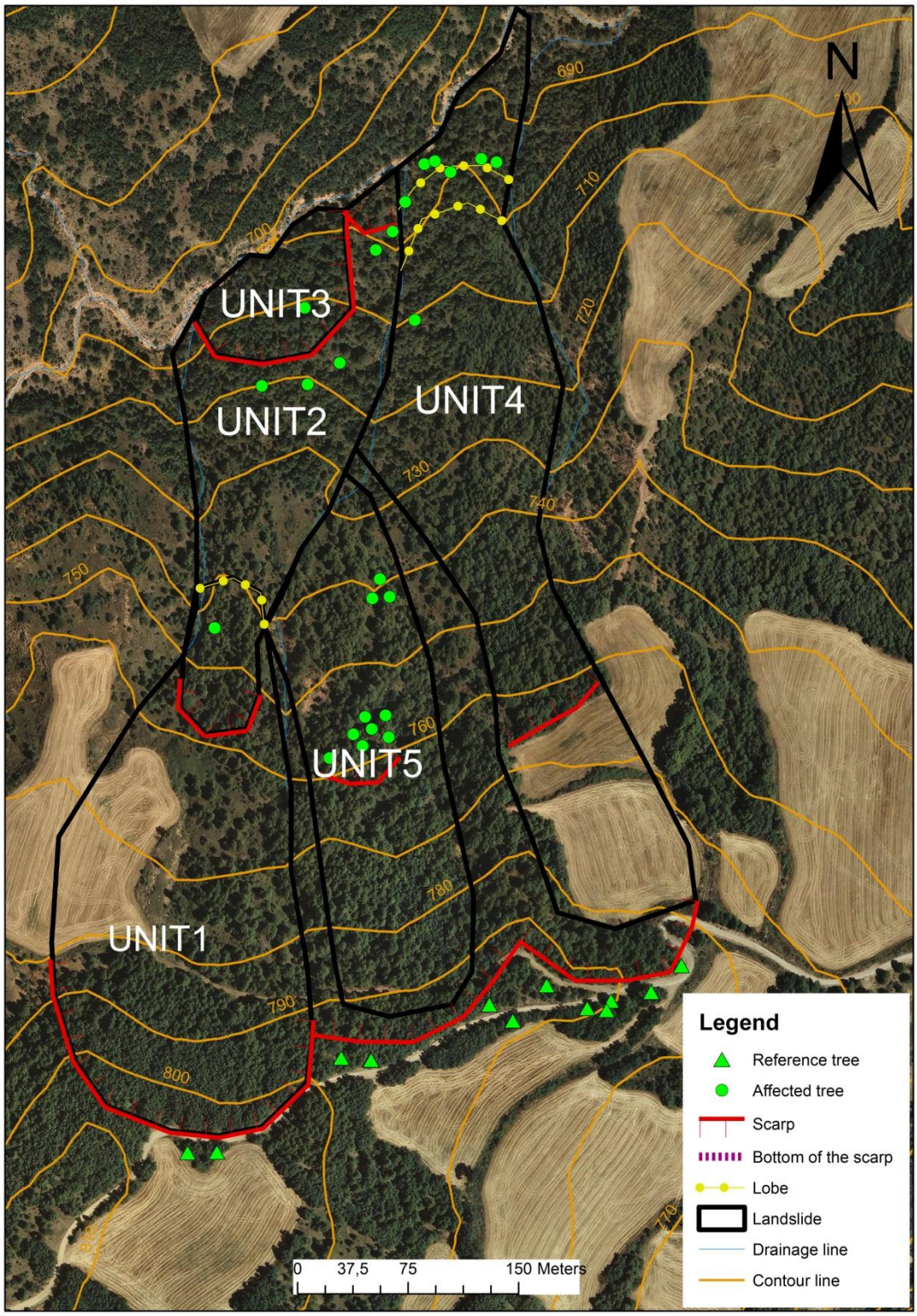

Figure 4-2: Clot dels Oms landslide composed of 5 units. Units 1 and 2 are earthflows, unit 3 is a rotational landslide and units 4 and 5 are translational landslides. Some features are shown in Table 4-1 and Table 4-2 (Oliveras, 2011).

Figure 4-3: View of the Clot dels Oms landslide from the north. Unit 4. Scarp indicated with a red line (GeoriscS.L., 2008).

Les Pales:

Located in the south part of the Tremp basin, with an approximate extension of 42,000 m^2 and an average slope of 12.7º, it is composed of three units of a low-medium plasticity clay with a residual friction angle of about 15º (Figure 4-4, Figure 4-5, Table 4-1 and Table 4-2). Geomophological cartography of such a landslide, as well as dendrological analysis has been done by (Montero, 2011).

Unit 1 has an extention of 26,800 m^2 with an average width of 79 m a length of 340 m and a crown scarp of 15 m. In the middle part, counter-slope areas with accumulated water can exist (Figure 4-6). They belong to rotational platforms with several scarps 2 m high. At the bottom, some lobes and tension cracks can be observed (Figure 4-7).

Unit 2 (Figure 4-8), with a scarp of 12 m high, presents a rotational component at the top, with counter-slope areas, and lobes and tension cracks at the bottom due to its flow component. It has an extention of 9,570 m^2, a width of 33 m and a length of 290 m.

Finally, unit 3 (Figure 4-8) is a smaller and more elongated eartflow with an extenxion of 6,020 m^2, a length of 215 m and a width of 28 m. It presents a crown scarp of 15 m high (similar to the scarp of unit1) with some rotational platforms at the top and lobes and traction cracks at the bottom. It is not completely clear the limit between unit 2 and 3 as both landslides are one next to the other and have the same behaviour at the bottom.

A total amount of 13 trees have been collected in unit 1, 37 trees in unit 2, and 20 trees in unit 3. 9 reference trees have been sampled (Montero, 2011). Most of trees have been sampled in the upper part of the landslide as there is a lack of vegetation in the upper part.

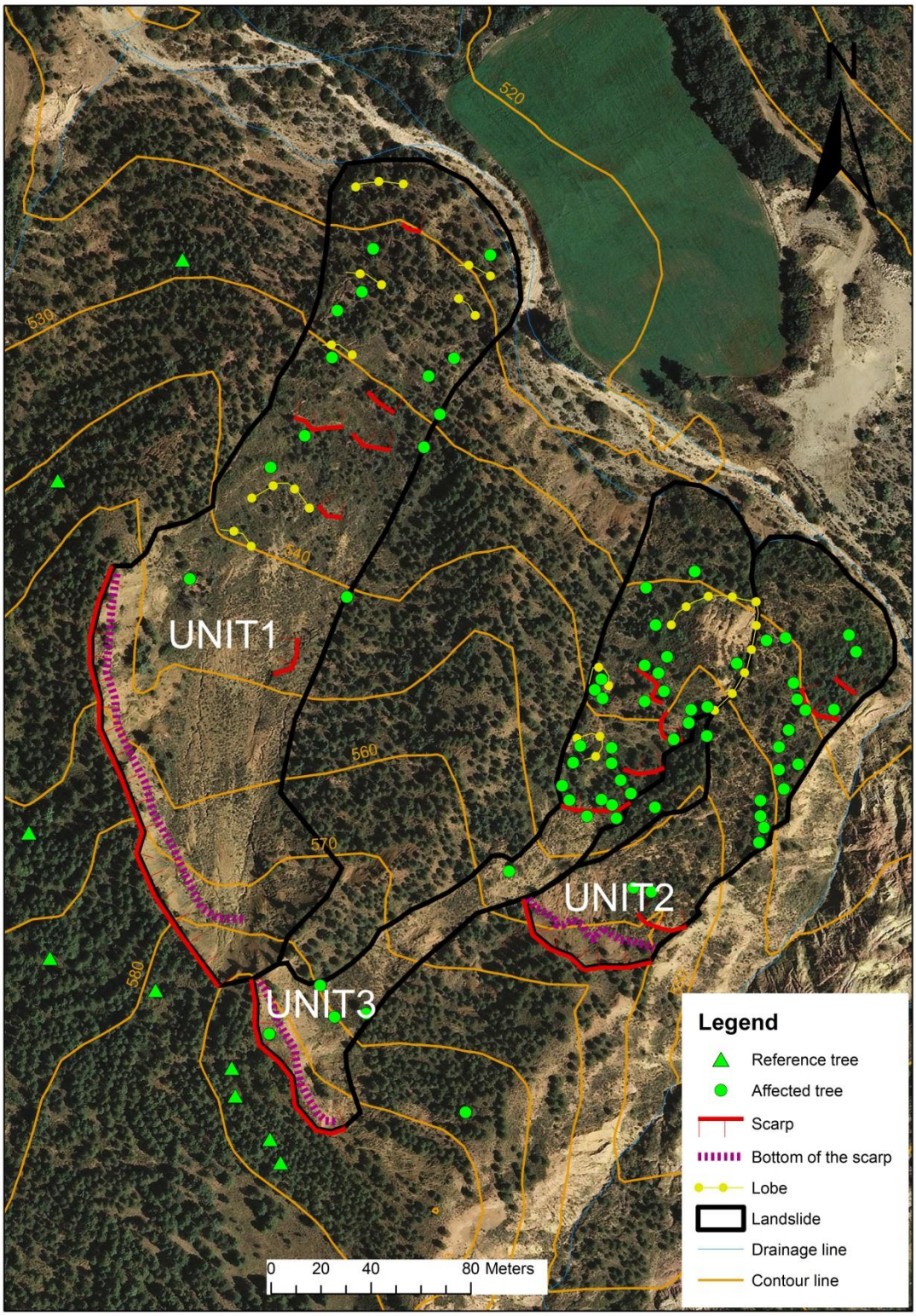

Figure 4-4: Les Pales landslide is composed of three units. Some features are shown in Table 4-1 and Table 4-2 (Montero, 2011).

Figure 4-5: View of Les Pales landslide from the north. Unit1. Cronw scarp in Garumnian materials can be seen (red line) (Georisc S. L., 2009).

Figure 4-6: Les pales landslide. Counter-slope area with inclined trees in the middle part of Unit1 (Montero, 2011).

Figure 4-7: Les Pales landslide. Tension cracks in the lower part of unit1 (Montero, 2011).

Figure 4-8: View of Les Pales landslide, from the north. Unit 2 and unit 3 can be observed in the middle of the photo. Scarp indicated with a red line (Georisc S. L., 2009).

Sant Salvador:

It is a large landslide located in the south part of the Tremp basin, near to the other movements; with an extension of about 800,000 m^2 and an average slope of 9.4º (Table 4-1, Figure 4-9 and Figure 4-10). Cartography and dendrological analysis have been obtained from a non-published work carried out in the Department of Geotechnical Engineering and Geosciences (ETCG) from the Technical University of Catalonia (UPC). It is a low-medium plasticity clay, according to the Casagrande soil classification, with a silty grain size and a residual friction angle of about 9º (Table 4-2). It can be classified as a complex movement, being considered the upper part as a rotational landslide and the lower part as an earthflow with some lobes. The failure surface is supposed to be located 10 m deep.

The crown scarp is formed by a semicircular large calcareous cliff of 125 m high from the cretaceous. It presents rockfall activity, since some blocs can be seen downslope.

In the upper part of the landslide but below the bottom of the main scarp, several minor scarps from 5 to 7 m. high and 40 to 100 m long can be identified with some counter-slope areas and accumulated water associated to rotational platforms (Figure 4-11). Tension cracks associated to a central earthflow of about 1,000 m long also exist. This is the most active part of the landslide (Figure 4-12).

The L-912 road divides the landslide in two parts. Hence, it is commonly affected by the movement. However, the presence of cultivated fields, mostly in the middle part of the failure (below the road) masks the original morphology of the movement.

The bottom of the central earthflow, located 20 m below the road, has been altered by an artificial lake. Some lobes close to that lake can be observed, which confirm the recent activity of the earthflow. A second earthflow of 100m long and 20 m width can be seen next to the central one, in the left margin of the landslide, and just below the main scarp. Its limits are difficult to identify, but the presence of lobes, tension cracks and water accumulations confirm this hypothesis.

Finally, in the right-central part, a third smaller earthflow can be identified with two crown scarps of about 20 m long, 1m high and a rotational component in the upper part.

114 samples of 106 pines have been dated (Figure 4-9). In such a case, all trees belong to the upper part of the landslide, above the road, since it is the most active part. They are relatively young trees, not older than 40 years.

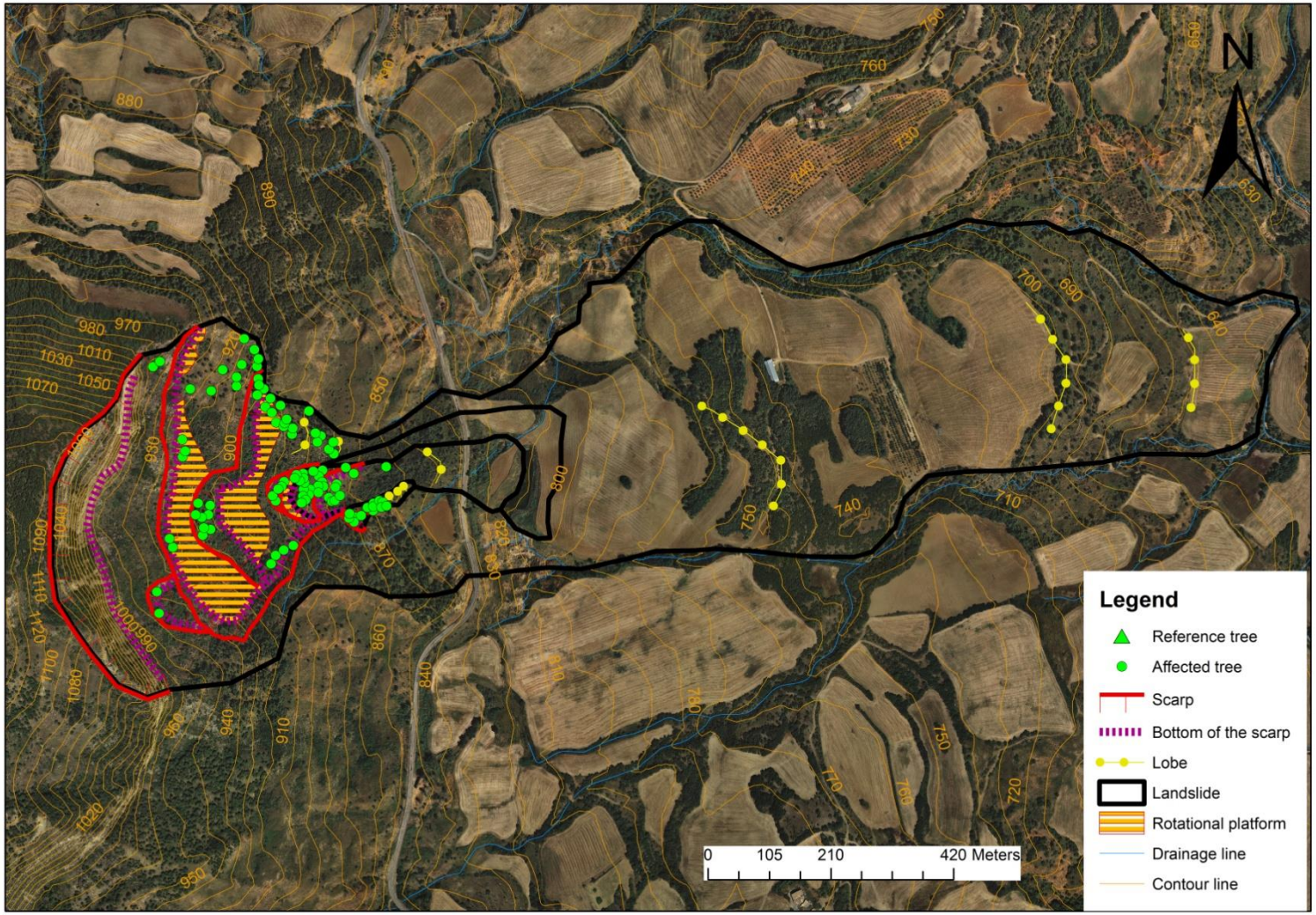

Figure 4-9: Sant Salvador Landslide. Some features are shown in Table 4-1and Table 4-2.

Figure 4-10: Sant Salvador landslide. General view from the south. Crown scar is delineated with a red line (Forné, 2004).

Figure 4-11: Sant Salvador landslide. Counter-slope areas with accumulated water.

Figure 4-12: Affected trees in the upper-middle part of the Sant Salvador landslide.

Mas Guillem:

Located in the south part of the Tremp basin, it is a translational landslide with an extent of about 50,000 m^2, a thickness of 20 m, a crown of 17 m high, a residual friction angle of about 15º and an average slope of 11.5º (Figure 4-13, Figure 4-14, Table 4-1 and Table 4-2). Cartography as well as dendrological analysis have been obtained from a non-published work carried out in the Department of Geotechnical Engineering and Geosciences (ETCG) from the Technical University of Catalonia (UPC). Granulometry resulted in a silty grain size. High presence of vegetation in the crown area, mostly oaks and pines exists. Both, left and right margins are defined by torrents and it can be seen the presence of cracks. The lower part of the landslide is quite plain with lobes and the torrent area is almost closed, probably due to the continuous reactivations. The upper part has been occupied by fields (Figure 4-15), hence, mostly of the original morphology has disappeared. As in the previous landslide, the movement is divided by the L-912 road and it produces continuous affections in that section.
45 trees (pines) for the dendrogeomorphology analysis have been sampled: 8 trees are located in the left margin, 14 in the right margin, 19 in the central part (between the road and the bottom) and 4 trees in the lower part of the landslide (Figure 4-13). Sampling near to the crown area has not been possible due to the absence of pines as well as in the part occupied by fields (just above the road). Finally, a total amount of 31 samples have been used for dating.

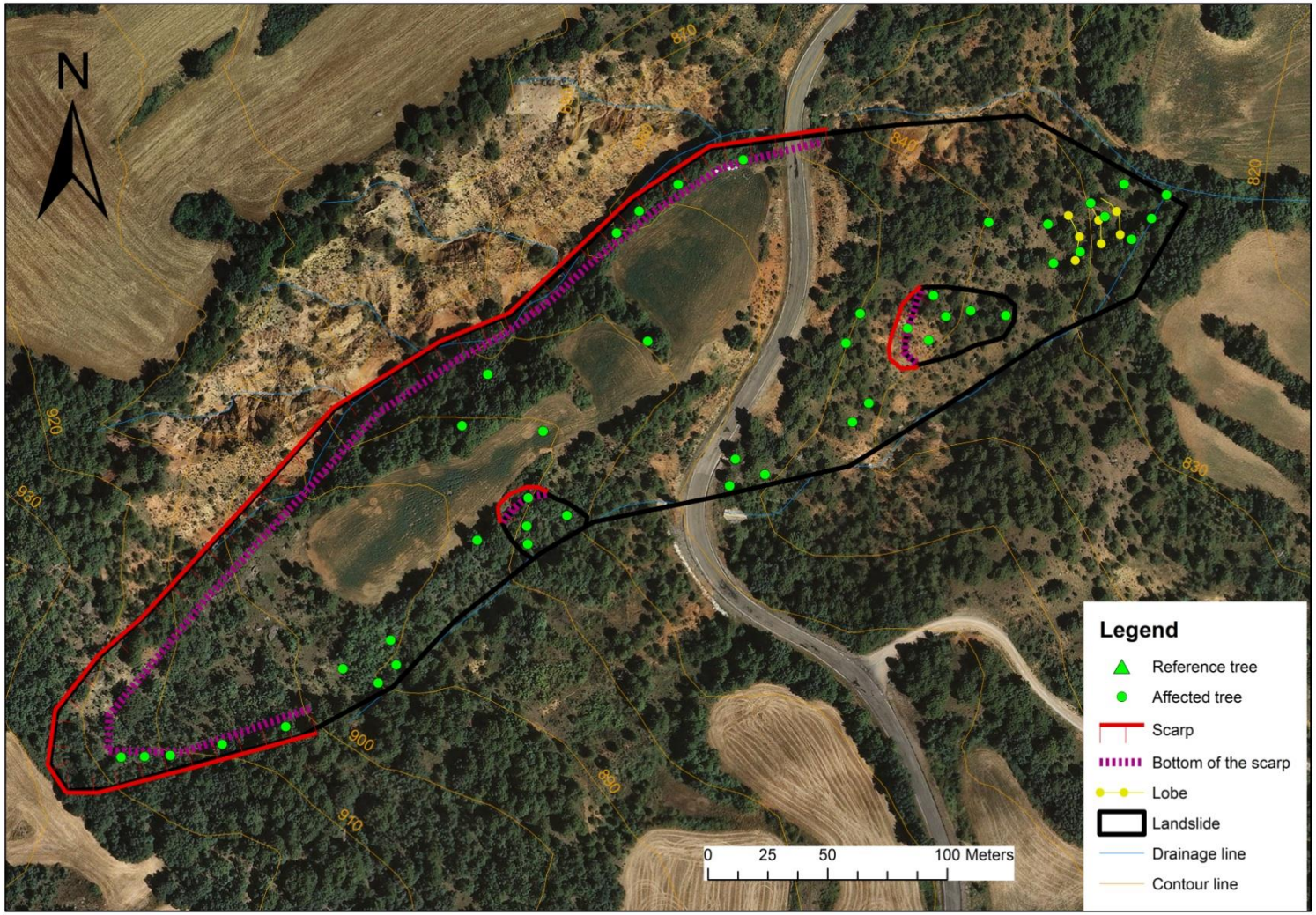

Figure 4-13: Mas Guillem landslide. Some features are shown in Table 4-1and Table 4-2

Figure 4-14: Mas Guillem landslide. Crown scar in Garumnian materials can be recognised from the L-912 road.

Figure 4-15: Mas Guillem landslide. General view of the movement. Crown scar located in the left margin (red line) as well as the central part occupied by fields can be seen.

4.6.2 b) Dendrogeomorphological sampling

As it has been said before, selected landslides have been analysed with dendrochronology (Figure 4-16). It permits dating, within one year (dendrological), anomalies in the tree rings caused by landslides. A dendrological year is expected to start in September and end in August (Moya et al., 1992). Number of trees showing tree-ring response to landsliding is presented in Figure 4-17. The earliest year from which data is available is 1950 and the latest is 2008. However, data from 2003 to 2008 has not been analysed as no rainfall data is available.

Figure 4-16: Dendrogeomorphological sampling procedure in Mas Guillem landslide.

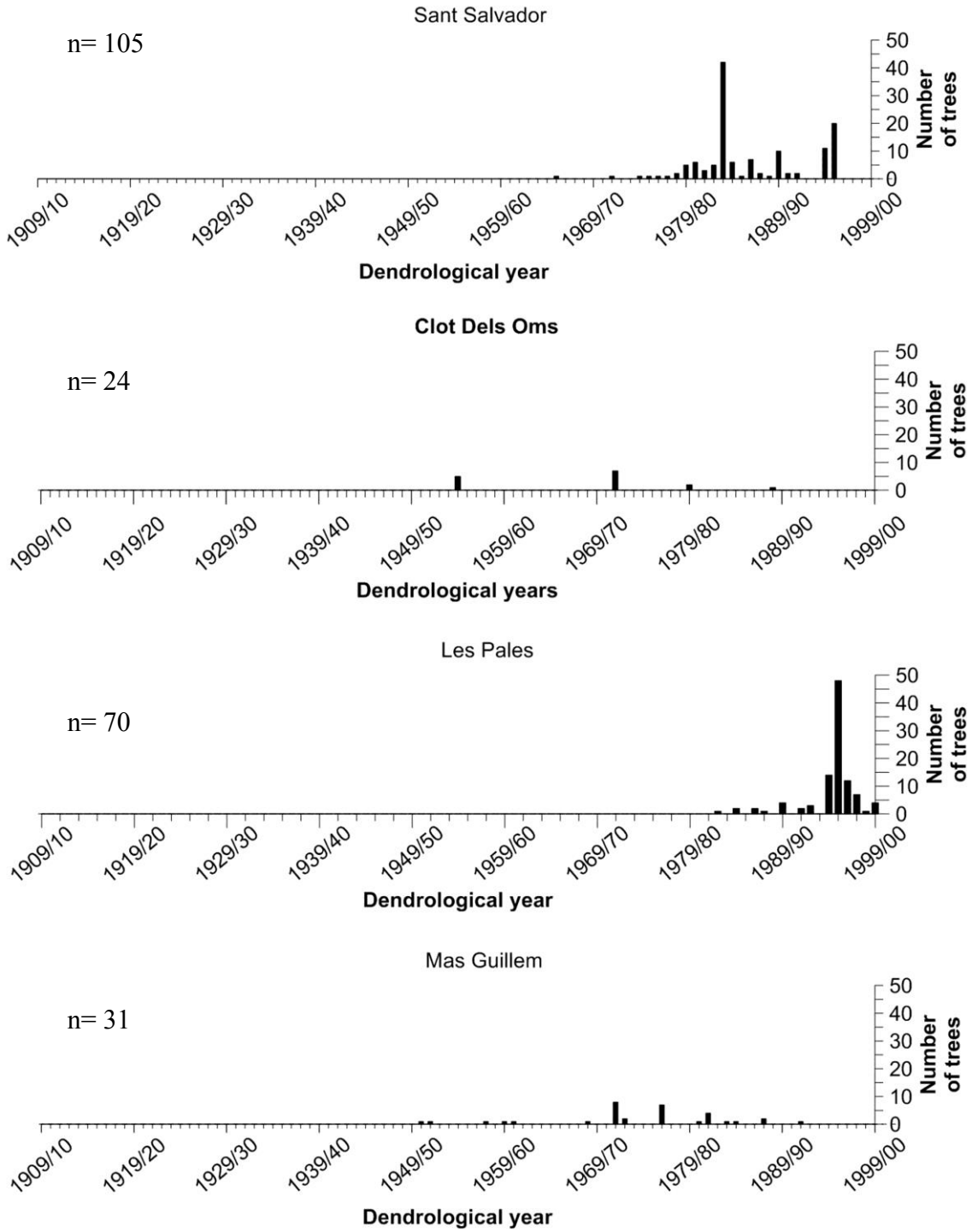

Figure 4-17: Results of the dendrological analysis. Number of trees showing tree-ring response to landsliding.

4.6.3 c) Determination of years with failures

It has been considered that a reactivation has occurred if three or more trees on the landslide show anomalies in their rings. The main handicap when working with this technique is that a direct relationship with triggering events cannot be established. On the other hand, it has been impossible to validate any data of failure obtained by tree-ring analysis due to the lack of information existing in the authorities' databases. 12 years with reactivations have been identified (Table 4-3).

In the Mas Guillem landslide, a clear response during the period 71/72 and 76/77 with 8 and 7 trees affected respectively can be observed. Reactivation in the period 71/72 can be considered as a general reactivation as it affects the major part of the landslide (with the exception of the central part and the bottom). On the other hand, reactivation observed in 76/77 is a local reactivation, affecting the right part of the movement. Finally, during the period 81/82, left margin and the central part present 4 responses (2 each), and two responses more can be identified the periods 83/84 and 84/85, which could be retarded responses.
In Les Pales landslide, a local response has been identified in the unit 2 being affected 3 trees. Another reactivation has been considered during the period 94/95 in which, 5 trees in unit 2 and 4 trees in unit 3 have been affected. Finally, a clear response has been detected during the period 95/96. It affects the tree units giving a total amount of 52 trees affected. Hence, it can be considered as a global reactivation.
In Sant Salvador landslide, a response of 5 trees affecting the central and upper area of the movement has been identified in the period 79/80 (local response). During the periods 80/81, 81/82 and 82/83 there is a response of 6, 3 and 5 trees respectively affecting the central and upper-left part of the landslide (local response). The clearest response has been detected during the dendrological year 83/84 since it affected the whole landslide and a large amount of trees (42). During the year 84/85, 6 trees presented another local response in the middle and the upper-left part with a delayed response in 85/86. During the dendrological year 86/87 a local reactivation affected 6 trees belonging to the little earthflow located in the middle-right part of the failure. Finally, periods 89/90, 94/95 and 95/96 show global responses with 10, 11 and 20 trees affected respectively.
In Clots dels Oms landslide, two reactivations have been indentified. The first one during the period 54/55 with 6 trees showing response, and the second one with 5 trees affected. Both are global reactivations.
In conclusion, 12 reactivations resulted, being half global and half local reactivations.

Table 4-3: Reactivation years. G: Global reactivation; L: Local reactivation.

Reactivation years according each landslide	Resulting reactivation years
Mas Guillem Landslide	54/55 (G)
71/72	71/72 (G)
76/77	76/77 (L)
81/82	79/80 (L)
Les Pales Landslide	81/82 (L)
89/90	82/83 (L)
94/95	83/84 (G)
95/96	84/85 (L)
Sant Salvador Landslide	86/87 (L)
79/80	89/90 (G)
80/81	94/95 (G)
81/82	95/96 (G)
82/83	
83/84	
84/85	
86/87	
89/90	
94/95	
95/96	
Clot dels Oms Landslide	
54/55	
71/72	

4.6.4 d) Collection and processing of rainfall data

Rainfall data were provided by the AEMET (Spanish meteorological Office). There are five gauges located between 1.5 and 17.5 km away from the sampled landslides (Figure 4-18) (Table 4-2).

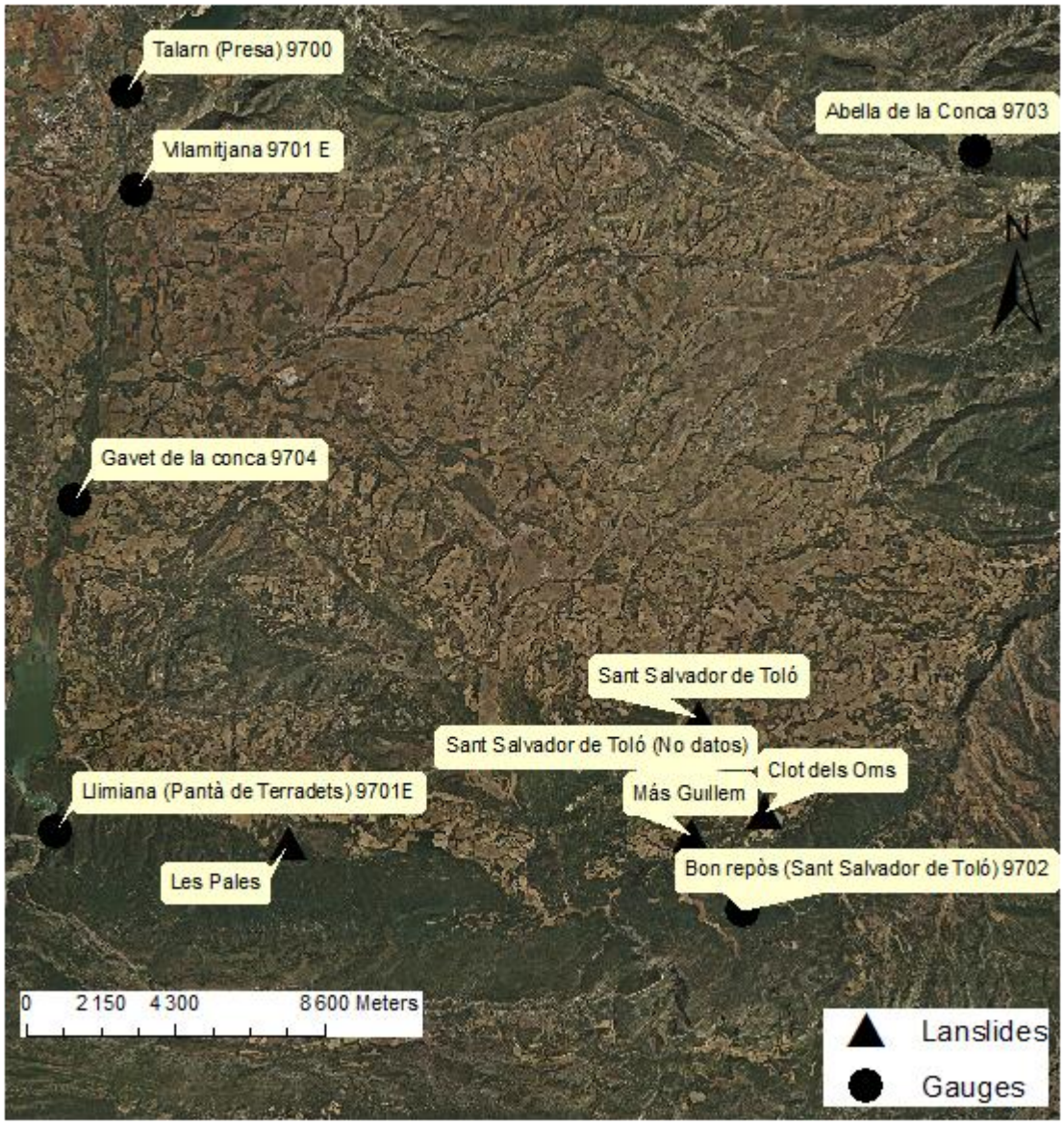

Figure 4-18: Gauges and landslides location.

Table 4-4: Gauges characteristics. European zone 31T.

Code	Name	X UTM(m)	Y UTM (m)	Z UTM (m)
9700	Talarn (Presa)	322,814	4,676,530	425
9702	Bon repos (Sant Salvador de Toló)	335,343	4,662,120	1,050
9701 E	Vilamitjana	323,105	4,674,690	415
9704	Gavet de la Conca	322,360	4,668,850	380
9708	Llimià (Pantà de Terradets)	322,458	4,662,670	399
9703	Abella de la Conca	838,709	4,676,510	956

These stations contain records of daily rainfall from 1915 to 2003 but significant information gaps exist (Figure 4-19). Rainfall data from Bon Repòs has been taken. It is the closest rain gauge to the landslides and located in the north face of Montsec (the same as landslides) at 1,050 m asl as well.

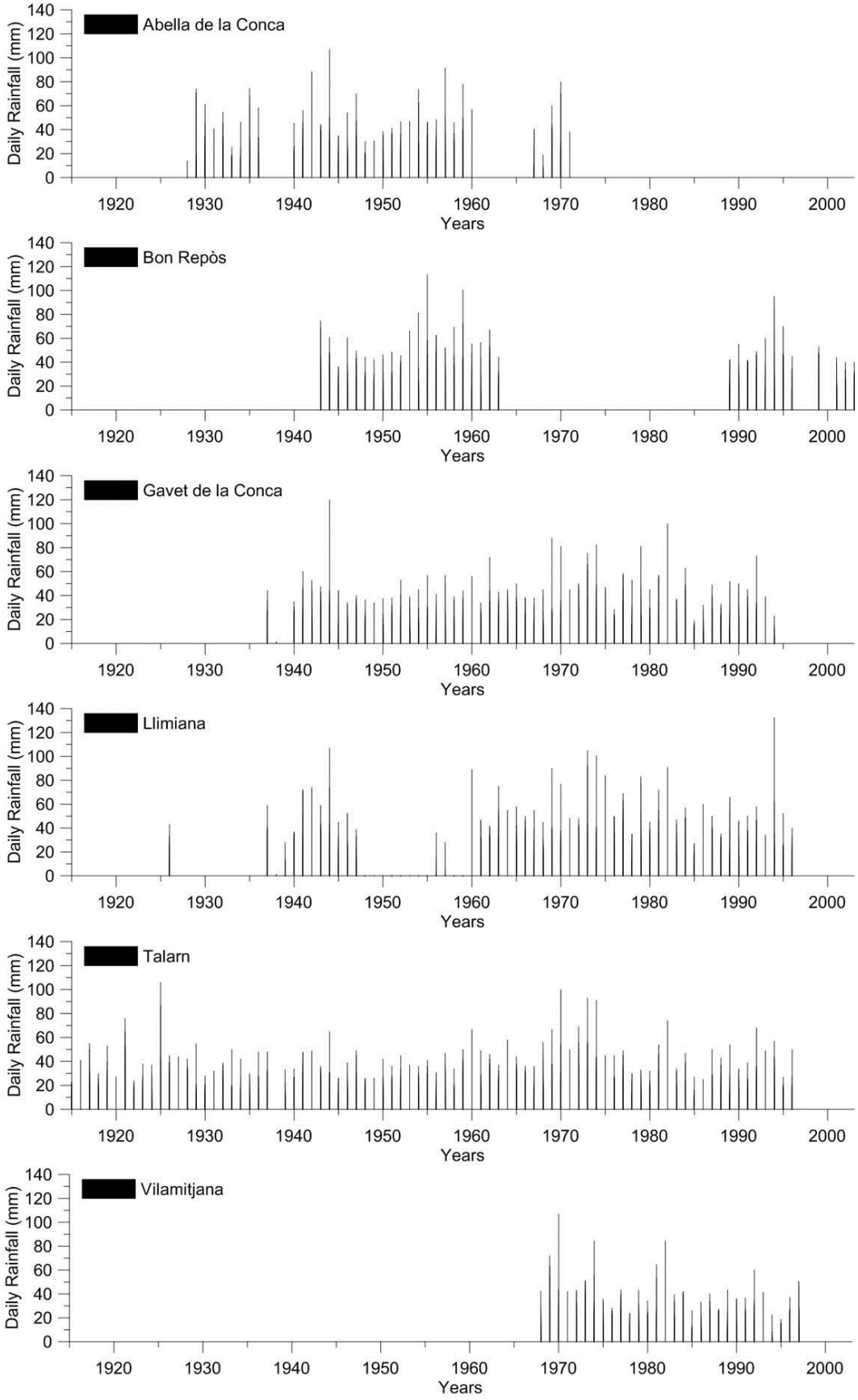

Figure 4-19: Daily rainfall of different gauges provided by AEMET (Spanish Meteorological Office).

Data gaps have been replaced with information from the other rain gauges using a polynomial potential adjustment. It is important to mention that other authors as Ko Ko et al. (2004) estimate data from other gauges adding the average variation in rainfall. This procedure is possible if not much gauges exist and if the day of the event is known, on the other hand, it is not straightforward. In such a case, more than one gauge needs to be considered to get as much rainfall data as possible in Bon Repòs gauge. Previously, a double mass analysis (Kohler, 1949) must be carried out to test the consistency of the records at a station. It consists in comparing its accumulated annual or seasonal precipitation with the concurrent accumulated values of mean precipitation for a group of surrounding stations. The result is a linear relation. A change due to meteorological causes would not cause a change in slope, as all the base stations would be similarly affected. On the other hand, a change in a gauge location would affect it (Linsley et al., 1975), hence, it should be dropped before other stations are tested or adjusted. It is very important to notice that any day without rainfall information is considered as "NoData", hence, the accumulated period containing that day will be considered as a period without information. On the contrary, it is being supposed that everyday without information, the amount of precipitation is 0 millimetres.

During the period which pluviometric information is available (from 1915 to 2003) there is not a single year in which data of all six gauges, from October to April, exist and it is impossible to perform such an analysis with all of them. Therefore, only four of them have been used (Bon Repòs, Talarn, Llimiana, Gavet de la Conca) (Figure 4-20A).This period has been considered as it is the one when mostly of precipitations occurs. On the other hand, analysis with rainfall data from May to April was also performed in order to understand the behaviour of the two missing gauges (Vilamitjana and Llimiana).

If double mass analysis is carried out with all the gauges except Vilamitjana, five years with information can be compared (Figure 4-20B). If the Abella de la Conca gauge is not considered, the number of comparable years is 4 (Figure 4-20C). It allows concluding that all of them can be used as any change in any gauge location has been done during this period.

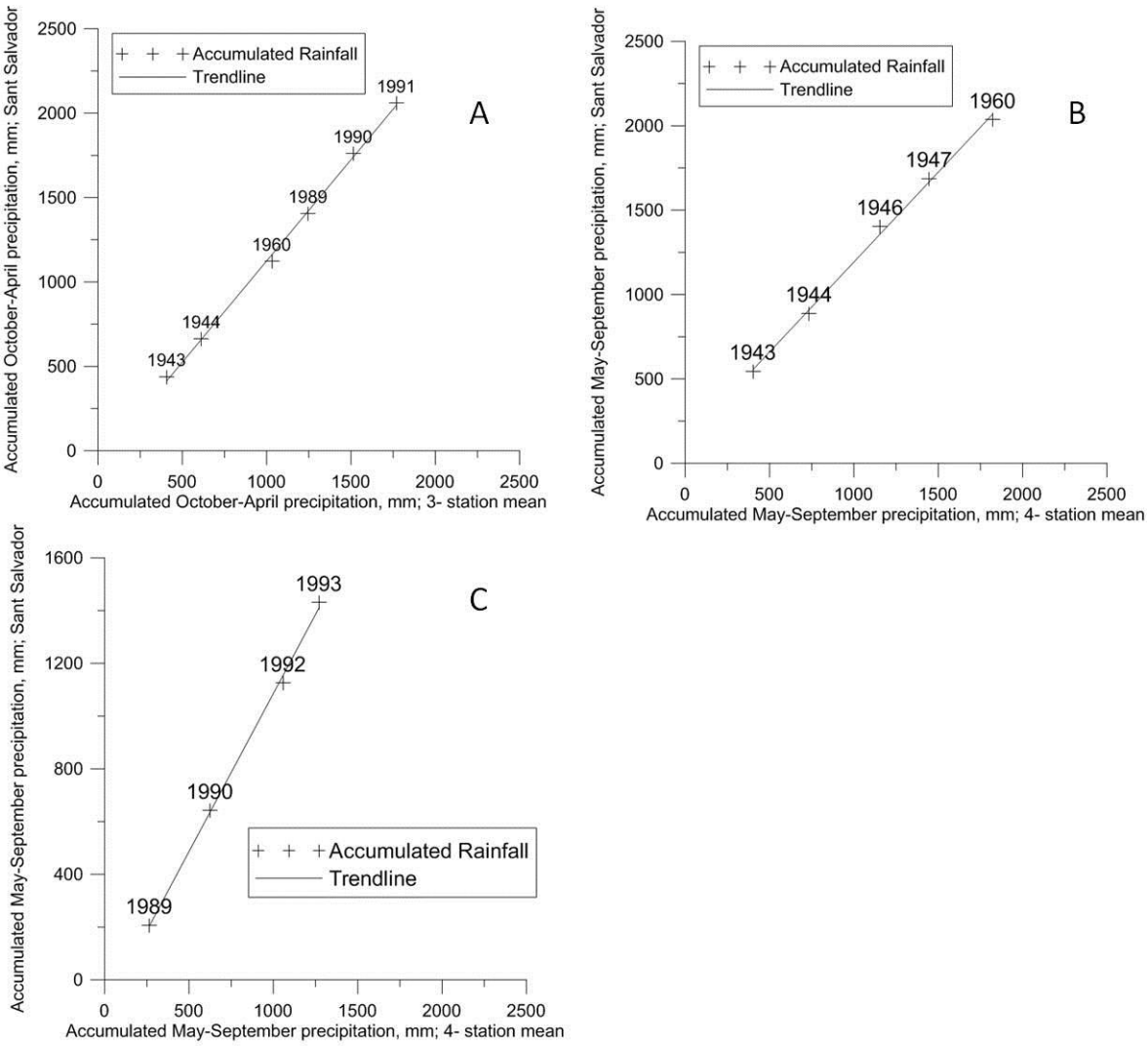

Figure 4-20: Adjustment of precipitation data for the Tremp basin by double-mass curve. A) From October to April. Vilamitjana and Abella de la Conca gauges are not include. B) From may to April. Vilamitjana gauge is not include. C) From May to April. Abella gauge is not included.

Monthly and daily accumulated rainfall have been adjusted by a polynomial function and compared in order to approximate the missing data in the gauge of Bon Repòs. In such a case, days with missing data and days with rain of 0 millimetres have not been considered as it has not sense to compare something with 0.

A total of 25 comparisons (all possible combinations) of monthly accumulated rainfall (30 days) between the Bon Repòs Gauge and other 5 gauges have been done (Table 4-5). Combinations of different gauges that show a best agreement have been selected and their daily rainfalls have been analysed obtaining a new adjustment (Table 4-6). It is important to notice that the coefficient of determination (R^2) is not very high, therefore, approximated rainfall from other stations will have high uncertainty. All these analyses can be found in Annex 4: Polynomial adjustment.

Table 4-5: Combination of gauges and the agreement of the polynomial potential function according to 30 day-accumulated-rainfalls. 1-Bon Repòs; 2-Talarn; 3-Llimiana; 4-Gavet de la Conca; 5-Vilamitjana; 6-Abella de la Conca.

Gauges	R^2	Gauges	R^2
1-2	0.59	1-4-6	0.7128
1-3	0.7	1-5-6	-
1-4	0.6	1-2-3-4	0.77
1-5	0.56	1-2-3-5	0.6939
1-6	0.6	1-2-3-6	0.7549
1-2-3	0.73	1-3-4-5	0.79
1-2-4	0.69	1-3-4-6	0.7604
1-2-5	0.63	1-4-5-6	-
1-2-6	0.7	1-2-3-4-5	0.77
1-3-4	0.77	1-2-3-4-6	0.761
1-3-5	0.7	1-3-4-5-6	-
1-3-6	0.7406	1-2-3-4-5-6	-
1-4-5	0.7645		

Table 4-6: Combination of gauges and the agreement of the polynomial potential function with daily rainfall. 1-Bon Repòs; 2-Talarn; 3-Llimiana; 4-Gavet de la Conca; 5-Vilamitjana; 6-Abella de la Conca.

Gauges	R^2
1-4-5	0.5
1-3-4-5	0.5238
1-2-3-4-5	0.5499

Gauges combination in better agreement with Bon Repòs is the one formed by Talarn, Llimiana, Gavet de la Conca and Vilamitjana with R^2=0.5499 (Equation 4-2).

$$P1=1.62P2^{0.73}+2.44P3^{0.56}-3.69P4^{0.06}+2.47P5^{-0.35}$$

Equation 4-2

in which P1 is the daily rainfall in Bon Repòs, P2 in Talarn, P3 in Llimiana, P4 in Gavet de la Conca and P5 in Vilamitjana.

4.6.5 e) Proposition of thresholds

Next step has been to identify possible combinations of rainfall that could justify the occurrence of failures in the past. As it has been said before, dendrogeomorphological results do not provide a specific date about landslide events. Furthermore, years with no dendrological response do not imply lack of failure or reactivation because trees might have not been affected. Thus, some basic inputs as the triggering rainy day and the type of threshold are unknown. For these reasons and considering we are working in a clayey material, two types of approaches have been used. The first one contemplates that to trigger a landslide an accumulated precipitation within a given period of time is needed (accumulated rainfall). A great variability

of thresholds have been defined in order to understand which is the best combination explaining the failures; from short periods with relatively intense events, to long periods with more gentle precipitations. It has been considered cumulative periods from 3 days to 2 months with a gradual increase of rainfall amount. It has been an iterative process and each new threshold has been proposed considering the previous and taking into account that the best threshold (dashed line) would be the one which is reached for all periods that are associated with landslide reactivation (L), but is higher than those that are not (N.L.). However, some periods without landslide reactivations present a higher amount of precipitation than periods with failures. An example is shown in
Figure 4-21. The defined threshold is reached during all years with landslide reactivations, but some years with no failures identified present a higher amount of rainfall. Hence, it is not a proper threshold.

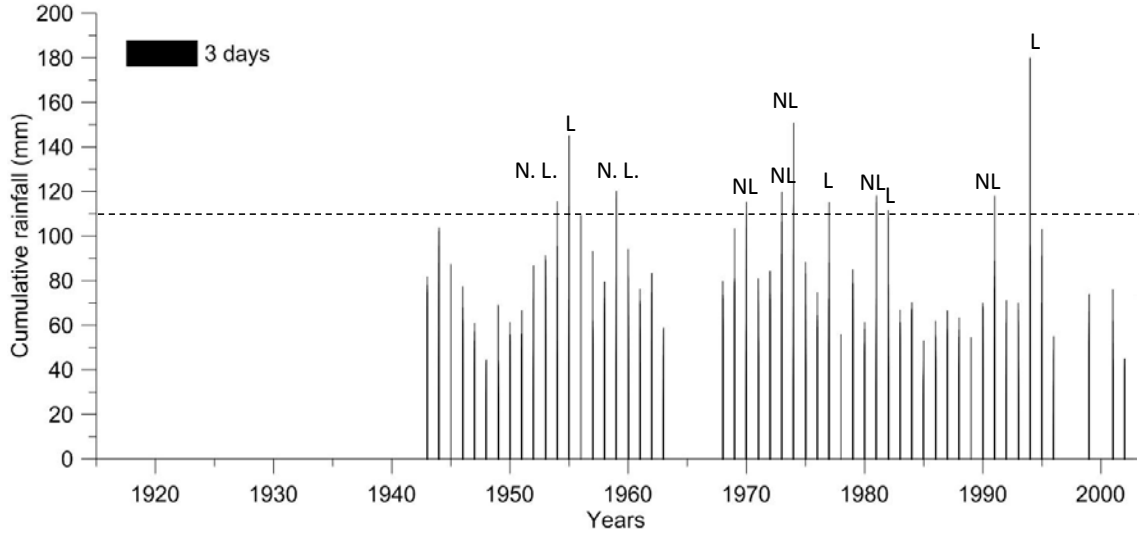

Figure 4-21: Cumulative rainfall and threshold (dashed line). 110mm within 3 days. L: Landsliding event. NL: No Landsliding event. The threshold is reached during all years with landslide reactivations, but some years with no failures identified, present a higher amount of rainfall. It is not a proper threshold.

Thus, another type of threshold with an accumulated rainfall followed by a minimum-daily-triggering precipitation has been considered (antecedent rainfall). Such a minimum-daily-triggering-precipitation must be a reasonable amount of water, common in that area, but not too much recurrent, since it would be exceeded in most cases. As in the afore-mentioned approximation, it is necessary to evaluate several types of rainfall, from short periods with intense precipitation to long periods with more gentle events. In such a case, different values of minimum-daily-triggering rainfall must be taken into account.

4.6.6 f) Thresholds validation

A receiver operating characteristics (ROC) analysis (Fawcett, 2006) has been conducted to evaluate the performance and reliability of different thresholds and decide which is the best that explain the failures. It is a technique for visualising, organising and selecting classifiers based on their performance. Each instance is mapped to one element of the set (p,n) of positive and negative class labels (e.g. dendrological years with observed reactivations, dendrological years without observed reactivations). A classification model (or classifier) is a mapping from instances to predicted classes. Labels Y and N are used for the class predictions produced by a

model. Given a rainfall threshold R_T, Y would be any dendrological year where, at least, one rainfall event exceeds such a threshold. On the other hand, N represents rainfall events where R_T is never reached. If the instance is positive and it is classified as positive, it is counted as a true positive; if it is classified as negative, it is counted as a false negative. If the instance is negative and it is classified as negative, it is counted as true negative; if it is classified as positive, it is counted as a false positive. Given a classifier and a set of instance (the test set), a two-by-two confusion matrix can be constructed representing the disposition of the set of instances (Figure 4-22).

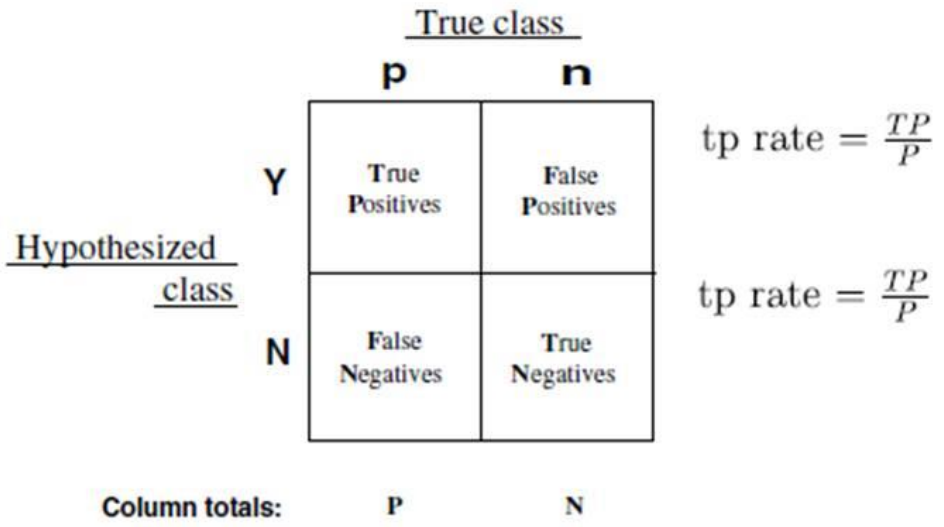

Figure 4-22: Confusion matrix and common performance metrics calculated from it.

The true positive (tp) rate of classifier (also called hit rate) is estimated as

$$Tprate \approx \frac{Positives\ correctly\ classified}{Total\ positives}$$

Equation 4-3

The false positive (fp) rate of the classifier (also called false alarm rate) is

$$Fprate \approx \frac{Negatives\ incorrectly\ classified}{Total\ negatives}$$

Equation 4-4

A ROC graph is used in order to plot tp rate (Equation 4-3) and fp rate (Equation 4-4). It depicts relative tradeoffs between benefits (tp) i.e. hit rate and costs (fp) i.e. false alarm rate. A discrete classifier outputs only a class label (Figure 4-23). The point (0,1) represents perfect classification. A point along a diagonal line (the so-called line of no-discrimination) from the left bottom to the top right corners means a completely random guess.

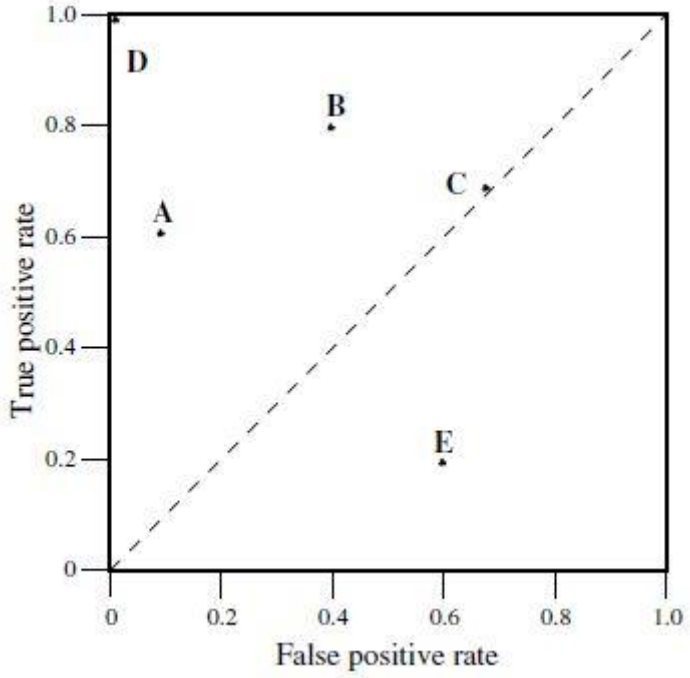

Figure 4-23: A basis ROC graph showing five discrete classifiers.

4.6.7 g) Calculation of temporal probability of failure

Finally, the average temporal probability of the whole Tremp basin has been evaluated. When working with rainfall triggered landslides, two factors must be considered. The first one is the probability that a threshold will be exceeded. Secondly is the probability that a landslide occurs given the exceedance.

As it has been done in Jaiswal & Van Westen (2009), the annual exceedance probability (AEP) of a rainfall (threshold) $P[R>R_T]$ is determined using a Poisson probability model (explained in previous sections). Hence, the exceedance probability or the probability of experiencing one or more rainfall events during time t is given by:

$$P[N(t)\geq 1]=1-e^{-t/\mu}$$

Equation 4-5

where μ is the mean recurrence interval between successive rainfall events.

On the other hand, the probability that a landslide occurs when the rainfall threshold has been exceeded $P[L|R>R_T]$ is given by the true positive rate in the ROC analysis.

Therefore, the temporal probability of failure will be $P[R>R_T] \times P[L|R>R_T]$.

4.7 Results

First of all, the relation between accumulated rainfall-cumulative period has been analysed (Table 4-7). Cumulative periods ranging from 3 to 61 days with accumulated rainfall from 60mm to 290 mm, respectively, have been used. All histograms prepared to evaluate such

thresholds can be found in Annex 5: Accumulated rainfall.

Table 4-7: ROC analysis for accumulated rainfall. Several thresholds with different cumulative days have been analysed.

Cumulative Period (days)	Accumulated rainfall (mm)	fp rate	tp rate
3	60	0.73	1.00
3	80	0.43	0.50
5	130	0.19	0.25
5	100	0.43	0.67
10	100	0.73	0.92
10	142	0.22	0.58
20	150	0.59	0.92
20	208	0.11	0.42
30	165	0.76	1.00
30	202	0.35	0.75
35	248	0.30	0.50
40	190	0.78	0.83
40	252	0.30	0.58
45	220	0.54	0.83
45	295	0.22	0.50
61	290	0.41	0.58

A first ROC analysis has been conducted with accumulated rainfall (Figure 4-24). Results are not very satisfactory as all different combinations are located close to the line X=Y what means that these rainfall events occurred in some years with and without landslide reactivations.

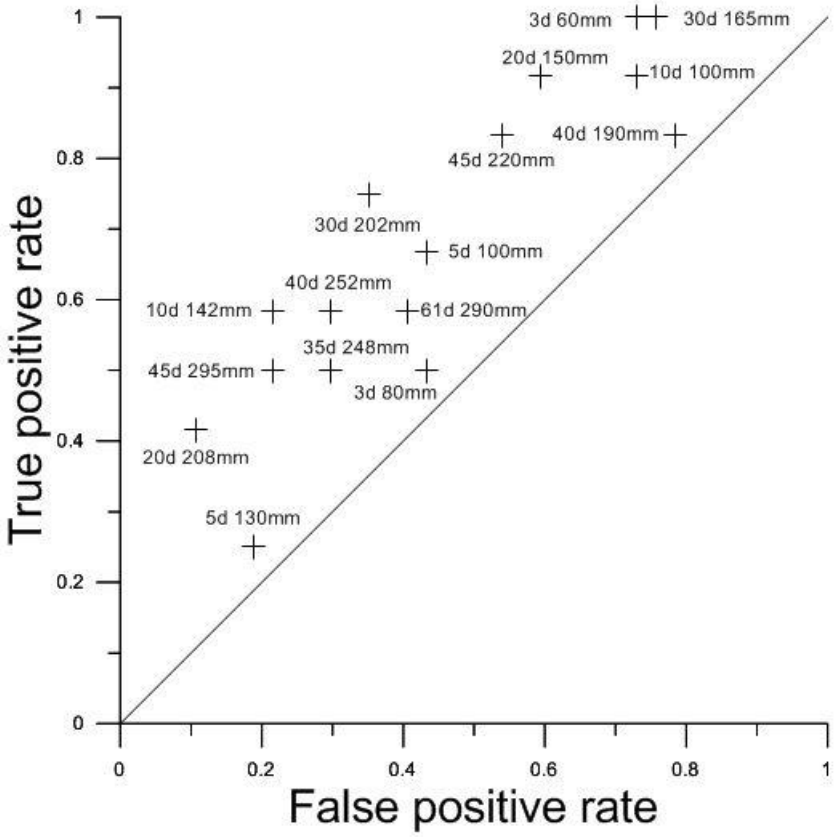

Figure 4-24: Roc analysis for accumulated rainfall.

On the other hand antecedent rainfall thresholds have also been defined (Table 4-8). In such a case, more variability exists, since a minimum triggering daily rainfall must be defined. All histograms prepared to evaluate such thresholds can be found in Annex 6: Antecedent rainfall.

Table 4-8: ROC analysis for antecedent rainfall. Several thresholds with different minimum triggering daily rainfall and cumulative period have been analysed.

Minimum triggering Daily Rainfall (mm)	Cumulative Period	Antecedent Rainfall(mm)	fp rate	tp rate
20	20 d	180	0.19	0.58
20	25 d	180	0.30	0.75
45	25 d	120	0.32	0.67
40	30 d	170	0.22	0.67
40	35 d	200	0.16	0.58
40	40 d	170	0.38	0.83
40	40 d	200	0.24	0.67
43	40 d	170	0.35	0.67
43	40 d	200	0.16	0.50
40	2 months	200	0.38	0.58
45	2 months	191	0.30	0.58
48	2 months	121	0.43	0.67
48	3 months	121	0.51	0.50

Better results can be seen as values obtained in the ROC graph are located closer to the point (0,1) than in the previous analysis (Figure 4-25). However, most of them show a big percentage of false alarms (fp rate).

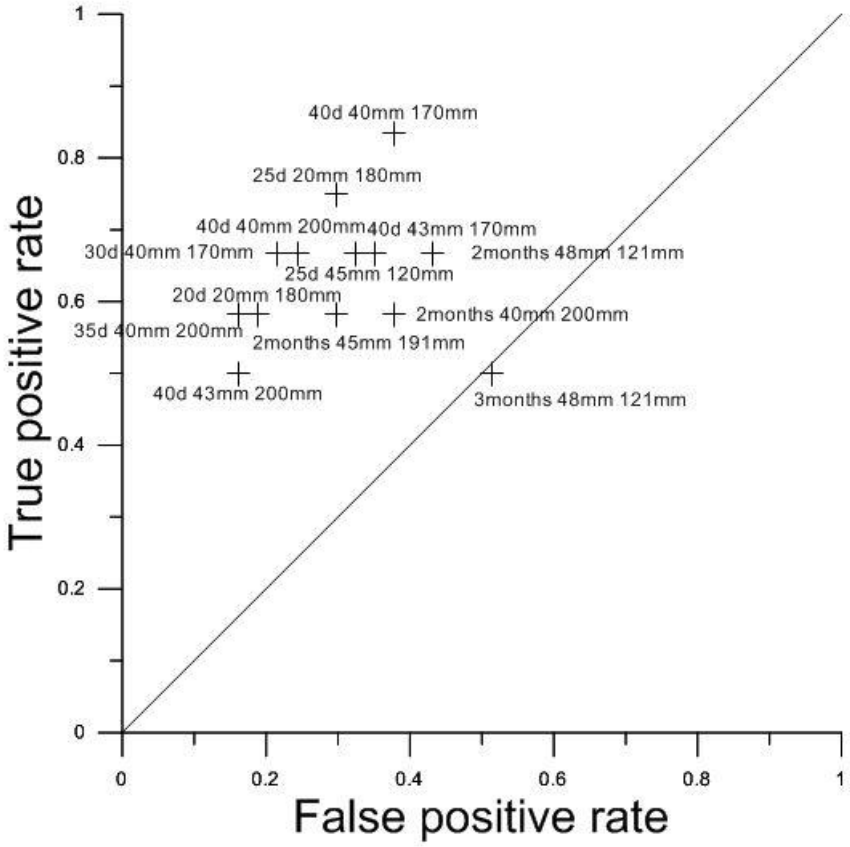

Figure 4-25: Roc analysis for antecedent rainfall.

Considering the antecedent rainfall, a last analysis, as the one done by Corominas & Moya (1999), has been carried out, since landslides are located in the same materials. Daily triggering rainfall higher than 30 mm (Figure 4-26) and 40 mm (Figure 4-27) and their respective antecedent rainfalls until six weeks have been used. It has been considered these two values of daily precipitation, since in Figure 4-25 best results are given by triggering rainfalls between 20 mm and 40 mm. However, 20 mm seems not to be a sufficient daily triggering rainfall as either fp rate is too much high when antecedent rainfall is very low, or tp rate is too much low when antecedent rainfall is higher (Table 4-8).

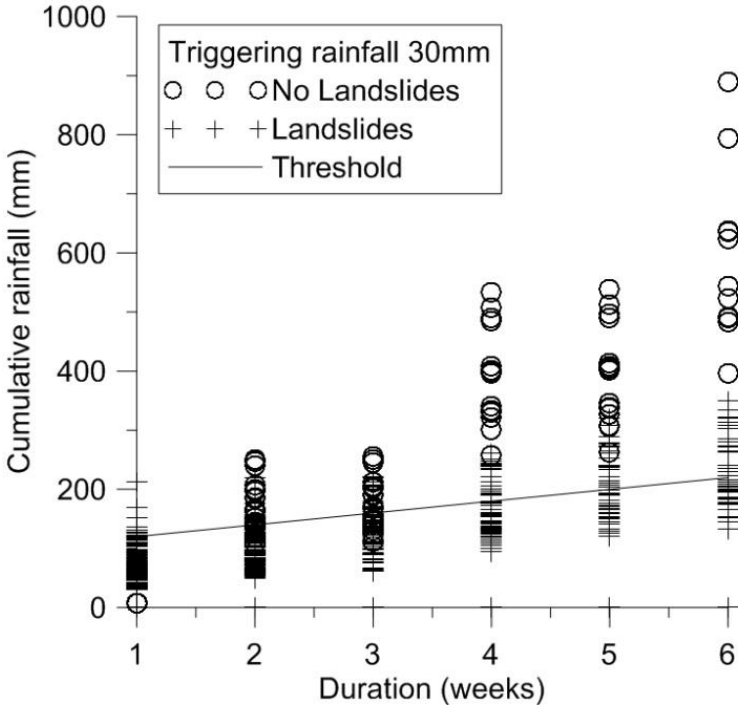

Figure 4-26: Threshold proposal for a 30 mm-daily-triggering rainfall and a six-week-antecedent rainfall.

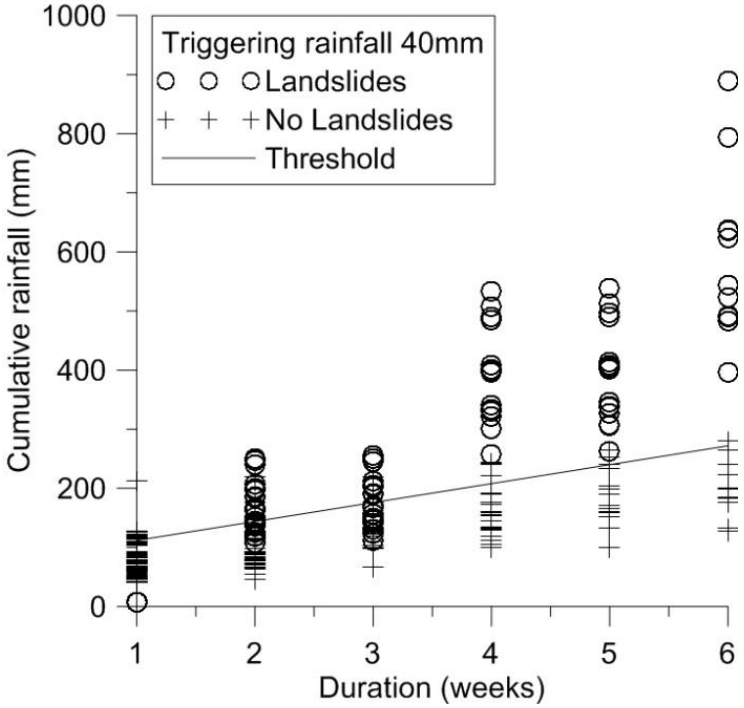

Figure 4-27: Threshold proposal for a 40 mm-daily-triggering rainfall and a six-week-antecedent rainfall.

In such a case, it has been considered that if in two consecutive weeks, the accumulated rainfall has not been higher than 10 mm, the previous precipitation has no effect in terms of soil saturation and it is not considered. This threshold has been defined as the best lineal relationship between antecedent rainfall (Ac) and weeks (D) that separates years with landslides and years

where no landslides occurred. Thus, this threshold is more restrictive and permits to evaluate a combination of rainfalls instead of a single one.
Results have been tested by means of ROC analysis (Figure 4-28). It shows that the best relation between false positive and true positive rates belongs to the 30 mm daily-triggering rainfall with Ac=20D+100 and a fp rate of 0.2 and a tp rate of 0.83 (Table 4-6).

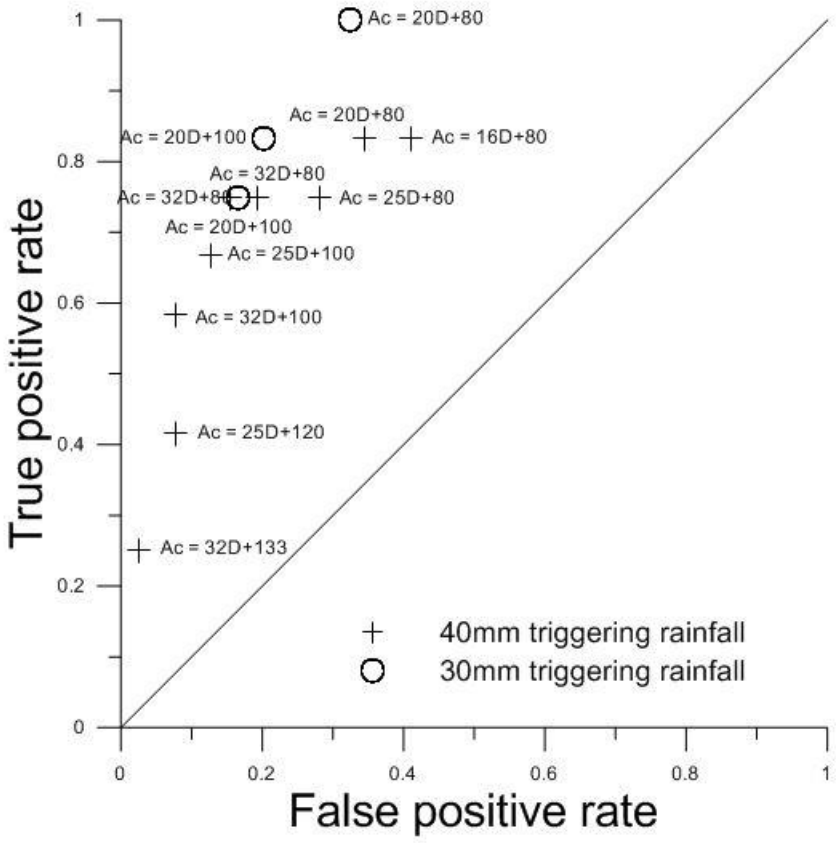

Figure 4-28: Roc analysis for antecedent rainfall similar to Corominas & Moya (1999).

Table 4-9: ROC analysis for antecedent rainfall-duration relationship. Several thresholds has been considered with a minimum triggering daily rainfall of 40 mm or 30 mm

	Threshold	fp rate	tp rate
Minimum triggering Daily Rainfall of 40mm			
	Ac = 32D+133	0.03	0.25
	Ac = 32D+100	0.08	0.58
	Ac = 32D+80	0.19	0.75
	Ac = 25D+120	0.08	0.42
	Ac = 25D+100	0.13	0.67
	Ac = 25D+80	0.28	0.75
	Ac = 20D+100	0.15	0.75
	Ac = 16D+80	0.41	0.83
	Ac = 20D+80	0.35	0.83
Minimum triggering Daily Rainfall of 30mm			
	Ac = 20D+100	0.20	0.83
	Ac = 32D+80	0.16	0.75
	Ac = 20D+80	0.32	1.00

Temporal probability of failure has been evaluated within the interval from which dendrological and rainfall data are available (i.e. from 1950 to 2003) with exception of these years with no data available (1964, 1965, 1966, 1967, 1997, 1998, 2000 and 2001). Therefore, a total of 45 years have been considered. In that period, the threshold defined as the best one to explain the different landslide events (Ac= 20D+10) has been reached or exceeded 71 times. According to Equation 4-5, the AEP of the threshold ($P[R>R_T]$) for a period of one year is 0.79. On the other hand, the probability of having a landslides when the threshold is reached ($P[L|R>R_T]$) is given by the Fp rate (0.83). Finally, temporal probability of landslide initiation is the product of the two previous mentioned parameters ($P[R>R_T] \times P[L|R>R_T]$) being 0.66 (Table 3-5).

Table 4-10: Temporal probability of landslides.

Threshold equation	Number of times the threshold exceeded	$P[R>R_T]$	$P[L|R>R_T]$	Temporal Probability $P[R>R_T] \times P[L|R>R_T]$
Ac= 20D+100	71	0.79	0.83	0.66

4.8 Conclusions

Assessment of rainfall thresholds responsible for landslide failures by means of ROC analysis permits to carry out an objective selection of these thresholds and optimise the analysis procedure since it is not an easy task attempt to establish the landslide causing rainfall event when the exact date of the failure is unknown and the rainfall data incomplete. Both rates obtained (tpr y fpr) are easy interpretable.

On the other hand, landslides in Tremp Basin do not present a clear response to the rainfall events. The best relationship has been obtained with daily triggering rainfall followed by an antecedent rainfall. The equation with best agreement is Ac=20D+100 for a minimum daily

triggering rainfall of 30 mm. However, some episodes exceeded such a threshold in periods with no reactivation. It suggests that the threshold must be improved or some failures have not been identified. Furthermore, the large amount of missing data in the closest gauge station (Bon Repòs) could affect the reliability of the estimated pluviometric data from the other gauges although the coefficient of determination of the polynomial adjustment (Equation 4-2) was R^2=0.5499 (not bad for hydrological approaches).
To conclude, an annual probability of occurrence of 0.66 has been determined as a first input data for quantitative landslide hazard assessment in the Tremp Basin.

4.9 Future research work

-More landslides should be analyse again in order to obtain more reactivation periods which could explain some years where thresholds have been exceeded and any failures were identified.
-Triggering factors such as landslide foot erosion by torrents should be also considered since some of them present erosion in the bottom.
-Tree-ring analysis in past failures close to rainfall gauges with complete data should be carried out within the Tremp basin. It would permit to work with more reliable rainfall data.
-A threshold for each landslide and its respective temporal probability of reactivation should be evaluated.
-A comparison of temporal probability between different landslides could be carried on in order to assess its spatial variation.
-Simply landslide database should be created by authorities when roads are affected by failures. It would be an extremely useful tool when finding out exact dates of movements as well as for ROC analysis validation.

Chapter 5

5 Frequency of first-time failures on intact slopes

5.1 Introduction

Magnitude-frequency (MF) relationships are required for the quantitative assessment of landslide hazard. To this end, the probability of occurrence of landslides of a given magnitude (which is often expressed in terms of landslide area) must be determined.

When dealing with landslides, the distinction between the reactivation of existing (dormant) landslides and first-time slope failures must be established. Dormant landslides often display gentle morphologies and residual strength conditions. Conversely, intact slopes are expected to mobilize peak strength conditions and form steep topographic profiles.

As stated in chapter 3, the analysis of intact slopes can be calculated by means of deterministic or probabilistic analysis.

Deterministic, also known as physically-based methods, which evaluate the slope stability based on the calculation of the Safety Factor (FS), have been widely used as a tool for landslide hazard assessment (e.g. Wu and Abdel-Latif., 2000; Frattini et al., 2004; Baum et al., 2005; Godt et al., 2008). They couple infinite slope stability models with hydrological models. Both models can be more or less complex including either steady-state or transient conditions (Baum et al., 2008; Montgomery and Dietrich, 1994). Usually, these deterministic models are two-dimensional, however, in the last years some efforts have been directed towards three-dimensional slope stability models. All of them are implemented within a GIS which calculates the FS for each pixel: Marchesini et al. (2009) implemented an algorithm which defines the 3D geometry of the sliding surface of rotational slides. Geotechnical parameters were estimated at regional scale from geological maps. Jia et al. (2012) evaluated the minimum FS within each Slope Unit (SU) using a Monte-Carlo simulation. It was calculated with a GIS-based 3D limit equilibrium model. Mergili et al. (2014) implemented a 3D slope stability model in GRASS GIS software which aimed at calculating the FS of the most critical slip surface for each cell. As already noted in the work of Mergili et al. (2014), some of these models incorporate a probabilistic package that calculates the probability of failure (probability of FS being less than 1) by evaluating the different slip surfaces as well as the uncertainty in the input values (e.g. Pack et al., 1998; Rossi et al., 2013).

This probability of failure, also called susceptibility index, may be turned into annual probability by correlating it with the temporal frequency of first-time slope failures.

As mentioned in chapter 3, the susceptibility is pixel-based and therefore, the mentioned methods permit to identify the unstable pixels under some given conditions. Nevertheless, there does not exist any methodology to define failures of variable magnitude (area), i.e. considering the number of neighbouring pixels that simultaneously fail leading to a rupture of higher dimensions than the pixel itself.

In Figure 5-1, A a mapped landslide with the crown scar (red line) and the direction of the movement (black arrows) is shown. In Figure 5-1, B the susceptibility of the mapped landslide has been calculated by means of a deterministic model called SINMAP (Pack et al., 2005).

Since the susceptibility has been calculated in each pixel, a great heterogeneity of susceptibility degrees exist within the landslide, mostly in the central part marked with a blue arrow.

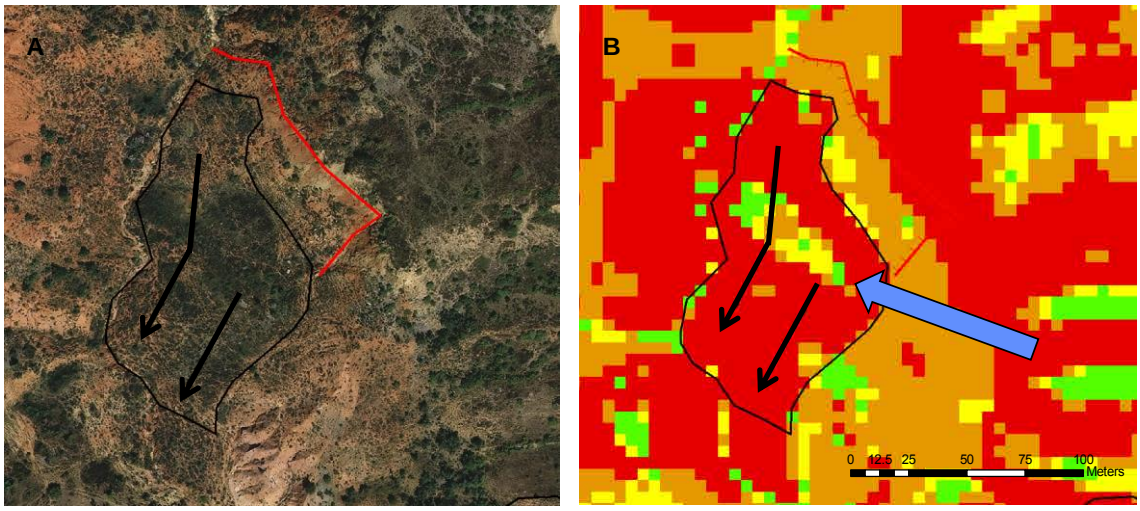

Figure 5-1: A: Orthophoto of a mapped landslide with the scar crown in red and the direction of the movement marked with black arrows. B: Reclassified susceptibility of the same mapped landslide using a deterministic model (SINMAP). It calculates the susceptibility in each pixel. In the central part of this large landslide (marked with a blue arrow) there exists an area with different susceptibility degrees.

On this basis two main challenges appear: 1) The characterization of the landslide susceptibility when it contains several pixels and 2) the obtaining of the susceptibility of intact slopes and prediction of first-time failures magnitude (area).
To this end, areal units larger than the pixel size must be used to evaluate the hazard (Xie et al., 2003). They will be treated as a unique entity.
These mapping units should divide the terrain in portions that have a set of common properties, different from the adjacent ones, across definable boundaries (Hansen, 1984). According to this definition, Guzzetti et al. (1999) defined the following mapping units among others:

-Terrain units
-Slope units
-Topographic units

It has been assumed by the geomorphologists that both geological and geomorphological features properly describe the boundaries resulting from the relationship between materials, forms and processes. Thus, terrain units are portions of the terrain with similar geological and geomorphological features.
Slope units (SUs) are the portion of terrain contained between the drainage (or valley) and divide lines (Carrara, 1988; Carrara et al., 1991) (Figure 5-2). These SUs can be later subdivided into hydro-morphological units called topographic units which are based on terrain gradient (Van Den Eeckhaut et al., 2009).
Usually, landslides are given downslope in areas with a certain gradient. Thus, as a first proxy, a landslide generation will be constrained between the highest and the lowest part for a given slope, i.e., between the divide and the drainage line, respectively. Therefore, SUs seem to be the most appropriate terrain partitioning for landslide hazard assessment (Xie et al., 2003).

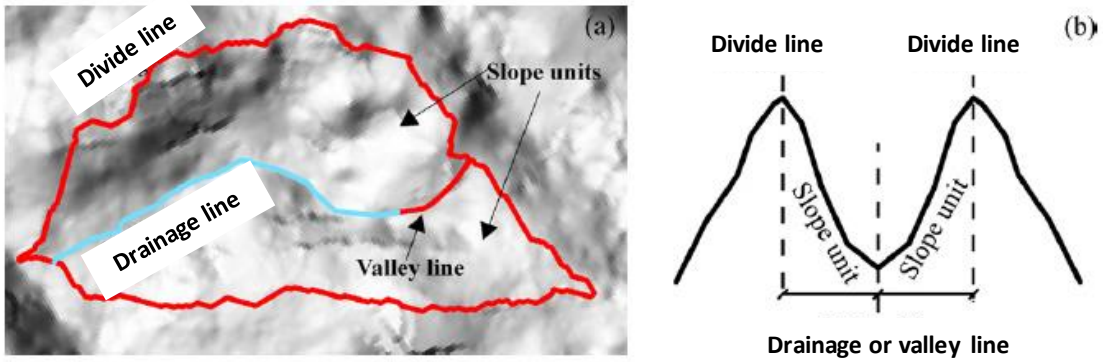

Figure 5-2: SUs obtained from a catchment: a) Planar view b) section view (modified from Jia et al. 2012).

The SU is defined from the catchment, which has been generated using a drainage network. Such a network has been determined by imposing that only pixels whose flow accumulation values are greater than a given threshold belong to the drainage line. This threshold is also known as Contributing Area Threshold (CAT). Conversely, pixels with flow accumulation value smaller than the CAT will not be considered as part of the drainage line. Thus, for a smaller CAT, the drainage line would follow the valley line shown in Figure 5-2, a.
Alvioli et al. (2014, 2015) considers the slope aspect of each portion comprised between the drainage and the divide lines in order to generate more homogeneous SUs.
Although SUs have been used by some authors (e.g. Giles, 1998; Guzzetti et al., 1999; Xie et al., 2003; Van Den Eeckhaut et al., 2009; Jia et al., 2012), their automatic delineation is not straightforward since the CAT necessary to extent the drainage line until the top of the catchment (red line named Valley line in Figure 5-2) should be 0. Consequently, all the pixels of the DEM would be considered as part of the drainage network.
Two alternative methodologies have been proposed to delineate SUs: Xie et al. (2003) used the Arc Hydro tool (David 2002) to draw the watershed. For the drainage lines, they reversed the DEM and calculated again the divide lines as mentioned before. In that case, when reversing the DEM, the drainage lines, which are supposed to be the low value points, become the high values and the watersheds are calculated again. Their boundaries correspond to the initial drainage lines. On the other hand, Alvioli et al. (2014, 2015) consider the catchment size as well as the generated SUs aspect (the maximum aspect variance to be accepted within each slope unit). It is important to highlight that there is no unique SU size. It will depend on the scale (regional, detailed, etc.) and the DEM resolution: SUs are delimited using the information provided by the DEM. If it is not capable to define small catchments with sufficient precision, small-sized SUs will not be properly defined.

5.1.1 Susceptibility assessment by means of slope units

When working with mapping units (e.g. SUs), it is not straightforward to evaluate their potential of failure: the susceptibility calculated by means of the deterministic model (SINMAP) at pixel scale must coincide with SU scale. In that case, the assignment of a unique susceptibility at each SU may be a feasible approach: for a given SU, the average susceptibility will be used. Consequently, the area of the SU may be used as a proxy for the magnitude.
This approach is shown in Figure 5-3: Two SUs have been delineated (SU1 and SU2). In figure A the susceptibility obtained at each pixel by means of a deterministic model has been calculated. Since the failures observed in the study area are larger than the pixel size, the

resulting susceptibility has been grouped according to the average class within each SU (Figure 5-3, B): Pixels with high (orange) and very low (green) susceptibility are grouped into the same class.
As it will be seen later, there is no unique SU size, so that the average susceptibility as well as the magnitude of the potential failures are still depending of the mapping unit size (SU instead of pixel) (Domènech, 2011).
Additionally, as the SU may not be equally affected by the instability process and show different stability degrees, we may not be in the safety side: in the Figure 5-3 A, a few pixels presenting high susceptibility (orange) are converted into low-susceptibility pixels (yellow).

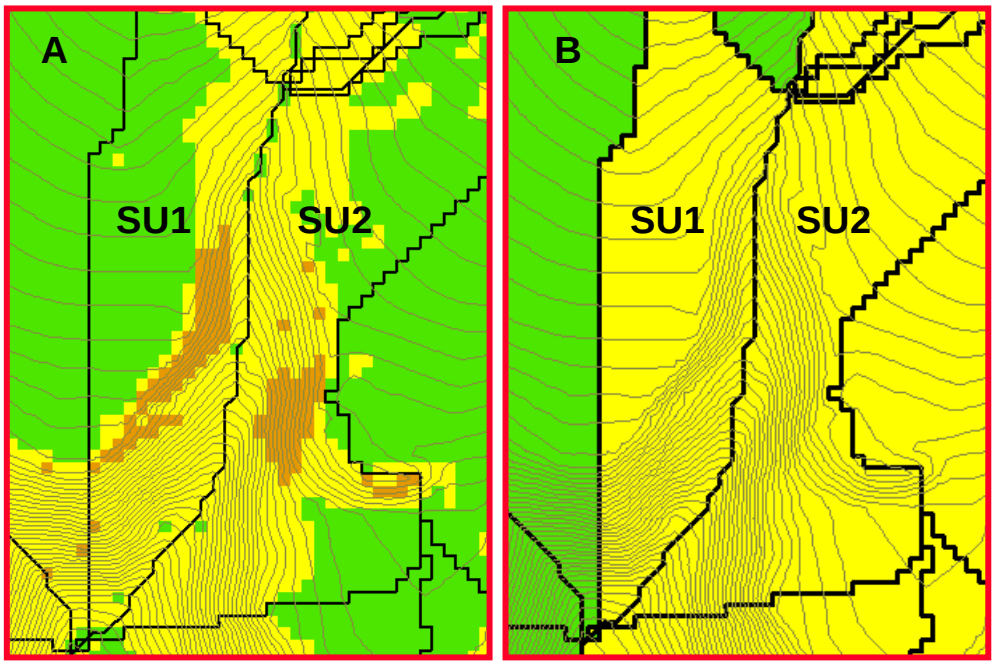

Figure 5-3: Two SUs are shown (SU1 and SU2). A: pixel-based susceptibility. B: SU-based susceptibility.

Finally, if the extension of the potential failure is smaller than the SU (Figure 5-4, red pixels pointed out with a blue arrow), the area of the latter is not a proper proxy of the future slope failure magnitude. Hence, an alternative procedure is required to evaluate more accurately the area of the potential failure, which is described in the following sections.
The objective of this chapter is to evaluate the potential for large slope failures (rotational slides and earthflows) of the intact slopes applying a deterministic model in the Barcedana Valley (Eastern Pyrenees, Spain) and using the area of the most susceptible cell-clusters as a proxy of the magnitude.

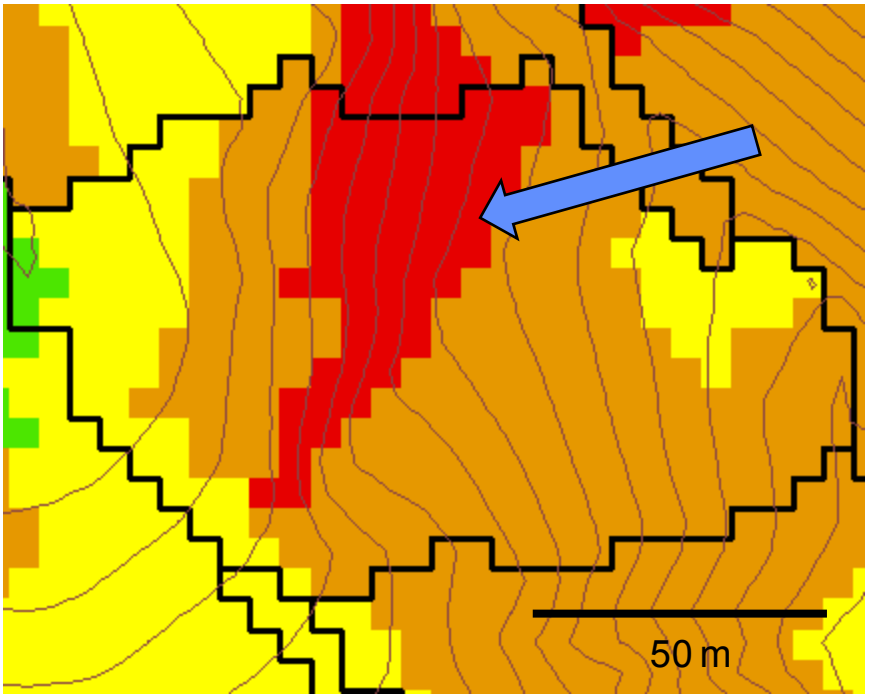

Figure 5-4: Red pixels (pointed out with a blue arrow) define a high susceptible region to failure smaller than the SU. Thus, the area of the latter would not be a good proxy for the magnitude of this potential failure.

5.2 Methodology

First, the stability index is calculated for each pixel using a slope stability model coupled with a hydrological model (SINMAP). These values are reclassified into four susceptibility classes. Then, the frequency of slope failures for each susceptibility class is calculated based on the observations of the first-time failures that occurred in the past. They have been obtained from the landslide field inventory map and from the observed orthophotos between 1956 and 2013 (Annex 7: First-time failures map and Table 5-7).

To evaluate the magnitude (area) of the potential failures a new methodology is presented. It comprises the automatic aggregation of adjacent pixels showing a similar stability index and located within the same SU. Finally, the MF matrix is prepared as well as the landslide hazard map.

5.2.1 Susceptibility assessment using a deterministic model

A first assessment of the susceptibility in the Tremp Basin, where the Barcedana Valley is located, was carried out by Abancó et al. (2009). They compared the susceptibility assessment accuracy obtained with three different techniques (two heuristic and one deterministic method). The deterministic model SINMAP (Stability Index MAPping) (Pack et al., 1998), which showed the best results, has been employed.

The SINMAP software was developed to analyse landslide susceptibility at regional scale in a GIS environment (Pack et al., 1998). It is based upon the infinite slope stability model coupled with a simple hydrological model using TOPMODEL (Beven and Kirby, 1979). This hydrological model calculates the topographic wetness index (*w)* for each pixel of a raster and the FS by using the Mohr-Coulomb criteria:

$$SI = \frac{C_{dl} + cos\Theta \left[1 - w\frac{\rho_w}{\rho_s}\right] tan\emptyset}{sin\Theta}$$

Equation 5-1

in which C_{dl} is the adimensional cohesion, ρ_w [kg/m^3] is the water density, ρ_s [kg/m^3] is the soil density, $\emptyset$ [º] is the friction angle, and Θ [º] is the slope angle. The adimensional cohesion is given by:

$$C_{dl} = \frac{C}{h\,\rho_s g}$$

Equation 5-2

in which C [N/m^2] is the soil cohesion, and g [9.81m/s^2] is the acceleration of gravity.

The hydrological model that calculates the wetness index (w) includes several considerations:

1-The surface runoff follows the topographic gradient. It allows calculating the specific catchment area at each pixel as:

$$a = A/b$$

Equation 5-3

in which a is the specific catchment area [m], A is the contributing area [m^2], and b is the unit contour length [m] (Figure 5-5).

2- The lateral discharge (q) at each point is in equilibrium with a steady state recharge, R [m/h].
3- The capacity for lateral flux at each point is given by:

$$Tsin\Theta$$

Equation 5-4

where T [m^2/h] is the soil transmissivity defined as the product of the permeability, K [m/h] and the soil thickness [m].

Considering assumption 1 and 2, the lateral discharge is:

$$q = Ra$$

Equation 5-5

where q is the lateral discharge [m^2/h].

Considering assumption 3, the wetness index (*w),* is calculated as follows:

$$w = \min(\frac{Ra}{Tsin\Theta}, 1)$$

Equation 5-6

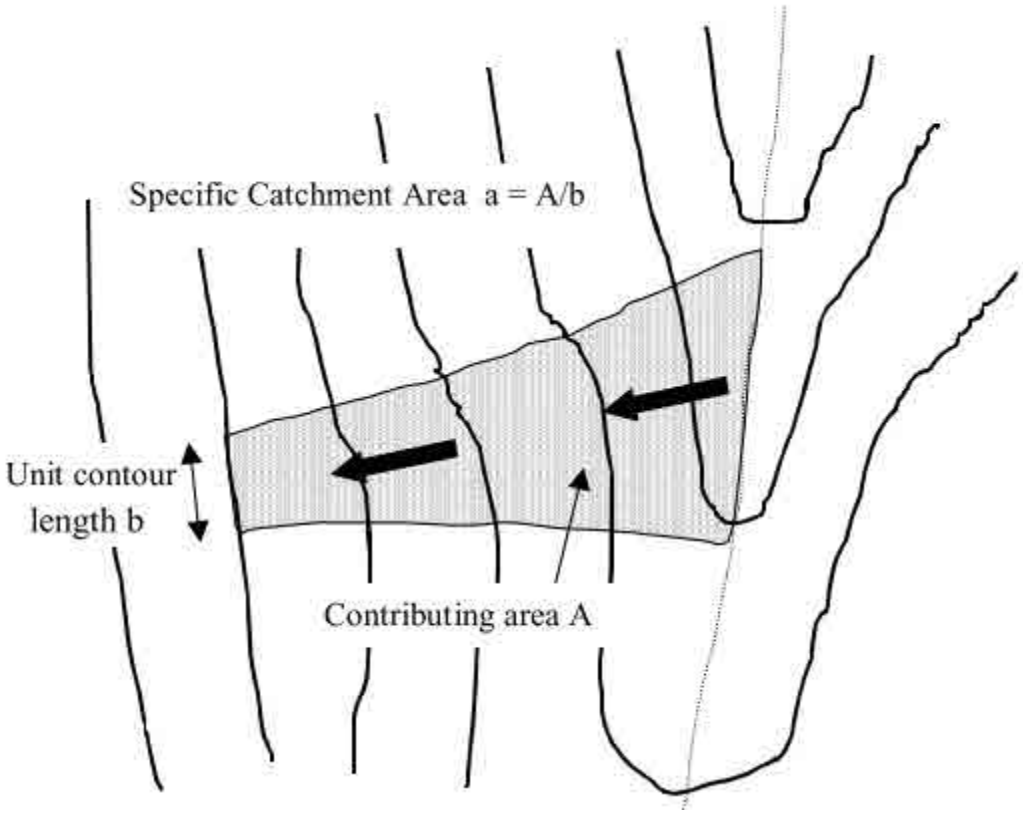

Figure 5-5: Definition of the specific catchment area (Pack et al., 1998).

Finally, the adimensional cohesion (C_{dl}), the friction angle (∅) as well as the ratio T/R (hydrological conditions) are selected. SINMAP does not permit to introduce a unique value, but a range of parameters, in case they are not constant or the exact value is not well constrained. Input parameters, which are shown in more detail in the following sections, have been obtained from different works carried out in the study area. Then, the code calculates the probability of failure according to the FS. It is named Stability Index (SI). SI values are finally grouped into four susceptibility classes.

5.2.2 Probability of (first-time) failure in intact slopes and validation of the model

The frequency of first-time failures for a given susceptibility class (F_i in Equation 3-1) has been calculated using the inventory of failures identified in the field and by means of orthophotos (Annex 7: First-time failures map).

The landslide inventory has been prepared by means of direct mapping in the field as well as by the analysis of the set of orthophotos obtained from the Geological Survey of Catalonia (ICGC, 2015) which covered a period of 57 years (from 1956 to 2013). More information about the landslide mapping can be found in chapter 3.

From the landslide inventory, it has been calculated the number of first-time slope failures

located within each susceptibility class (N_i) over the total number of first-time slope failures (N_T). Then, this ratio has been divided by the observed period of time (P) and normalised by the area occupied by each susceptibility class (A_i). This frequency has been expressed in terms of number of first-time slope failures per year and per square kilometres:

$$F_i = \frac{\frac{N_i}{N_T}}{P \times A_i}$$

Equation 5-7

In order to validate the model, F_i has been used. Thus, the more susceptible a class is, the higher the ratio should be.

5.2.3 Magnitude of first-time slope failures

The magnitude of the potential failures has been evaluated considering the size of the susceptible cell clusters showing the same susceptibility class and located within the same SU.

5.2.3.1 Delineation of the Slope units

The SUs of each catchment are obtained using the procedure created by Alvioli et al. (2014, 2015) from the Istituto di Ricerca per la Prevenzione Idrogeologica (CNR-IRPI) located in Perugia (Italy).

They adopted an iterative approach using a DEM of the study area, and introduce a set of input parameters, by means of a publicly accessible Web Processing Service (WPS) in QGIS (QGIS Development Team, 2015). The resulting SUs are delineated (Figure 5-6). A more recent version of the code for use in GRASS GIS (Neteler and Mitasova, 2008) is available at http://geomorphology.irpi.cnr.it/tools/slope-units (Alvioli et al., 2015). The input parameters are:

1) CAT (m^2): Minimum value of flow accumulation for accepting a pixel to be considered as part of the drainage network. Such a network will be used for the latter generation of the basins.
2) Number of iterations [N] in which the initial CAT will be reduced.
3) Reduction factor [RF]: Reduction of the initial CAT at each iteration. It works as follows:

$$CAT_{p+1} = CAT_p - \frac{CAT_p}{RF} \qquad (p = 0, \dots, N)$$

Equation 5-8

in which CAT_p is the initial CAT at step p.

4) Aspect circular variance [circularvariance]: Maximum aspect variance to be accepted within each SU to not be further partitioned.
5) Minimum area [areamin] (m^2): Minimum value of the SUs.

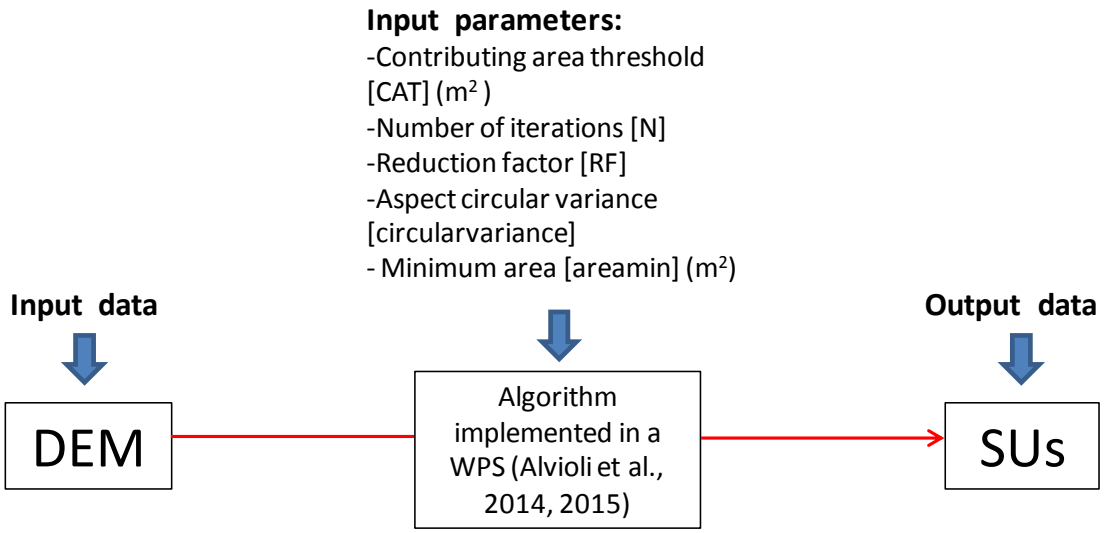

Figure 5-6: Schematic procedure developed by Alvioli et al. (2014, 2015). Input parameters are introduced into the algorithm by means of the WPS to be later applied to the DEM. Finally, resulting SUs are delineated.

The method consists in delineating slope units that fulfil simultaneously two criteria. The first one is a hydrological criterion; each slope unit is a half-basin obtained with the CAT at a given iteration step, according to Equation 1-8. The second one is a constraint on aspect direction of the slope units, which, on average, is required to be homogeneous enough within each slope unit. The two constraints are implemented into the numerical code in such a way that they fulfil the general definition of slope units, i.e. maximization of inter-unit homogeneity and extra-unit inhomogeneity.

Once the DEM is uploaded, the terrain is first partitioned into half-basins using an input CAT using the r.watershed algorithm of GRASS GIS (Neteler and Mitasova, 2008). Those units with an aspect's standard deviation smaller than the circularvariance and an area larger than the areamin are marked as SU. The remaining part of the study area is later partitioned in the next iteration but using a smaller CAT according to Equation 5-8. Thus, smaller half-basins will be delineated and some of them will be marked as SUs following the procedure mentioned above. The remaining part will be partitioned again until either no area is left as unclassified or the number of iterations is reached. Finally, a further iteration is performed to aggregate those small areas. It is based on the aspect values and a violation on the hydrological criterion may be produced.

In the Figure 5-7, the process developed by Alvioli et al. (2014, 2015) is shown.

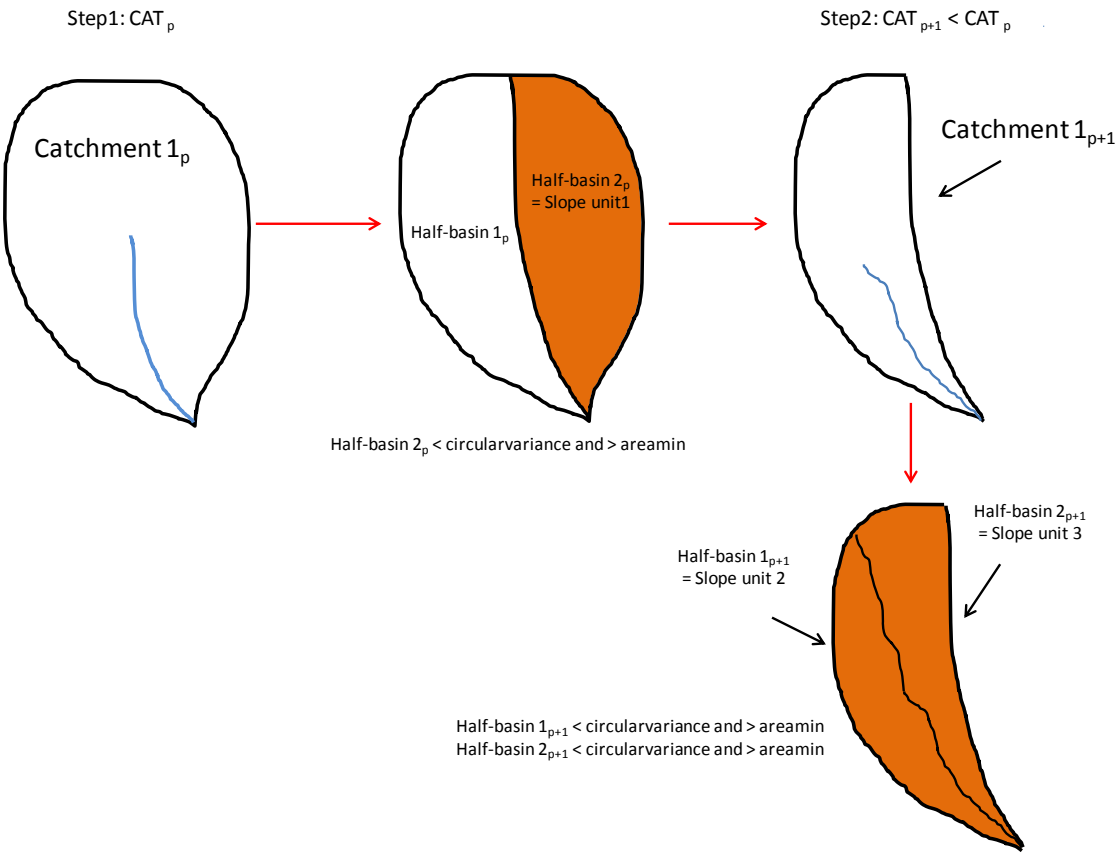

Figure 5-7: Schema of the SUs generation applying the procedure created by Alvioli et al. (2014, 2015). In the step 1, the Half-basin 1_p has an aspect standard deviation higher than the input value and an area smaller than the minimum area. Therefore, it is not delineated as SU and a second iteration is needed using a CAT_{p+1} smaller than in the previous step (CAT_p).

To this end, several SUs of different sizes have been generated. Input values have been modified following the advices of Dr. Alvioli.

In order to analyze the interaction between the delineated SUs and the inventoried landslides, the ratio of landslides cut by SUs has been calculated. This ratio considers the number of the inventoried landslides cut by the SUs over the total number of inventoried landslides (N). It is assumed that the most suitable combination of input parameters to generate the SUs will be the one respecting the boundaries of the mapped landslides, i.e. the combination of input parameters that minimizes this ratio. However, large SUs with ratio equal to 0 are not the most suitable since they do not properly delineate the slopes present in the study area. Therefore, the minimization of this ratio gives a first proxy of the SUs size, which will later be visually checked in the map as well as in the field if needed.

First of all, some trials have been carried out using a CAT of 10^6 m^2 and circularvariance of 0.1. Usually, the areamin for the SUs is 10 o 20 times smaller than the CAT (oral communication of Dr. Alvioli); hence a first value of 10^5 m^2 has been used. RF and N have been modified: for values of RF higher than 20 no differences exist; concerning N, it has been observed that for 100 or more iterations the final result is the same (Table 5-1).

Table 5-1: Values for SU generation and ratio of landslides cut by SUs. CAT values of 10^6 m^2, aspect circular variance of 0.1 and minimum area values 10 times smaller than the CAT have been used.

SU	Contributing area threshold [CAT] (m^2)	Reduction factor [RF]	Aspect circular variance [circularvariance]	Minimum area (m^2) [areamin]	Number of iterations [N]	Ratio of landslides cut by SUs
1	10^6	10	0.1	10^5	10^6	0.28
2	10^6	10	0.1	10^5	100	0.28
3	10^6	10	0.1	10^5	10^{10}	0.28
4	10^6	2	0.1	10^5	10^{10}	0.28
5	10^6	3	0.1	10^5	10^{10}	0.28
6	10^6	4	0.1	10^5	10^{10}	0.28
7	10^6	5	0.1	10^5	10^{10}	0.28
8	10^6	5	0.1	10^5	10^{20}	0.28
9	10^6	6	0.1	10^5	10^{10}	0.28
10	10^6	7	0.1	10^5	10^{10}	0.28
11	10^6	8	0.1	10^5	10^{10}	0.28
12	10^6	12	0.1	10^5	10^{10}	0.28
13	10^6	15	0.1	10^5	10^{10}	0.28
14	10^6	20	0.1	10^5	10^{10}	0.29
15	10^6	40	0.1	10^5	10^{10}	0.31

Thereafter, CAT, RF and areamin have been fixed and circularvariance values ranging from 0.05-0.7 have been used. It has been observed that this input parameter is extremely sensitive for values between 0.1 and 0.2 (SU no. 4 and no. 18, respectively) (Table 5-2).

Table 5-2: Values for SU generation and ratio of landslides cut by SUs. CAT, RF and areamin have been fixed. Different values of circularvariance have been used.

SU	Contributing area threshold [CAT] (m^2)	Reduction factor [RF]	Aspect circular variance [circularvariance]	Minimum area (m^2) [areamin]	Number of iterations [N]	Ratio of landslides cut by SUs
4	10^6	2	0.1	10^5	10^{10}	0.28
17	10^6	2	0.05	10^5	10^{10}	0.28
18	10^6	2	0.2	10^5	10^{10}	0.18
19	10^6	2	0.5	10^5	10^{10}	0.14
20	10^6	2	0.7	10^5	10^{10}	0.14

Then, several trials reducing CAT to 10^5 have been performed. RF of 2, 10 and 15 and circularvariances from 0.1 to 0.5 have been combined with areamin values equal, 10, 20 and 100 times smaller than CAT. RF has been identified as the less influent input parameter followed by the areamin and the circularvariance, which is the most sensitive one (Table 5-3).

Table 5-3: Values for SU generation and ratio of landslides cut by SUs. CAT values until 10^5, RF of 2, 10 and 15, circularvariance from 0.1 tot 0.5 and areamin equal, 10, 20 and 100 times smaller than CAT have been used.

SU	Contributing area threshold [CAT] (m^2)	Reduction factor [RF]	Aspect circular variance [circularvariance]	Minimum area (m^2) [areamin]	Number of iterations [N]	Ratio of landslides cut by SUs
24	10^6	2	0.1	10^4	10^{10}	0.47
25	10^5	2	0.1	10^5	10^{10}	0.22
26	10^6	2	0.1	10^5	10^{10}	0.28
27	10^7	15	0.1	10^5	10^{10}	0.30
28	10^5	15	0.1	10^4	10^{10}	0.51
29	10^5	15	0.2	10^4	10^{10}	0.31
30	10^5	15	0.2	$5*10^3$	10^{10}	0.34
31	10^5	2	0.2	10^4	1000	0.31
32	10^5	10	0.2	10^4	1000	0.31
33	10^5	10	0.3	10^4	1000	0.30
34	10^5	15	0.3	$5*10^3$	10^{10}	0.33
35	10^5	15	0.5	$5*10^3$	10^{10}	0.33
36	10^5	15	0.4	10^4	1000	0.30

Finally, RF of 10 has been set. CAT values of 10^5 and 10^6 have been employed again with areamins values about 10 or 20 times smaller than CAT, and a circularvariance ranging from 0.1 to 0.5. Again the most sensitive value is the circularvariance, especially for values between 0.1 and 0.2 (Table 5-4).

Table 5-4: Values for SU generation and ratio of landslides cut by SUs. RF of 10, CAT values of 10^5 and 10^6 and areamins 10 or 20 times smaller than the CAT have been used. Circular variance values ranging from 0.1 to 0.5 have been used.

SU	Contributing area threshold [CAT] (m^2)	Reduction factor [RF]	Aspect circular variance [circularvariance]	Minimum area (m^2) [areamin]	Number of iterations [N]	Ratio of landslides cut by SUs
37	10^5	10	0.5	10^4	1000	0.30
39	10^6	10	0.2	10^5	10^{10}	0.20
40	10^6	10	0.3	10^5	10^{10}	0.19
41	10^6	10	0.4	10^5	10^{10}	0.14
42	10^6	10	0.5	10^5	10^{10}	0.14
44	10^5	10	0.1	$5*10^3$	10^{10}	0.57
45	10^5	10	0.4	$5*10^3$	10^{10}	0.33

5.2.3.2 Pixels clustering

As mentioned above, if current landslides observed in the study area occupy just a part of the SU, the area of the latter will not be a proper size proxy of the future slope failure. To overcome this restriction we propose an automatic aggregation of adjacent pixels belonging to the same SU and showing the same susceptibility class. Thus, the area of the high susceptible pixel clusters is obtained and its size can be associated to the size of the potential failure. This

aggregation allows the user to specify a minimum area, below which pixel clusters of the same susceptibility class and belonging to the same SU will be automatically reclassified and merged within a bigger adjacent cluster. In Figure 5-8 A, 5 pixel clusters located within the same SU have been pointed out with a black circle. Since their area is smaller than a given threshold (previously defined by the user), they have been automatically reclassified and merged within the bigger adjacent cluster (Figure 5-8 B).

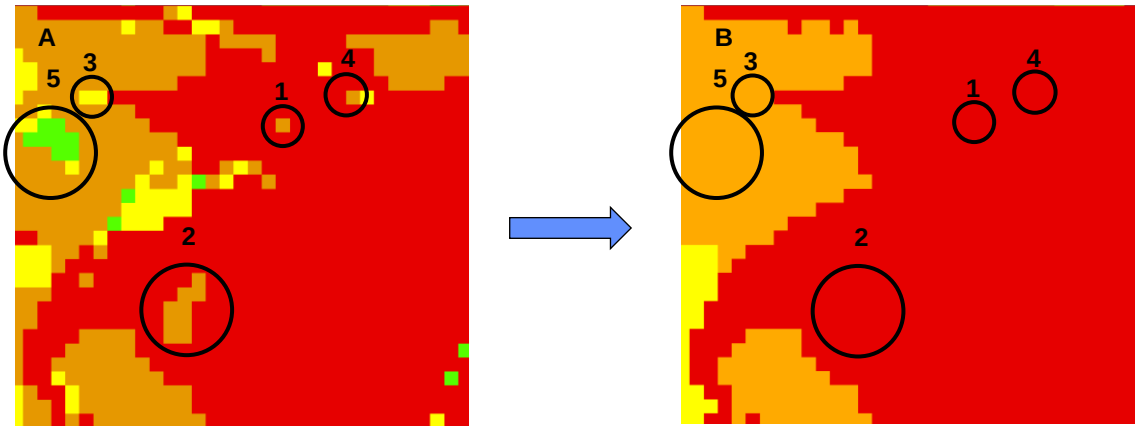

Figure 5-8: A: Pixel clusters of the same susceptibility, whose area is smaller than a given threshold (previously defined by the user), have been pointed out with a black circle. B: These clusters have been reclassified and merged within the bigger adjacent cluster.

At this point it is important to notice that different SU sizes imply different pixel clusters and consequently different area occupied by each susceptibility class: the smaller the SU's size, the smaller the pixel clusters. Thus, the probability of these smaller clusters to be reclassified and merged within the bigger adjacent cluster is higher than if working with larger SUs and consequently with larger pixel clusters.

In Figure 5-9 an example about this dependency is shown. Pixels of the same susceptibility map have been clustered using different SU sizes (SU28, SU35 and SU40). In SU 28, two resulting pixel clusters are different from SU35 and SU4 (red circles 1 and 2). If comparing maps obtained with SU35 and SU40, some differences between pixel clusters are also evident (red circle 3).

Since the area of each susceptibility class will be slightly different depending on the SU size, the frequency of failure assigned to each susceptibility class (number of fist-time slope failures $\times$ yr^{-1} $\times$ $(km^2)^{-1}$) may be slightly different. For that purpose, four different SU sizes will be used. It is not simple to define the proper SU size; it will be a compromise between the field observations and the pixel size distribution obtained for the different SU sizes.

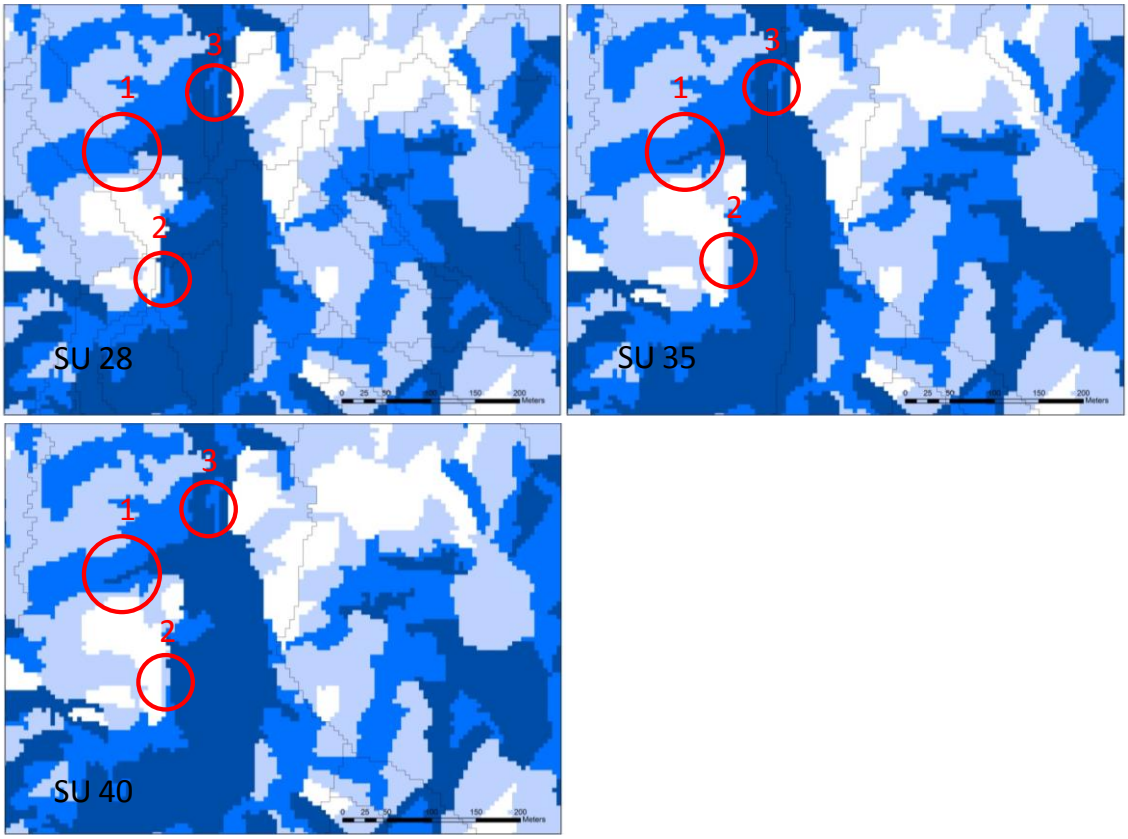

Figure 5-9: Susceptibility maps obtained with SINMAP. Three types of slope units presenting different sizes (SU 28, Su 35 and SU 40) have been applied. Since different SU sizes imply different pixel clusters and different area occupied by each susceptibility class, the red circles point out the differences in the clustering process according to the size of the SUs used.

5.2.3.3 Calculation of the magnitude

Assuming that the minimum size of the potential failures will be the same as the landslides given in the past, this minimum area will be the area of the smallest first-time failure identified in the study site. The area of each potential failure within each SU is calculated using GIS software (ArcGIS 9.3® by ESRI and ILWIS 3.4 by International Institute for Geo-information Science and Earth Observation, ITC).

5.2.4 Magnitude-Frequency matrix

As stated in chapter 3, the MF matrices are used to map the landslide hazard. These matrices express the hazard by combining the magnitude and the frequency of the slope failures. Both parameters will play a different role depending on the type of landslide, hence, the MF frequency will be different for each process (rockfalls, landslides, collapses, etc.) (Strozzi et al., 2013). In this work, the hazard has been defined according to the degrees of hazard established in the Swiss Federal Guidelines (Raetzo et al., 2002) and the SINMAP stability class definition (modified from Pack et al., 2005). The magnitude thresholds have been defined according to the typical landslide size.

5.3 Application

Input values necessary to calculate the susceptibility by means of SINMAP (Pack et al., 1998) (C_{dl}, T/R) are found in Table 5-5 (highlighted in green). Some of them have been obtained from different studies carried out either in the Tremp basin or close to the study area (Canales, 2011; Montero, 2011; Oliveras, 2011; Pinyol et al., 2012; Alcalá and Custodio, 2014, 2015). Other values have been obtained from text books (e.g. González de Vallejo et al., 2002) and measurements performed by the author (Annex 19: DATING WITH IN SITU TERRESTRIAL COSMOGENIC ISOTOPES).

Once SI values have been calculated (Annex 8: Susceptibility map), they have been reclassified in 4 susceptibility classes according to Table 5-6 (Annex 9: Reclassified susceptibility map). This classification has been modified from Pack et al. (2005).

As stated in chapter 3, some activity indicators and morphological features were mapped after several field trips. The following ones were used to calibrate both input parameters and susceptibility classes:

Activity indicators:
Fallen trees
Disturbed trees
Trees with impact marks
Intact bedding
Disturbed bedding
Terrain cracks
Structure with slight pathologies
Structure with severe pathologies

Morphological features:
Slopes with swollen and remoulded material
Discontinuity between landslides
Landslide lobe

Table 5-5: Input values used to calculate the susceptibility by means of SINMAP.

	Hard rock	Interbedded weak and hard rocks	Weak rock	Coarse colluvium	Fine colluvium	Slide material
C (min) [MPa]	**19.62** (González de Vallejo et al., 2002)	**2.45** (González de Vallejo et al., 2002)	**0** (González de Vallejo et al., 2002)	**0** (Field observation + Expert criterion)	**0** (Canales, 2011)	**0** (Canales, 2011; Montero, 2011; Oliveras, 2011; Pinyol et al., 2012)
C (max) [MPA]	**39.24** (González de Vallejo et al., 2002)	**39.24** (González de Vallejo et al., 2002)	**0.2** (González de Vallejo et al., 2002)	**0** (Field observation + Expert criterion)	**0** (Canales, 2011)	**0** (Canales, 2011; Montero, 2011; Oliveras, 2011; Pinyol et al., 2012)
h soil [m]	**0.01** (field observation)	**0.01** (field observation)	**15** (field observation)	**15** (Oliveras, 2011)	**15** (Oliveras, 2011)	**15** (Canales, 2011; Montero, 2011; Oliveras, 2011)
ρ_s [kg/m^3]	**2600** (Annex 19: DATING WITH IN SITU TERRESTRIAL COSMOGENIC ISOTOPES)	**2600** (Annex 19: DATING WITH IN SITU TERRESTRIAL COSMOGENIC ISOTOPES)	**2500** (Annex 19: DATING WITH IN SITU TERRESTRIAL COSMOGENIC ISOTOPES)	**2300** (Expert criterion)	**2200** (Canales, 2011)	**2200** (Canales, 2011; Montero, 2011; Oliveras, 2011)
g [m/s^2]	9.81	9.81	9.81	9.81	9.81	9.81
K min [m/s]	**1*10^{-12}** (González de Vallejo et al., 2002)	**1*10^{-11}** (González de Vallejo et al., 2002)	**1*10^{-10}** (González de Vallejo et al., 2002)	**1*10^{-9}** (Coduto, 1999)	**1*10^{-10}** (Coduto, 1999)	**1*10^{-10}** (Coduto, 1999)
K max [m/s]	**1*10^{-6}** (González de Vallejo et al., 2002)	**1*10^{-5}** (González de Vallejo et al., 2002)	**1*10^{-5}** (González de Vallejo et al., 2002)	**1*10^{-7}** (Coduto, 1999)	**1*10^{-5}** (Coduto, 1999)	**1*10^{-4}** (Coduto, 1999)
T min [m^2/s]	1*10^{-14}	1-10^{-13}	1.5*10^{-9}	1.5*10^{-8}	1.5*10^{-9}	1.5*10^{-9}
T max [m^2/s]	1*10^{-8}	1-10^{-7}	1.5*10^{-4}	1.5*10^{-6}	1.5*10^{-4}	1.5*10^{-3}

R min [m/s]	**$7.48*10^{-9}$** (Alcalá and Custodio, 2015, 2014)	**$7.48*10^{-9}$** (Alcalá and Custodio, 2015, 2014)	**$7.48*10^{-9}$** (Alcalá and Custodio, 2015, 2014)	**$7.48*10^{-9}$** (Alcalá and Custodio, 2015, 2014)	**$7.48*10^{-9}$** (Alcalá and Custodio, 2015, 2014)	**$7.48*10^{-9}$** (Alcalá and Custodio, 2015, 2014)
R max [m/s]	**$1.078*10^{-8}$** (Alcalá and Custodio, 2015, 2014)	**$1.078*10^{-8}$** (Alcalá and Custodio, 2015, 2014)	**$1.078*10^{-8}$** (Alcalá and Custodio, 2015, 2014)	**$1.078*10^{-8}$** (Alcalá and Custodio, 2015, 2014)	**$1.078*10^{-8}$** (Alcalá and Custodio, 2015, 2014)	**$1.078*10^{-8}$** (Alcalá and Custodio, 2015, 2014)
C_{dl} min	76923	9615	0	0	0	0
C_{dl} max	153846	153846	0.5	0	0	0
$\emptyset$ min [º]	**40** (González de Vallejo et al., 2002)	**30** (González de Vallejo et al., 2002)	**30** (González de Vallejo et al., 2002)	**18** (Field observation + expert criterion)	**18** (Field observation + Expert criterion)	**9** (Canales, 2011; Montero, 2011; Oliveras, 2011; Pinyol et al., 2012)
$\emptyset$ max [º]	**50** (González de Vallejo et al., 2002)	**50** (González de Vallejo et al., 2002)	**35** (González de Vallejo et al., 2002)	**30** (González de Vallejo et al., 2002)	**25** (Canales, 2011)	**13** (Canales, 2011; Montero, 2011; Oliveras, 2011; Pinyol et al., 2012)
T/R min [m]	$1*10^{-6}$	$9.27*10^{-6}$	0.1	1.4	0.14	0.14
T/R max [m]	1.33	13.36	20053	200.5	20053	200534

Table 5-6: SINMAP stability class definition (modified from Pack et al., 2005)

Condition (directly from SINMAP)	Predicted State	Parameter Range	Possible Influence of Factors Not Modelled	Modified condition	Proposed susceptibility
SI>1.5	Stable slope zone	Range cannot model instability	Significant destabilizing factors are required for instability	SI>1.5	Very Low
1.5>SI>1.25	Moderately stable zone	Range cannot model instability	Moderate destabilizing factors are required for instability	1.5>SI>1.0	Low
				1.0>SI>0.25	Medium
1.25>SI>1.0	Quasi-stable slope zone	Range cannot model instability	Minor destabilizing factors could lead to instability		
1.0>SI>0.5	Lower threshold slope zone	Pessimistic half of range required for instability	Destabilizing factors are not required for instability		
0.5>SI>0.0	Upper threshold slope zone	Optimistic half of range required for instability	Stabilizing factors may be responsible for stability	0.25>SI≥0.0	High
0.0>SI	Instable slope zone	Range cannot model stability	Stabilizing factors are required for stability		

Then, frequency of the first-time slope failure for each susceptibility class has been calculated. It has been normalised by the total area occupied by each susceptibility class. Since the number of pixels of a given susceptibility depend on the aggregation process and therefore on the SU size, the frequency for a given susceptibility will be dependent on the SUs size as well.

At this point, it is important to notice that although a unique SU size does not exist, in mountainous areas SUs can be easily identified compared with plane areas. In the latter, the topography has not been sufficiently moulded by the erosive processes and therefore, the drainage lines and the subsequent catchments to be later partitioned into SUs are more difficult to delineate (Figure 5-10). In our study area, earthflows are located in gentle slopes where the delineation of the SUs is not straightforward and thus, a previous analysis to evaluate the proper size of the SUs has been performed.

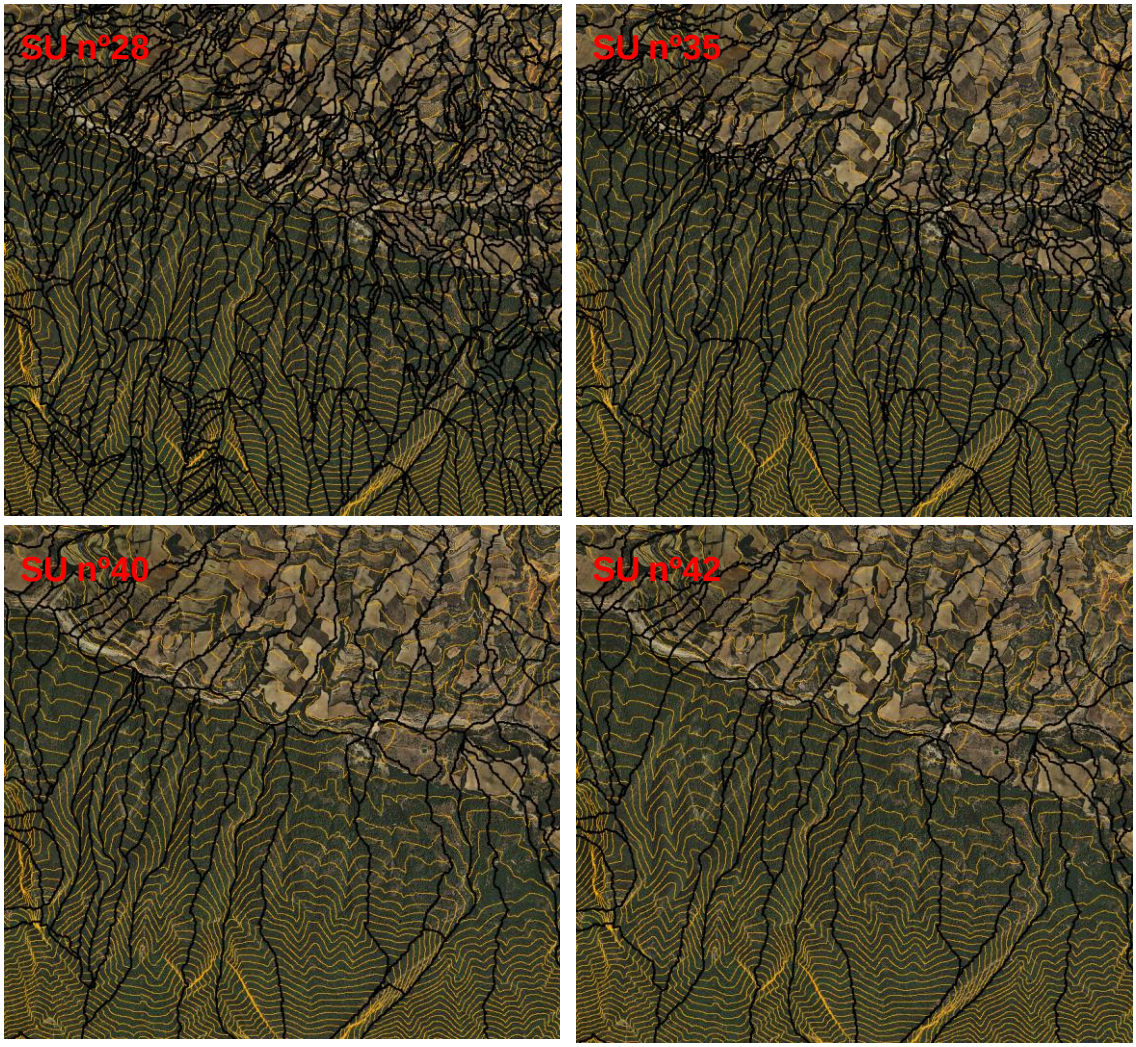

Figure 5-10: View of SUs of different sizes generated at the study site at scale 1:20,000. It can be seen as in the mountainous area (lower and central part of the each view), the generated SUs are easy to identify rather than in the more plane area (upper part of the view) where it is not trivial to check whether they have been properly delineated.

The different SUs have been generated by modifying the two most sensitive parameters (CAT [x] and circularvariance [y]) (Figure 5-11). In this calibration, the 109 landslides identified in Barcedana Valley (chapter 3) have been used (first-time slope failures as well as reactivations).
As it was expected, the maximum number of landslides cut by SUs (0.51) is given when small circularvariance and CAT values are used, i.e. when small SUs are generated. Additionally, for a given CAT, the less restrictive the circularvariance is, the smaller the ratio. For a fixed circularvariance value, the ratio of landslides cut by SUs decreases with smaller CATs (larger catchments).
Nevertheless, the ratio that describes the best SU size does not exist. It depends on the role of these SU as well as the study area (catchments and landslides) and the scale of analysis. Consequently four different SUs of different sizes have been chosen from Table 5-1, Table 5-2, Table 5-3 and Table 5-4, in order to evaluate the influence of their size when correlating the SI (obtained from SINMAP) with the temporal frequency of each susceptibility class: SU no. 28 (Figure 5-11, red circle), SU no. 35 (Figure 5-11, green circle) and SU no. 40 (Figure 5-11, purple circle) and SU no. 42 (Figure 5-11, orange circle). Features of these SUs are shown in Table 5-8.

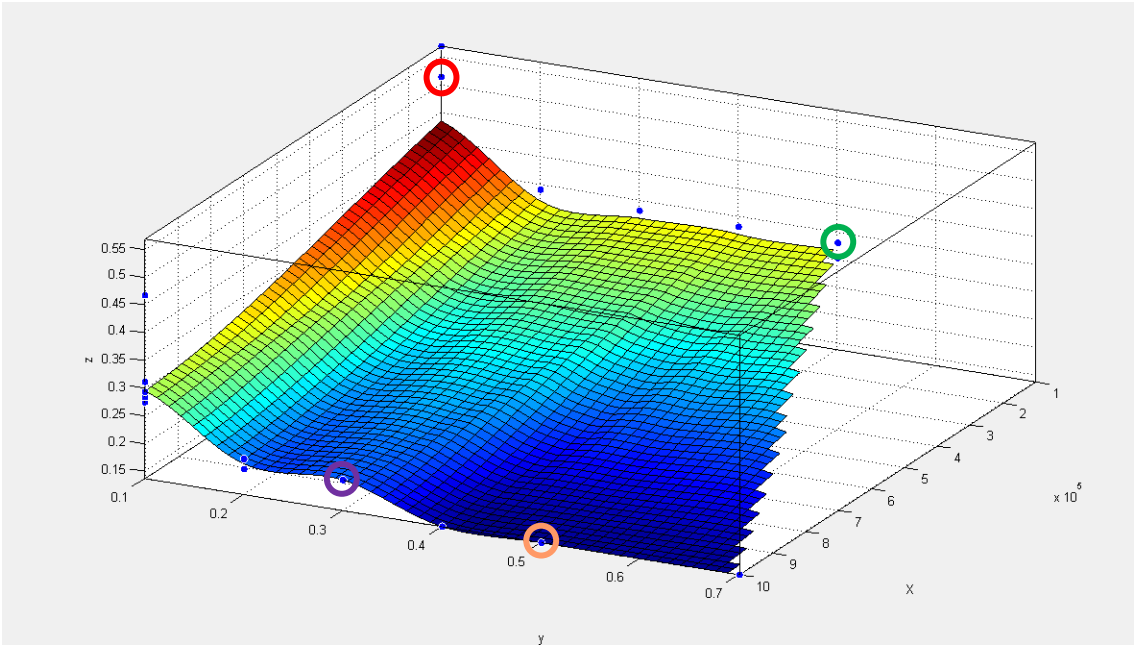

Figure 5-11: Ratio of landslides cut by SUs (N) according to the CAT (m^2) (X) and the aspect circular variance (Y). Red, green purple and orange circles correspond to SU no. 28, 35, 40 and 42, respectively (Table 5-1, Table 5-2, Table 5-3 and Table 5-4).

To this end, the number of first-time slope failures has been identified in the orthophotos set (Table 5-7) (ICGC, 2015). Then, the number of first-time slope failures that occurred within each susceptibility class has been calculated (Table 5-9). As mentioned above, this ratio has also been used to validate the model since the highest susceptibility classes are expected to contain a bigger number of failures. Finally, they have been divided by the observation's period of time (from 1956 to 2013) and normalized by the extension occupied by each susceptibility class. The influence of the SU size on the frequency of the potential failures is shown in Table 5-9.

Table 5-7: First-time slope failures identified in the Barcedana Valley. NA: Not identified; F: Failure. Area of the failure is shown.

Landslide	1956	1990	1993	1997	2003	2005	2007	2008	2009	2011	2013	Area (m^2)	Lithological unit
1						F						816	3
2		F	NA	NA								1053	3
3											F	1091	3
4											F	1229	5
5						F						2961	5
6		F	NA	NA								7002	4
7		F										7153	5
8			F									8849	5
9									F			11540	5
10											F	11550	5
11					F							15110	4
12					F							15120	5
13		F										19590	4
14										F		23700	5
15				F								27700	5
16				F								28450	4
17		F										52010	4

Table 5-8: Features of the SUs selected to evaluate the influence of the SU size over the landslide magnitude.

SU	No. of SUs	Minimum SU area (m^2)	Maximum SU area (m^2)	Average SU area (m^2)
28	1360	3350	328525	17341
35	472	1800	595150	50175
40	83	34625	1043525	275525
42	57	35575	3469650	407374

Table 5-9: Frequency of first-time slope failures in Barcedana Valley (# failures/yr/km^2)

Susceptibility class	No. of first-time slope failures	Ratio (# first-time slope failures of each susceptibility class/overall)	Observation period (yr) (1956-2013)	Area of intact slopes in 1956 (km^2)				Frequency of first-time slope failures (# /yr/km^2)			
				SU no. 28	SU no. 35	SU no. 40	SU no. 42	SU no. 28	SU no. 35	SU no. 40	SU no. 42
1	0	0	57	8.55	8.56	8.58	8.59	0	0	0	0
2	0	0	57	2.15	2.21	2.24	2.25	0	0	0	0
3	1	0.059	57	3.25	3.26	3.26	3.26	0.005	0.005	0.005	0.005
4	16	0.941	57	5.68	5.60	5.56	5.54	0.049	0.05	0.051	0.051

As it can be seen in the Table 5-9, the higher the susceptibility class, the higher the frequency of first-time slope failures. Furthermore, the frequency remains similar even when using different SU sizes.

On the other hand, to evaluate the SUs size's influence during the pixel clustering process, the pixel cluster size distribution for each susceptibility class and each SU has been analysed and compared to the results obtained with the reclassified susceptibility map obtained from SINMAP. In this case, neither have SUs been considered; nor has the automatic aggregation of adjacent pixels been performed. The area of adjacent pixels has just been calculated with the same susceptibility class (pixels clusters) (Figure 5-12, Figure 5-13, Figure 5-14 and Figure 5-15). The highest susceptibility class distribution (Figure 5-15) has been compared with the size distribution of the mapped first-time failures since most of them (94.1%) are located within this class (Table 5-9).

In general, the susceptibility map obtained directly from SINMAP comprises a higher number of small clusters, as expected. Furthermore, for very low and high susceptibility classes (Figure 5-12 and Figure 5-15), a wider range of areas is given than for low and medium susceptibility classes.

Concerning the very low and high susceptibility classes, there exist a few pixel clusters, generated directly from SINMAP, which are reduced after the grouping process. For the high susceptibility class, this is a consequence of the large landslides identified in the field and introduced into the SINMAP. Since they are larger than the SUs, pixel clusters generated within the SUs will be smaller: we are referring to landslide sizes larger than 10^6 m^2. These are really large landslides which need to be individually treated. Regarding the very low susceptibility class, this is conditioned by the imposition of high resistant geomechanical properties to a given material. If this material widely extends in the study area, a few pixel clusters obtained directly from SINMAP will be larger than the SUs and therefore, larger than the clusters generated within the SUs.

Concerning low and medium susceptibility classes, the reclassified map obtained from SINMAP does not contain these large clusters but smaller pixel aggregations sometimes given even by one single pixel. Therefore, when applying the automatic aggregation of pixels using SUs of large sizes (SU no. 40 and 42), the generation of clusters of pixels, larger than in the reclassified map, is given.

When comparing the distribution of the mapped first-time failures with the pixel clusters (Figure 5-15) it can be observed that the predicted failures that better fit with the mapped first-time failures are the ones obtained with the SU no. 35. If using the SU no. 28, the predicted failures are smaller than the mapped first-time failures. Conversely, with the SU no. 40 and 42, the modelled failures are larger than the first-time failures of the study site.

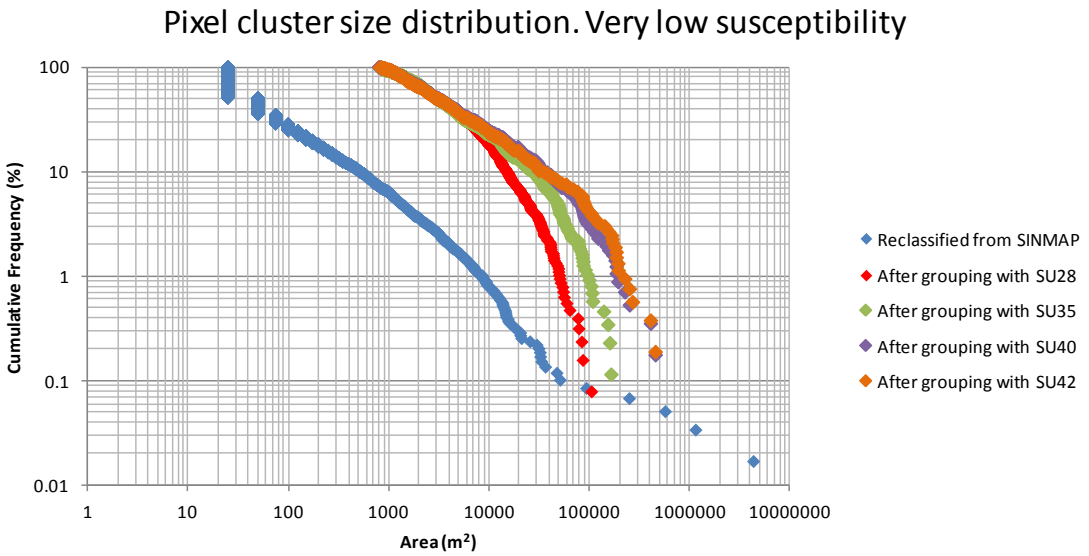

Figure 5-12: Pixel cluster size distribution of susceptibility class 1 obtained from the reclassification of SINMAP, after grouping using SU no. 28, 35, 40 and 42.

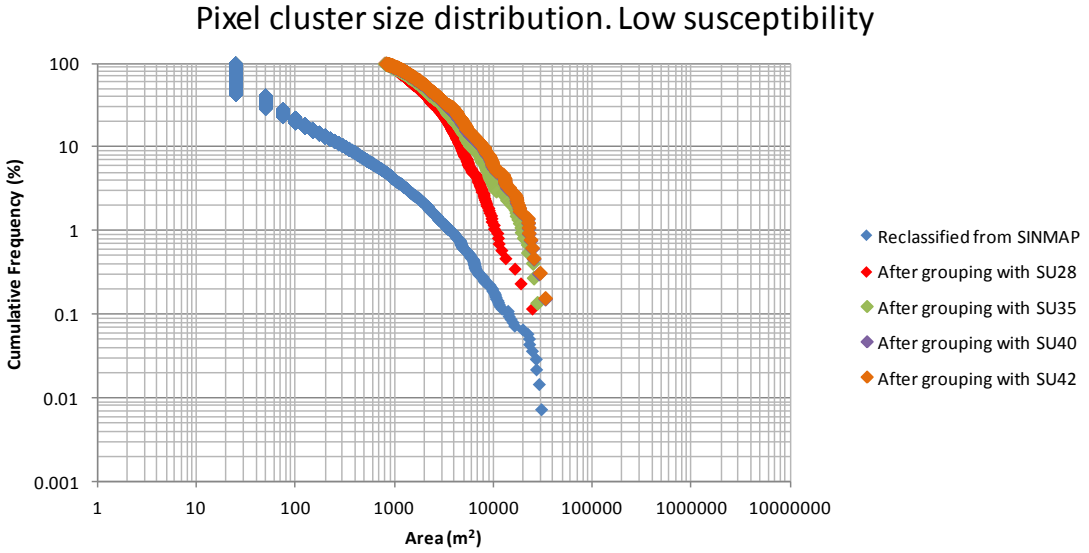

Figure 5-13: Pixel cluster size distribution of susceptibility class 2 obtained directly from SINMAP, after grouping using SU no. 28, 35, 40 and 42.

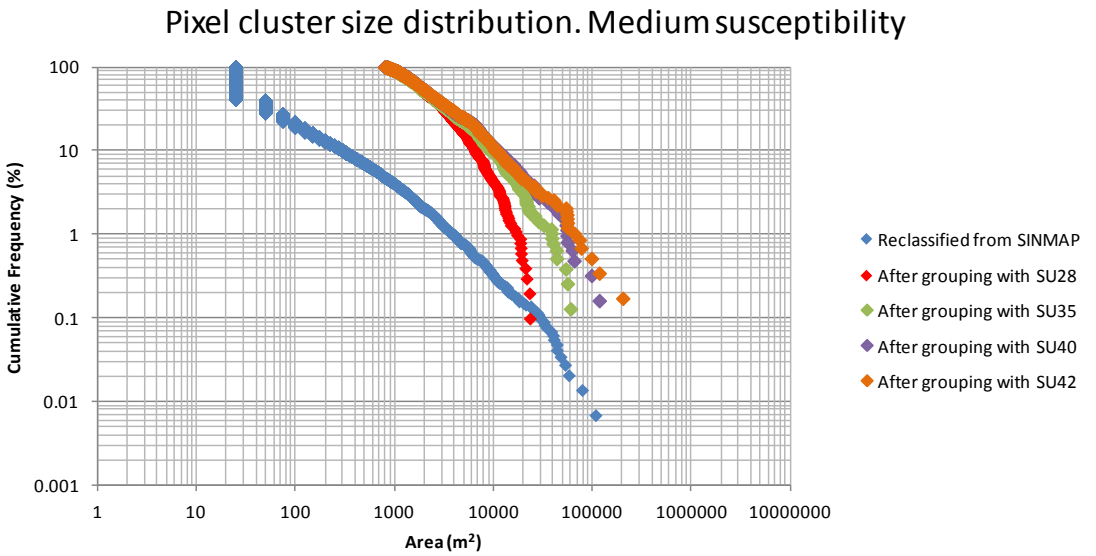

Figure 5-14: Pixel cluster size distribution of susceptibility class 3 obtained directly from SINMAP, after grouping using SU no. 28, 35, 40 and 42.

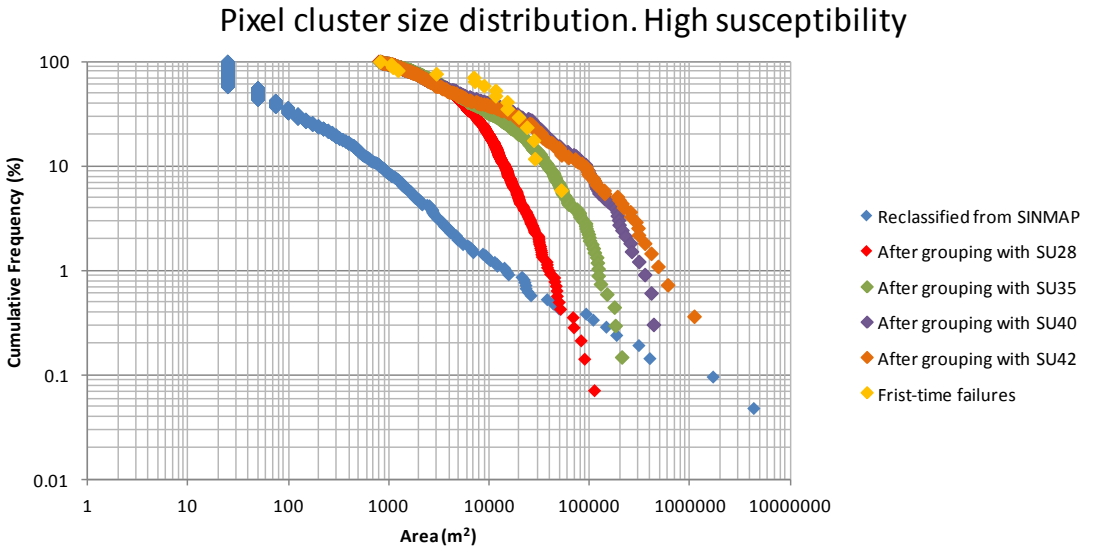

Figure 5-15: Pixel cluster size distribution of susceptibility class 4 obtained directly from SINMAP, after grouping using SU no. 28, 35, 40 and 42.

The area of the mapped first-time failures has been compared with the area of the predicted failures (high susceptible areas) calculated by SINMAP for a given SU size (Figure 5-16). As it can be seen, there does not exist any significant correlation between them. The best one is given when using the smaller SU size (SU28). In that case, the coefficient of determination is R^2= 0.68. However, the slope of the trend line is smaller than 1 and therefore, the predicted failures are smaller than the ones mapped in the field. Therefore, although the prediction improves, an underestimation of the magnitude of the potential failures still exists.

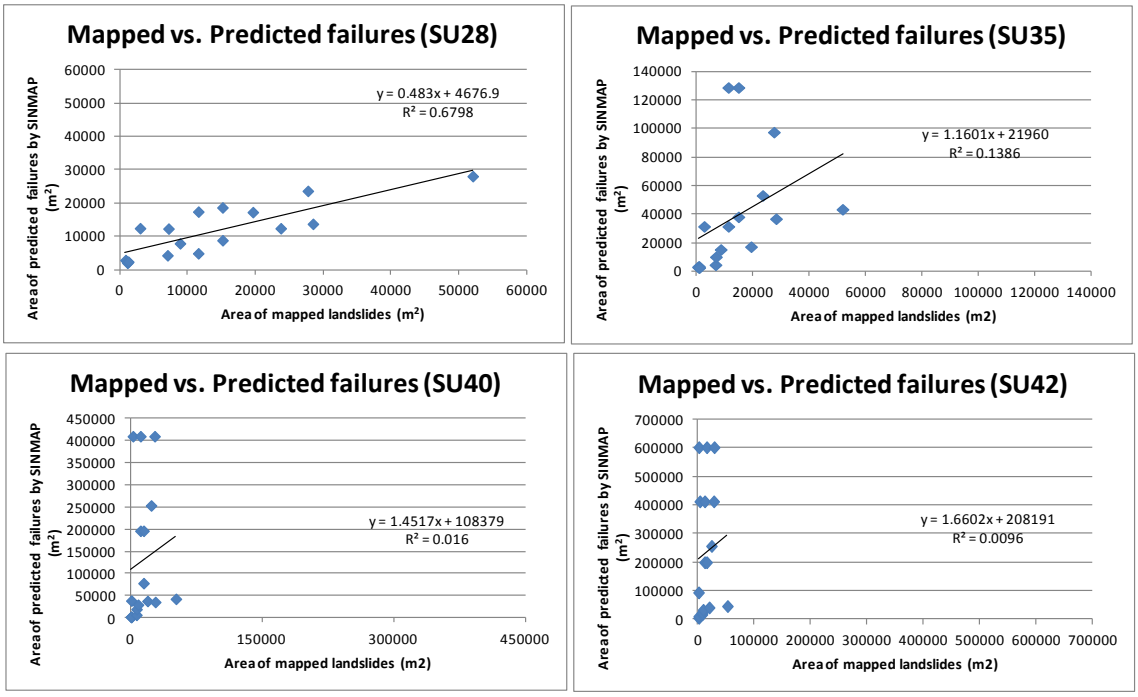

Figure 5-16: Relationship between the area of the mapped first-time failures and the predicted failure by SINMAP according to the different SU size.

As it can be seen in Figure 5-17, when using too small SUs (SU no. 28) they may cut the mapped landsides and therefore the predicted failure have a smaller area. Thus, larger mapping units, which better fit the existing failures of the study site, should be defined (Figure 5-17, SU no. 35).

Figure 5-17: Left: Mapped landslide (red) cut by SUs when using too small mapping units (SU no. 28). Right: SUs of higher areas have been delineated to fit better with the mapped failures (SU no. 35).

Conversely, if too large SUs are used (SU no. 40 or 42), the cluster of adjacent pixels with the same susceptibility class and located within the same SU may be larger than the mapped failures and thus, the magnitude of the potential failures will be overestimated (Figure 5-18).
Therefore the most suitable SU has been considered to be the SU no. 35 (Annex 12: Hazard

map obtained after pixel clustering by SU no. 35).

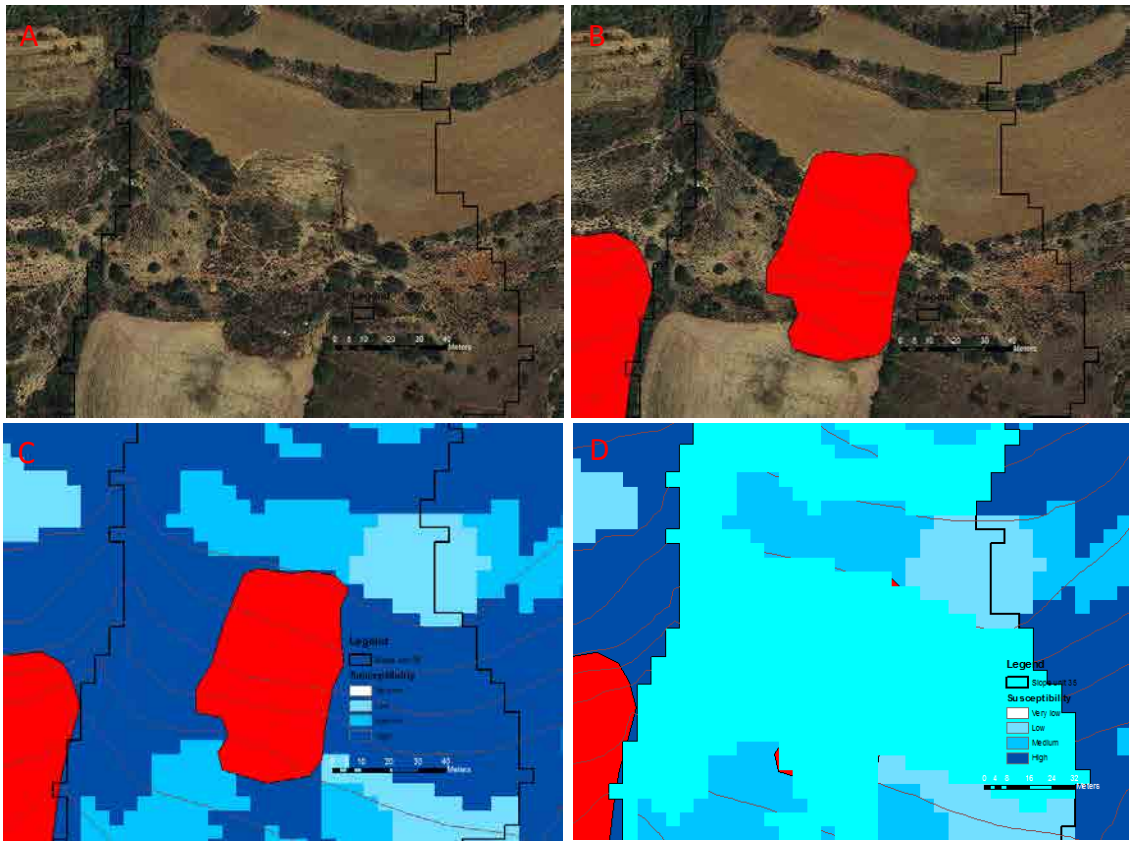

Figure 5-18: A) Orthophoto of the study site; B) Mapped first-time failure in red located in the central part of the view; C) Susceptibility map with the automatic aggregation of pixels; D) Area of the group of adjacent pixels with high susceptibility and located within the same SU.

The main reason that may explain this poor correlation between mapped and calculated first-time failures is that most of the failures are located within gentle slopes where de delineation of the SUs is not trivial. Consequently, the resulting SUs are either smaller or larger than the expected ones and the area of the potential failures is being either underestimated or overestimated.

Finally, the MF matrix (Table 5-12) has been defined considering the degrees of hazard of the Swiss Federal Guidelines (Raetzo et al., 2002) (Table 5-10).

Despite the number of studies and methodologies developed for the landslide hazard mapping, a clear consensus does not exist when defining the degrees of hazard of the MF matrix for a given frequency and magnitude (or intensity). As stated by Cardinali et al. (2002), extreme values may be easy to define; however, intermediate conditions may be more difficult to rank. The hazard levels of the MF matrix may also be defined using two-digit positional index. One number identifies the magnitude and the other one the frequency. In such a case, the user can perfectly understand the contribution of each input parameter to the hazard (Table 5-11).

Table 5-10: Definition of the degrees of hazard of the MF matrix (Table 5-12) (modified from BMLFUW, 2011).

Swiss Federal Guidelines (Raetzo et al., 2002)	Degree of hazard of the MF matrix (Table 5-12).
Red: high hazard	Red: high hazard
-People are at risk of injury both inside and outside buildings.	
-A rapid destruction of buildings is possible.	
Or	
-Events occurring with a lower intensity, but with a higher probability of occurrence. In this case, people are mainly at risk outside buildings, or buildings can no longer house people.	
The red zone mainly designates a prohibition domain (area where development is prohibited).	
Blue: moderate hazard	Orange: medium hazard
-People are at risk of injury outside buildings. Risk is considerably lower inside buildings.	
-Damage to buildings should be expected, but not a rapid destruction, as long as the construction type has been adapted at the present conditions.	
The blue zone is mainly a regulation domain, in which severe damage can be reduced by means of appropriate protective measures (area with restrictive regulations).	
Yellow: low hazard	Yellow: low hazard
People are at slow risk of injury	
Slight damage to buildings is possible	
The yellow zone is mainly an alerting domain (area where people are notified at possible hazard).	
Yellow-white hatching: residual danger	Green: very low hazard
Low probability of high intensity event occurrence can be designated by yellow-white hatching. The yellow-white hatched zone is mainly an alerting domain, highlighting a residual danger	
White: no danger	
No danger or negligible danger, according to currently available information	

Table 5-11: Magnitude-Frequency matrix. The hazard levels are defined using two-digit positional index (modified from Cardinali et al., 2002).

Magnitude			
High (3)	13	23	33
Medium (2)	12	22	32
Low (1)	11	21	31
	Low (1)	**Medium (2)**	**High (3)**
	Frequency		

Earthflows are usually very slow movements in which large failures may imply affectations to a higher part of the territory rather than a higher intensity. Therefore, the frequency was considered to prevail over the magnitude when evaluating the degree of hazard for not much

recurrent events (very low and low frequency). On the other hand, with medium and high-frequency earthflows, the magnitude has been seen to play a more important role since the affectation to infrastructures and/or people will be more recurrent. For medium and high frequencies combined with low magnitude (index 13 and 14, Table 5-12) the degree of hazard is considered to be low and medium, respectively, as the dimensions of the failures are considerably small. However, when having a medium frequency and high magnitude (33, Table 5-12), the large area of the movements suggests that the damage produced to the buildings may be more severe.

Table 5-12: MF matrix for the evaluation of the first-time slope failure hazard.

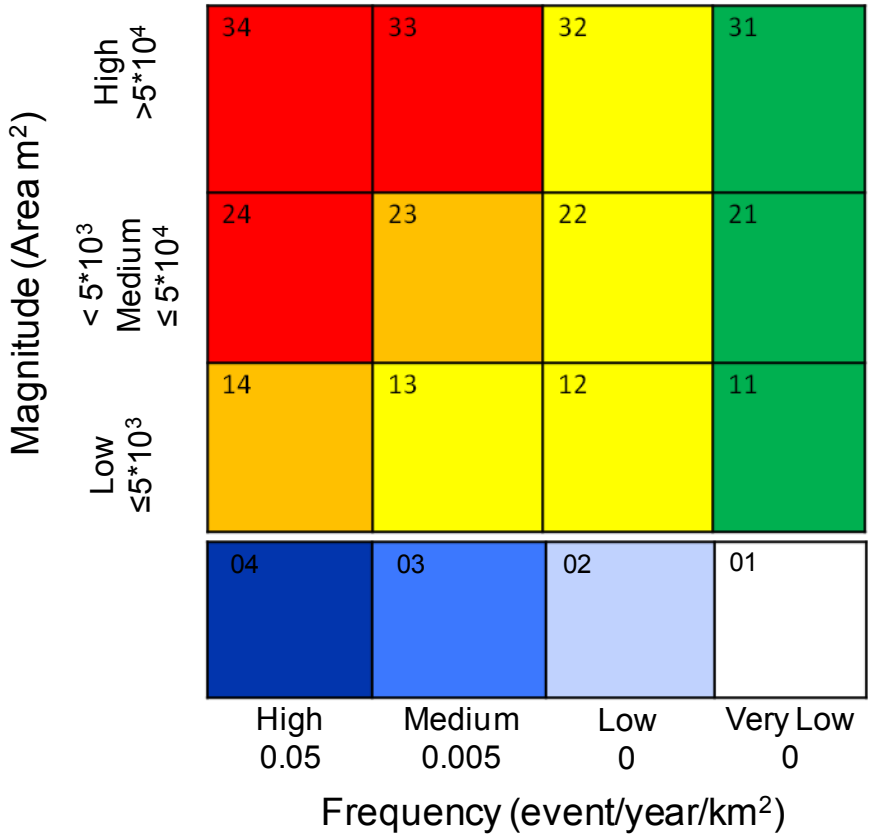

A comparison between the reclassified susceptibility map obtained from SINMAP, the susceptibility map after the automatic pixel aggregation and the hazard map obtained after the application of the MF matrix is shown in Figure 5-19, Figure 5-20, Figure 5-21 and Figure 5-22 for SU no. 28, 35, 40 and 42, respectively. In this case, a south and south-east-facing slope is shown with a high susceptibility in most of the slope (Figure 5-19 A, Figure 5-20 A, Figure 5-21 A and Figure 5-22 A). However, some pixels with medium, low, and very low susceptibility (indicated with black arrows) have been calculated by SINMAP in the middle of such slopes. Obviously, if a landslide hazard mapping is performed, these small parts of the terrain showing susceptibility classes smaller than the surrounding materials will not be considered as less susceptible, but as an artefact due to the pixel-based nature of the FS. Therefore, the susceptibility has been homogenised along the slope and the area of the clusters has been calculated (Figure 5-19 B, Figure 5-20 B, Figure 5-21 B and Figure 5-22 B). Thereafter, the MF matrix has been applied (Figure 5-19 C, Figure 5-20 C, Figure 5-21 C, Figure 5-22 C).

In the Figure 5-19, the SU no. 28 has been used. Since some pixel clusters located within a SU have a low magnitude (according to Table 5-12), the degree of hazard (Figure 5-19 C) is reduced compared to the susceptibility one (Figure 5-19 B).

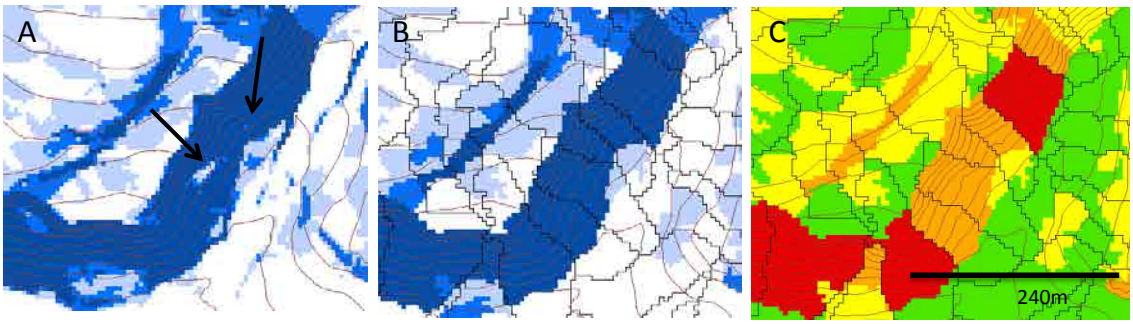

Figure 5-19: A) Reclassified susceptibility map obtained from SINMAP; B) Susceptibility map after pixel clustering using SU no. 28; C) Hazard map obtained after the application of the MF matrix (Table 5-12).

When using the SU no. 35, the hazard degree is reduced in most cases (Figure 5-20 C). Although they are generally larger than the SU no. 28, in this slope they are smaller, probably due to the smaller areamin used in SU no. 35.

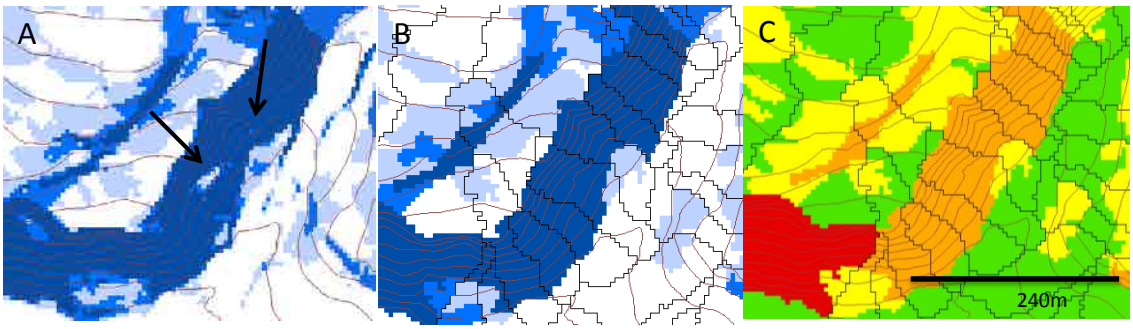

Figure 5-20: A) Reclassified susceptibility map obtained from SINMAP; B) Susceptibility map after pixel clustering using the SU no. 35; C) Hazard map obtained after the application of the MF matrix (Table 5-12).

SU no. 40 (Figure 5-21) and no. 42 (Figure 5-22) are undoubtedly the largest ones of the three studied approaches. In that case, any of the slope pixel groups have been modified during the application of the MF matrix due to their large sizes.

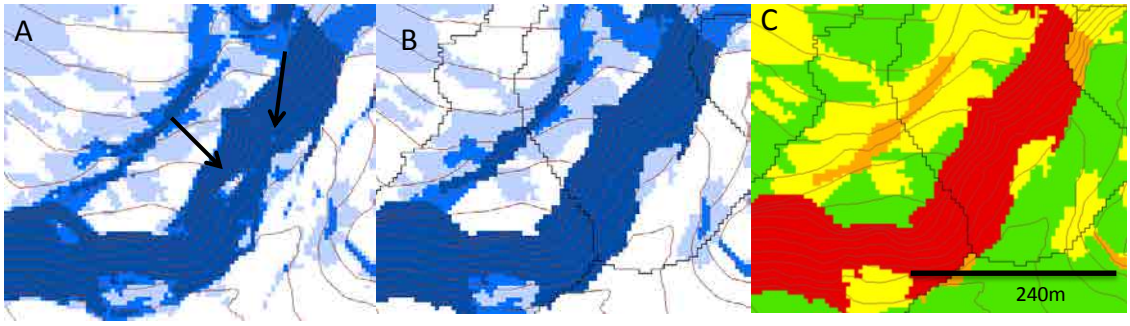

Figure 5-21: A) Reclassified susceptibility map obtained from SINMAP; B) Susceptibility map after pixel clustering using SU no. 40; C) Hazard map obtained after the application of the MF matrix (Table 5-12).

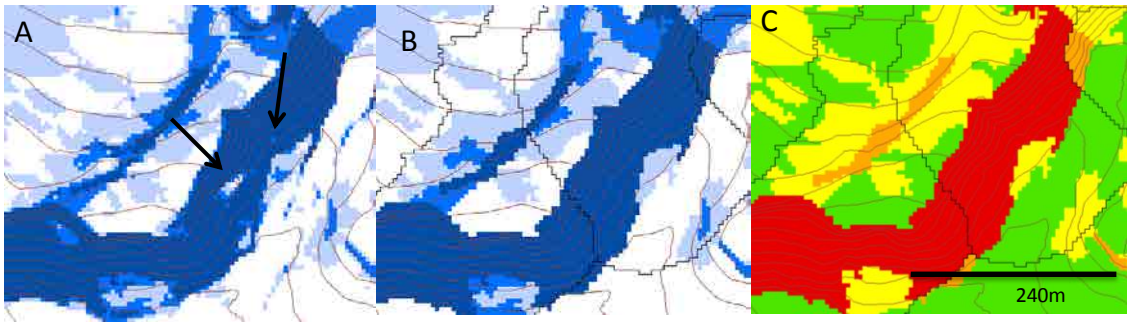

Figure 5-22: A) Reclassified susceptibility map obtained from SINMAP; B) Susceptibility map after pixel clustering using SU no. 42; C) Hazard map obtained after the application of the MF matrix (Table 5-12).

5.4 Conclusions

A supervised procedure has been developed in the Barcedana Valley (Eastern Pyrenees, Spain) to evaluate the frequency and magnitude of first-time slope failures, larger than the pixel size, applying a deterministic model for the later hazard mapping using the magnitude-frequency matrix.

The frequency has been calculated using the first-time slope failure inventory and the stability index that has been reclassified into four susceptibility classes. This index has been calculated in each pixel by means of a deterministic model named SINMAP (Pack et al., 2005). It couples a slope stability model with a simple hydrological model.

The area of the potential failures has been obtained by performing an automatic aggregation of groups of adjacent pixels with the same susceptibility class, located within the same SU and having an area smaller than a given threshold.

Input parameters of the deterministic model (friction angle, dimensionless cohesion and the T/R rate) have been obtained from several works carried out at UPC, references and observations performed after several field campaigns. They have been very useful for the later calibration of the model as well.

The first-time slope failures, determined after the analysis of a set of orthophotos covering a 57 years period, have been used to validate the model as well as to calculate the frequency of each susceptibility class. The reliability of SINMAP has been evaluated by calculating the percentage of first-time slope failures located within each susceptibility class. The frequency has been calculated by dividing this percentage among the elapsed time covered by the orthophotos.

Thereafter, it has been normalised by the area occupied for each susceptibility class. A unique SU size does not exist. Furthermore, for different SU sizes, the pixel clusters will be different and the frequency of the potential failures could be different as well. Therefore, several approaches using SUs of different sizes have been carried out. For that purpose, an iterative algorithm developed by the CNR-IRPI (Perugia, Italy) (Alvioli et al., 2014; 2015) has been used. It performs an automatic delineation of SUs through a Web Processing Service (WPS). It has been checked that the number of pixels of a given susceptibility class depends on the SU size. Nevertheless, its influence is insignificant concerning the frequency of the potential failures.

The magnitude has been obtained by implementing an algorithm within ArcGIS 9.3®. It comprises an automatic aggregation of a pixel or a group of pixels located within the same SU, showing the same susceptibility class and having an area smaller than a given threshold. In that case, the distribution of the pixel cluster areas does present differences according to the SU size: with smaller SUs (SUs no. 28 and 35), the maximum area of the pixel clusters is smaller. Conversely, when generating larger SUs (SUs no. 40 and 42), the area reached by potential failures is larger.

The pixel cluster size distributions belonging to the high susceptible area have been compared with the distribution of the mapped first-time failures. It has been observed that the distribution of the mapped first-time failures is best fitted with the distribution belonging to the SU no. 35.

Furthermore, the area of the first-time failures has been compared with the area of the potential failures, calculated with SINMAP, for the different SU sizes. The obtained poor correlation may be explained by the difficulty to generate proper SUs within the gentle slopes where most of the landslides are located. Thus, the resulting SUs are either smaller or larger than the expected ones, and the consequent area of potential failures is being either underestimated or overestimated. However, a significant relation between the cluster sizes and landslide sizes has been obtained for SU28.

Then, the MF matrix has been obtained considering that the frequency prevails over the magnitude for low and very low frequency classes. For high and very high classes, it has been assumed that a small magnitude can reduce the degree of hazard. Conversely, a large magnitude implies an increase of the hazard degree. The definition of each hazard degree has been adopted from the Swiss Federal Guidelines (Raetzo et al., 2002).

Finally, the landslide hazard maps have been obtained applying the MF matrix and considering the three SU sizes. Results show that a good pixel clustering has been performed in order to avoid the generation of single or small groups of pixels with a different degree of susceptibility. Moreover, the pixel grouping has been carried out successfully between pixels located just within the same SU. The area of the clusters has been calculated in order to be used as the magnitude when evaluating the landslide hazard. For small SUs, the final hazard degree will tend to be smaller, and vice versa. Hence, the SU size is still playing an important role in the final hazard mapping. Nevertheless, this methodology allows assessing the hazard in a semi automatic and objective way and considering the landslide area instead of the whole mapping unit.

5.5 Future works

-The local authorities should perform a systematic classification of landslides in order to provide an extensive failure database, aiming at calibrating and/or validating the models.

-To evaluate the susceptibility without the landslides identified in the field in order to use them for the later validation.

-It would be interesting to perform a first pixel clustering before reclassifying the stability index, calculated with SINMAP, into four susceptibility classes.
-Although the methodology developed by Alvioli et al. (2014; 2015) has been a great advance concerning the delineation of the SUs, more improvement is still needed focused on the possibility to add a layer of existing landslides before the generation of the mapping units. It should interfere as little as possible during the delineation process, mostly when these landsides are larger than some SUs.
-It would be very interesting to apply this methodology to mountainous areas where SUs could be easily delineated.

Part II: Rockfalls

Chapter 6

6 Evaluation of the rockfall scar volume distribution using a terrestrial laser scanner

6.1 Introduction

Magnitude-Cumulative Frequency (MCF) relations are required to quantify the rockfall hazard (Fell et al., 2005; Picarelli et al., 2005). The magnitude of the rockfall is characterized by the volume (Corominas and Moya, 2008), hence, size statistics of rockfalls must be provided (Guzzetti et al., 2004). MCF are typically obtained by means of 1) rockfall records, 2) inventories obtained from photos if available data of past events exists, 3) dendrogeomorphology, 4) interpretation of photos of different ages or 5) use of new technologies for data acquisition such as Terrestrial Laser Scanner (TLS) or photogrammetry in order to compare the slope face before and after the event.

Examples using databases of past events from road maintenance records or inventories obtained by in situ observations were provided by Hungr et al. (1999). He obtained 3538 records of rockfalls and slides, covering four decades, from road maintenance records and impacts on the road along the main rail and highway routes of South Western British Columbia. Guzzetti et al. (2003 and 2004) obtained the frequency-volume statistics of 463 and 111 rockfall events in the Yosemite Valley (USA) and Nera Valley (Italy), respectively, from observations and historical accounts. Dussauge-Peisser et al. (2002) used three rockfall inventories in order to build up a volume distribution for the French Alps (Grenoble) from 1935 to 1995, for the Yosemite Valley (USA) covering the 1912-1992 period and for the Arly gorges on the French Alps as well from 1954 to 1976. Nevertheless, quite often, such inventories are not available or are incomplete. To overcome this difficulty, Stoffel et al. (2005) used dendrogeomorphology (Alestalo, 1971) to evaluate the spatial and temporal variations of rockfall activity in a forested slope for the last 4 years. Later, Corominas & Moya (2010) used dendrogeomorphology to determine the frequency and magnitude of rockfalls, debris flows and complex slides in Andorra. In the same way, Moya et al. (2010) evaluated the rockfall activity at the Solà d'Andorra (Eastern Pyrenees, Andorra). They sampled 265 injured trees covering a period of four decades. Another technique when no inventories are available consists in the interpretation of aerial photographs: Copons & Vilaplana (2008) combined such a method with visual observations in situ and from an helicopter in order to develop a geomorphological inventory for the analysis of the rockfall susceptibility in a rocky slope of Andorra. Frattini et al. (2008) used five time-sets of aerial photographs, ranging from 1954 to 1998 to prepare a dataset of rockfall source areas as well as an inventory of rockfall deposits in Val di Fassa (Dolomites, Eastern Italian Alps).

Alternatively, when historical records are missing, some indirect methods such as the calculation of the in situ block size distribution (IBSD) or of the rockfall scar size distribution (RSSD) can be applied as an approximation for the rockfall size distribution.

The generation of blocks of a specific size and shape is mainly controlled by the intersection of discontinuity sets within a rock mass. The spacing, the persistence, the orientation and the

number of discontinuity sets are the most important parameters controlling the dimensions of these scars. The recognition of these parameters as key factors for the definition of the IBSD has already been recognised by ISRM (1978). Thereafter, several studies have been carried out which aim at a better understanding of the IBSD and RSSD relations (e.g. Lu & Latham 1999; Wang et al. 2003; Elmouttie & Poropat 2012; Lambert et al. 2012). Wang et al. (2003) outlined that the size and shape distribution of the fragments are strongly controlled by the persistence and the density of the discontinuities. Assuming fully persistent joints, an underestimation of block sizes is produced as well as an overestimation of their frequency (Kim et al., 2007). However, a very persistent set displacing all the other existing sets can generate large rockfall volumes. Ahn & Lee (2004) considered the non-persistence of discontinuities as well as their variable orientation. Cho et al. (2012) developed an algorithm where the persistence of circular discontinuity of planar surface can be considered and thus, more realistic analysis can be performed. On the other hand, the rockfall scars of past events, present on the cliff, are a clue for the evaluation of the RSSD, wherever such visual observations are possible. As it will be explained later, in that case, the distribution of the scar volumes formed by the detached blocks in the past is considered.
For assessing both IBSD and RSSD the characterization of the discontinuities and their interaction within the massif is required (Baecher 1980; Baecher 1983; Goodman 1989; Vöge et al. 2013; Fityus et al. 2013).

6.2 Methods for the characterization of rock mass discontinuities

Orientations, spacings, joints aspect and slope can be measured performing several scanlines (Priest and Hudson, 1981) or applying the window method (Priest, 1993) in accessible areas. The scan line survey consists in measuring the properties of the discontinuities that intersect a line. Detailed information for each fracture of each set should be collected. However, it is more time consuming than the window method. For the window method average discontinuity data about each set is collected usually at the bottom of the slope, for access purposes. However, this might not be representative of the whole area.
In the last decades, the rapid development of new technologies for data acquisition has allowed to obtain high resolution Digital Surface Models (DSMs) and the characterization of joint sets which are present in a rock mass using aerial sensors, ALS (i.e.: aerial photography and airborne Light detection and Ranging, LIDAR) (Abellán et al., 2006). When working with vertical slope faces, several limitations are present for high resolution data acquisition due to the occlusion of objects from given aerial perspectives (Armesto et al., 2009). A considerable advance at this camp has been the use of the terrestrial sensors such as the Terrestrial Laser Scanner (TLS) which is based on the same principle as the ALS but it is placed on the ground surface as well as the application of the digital photogrammetry for obtaining high resolution DSMs. Several works have been performed using these techniques. An interesting review on close-range terrestrial digital photogrammetry and TLS applications can be found in Abellán et al. (2014) as well as in Sturzenegger and Stead (2009). Further interesting applications can be found in Riquelme et al. (2014) who used the Matlab software (MathWorks Inc, http://www.mathworks.com/) to identify and characterize flat surfaces present in a slope using a point cloud obtained with LIDAR. Gigli & Casagli (2011) designed a Matlab tool called DiAna (Discontinuity Analysis) for the extraction of rock mass parameters such as orientation, persistence, roughness, number of sets, spacing/frequency and block size from a LIDAR point cloud. Umili et al. (2013) designed an automatic method for discontinuity traces mapping.

Garcia-Sellés et al. (2009, 2011) created a software called SEFL for the extraction of planar geological surfaces from a point cloud. In relation with photogrammetry, Kemeny and Post (2003) used an approach for estimating the fracture orientation of rock masses using digital images. Deb et al. (2008) developed several codes in Matlab that permitted the automated identification of discontinuities and the analysis of their geometry. Lato and Vöge (2012) and Vöge et al. (2013) developed a software for the automatic mapping of joints in DSMs obtained by means of a TLS or digital photogrammetry.
In these cases, the scar preservation plays an important role when defining the discontinuity planes using remote techniques. Eroded and irregular surfaces are difficult to define affecting the proper definition of the scars persistence and the consequent RSSD as well as the IBSD. For that purpose, it is essential to have enough accurate data.

6.3 Preparation of a rockfall scar volume distribution. Advanced methods

In the last decades, the use of TLS has become a common technique for the characterization of the rock mass exposure. It allows gathering large data sets providing high resolution DSMs in a relatively short period of time (a few days): Deline et al. (2011) compared the topography before and after the occurrence of a rock avalanche occurred in the Mont Blanc massif on December 2008. He subtracted the pre from the post-failure DSM using the ArcGIS Spatial Analyst (Giardino et al., 2005) and the PolyWorks software (Polyworks, .http://www.innovmetric.com/) to get the rockfall volume. The used DSMs were obtained by airborne and helicopter borne LIDAR respectively.
The evaluation of the rockfall scar volume distribution can be carried out in different ways depending on the available information: 1) Comparing the topography, obtained by means of TLS, before and after the event (e.g. Abellán et al., 2011), 2) using photos to reconstruct the original topography on a post-failure ground based-LIDAR DSM (e.g. Ravanel & Deline 2008) or 3) estimating the rockfall scar missing volumes using a post-failure point cloud obtained with a TLS (e.g. Santana et al. 2012). In the latter, as no information about the original topography was available the volume estimations are less precise than in the other two cases.
Santana et al. (2012) calculated the RSSD using a high resolution point cloud obtained by a TLS. They presented a supervised methodology for the detection of discontinuity surfaces belonging to rockfall scars from the past and the calculation of the missing volumes. This work was carried out at an intense fractured outcrop made of granodiorites which was affected by several rockfalls leaving numerous and well defined rockfall scars. The volume of the past rockfall events was assumed to be given by the mass defined between a sliding plane and the intersection of two other discontinuity planes acting as tension cracks. The distribution of the scar volumes was evaluated by multiplying the areas of the basal planes with the heights of the scars (given by the intersection of the two other discontinuity surfaces) using a Montecarlo simulation. To identify the discontinuity sets, the points from the point cloud having similar dip and dip directions were classified into sets. For the generation of discontinuity surfaces, the undulation of discontinuity planes was taken into account as well as the spacing of the discontinuity sets. The obtained discontinuity planes were in good agreement with those observed in field. The obtained rockfall scar volume distribution was found to be well fitted by an inverse power-law of exponent -0.9.
In this work, an adaptation of the methodology developed by Santana et al. (2012) is used to obtain the size distribution of rockfall scars at the Montsec Range (North-eastern Pyrenees, Spain). The study area is a limestone cliff where overhanging blocks that have been detached

from the slope face can be observed. These characteristics result in the following: (i) the dissolution processes in the limestones complicate the definition of the discontinuity surfaces with the TLS and the subsequent volume calculation (Figure 6-1, A) due to the high amount of surface irregularities and additionally because their boundaries cannot be clearly established. (ii) it is now well known whether the scars produced by the detached blocks are the result of one or several rockfall events. Because of this, the methodology of Santana et al. (2012) has to be adapted accordingly, following a different approach, as described in the following.

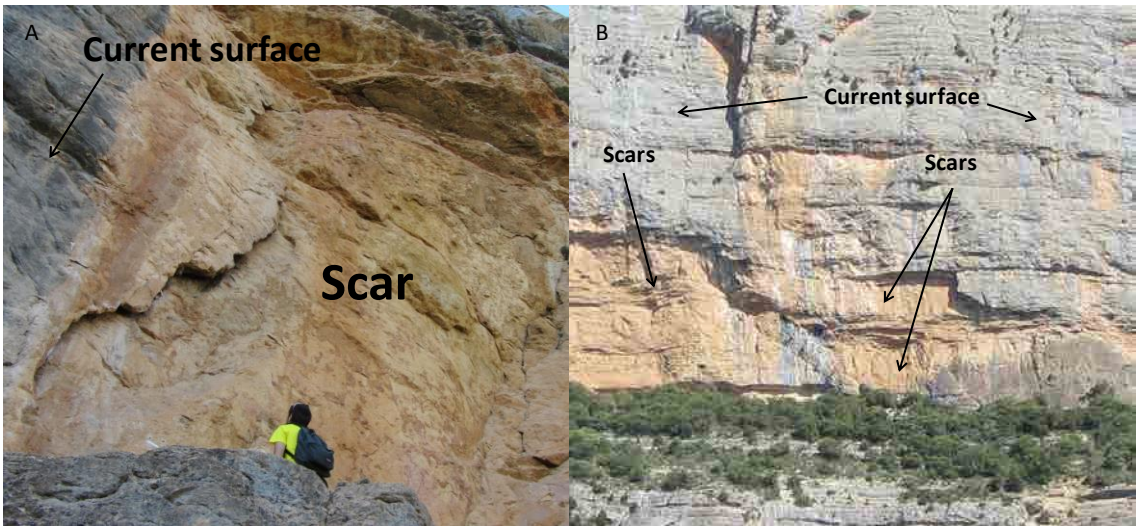

Figure 6-1: Scars present in the massif (reddish colour) differentiated from the reference rock wall surface (grey colour). A: Big scar. B: Zoom out of the scar.

The volume of the rockfall scars is approximated by a prism defined by the area of the overhangs above the scars (Figure 6-2, set A) multiplied by the scar height (vertical joint set) (Figure 6-2, set B). The latter may cross one or several spacings of bedding planes. The rockfall scar volume distribution is obtained probabilistically by means of a Monte Carlo simulation multiplying the basal area distribution of the overhangs with the length distribution of the scar heights. Rockfall scars are distinguished from the rest of the rock mass by their reddish colour and the empty space below overhangs left by the detached block (Figure 6-1).

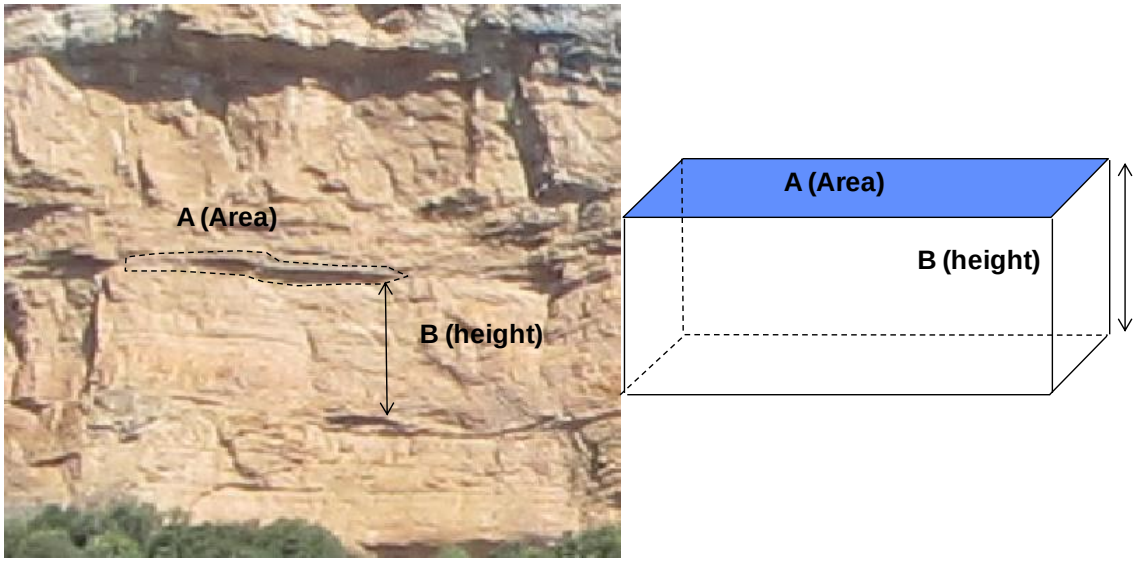

Figure 6-2: Rockfall scar volume calculation multiplying the overhang exposed area and the scar height (B).

6.4 Study area

This methodology has been applied to the Montsec Range, Spain (Eastern Pyrenees), which is situated within the Montsec thrust, developed during the Eocene (Soriano et al., 2006), in the central part of the South Pyrenean Unit (Seguret, 1972). The Montsec range is oriented E-W with an extension of about 40 km. In the frontal part of the unit, where the slope is located, outcrop materials from the Upper-Cretaceous exist (Caus et al., 1999). The cliff is composed of limestones which are not very fractured (Figure 6-3). It has been affected by rockfalls and consequently, several scars from detached blocks can be observed in the wall as well as fallen boulders at the bottom of it, mostly, covered by vegetation. It is located at 1,500 m asl with a Mediterranean continental climate. This area is not affected by the human activity and no data about past rockfall events is available.

The study area has been split into 2 smaller zones where recent rockfall scars can be observed. Zone 1 (Z1) covers an area of 14,010 m^2. It is located in the west part of the massif. Large rockfall scars as well as smaller ones are present. Blocks from past events can be seen at the bottom of the slope. They are mostly covered by vegetation. Zone 2 (Z2) has an extension of 6,802 m^2. It is located in the east part of the slope face. In that case, rockfall scars are smaller than in Z1.

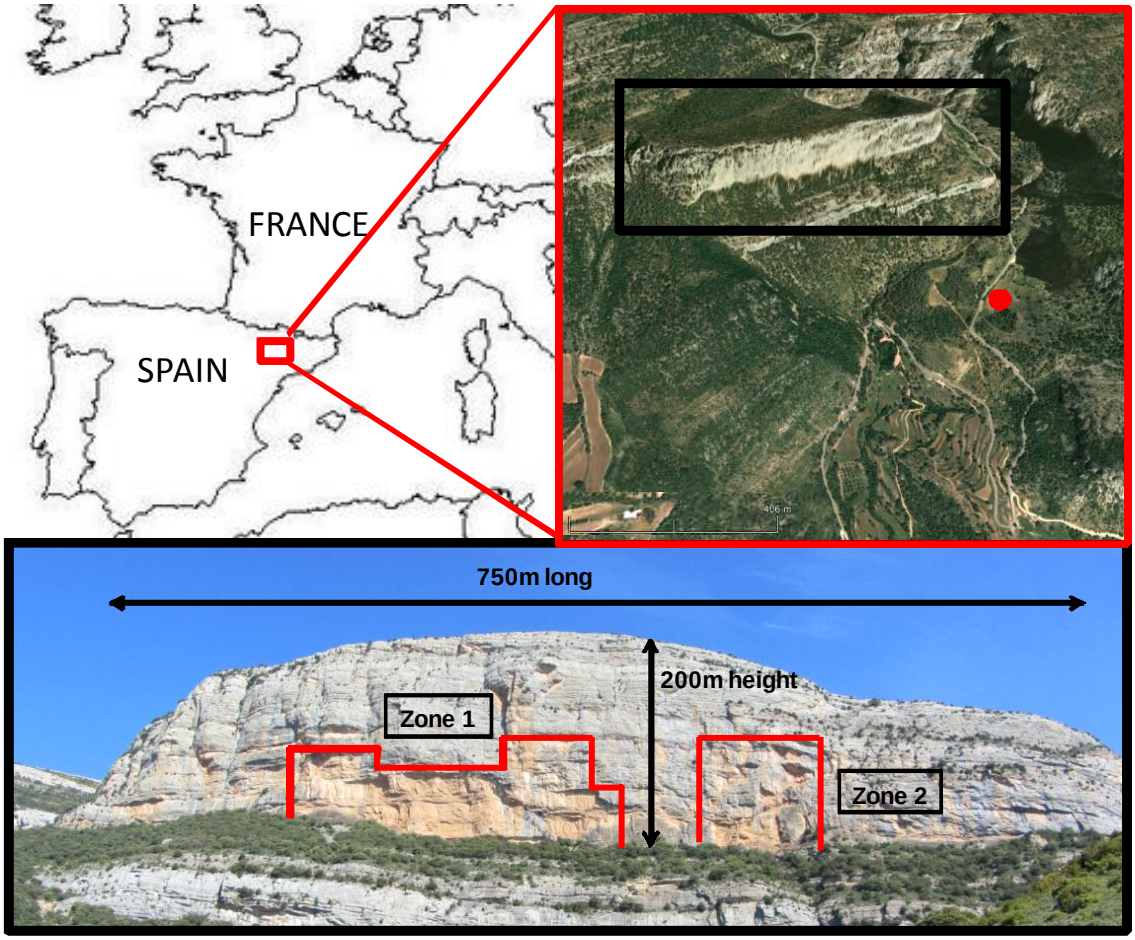

Figure 6-3: Location of the study site (up left). The boundaries of the scanned area can be seen as well as the location of the scan station (red point) (up right). The limits of the analysed area on the wall are marked with red line (lower part).

When working in massifs where small-sized rockfall scars have been degraded due to erosion processes (e.g. dissolution), their boundaries cannot be clearly defined affecting, on one hand, the identification of small rockfall scars and, on the other hand, the definition of the lateral extent. Both restrictions will affect the preparation of a RSSD.

Figure 6-4 (lower left photo) shows an outcrop of granodiorites from Andorra. Well defined scar volumes can be identified. In the lower right, a rock wall in the Montsec range, made of limestones is shown. Dashed black lines indicate hardly identifiable small-sized rockfall scars bounded by well-defined almost horizontal discontinuity planes (bedding planes) as well as irregular and partially eroded surfaces (parallel to the slope face). The fact that the scar boundary on the left (Figure 6-4, top) is not well defined in this case as in many cases, makes difficult the evaluation of the RSSD.

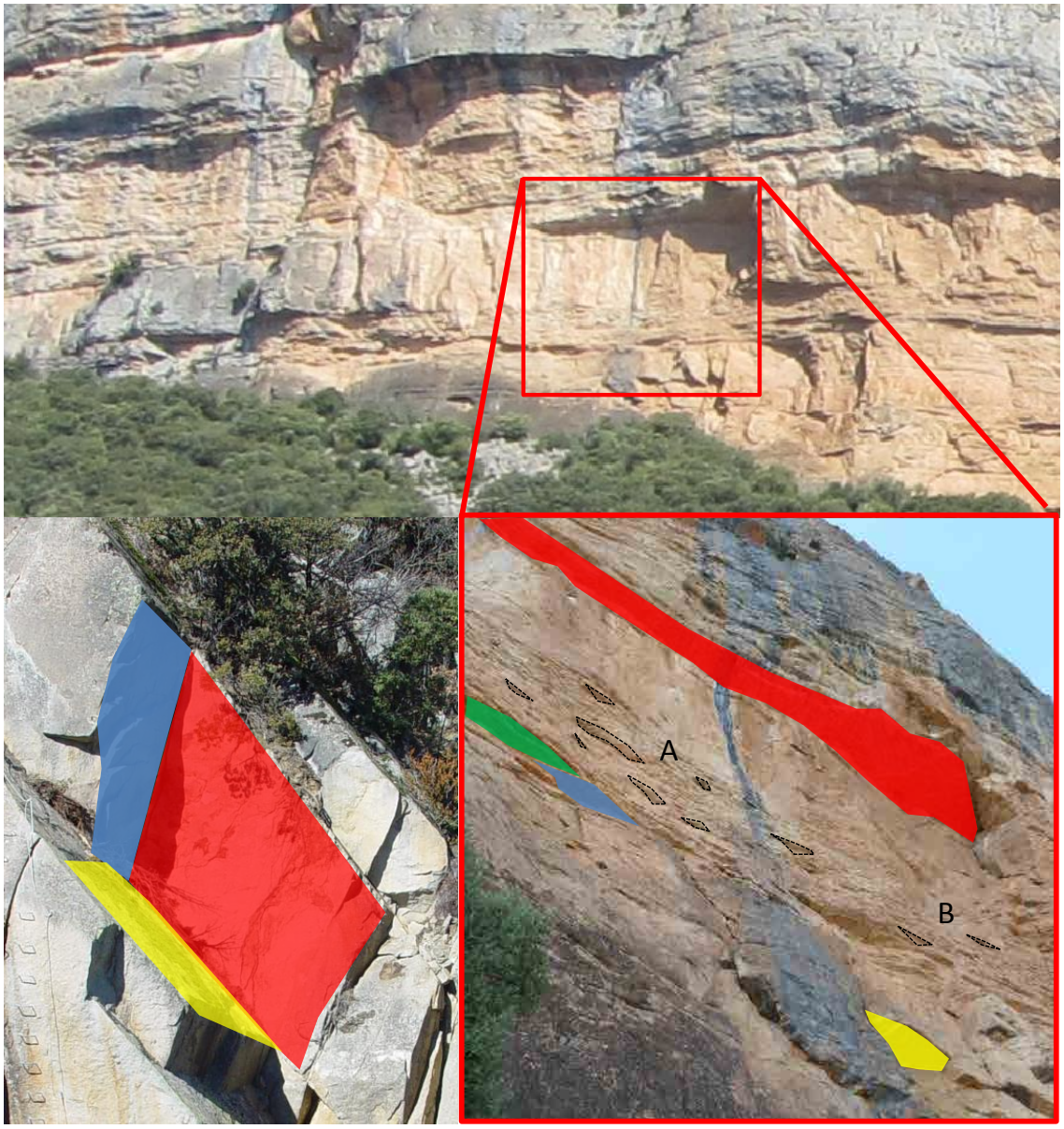

Figure 6-4: The lower left photo corresponds to a granodiorites outcrop from Andorra (Santana et al., 2012) with well defined rockfall scars. The upper and lower right photos belong to the limestone massif from the study area in Montsec (Spain). In the lower right photo, points A and B indicate overhangs formed by stepped surfaces (bedding planes) as a result of either a single or successive rockfall events. The lateral extent of the scars is imprecise.

The main difficulty arises when deciding whether a stepped-path overhang is the result of a sequence of small-sized rockfall events (Figure 6-5, A and B) or is ought to a single large failure (Figure 6-5, A+B). A given scar at its turn can be the result of the detachment of one or several detached blocks from the wall (e.g. the volume A may be the result of one bigger or two smaller volumes). To that purpose, several scenarios have been considered for the evaluation of the RSSD. More details can be found at the next section.

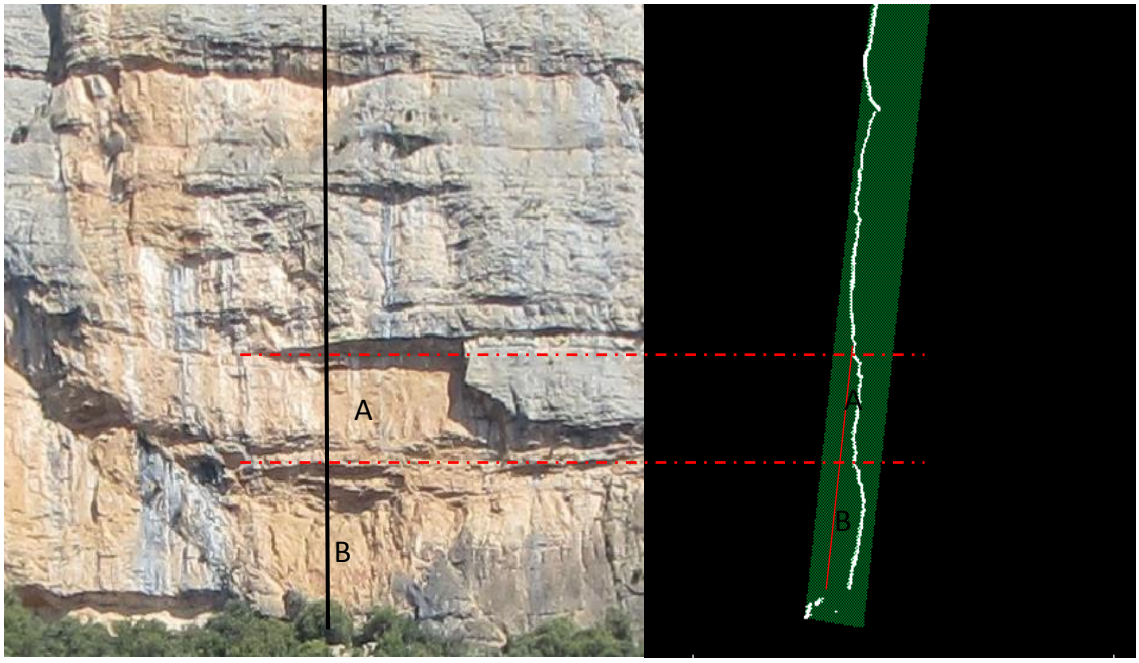

Figure 6-5: Slope face with several rockfall scars (left): The black vertical line indicates the position of the cross-section shown on the right. A and B indicate the considered rockfall scars.

6.5 Methodology

The methodology aims at the identification of the scars on the wall and the calculation of their volume distribution considering all the possibilities of rock mass detachment. The main steps, which are based on the methodology of Santana et al. (2012), are: A) Construction of the topography using a high resolution point cloud obtained with Terrestrial Laser Scanner (TLS), B) Identification of discontinuity sets, C) Generation of discontinuity surfaces and D) Calculation of the volume of the existing scars.

6.5.1 a) Construction of the topography using a high resolution point cloud obtained with a Terrestrial Laser Scanner (TLS)

The data required for this analysis is obtained using a TLS which can provide a high resolution point cloud suitable for the rock slope characterization. After the data acquisition, the scans are aligned identifying common points following an automatic process which minimizes the alignment errors. The alignment can be carried out using commercial software such as PolyWorks (Polyworks, .http://www.innovmetric.com/).

6.5.2 b) Identification of discontinuity sets

As the objective of this work is to generate the rockfall scar volume distribution based on the existing joint sets, first, the principal discontinuity sets contributing to the formation of the rockfall volumes must be identified.

A first visual field inspection and the observation of photos of the slope are carried out in order to evaluate the approximately the number of joint sets and their orientation. Then, the point cloud is rotated and observed in detail using both Gocad software (Earth Decision Sciences, http://www.earthdecision.com/) and Cloud Compare (Girardeau-Montant, 2006) to get a better idea of the principal sets. Joint sets are formed by points having a similar orientation and dip

angle, and therefore, the properties of each point such as the dip and dip direction are obtained by fitting planes and evaluating their normal vector. For each point, a plane is fitted using a minimum number of neighbouring points within a search radius and satisfying a maximum collinearity index (K) and a minimum coplanarity index (M) (Figure 6-6). This approach is based on the moment-of-inertia method (Woodcoock 1977; Fernández 2005 and García-Sellés et al. 2011). The smaller the K-values, the better the points are fitted in a line. The larger the M-values, the better the points are fitted in a plane.

Noise (e.g. ought to vegetation) displays non acceptable M and K values and the respective points are filtered out using the SEFL software (Garcia-Sellés et al. 2009, 2011). The remaining points are represented in a stereoplot for identification of the discontinuity sets. As shown in Figure 6-4, since not all the discontinuity surfaces are large, flat and smooth, some planes, mostly the small and eroded ones, display as well non suitable K and M indexes and are eliminated. However, most of them could form part of existing small rockfall scars and thus, being necessary for the subsequent analysis. Since it is not known which type of planes (large and/or smaller) correspond to the past events, all possibilities must be considered. Therefore, two approaches based on different criteria (K, M and search radius) are followed for the identification of the discontinuity sets. The approach A takes into account irregular surfaces, and both, large and small (including eroded) scars are considered. In that case, less restricting criteria (K, M and search radius) are used, and the remaining points belonging to vegetation should be manually removed. The approach B provides planes which satisfy more restricting criteria, and thus only large and smooth scars are obtained in this case. More details about both approaches will be given later.

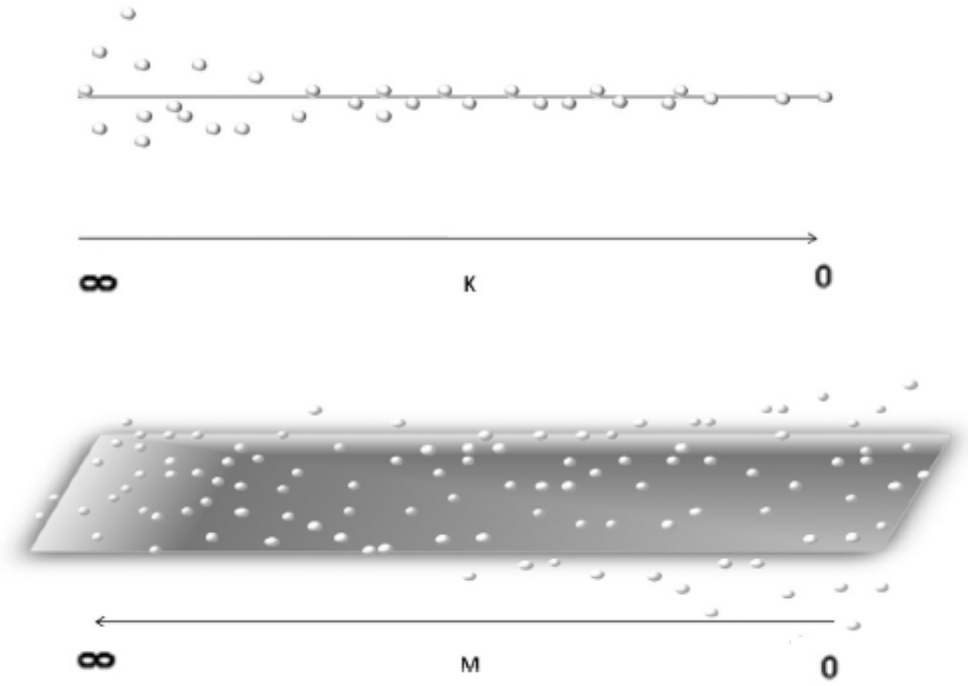

Figure 6-6: K-value is the collinearity index. The smaller its value, the better the points are fitted in a line. M-value is the coplanarity index. The larger its value, the better the points are fitted in a plane (modified from Santana et al.,2012).

6.5.3 c) Generation of discontinuity surfaces

Once the different discontinuity sets have been identified, point clusters defining plane surfaces are selected for each discontinuity set. Two neighboring points located at a different height and having a similar orientation can belong either to the same discontinuity plane due to the undulation (Figure 6-7, red points) or to different surfaces of the same set separated by spacing (Figure 6-7, green points).

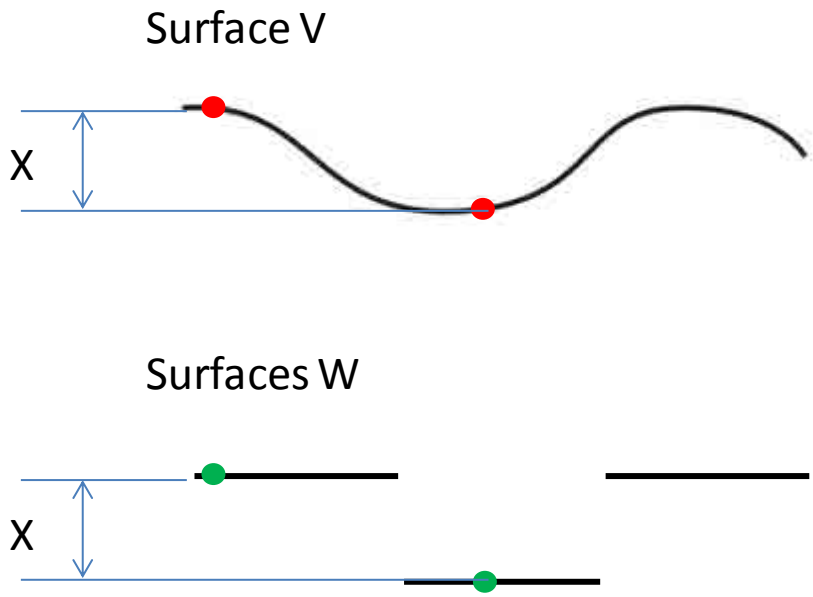

Figure 6-7: Profiles of different surfaces. The surface V is undulated. The surfaces W are three different planes. Red and green points are all neighbouring points located at a distance X. The red points belong to the same surface. The green points belong to different surfaces planes.

To decide whether two neighboring points belong to one undulated or two different surfaces the following criterion is used (Santana et al., 2012): if the distance between the two points is greater than the minimum spacing of the discontinuity set, then the two points belong to different surfaces. If the distance is smaller than the spacing they belong to the same undulated surface. This condition is shown graphically in Figure 6-8 and should be implemented separately for points belonging to each discontinuity sets, applying for each set appropriate thresholds for the distance D and the angular tolerance α (Figure 6-8). This procedure is automatic using the software SEFL which permits the generation of planes for each set separately. After the generation of the planes, a visual check is carried out to check whether points belonging to different surfaces have been grouped into the same cluster (under-segmentation) or points belonging to the same surface have been attributed to different groups (over-segmentation). This check can be done using the Gocad or Cloud Compare programs.

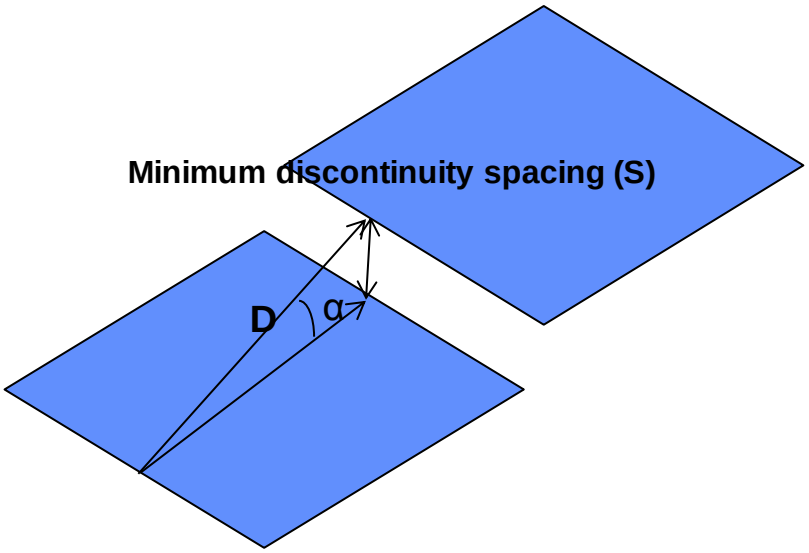

Figure 6-8: If the difference in height between two points is smaller than S, they are considered to belong to the same surface.

6.5.4 d) Calculation of the volume of the existing scars

The next step is the calculation of the dimensions of the rockfall scars. In order to evaluate the volumes for the whole slope face automatically, a procedure similar to the applied by Santana et al. (2012) is used. First of all, it is assumed that rockfall scars can be defined as prisms whose volume is the product of the area of the overhanging discontinuity (Figure 6-2, set A) with the height of the scar (Figure 6-2, set B). This is performed using an algorithm developed by Santana et al. (2012) and integrated in the program SEFL by which, areas and heights of the surface planes can be determined. The data for the scar areas and heights evaluated on the point cloud are fitted by statistical distributions. The respective Probability Density Functions (PDFs) are obtained using the program EasyFit (http://www.mathwave.com/). Then, the volume distribution is calculated by means of a Monte Carlo simulation.

As aforementioned, in case of overhangs having a stepped profile, the reconstruction of the rockfall volume detached from a scar is not trivial, as it is not known whether such scars are the result of several small rockfall events or of a single larger event involving several bedding planes. Each scenario leads to different RSSDs.

For that purpose three different scenarios are analysed using the approaches A and B: 1) Small scars are part of larger events generated by the intersection of large discontinuity surfaces. A retreat of the rock wall parallel to the slope face is assumed. The scar is generated by the detachment of a few large blocks (Figure 6-9, 1). 2) Scars have been generated by successive small-sized rockfall events. In this case, it is assumed that the cliff retreats parallel to the original topographic surface (Figure 6-9, 2). The scar size is determined by the height of the scar below the overhang. Finally, 3) Scars have been generated by several small-sized rockfall events. Thus, both large and small rockfall scars have occurred. The main difference from scenario 2 is that the cliff retreat is considered from a homogeneous original reference topographic surface producing a wider range of scar heights and, consequently, a wider range of volume sizes (Figure 6-9, 3).

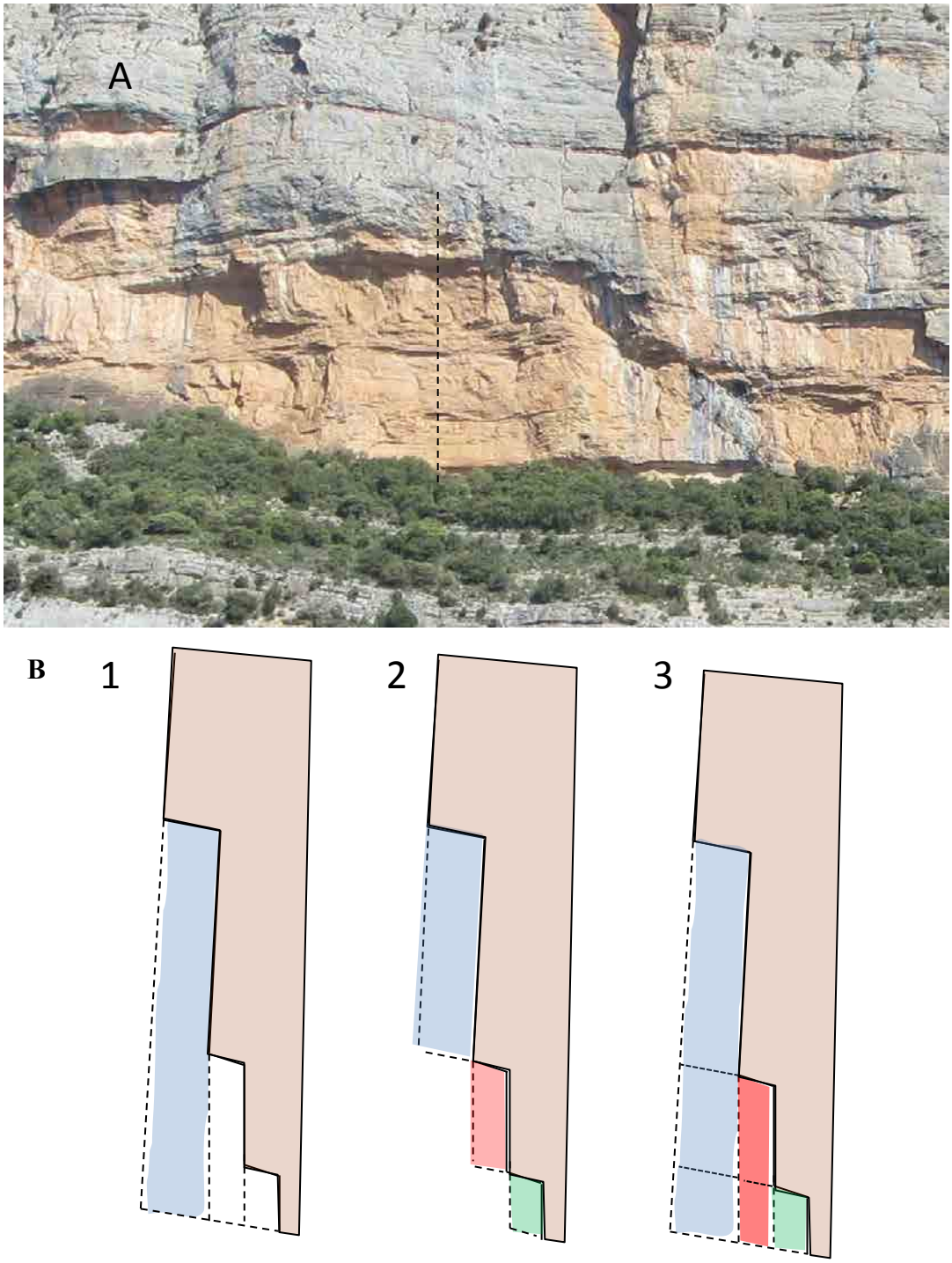

Figure 6-9: Cross sections of the massif showing the possible scenarios of detachment evolution. A: View of the massif. The dashed line indicates the location of the cross section; B 1: Big elongated rock prisms are detached from the cliff; 2: Small rockfalls take place in a staggered slope and 3: Large rockfall scars are the result of several small-size rockfall events. In all the scenarios, a staggered profile is generated.

For each scenario, areas and heights are calculated as follows:

Scenario 1 (Figure 6-9, 1):
Restrictive K and M criteria to generate discontinuity surfaces are used (approach B), resulting in both large and smooth surfaces. The area of the large overhanging surfaces is used as an

approximation of the basal area. Regarding the height of the scar, the length of the discontinuity planes belonging to the vertical set is used (Figure 6-10, A).

Scenario 2 (Figure 6-9, 2):
Flexible K and M criteria to generate discontinuity surfaces are used (approach A), obtaining small-sized, irregular and undulated overhanging surfaces (bedding planes or set 1). The vertical discontinuity surfaces (or set 2) generated with the approach B are too irregular and rough to be identified as surfaces that could yield reliable heights of the scars (Figure 6-10, B). Alternatively, the spacing between successive overhanging planes located one on top of the other (bedding planes or set 1) is used. This provides a minimum height as rockfall scars can have heights involving one or more spacings.

Scenario 3 (Figure 6-9, 3):
The surfaces of the overhangs (bedding planes or set 1) are obtained following the same procedure as for the previous scenario. The definition of the scar height is also evaluated using the spacing of the overhanging planes (bedding planes or set 1). In this case, not only the spacing between consecutive bedding planes located one on top of the other is considered but also the distance between planes located at different parts of the cliff (rock wall retreat parallel to the massif) (Figure 6-10, B).

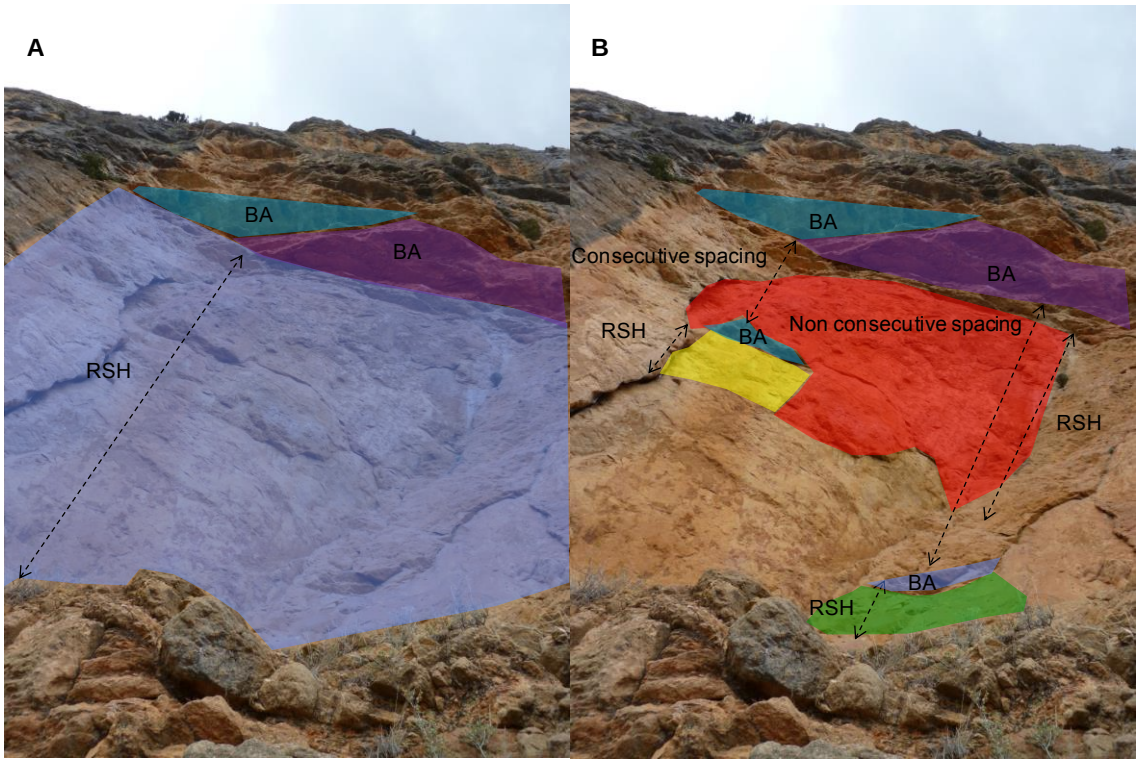

Figure 6-10: A: Large vertical discontinuity surface generated with the approach B (scenario 1). B: Different small-size vertical discontinuity surfaces generated with the approach A (scenarios 2 and 3). BA: Basal Area of the overhang (bedding plane); RSH: Rockfall scar height.

6.6 Application

Data collection was carried out in collaboration with the University of Lausanne (UNIL). The TLS used was the OPTECH Ilris 3D Long. It has an accuracy of 7 mm at 100 m and a

maximum range of 1,330 m as well as a high data acquisition speed (up to 10000 points/second) (http://www.optech.com/). A total of 3 scans were performed at a maximum distance of 700 m obtaining 20,251,588 points that cover an area about 150,000 m^2. This represents a resolution of about 1.4 points/cm. The scans were later aligned with PolyWorks software (Polyworks, .http://www.innovmetric.com/). Zone 1 (Z1), covers an area of 14,010 m^2. Its corresponding point cloud can be seen in Figure 6-11. Zone 2 (Z2), with an extension of 6,802 m^2, is shown at Figure 6-12.

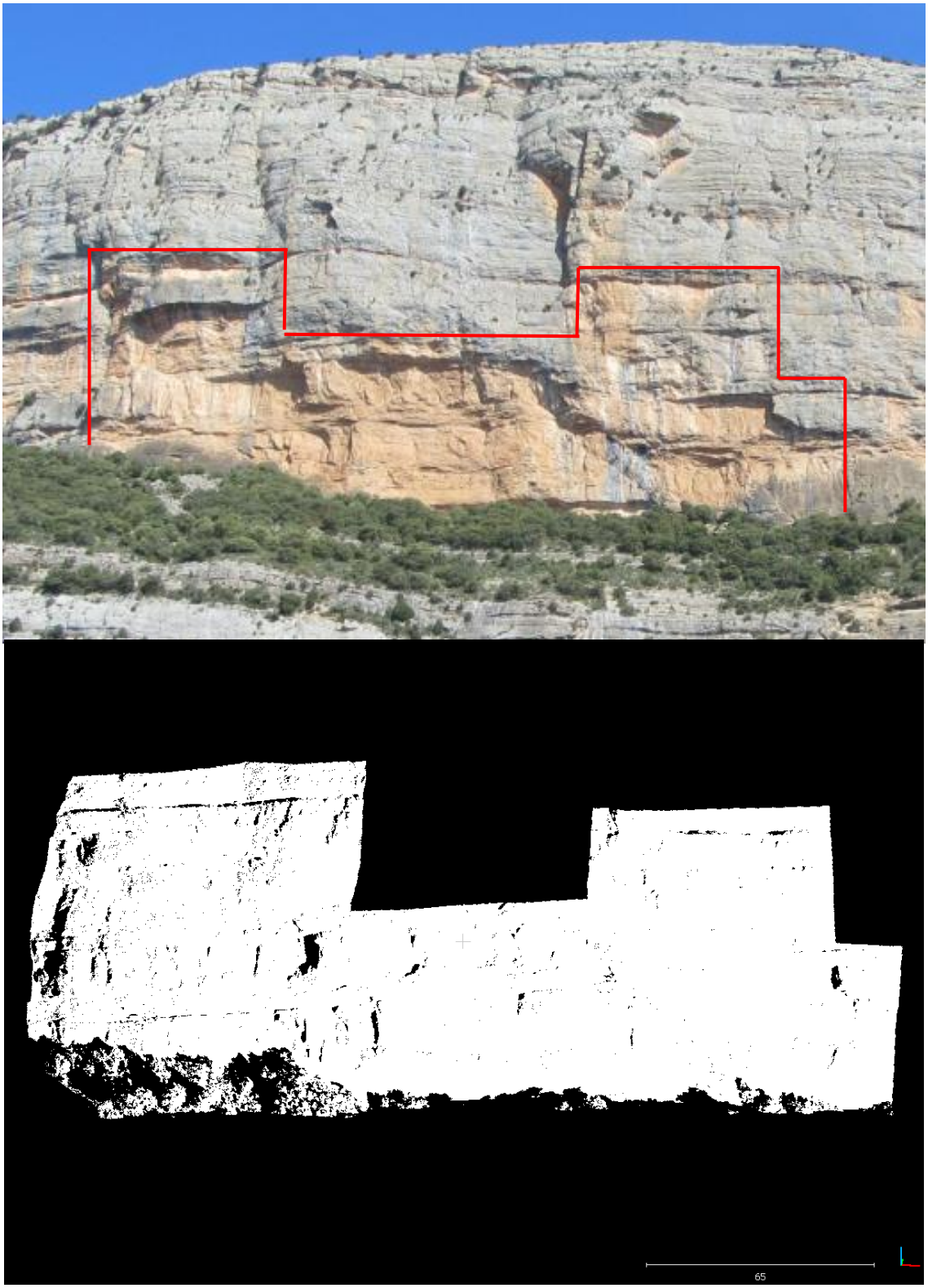

Figure 6-11: Point cloud of zone 1 covering an area of 14,010 m^2.

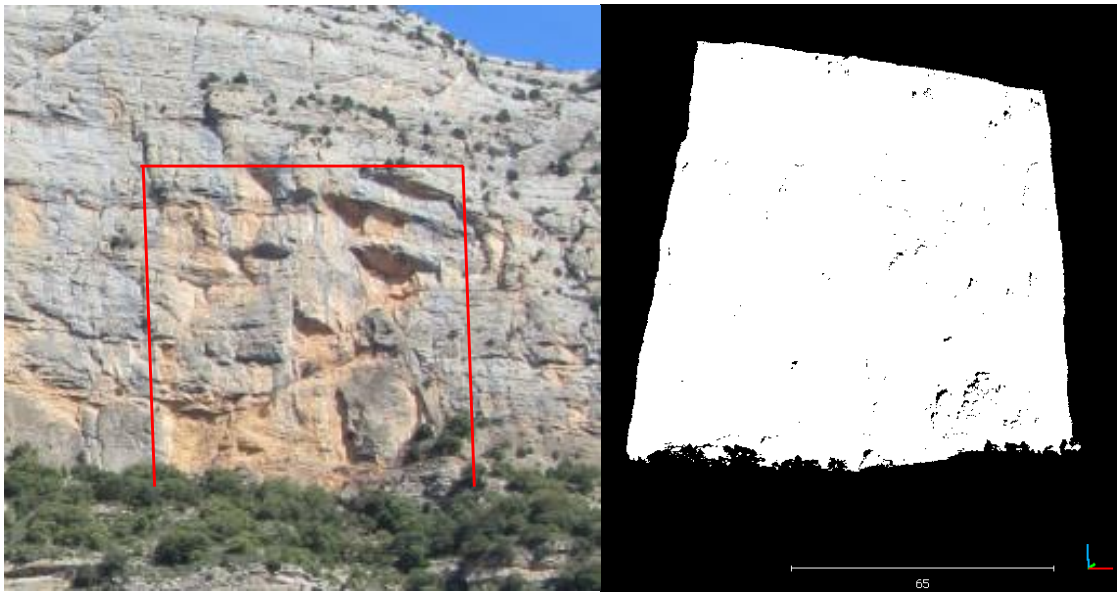

Figure 6-12: Point cloud of zone 2 covering an area of 6,802 m^2.

Once the point cloud was prepared, the discontinuity sets were identified. A first visual inspection, in the field and using photos was carried out obtaining three principal discontinuity sets (set 1, set 2 and set 3) (Figure 6-13). Set 1 includes the quasi-horizontal bedding planes which form the roof of the rockfall scars from which the rock mass has been detached by tension failure. These are mostly large, smooth, and regular surfaces although smaller, rough and irregular planes may be present as well due to erosion and dissolution of the initially formed surfaces. Set 2 includes very undulated vertical planes parallel to the slope face. They are less persistent than set 1. Set 3 includes vertical planes, perpendicular to the rock wall. It is a very irregular set which is not present in most of the rockfall scars and thus, its contribution to the rockfall detachment is minor. Hence, set 3 is considered in the following steps.

Thereafter, a sensitivity analysis for the parameters M, K and search radius was performed in order to fit planes at each point (Annex 15: Sensitivity analysis for planar regression; normal vector definition for each point) and obtain their dip and dip direction.

According to Fernández (2005), values for M greater than 4 and values for K smaller than 0.8 provide the best-fit planes. García-Sellés et al. (2011) used a less restrictive M-value of 3.5 since they worked with more irregular surfaces ought to their tectonic origin. Other examples of M and K values can be found at Santana et al. (2012) who used a minimum M-value of 3.5 and a maximum K-value of 1.2 for granodiorites at an intensely fractured slope in Andorra. Hence, the election of both values, K and M, depends of the genesis and the type of discontinuity surfaces as well as the degree of resolution required for the analysis.

Changes in the K-value slightly affect the results, therefore a typical value equal to 1.2 in accordance with the suggested values in the literature was chosen. The results were checked by visual inspection of the point cloud using the Cloud Compare software. Conversely, the generated surfaces are very sensitive to the variations of the coplanarity index (M). For large and smooth surfaces, restrictive parameters as the ones proposed by Fernández (2005) can be used. Nevertheless, when working with smaller and irregular surfaces (e.g. dissolved limestone surfaces) the afore-mentioned values must be less restrictive.

For values greater than 3.5, the points that belong to the small and irregular surfaces of set 1 are removed from the point cloud. For the case study the smallest M-value found preserving all the points belonging to the small surfaces of the set 1 was 2.5. Concerning the radius, 2.5 cm provides realistic surfaces. For a smaller radius, important data is lost as several points are

removed in areas oblique to the laser beam where the density of the point cloud is lower. On the other hand, for the irregular surfaces of the discontinuity boundaries and small surfaces, the greater the radius, the worse the coplanarity index.

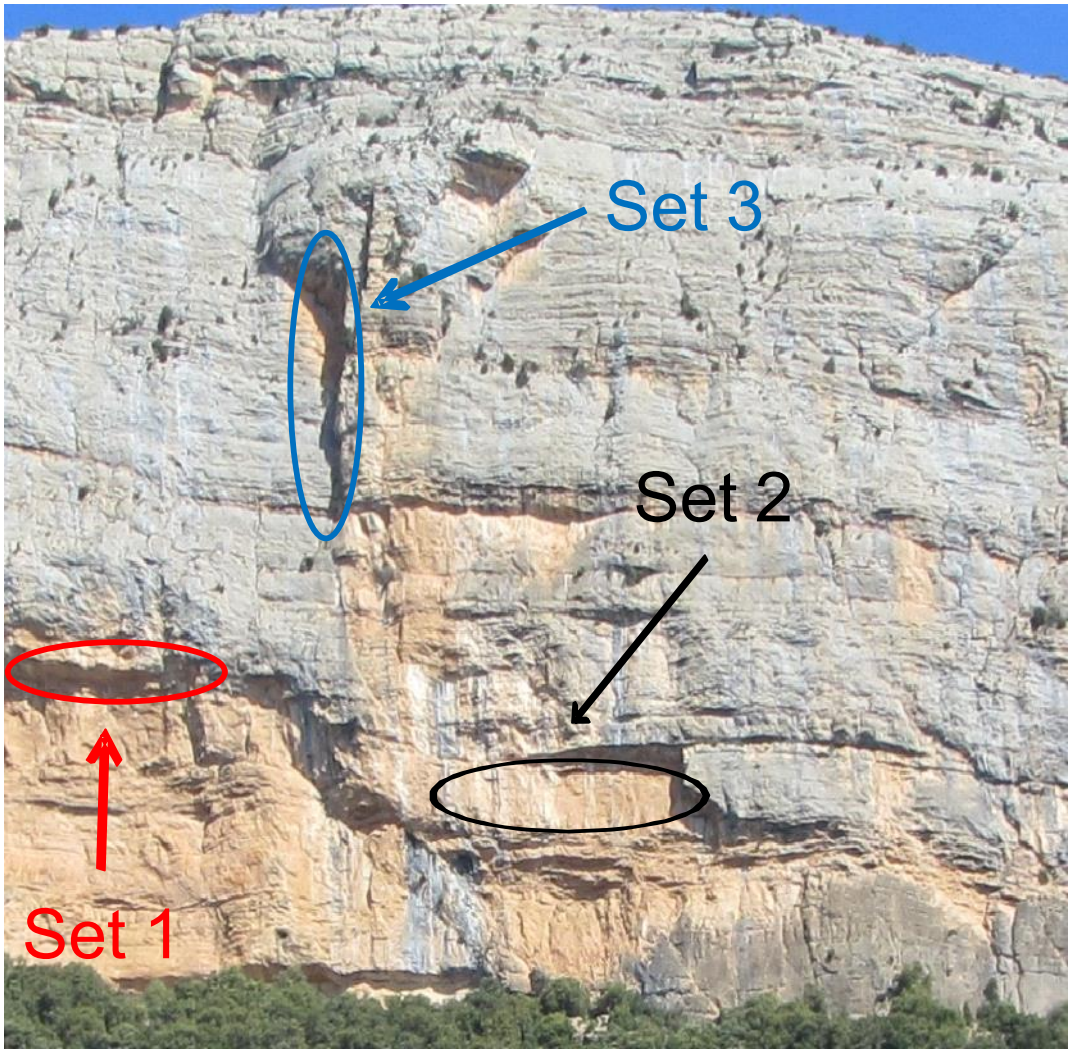

Figure 6-13: Three main discontinuity sets identified in the massif by visual checking.

At this point, two approaches were followed. In approach A, the afore-mentioned small-sized, eroded and irregular surfaces were obtained. Thus an M larger than 2.5, a K below 1.5 and a search radius of 2.5 cm were used. In approach B, only large scar surfaces were obtained using M-values larger than 3.5 were used.
For the two approaches, planes were fitted to each point and the dip and dip direction of the normal vector (pole), and the degree of fit (M and K) were calculated. The derived stereoplots are shown in Figure 6-14. Two main orientations were obtained using both approaches. Points of each orientation were grouped into set 1 and set 2, respectively, according to the dip and dip direction (Table 6-1).

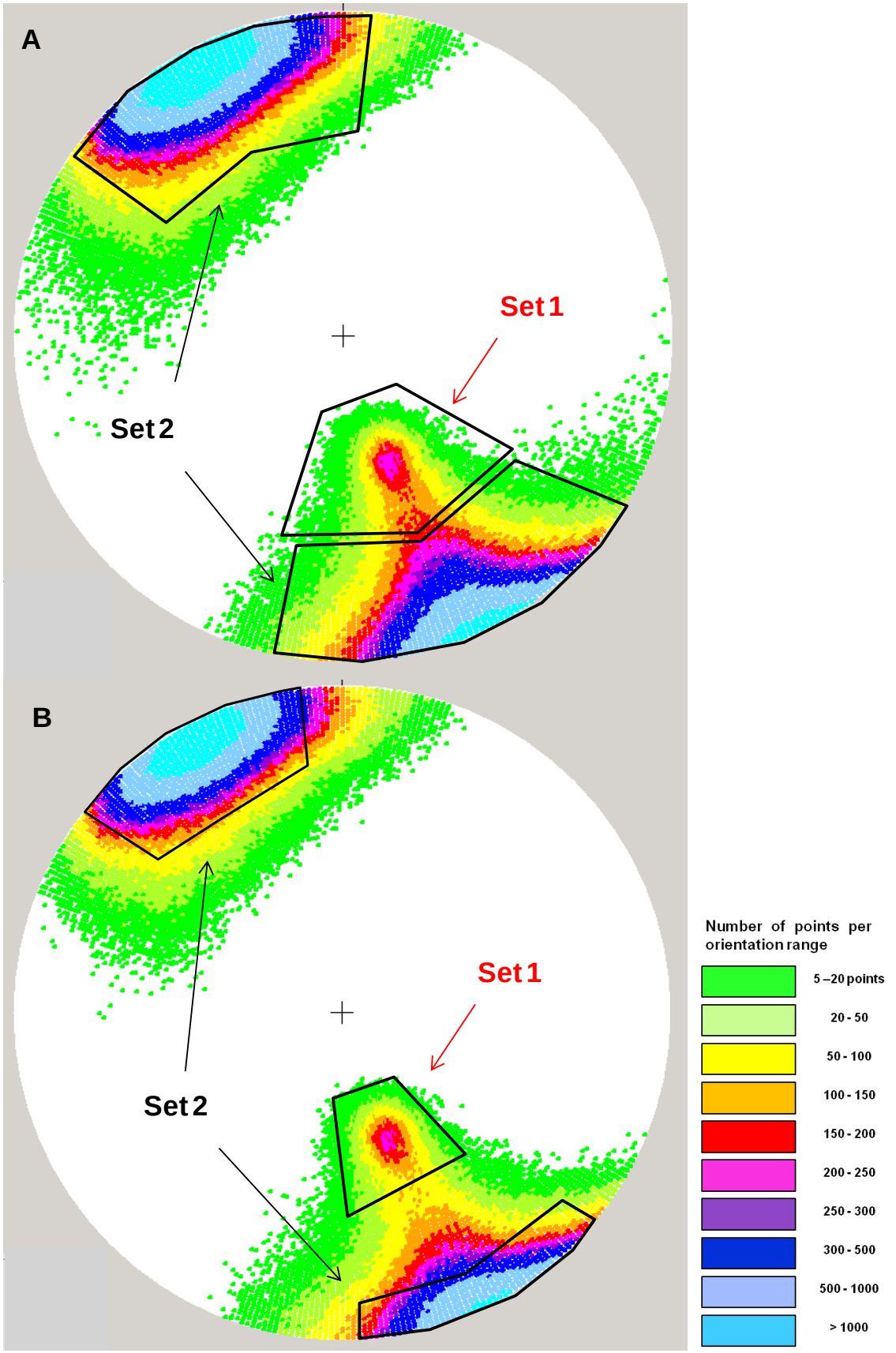

Figure 6-14: Stereographic density plots derived from the point cloud. In the upper plot, M larger than 2.5, K smaller than 1.5 and a search radius of 2.5 cm has been applied. In the lower plot, M larger than 3.5, K below 1.5 and a search radius of 2.5 cm is used. Both sets can be identified in the field as well.

Table 6-1: Dip direction and dip of the two sets identified using approach A and B.

Approach	Set	Dip direction	Dip	M	K	Radius (cm)
A						
	1	341 ± 35	39 ± 17	>2.5	<1.2	2.5
	2	155 ± 30	90 ± 35	>2.5	<1.2	2.5
B						
	1	338 ± 22	39 ± 17	>3.5	<1.2	2.5
	2	145 ± 23	90 ± 10	>3.5	<1.2	2.5

For each set, isolated points (noise) were removed applying a continuity filter (Annex 16: Sensitivity analysis for filter continuity; removal of isolated points). The inclusion criteria are:
For the approach A, only points surrounded by a minimum number of 6 points located within an angular distance smaller than 20º and a maximum radius of 0.4 m were considered in set 1. Concerning set 2, which is a more continuous set and with larger surfaces, less restrictive conditions were applied: 1 m of maximum radius, 40 points and 20º of angular distance were considered, accordingly.
For the approach B, since only larger surfaces were identified, a minimum number of 6 points, 0.4 m of radius and 15º of angular distance were selected.
The next step was the generation of the discontinuity surfaces for the two sets. The parameters S, D and α must be determined for both approach A and B.

Approach A: Generation of small surfaces.
For set 1, to optimize the parameters S and α, a sensitivity analysis was performed for D = 1m (Table 0-6, Annex 17: Sensitivity analysis for the definition of discontinuity sets). It was observed that for values of S smaller than 0.25 m over-segmentation was produced. On the contrary, for values larger than 0.25 m, under-segmentation was observed. The appropriateness of the S and α values was checked plotting the obtained planes by means of the Gocad software. Furthermore, the spacings between the surfaces of set 1 were also measured in order to validate the selected distance S. If discontinuities were persistent, the spacing would be measured perpendicular to the average orientation of each set. Since discontinuities are non-persistent (Figure 6-16, A), several scanlines (measurements along a predefined line or row) were needed in order to obtain the minimum spacing (Kemeny and Turner, 2008) (Figure 6-15).

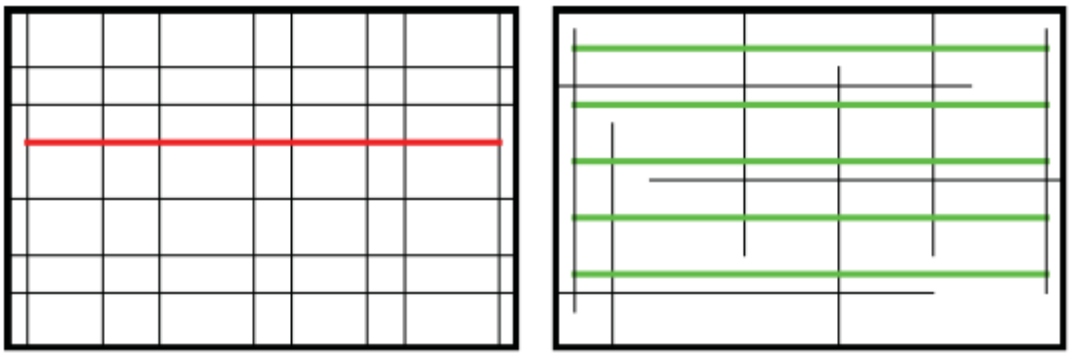

Figure 6-15: a) Persistent joints (Black lines) giving a single and well-defined spacing with a single scanline (Red line) measured perpendicular to the average orientation. b) Non-persistent joints (Black lines) yield a varied range of spacings which are calculated by several scanlines (Green lines) (Kemeny and Turner, 2008).

The accessibility of the slope is limited only at its lower part, which complicates the measurement of the spacing by means of scanlines using the methodology described by Priest & Hudson (1981). Therefore, 31 vertical cross sections of the study area (19 for zone 1 and 12 for zone 2) were made using the point cloud instead (Figure 6-16 B and D). They were carried out with the Matlab software. Then, the perpendicular distances between the discontinuity planes were measured at each cross section.

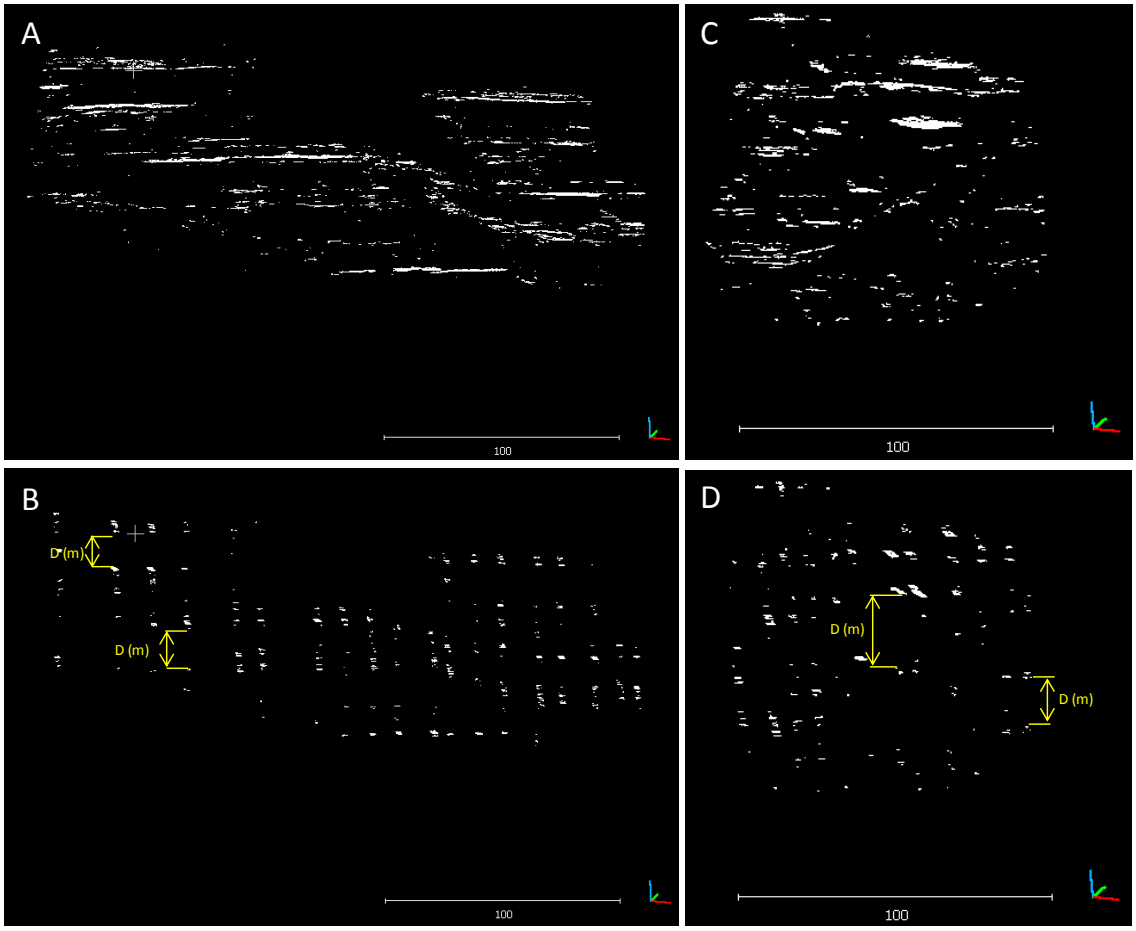

Figure 6-16: A) Point cloud of zone 1 (Figure 6-3) representing the discontinuity surfaces belonging to set 1 obtained using approach A; B) 19 vertical cross sections made at zone 1 to obtain the spacing distribution between the discontinuities of the subfigure A. C) Point cloud of zone 2 showing the discontinuity surfaces of the set 1 obtained using Approach A; D) 12 vertical cross sections made at zone 2 to obtain the range of spacings between the afore-mentioned discontinuities of the subfigure C.

As it can be seen in Figure 6-17, 400 spacings were measured between the discontinuities of set 1. Some of them are smaller than 0.25 m. As aforementioned, for values smaller than 0.25 m over-segmentation is produced (probably due to the undulation of planes of set 1). Thus, for values smaller than 0.25 m we are not able to discriminate between undulation and spacing.
To this end, for an S of 0.25 m, a value of D =1 m and α=14.48º have been chosen.

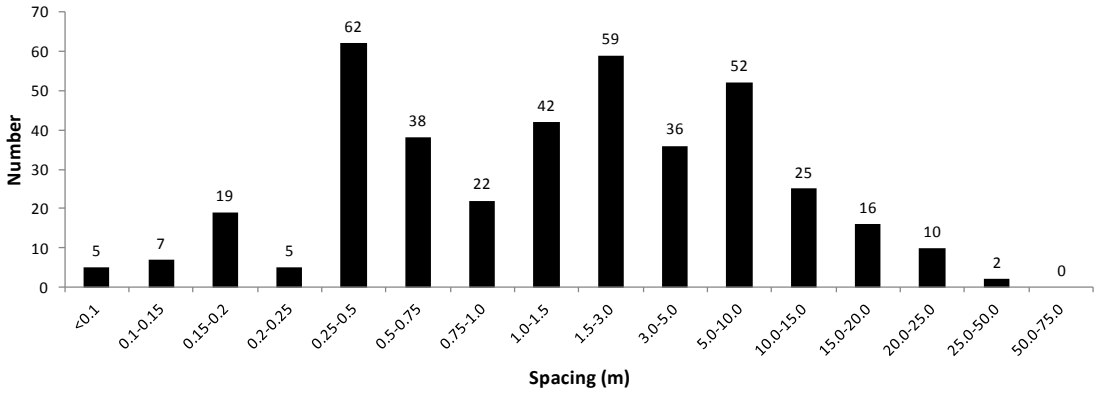

Figure 6-17: Distribution of the 400 spacings measured between planes of set 1 following the approach A. Spacings longer than 0.25 m are the most frequent.

For set 2, it was not possible to generate small-size discontinuity surfaces. They are not sufficiently persistent to be automatically detected and the undulation of set 2 masks them producing over-segmentation in most cases. Alternatively, the height of the rockfall scars, given by the length of the discontinuity planes of set 2, was obtained using the spacings of set 1. Due to the low persistence of set 2, the spacing is sensitive to the location of the cliff where it is measured. In some cases, the spacing between successive overhanging planes located one over the other (bedding planes or set 1) is used. In addition to this, not only the spacing between consecutive bedding planes is considered but also the distance between planes located at different parts of the cliff.

Approach B: Considering only large planes

For set 1, the obtained scar planes are larger, more uniform and better well-spaced than following the previous approach. A sensitivity analysis was performed for D = 1 m (Table 0-7, Annex 17: Sensitivity analysis for the definition of discontinuity sets). It was observed that for values of S lower than 0.4 m over-segmentation was produced. On the contrary, for higher values, under-segmentation was observed. Therefore, a D=1 m and α= 24º were used for a minimum spacing of 0.4 m. The obtained planes were checked against the point cloud by means of the Gocad software. Furthermore, since only large planes are considered using this approach, only surfaces formed by a minimum number of 40 points per cluster were accepted.

Unlike approach A, with approach B the discontinuity planes of set 2 are detected. Nevertheless, the high undulation of this set still complicates the calculation of the minimum spacing (S) To overcome this, the spacing between the discontinuities of set 2 was approximated by the minimum width of the planes of set 1 (Figure 6-18) which can be calculated by means of the SEFL software. The minimum spacing obtained was 0.4 m. For D=1, an angular distance of α=24º was assumed. Over-segmentation due to undulation could be avoided requiring a minimum threshold of 100 points per cluster. In Table 6-2 the final values are presented.

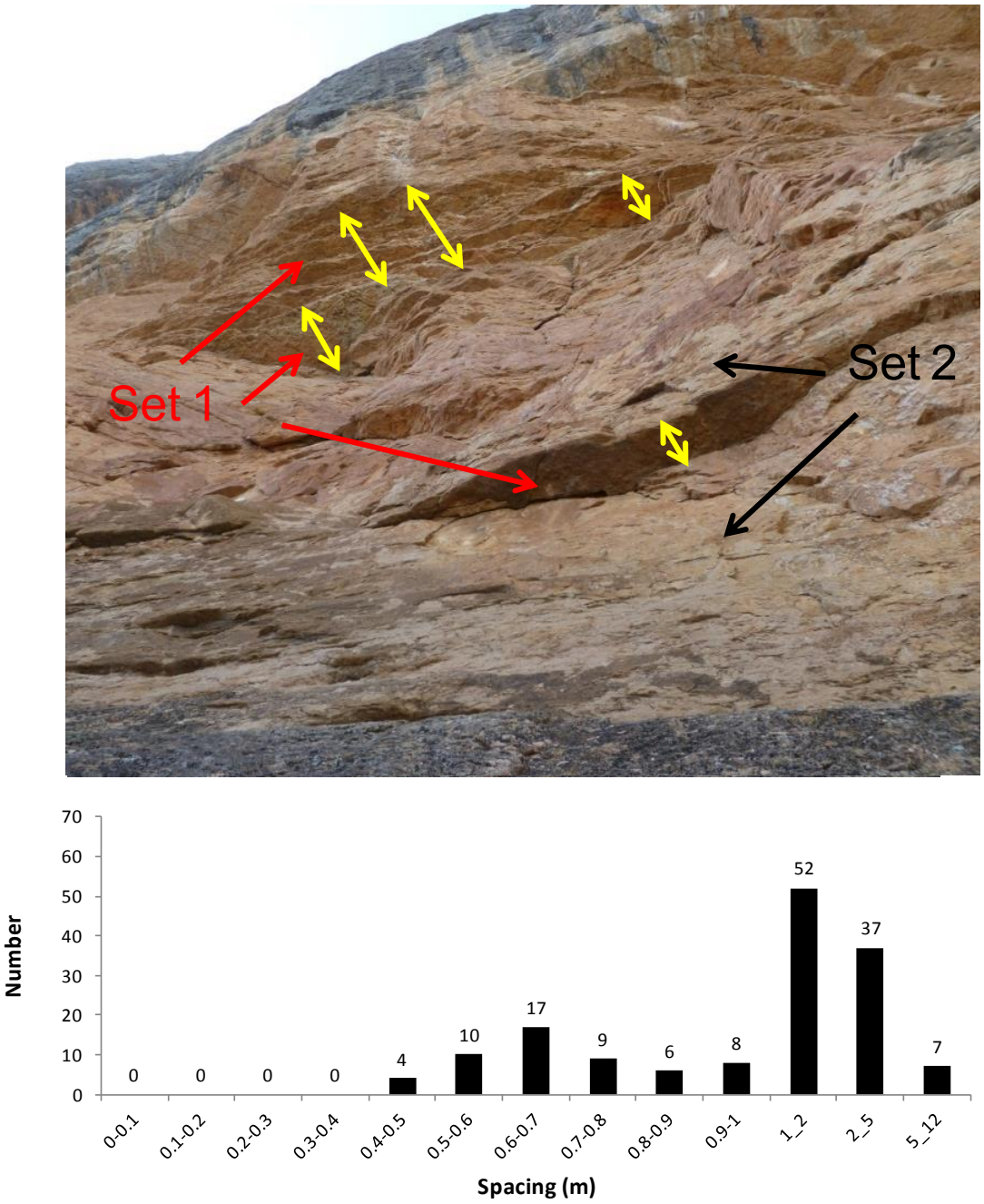

Figure 6-18: Spacing measured between 150 discontinuities of set 2 for approach B. A minimum spacing of 0.4 m was chosen.

The results confirm that for set 1, following approach A which includes small surfaces, the minimum spacing calculated (0.25 m) is smaller than following approach B (0.4 m) that considers only large planes. With relation to set 2 (approach A), the high undulation of the vertical slope face prevents the generation of small vertical planes and the determination of their minimum spacing. So, the minimum width of planes of set 1 was used instead. When considering larger planes (approach B), discontinuity surfaces of set 2 could be generated. However, the minimum spacing also must be approximated using the minimum width of planes belonging to set 1 due to the afore-mentioned high undulation. Details for the parameters used for each approach can be seen in Table 6-2.

Table 6-2: Data used to define the discontinuity sets in each approach.

Approach	Set	D (m)	α (°)	Minimum spacing (m)	Minimum number of points per cluster
A					
	1	1	14.48	0.25	-
	2	-	-	-	-
B					
	1	1	24	0.4	40
	2	1	24	0.4	100

6.6.1 Definition of different scenarios for the evaluation of the rockfall scar volumes

The volume of the rockfall scars was evaluated assuming that: 1) The discontinuities of set 1 correspond to the basal surfaces of the rockfall scars and 2) The rockfall scar height can be defined by the length of discontinuity planes of set 2.

As described previously, for large rockfall scars (approach B) (Figure 6-9, B), the height of the scar is obtained using the length of the discontinuity planes of set 2. Nevertheless, when considering also smaller, eroded and irregular rockfall scars (approach A, Figure 6-9, C and D), planes belonging to the set 2 cannot be obtained due to its high undulation. Hence, the spacing between discontinuities of set 1 obtained following approach A, was used instead (Figure 6-17).

For the subsequent Monte Carlo simulation to obtain the RSSD, 100,000 random volumes were created by multiplication of the scar basal areas with the heights. To take into account all the afore-mentioned possibilities about these two Monte Carlo variables, three scenarios were considered (Table 6-3). The random volume samples were then generated assuming for the variables the distributions of Table 1-4 and calculating their product.

Table 6-3: Scenarios carried out to consider all the different rockfall scar volumes given by different detachment mechanisms. Scenario 1, considers only large events, scenario 2, small-sized rockfall events and scenario 3, large and small rockfall events.

Scenario	Basal shape	Length
1	Large discontinuities of set 1 (Approach B)	Height of discontinuities of set 2 (Approach B)
2	Large and small discontinuities of set 1 (Approach A)	Spacing measured between successive discontinuities of set 1 (Approach A).
3	Large and small discontinuities of set 1 (Approach A)	All spacings measured between discontinuities of set 1 (Approach A).

Table 6-4: Distribution of areas and heights according to the different approaches and zones.

Scenario	Zone 1		Zone 2	
	Area	Height/Spacing	Area	Height/Spacing

1	Lognormal	Pearson6	Lognormal	Pearson6
2	Beta	Normal	Beta	Beta
3		Pearson5		Pearson5

Scenario 1:
Areas of the exposed bedding planes of set 1 (Table 6-1, approach B) were combined with heights of discontinuities of set 2 (Table 6-1, approach B), generating only large rockfall prisms (Blue prism in Figure 6-19). Thus, the number of large volumes is maximized and of mid-sized and small volumes minimized. Figure 6-19 depicts the estimated missing volumes including a frontal view (left) and a cross section (right) of the rock wall. The location of the cross section is indicated with a dashed line on the frontal view.
The areas of the planes of set 1 are well fitted by a lognormal distribution (Annex 18: Calculation of areas, lengths and spacings of discontinuity sets; application to the different scenarios, Figure 0-64) and the heights of the planes of set 2 by a Pearson6, accordingly, in both zones 1 and zone 2 (Annex 18: Calculation of areas, lengths and spacings of discontinuity sets; application to the different scenarios, Figure 0-66 and Figure 0-71).
The rollover effect observed for volumes smaller than 8 m^3 (Figure 6-22) can be interpreted by the minimization of the calculation of mid-sized and small rockfall scars in zone 1 (Guzzetti et al., 2002; Stark and Hovius, 2001). The maximum volume is 8,700 m^3.
The results for zone 2 as well as the whole area – both zones 1 and 2 -, presented at Figure 6-22, follow a similar pattern. The minimum calculated volume is 6 m^3 and 8 m^3 and the maximum volume is 3,400 m^3 and 8,700 m^3, respectively in zone 2 and in the whole area.

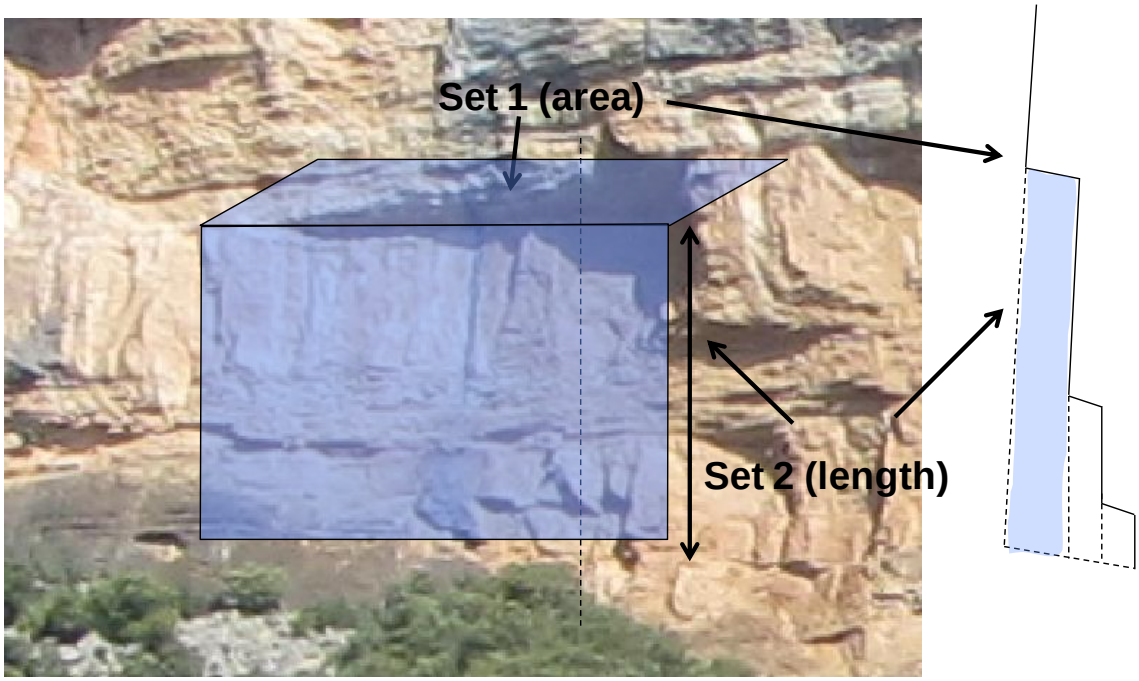

Figure 6-19: Scenario 1. Large discontinuity planes belonging to set 1 (Approach B in Table 6-1) and set 2 (Approach B in Table 6-1) are considered.

Scenario 2:

The areas of all the discontinuity planes belonging to set 1 (Table 6-1, approach A) have been combined with the spacings of set 1 considering the smallest rockfall scar heights (solid lines in Figure 6-20). Since the spacings of set 1 are generally smaller than the scar heights calculated for scenario 1, the rockfall scar volumes will be smaller as well. This leads to the minimization of mid-sized and large volumes and the maximization of small volumes. In the right part of Figure 6-20 the estimated missing volumes (grey, yellow and green prisms) are depicted, together with the volumes that were not considered (red prisms) at a cross section of the rock wall (thinnest dashed line on the left).

The spacings in zone 1 (Annex 18: Calculation of areas, lengths and spacings of discontinuity sets; application to the different scenarios, Figure 0-67) follow a normal distribution, while in zone 2, the best fit has been obtained with a beta distribution (Annex 18: Calculation of areas, lengths and spacings of discontinuity sets; application to the different scenarios, Figure 0-72). Areas follow a beta distribution in both zones (Annex 18: Calculation of areas, lengths and spacings of discontinuity sets; application to the different scenarios, Figure 0-65 and Figure 0-70).

For this scenario, where a large amount of small areas and spacings than larger ones has been obtained, for when fitting a PDF (Probability Density Function), working at logarithmic scale is strongly recommended. The advantage is that as logarithm is a monotonous function, probabilities remain constant and changes do not affect the data distribution (Egozcue and Ortego, 2006; Pawlowsky-Glahn and Egozcue, 2001; Tarantola, 2006).

Concerning zone 1, the roll over effect is not so accentuated since a minimum rockfall scar of 0.3 m^3 has been obtained (Figure 6-22). The maximum volume has been 4,100 m^3, being smaller than in scenario 1.

Results from zone 2 and from the whole area (Figure 6-22) indicate the same pattern as the minimum volume considered in both analyses is of 0.3 m^3. The maximum volume calculated has been 2,900 m^3 in zone 2 and 4,100 m^3 in the whole area.

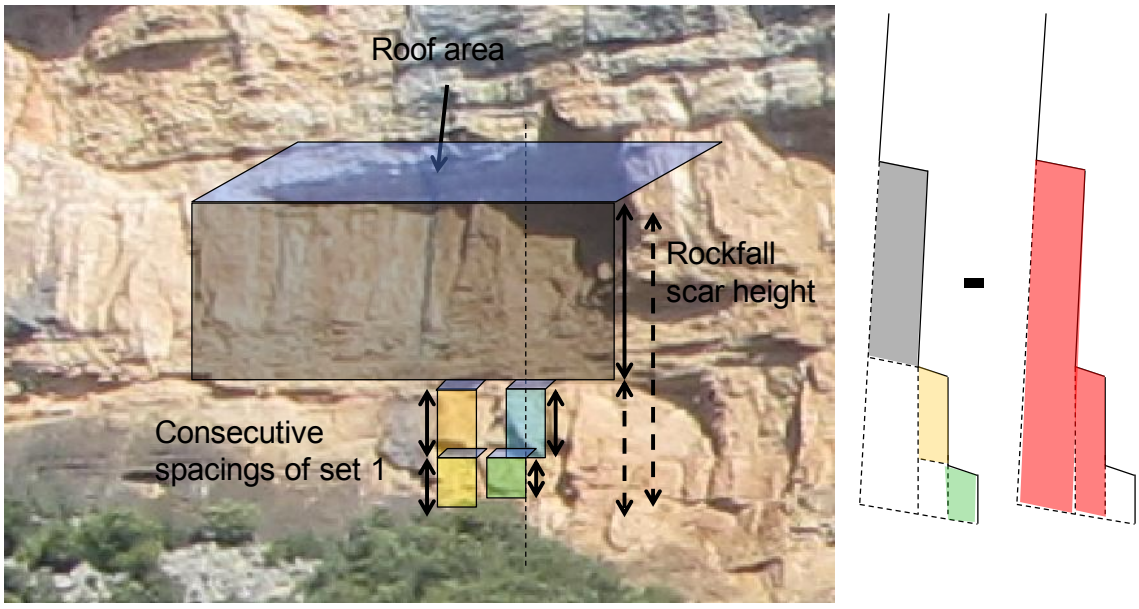

Figure 6-20: Scenario 2. Mid-sized and small volumes have been calculated combining all the areas of the overhangs (discontinuity surfaces of set 1) (Approach A, Table 6-1) and the spacings between consecutive planes of set 1 (solid lines). The number of mid-sized and large volumes (red prisms) is minimized and of small volumes maximized.

Scenario 3:

The areas of all planes belonging to set 1 (Approach A, Table 6-1) were combined with all the spacings calculated between the planes of set 1 used to approximate the rockfall scar height. All the spacings calculated in the 31 vertical cross sections (Figure 6-16, B and D) have been considered (represented as solid lines in Figure 6-21). The number of large volumes is minimized since the largest spacings are omitted (Figure 6-21). In the right part of the Figure 6-21 the estimated missing volumes (grey, yellow, green and red prisms) are depicted at a cross section of the rock wall (at the dashed line).

Spacings follow a Pearson 5 distribution (Annex 18: Calculation of areas, lengths and spacings of discontinuity sets; application to the different scenarios, Figure 0-68 and Figure 0-73). Areas follow a beta distribution in both zones (Annex 18: Calculation of areas, lengths and spacings of discontinuity sets; application to the different scenarios, Figure 0-65 and Figure 0-70). As for scenario 2 the logarithmic scale has been used during the fitting of the data.

Regarding zone 1, the observed roll over is very slight since a minimum rockfall scar of 0.3 m^3 has been considered (Figure 6-22). The maximum volume has been 4,100 m^3 being smaller than for scenario 1.

The results for zone 2 and for the whole area (Figure 6-22) follow the same pattern as for zone 1, with a minimum volume equal to 0.3 m^3 in both analyses. The maximum volume has been 3,300 m^3 and 4,100 m^3, in zone 2 and in the whole area, respectively.

Scenario 3 represents an intermediate situation which excludes large rockfall scar volumes (scenario 1) and does not maximize small rockfall scars (scenario 2).

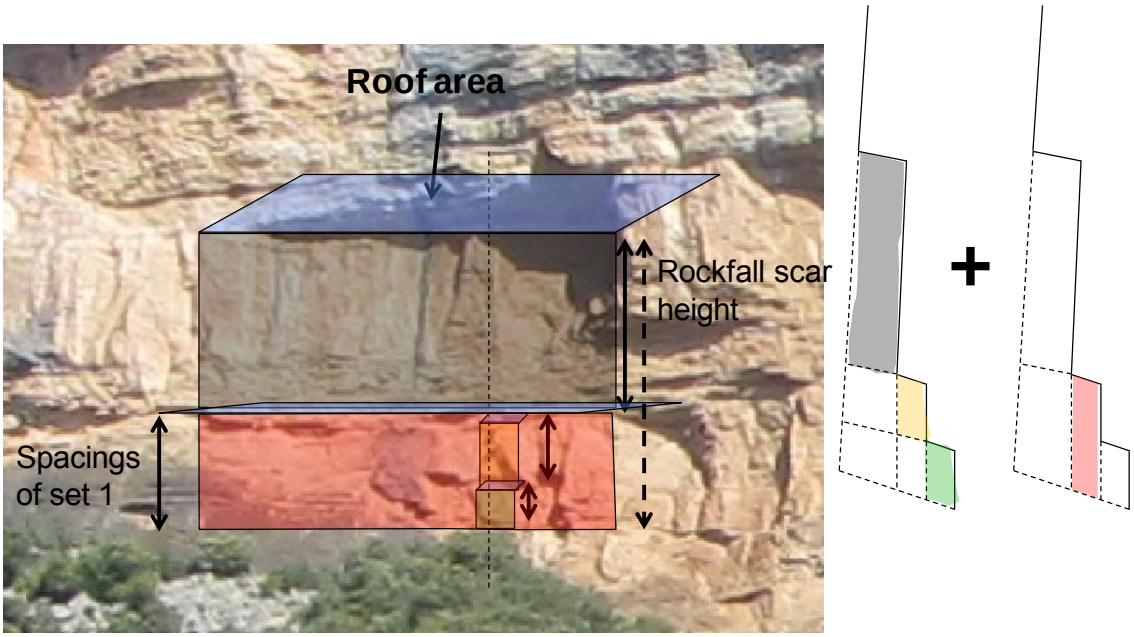

Figure 6-21: Scenario 3. The distribution of the rockfall scar volumes has been calculated combining the planes identified in set 1 (Approach A, Table 6-1) with the spacings obtained by scanlines. The number of large volumes is minimized.

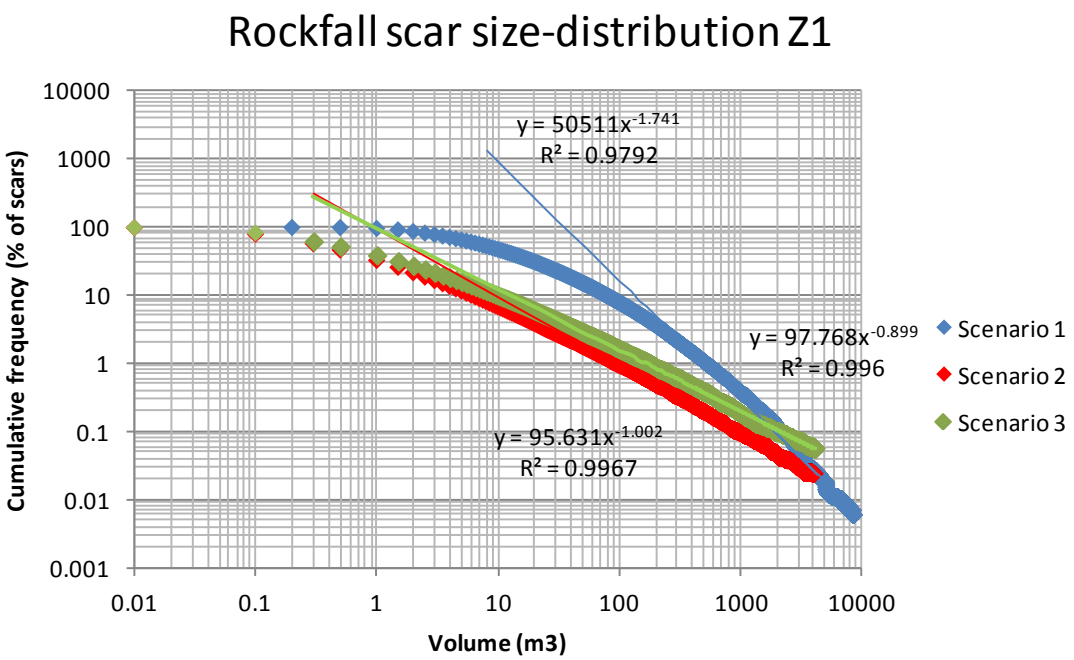
Rockfall scar size-distribution Z1
Cumulative frequency (% of scars)
10000
1000
100
10
1
0.1
0.01
0.001
0.01
0.1
1
10
100
1000
10000
Volume (m3)
y = 50511x-1.741
R² = 0.9792
y = 97.768x-0.899
R² = 0.996
y = 95.631x-1.002
R² = 0.9967
Scenario 1
Scenario 2
Scenario 3

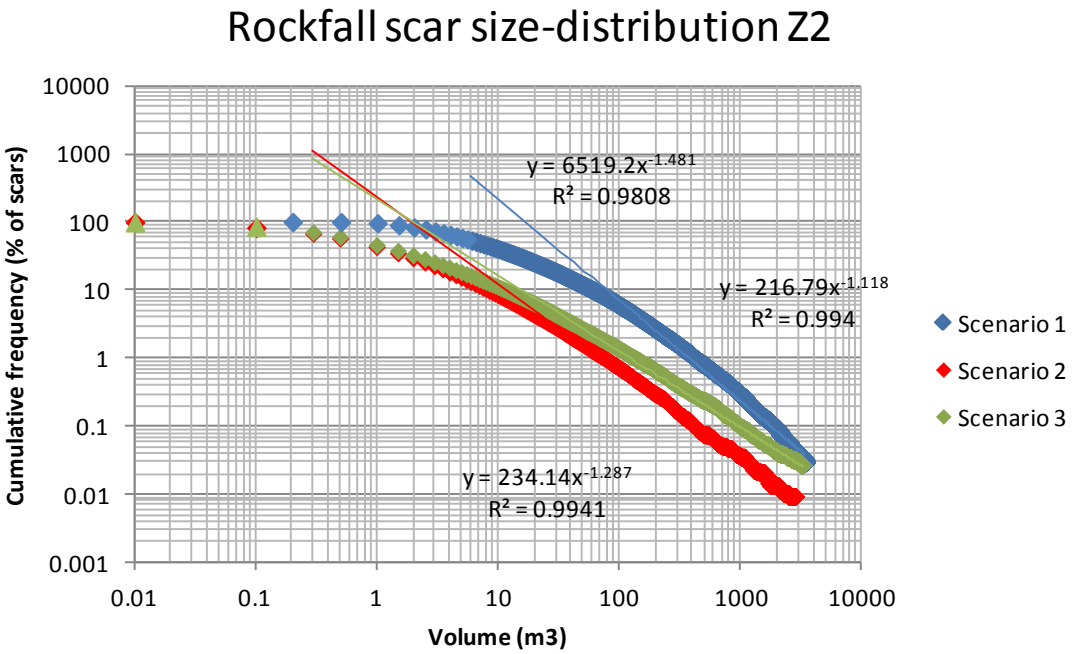
Rockfall scar size-distribution Z2
Cumulative frequency (% of scars)
10000
1000
100
10
1
0.1
0.01
0.001
0.01
0.1
1
10
100
1000
10000
Volume (m3)
y = 6519.2x-1.481
R² = 0.9808
y = 216.79x-1.118
R² = 0.994
y = 234.14x-1.287
R² = 0.9941
Scenario 1
Scenario 2
Scenario 3

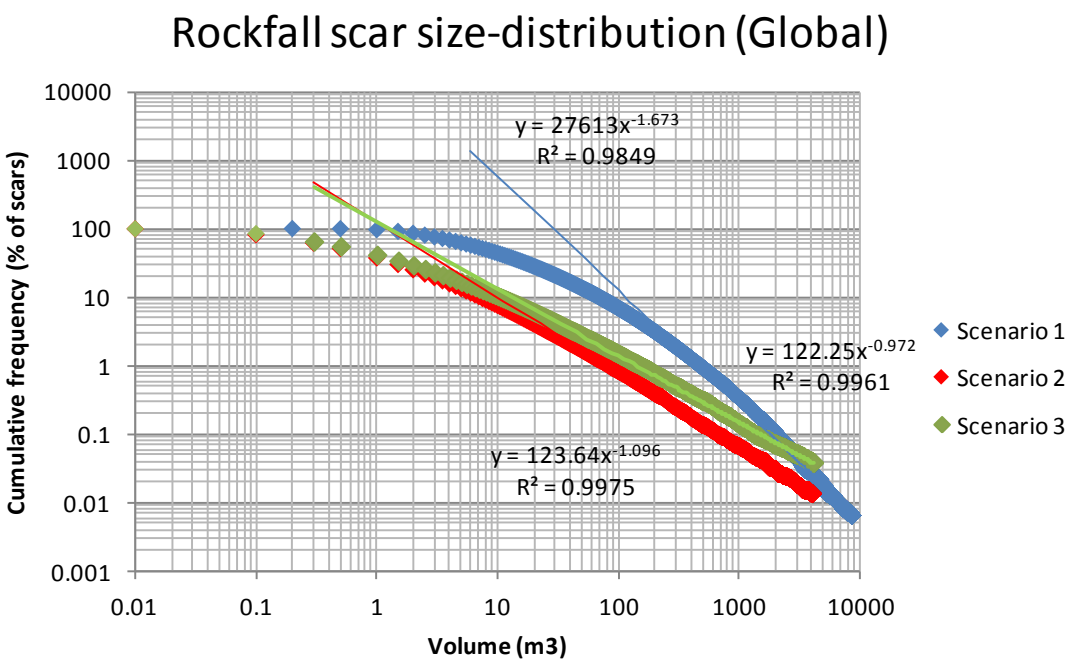

Figure 6-22: RSSD of zone 1 (Z1), zone 2 (Z2) and of the whole area (Global), for different scenarios.

6.7 Discussion

The rockfall scar volume distribution was indicated to be well fitted by inverse power laws at zones 1 and 2 and their combination (Table 6-5; Figure 6-22). Observing the distributions in zones 1, 2 and in the whole area, it is observed that scenario 1 yields a higher exponent (absolute value) than scenario 2, and scenario 2 than 3, ought to the inclusion of large rockfall scar volumes and exclusion of mid-sized and small volumes given for scenario 1 and vice versa for scenarios 2 and 3.

Furthermore, when comparing exponents belonging to the same scenario but at different zones the following is observed: for scenario 1, the exponent in zone 1 is higher than in zone 2, which denotes the existence of higher rockfall scars in zone 1 compared with zone 2. However, for scenarios 2 and 3, exponents are smaller in zone 1 than in zone 2 suggesting that in zone 1 the scar volumes are more homogeneous. The exponents calculated for the whole area vary between the values of zone 1 and zone 2, as expected.

Table 6-5: Inverse power laws fitted for each scenario in zone 1, zone 2 and in the whole area.

Scenario	Expression		
	Zone 1	**Zone 2**	**Whole area (Global)**
1	$F(x \geq X) = 50511x^{-1.741}$	$F(x \geq X) = 6519.2x^{-1.481}$	$F(x \geq X) = 27613x^{-1.673}$
2	$F(x \geq X) = 95.63x^{-1.002}$	$F(x \geq X) = 234.14x^{-1.287}$	$F(x \geq X) = 123.64x^{-1.096}$
3	$F(x \geq X) = 97.77x^{-0.899}$	$F(x \geq X) = 216.79x^{-1.118}$	$F(x \geq X) = 122.25x^{-0.972}$

The degree of validity of the assumed scenarios is difficult to be verified for the selection of the most realistic one. Nevertheless, given the uncertainties that are involved into the described procedure and the results, scenario 3 seems to be the most credible since it excludes large rockfall scar volumes (scenario 1) and does not maximize small rockfall scars (scenario 2).
The exponents of the power laws that were calculated for scenario 2 and 3 approximate very well the correspondent values in similar works by other researchers (Table 3-6), mostly in scenario 3 for zone 1 and for the whole area. Scenario 1 provides exponents that slightly vary from these values. Although the geological context is completely different, exponents for scenario 2 and 3 are very similar to the one obtained by Santana et al. (2012).

Table 6-6: Characteristics of rockfall and rockfall scar volume distributions (taken from Santana et al. (2012) and later adapted).

Author	Site	Method	Geological setting	b
Hungr et al. (1999)[a]	British Columbia, Canada	Rail and highway inventories	Massive felsic rock, road cuts	0.43
			Massive felsic rock, road cuts	0.4
			Jointed metamorphic, rock, road cuts	0.7
			Jointed metamorphic, rock, road cuts	0.65
Rousseau (1999)[a]	Mahaval, La Reunión	Instrumental measurements	Single natural basaltic cliff	1
Dussauge-Peisser et al. (2002)[a]	Upper Arly Gorges, French Alps	Historical data	Metamorphic and sedimentary rocks	0.45±0.15
	Grenoble, French Alps		Calcareous cliffs	0.41±0.11
	Yosemite Valley, California		Granitic cliffs	0.46±0.11
Santana et al. (2012)	Andorra, Eastern Pyrenees	Rockfall scar volume distribution using TLS	Intensely fractured granodioritic cliff	0.92

[a] taken from Dussauge-Peisser et al. (2002)

6.8 Conclusions

A supervised procedure based on the methodology developed by Santana et al. (2012) has been adapted to fit the peculiarities of a given study area, at Montsec Range, for the calculation of the RSSD (Rockfall Scar Size Distribution). This methodology, which requires a high resolution point cloud data obtained by a LIDAR, can be used when complete historical rockfall series are not available and/or the access to the outcrop is limited. It permits a safe, quantitative, objective and systematic evaluation of the rockfall scar sizes.

The application of the methodology to the study site at Montsec Range indicated the presence of two main discontinuity sets.

Using the point cloud, we calculated the distribution of the basal areas of the overhangs and the length distribution of scar heights and we performed a Monte Carlo simulation to get the scar volume distribution by multiplying random samples of the two former variables. Some scars used to calculate the rockfall height, which are not sufficiently persistent to be automatically detected, cannot be detected, additionally due to their high undulation. In that case, the scar height was obtained, alternatively, using the spacing between the basal planes.

A further complication in the calculation of the RSSD originates in the lithology of the study area which permits the dissolution of the rock, generating irregularities in the surface of the discontinuity planes. As a consequence, scars limits are difficult to be distinguished and many small volumes cannot be detected, even when working with a high resolution point cloud. Moreover the inclusion of these irregular planes is arguable; it is not known whether they correspond to a single big rockfall or various smaller events. Therefore, two approaches have been followed to generate the discontinuity sets from the LIDAR point cloud: A) Use of flexible K and M parameters producing both large and small discontinuity surfaces and B) Use of restrictive K and M parameters, filtering both irregular and small discontinuity surfaces and generating only large surfaces.

Another important difficulty arises when deciding whether a staggered stepwise overhang (sometimes given by the afore-mentioned small, eroded and non persistent small surfaces) is the result of a sequence of small-sized rockfall events or due to a single large failure.To deal with this uncertainty, three different scenarios are considered in the 2 analysed zones of the study site: Scenario 1 in which large rockfall scars are generated by a single large rockfall event; Scenario 2 that considers mostly small, eroded and irregular surfaces, some of them difficult to identify, which may be the result of small occurrences; and Scenario 3 that suggests that rockfall scars can be the result of one or several rockfall events and thus, an intermediate distribution of scar volumes is contemplated.

According to the obtained results, in zone 1, the generated scar distributions were fitted by inverse power-laws with exponents ranging from -0.899 to -1.741 for the three different scenarios. In zone 2, the respective exponents range from -1.118 to -1.481. Considering the whole area, the exponents range from -1.673 to -0.972.

Scenario 3 seems to be the most realistic. It excludes large rockfall scar volumes considered by scenario 1 and does not maximize small scar volumes as for scenario 2. Furthermore, scenario 3 contemplates several block detachment possibilities.

Roll over effects were observed for all scenarios and zones for volumes smaller than 8 m^3 for scenario 1 and 0.3 m^3 for scenario 2 and 3. In scenario 1, the rollover effect is most probably ought to undersampling (Stark and Hovius, 2001) since only large rockfall scar volumes have been considered. Nevertheless, for the rest of the scenarios, the roll over effect should not attributed to undersampling given that the precision in detecting small volumes in both zones 1 and 2 is high. The same conclusion was also reached by Santana et al. (2012) who attributed this phenomenon to the existent fracture patterns of their study site. On the other hand, Brunetti et

al. (2009) suggested that it could be the result of a change in the morphological property governing the rockfall process (Guzzetti et al. 2002, 2008; Katz & Aharonov 2006; Malamud et al. 2004).

6.9 Future research work

-Further investigation about the most appropriate rockfall scar volume distribution is needed when several detachment mechanisms exist.
-Factors causing the rollover effects observed at small volumes (bellow 0.3 m^3), even if working with very small rockfall scars, should be investigated.
-The next step after the evaluation of the statistical rockfall volume distribution is the calculation of the rockfall frequency-magnitude relation in terms of annual probability.
-It would be interesting to repeat the same procedure in other areas with different geological settings (rock types, geological history, genesis of the discontinuities, etc.) and to compare the results.

Chapter 7

7 Obtaining magnitude-cumulative frequency curves from rockfall scar size distribution using cosmogenic 36Cl

7.1 Introduction

Magnitude-Cumulative Frequency (MCF) relations are a key issue when evaluating rockfall hazard. Two essential input data are necessary to prepare such relations: the magnitude, which is characterized by the volume, and the frequency, which can be expressed as the total number of occurrences per year.

To assess the probability of future instabilities two procedures are often followed: the evaluation of the potential for the slope failure (e.g. Hantz et al. 2003) and the observation of the past landslide events and its statistical treatment (Corominas and Moya, 2008). The analysis of past events is widely used. It requires data collection from road maintenance records or inventories obtained by field observations (Hungr et al., 2008). Many works have been published on the calculation of Magnitude-Frequency (MF) using historical data. Hungr et al. (1999) obtained 3,538 records of rockfalls and slides from road maintenance records and impacts on the road. They covered four decades along the main rail and highway routes of south-western British Columbia. Guzzetti et al. (2004, 2003) obtained the frequency-volume statistics of 463 and 111 rockfall events in the Yosemite Valley (USA) and Nera Valley (Italy), respectively, from observations and historical accounts. However, in some cases, such inventories are not available or are incomplete. The larger the volume, the longer the observation period must be (Hantz et al., 2003). To overcome this restriction, different methodologies have been proposed. Bunce et al. (1997) used the impact marks of past rockfall events on the road pavement to extent the record of past events. Corominas and Moya (2010) used dendrogeomorphology (Alestalo, 1971) to determine the frequency and magnitude of rockfall events, among other processes, by means of the spatial analysis of damaged trees. Corona et al. (2013) used the dendrogeomorphology to determine the source areas and the rockfall MF. Another technique which consists in counting visible scars resulting from the impact of a detached block on the stem surface of f. Sylvatica was applied by Trappmann and Stoffel (2013).

When dealing with temporal probability, the approximated date or, at least, the time span between occurrences must be known. Despite various studies using the above-mentioned techniques (e.g. Stoffel et al., 2005; Moya et al., 2010; Schneuwly and Stoffel, 2008; Perret et al., 2006), if complete inventories are not available and/or classical dating techniques are not feasible, other strategies must be investigated.

Here we propose an indirect way to determine the long-term past rockfall frequency based on the average cliff retreat rate, i.e., the amount of rock mass lost during a defined period of time.

It is assumed the existence of an initial reference surface (S_0) present in the massif at an initial time T= 0 (Figure 7-1). Over time, the slope face recedes, mainly by rockfalls of several volumes and shapes but also due to other processes such dissolution, until the present day giving the actual slope face. The total volume of material released can be obtained by

subtracting the current slope face from the reference surface S_0 (Figure 7-1). The elapsed time during which the material has been released until the present day can be obtained by calculating the exposure age of S_0 (t_0). It can be carried out by collecting several samples which are expected to belong to S_0 (visual observation) and check whether they have similar ages or not. Furthermore, if samples from younger scar surfaces located at different depths from S_0 are dated, information about the evolution of the retreat rate of the massif can be obtained.

Regarding the volume of material lost, it may be distributed in the Rockfall Scar Size Distribution (RSSD) of the cliff obtained in chapter 6 of this thesis. At this point, two important assumptions have been done: 1) the rockfall scar volumes may be used as a first approximation to the volume of the rockfall events, 2) the volume of each rockfall scar is approximated by a prism defined as the area of the overhangs, from which the rock block has been detached, multiplied by the scar height. It has been assumed that a roof corresponds to a single event. Nevertheless, each roof could be the result of several rockfall events or conversely, a roof might belong to a bigger stepped failure. Consequently, the rockfall volume might be either overestimated or underestimated, respectively.

Dividing the number of rockfall scar volumes by the elapsed time t_0, the MCF curve of the rockfall scars is obtained. The method is based on the formation of radioactive nuclides within minerals by cosmic radiation exposure. The amount of nuclide formed is proportional to its exposure age and thus, to the exposure age of the material where it is located. However, some corrections must be applied before obtaining of the sample's age. The most commonly used cosmogenic isotopes are ^{10}Be, ^{36}Cl and ^{26}Al. More information about Terrestrial Cosmogenic Nuclides (TCN) can be found Annex 19: DATING WITH IN SITU TERRESTRIAL COSMOGENIC ISOTOPES. In this work, ^{36}Cl has been used due to the high amount of Ca in the rock wall (limestone massif). When working with ^{36}Cl, the retreat rate (among other parameters) is an input. The retreat rate gives an indication of the expected amount of inherited ^{36}Cl in the sample. ^{36}Cl is produced at depth due to the high penetration power in the subsurface of the muonic component of the secondary radiation (radiation produced by the interaction of primary cosmic-ray flux with nuclei of atoms in the atmosphere) (Dunai, 2010) and the presence of U, Th and ^{nat}Cl. Inherited ^{36}Cl can contribute significantly to the concentration of ^{36}Cl produced by exposure, and consequently, it affects the estimation of the sample exposure age, mostly in shallow samples (<15 m aprox). In massifs with a high content of inherited ^{36}Cl, a slight variation of the denudation rate produces great changes in the exposure age (e.g. Merchel et al. 2013). Thus, a proper cliff retreat rate (retreat rate input) must be defined for dating the S_0. Since the calculation of the cliff retreat rate is the target of this work, an iterative process must be performed until the retreat rate input and the calculated retreat rate (retreat rate output) are similar.

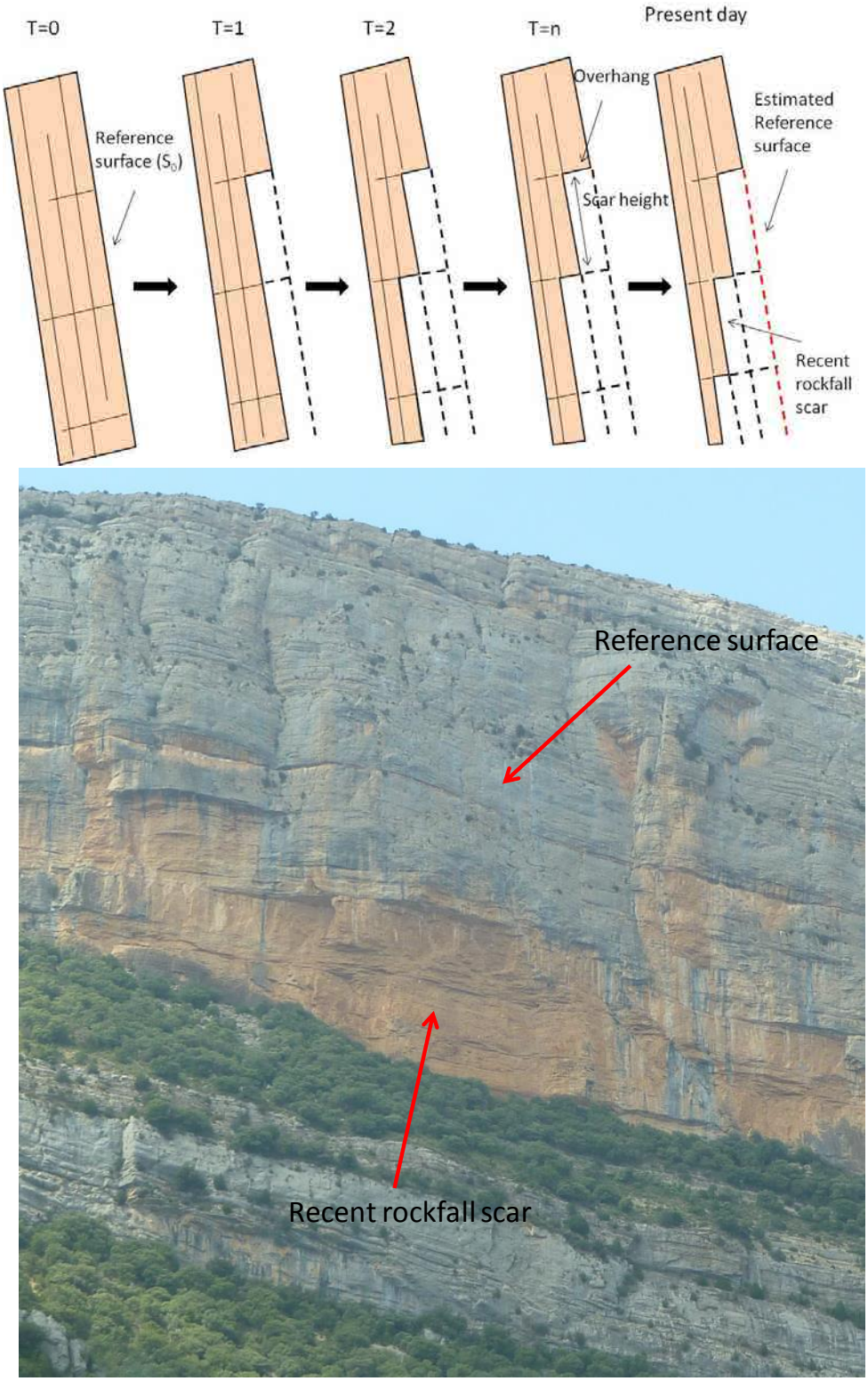

Figure 7-1: Evolution of the cliff from the reference surface S_0 at time T = 0 until the present day. Rockfall scars appear progressively with time. Reference surface S_0 (Top). Reference surface S_0 and more recent rockfall scars, identified by their reddish colour, are indicated (Bottom).

7.2 Study Area

This technique has been applied in the Montsec Range, Spain (Eastern Pyrenees). It is located within the Montsec thrust, developed during the Eocene (Soriano et al., 2006), in the central part of the South Pyrenean Unit (Seguret, 1972). The Montsec Range is oriented E-W with an extension about 40 km. In the frontal part of the unit, where the rock wall is located, outcrop materials from the Upper-cretaceous (Caus et al., 1999). The cliff is composed of slightly fractured limestones (Figure 6-3) and it is being affected by rockfalls. Consequently, several scars from detached blocks can be observed in the wall as well as fallen boulders at the bottom, mostly covered by vegetation. The Montsec Range is located at 1,500 m asl with a Mediterranean continental climate. This area is not affected by the human activity and no data about past rockfall events are available.

The study site has been split into 2 smaller zones where recent rockfall scars can be observed (Figure 6-3). Zone 1 (Z1) is located at the west part of the massif. Large to small rockfall scars are present and blocks from past events can be identified at the bottom of the slope, mostly covered by vegetation.

Zone 2 (Z2) is located at the east part of the slope face and has rockfall scars smaller than those in Z1.

The blue dot in the upper-right Figure 6-3 refers to the location of the scanning station. Red dots numbered from 1 to 9, in the lower part of Figure 6-3, indicate the nine samples collected from the massif and later dated using cosmogenic ^{36}Cl.

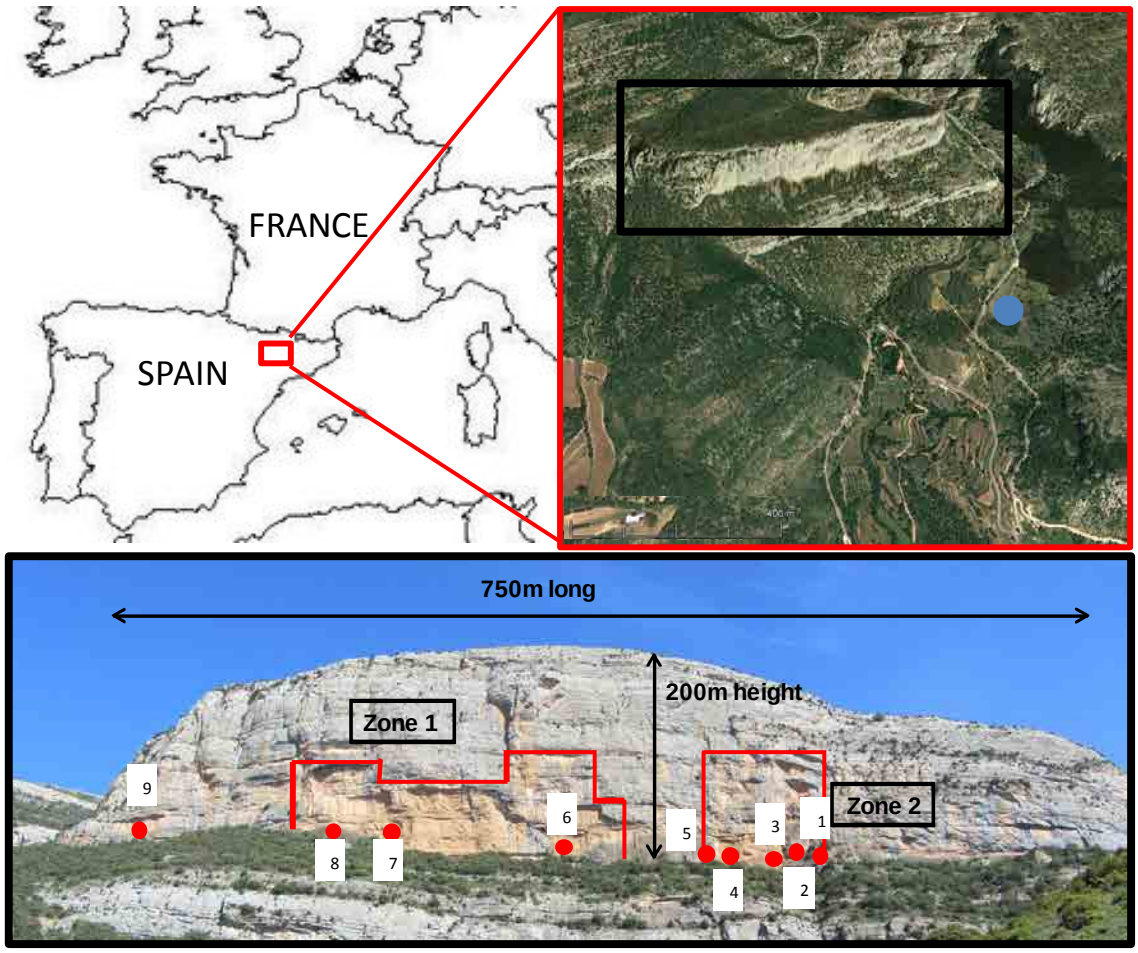

Figure 7-2: Study site. In the upper-right, the scanned area is shown as well as the location of the scan station (blue point). Areas of study are boundary with red (lower part). Red points indicate the sample place where they were collected.

7.3 Methodology

In chapter 6, the RSSD was obtained in the Montsec Range (Eastern Pyrenees) following the methodology based on Santana et al. (2012) which does not consider the temporal frequency.

The methodology presented in this chapter aims to get the frequency by using the RSSD calculated from the total volume of material released and the time necessary to generate this distribution. This period of time comprises from the age of the reference cliff surface (t_0) to the present-day surface. The end result of this methodology is the MCF curve.

The main steps are: a) volume calculation of material lost, b) area calculation of material lost, c) calculation of the reference surface exposure age (t_0) and the cliff retreat rate (R_r), and d) conversion from cumulative percentage of rockfall scar volumes to cumulative number per year. The flow diagram with the applied methodology is shown in Figure 7-3.

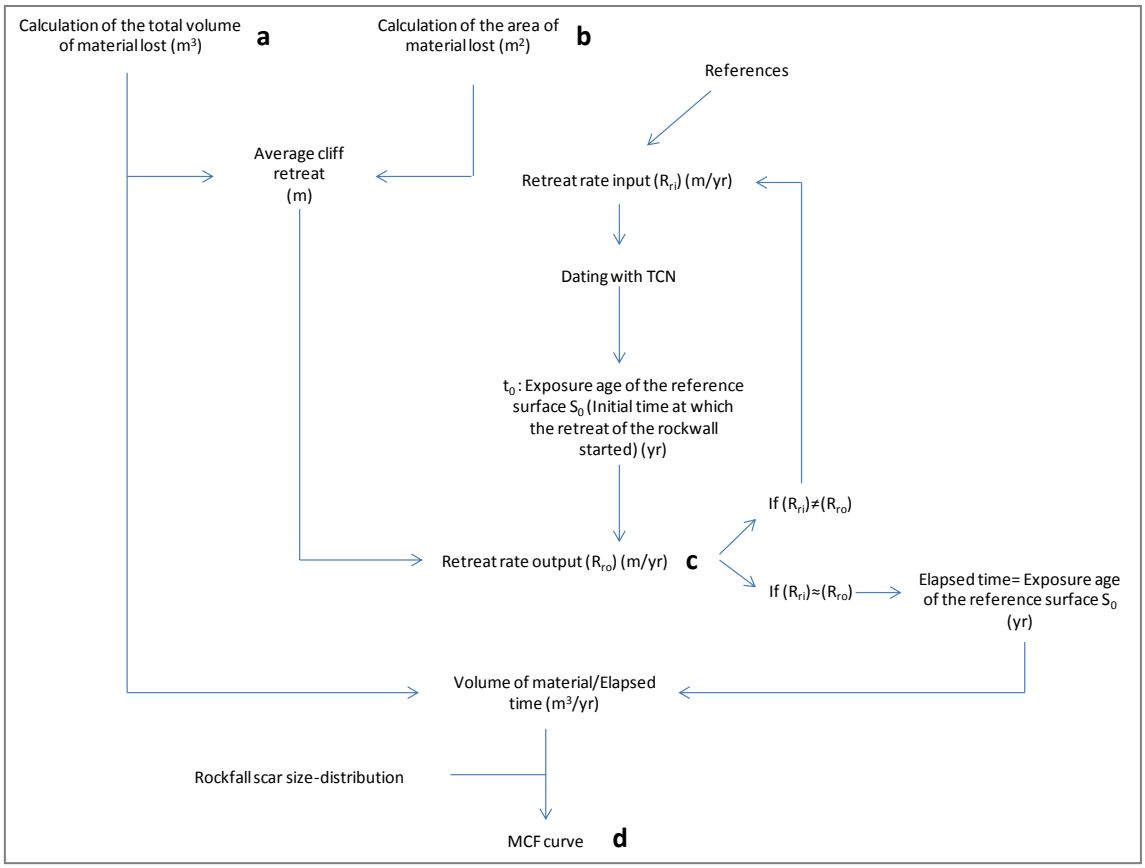

Figure 7-3: Flow chart indicating the followed methodology. Letters "a", "b", "c" and "d" refer to the main steps.

7.3.1 a) Volume calculation

It consists in the evaluation of the total volume released in the rock wall using a point cloud obtained with a Terrestrial Laser Scanner (TLS). Several methods exist for its calculation: 1) subtraction of Digital Surface Models (DSM's) obtained before and after the event (e.g. Deline et al. 2011) 2) reconstruction of the original topography over a present day DSM using photos taken before the event (Ravanel and Deline, 2008). It can be applied when images with sufficient resolution exist (up to a hundred years) and 3) reconstruction of the pre-failure cliff surface using an existing DSM and subtracting the present day surface (Figure 7-4).

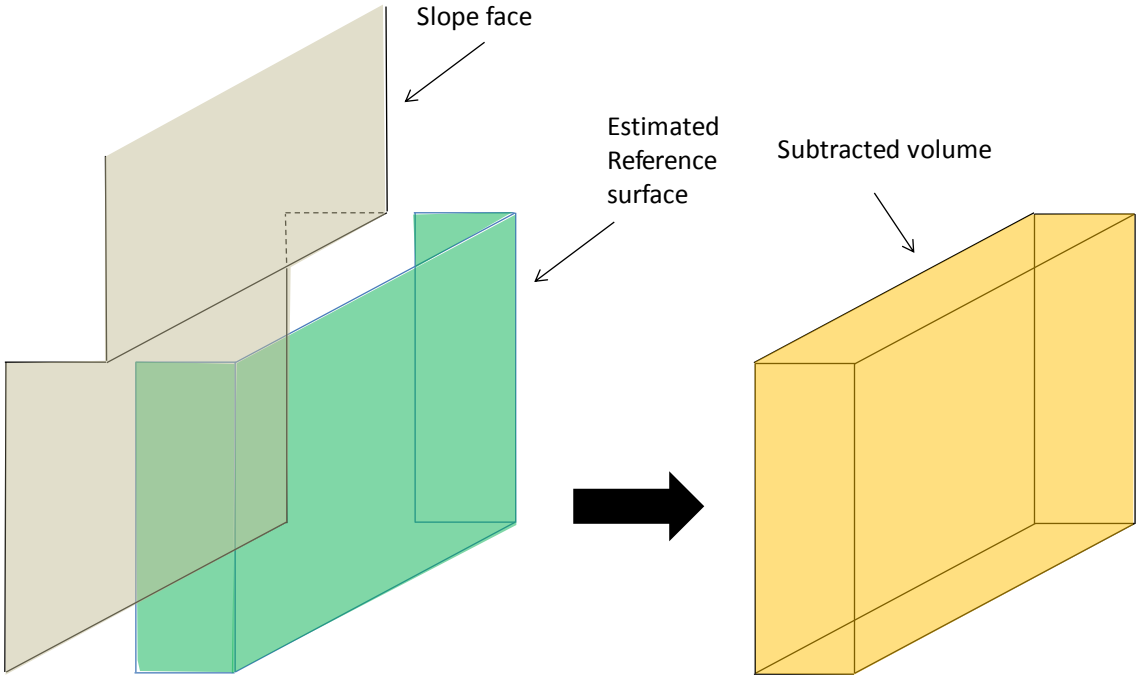

Figure 7-4: Schematic process to obtain the volume lost from the cliff for a time period. The reconstructed reference surface is subtracted from the present-day slope face.

The detailed DSMs can be obtained by means of photogrammetry or TLS. The latter is a terrestrial sensor for data acquisition based on the same principle as airborne LIDAR (Light detection and Ranging). It allows obtaining high resolution DSMs in a short time period (hours) for the extraction of rock mass parameters such as orientation, persistence, roughness, number of sets and spacing/frequency. More information about TLS applications can be found in Abellán et al. (2014).

In this work, the volume of material lost until present has been obtained by subtracting the reconstructed cliff surface, existing at a certain time t_0 (reference surface), from the present-day slope face. The reference surface has been reconstructed from a TLS-scan generated DSM of the rock wall at the present day. The recession of the cliff has been assumed parallel to the slope face (Figure 7-5). Recent rockfall scars are distinguished from the rest of the rock mass by their reddish colour (Figure 7-1).

As explained later, this volume (Figure 7-3 a) is also used to calibrate the R_{ro} of the massif in order to check the consistency of the dates obtained with ^{36}Cl.

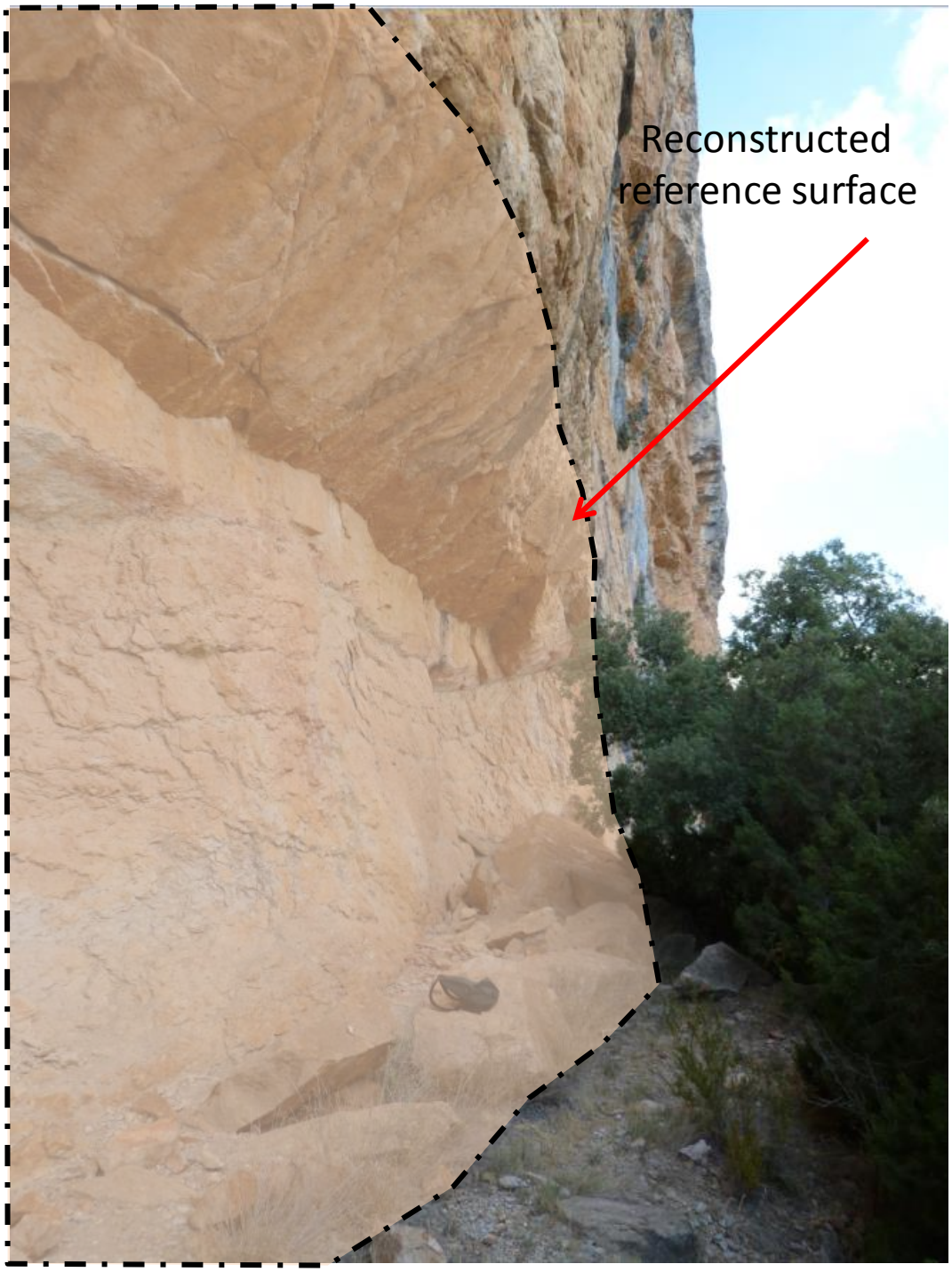

Figure 7-5: Reconstructed reference surface delimitated with a black-dashed line.

7.3.2 b) Area calculation

The area of the massif affected by the rockfalls has been computed to calculate the average cliff retreat and the subsequent calibration of the R_{ro} (Figure 7-3 b). Using a photo and the Matlab software (MathWorks Inc, http://www.mathworks.com/), a white mask has been overlaid covering the area of study. Then, the number of pixels has been counted. If the pixel size is known, the area can be easily determined.

7.3.3 c) Calculation of the reference surface exposure age and the retreat rate

It is necessary to know the elapsed time during which the rockfall volume has been released. Furthermore, dating surfaces located between the reference surface and the present-day surface would give an insight of the rate of recession. To this end, different stepped surfaces of the slope have been dated using cosmogenic ^{36}Cl.

As mentioned before, when dating shallow rock samples (<15 m.) the content of inherited ^{36}Cl can affect the calculated sample exposure age. Since the content is mostly controlled by the retreat rate, this must be defined beforehand. For that purpose, an iterative process has been followed (Figure 7-3): a first retreat rate called retreat rate input (R_{ri}) has been used to calculate the exposure age of samples belonging to S_0. This retreat rate is based on published research works which are shown later on. If the exposure ages are of the same order of magnitude, the average cliff retreat rate (R_{av}), which has been obtained by dividing the volume of material lost over the area affected by rockfalls (Figure 7-3 a and b), is divided by these ages (Figure 7-3C). The resulting ratio is named retreat rate output (R_{ro}) and is compared to R_{ri} (Figure 7-3). If both rates are similar, the obtained t_0 exposure age is considered correct. On the contrary, another R_{ri} must be introduced until both retreat rates converge.

Many works exist in the literature related with the retreat rate (e.g.: Sancho et al. 1988; André, 1997; Gutierrez and Sancho, 1998; Gutierrez and Sese, 2001; Schuster and Highland, 2001; Buoncristiani et al. 2002; Curry and Morris, 2004; Haeuselmann et al., 2007; Brenot et al., 2008; Delmas et al., 2009; Brooks and Spencer, 2010; Züst et al., 2014) (Table 7-1). A summary of retreat rates at different geological settings and for different types of deposits and processes are shown in Table 7-1. It is shown that some retreat scarp rates in arid zones from Spain, close to the study are, having similar geology and affected by rockfalls range from 0.1 to 0.7 mm/yr. Thus, a first value of 350 mm/ka has been taken. This value will be later validated.

Table 7-1: Erosion/retreat rate values of different authors according to the location, geology and process.

Author	Site	Geology	Process	Erosion/retreat rate (mm/yr)
(Gutierrez and Sancho, 1998)	Duero basin (Spain)	Limestones (Miocene)	Rockfalls, climatic change, human activity	0.1-7
(Sancho et al., 1988)	Ebre basin (Spain)	Limestones (Miocene)	Rockfalls, climatic change, human activity	0.3
(Curry and Morris, 2004)	Mynydd Du (Wales)	Sandstone (Devonian)	Microgelivation	1.23 (Lateglacial); 0.12 (Holocene)
	Mynydd Du (Wales)	Sandstone (Devonian)	Rockfall	0.018
(Delmas et al., 2009)	Massif du Carlit (Pyrenees, France)	Granite (Paleozoic)	Glacial erosion	0.001 - 10
(Haeuselmann et al., 2007)	Switzerland	Limestones	Glacial erosion	1.2
(Züst et al., 2014)	(Sinks Canyon, Wyoming, USA)	Till deposit	Glacial erosion	0.52 – 0.72
(Buoncristiani et al., 2002)	Southern French Alps	Limestones (Jurassic)	Rockfall	0.68

7.3.4 d) From cumulative percentage of rockfall scar volumes to cumulative number per year

The last step of the methodology is the conversion of the RSSD to MCF curve, i.e. from the cumulative percentage of rockfall scars larger than a specific size to the number of rockfall scars per year larger than a specific size.

If both the total volume of material released (V_T) and the ratio of rockfall scars of each size (X_n) (obtained from the RSSD, chapter 6) are known, the total number of rockfall scars is given by:

$$N_T = \frac{V_T}{X_1 \times V_1 + X_2 \times V_2 + \cdots + X_n \times V_N}$$

Equation 7-1

and the number of rockfall scars of a given size is:

$$N_n = N_T \times X_n$$

Equation 7-2

Finally, if the elapsed time is known (t_0), the number of events per year of a given volume is:

$$\frac{N_n}{t_0}$$

Equation 7-3

A flowchart of the process is presented in Figure 7-6.

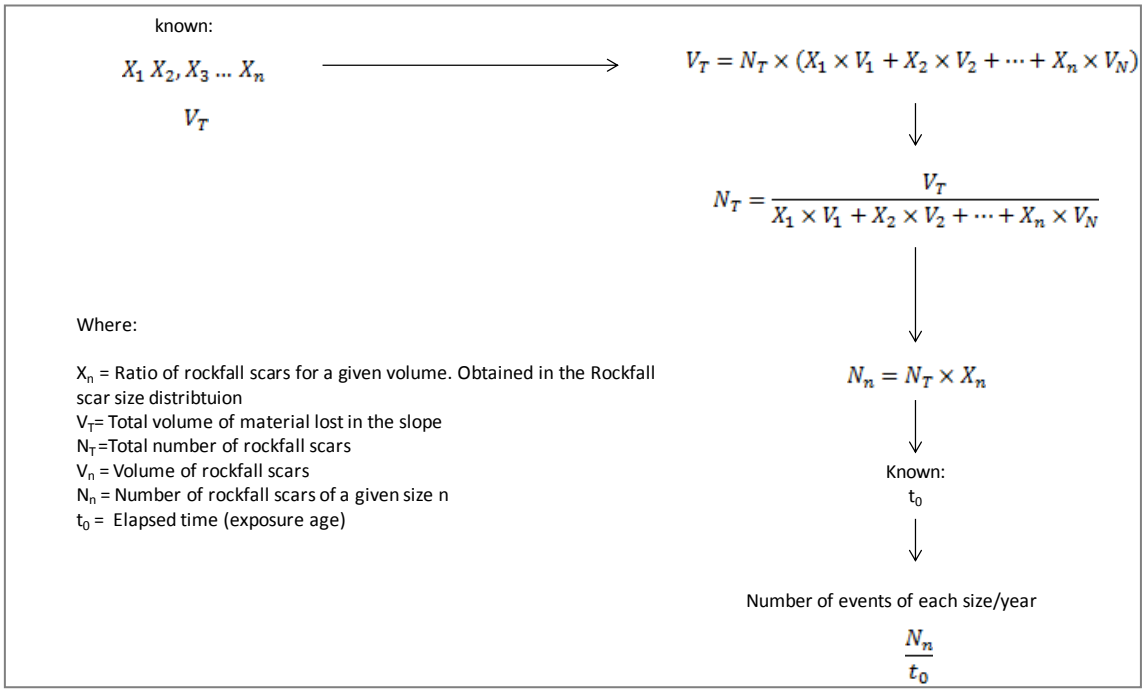

Figure 7-6: Flowchart representing the steps followed to convert the percentage of rockfall scars into the number of rockfall scars per year.

7.4 Application

The amount of rock mass released in the cliff face and the volume distribution of the rockfall scars were obtained from a DSM generated with a TLS. The work was carried out in collaboration with University of Lausanne (UNIL). The TLS used was the OPTECH Ilris 3D Long. It has an accuracy of 7 mm at 100 m, a maximum range of 1,330 m, and a high data acquisition speed of up to 10,000 points/second (http://www.optech.com/). A total of 3 scans were performed at a maximum distance of 900 m obtaining 20,251,588 points that cover an area about 150,000 m^2. This represents a resolution about 1.4 points/cm. The scans were later aligned with PolyWorks software (Polyworks, .http://www.innovmetric.com/).

As mentioned before, this area was split into 2 zones where recent rockfall scars can be observed. For each zone (Z1 and Z2), a triangulated mesh representing the initial surface, S_0, was reconstructed over the DSM. It was assumed that the cliff recedes parallel to the slope face. Control points were used where no information was available (Figure 7-7 for Z1 and Figure 7-8 for Z2) assuming that: 1) recent rockfall scar surfaces are characterised by a fresh and reddish appearance and 2) S_0 is characterised by a dark grey colour. Both hypotheses will be validated when the samples are dated.

The missing rock mass volume from the cliff face was obtained with the PolyWorks software. The volume between the reconstructed S_0 and the present day cliff surface was calculated by subtracting both meshes following the procedure developed by Broccolato et al. (2006). The calculated volumes were 78,903.48 m^3 and 16,764.48 m^3 for Z1 and Z2 respectively.

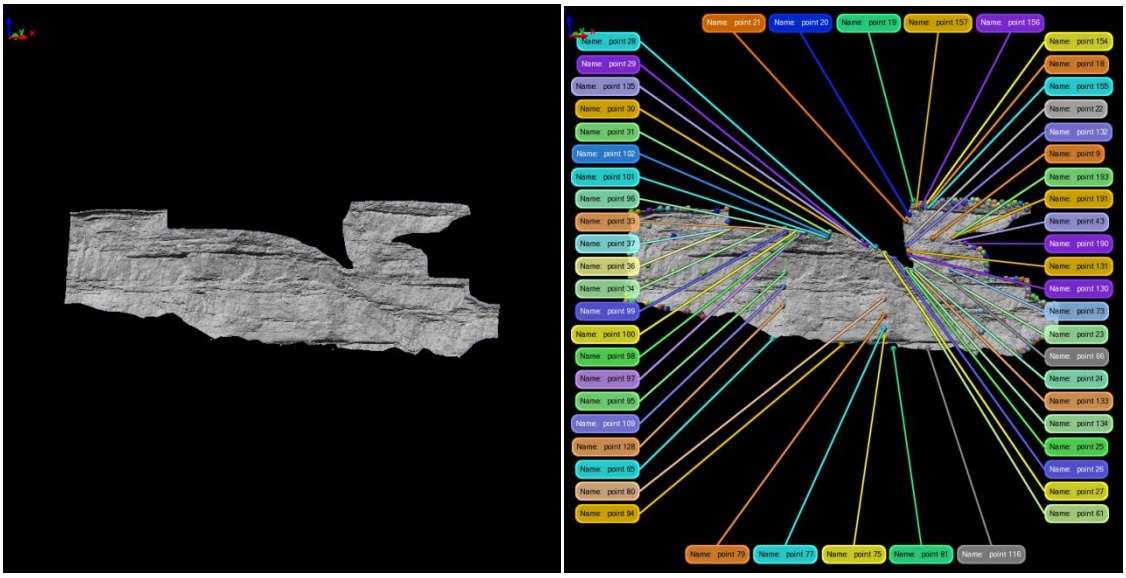

Figure 7-7: DSM from the study area obtained with TLS (Z1) (Left). The reference surface S_0 was created by defining points contained within this envelope (Right) using the assumptions stated in the text above.

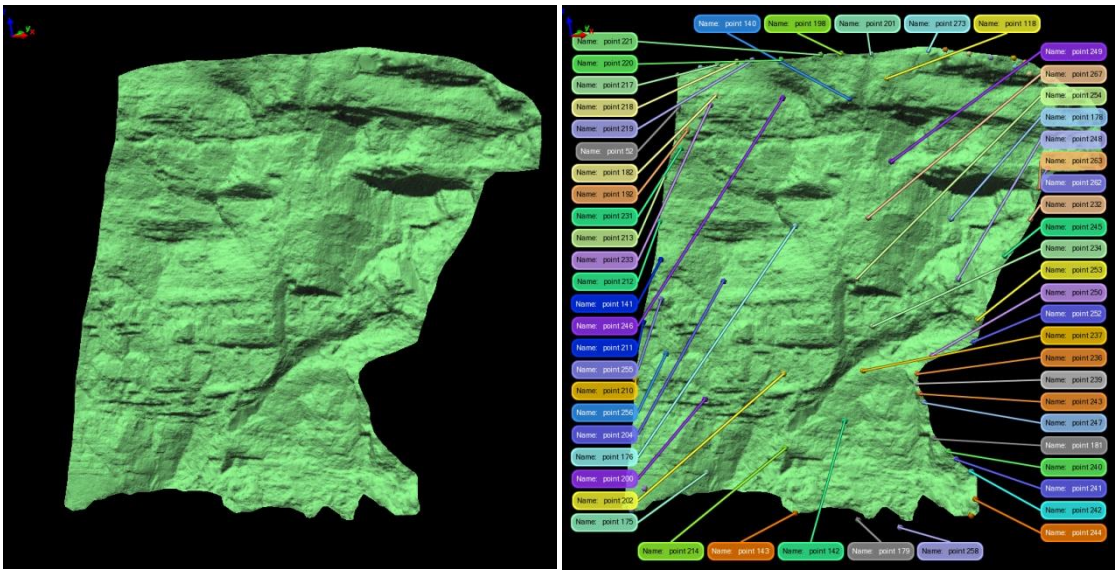

Figure 7-8: DSM from the study area obtained with TLS (Z2) (Left). The reference surface S_0 was created by defining points contained within this envelope (Right) using the assumptions stated in the text above.

Once the missing rock mass volume was calculated, the next step was the evaluation of the area affected by rockfalls. Figure 7-9 and

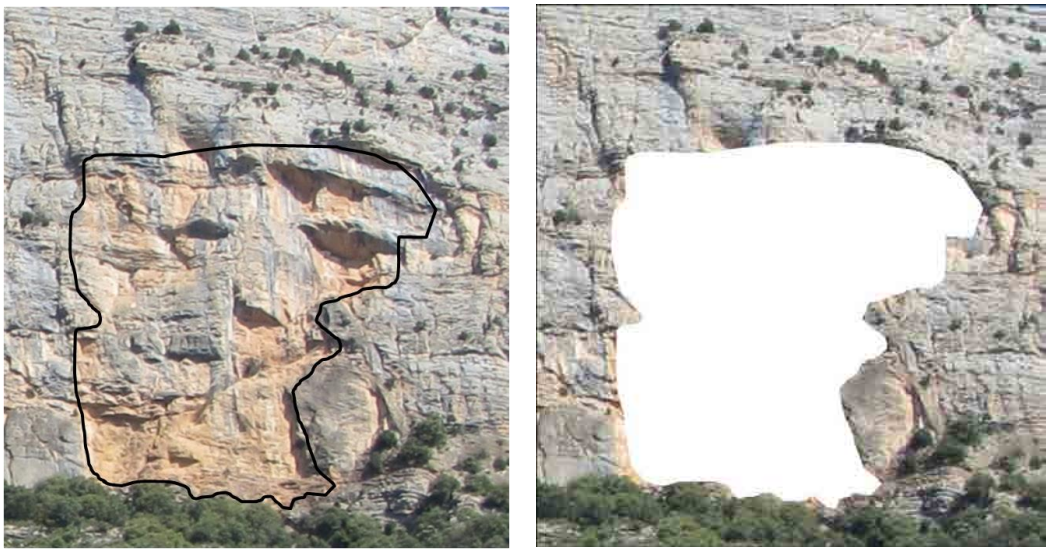

Figure 7-10 show the boundary of Z1 and Z2 respectively. A white mask was overlaid over Z1 and Z2 and the number of pixels of each mask was counted using Matlab. If the pixel size is known, the area can be easily determined. The area obtained were 14,010 m^2 (Z1) and 6,801.65 m^2 (Z2). At this point, it is important to notice that the average cliff retreat (volume lost/area affected) (Figure 7-3) of 5,631.94 mm in Z1 is higher than that of 2,464.77 mm in Z2. This indicates that the rockfall activity is higher in Z1 than in Z2.

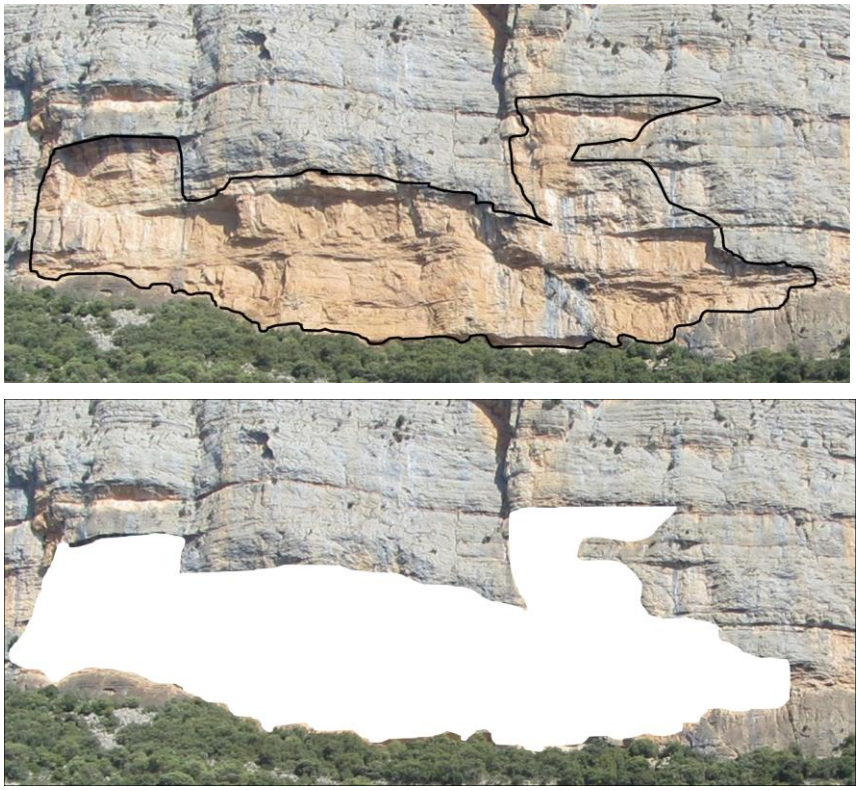

Figure 7-9: Delimitation of the rockfall scars area based on its colour and the depression of the topographic surface (Z1) (Top). White mask overlaying the area affected by rockfall scars (Z1) (Bottom).

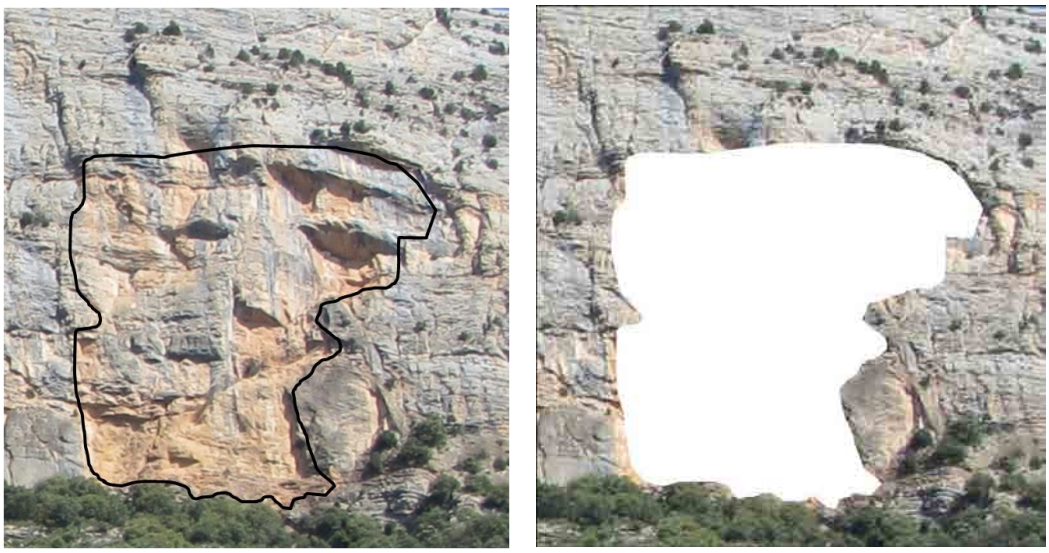

Figure 7-10: Delimitation of the rockfall scars area based on its colour and the depression of the topographic surface (Z2) (Left). White mask overlaying the area affected by rockfall scars (Z2) (Right).

Nine samples were collected from the massif and dated by means of cosmogenic ^{36}Cl (Figure 6-3). Samples 1, 5, 7, and 8 were assumed to belong to S_0. The objective was their dating to determine the time span during which the volume of the rock wall was released. Samples 2, 3, 4, 6 and 9 were taken from the current slope face at different depths from S_0. The initial idea was

to calculate other retreat rates and thus give information about the cliff evolution. Although this was not possible, it was checked that, in general, samples located at greater depths from S_0 correspond to younger scars. To this end, the spreadsheet provided by (Schimmelpfennig et al., 2009) and modified later by (Braucher et al., 2011) was used. The description of the sampling places and work done for obtaining the samples exposure age can be found in Annex 19: DATING WITH IN SITU TERRESTRIAL COSMOGENIC ISOTOPES.

As mentioned before, for shallow samples (<15 m depth), an accurate value of R_{ri} (Figure 7-3) is crucial for a correct definition of the exposure age of each sample. Typical values of cliff recession rates for limestone massifs from the Jurassic, Upper Cretaceous and Tertiary, affected by rockfalls and relatively close to the study area range from 0.1 to 0.68 mm/a (Buoncristiani et al., 2002; Gutierrez and Sancho, 1998; Sancho et al., 1988) so that, a retreat rate of 350 mm/ka, was initially assumed. In Table 7-2, the exposure age of each sample and associated uncertainty are shown. Samples 1, 5, 7 and 8 seemed to be the oldest ones with an average exposure age of 15,256 years and an uncertainty of 10.6%. This confirms they belong to S_0 as it was suggested.

Table 7-2: Exposure age and uncertainty of each sample assuming a retreat rate of 350 mm/ka.

Sample	Exposure age (a)	Uncertainty (%)
1	13,854	10.71
2	8,693	10.7
3	1,492	13.8
4	11,257	10.5
5	14,596	10.82
6	5,555	10.77
7	16,697	10.83
8	15,875	10.6
9	6,814	10.62

A sensitivity analysis for various input retreat rates was performed (Figure 7-11). It can be observed that the exposure ages are strongly dependent on the retreat rate particularly when it is smaller than 400 mm/ka. For retreat rate values higher than 1,000 mm/ka, exposure ages tend to remain constant.

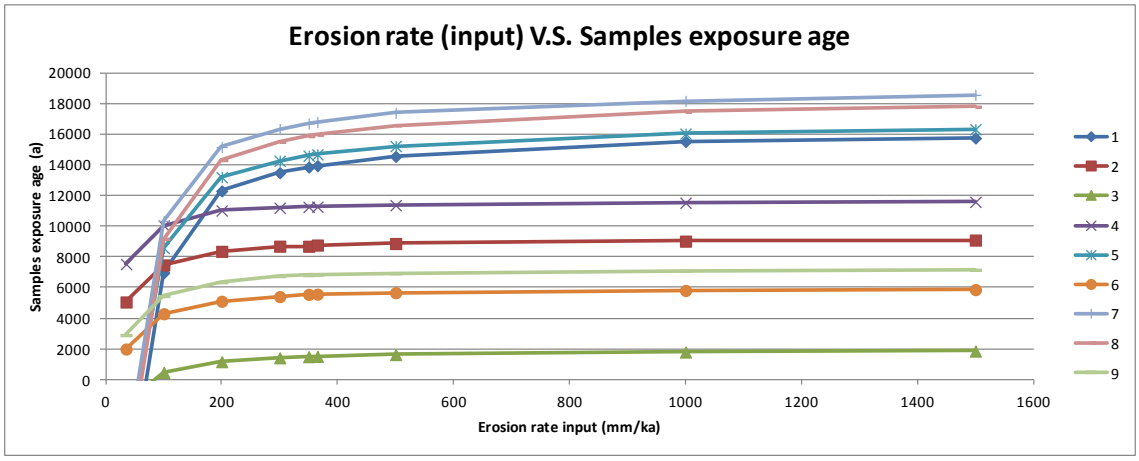

Figure 7-11: Sensitivity analysis carried out in order to analyse the role of the retreat rate in the sample's exposure age.

It is crucial to obtain exposure ages not affected by the retreat rate. Otherwise, the inherited ^{36}Cl concentration may interfere in the final results. The difference between the exposure age obtained from smaller retreat rates and the retreat rate of 1,000 mm/ka is shown in (Table 7-3). In this table it has been assumed that for a retreat rate of 1,000 mm/ka the exposure ages are not affected by the inheritance of ^{36}Cl. For a retreat rate of 350 mm/ka, the maximum variation in the exposure age is 10.74% (sample 1). On the other hand, the maximum uncertainty when calculating the exposure ages using the same retreat rate (350 mm/ka) is 10.83% (sample 7, Table 7-2). Therefore, for retreat rates around 350 mm/ka or higher, the variation of the exposure age due to the inherited ^{36}Cl is smaller than the precision of the method and consequently, it is not interfering in the final results. Therefore, retreat rates similar or higher than 350 mm/ka were considered to be acceptable.

Table 7-3: Variation of the exposure age for samples 1, 5, 7 and 8 comparing a retreat rate of 1,000 mm/ka with four smaller rates (100, 200, 300 and 350 mm/ka).

	Exposure age variation (%)			
Sample	**1**	**5**	**7**	**8**
Compared retreat rates (mm/ka)				
1,000-350	10.74	8.97	8.1	9.12
1,000-300	13.1	11.04	10.08	11.23
1,000-200	20.75	17.71	16.54	18.07
1,000-100	55.11	46.5	43.08	47.5

In order to obtain the appropriate R_{ri} and the subsequent exposure age of the samples, Z1, Z2 and the whole area were studied separately.

Zone 1

A first R_{ri} of 350 mm/ka (according to the literature; Table 7-1) was used (Table 7-4). For this value, the average exposure age of samples belonging to S_0 was 15,255.5 years. Considering an average cliff retreat (Figure 7-3) of 5,630 mm (78,903.48 m^3/14,010 m^2) a R_{ro} of 368 mm/ka (5,630 mm/15,255.5 a) was calculated. Since R_{ro} is a bit higher than R_{ri} another value of R_{ri} =500 mm/ka was used giving an average t_0 exposure age of 15,935 years and a subsequent R_{ro}

of 352 mm/ka. A third attempt was done using an intermediate R_{ri} of 365 mm/k giving an average t_0 exposure age of 15,346 years and a R_{ro} of 366 mm/ka. This is in good agreement with the R_{ri} of 365 mm/ka.

Table 7-4: Retreat rate output (R_{ro}) for different retreat rate inputs (R_{ri}) in Z1. The average exposure age of samples belonging to S_0 was used. The average cliff retreat was obtained dividing the missing volume by the missing area.

Retreat rate input (R_{ri}) (mm/ka)	**Exposure age (a)**				**Average exposure age (Ka)**	**Average cliff retreat (mm)**	**Retreat rate output (R_{ro}) (mm/ka)**
	Sample						
	1	**5**	**7**	**8**			
350	13,854	14,596	16,697	15,875	15.3	5630	368
365	13,946	14,680	16,788	15,968	15.4	"	366
500	14,550	15,228	17,384	16,577	16	"	352

Zone 2

In this case, the average cliff retreat was 2,465 mm (14,764.48m^3/6,801.65m^2). For an average age of the reference surface of 15,255.5 years calculated using a R_{ri} of 350 mm/ka, the resulting R_{ro} was 62 mm/ka (2,465 mm/15,255.5 a). It means that smaller values of R_{ri} were needed. Values of R_{ri} of 100 and 200 mm/ka were used resulting in R_{ro} of 281 and 181 mm/ka, respectively. Therefore, the appropriate R_{ri} would be between 100 and 200 mm/ka. Since the average cliff retreats from Z1 and Z2 are different, for a given t_0 age, it is obvious that retreat rates will be different in each zone as well. However, as it was mentioned before, smaller values than 350 mm/ka may imply high amounts of inherited ^{36}Cl (Table 7-6) that interfere in the resulting exposure age.

Table 7-5: Retreat rate output (R_{ro}) for different retreat rate inputs (R_{ri}) in Z2. The average exposure age of samples belonging to S_0 was used. The average cliff retreat was obtained from the ratio between the missing volume and the missing area.

Retreat rate input (R_{ri}) (mm/ka)	**Exposure age (a)**				**Average exposure age (Ka)**	**Average cliff retreat (mm)**	**Retreat rate output (R_{ro}) (mm/ka)**
	Sample						
	1	**5**	**7**	**8**			
100	6,968	8,579	10,342	9,172	8.8	2,465	280
200	1,2301	13,195	15,164	14,311	13.7	"	180
350	1,3854	14,596	16,697	15,875	15.3	"	161

In Table 7-6, the amount of inherited ^{36}Cl according to different retreat rates is shown for each sample belonging to S_0. As expected, the higher the retreat rate the lower the ^{36}Cl produced by inheritance. Since the cliff retreat rate is high, the slope face material is replaced with a high velocity and the time to produce the inherited ^{36}Cl is reduced.

Table 7-6: ^{36}Cl from inheritance (%) according to the sample and the retreat rate input (R_{ri}) (mm/ka).

Retreat rate input (R_{ri}) (mm/ka)	**100**	**200**	**300**	**350**	**365**	**500**	**1,000**
Samples belonging to S_0	**^{36}Cl inherited (%)**						
1	59	30.8	20.9	18	17.3	12.8	6.63
5	52.2	27.2	18.4	15.9	15.3	11.2	5.73
7	49.7	26.2	18	15.6	15	11.3	6.14
8	52.8	27.6	18.8	16.2	15.6	11.6	6.03

Whole area (Z1 and Z2)

Finally, the whole area was considered as a unique entity (Table 7-7). The average cliff retreat was calculated using the total volume of material released divided by the area that it occupied. Thus, the average cliff retreat is 4,597 mm. Considering a R_{ri} of 350 mm/ka and an average exposure age of 15.3 ka, a R_{ro} of 301 mm/ka is obtained. For a R_{ri} of 300 mm/ka and a exposure age of 15 Ka, a R_{ro} of is 309 mm/ka is obtained. A third R_{ri} of 310 mm/ka was used giving a R_{ro} of 307 mm/ka. Therefore, taking into account the whole area, the appropriate R_{ri} would be around 310 mm/ka.

Table 7-7: Retreat rate output (R_{ro}) for different retreat rate inputs (R_{ri}) in the whole area (Z1 and Z2). The average exposure age of samples belonging to S_0 was used. The average cliff retreat was obtained from the ratio between the missing volume and the missing area.

Retreat rate input (R_{ri}) (mm/ka)	**Exposure age (a)**				**Average exposure age (Ka)**	**Average cliff retreat (mm)**	**Retreat rate output (R_{ro}) (mm/ka)**
	Sample						
	1	**5**	**7**	**8**			
300	13,488	14,264	16,336	15,506	14.9	4,597	309
310	13,569	14,338	16,416	15,588	15	"	307
350	13,854	14,596	16,697	15,875	15.3	"	301

Results of Z2 were rejected since exposure ages of S_0 were affected by the high amount of inherited ^{36}Cl. On the contrary, the analyses performed in Z1 and in the whole area were considered to give exposure ages of S_0 not affected by the inherited ^{36}Cl with R_{ri} values ranging from 310 to 365 mm/ka. Since the higher the retreat rate the lower the concentration of ^{36}Cl inherited, a R_{ri} of 365 mm/ka was chosen.

Exposure ages, uncertainty and depth (distance from the reference surface) of each sample for a R_{ri} of 365 mm/ka were calculated. Results are shown in Table 7-8. For samples belonging to the current slope face (2, 3, 4, 6 and 9) it was checked that, in general, the deeper the samples they younger they are, except for sample 9. The different results obtained with sample 9 may be due to its location, far away from the other samples, in the western part of the study area where the rock mass gets curved. This hinders the measurement of its depth. In Table 7-8 the relation between the depth and the exposure age of each sample is shown.

Finally, the average exposure age of samples belonging to S_0 for a R_{ri} of 365 mm/ka was 15,346

years.

Table 7-8: Exposure age, uncertainty and depth (distance from the reference surface) of each sample assuming a retreat rate of 365 mm/ka.

Sample	Exposure age (a)	Uncertainty (%)	Sample depth (cm)
1	13,946	10.7	0
2	8,769	10.69	670
3	1,511	13.71	730
4	11,272	10.49	664
5	14,680	10.82	0
6	5,569	10.76	697
7	16,788	10.81	0
8	15,968	10.59	0
9	6,830	10.62	611

In the last step, the conversion from RSSD to MCF curves was performed. It is important to note that they were built up considering the three rockfall scenarios afore-mentioned: 1) occurrence of large rockfall scars leading to the generation of considerable volumes (Figure 7-12, 1), 2) small, eroded and irregular rockfall scar surfaces which may be the result of smaller occurrences (Figure 7-12, 2), and 3) the rockfall scars can be the result of one or several rockfall events excluding large volumes from scenario 1 but including larger scars than in scenario 2 (Figure 7-12, 3). For each scenario, an inverse power law was fitted to the RSSD in Z1 and Z2, and in the whole area (Figure 7-13, Figure 7-16 and Figure 7-19). Results are shown in Table 7-9.

Table 7-9: Inverse power laws fitted in the RSSD (Figure 7-13, Figure 7-16 and Figure 7-19) for each scenario in Z1, Z2 and in the whole area.

Scenario	Expression		
	Zone 1	Zone 2	Whole area (Global)
1	$F(x \geq X) = 50511x^{-1.74}$	$F(x \geq X) = 6519.2x^{-1.481}$	$F(x \geq X) = 27613x^{-1.673}$
2	$F(x \geq X) = 95.63x^{-1.002}$	$F(x \geq X) = 234.14x^{-1.287}$	$F(x \geq X) = 123.64x^{-1.096}$
3	$F(x \geq X) = 97.77x^{-0.899}$	$F(x \geq X) = 216.79x^{-1.118}$	$F(x \geq X) = 122.25x^{-0.972}$

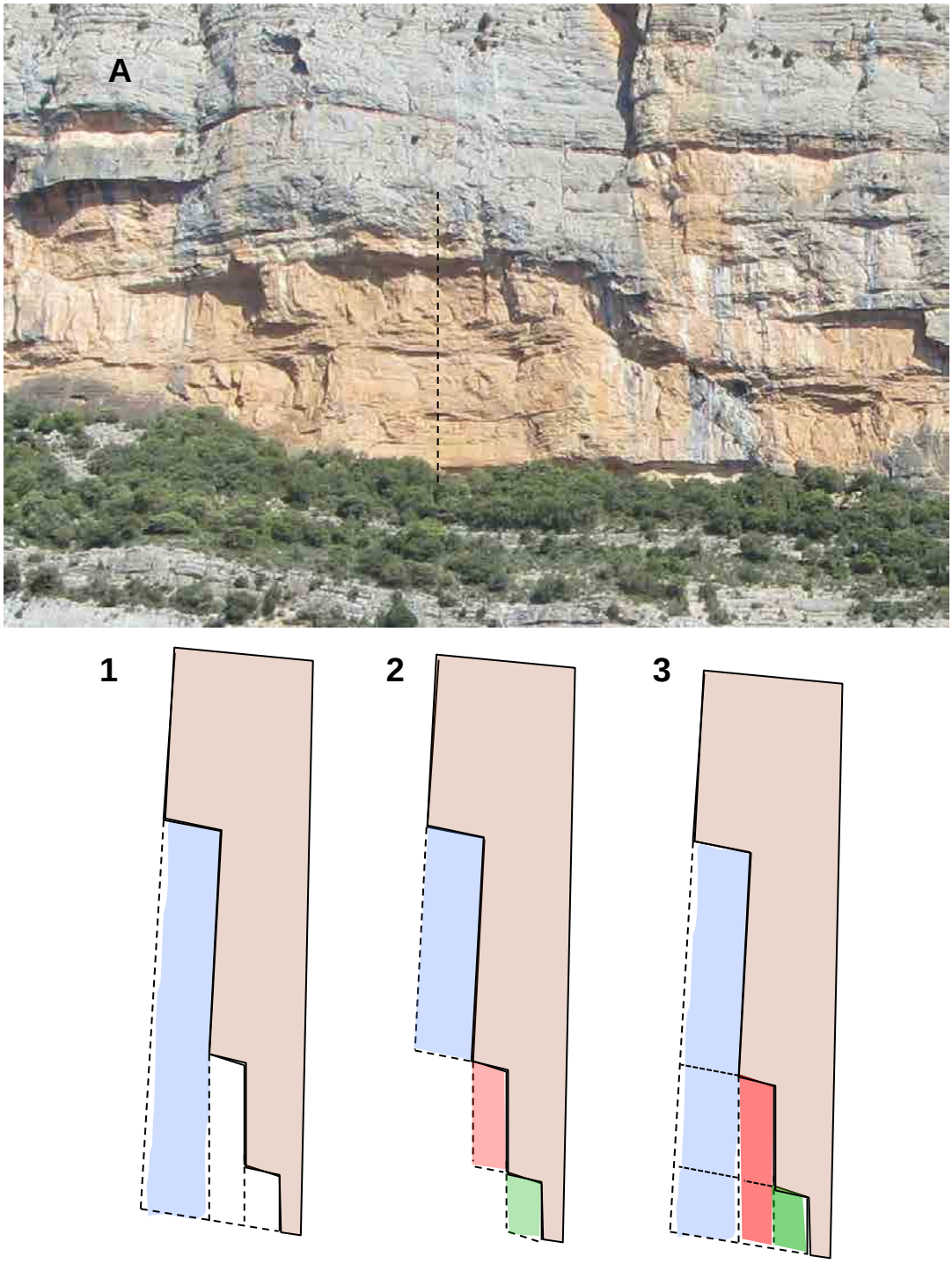

Figure 7-12: Cross sections of the massif showing the possible scenarios according to different detachment mechanisms. A: View of the massif. Dashed line indicates the location of the vertical cross section; 1: Elongated and large prisms are formed; 2: Small-sized rockfalls take place in a staggered slope and 3: Large rockfall scars are the results of various rockfall events.

The input data are the total volume of material lost (V_T) in the cliff face (78,903 and 16,764 m^3) within the last 15,346 years and the ratio of rockfall scars of a given size X_n (Figure 7-6) obtained in the RSSD. Combining V_T with X_n, the number of rockfall scars of a given volume was obtained (Figure 7-14, Figure 7-17 and Figure 7-20). Using the elapsed time (t_0), the number of rockfall scars per year of a given size was calculated (Figure 7-15, Figure 7-18 and Figure 7-21). In Table 7-10 the total volume of material lost, the number of calculated scars and the elapsed time considered are shown.

Table 7-10: Total volume of material lost, total number of scars and elapsed time for each zone and the whole area.

Zone	Scenario	Total volume of material lost (V_T) (m^3)	Total number of scars calculated (N_T)	Elapsed time (t_0) (years)
1	1	78,903.48	1,891	15,346
	2	"	8,903	"
	3	"	5,004	"
2	1	16,764.48	514	"
	2	"	2,876	"
	3	"	1,671	"
Whole area	1	95,667.96	2,573	"
	2	"	13,023	"
	3	"	7,416	"

For each zone, when introducing the total volume of material lost (V_T) (Figure 7-14, Figure 7-17 and Figure 7-20) and the elapsed time (t_0) (Figure 7-15, Figure 7-18 and Figure 7-21) the exponent of the fitted power laws remains constant since the size distribution of each scenario is not affected. Hence, characteristics of the MCF curves such as roll over effect and minimum and maximum volume calculated will remain constant as in the RSSD. Furthermore, since scenario 1 considers scar volumes larger than scenario 2 and 3, for the same volume of material lost, the number of scars is smaller than in the two other scenarios. The number of rockfall scars is highest in scenario 2 as it takes into account the smallest volumes in both zones (Table 7-10).
A brief reminder about the characteristics of the three scenarios is presented below:

Scenario 1:
In Z1, this scenario includes mainly large rockfall scar volumes, hence the minimization of mid-sized and small volumes can be observed as a strong rollover effect (Guzzetti et al., 2002; Stark and Hovius, 2001) for scar volumes smaller than 8 m^3 (Figure 7-15). The maximum volume calculated was 8,700 m^3.
Results from Z2 and the whole area (Figure 7-18) seem to have the same pattern as that in Z1 with a minimum volume considered of 6 m^3 (Z2) and 8 m^3 (whole area). The maximum volume calculated was 3,400 m^3 in Z2 and 8,700 m^3 in the whole area (Figure 7-21).

Scenario 2:
In Z1, the roll over effect is not so accentuated since a minimum rockfall scar volumes of 0.3 m^3 were considered (Figure 7-15). The maximum volume obtained was 4,100 m^3 being smaller

than in scenario 1. The minimization of mid-sized and large volumes can be observed.
Results from Z2 and the whole area (Figure 7-18 and Figure 7-21) seem to have the same pattern as that in Z1 with a minimum volume considered of 0.3 m^3 in both analyses. The maximum volume calculated was 2,900 m^3 in Z2 and 4,100 m^3 in the whole area.

Scenario 3:
In Z1, the roll over effect is not so accentuated since a minimum rockfall scar volume of 0.3 m^3 was considered (Figure 7-15). The maximum volume obtained was 4,100 m^3, smaller than that in scenario 1. This scenario seems to be an intermediate procedure which excludes large volumes and does not maximize small rockfall scars.
Results from Z2 and the whole area (Figure 7-18 and Figure 7-21) seem to have the same pattern as that in Z1 with a minimum volume considered of 0.3 m^3 in both analyses. The maximum volume calculated was 3,300 m^3 in Z2 and 4,100 m^3 in the whole area.

Zone1

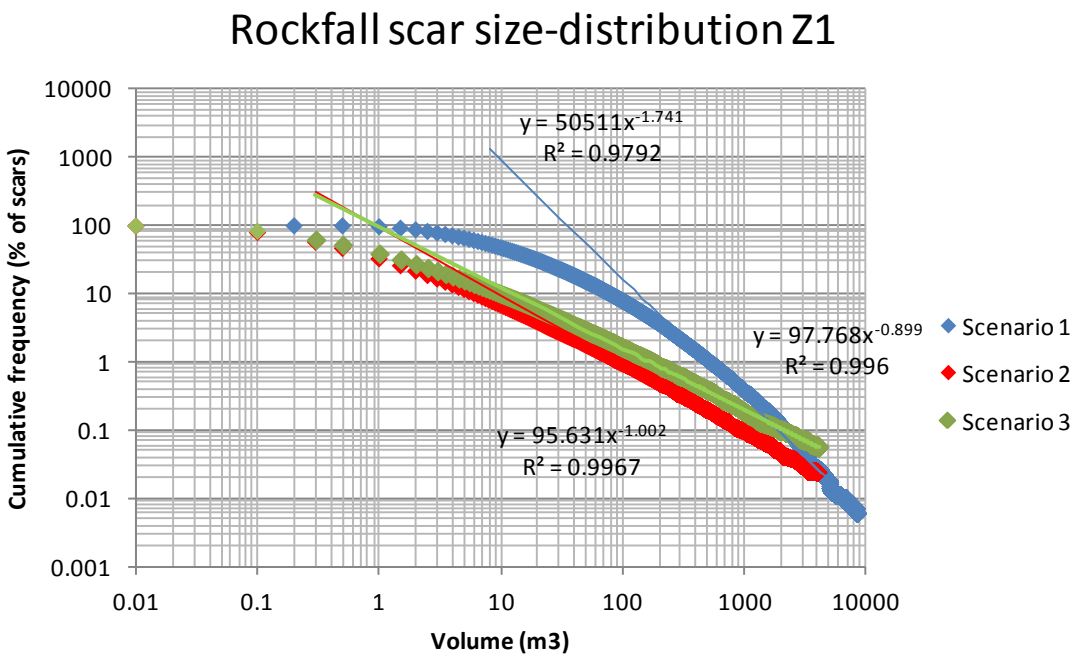

Figure 7-13: Rockfall scar size distribution of Z1 in terms of % of rockfall scars (obtained in chapter 6).

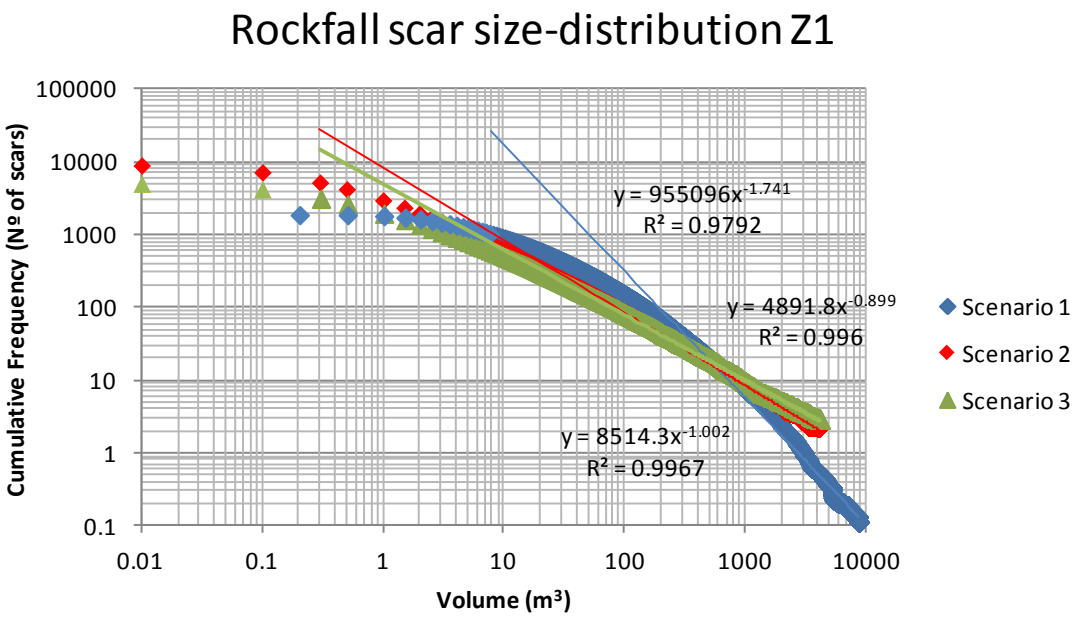

Figure 7-14: Rockfall scar size distribution of Z1 in terms of number of scars.

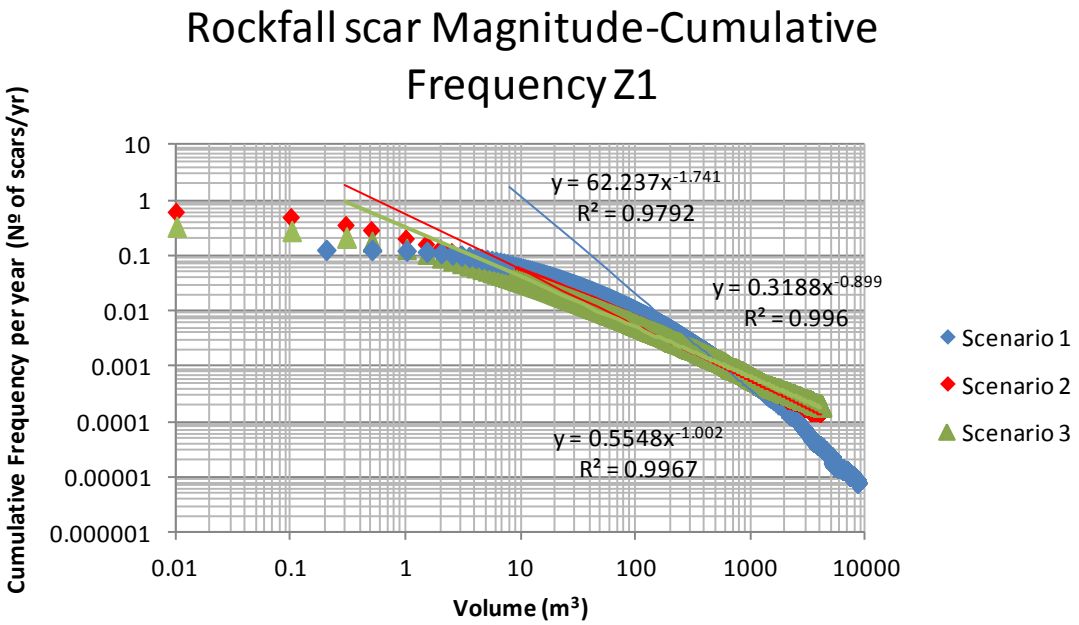

Figure 7-15: Derived MCF curves for each scenario in Z1.

Zone 2

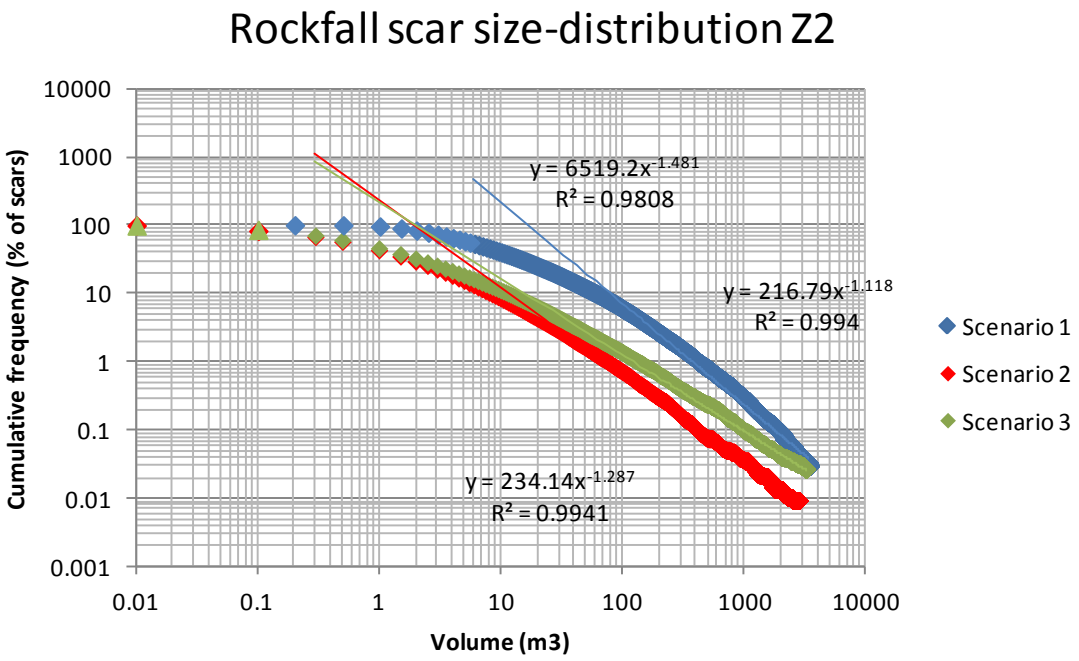

Figure 7-16: Rockfall scar size distribution of Z2 in terms of % of scars (obtained in chapter 6).

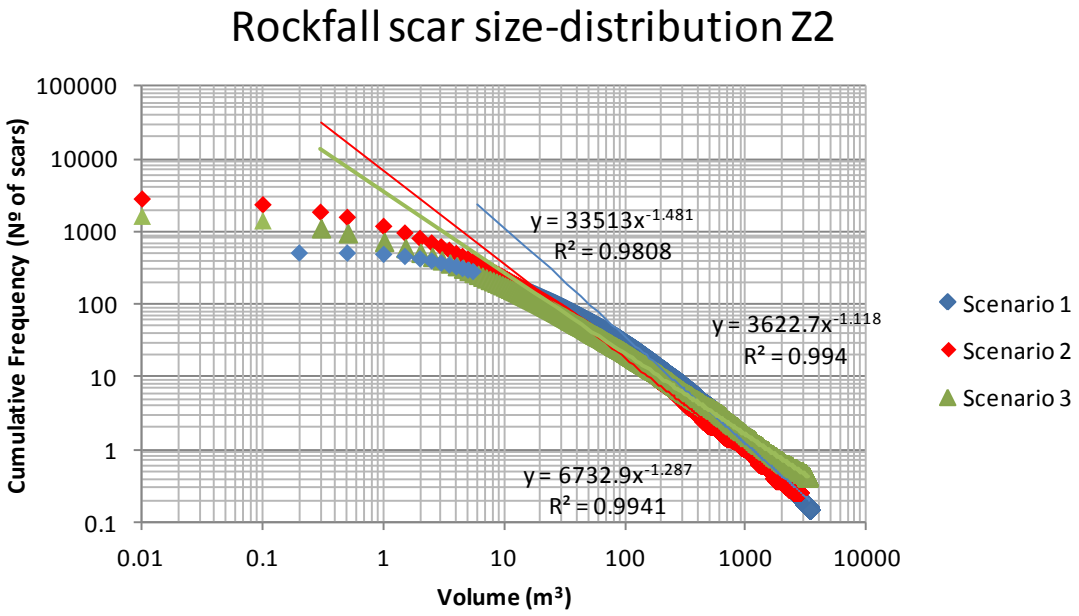

Figure 7-17: Rockfall scar size distribution of Z2 in terms of number of scars

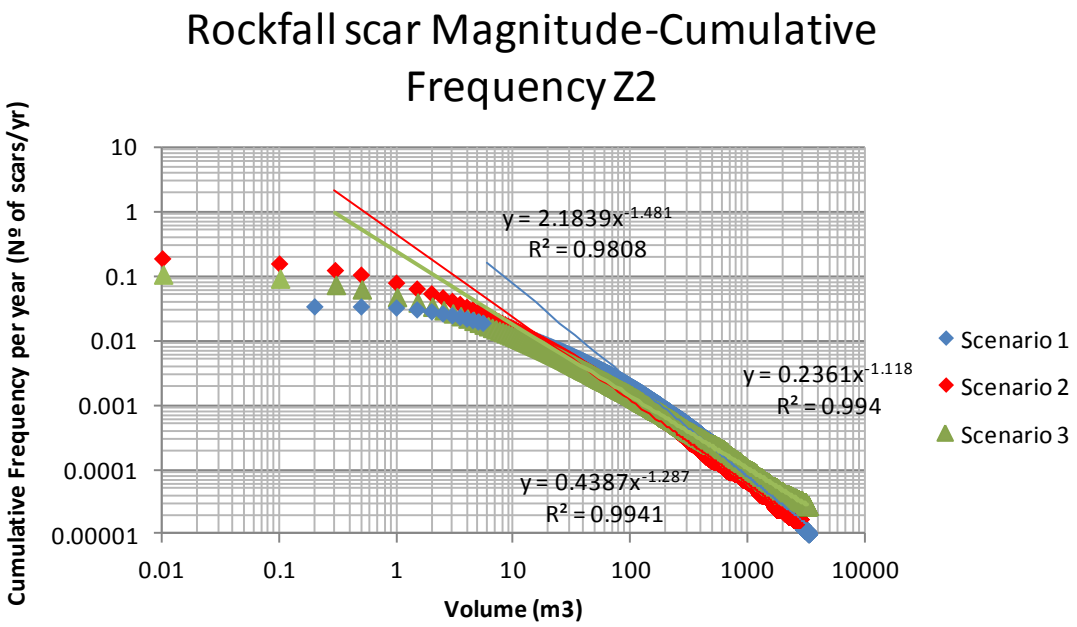

Figure 7-18: Derived MCF curves for each scenario in Z2.

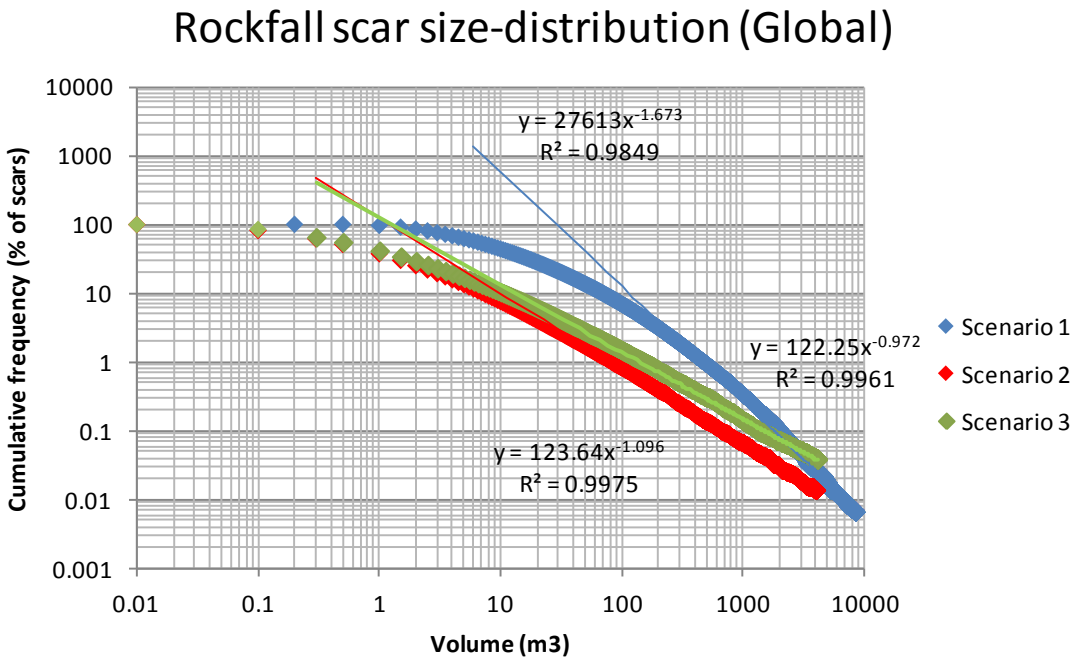

Figure 7-19: Rockfall scar size distribution of the whole area in terms of % of scars.

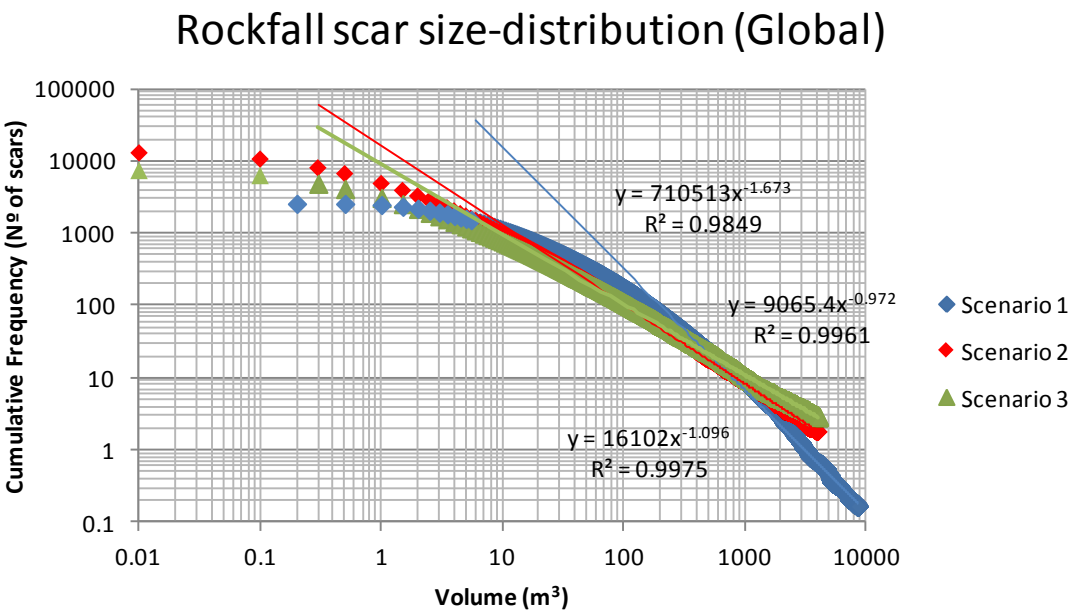

Figure 7-20: Rockfall scar size distribution of the whole area in terms of number of scars.

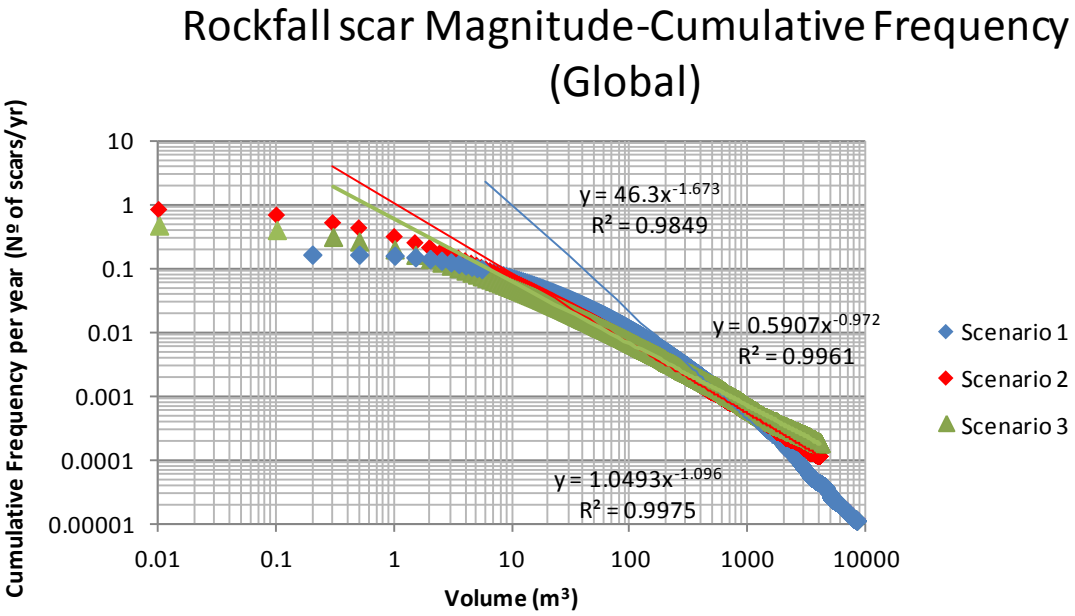

Figure 7-21: Derived MCF curves for each scenario in the whole area.

7.5 Discussion

In Table 7-11, the inverse power laws fitted to the MCF curves are shown. In both zones, the frequency of rockfall scar volumes is low. In Z1, for volumes of 1 m^3 or greater, the highest frequency is 0.19 rockfall scars per year (scenario 2), i.e., one rockfall scar each 5.3 years. In Z2, 0.078 rockfall scars per year for a volume of 1 m^3 or higher are expected, which gives one event each 12.8 years. In the whole area, for rockfall scars of 1 m^3 or higher, 0.316 rockfalls scars per year are expected (one rockfall scar each 3.16 years).

Comparing the MCF curves from Z1 and Z2 it can be observed that the frequency of rockfall scar volumes is lower in Z2 than in Z1. This means, for a specific volume, the number of rockfall scars per year is smaller in Z2. This confirms that Z1 is more active than Z2 in terms of rockfalls (Figure 6-3). In the whole area, the frequency is slightly higher than in Z1 and Z2. Since the volume of material used in the whole area is higher (volume from Z1 and Z2), its frequency increases as well.

Table 7-11: Inverse power laws fitted in the MCF curves (Figure 7-15, Figure 7-18 and Figure 7-21) for each scenario in both Z1 and Z2 and in the whole area

Scenario	**Expression**		
	Zone 1	**Zone 2**	**Whole area (Global)**
1	$F(x \geq X) = 62.237x^{-1.74}$	$F(x \geq X) = 2.1839x^{-1.481}$	$F(x \geq X) = 46.3x^{-1.673}$
2	$F(x \geq X) = 0.5548x^{-1.002}$	$F(x \geq X) = 0.4387x^{-1.287}$	$F(x \geq X) = 1.0493x^{-1.096}$
3	$F(x \geq X) = 0.3188x^{-0.899}$	$F(x \geq X) = 0.2361x^{-1.118}$	$F(x \geq X) = 0.5907x^{-0.972}$

As mentioned in chapter 6, it is not straightforward to decide which is the correct scenario for this area. However, given the uncertainties described during the methodology and the results commented above, scenario 3 seems to be the most appropriated since it excludes large rockfall scar volumes (scenario 1) and does not maximize small rockfall scars (scenario 2).
If comparing exponents of the power laws fitted for each scenario, with other values of published works shown in Table 3-6, it seems that the ones belonging to scenario 2 and 3 could be the most reliable, specially the MCF curve exponents of scenario 3 calculated in Z1 and in the whole area. Although the geological context is completely different, both exponents are very similar to the one obtained by Santana et al. (2012) whose study are (Andorra) is relatively close. Therefore, if a rockfall hazard map of the whole cliff was needed, the MCF curve of the scenario 3 calculated in the whole area should be taken (Figure 7-21).

Table 7-12: Characteristics of rockfall and rockfall scars volumes distributions (Taken from Santana et al. (2012) and later adapted).

Author	Site	Method	Geological setting	b
Hungr et al. (1999)[a]	British Columbia, Canada	Rail and highway inventories	Massive felsic rock, road cuts	0.43
			Massive felsic rock, road cuts	0.4
			Jointed metamorphic, rock, road cuts	0.7
			Jointed metamorphic, rock, road cuts	0.65
Rousseau (1999)[a]	Mahaval, La Reunión	Instrumental measurements	Single natural basaltic cliff	1
Dussauge-Peisser et al. (2002)[a]	Upper Arly Gorges, French Alps	Historical data	Metamorphic and sedimentary rocks	0.45±0.15
	Grenoble, French Alps		Calcareous cliffs	0.41±0.11
	Yosemite Valley, California		Granitic cliffs	0.46±0.11
Santana et al. (2012)	Andorra, Eastern Pyrenees	Rockfall scar volume distribution using TLS	Intensely fractured granodioritic cliff	0.92

[a] taken from Dussauge-Peisser et al. (2002)

7.6 Conclusions

A methodology has been proposed for obtaining the rockfall magnitude-cumulative frequency relation in the study area using the rockfall scar size distribution and dating by terrestrial cosmogenic nuclide. The rockfall scar size distribution and the total volume of material released have been obtained using a point cloud acquired with a terrestrial laser scanner (see chapter 6 of this thesis). The elapsed time has been calculated by dating several parts of the massif with cosmogenic ^{36}Cl. This technique permits a safe, quantitative, objective and systematic evaluation of the cumulative frequency-volume relation for rockfall scars when no databases of past events exist.

The total volume of material lost has been calculated by subtracting a post failure DSM, obtained with a TLS, from a pre-failure DSM. Since the pre-failure DSM was not available it was obtained by defining an approximated pre-existing surface called S_0 which represents the initial position of the cliff just before the blocks detached from the current scars at a certain time T=0. The S_0 surface has been defined assuming the recession of the cliff is parallel to the slope face.

The elapsed time started at T=0 until the present day. For that purpose, 9 samples have been dated using cosmogenic ^{36}Cl. The samples with a similar age define the S_0. It has been confirmed that grey surfaces are older and surfaces at a certain distance from S_0 are younger (a few thousands of years of difference). The definition of a proper input retreat rate, indispensable when working with shallow samples due to the interference of the inherited ^{36}Cl with the final exposure age, was one of the most difficult challenges of the proposed methodology.

The methodology has been applied to two separated zones of a rock wall cliff of the Montsec Range (Eastern Pyrenees, Spain) as well as in the whole area, and considering three different scenarios. Scenario 1 considers large scars and includes, mainly, large rockfall scar volumes. Scenario 2 considers smaller, eroded and irregular surfaces, some of them difficult to identify, which may be the result of smaller occurrences. Scenario 3 assumes that rockfall scars can be the result of one or several rockfall events and thus, a wider range of detachment possibilities are considered. The retreat rate obtained in Z2 has been lower than in Z1. A global retreat rate of 365 mm/ka has been used for the whole area in order to avoid retreat rate-dependent exposure ages (Merchel et al., 2013). Such a retreat rate is between those found in the literature ranging from 0.1 to 0.68 mm/a. The frequency of rockfall scars of a specific volume is lower in Z2 than in Z1, confirming the lower activity observed at first sight in Z2. The frequency of rockfall scars calculated in the whole area is higher since the amount of material used is higher as well.

Exponents showing the best agreement with published works are those from scenario 3 for Z1 and for the whole area. If a rockfall hazard map from the cliff was required, the MCF curve from scenario 3 calculated in the whole area would be the most appropriated option.

7.7 Future research work

-To work in cliffs where information about the initial slope surface was available (e.g.: photos, pre-failure DSM, etc.). This would allow a better calculation of the released volume.

-To apply the proposed methodology in areas where sufficient databases are available to validate MCF curves. However, it should be noted that a scar can be the result of one or several rockfall events and detached blocks can spread into smaller blocks due to fragmentation.

-To use other cosmogenic isotopes like ^{10}Be or ^{26}Al which are not affected by depth, because when dating shallow samples of relatively small rockfall events, ^{36}Cl exhibit some difficulties by inheritance.

Chapter 8

8 Concluding remarks

In this chapter the general conclusions of the thesis are shown corresponding to the objective announced in chapter 1: development of a rigorous, objective and reproducible methodology to establish the magnitude-frequency relationship of earthflows and rockfalls for the latter application to the hazard mapping at regional scale.
More detailed conclusions are found at the end of each chapter.

8.1 Summary of the conclusions

This work contributed to the development of two methodologies to obtain the Magnitude-Cumulative frequency curves of earthflows and rockfalls in the Tremp Basin (eastern Pyrenees).

8.1.1 Earthflows

The study area is located in the Barcedana Valley, where Garumnian Clays are responsible of several earthflows and translational landslides. It has been performed the landslide cartography and the obtaining of the magnitude-cumulative frequency curve. From this, the annual reactivation probability for a given volume can be derived.
Additionally, a first rainfall threshold responsible for landslide reactivations, by means of dendrogeomorphology and ROC analysis, has been calculated. The annual probability of reactivation has been derived from that rainfall threshold and it has been later used for the validation of the results obtained from the landslide inventory. The annual probability of reactivations has been of 0.66
The comparison between both probabilities confirmed that the obtaining of the landslide triggering rainfall thresholds using dendrogeomorphology and ROC points is a good method to obtain the probability of landslide reactivation when there is a lack of databases.
For first-time slope failures, a supervised procedure has been developed in the Barcedana Valley (Eastern Pyrenees, Spain) to evaluate the frequency and magnitude of first-time slope failures, larger than the pixel size, applying a deterministic model for the later hazard mapping using the magnitude-frequency matrix.
The frequency has been calculated from the first-time slope failure inventory and the stability index, calculated with a deterministic model (SINMAP Pack et al., 2005), has been reclassified into four susceptibility classes.
The area of the potential failures has been obtained by performing an automatic aggregation of groups of adjacent pixels with the same susceptibility class, located within the same slope and having an area smaller than a given threshold. To isolate each slope, a mapping unit called slope units has been defined using an iterative algorithm developed by the CNR-IRPI (Perugia, Italy) (Alvioli et al., 2014; 2015).
The automatic aggregation of pixels has been calculated by implementing an algorithm within ArcGIS 9.3®.
The pixel cluster size distribution has been compared with the first-time slope failures distribution. It denoted a great improvement compared with the pixel-based results obtained

directly from the deterministic model.
Finally, the MF matrix has been defined for the landslide hazard mapping.
This methodology permitted to assess the hazard of potential failures in a semi-automatic and objective way and considering the landslide area.

8.1.2 Rockfalls

A supervised procedure based on the methodology developed by Santana et al. (2012) has been developed for the calculation of the rockfall scar size distribution (RSSD). This methodology requires high resolution point cloud data obtained by a LIDAR and it can be used when historical rockfall series are not available and/or the access to the outcrop is limited. It permits a safe, quantitative, objective and systematic evaluation of the rockfall scar sizes assuming that the RSSD can be an approximation of the Rockfall Volume Distribution (RVD).
The methodology has been applied to two separated zones of a rock wall cliff of the Montsec Range (Eastern Pyrenees, Spain) as well as in the whole area, and considering three different scenarios.
To contemplate the different failure mechanics and thus all the possible volume distributions, three different scenarios were considered: Scenario 1 considers that large rockfall scars are generated by a single large rockfall event, scenario 2 takes in account small eroded and irregular surfaces which lead to the generation of small occurrences. Finally, scenario 3 considers a wider range of rockfall scar volumes.
Then, the temporal frequency of the rockfall scar volumes distribution has been obtained to convert from RSSD to magnitude-cumulative frequency curve. To this, the elapsed time and the total volume of material needed to generate the calculated RSSD have been calculated.
The elapse time has been computed by dating different parts of the rockwall using Terrestrial Cosmogenic Nuclide (TCN), ^{36}Cl. It permitted to obtain a retreat rate of the massif of 365mm/ka. Although there does not exist similar studies carried out in the study area, this value agree with those found in the literature in similar geological conditions (0.1 to 0.68 mm/a)
The total volume of material lost has been obtained using the point cloud obtained with the TLS and by defining a reference surface which represents the initial position of the cliff just before the blocks detached from the current scars.
In the whole area, for rockfall scars of 1 m^3 or higher, the higher frequency (scenario 2) is of 0.316 rockfalls scars per year (one rockfall scar each 3.16 years).
Scenario 3 was considered to be the most feasible one since it excludes large rockfall scar volumes, considered in scenario 1, and does not maximize small scar volumes as in scenario 2.

8.2 Future research work

This work has brought to light to the obtaining of the magnitude-cumulative frequency curves of earthflows and rockfalls for their application during the landslide hazard assessment. Nevertheless, many questions and/or recommendations have appeared throughout this research. Although more detailed future works are found at the end of each chapter, in this section, some general recommendations are shown:

-A systematic classification of landslides should be performed by the local authorities in order to provide an extensive database about failures aimed to find out exact dates of movements for the obtaining of the proper rainfall thresholds as well as for the calibration and/or validation of the models.
-Although the methodology developed by Alvioli et al. (2014; 2015) has been a great advance

concerning the delineation of the slope units, more improvement is still needed focused on the possibility to add a layer of existing landslides before the generation of the mapping units. It should interfere as minimum as possible during the delineation process, mostly, when these landsides are larger than some slope units.

-Further investigation about the most appropriate rockfall scar volume distribution is needed when several detachment mechanisms exist.

-To apply the proposed methodology in areas with different geological settings (rock types, geological history, genesis of the discontinuities, etc.) and with sufficient available databases to validate MCF curves and to compare the results. However, it should be noted that a scar can be the result of one or several rockfall events and detached blocks can spread into smaller blocks due to fragmentation.

-To work in cliffs where information about the initial slope surface was available (e.g.: photos, pre-failure DSM, etc.). This would allow a better calculation of the released volume.

-To use other cosmogenic isotopes like ^{10}Be or ^{26}Al which are not affected by depth, because when dating shallow samples of relatively small rockfall events, ^{36}Cl exhibit some difficulties by inheritance.

References

Abancó, C., Hürlimann, M., Lantada, N., 2009a. Validació de mapes de susceptibilitat d'esllavissaments elaborats mitjançant diferents tècniques a la zona de Sant Salvador de Toló; caracterització de les zones inestables i estudi de la seva activitat. Technical University of Catalonia.

Abancó, C., Lantada, N., Hürlimann, M., Corominas, J., Copons, R., 2009b. Validación de mapas de susceptibilidad de deslizamientos elaborados mediante diferentes técnicas. Aplicación a la zona de Sant Salvador de Toló (Cataluña), in: Alonso, E., Corominas, J., Hürlimann, M. (Eds.), VII Simposio Nacional Sobre Taludes Y Laderas Inestables. CIMNE, Barcelona, pp. 725–736.

Abbruzzese, J.M., Labiouse, V., 2013. New Cadanav methodology for quantitative rock fall hazard assessment and zoning at the local scale. Landslides 11, 551–564. doi:10.1007/s10346-013-0411-7

Abellán, a., Vilaplana, J.M., Calvet, J., García-Sellés, D., Asensio, E., 2011. Rockfall monitoring by Terrestrial Laser Scanning – case study of the basaltic rock face at Castellfollit de la Roca (Catalonia, Spain). Nat. Hazards Earth Syst. Sci. 11, 829–841. doi:10.5194/nhess-11-829-2011

Abellán, a., Vilaplana, J.M., Martínez, J., 2006. Application of a long-range Terrestrial Laser Scanner to a detailed rockfall study at Vall de Núria (Eastern Pyrenees, Spain). Eng. Geol. 88, 136–148. doi:10.1016/j.enggeo.2006.09.012

Abellán, A., Oppikofer, T., Jaboyedoff, M., Rosser, N.J., Lim, M., Lato, M.J., 2014. Terrestrial laser scanning of rock slope instabilities. Earth Surf. Process. Landforms 39, 80–97. doi:10.1002/esp.3493

Adapt Alp 5.1, 2010. Hazard Mapping- Geological Hazards. Literature Survey - Final Report.

AGS, 2007. Guidelines for Landslide Susceptibility, Hazard and Risk Zoning for Land Use Planning. Australian Geomechanics Society Landslide Taskforce Landslide Zoning Working Group. Australian Geomechanics Society.

Ahn, S.-H., Lee, C.-I., 2004. Removability Analysis of Rock Blocks By Block Theory and a Probabilistic Approach. Int. J. Rock Mech. Min. Sci. 41, 429. doi:10.1016/j.ijrmms.2003.12.069

Akhmadaliev, S., Heller, R., Hanf, D., Rugel, G., Merchel, S., 2013. The new 6MV AMS-facility DREAMS at Dresden. Nucl. Instruments Methods Phys. Res. Sect. B Beam Interact. with Mater. Atoms 294, 5–10. doi:10.1016/j.nimb.2012.01.053

Alcalá, F.J., Custodio, E., 2015. Natural uncertainty of spatial average aquifer recharge through atmospheric chloride mass bal- ance in continental Spain. J. Hydrol. doi:http://dx.doi.org/10.1016/j.jhydrol.2015.03.018

Alcalá, F.J., Custodio, E., 2014. Spatial average aquifer recharge through atmospheric chloride mass balance and its uncertainty in continental Spain. Hydrol. Process. 28, 218–236. doi:10.1002/hyp.9556

Aleotti, P., 2004. A warning system for rainfall-induced shallow failures. Eng. Geol. 73, 247–265.

Alestalo, J., 1971. Dendrochronological interpretation of geomorphic processes. Fennia 105, 1–140.

Alvioli, M., Marchesini, I., Fiorucci, F., Ardizzone, F., Rossi, M., Reichenbach, P., Guzzetti, F., 2014. Automatic delineation of geomorphological slope units. Geophysical Research Abstracts 16. EGU General Assembly. Vienna.

Alvioli, M., Marchesini, I., Reichenbach, P., Rossi, M., Fiorucci, F., Ardizzone, F., Guzzetti, F., 2015. Manuscript in preparation.

Anderson, M.G., Kemp, M.J., Shen, J.M., 1987. On the use of resistance envelopes to identify the controls on slope stability in the tropics. Earth Surf. Process. Landforms 12, 637–648.

André, M.-F., 1997. Holocene Rockwall Retreat in Svalbard: A Triple-Rate Evolution. Earth Surf. Process. Landforms 22, 423–440. doi:10.1002/(SICI)1096-9837(199705)22:5<423::AID-ESP706>3.0.CO;2-6

Annaka, T., Satake, K., Sakakiyama, T., Yanagisawa, K., Shuto, N., 2007. Logic-tree approach for Probabilistic Tsunami Hazard Analysis and its applications to the Japanese coasts. Pure Appl. Geophys. 164, 577–592. doi:10.1007/s00024-006-0174-3

Armesto, J., Ordóñez, C., Alejano, L., Arias, P., 2009. Terrestrial laser scanning used to determine the geometry of a granite boulder for stability analysis purposes. Geomorphology 106, 271–277. doi:10.1016/j.geomorph.2008.11.005

Ayalew, L., Yamagishi, H., 2005. The application of GIS-based logistic regression for landslide susceptibility mapping in the Kakuda-Yahiko Mountains, Central Japan. Geomorphology 65, 15–31. doi:10.1016/j.geomorph.2004.06.010

Baecher, G.B., 1983. Statistical analysis of rockmass fracturing. J. Int. Assoc. Math. Geol. 15, 329–348.

Baecher, G.B., 1980. Progressively censored sampling of rock joint traces. J. Int. Assoc. Math. Geol. 12, 33–40.

Balco, G., 2006. Geometric shielding calculator [WWW Document]. URL http://hess.ess.washington.edu/math/general/skyline_input.php

Baltzer, A., 1875. Über bergstürze in den Alpen. Verlag der Schabelitz'schen buchhandlung (C. Schmidt)Zurich, 50p.

Baum, R.L., Coe, J.A., Godt, J.W., Harp, E.L., Reid, M.E., Savage, W.Z., Schulz, W.H., Brien, D.L., Chleborad, A.F., McKenna, J.P., Michael, J.A., 2005. Regional landslide-hazard assessment for Seattle, Washington, USA. Landslides 2, 266–279.

Baum, R.L., Savage, W.Z., Godt, J.W., 2008. TRIGRS — A Fortran Program for Transient Rainfall Infiltration and Grid Based Regional Slope-Stability Analysis, Version 2.0. USGS Open File Report 2008 1159.

Bell, R., Glade, T., 2004. Quantitative risk analysis for landslides – Examples from Bíldudalur, NW-Iceland. Nat. Hazards Earth Syst. Sci. 4, 117–131. doi:10.5194/nhess-4-117-2004

Bertolini, G., Guida, M., Pizziolo, M., 2005. Landslides in Emilia-Romagna region (Italy): Strategies for hazard assessment and risk management. Landslides 2, 302–312. doi:10.1007/s10346-005-0020-1

Bertolini, G., Pizziolo, M., 2008. Risk assessment strategies for the reactivation of earth flows in the Northern Apennines (Italy). Eng. Geol. 102, 178–192. doi:10.1016/j.enggeo.2008.03.017

Beven, K.J., Kirby, M.J., 1979. A physically based variable contributing area model of basin hydrology. Hydrol. Sci. Bull. 24 (4), 43–69.

BMLFUW, 2011. Alpine Mass Movements: Implications for hazard assessment and mapping, Special Edition of Journal of Torrent, Avalanche, Landslide and Rock Fall Engineering No. 166.

Bonnard, C., Noverraz, F., 2001. Influence of climate change on large landslides: assessment of long term movements and trends., in: Proc. of the International Conference on Landslides: Causes Impact and Countermeasures. Gluckauf, Essen, Davos, pp. 121–138.

Bourrier, F., Dorren, L., Hungr, O., 2013. The use of ballistic trajectory and granular flow models in predicting rockfall propagation. Earth Surf. Process. Landforms 38, 435–440. doi:10.1002/esp.3372

Brardinoni, F., Church, M., 2004. Representing the landslide magnitude–frequency relation: Capilano River basin, British Columbia. Earth Surf. Process. Landforms 29, 115–124. doi:10.1002/esp.1029

Braucher, R., Merchel, S., Borgomano, J., Bourlès, D.L., 2011. Production of cosmogenic radionuclides at great depth: A multi element approach. Earth Planet. Sci. Lett. 309, 1–9.

Brenot, J., Quiquerez, A., Petit, C., Garcia, J.-P., 2008. Erosion rates and sediment budgets in vineyards at 1-m resolution based on stock unearthing (Burgundy, France). Geomorphology 100, 345–355. doi:10.1016/j.geomorph.2008.01.005

Broccolato, M., Martelli, D.. C.G., Tamburini, A., 2006. Il rilievo geomeccanico di pareti rocciose instabili difficilmente accessibili mediante impiego di laser scanner

terrestre. Applicazione al caso di Ozein (vale di Cogne, Aosta). Geoing. Ambient. e Mineraria 119, 39–46.

Brooks, S.M., Spencer, T., 2010. Temporal and spatial variations in recession rates and sediment release from soft rock cliffs, Suffolk coast, UK. Geomorphology 124, 26–41. doi:10.1016/j.geomorph.2010.08.005

Brown, E.T., Edmond, J.M., Raisbeck, G.M., Yiou, F., Kurz, M.D., Brook, E.J., 1991. Examination of surface exposure ages of Antartic moraines using in situ produced Berillium-10 and Aluminium-26. Geochim. Cosmochim. Acta 55, 2269–2283.

Brunetti, M.T., Guzzetti, F., Rossi, M., 2009. Probability distributions of landslide volumes. Nonlinear Process. Geophys. 16, 179–188.

Bunce, C.M., Cruden, D.M., Morgenstern, N.R., 1997. Assessment of the hazard from rock fall on a highway. Can. Geotech. J. 34, 344–356. doi:10.1139/cgj-34-3-344

Buoncristiani, J.-F., Petit, C., Campy, M., Bossuet, G., Richard, H., 2002. Quantification de l'ablation d'un bassin versant marno calcaire alpin durant le Petit Age Glaciaire par l'étude d'un système lacustre (cas du lac du <<Claps>> de Luc-en- Diois Drôme, France) (in French). Geodin. Acta 15, 103–111.

Caine, N., 1980. The rainfall intensity: duration control of shallow landslides and debris flows. Geogr Ann A 62, 23–27.

Campbell, R.H., 1975. Soil Slips, debris flows, and rainstorms in the Santa Monica Mountains and vicinity, Southern California, in: U.S. Geological Survey Professional Paper 851. Washington DC, p. 51.

Can, T., Nefeslioglu, H. a., Gokceoglu, C., Sonmez, H., Duman, T.Y., 2005. Susceptibility assessments of shallow earthflows triggered by heavy rainfall at three catchments by logistic regression analyses. Geomorphology 72, 250–271. doi:10.1016/j.geomorph.2005.05.011

Canales, C.J., 2011. Soil strenght parameters and stability conditions of the slopes of the Tremp basin (Eastern Pyrenees, Spain) derived from back-analysis and field reconnaissance. Master thesis. Technical Univesity of Catalonia. Barcelona. Technical University of Catalonia, Barcelona.

Cannon, S.H., Ellen, S.D., 1985. Rainfall conditions for abundant debris avalanches, San Francisco Bay region, California. Calif. Geol. 38, 267–272.

Cannon, S.H., Gartner, J.E., 2005. Wildfire-related debris flow from a hazards perspective., in: Jakob, M., Hungr, O. (Eds.), Debris Flow Hazards and Related Phenomena. Springer, Berlin Heidelberg, pp. 363–385.

Cardinali, M., Galli, M., Guzzetti, F., Ardizzone, F., Reichenbach, P., Bartoccini, P., 2006. Rainfall induced landslides in December 2004 in south-western Umbria, central Italy: types, extent, damage and risk assessment. Nat. Hazards Earth Syst. Sci. 6, 237–260. doi:10.5194/nhess-6-237-2006

Cardinali, M., Reichenbach, P., Guzzetti, F., Ardizzone, F., Antonini, G., Galli, M., Cacciano, M., Castellani, M., A, V.V., 2002. A geomorphological approach to the estimation of landslide hazards and risks in Umbria , Central Italy. Nat. Hazards Earth Syst. Sci. 2, 57–72.

Carrara, A., 1988. Drainage and divide networks derived from high-fidelity digital terrain models, in: Chung, C.F. (Ed.), Quantitative Analysis of Mineral and Energy Resources. Dordrecht, The Netherlands, pp. 581–597.

Carrara, A., Cardinali, M., Detti, R., Guzzetti, F., Pasqui, V., Reichenbach, P., 1991. GIS TECHNIQUES AND STATISTICAL MODELS IN EVALUATING LANDSLIDE HAZARD. Earth Surf. Process. Landforms 427–445.

Casagrande, A., 1942. Sistema unificado de clasificación de suelos. En: JUÁREZ, E. et. al., 2004. Mecánica de suelos. V. 2: teoría y aplicaciones de la mecánica de suelos. México, DF (México), Grupo Noriega. v. 2-3.

Cascini, L., 2008. Applicability of landslide susceptibility and hazard zoning at different scales. Eng. Geol. 102, 164–177. doi:10.1016/j.enggeo.2008.03.016

Castellanos Abella, E.A., 2008. Discussions, conclusions and recomendations. In: Castellanos Abella, E. A., Multi-scale landslide risk assessment in Cuba, Utrecht, Utrecht University, 2008. ITC Disertation 154, 227-244p. ISBN: 978-90-6164-268-8.

Castellanos Abellan, E. a., Van Westen, C.J., 2007. Generation of a landslide risk index map for Cuba using spatial multi-criteria evaluation. Landslides 4, 311–325. doi:10.1007/s10346-007-0087-y

Caus, E., Llompart, J., Rossell, J., Bernaus, J.M., 1999. El coniaciense superior-santoniense inferior de la sierra del Montsec (Pirineos, NE de España). Rev. Soc. Geol. España 12, 269–280.

Chen, Z., Wang, J., 2007. Landslide hazard mapping using logistic regression model in Mackenzie Valley, Canada. Nat. Hazards 42, 75–89. doi:10.1007/s11069-006-9061-6

Cho, T.F., Lee, S.B., Won, K.S., 2012. Three-dimensional deterministic block analysis model for information-oriented excavation design. Int. J. Rock Mech. Min. Sci. 55, 63–70. doi:10.1016/j.ijrmms.2012.05.003

Clarizia, M., Gullà, G., Sorbino, G., 1996. Sui meccanismi di innesco dei soil slip, in: Luino, F. (Ed.), Int. Conf. Prevention of Hydrogeological Hazards: The Role of Scientific Research. Alba: L'Artistica Savigliano pub, pp. 585–597.

Codilean, A.T., 2006. Calculation of the cosmogenic nuclide production topographic shielding scaling factor for large areas using DEMs. Earth Surf. Process. Landf. 31, 785–794.

Coduto, D., 1999. Geotechnical Engineering: Principles and Practices. Prentice-Hall, New Jersey.

Conrad, N., Elmore, D., Kubik, P., Gave, H., Tubbs, L., Chrunyk, B., Wahlen, M., 1986. The chemical preparation of AgCl for measuring 36Cl in polar ice with accelerometer mass spectrometry. Radiocarbon 28, 556–560.

Copons, R., Vilaplana, J., 2008. Rockfall susceptibility zoning at a large scale: From geomorphological inventory to preliminary land use planning. Eng. Geol. 102, 142–151. doi:10.1016/j.enggeo.2008.03.020

Corominas, J., 2000. Landslide and climate, in: Proc of the VIII International Symposium on Landslides. Cardiff.

Corominas, J., Moya, J., 2010. Contribution of dendrochronology to the determination of magnitude–frequency relationships for landslides. Geomorphology 124, 137–149. doi:10.1016/j.geomorph.2010.09.001

Corominas, J., Moya, J., 2008. A review of assessing landslide frequency for hazard zoning purposes. Eng. Geol. 102, 193–213. doi:10.1016/j.enggeo.2008.03.018

Corominas, J., Moya, J., 1999. Reconstructing recent landslide activity in relation to rainfall in the Llobregat River basin, Eastern Pyrenees, Spain. Geomorphology 30, 79–93.

Corominas, J., van Westen, C., Frattini, P., Cascini, L., Malet, J.-P., Fotopoulou, S., Catani, F., Van Den Eeckhaut, M., Mavrouli, O., Agliardi, F., Pitilakis, K., Winter, M.G., Pastor, M., Ferlisi, S., Tofani, V., Hervás, J., Smith, J.T., 2014. Recommendations for the quantitative analysis of landslide risk. Bull. Eng. Geol. Environ. 73, 209–263. doi:10.1007/s10064-013-0538-8

Corona, C., Trappmann, D., Stoffel, M., 2013. Parameterization of rockfall source areas and magnitudes with ecological recorders: When disturbances in trees serve the calibration and validation of simulation runs. Geomorphology 202, 33–42. doi:10.1016/j.geomorph.2013.02.001

Crosta, G.B., 1989. A study of slope movements caused by heavy rainfall in Valtellina (Italy-July 1987)., in: Cancelli, A. (Ed.), Proc. 6th Int. Conf. and Field Workshop on Landslides ALPS 90. Ricerca Scientifica ed Educazione Permanente, Milano, pp. 247–258.

Crosta, G.B., Frattini, P., 2001. Rainfall thresholds for triggering soil slips and debris flow, in: Mugnai, A., Guzzetti, F., Roth, G. (Eds.), Proc. 2nd EGS Plinius Conf. on Mediterranean Storms. Siena, pp. 463–487.

Crovelli, R.A., 2000. Probability models for estimation of number and costs of landslides. United States Geological Survey Open File Report 00-249.

Cruden, D.M., 1991. A simple definition of a landslide. Bull. Int. Assoc. Eng. Geol. 43, 27–29.

Cruden, D.M., Varnes, D.J., 1996. Landslide types and processes, in: Turner, A.K., Schuster, R.L. (Eds.), Landslides. Investigation and Mitigation. Transportation Research Board Special Report 247. National Academy Press. Washington DC., pp. 36–75.

Cuevas, J.L., 1992. Estratigrafía del "Garumniense" de la Conca de Tremp. Prepirineo de Lérida. Acta Geológica Hispánica 27, 95–108.

Cuevas, J.L., Dreyer, T., Mercadé, L., 1991. En: Guidebook of 4th Intern. Conference on Fluvial Sedimentology (M. Marzo y C. Puigdefàbregas, Eds),. Publicaciones Servei Geològic de Catalunya, 2ª Edició, 23-26 y 103-105.

Curry, A.M., Morris, C.J., 2004. Lateglacial and Holocene talus slope development and rockwall retreat on Mynydd Du, UK. Geomorphology 58, 85–106. doi:10.1016/S0169-555X(03)00226-5

Dahal, R.K., Hasegawa, S., 2008. Representative rainfall thresholds for landslides in the Nepal Himalaya. Geomorphology 100, 429–443. doi:10.1016/j.geomorph.2008.01.014

Davies, T., Phillips, C., Warburton, J., 2013. Processes, transport, deposition, and landforms: flow In: Shroder, J. (Editor in Chief), Marston, R.A., Stoffel, M. (Eds.), Treatise on Geomorphology. Academic Press, San Diego, CA, vol. 7, Mountain and Hillslope Geomorphology, pp. 158–170.

Davis, R.J., Schaeffer, O.A., 1955. Chlorine-36 in nature. Ann. New York Acad. Sci. 62, 105–122.

Deb, D., Hariharan, S., Rao, U.M., Ryu, C.-H., 2008. Automatic detection and analysis of discontinuity geometry of rock mass from digital images. Comput. Geosci. 34, 115–126. doi:10.1016/j.cageo.2007.03.007

Deline, P., Alberto, W., Broccolato, M., Hungr, O., Noetzli, J., Ravanel, L., Tamburini, a., 2011. The December 2008 Crammont rock avalanche, Mont Blanc massif area, Italy. Nat. Hazards Earth Syst. Sci. 11, 3307–3318. doi:10.5194/nhess-11-3307-2011

Delmas, M., Calvet, M., Gunnell, Y., 2009. Variability of Quaternary glacial erosion rates – A global perspective with special reference to the Eastern Pyrenees. Quat. Sci. Rev. 28, 484–498. doi:10.1016/j.quascirev.2008.11.006

Delong, S.B., Prentice, C.S., Hilley, G.E., Ebert, Y., 2012. Multitemporal ALSM change detection, sediment delivery, and process mapping at an active earthflow. Earth Surf. Process. Landforms 37, 262–272. doi:10.1002/esp.2234

Diehl, R., Halloin, H., Kretschmer, K., Lichti, G.G., Schönfelder, V., Strong, A.W., von Kienlin, A., Wang, W., Jean, P., Knödlseder, J., Roques, J.-P., Weidenspointner, G., Schanne, S., Hartmann, D.H., Winkler, C., Wunderer, C., 2006. Radioactive 26Al from massive stars in the Galaxy. Nature 439, 45–47. doi:10.1038/nature04364

Domènech, G., 2011. Obtenció de mapes de perillositat d'esllavissades a partir del càlcul de la susceptibilitat mitjançant un model determinista. Master thesis. Technical Univesity of Catalonia. Barcelona.

Dunai, T.J., 2010. COSMOGENIC NUCLIDES Principles, Concepts and Applications in the Earth Surface Sciences. Cambridge University Press, New York.

Dunai, T.J., 2001. Influence of secular variation of the geomagnetic field on production rates of in situ produced cosmogenic nuclides 193.

Dunai, T.J., 2000. Scaling factors for production rates of in situ produced cosmogenic nuclides: a critical reevaluation. Earth Planet. Sci. Lett. 176, 157–169.

Dunne, J., Elmore, D., Muzikar, P., 1999. Scaling factors for the rates of production of cosmogenic nuclides for geometric shielding and attenuation at depth on sloped surfaces. Geomorphology 27, 3–11.

Dussauge-Peisser, C., Helmstetter, A., Grasso, J.-R., Hantz, D., Desvarreux, P., Jeannin, M., Giraud, A., 2002. Probabilistic approach to rock fall hazard assessment: potential of historical data analysis. Nat. Hazards Earth Syst. Sci. 2, 15–26. doi:10.5194/nhess-2-15-2002

EasyFit, T., n.d. Mathwave - data analysis and simulation http://www.mathwave.com.

Egozcue, J.J., Ortego, M.I., 2006. The effect of scale in daily precipitation hazard assessment. Nat. Hazards Earth Syst. Sci. 459–470.

Eidelman, S., Hayes, K.G., Olive, K.A., Aguilar-Benitez, M., Amsler, C., Asner, D., Babu, K.S., Barnett, R.M., Beringer, J., Burchat, P.R., Carone, C.D., Caso, S., Conforto, G., Dahl, O., D'Ambrosio, G., Doser, M., Feng, J.L., Gherghetta, T., Gibbons, L., Goodman, M., Grab, C., Groom, D.E., Gurtu, A., Hagiwara, K., Hernández-Rey, J.J., Hikasa, K., Honscheid, K., Jawahery, H., Kolda, C., Kwon, Y., Mangano, M.L., Manohar, A. V., March-Russell, J., Masoni, A., Miquel, R., Mönig, K., Murayama, H., Nakamura, K., Navas, S., Pape, L., Patrignani, C., Piepke, A., Raffelt, G., Roos, M., Tanabashi, M., Terning, J., Törnqvist, N. a., Trippe, T.G., Vogel, P., Wohl, C.G., Workman, R.L., Yao, W.-M., Zyla, P. a., 2004. Review of Particle Physics. Phys. Lett. B 592, 1–1109. doi:10.1016/j.physletb.2004.06.001

Elmouttie, M.K., Poropat, G. V., 2012. A Method to Estimate In Situ Block Size Distribution. Rock Mech. Rock Eng. 45, 401–407. doi:10.1007/s00603-011-0175-0

Erener, A., Düzgün, H.B.S., 2013. A regional scale quantitative risk assessment for landslides: Case of Kumluca watershed in Bartin, Turkey. Landslides 10, 55–73. doi:10.1007/s10346-012-0317-9

Evans, S.G., Hungr, O., 1993. The assessment of rockfall hazard at the base of talus slopes. Can. Geotech. J. 30, 620–636. doi:10.1139/t93-054

Faraji Sabokbar, H., Shadman Roodposhti, M., Tazik, E., 2014. Landslide susceptibility mapping using geographically-weighted principal component analysis. Geomorphology 226, 15–24. doi:10.1016/j.geomorph.2014.07.026

Fawcett, T., 2006. An introduction to ROC analysis. Pattern Recognit. Lett. 27, 861–874. doi:10.1016/j.patrec.2005.10.010

Fell, R., Corominas, J., Bonnard, C., Cascini, L., Leroi, E., Savage, W.Z., 2008. Guidelines for landslide susceptibility, hazard and risk zoning for land use planning. Eng. Geol. 102, 85–98. doi:10.1016/j.enggeo.2008.03.022

Fell, R., Ho, K.K.S., Lacasse, S., Leroi, E., 2005. A framework for landslide risk assessment and management, in: Hungr, O., Fell, R., Couture, R., Eberhardt, E. (Eds.), Landslide Risk Management. Taylor and Francis, London, pp. 3–19.

Fernández, O., 2005. Obtaining a best fitting plane through 3D georeferenced data. J. Struct. Geol. 27, 855–858. doi:10.1016/j.jsg.2004.12.004

Fillon, C., Gautheron, C., van der Beek, P., 2013. Oligocene-Miocene burial and exhumation of the Southern Pyrenean foreland quantified by low-temperature thermochronology. J. Geol. Soc. London. 170, 67–77. doi:10.1144/jgs2012-051

Finlay, P.J., Fell, R., Maguire, P.K., 1997. The relationship between the probability of landslide occurrence and rainfall. Can. Geotech. J. 34, 811–824. doi:10.1139/cgj-34-6-811

Fityus, S.G., Giacomini, a., Buzzi, O., 2013. The significance of geology for the morphology of potentially unstable rocks. Eng. Geol. 162, 43–52. doi:10.1016/j.enggeo.2013.05.007

Forné, D., 2004. Anàlisi d'estabilitat de diferents esllavissaments al Pirineu mitjançant el mètode de l'equilibri límit. Influència del nivell freàtic en les reactivacions.Master thesis. Technical Univesity of Catalonia. Barcelona. Technical University of Catalonia, Barcelona.

Frattini, P., Crosta, G., Carrara, A., Agliardi, F., 2008. Assessment of rockfall susceptibility by integrating statistical and physically-based approaches. Geomorphology 94, 419–437. doi:10.1016/j.geomorph.2006.10.037

Frattini, P., Crosta, G., Fusi, N., Dalnegro, P., 2004. Shallow landslides in pyroclastic soils: a distributed modelling approach for hazard assessment. Eng. Geol. 73, 277–295. doi:10.1016/j.enggeo.2004.01.009

Frequency-volume relation and prediction of rainfall induced landslides, 2001. . Eng. Geol. 59, 253–266.

Fuchs, M., Torizin, J., Kühn, F., 2014. The effect of DEM resolution on the computation of the factor of safety using an infinite slope model. Geomorphology 224, 16–26. doi:10.1016/j.geomorph.2014.07.015

Garcia-Sellés, D., Arbués, P., -Falivene, O., Gratacós, O., Tavanil, S., Muñoz, J., 2009. Metodología para la caracterización automatica de las estructuras geológicas a partir de datos LIDAR (CIMNE). VII Simp. Nac. sobre Taludes y Laderas Inestables.

García-Sellés, D., Falivene, O., Arbués, P., Gratacos, O., Tavani, S., Muñoz, J. a., 2011. Supervised identification and reconstruction of near-planar geological surfaces from terrestrial laser scanning. Comput. Geosci. 37, 1584–1594. doi:10.1016/j.cageo.2011.03.007

Georisc S. L., 2009. Adquisició de dades per a l'anàlisi metodològica posterior de la susceptibilitat i la perillositat en el sector Barcedana-Montsec. Ref. Comanda Institut Geològic de Catalunya: 07-5/2009.

GeoriscS.L., 2008. Adquisició de dades per a l'anàlisi posterior de la susceptibilitat i la perillositat en una zona pilot situada a Sant Salvador de Toló.Ref. Comanda Institut Geològic de Catalunya: 06-249/2008. Ref. Estudi Georisc S.L.:08019.

Giardino, M., Borgogno Mondino, E., Perotti, L., 2005. Geomatics application for geological and geomorphological mapping and landslide hazard evaluation: case studies in the Italian NW-Alps, in: Proceedings of the 31st Symposium on Remote Sensing of Environment. Saint Petersburg (CSI), p. unpaginated CD–ROM, 4 pp.

Gigli, G., Casagli, N., 2011. Semi-automatic extraction of rock mass structural data from high resolution LIDAR point clouds. Int. J. Rock Mech. Min. Sci. 48, 187–198. doi:10.1016/j.ijrmms.2010.11.009

Giles, P., 1998. An automated approach to the classification of the slope units using digital data. Geomorphology 21, 251–264. doi:10.1016/S0169-555X(97)00064-0

Giordan, D., Allasia, P., Manconi, A., Baldo, M., Santangelo, M., Cardinali, M., Corazza, A., Albanese, V., Lollino, G., Guzzetti, F., 2013. Morphological and kinematic evolution of a large earthflow: The Montaguto landslide, southern Italy. Geomorphology 187, 61–79. doi:10.1016/j.geomorph.2012.12.035

Girardeau-Montant, D., 2006. Détection de changement sur des données géométriques tridimensionnelles - Ph.D thesis. Telecom Paris.

Gocad, D., n.d. Earth Decision Sciences http://www.earthdecision.com.

Godt, J.W., Baum, R.L., Savag, e W.Z., Salciarini, D., Schulz, W.H., Harp, E.L., 2008. Transient deterministic shallow landslide modeling: Requirements for susceptibility and hazard assessments in a GIS framework. Eng. Geol. 102, 214–226.

González de Vallejo, L.I., Ferrer, M., Ortuño, L., Oteo, C., 2002. Ingeniería Geológica. PEARSON EDUCACIÓN, Madrid.

Goodman, R.E., 1989. Introduction to Rock Mechanics. John Wiley and sons, New York, p. 561.

Gosse, J.C., Evenson, E.B., Klein, J., Lawn, B., Middleton, R., 1995. Precise cosmogenic Berillium-10 measurements in western NorthAmerica: Support for a global Younger Dryas cooling event. Geology 23, 877–880.

Gosse, J.C., Phillips, F.M., 2001. Terrestrial in situ cosmogenic nuclides: theory and application. Quat. Sci. Rev. 20, 1475–1560.

Greco, R., Sorrisovalvo, M., Catalano, E., 2006. Logistic Regression analysis in the evaluation of mass movements susceptibility: The Aspromonte case study, Calabria, Italy. Eng. Geol. 89, 47–66. doi:10.1016/j.enggeo.2006.09.006

Günther, A., Eeckhaut, M. Van Den, Malet, J., Reichenbach, P., Hervás, J., 2014. Climate-physiographically differentiated Pan-European landslide susceptibility assessment using spatial multi-criteria evaluation and transnational landslide information. Geomorphology 224, 69–85. doi:10.1016/j.geomorph.2014.07.011

Gutenberg, B., Richter, C.F., 1954. Seismicity of the earth. 2nd ed. Princeton University Press, Princeton, N.J.

Guthrie, R.., Evans, S.., 2005. The role of magnitude–frequency relations in regional landslide risk analysis. In: Hungr O, Fell R, Couture R, Eberhardt E (eds) Landslide risk management. A.A. Balkema, London, pp 375–380.

Guthrie, R.H., Deadman, P.J., Cabrera, a. R., Evans, S.G., 2008. Exploring the magnitude–frequency distribution: a cellular automata model for landslides. Landslides 5, 151–159. doi:10.1007/s10346-007-0104-1

Gutierrez Elorza, M., Sesé Martínez, V.H., 2001. Multiple talus flatirons , variations of scarp retreat rates and the evolution of slopes in Almazán Basin (semi-arid central Spain). Geomorphology 38, 19–29.

Gutierrez, M., Sancho, C., 1998. Scarp retreat rates in semiarid environments from talus flatirons ž Ebro Basin , NE Spain / 111–121.

Guzzetti, F., Ardizzone, F., Cardinali, M., Galli, M., Reichenbach, P., Rossi, M., 2008. Distribution of landslides in the Upper Tiber River basin, central Italy. Geomorphology 96, 105–122. doi:10.1016/j.geomorph.2007.07.015

Guzzetti, F., Ardizzone, F., Cardinali, M., Rossi, M., Valigi, D., 2009. Landslide volumes and landslide mobilization rates in Umbria, central Italy. Earth Planet. Sci. Lett. 279, 222–229. doi:10.1016/j.epsl.2009.01.005

Guzzetti, F., Carrara, A., Cardinali, M., Reichenbach, P., 1999. Landslide hazard evaluation: a review of current techniques and their application in a multi-scale study, Central Italy. Geomorphology 31, 181–216. doi:10.1016/S0169-555X(99)00078-1

Guzzetti, F., Carrara, A., Cardinali, M., Reichenbach, P., 1997. Landslide hazard evaluation: a review of current techniques and their application in a multi-scale study, Central Italy. Geomorphology 31, 181–216.

Guzzetti, F., Costa, G., Marchetti, M., Reichenbach, P., 1992. Debris flows triggered by the July, 17-19, 1987 storm in the Valtellina Area (Northern Italy), in: Proc. of the VII International Congress Interpraevent. Bern, pp. 193–204.

Guzzetti, F., Malamud, B.D., Turcotte, D.L., Reichenbach, P., 2002. Power-law correlations of landslide areas in central Italy. Earth Planet. Sci. Lett. 195, 169–183. doi:10.1016/S0012-821X(01)00589-1

Guzzetti, F., Peruccacci, S., Rossi, M., Colin, P.S., 2008. The rainfall intensity – duration control of shallow landslides and debris flows : an update. Landslides 5, 3–17. doi:10.1007/s10346-007-0112-1

Guzzetti, F., Peruccacci, S., Rossi, M., Stark, C.P., 2007. Rainfall thresholds for the initiation of landslides in central and southern Europe. Meteorol. Atmos. Phys. 98, 239–267. doi:10.1007/s00703-007-0262-7

Guzzetti, F., Reichenbach, P., Cardinali, M., Galli, M., Ardizzone, F., 2005. Probabilistic landslide hazard assessment at the basin scale. Geomorphology 72, 272–299. doi:10.1016/j.geomorph.2005.06.002

Guzzetti, F., Reichenbach, P., Ghigi, S., 2004. Rockfall Hazard and Risk Assessment Along a Transportation Corridor in the Nera Valley, Central Italy. Environ. Manage. 34, 191–208. doi:10.1007/s00267-003-0021-6

Guzzetti, F., Reichenbach, P., Wieczorek, G.F., 2003. Rockfall hazard and risk assessment in the Yosemite Valley, California, USA. Nat. Hazards Earth Syst. Sci. 3, 491–503. doi:10.5194/nhess-3-491-2003

Haeuselmann, P., Granger, D.E., Jeannin, P.Y., Lauritzen, S.E., 2007. Abrupt glacial valley incision at 0.8 Ma dated from cave deposits in Switzerland. Geology 35, 143–146.

Haneberg, W.C., 2006. Effects of Digital Elevation Model Errors on Spatially Distributed Seismic Slope Stability Calculations: An Example from Seattle, Washington. Environ. Eng. Geosci. 12, 247–260. doi:10.2113/gseegeosci.12.3.247

Haneberg, W.C., 2004. A Rational Probabilistic Method for Spatially Distributed Landslide Hazard Assessment. Environ. Eng. Geosci. 10, 27–43. doi:10.2113/10.1.27

Hansen, A., 1984. Landslide hazard analysis, in: Brunsden, D., Prior, D.B. (Eds.), . Wiley, New York, pp. 523–602.

Hansen, A., Brimicombe, A.J., Franks, C.A.M., Kirk P.A. Tung, F., 1995. Application of GIS to hazard assessment, with particular reference to landslides in Hong Kong., in: Carrara, A., Guzzetti, F. (Eds.), Geographical Information Systems in Assessing Natural Hazards. Kluwer Academic Publishers, Dordrecht, the Netherlands, pp. 273–298.

Hantz, D., Vengeon, J.M., Dussauge-Peisser, C., 2003. An historical, geomechanical and probabilistic approach to rock-fall hazard assessment. Nat. Hazards Earth Syst. Sci. 3, 693–701. doi:10.5194/nhess-3-693-2003

Heim, A., 1932. Landslides and human lives (Bergsturz and Menschenleben). In: Skermer, N. (ed) Bi-Tech Publishers, Vancouver, BC, 196p.

Holden, N.E., 1990. Total half-lives for selected nuclides. Pure Appl. Chem. 62, 941–958.

Hovius, N., Stark, C.P., Allen, P. a., 1997. Sediment flux from a mountain belt derived by landslide mapping. Geology 25, 231. doi:10.1130/0091-7613(1997)025<0231:SFFAMB>2.3.CO;2

Hovius, N., Stark, C.P., Hao-Tsu, C., Jiun-Chuan, L., 2000. Supply and removal of sediment in a landslide dominated mountain belt: Central Range, Taiwan. J. Geol. 108, 73–89.

Hungr, O., Evans, S.G., Hazzard, J., 1999. Magnitude and frequency of rock falls and rock slides along the main transportation corridors of southwestern British Columbia. Can. Geotech. J. 36, 224–238. doi:10.1139/cgj-36-2-224

Hungr, O., Leroueil, S., Picarelli, L., 2014. The Varnes classification of landslide types, an update. Landslides 11, 167–194. doi:10.1007/s10346-013-0436-y

Hungr, O., Mcdougall, S., Wise, M., Cullen, M., 2008. Magnitude–frequency relationships of debris flows and debris avalanches in relation to slope relief. Geomorphology 96, 355–365. doi:10.1016/j.geomorph.2007.03.020

Hutchinson, J., 1968. Mass movement. In: Fairbridge RW (ed) Encyclopedia of geomorphology. Reinhold Publishers, New York, pp 688–695.

Hutchinson, J.N., 1988. Morphological and geotechnical parameters of landslides in relation to geology and hydrogeology. Landslides. Proceedings 5th International Conference on Landslides, Lausanne.

ICGC, 2015. Mapa Geològic de Catalunya [WWW Document]. URL http://www.icgc.cat/ (accessed 2.24.15).

Innes, J.L., 1983. Debris flow. Prog. Phys. Geogr. 7, 469–501.

ISRM, 1978. Commission on standardization of laboratory and field tests. Suggested methods for the quantitative description of discontinuities in rock masses. Int. J. Rock Mech. Min. Sci. Geomech. 15, 319–368.

Iverson, R.. M., Major, J.J., 1987. Rainfall, groundwaterf low, and seasonal motion at Minor Creek landslide, northwestern California: Physical interpretation of empirical relations, Geol. Soc. Am. Bull., 99, 579 -594, 1987.

Iverson, R.M., 2000. Landslide triggering by rainfall infiltration. Water Resour. Res. 36, 1897–1910.

Ivy-Ochs, S., Kubik, P.W., Masarik, J., Wieler, R., Bruno, L., Schluechter, C., 1998. Preliminary results on the use of pyroxene for Berillium-10 surface exposure dating. Schweizerische Mineral. und Petrogr. Mitteilungen 78, 375–382.

Jaiswal, P., van Westen, C.J., 2009. Estimating temporal probability for landslide initiation along transportation routes based on rainfall thresholds. Geomorphology 112, 96–105. doi:10.1016/j.geomorph.2009.05.008

Jaiswal, P., van Westen, C.J., Jetten, V., 2011. Quantitative assessment of landslide hazard along transportation lines using historical records. Landslides 8, 279–291. doi:10.1007/s10346-011-0252-1

Jakob, M., Weatherly, H., 2003. A hydroclimatic threshold for landslide initiation on the North Shore Mountains of Vancouver, British Columbia. Geomorphology 54, 137–156. doi:10.1016/S0169-555X(02)00339-2

Jia, N., Mitani, Y., Xie, M., Djamaluddin, I., 2012. Shallow landslide hazard assessment using a three-dimensional deterministic model in a mountainous area. Comput. Geotech. 45, 1–10. doi:10.1016/j.compgeo.2012.04.007

Jibson, R.W., 1989. Debris flow in southern Porto Rico. Geol. Soc. Am. Spec. Pap. 236, 29–55.

Katz, O., Aharonov, E., 2006. Landslides in vibrating sand box: What controls types of slope failure and frequency magnitude relations? Earth Planet. Sci. Lett. 247, 280–294. doi:10.1016/j.epsl.2006.05.009

Keefer, D.K., Johnson, A.M., 1983. Earthflows: morphology, mobilization and movement. USGS Prof. Paper 1264. (56 pp.).

Kemeny, J., Post, R., 2003. Estimating three-dimensional rock discontinuity orientation from digital images of fracture traces. Comput. Geosci. 29, 65–77. doi:10.1016/S0098-3004(02)00106-1

Kemeny, J., Turner, K., 2008. Gound-Based LiDAR: Rock Slope Mapping and Assessment. Federal Highway Administration Report FHWACFL/ TD-08-006.

Kim, B.H., Cai, M., Kaiser, P.K., Yang, H.S., 2007. Estimation of Block Sizes for Rock Masses with Non-persistent Joints. Rock Mech. Rock Eng. 40, 169–192. doi:10.1007/s00603-006-0093-8

Klein, J., Lawn, B., Gosse, J., Harrington, C., 1997. Can terrestrial cosmogenic Be-10 be measured in whole rock samples to decipher surface exposure histories. Geol. Soc. Am. Abstr. with Programs 29.

Ko Ko, C., Flentje, P., Chowdhury, R., 2004. Interpretation of probability of landsliding triggered by rainfall. Landslides 1, 263–275. doi:10.1007/s10346-004-0031-3

Kohl, C.P., Nishiizumi, K., 1992. Chemical isolation of quartz for measurement of in situ-produced cosmogenic nuclides. Geochim. Cosmochim. Acta 56, 3583–3587.

Kohler, M.A., 1949. Double-Mass Analysis for Testing the Consistency of Records and for Making Required Adjustments. Bull. Am. Meteorol. Soc. 30, 188–189.

Kong, W.K., 2002. Risk assessment of slopes. Q. J. Eng. Geol. Hydrogeol. 35, 213–222. doi:10.1144/1470-9236/2000-39

Kranitz, F., Bensi, S., 2009. in: Posch-Trözmüller, G. (Ed.): Second Scientific Report to the INTERREG IV A project MASSMOVE - Minimal standards for compilation of danger maps like landslides and rock fall as a tool for disaster prevention. Attachment 4 to the second progress report, .

Lal, D., 1991. Cosmic ray labeling of erosion surfaces: in situ nuclide production rates and erosion models. Earth Planet. Sci. Lett. 104, 424–43.

Lal, D., Arnold, J.R., 1985. Tracing quartz throught the environment, in: Indian Adademy of Sciences. pp. 1–5.

Lal, D., Peters, B., 1967. Cosmic ray produced radioactivity on the earth. Handb. der Phys.

Lambe, T., Whitman, R. V, 1979. Soil mechanic, in: John Wiley & Sons. N. Y.

Lambert, C., Thoeni, K., Giacomini, A., Casagrande, D., Sloan, S., 2012. Rockfall Hazard Analysis From Discrete Fracture Network Modelling with Finite Persistence Discontinuities. Rock Mech. Rock Eng. 871–884. doi:10.1007/s00603-012-0250-1

Lari, S., Frattini, P., Crosta, G.B., 2014. A probabilistic approach for landslide hazard analysis. Eng. Geol. 182, 3–14. doi:10.1016/j.enggeo.2014.07.015

Lateltin, O., Haemmig, C., Raetzo, H., Bonnard, C., 2005. Landslide risk management in Switzerland. Landslides 2, 313–320. doi:10.1007/s10346-005-0018-8

Lato, M.J., Vöge, M., 2012. Automated mapping of rock discontinuities in 3D lidar and photogrammetry models. Int. J. Rock Mech. Min. Sci. 54, 150–158. doi:10.1016/j.ijrmms.2012.06.003

Leymerie, A., 1862. Apercu géognostique des Petites Pyrénées et particulierement de la montagne d'Ausseing. Bulletin de la Societé Géologique (le Fiaízce, 19: 1091-1096.

Licciardi, J.., Kurz, M.., Clark, P.., Brook, E.., 1999. Calibration of cosmogenic 3He production rates from Holocene lava flows in Oregon, USA, and effects of the Earth's magnetic field. Earth Planet. Sci. Lett. 172, 261–271.

Licciardi, J.M., Denoncourt, C.L., Finkel, R.C., 2008. Cosmogenic 36Cl production rates from Ca spallation in Iceland. Earth Planet. Sci. Lett. 267, 365–377.

Linares, R., Rosell, J., Pallí, L., Roqué, C., 2002. Afforestation by slope terracing accelerates erosion. A case study in the Barranco de Barcedana (Conca de Tremp, NE Spain). Environ. Geol. 42, 11–18. doi:10.1007/s00254-002-0527-x

Linsley, R.K., Kohler, M.A., H., P.J.L., 1975. Hydrology for Engineers, 2nd ed, Water Resources and Environmental Engineering. McGraw-Hill, New York.

Lu, P., Latham, J.-P., 1999. Developments in the Assessment of In-situ Block Size Distributions of Rock Masses. Rock Mech. Rock Eng. 32, 29–49. doi:10.1007/s006030050042

Luzi, L., Pergalani, F., Terlien, M.T.J., 2000. Slope vulnerability to earthquakes at subregional scale, using probabilistic techniques and geographic information systems. Eng. Geol. 58, 313–336. doi:10.1016/S0013-7952(00)00041-7

Mackey, B.H., Roering, J.J., 2011. Sediment yield, spatial characteristics, and the long-term evolution of active earthflows determined from airborne LiDAR and historical photographs, Eel River, California. GSA Bull. 123, 1560–1576. doi:10.1130/B30306.1

Malamud, B.D., Turcotte, D.L., Guzzetti, F., Reichenbach, P., 2004a. Landslide inventories and their statistical properties. Earth Surf. Process. Landforms 29, 687–711. doi:10.1002/esp.1064

Malamud, B.D., Turcotte, D.L., Guzzetti, F., Reichenbach, P., 2004b. Landslides, earthquakes, and erosion. Earth Planet. Sci. Lett. 229, 45–59. doi:10.1016/j.epsl.2004.10.018

Malet, J.P., Laigle, D., Remaître, a., Maquaire, O., 2005. Triggering conditions and mobility of debris flows associated to complex earthflows. Geomorphology 66, 215–235. doi:10.1016/j.geomorph.2004.09.014

Malet, M.O., 2002. The use of global positioning system techniques for the continuous monitoring of landslides: Application to the Super-Sauze earthflow (Alpes-de-Haute-Provence, France). Geomorphology 43, 33–54. doi:10.1016/S0169-555X(01)00098-8

Marchesini, I., Cencetti, C., De Rosa, P., 2009. A preliminary method for the evaluation of the landslides volume at a regional scale. Geoinformatica 13, 277–289. doi:10.1007/s10707-008-0060-5

Martha, T.R., van Westen, C.J., Kerle, N., Jetten, V., Vinod Kumar, K., 2013. Landslide hazard and risk assessment using semi-automatically created landslide inventories. Geomorphology 184, 139–150. doi:10.1016/j.geomorph.2012.12.001

MathWorks Inc, n.d. MATLAB, the language of technical computing http://www.mathworks.com.

Merchel, S., Arnold, M., Aumaître, G., Benedetti, L., Bourlès, D.L., Braucher, R., Alfimov, V., Freeman, S.P.H.T., Steier, P., Wallner, a., 2008a. Towards more

precise 10Be and 36Cl data from measurements at the 10−14 level: Influence of sample preparation. Nucl. Instruments Methods Phys. Res. Sect. B Beam Interact. with Mater. Atoms 266, 4921–4926. doi:10.1016/j.nimb.2008.07.031

Merchel, S., Benedetti, L., Bourlès, D.L., Braucher, R., Dewald, A., Faestermann, T., Finkel, R.C., Korschinek, G., Masarik, J., Poutivtsev, M., Rochette, P., Rugel, G., Zell, K.-O., 2010. A multi-radionuclide approach for in situ produced terrestrial cosmogenic nuclides: 10Be, 26Al, 36Cl and 41Ca from carbonate rocks. Nucl. Instruments Methods Phys. Res. Sect. B Beam Interact. with Mater. Atoms 268, 1179–1184.

Merchel, S., Braucher, R., Alfimov, V., Bichler, M., Bourlès, D.L., Reitner, J.M., 2013. The potential of historic rock avalanches and man-made structures as chlorine-36 production rate calibration sites. Quat. Geochronol. 18, 54–62. doi:10.1016/j.quageo.2013.07.004

Merchel, S., Braucher, R., Benedetti, L., Grauby, O., Bourlès, D.L., 2008b. Dating carbonate rocks with in-situ produced cosmogenic 10Be: Why it often fails. Quat. Geochronol. 3, 299–307.

Merchel, S., Bremser, W., Alfimov, V., Arnold, M., Aumaître, G., Benedetti, L., Bourlès, D.L., Caffee, M., Fifield, L.K., Finkel, R.C., Freeman, S.P.H.T., Martschini, M., Matsushi, Y., Rood, D.H., Sasa, K., Steier, P., Takahashi, T., Tamari, M., Tims, S.G., Tosaki, Y., Wilcken, K.M., Xu, S., 2011. Ultra-trace analysis of 36Cl by accelerator mass spectrometry: an interlaboratory study. Anal. Bioanal. Chem. 400, 3125–32. doi:10.1007/s00216-011-4979-2

Mergili, M., Marchesini, I., Rossi, M., Guzzetti, F., Fellin, W., 2014. Spatially distributed three-dimensional slope stability modelling in a raster GIS. Geomorphology 206, 178–195. doi:10.1016/j.geomorph.2013.10.008

Mey, P.H.W., Nagtegaal, P.J.C., Roberti, K.J., Hartevelt, J.J.A., 1968. Leidse Geologische Mededelingen, 41, 221-228.

Montero, I., 2011. Determinación y análisis de la actividad del deslizamiento de Les Pales (Cuenca de Tremp, Lleida). Master thesis. Technical Univesity of Catalonia. Barcelona.

Montgomery, D.R., Dietrich, W.E., 1994. A physically based model for the topographic control on shallow landsliding. Water Resour. Res., 30, 1153–1171.

Motamedi, M., Liang, R.Y., 2013. Probabilistic landslide hazard assessment using Copula modeling technique. Landslides 1–9. doi:10.1007/s10346-013-0399-z

Moya, J., Corominas, J., Gutiérrez, E., Vilaplana, J.M., 1992. Datación de movimientos de ladera mediante la dendrocronología. Ejemplos de aplicación en el Prepirineo Oriental., in: Proc. III Simposio Nacional Taludes Y Laderas Inestables. La Coruña, España, pp. 27–38.

Moya, J., Corominas, J., Pérez Arcas, J., Baeza, C., 2010. Tree-ring based assessment of rockfall frequency on talus slopes at Solà d'Andorra, Eastern Pyrenees. Geomorphology 118, 393–408. doi:10.1016/j.geomorph.2010.02.007

Muñoz, J.A., 1992. Evolution of a continental collision belt: ECORS Pyrenees crustal balanced cross section. In: mcclAy, k.R. (ed.) Thrust Tectonics. Chapman & Hall, London, 235–246.

Nadim, F., Cepeda, J., Sandersen, F., Jaedicke, C., Heyerdahl, H., 2009. Prediction of rainfall-induced landslides through empirical and numerical models., in: Rainfall-Induced Landslides: Mechanisms, Monitoring Techniques and Nowcasting Models for Early-Warning Systems. First Italian Workshop on Landslides. Naples, pp. 1–10.

Neteler, M., Mitasova, H., 2008. Open Source GIS: A GRASS GIS Approach, third ed. Springer, New York.

Novoa, M., 1984. Precipitaciones y avenidas extraordinarias en Catalunya. J Trab Inestabilidades Laderas Pirineo Barcelona, pp I.1.1–I.1.15.

Oliveras, G., 2011. Determinació i analisi de l'activitat de l'esllavissada de Clot del Oms (Conca de Tremps, Lleida). Master thesis. Technical Univesity of Catalonia. Barcelona.

ONR-24-800, 2007. Schutzbauwerke der Wildbachverbauung – Begriffsbestimmungen und Klassifizierungen. In: Österreichisches and Normungsinstitut (Editors).

Pack, R.T., Tarboton, D.G., Goodwin, C.N., 1998. The SINMAP Approach to Terrain Stability Mapping, in: Eighth Congres of the International Association of Engineering Geology.

Pack, R.T., Tarboton, D.G., Goodwin, C.N., A, P., 2005. SINMAP. A Stability Index Approach to Terrain Stability Hazard Mapping. Version for ArcGIS 9.x and Higher. Utah State University.

Pavetich, S., Akhmadaliev, S., Arnold, M., Aumaître, G., Bourlès, D., Buchriegler, J., Golser, R., Keddadouche, K., Martschini, M., Merchel, S., Rugel, G., Steier, P., 2014. Interlaboratory study of the ion source memory effect in 36Cl accelerator mass spectrometry. Nucl. Instruments Methods Phys. Res. Sect. B Beam Interact. with Mater. Atoms 329, 22–29. doi:10.1016/j.nimb.2014.02.130

Pawlowsky-Glahn, V., Egozcue, J.J., 2001. Geometric approach to statistical analysis on the simplex. Stoch. Environ. Res. Risk Assess. 15, 384–398. doi:10.1007/s004770100077

Pelletier, J.D., Malamud, B.D., Blodgett, T., Turcotte, D.L., 1997. Scale-invariance of soil moisture variability and its implications for the frequency-size distribution of landslides. Eng. Geol. 48, 255–268. doi:10.1016/S0013-7952(97)00041-0

Perret, S., Stoffel, M., Kienholz, H., 2006. Spatial and temporal rockfall activity in a forest stand in the Swiss Prealps—A dendrogeomorphological case study. Geomorphology 74, 219–231. doi:10.1016/j.geomorph.2005.08.009

Petley, D.N., Mantovani, F., Bulmer, M.H., Zannoni, a., 2005. The use of surface monitoring data for the interpretation of landslide movement patterns. Geomorphology 66, 133–147. doi:10.1016/j.geomorph.2004.09.011

Phillips, C.J., Davies, T.R.H., 1991. Determining rheologic parameters of debris flow material. Geomorphology 4, 101–110.

Phillips, F.., Leavy, B.D., Jannik, N.O., Elmore, D., Kubik, P.W., 1986. The accumulation of cosmogenic chlorine-36 in rocks: a method for surface exposure dating. Science (80-.). 231, 41–43.

Phillips, F.M., Stone, W.D., Fabryka-Martin, J., 2000. An improved approach to calculating low-energy cosmic ray neutron fluxes near the land/atmosphere interface. Chem. Geol.

Phillips, F.M., Stone, W.D., Fabryka-martin, J.T., 2001. An improved approach to calculating low-energy cosmic-ray neutron fluxes near the landratmosphere interface. Chem. Geol. 175, 689–701.

Phillips, W.M., Mc Donald, E. V., Reneau, S.L., Poths, J., 1996. Resolving inherited cosmogenic nuclides in soils: a case study from the Pajarito Plateau: New Mexico, USA. Geol. Soc. Am. Abstr. with Programs 28, A180.

Picarelli, L., 2001. Transition from slide to earthflow and the reverse. In: Sassa, K. (Ed.), Transition from Slide to Flow. Mechanisms and Remedial Measures, Proceedings of the Conference, Trabzon, pp. 21– 54.

Picarelli, L., Oboni, F., Evans, S.G., Mostyn, G., Fell, R., 2005. Hazard characterization and quantification, in: Hungr, O., Fell, R., Couture, R., Eberthardt, E. (Eds.), Landslide Risk Management. Taylor and Francis, London, pp. 27–61.

Pinyol, N.M., Alonso, E.E., Corominas, J., Moya, J., 2012. Canelles landslide: Modelling rapid drawdown and fast potential sliding. Landslides 9, 33–51. doi:10.1007/s10346-011-0264-x

Pizziolo, M., 1996. Carta Inventario del Dissesto. Regione Emilia-Romagna, Bologna, Italy.

Poisel, R., Preh, A., 2011. Rock Fall Detachment Mechanisms. Interdisciplinary Rockfall Workshop. Innsbruck-Igls.

Poisel, R., Preh, A., 2004. Rock slope initial failure mechanisms and their mechanical models. Felsbau 22, 40–45.

Polyworks, S., n.d. Innovmetric Software. http://www.innovmetric.com.

Pradhan, B., 2013. A comparative study on the predictive ability of the decision tree, support vector machine and neuro-fuzzy models in landslide susceptibility mapping using GIS. Comput. Geosci. 51, 350–365. doi:10.1016/j.cageo.2012.08.023

Priest, S.D., 1993. Discontinuity analysis for rock engineering. Chapman and Hall, London, p. 473.

Priest, S.D., Hudson, J.A., 1981. Estimation of discontinuity spacing and trace length using scan line surveys. Int. J. Rock Mech. Min. Sci. Geomech. Abstr. 18, 183–197.

Prokešová, R., Kardoš, M., Tábořík, P., Medveďová, A., Stacke, V., Chudý, F., 2014. Kinematic behaviour of a large earthflow defined by surface displacement monitoring, DEM differencing, and ERT imaging. Geomorphology 224, 86–101. doi:10.1016/j.geomorph.2014.06.029

Pujalte, V., Schmitz, B., 2005. The stratigraphy of the Tremp Group revisited (Garumnian, Tremp-Graus basin, South Pyrenees). Geogaceta 38, 79–82.

QGIS Development Team, 2015. QGIS Geographic Information System. Open Source Geospatial Foundation Project. http://qgis.osgeo.org.

Raetzo, H., Lateltin, O., Bollinger, D., Tripet, J., 2002. Hazard assessment in Switzerland - Codes of Practice for mass movements. Bull. Eng. Geol. Environ. 61, 263–268. doi:10.1007/s10064-002-0163-4

Raetzo, H., Loup, B., 2009. Bafu Schutz vor Massenbewegungen. Technische Richtlinie als Vollzugshilfe. Entwurf 9. Sept.

Rahardjo, H., Li, X.W., Toll, D.G., Leong, E.C., 2001. The effect of antecedent rainfall on slope stability. Geotech. Geol. Eng. 19, 371–399.

Ravanel, L., Deline, P., 2008. La face ouest des Drus (massif du Mont-Blanc) : évolution de l'instabilité d'une paroi rocheuse dans la haute montagne alpine depuis la fin du petit âge glaciaire. Géomorphologie Reli. Process. Environ. 4, 261–272.

Reichenbach, P., Cardinali, M., De Vita, P., Guzzetti, F., 1998. Regional hydrological thresholds for landslides and floods in the Tiber River Basin (Central Italy). Environ. Geol. 35, 146–159.

Revellino, P., Grelle, G., Donnarumma, a., Guadagno, F.M., 2010. Structurally controlled earth flows of the Benevento province (Southern Italy). Bull. Eng. Geol. Environ. 69, 487–500. doi:10.1007/s10064-010-0288-9

Riquelme, A.J., Abellán, a., Tomás, R., Jaboyedoff, M., 2014. A new approach for semi-automatic rock mass joints recognition from 3D point clouds. Comput. Geosci. 68, 38–52. doi:10.1016/j.cageo.2014.03.014

Rosell, J., Llompart, R., Linares, C., 2001. El “garumniense” prepirenaico. Rev. Soc. Geol. España 14, 47–56.

Rossi, G., Catani, F., Leoni, L., Segoni, S., Tofani, V., 2013. HIRESSS: A physically based slope stability simulator for HPC applications. Nat. Hazards Earth Syst. Sci. 13, 151–166. doi:10.5194/nhess-13-151-2013

Rousseau, N., 1999. Study of seismic signals associated with rockfalls at 2 sites on the Reunion Island (Mahavek Cascade and souffriére cavity) - Ph.D thesis, Inst. de Phys. du Globe de Paris.

Ruiz, R., 2013. Caracterització de la fragmentació en els despreniments rocosos. Master thesis. Technical Univesity of Catalonia. Barcelona.

Sancho, C., Gutiérrez, M., Peña, J.L., Burillo, F., 1988. A quantitative approach to scarp retreat starting from triangular slope facets, central Ebro Basin, Spain. Catena Suppl. 13, 139–146.

Santana, D., Corominas, J., Mavrouli, O., Garcia-Sellés, D., 2012. Magnitude–frequency relation for rockfall scars using a Terrestrial Laser Scanner. Eng. Geol. 145-146, 50–64. doi:10.1016/j.enggeo.2012.07.001

Schimmelpfennig, I., Benedetti, L., Finkel, R., Pik, R., Blard, P., Bourlès, D., Burnard, P., Williams, A., 2009. Sources of in-situ 36Cl in basaltic rocks. Implications for calibration of production rates. Quat. Geochronol. 4, 441–461.

Schimmelpfennig, I., Benedetti, L., Garreta, V., Pik, R., Blard, P., Burnard, P., Bourlès, D., Finkel, R., Ammon, K., Dunai, T., 2011. Calibration of cosmogenic 36Cl production rates from Ca and K spallation in lava flows from Mt. Etna (38°N, Italy) and Payun Matru (36°S, Argentina). Geochim. Cosmochim. Acta 75, 2611–2632.

Schlagenhauf, A., Gaudemer, Y., Benedetti, L., Manighetti, I., Palumbo, L., Schimmelpfennig, I., Finkel, R., Pou, K., 2010. Using in situ Chlorine-36 cosmonuclide to recover past earthquake histories on limestone normal fault scarps: a reappraisal of methodology and interpretations. Geophys. J. Int. 182, 36–72.

Schneuwly, D.M., Stoffel, M., 2008. Spatial analysis of rockfall activity, bounce heights and geomorphic changes over the last 50 years – A case study using dendrogeomorphology. Geomorphology 102, 522–531. doi:10.1016/j.geomorph.2008.05.043

Schuster, R.L., Highland, L.M., 2001. Socioeconomic and environmental impacts of landslides in the Western Hemisphere, in: Open-File Rep. 01-0276. U.S. Geological Survey, Reston, Va.

Seguret, M., 1972. Etude tectonique des nappes et séries décollées de la partie centrale du vessant du des Pyrénées - Ph.D thesis. University of Montpellier.

Sengupta, A., Gupta, S., Anbarasu, K., 2010. Rainfall thresholds for the initiation of landslides at Lanta Khola in north Sikkim, India. Nat. Hazards 52, 31–42.

Simoni, A., Ponza, A., Picotti, V., Berti, M., Dinelli, E., 2013. Earthflow sediment production and Holocene sediment record in a large Apennine catchment. Geomorphology 188, 42–53. doi:10.1016/j.geomorph.2012.12.006

Soriano, C., Gratshev, V.G., Delclòs, X., 2006. New Early Cretaceous weevils (Insecta, Coleoptera, Curculionoidea) from El Montsec, Spain. Cretac. Res. 27, 555–564. doi:10.1016/j.cretres.2005.10.015

Stark, C.P., Hovius, N., 2001. The characterization of landslide size distributions. Geophys. Res. Lett. 28, 1091–1094.

Sterlacchini, S., Frigerio, S., Giacomelli, P., Brambilla, M., 2007. Landslide risk analysis: a multi-disciplinary methodological approach. Nat. Hazards Earth Syst. Sci. 7, 657–675. doi:10.5194/nhess-7-657-2007

Stoffel, M., 2010. Magnitude–frequency relationships of debris flows — A case study based on field surveys and tree-ring records. Geomorphology 116, 67–76. doi:10.1016/j.geomorph.2009.10.009

Stoffel, M., Schneuwly, D., Bollschweiler, M., Lievre, I., Delaloye, R., Myint, M., Monbaron, M., 2005. Analyzing rockfall activity (1600–2002) in a protection forest—a case study using dendrogeomorphology. Geomorphology 68, 224–241. doi:10.1016/j.geomorph.2004.11.017

Stone, J.O., 2000. Air pressure and cosmogenic isotope production. J. Geophys. Res. 105, 753–759.

Stone, J.O., Allan, G.L., Fifield, L.K., Cresswell, R.G., 1996. Cosmogenic chlorine-36 from calcium spallation. Geochim. Cosmochim. Acta 60, 679–692.

Strozzi, T., Ambrosi, C., Raetzo, H., 2013. Interpretation of Aerial Photographs and Satellite SAR Interferometry for the Inventory of Landslides. Remote Sens. 5, 2554–2570. doi:10.3390/rs5052554

Stuart, F.M., Dunai, T.J., 2009. No Title. quat Geochronol 4, 435–436.

Sturzenegger, M., Stead, D., 2009. Close-range terrestrial digital photogrammetry and terrestrial laser scanning for discontinuity characterization on rock cuts. Eng. Geol. 106, 163–182. doi:10.1016/j.enggeo.2009.03.004

Swanson, T.W., Caffee, M.L., 2001. Determination of 36Cl Production Rates Derived from the Well-Dated Deglaciation Surfaces of Whidbey and Fidalgo Islands, Washington. Quat. Res. 56, 366–382.

Tarantola, A., 2006. Elements for Physics. Quantities, Qualities and Intrinsic Theories. Springer, Germany.

Tarolli, P., Borga, M., Chang, K.T., Chiang, S.H., 2011. Modeling shallow landsliding susceptibility by incorporating heavy rainfall statistical properties. Geomorphology 133, 199–211. doi:10.1016/j.geomorph.2011.02.033

Terlien, M.T.J., 1998. The determination of statistical and deterministic hydrological landslide-triggering thresholds. Environ. Geol. 35, 125–130.

Trappmann, D., Stoffel, M., 2013. Counting scars on tree stems to assess rockfall hazards: A low effort approach, but how reliable? Geomorphology 180-181, 180–186. doi:10.1016/j.geomorph.2012.10.009

Turcotte, D.L., Malamud, B.D., Guzzetti, F., Reichenbach, P., 2002. Self-organization, the cascade model, and natural hazards. Proc Natl Acad Sci USA 19:2530–2537 Von Neumann J (1966) Theory of self-reproducing automata. University of Illinois Press, Urbana.

Umili, G., Ferrero, a., Einstein, H.H., 2013. A new method for automatic discontinuity traces sampling on rock mass 3D model. Comput. Geosci. 51, 182–192. doi:10.1016/j.cageo.2012.07.026

Van Den Eeckhaut, M., Poesen, J., Govers, G., Verstraeten, G., Demoulin, a., 2007. Characteristics of the size distribution of recent and historical landslides in a populated hilly region. Earth Planet. Sci. Lett. 256, 588–603. doi:10.1016/j.epsl.2007.01.040

Van Den Eeckhaut, M., Reichenbach, P., Guzzetti, F., Rossi, M., Poesen, J., 2009. Combined landslide inventory and susceptibility assessment based on different mapping units: an example from the Flemish Ardennes, Belgium. Nat. Hazards Earth Syst. Sci. 9, 507–521. doi:10.5194/nhess-9-507-2009

Van Westen, C.J., 2000. The modelling of landslide hazards using GIS. Surv Geophys 21, 241–255.

Van Westen, C.J., Rengers, N., Soeters, R., 2003. Use of geomorphological information in indirect landslide susceptibility assessment. Nat. Hazards 30, 399–419. doi:10.1023/B:NHAZ.0000007097.42735.9e

Varnes, D.J., 1984. Landslide hazard zonation: a review of principles and practice, in: UNESCO. Daramtiere, París, p. 61.

Varnes, D.J., 1978. Slope movement types and processes, in: Krizek, R.J., Schuster, R.L. (Eds.), Landslides: Analysis and Control, Special Report 176. Transportation Research Board, National Research Council. Washington, pp. 11–33.

Vermeesch, P., 2007. CosmoCalc: an Excel add-in for cosmogenic nuclide calculations. Geochemistry Geophys. Geosystems 8, Q08003.

Vöge, M., Lato, M.J., Diederichs, M.S., 2013. Automated rockmass discontinuity mapping from 3-dimensional surface data. Eng. Geol. 164, 155–162. doi:10.1016/j.enggeo.2013.07.008

Vranken, L., Vantilt, G., Van Den Eeckhaut, M., Vandekerckhove, L., Poesen, J., 2014. Landslide risk assessment in a densely populated hilly area. Landslides. doi:10.1007/s10346-014-0506-9

Wang, L.G., Yamashita, S., Sugimoto, F., Pan, C., Tan, G., 2003. A Methodology for Predicting the In Situ Size and Shape Distribution of Rock Blocks. Rock Mech. Rock Eng. 36, 121–142. doi:10.1007/s00603-002-0039-8

Westen, C.J., Asch, T.W.J., Soeters, R., 2006. Landslide hazard and risk zonation—why is it still so difficult? Bull. Eng. Geol. Environ. 65, 167–184. doi:10.1007/s10064-005-0023-0

White, I.D., Mottershead, D.N., Harrison, J.J., 1996. Environmental systems, 2nd ed. Chapman and Hall, London.

Wieczorek, G.F., 1996. Landslide triggering mechanisms., in: Turner, A.K., Schuster, R.L. (Eds.), Landslides: Investigation and Mitigation. Transportation Research board, National Research Council, special report, Washington DC, pp. 76–90.

Wieczorek, G.F., Morgan, B.A., Campbell, R.H., 2000. Debris flow hazards in the Blue Ridge of Central Virginia. Environ. Eng. Geosci. 6, 3–23.

Wilson, R.C., 1989. Rainstorms, pore pressures, and debris flows: a theoretical framework., in: Morton, D.M., Sadler, P.M. (Eds.), Landslides in a Semi-Arid Environmental. Publications of the Inland Geological Society, California, pp. 101–117.

Wilson, R.C., Wieczorek, G.F., 1995. Rainfall thresholds for the initiation of debris flow at La Honda, California. Environ. Eng. Geosci. 1, 11–27.

Woodcoock, N.H., 1977. Specification of fabric shapes using an eigenvalue method. Geol. Soc. Am. Bull. 88, 1231–1236.

Wu, T.H., Abdel-Latif, M. a, 2000. Prediction and mapping of landslide hazard. Can. Geotech. J. 37, 781–795. doi:10.1139/t00-006

Xie, M., Esaki, T., Zhou, G., Mitani, Y., 2003. Geographic Information Systems-Based Three-Dimensional Critical Slope Stability Analysis and Landslide Hazard Assessment. J. Geotech. Geoenvironmental Eng. 129, 1109–1118. doi:10.1061/(ASCE)1090-0241(2003)129:12(1109)

Zaruba, Q., Mencl, V., 1969. Landslides and their control. Elsevier, New York, 238p.

Zêzere, J.L., Trigo, R.M., Trigo, I.F., 2005. Shallow and deep landslides induced by rainfall in the Lisbon region (Portugal): assessment of relationships with the North Atlantic Oscillation. Nat. Hazards Earth Syst. Sci. 5, 331–344.

Züst, F., Dahms, D., Purves, R., Egli, M., 2014. Surface reconstruction and derivation of erosion rates over several glaciations (1Ma) in an alpine setting (Sinks Canyon,

Wyoming, USA). Geomorphology 219, 232–247.
doi:10.1016/j.geomorph.2014.05.017

List of figures

List of tables

ANNEXES

Annex 1: Landslide characteristics

Table 0-1: Characteristics of mapped landslides. F: New failure/reactivation observed; NA: Not identified due to the poor orthophotos's resolution. Area and lithological unit where the landslide occurred are shown.

				Sets of aerial orthophotos									
	1956	1990	1993	1997	2003	2005	2007	2008	2009	2011	2013	Area (m^2)	Lithological unit
1	F	NA	NA	NA	NA	F	F					1913	3
2						F						816	3
3	F	NA	NA									780	3
4	F											2533	3
5	F											5582	3
6		F	NA	NA								1053	3
7	F											874	3
8	F	NA	NA									444	3
9	F	NA	F	F								813	3
10	F	NA	NA	NA	NA	F						2892	3
11	F	F	NA	F								1131	3
12	F	NA	NA	NA		F						943	3
13	F											2028	3
14	F	NA	NA	NA								1872	3
15	F	NA	NA	NA								682	3
16	F	NA	NA	NA		F	F					3332	3
17		F	NA	F	F	F						725	3
18	F	NA	NA	NA								2887	3
19	F	NA	NA	NA								11000	3
20	F	NA	NA	NA								13260	3
21	F	NA	NA	NA	NA	F	F					1148	3
22	F	NA	NA	F								963	3
23	F	NA	NA	F								1282	3
24	F	NA	NA	NA		F						1186	3
25	F	F	NA	NA								1092	3
26	F	NA	NA	NA								1189	3
27	F	NA	NA	NA								380	3
28	F	NA	NA	NA					F	F		1546	3
29	F	NA	F									2079	3
30		NA	NA	F	F	F	F			F		3679	3
31	F	NA	NA	NA								7889	3
32	F	NA	NA	NA								2231	3
33	F	NA	NA	NA								2499	3
34	F	NA	NA	NA								4274	3
35	F	NA	NA	NA								1329	3
36	F	NA	NA	NA								5035	3
37	F	NA	NA	NA								2504	3
38	F	NA	NA	NA					F	F		1270	3
39											F	1091	3
40	F	NA	NA	NA								9288	4
41	F	F										8489	4
42	F	F				F						30070	4
43	F	NA	NA		F			F	F			830	4
44	F	NA	NA	NA	F	F						543	4
45	F	NA	NA	NA								1177	4
46	F	NA	NA	NA								16680	4
47				F								28450	4
48					F							15110	4

49	F											15260	4
50	F											9654	4
51		F										19590	4
52	F											11390	4
53	F	NA										11070	4
54	F	F										13070	4
55		F										52010	4
56	F	NA	NA	NA								1661	4
57	NA	NA	NA						F			1983	4
58		F	NA	NA								7002	4
59	F	NA	NA	NA								10600	4
60	F	NA	NA	NA								3144	4
61	F	NA	NA	NA								2918	4
62	F	NA	NA	NA								9510	4
63	F	NA	F	NA	F	F			F	F		1887	5
64		F		F		F						1912	5
65						F						2961	5
66									F			11540	5
67					F							15120	5
68	F			F								8643	5
69										F		23700	5
70	NA	NA	NA	F								3375	5
71	NA								F			14340	5
72			F									8849	5
73		F										7153	5
74				F								27700	5
75	F	NA	NA	NA	NA	F						4380	5
76	F	F	NA	F	NA	F	F			F	F	4068	5
77	F	F	NA	NA	F	F	F		F			24030	5
78	F	NA	F	F								15410	5
79	F	F	F	NA	F	F	F			F		126000	5
80	F	NA	NA									15600	5
81	F											7055	5
82	F	NA	NA	NA		F						12500	5
83	F	NA	NA	NA		F						2741	5
84	F	NA	NA	NA								6675	5
85	F	F	NA	NA								7512	5
86	F	NA	NA	NA		F						1933	5
87	F	NA	NA	F								2994	5
88	F	NA	NA	NA		F	F			F		1397	5
89	F	F				F						3350	5
90	F	NA	NA	NA		F						3905	5
91	NA		F		F				F	F		60550	5
92	F	NA	NA	NA								12990	5
93	F											56230	5
94	NA											56300	5
95	NA											585700	5
96	NA											911900	5
97	F	NA	NA	NA		F		F				10150	5
98	F	NA	NA	NA					F			12230	5
99	F	NA	NA	NA								19860	5
100	F	NA	NA	NA								11280	5
101	F	NA	NA									142700	5
102	F	NA	NA	NA								17660	5
103	F	NA	NA									32150	5

104	F	NA	NA	NA								194900	5
105	F	NA	NA	NA			F				F	178500	5
106	F	NA	NA	NA		F			F	F		416700	5
107	NA											443200	5
108											F	1229	5
109											F	11550	5

Annex 2: Lithological and morphological map with activity indicators

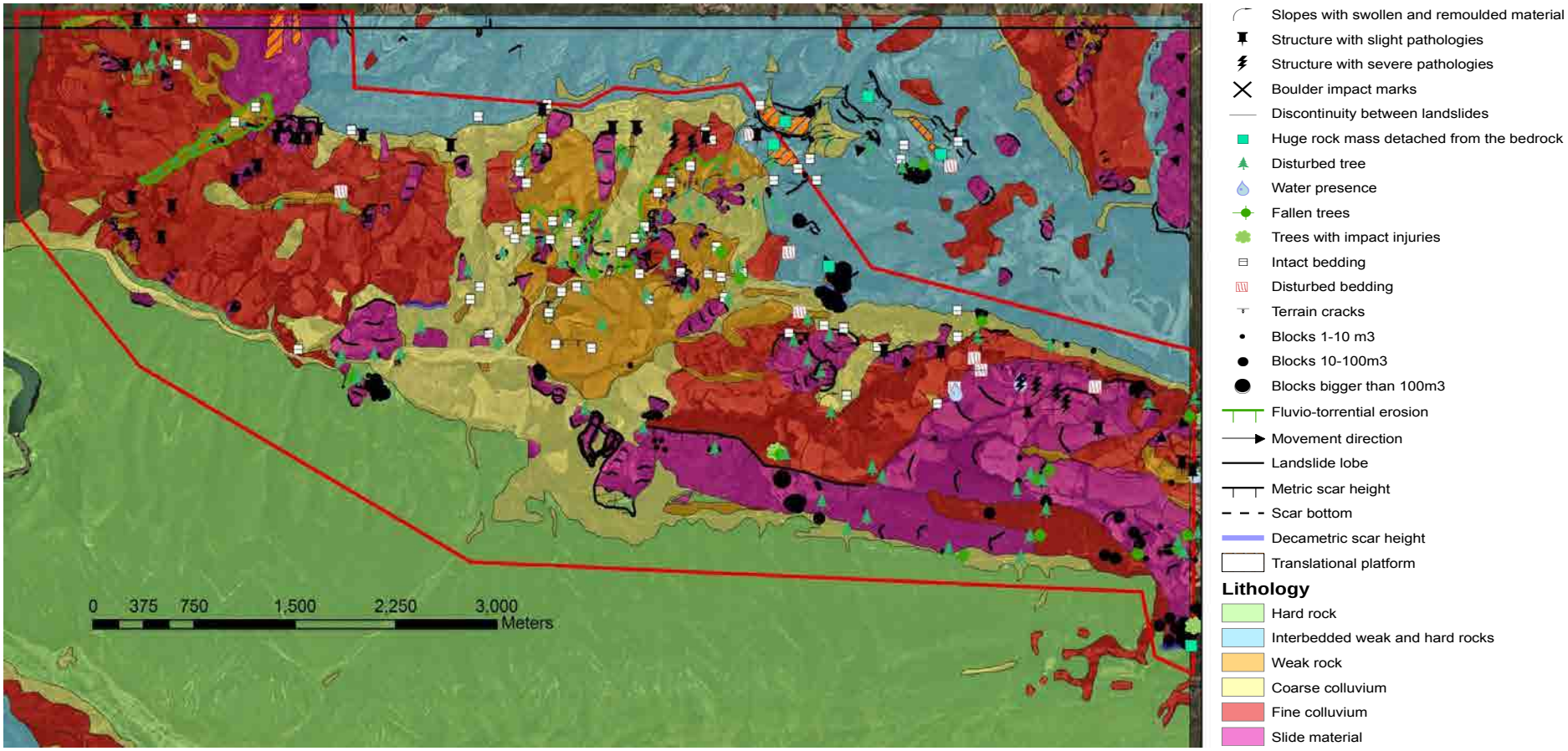

Figure 0-1: Lithological and morphological map with activity indicators.

.

Annex 3: Reactivations map

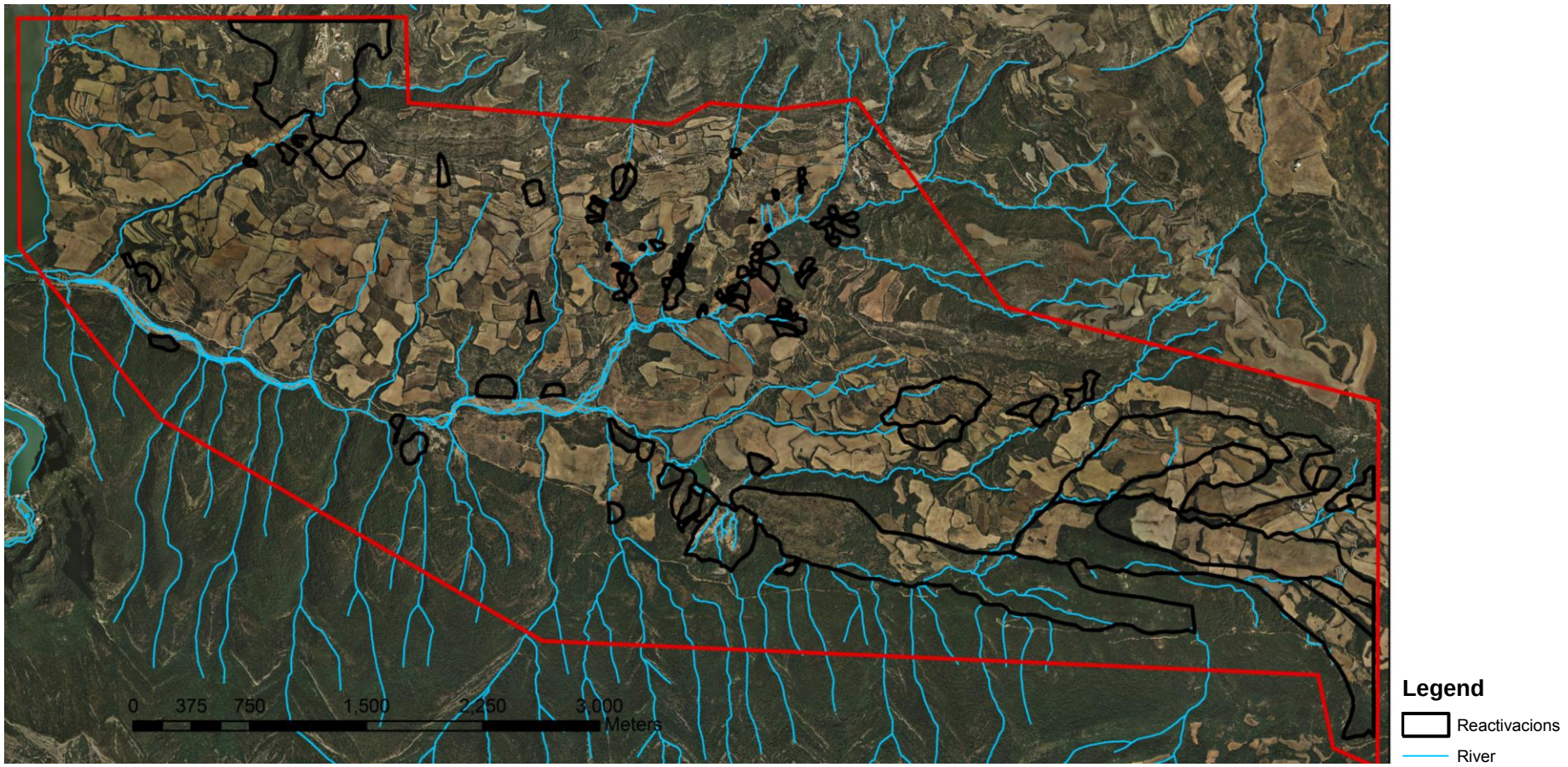

Figure 0-2: Reactivations.

Annex 4: Polynomial adjustment

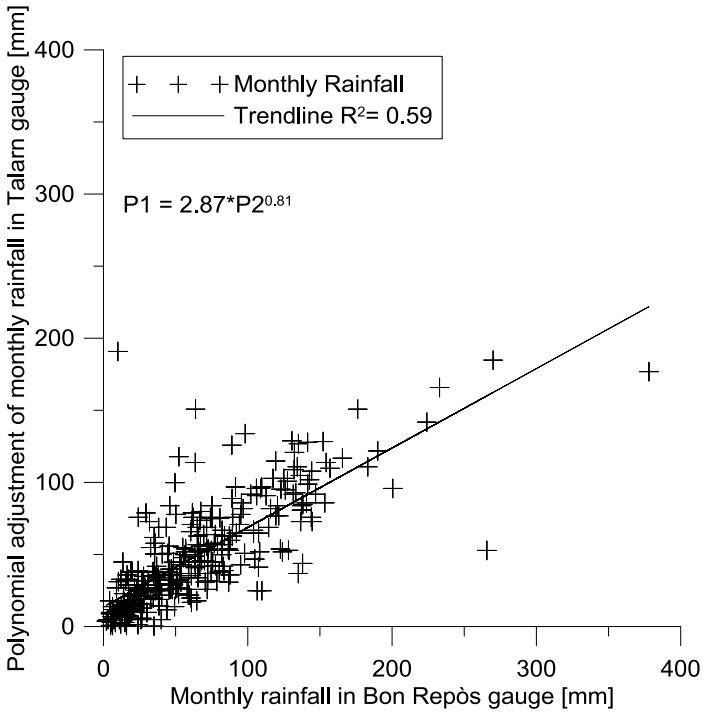

Figure 0-3: Comparison between monthly rainfall in the Bon Repòs gauge and its polynomial adjustment using the Talarn gauge. Polynomial adjustment equation and coefficient of determination are shown. 1-Bon Repòs gauge; 2-Talarn gauge.

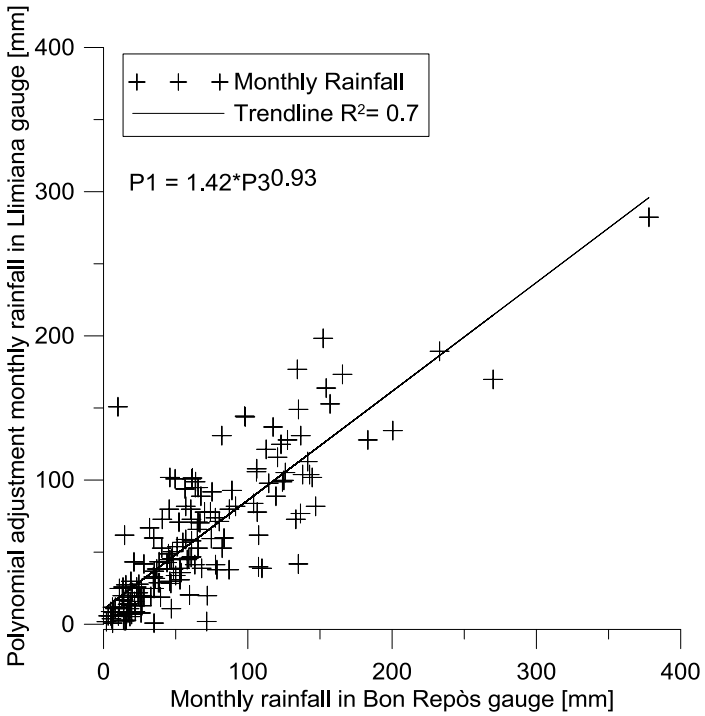

Figure 0-4: Comparison between monthly rainfall in the Bon Repòs gauge and its polynomial adjustment using the Llimiana gauge. Polynomial adjustment equation and coefficient of determination are shown. 1-Bon Repòs gauge; 2-Llimiana gauge.

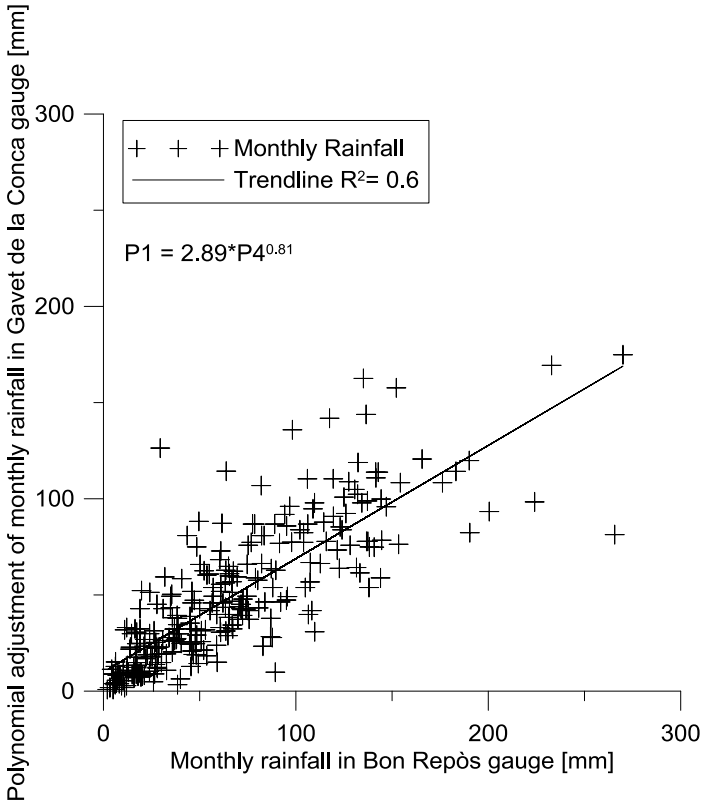

Figure 0-5: Comparison between monthly rainfall in the Bon Repòs gauge and its polynomial adjustment using the Gavet de la Conca gauge. Polynomial adjustment equation and coefficient of determination are shown. 1-Bon Repòs gauge; 2-Gavet de la Conca gauge.

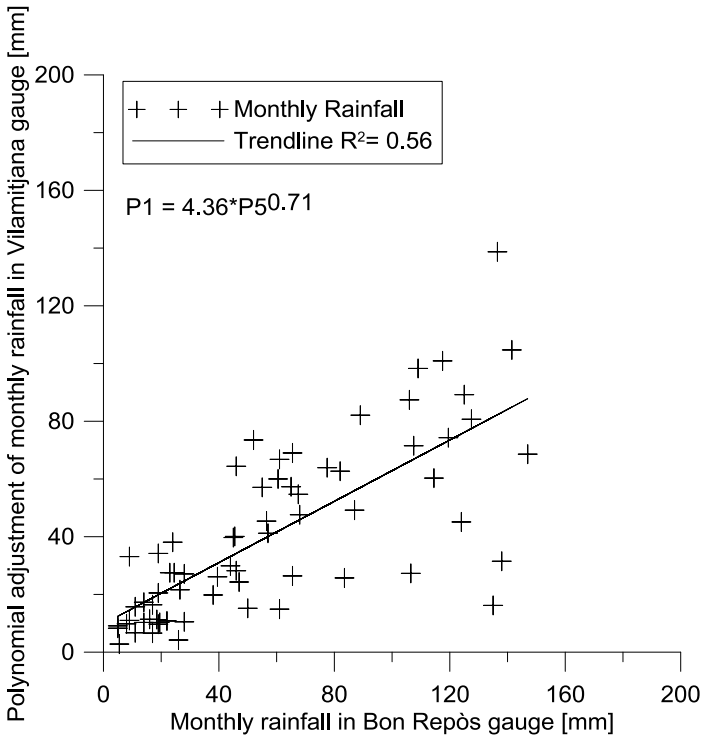

Figure 0-6: Comparison between monthly rainfall in the Bon Repòs gauge and its polynomial adjustment using the Vilamitjana gauge. Polynomial adjustment equation and coefficient of determination are shown. 1-Bon Repòs gauge; 2-Vilamitjana gauge.

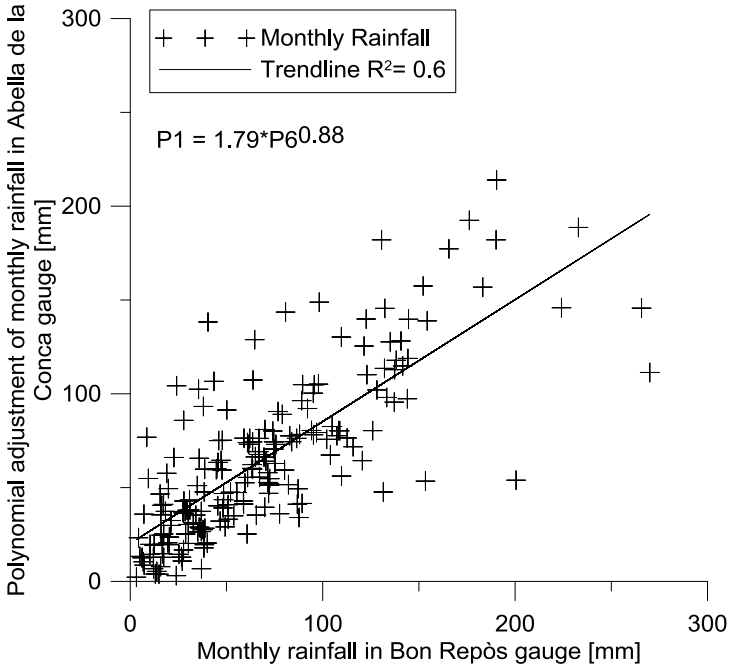

Figure 0-7: Comparison between monthly rainfall in the Bon Repòs gauge and its polynomial adjustment using the Abella de la Conca gauge. Polynomial adjustment equation and coefficient of determination are shown. 1-Bon Repòs gauge; 2-Abella de la Conca gauge.

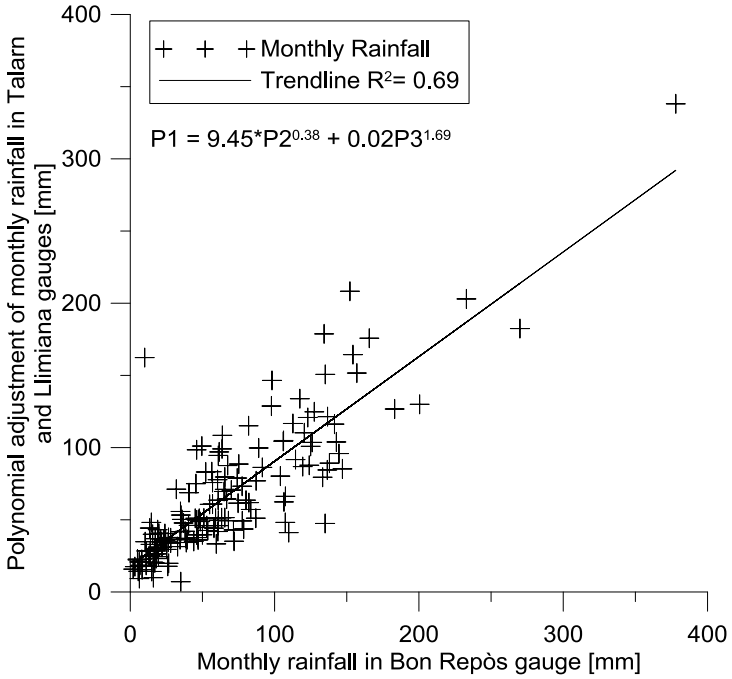

Figure 0-8: Comparison between monthly rainfall in the Bon Repòs gauge and its polynomial adjustment using the Talarn and Lliminana gauges. Polynomial adjustment equation and coefficient of determination are shown. 1-Bon Repòs gauge; 2-Talarn gauge; 3-Lliminana gauge.

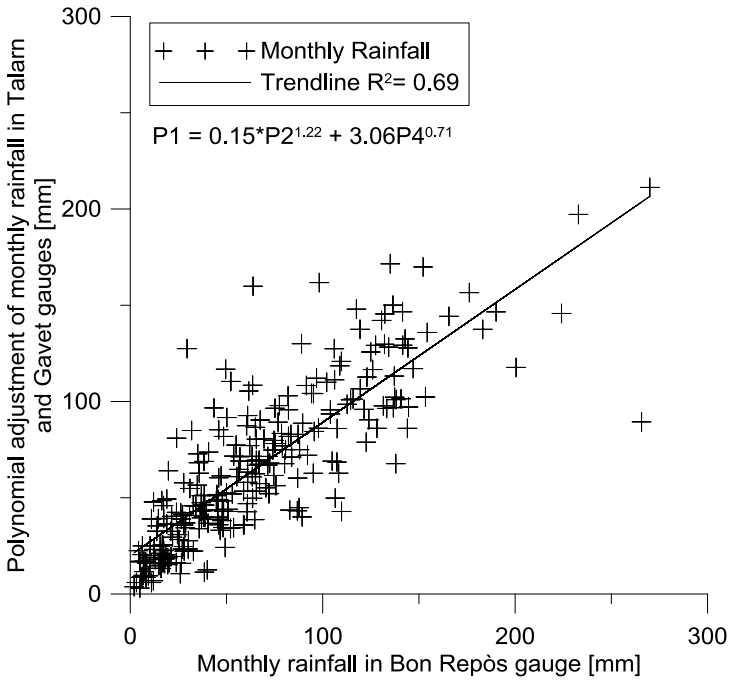

Figure 0-9: Comparison between monthly rainfall in the Bon Repòs gauge and its polynomial adjustment using the Talarn and Gavet de la Conca gauges. Polynomial adjustment equation and coefficient of determination are shown. 1-Bon Repòs gauge; 2-Talarn gauge; 4-Gavet de la Conca gauge.

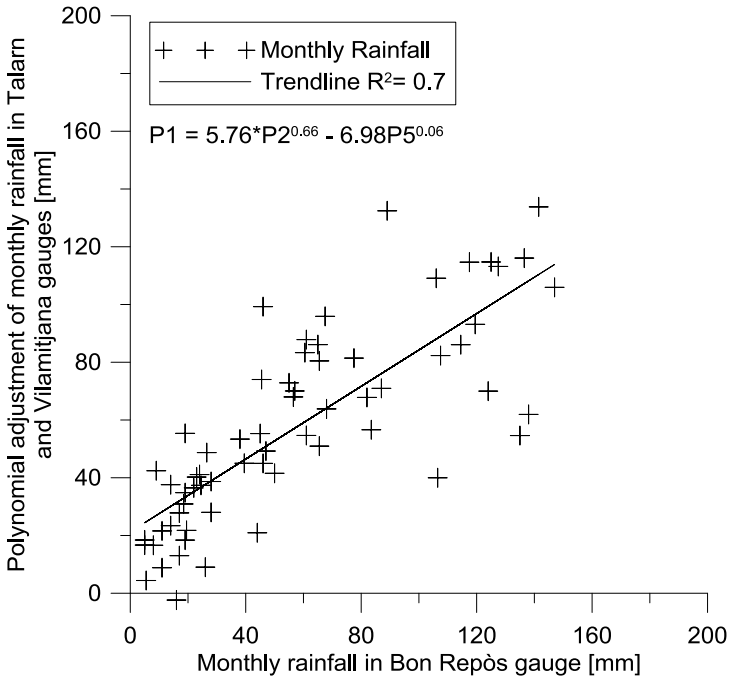

Figure 0-10: Comparison between monthly rainfall in the Bon Repòs gauge and its polynomial adjustment using the Talarn and Vilamitjana gauges. Polynomial adjustment equation and coefficient of determination are shown. 1-Bon Repòs gauge; 2-Talarn gauge; 5-Vilamitjana gauge.

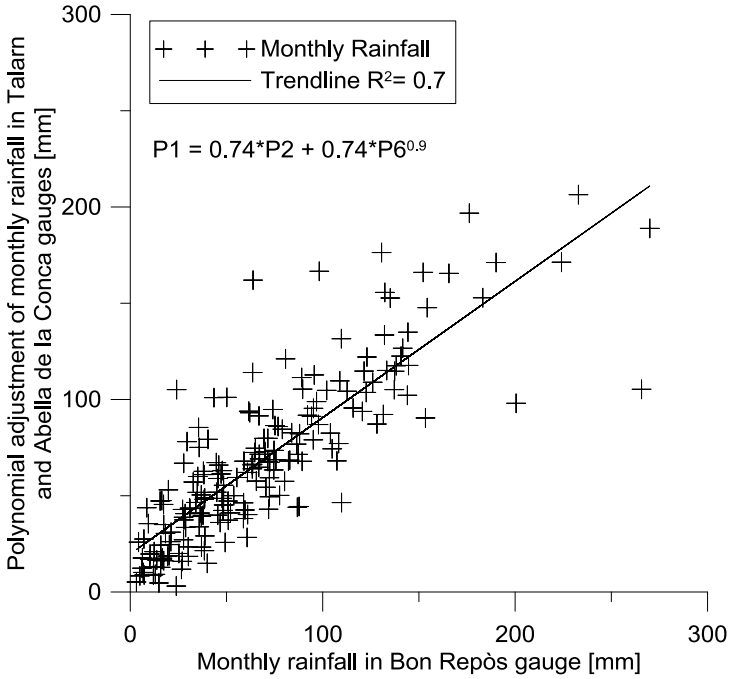

Figure 0-11: Comparison between monthly rainfall in the Bon Repòs gauge and its polynomial adjustment using the Talarn and Abella de la Conca gauges. Polynomial adjustment equation and coefficient of determination are shown. 1-Bon Repòs gauge; 2-Talarn gauge; 6-Abella de la Conca gauge.

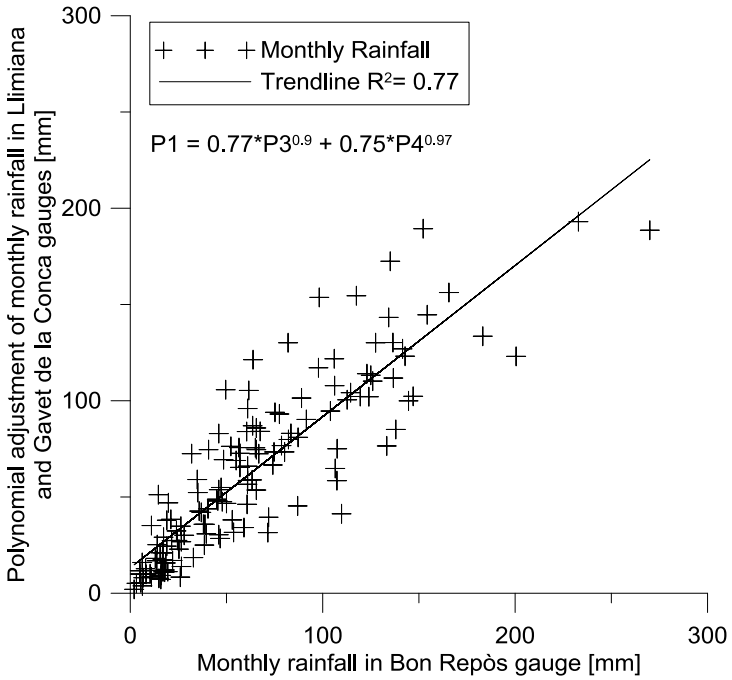

Figure 0-12: Comparison between monthly rainfall in the Bon Repòs gauge and its polynomial adjustment using the Llimiana and Gavet de la Conca gauges. Polynomial adjustment equation and coefficient of determination are shown. 1-Bon Repòs gauge; 3-Llimiana gauge; 4-Gavet de la Conca gauge.

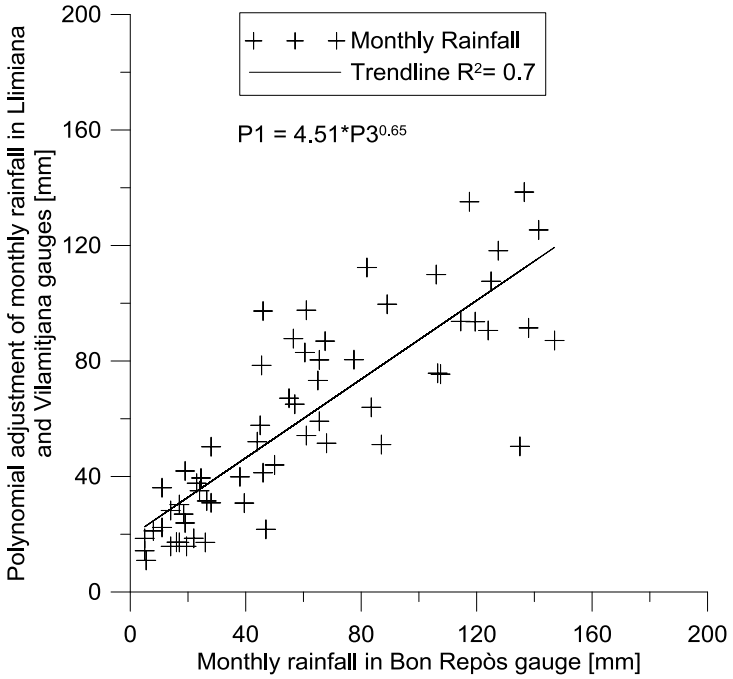

Figure 0-13: Comparison between monthly rainfall in the Bon Repòs gauge and its polynomial adjustment using the Talarn and Vilamitjana gauges. Polynomial adjustment equation and coefficient of determination are shown. 1-Bon Repòs gauge; 2-Talarn gauge; 3-Vilamitjana gauge.

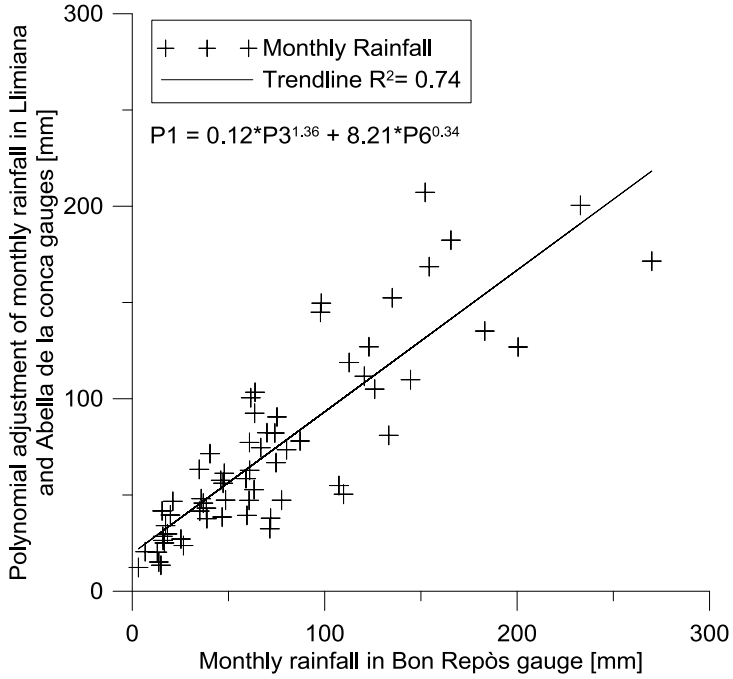

Figure 0-14: Comparison between monthly rainfall in the Bon Repòs gauge and its polynomial adjustment using the Llimiana and Abella de la Conca gauges. Polynomial adjustment equation and coefficient of determination are shown. 1-Bon Repòs gauge; 3-Llimiana gauge; 3-Abella de la Conca gauge.

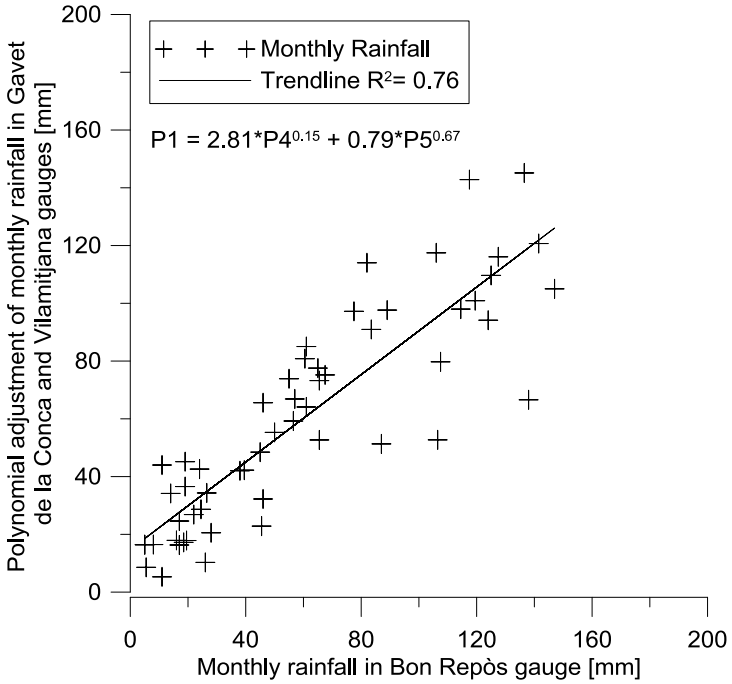

Figure 0-15: Comparison between monthly rainfall in the Bon Repòs gauge and its polynomial adjustment using the Gavet de la Conca and Vilamitjana gauges. Polynomial adjustment equation and coefficient of determination are shown. 1-Bon Repòs gauge; 4-Gavet de la Conca gauge; 5-Vilamitjana gauge.

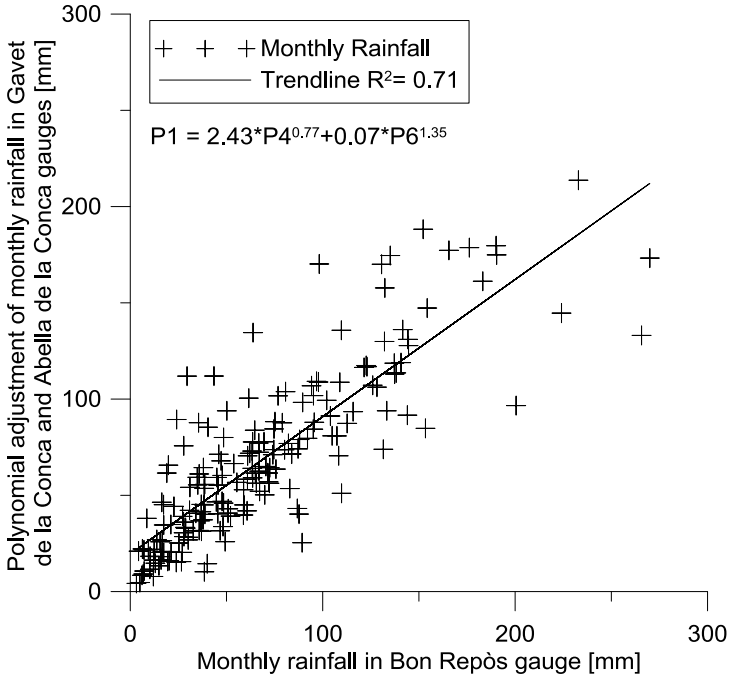

Figure 0-16: Comparison between monthly rainfall in the Bon Repòs gauge and its polynomial adjustment using the Gavet de la Conca and Abella de la Conca gauges. Polynomial adjustment equation and coefficient of determination are shown. 1-Bon Repòs gauge; 4-Gavet de la Conca gauge; 5-Abella de la Conca gauge.

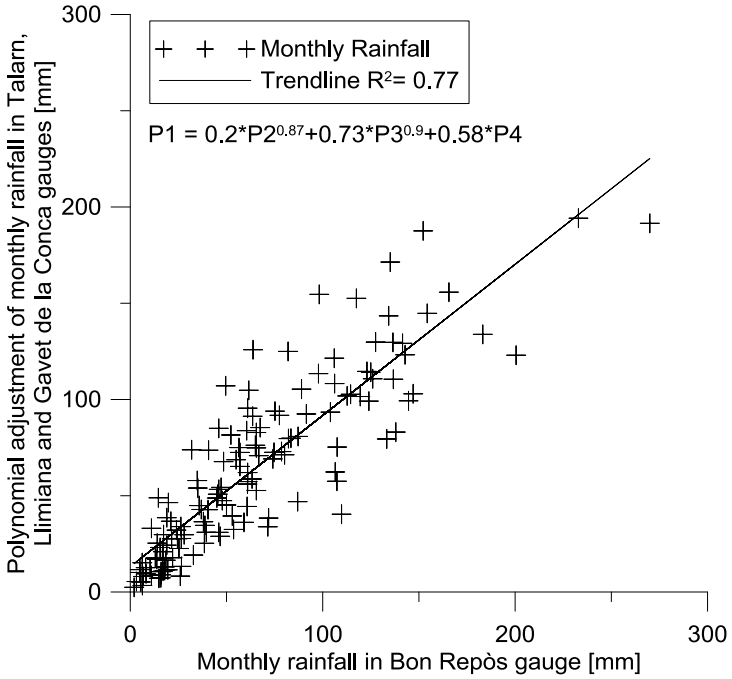

Figure 0-17: Comparison between monthly rainfall in the Bon Repòs gauge and its polynomial adjustment using the Talarn, Llimiana and Gavet de la conca gauges. Polynomial adjustment equation and coefficient of determination are shown. 1-Bon Repòs gauge; 2-Talarn gauge; 3-Llimiana gauge; 4-Gavet de la Conca gauge.

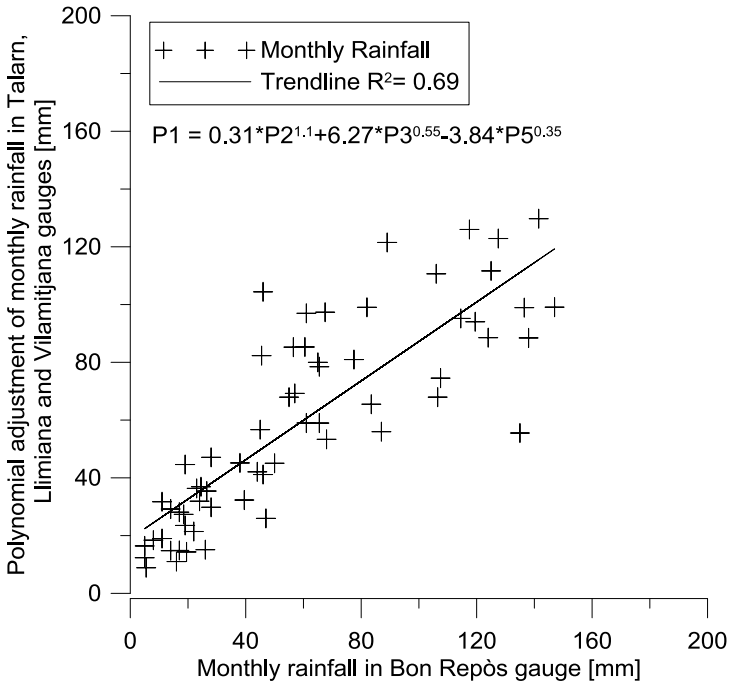

Figure 0-18: Comparison between monthly rainfall in the Bon Repòs gauge and its polynomial adjustment using the Talarn, Llimiana and Vilamitjana gauges. Polynomial adjustment equation and coefficient of determination are shown. 1-Bon Repòs gauge; 2-Talarn gauge; 3-Llimiana gauge; 5-Vilamitjana gauge.

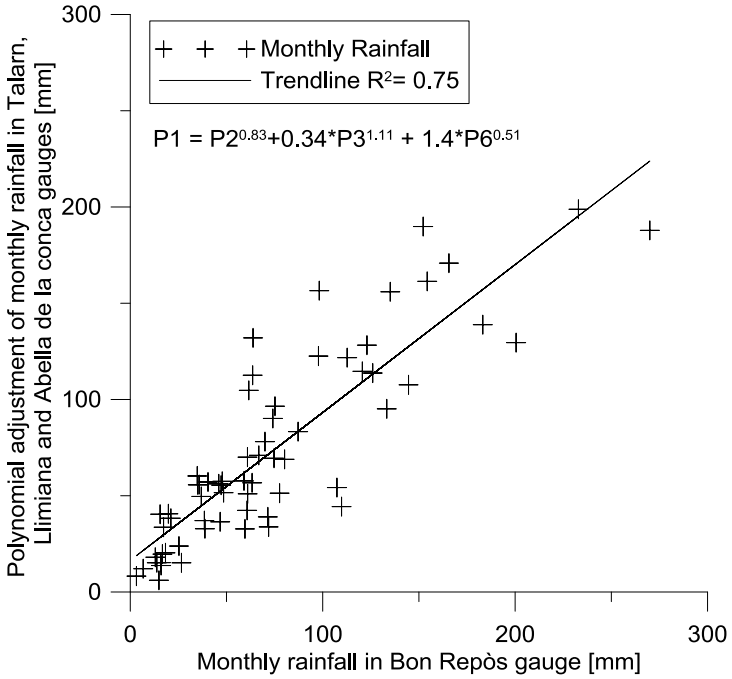

Figure 0-19: Comparison between monthly rainfall in the Bon Repòs gauge and its polynomial adjustment using the Talarn, Llimiana and Abella de la conca gauges. Polynomial adjustment equation and coefficient of determination are shown. 1-Bon Repòs gauge; 2-Talarn gauge; 3-Llimiana gauge; 6-Abella de la Conca gauge.

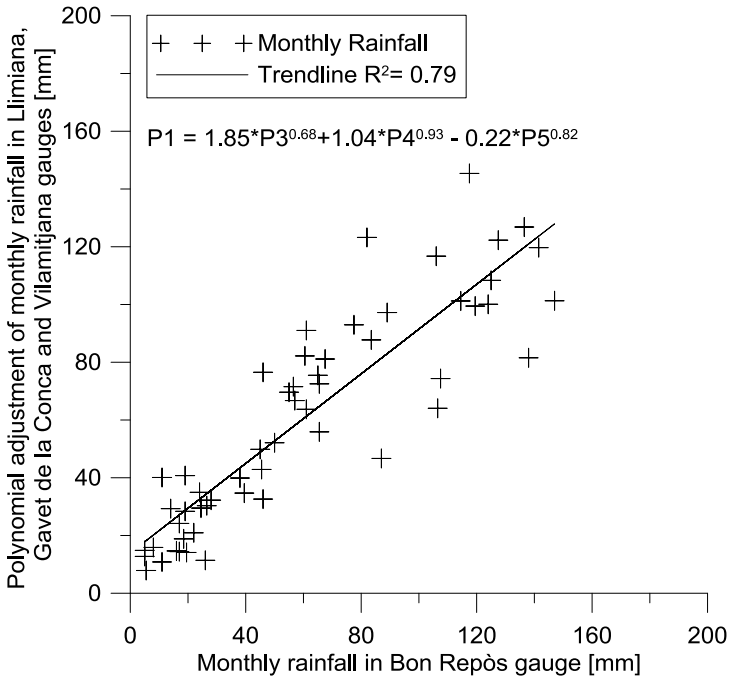

Figure 0-20: Comparison between monthly rainfall in the Bon Repòs gauge and its polynomial adjustment using the Llimiana, Gavet de la conca and Vilamitjana gauges. Polynomial adjustment equation and coefficient of determination are shown. 1-Bon Repòs gauge; 3-Llimiana gauge; 4-Gavet de la Conca gauge; 5-Vilamitjana gauge.

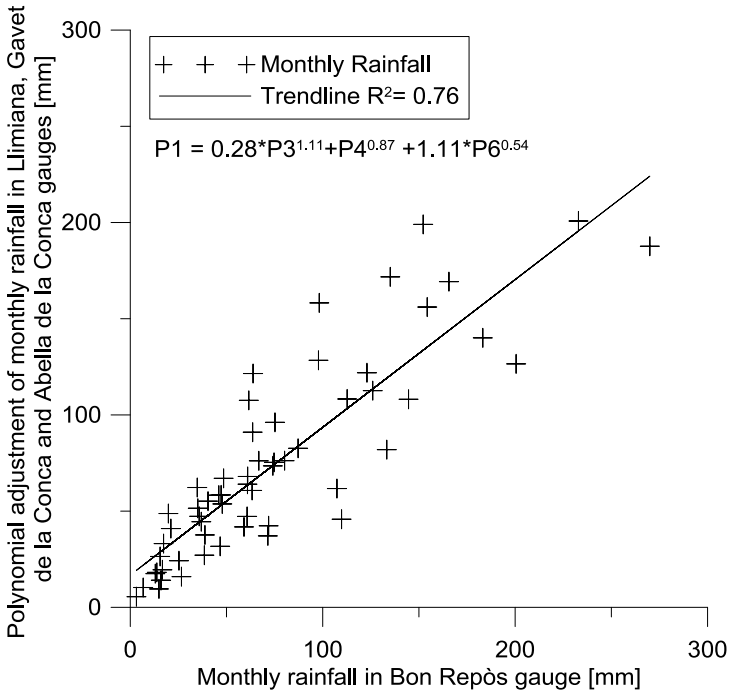

Figure 0-21: Comparison between monthly rainfall in the Bon Repòs gauge and its polynomial adjustment using the Llimiana, Gavet de la conca and Abella de la Conca gauges. Polynomial adjustment equation and coefficient of determination are shown. 1-Bon Repòs gauge; 3-Llimiana gauge; 4-Gavet de la Conca gauge; 6-Abella de la Conca gauge.

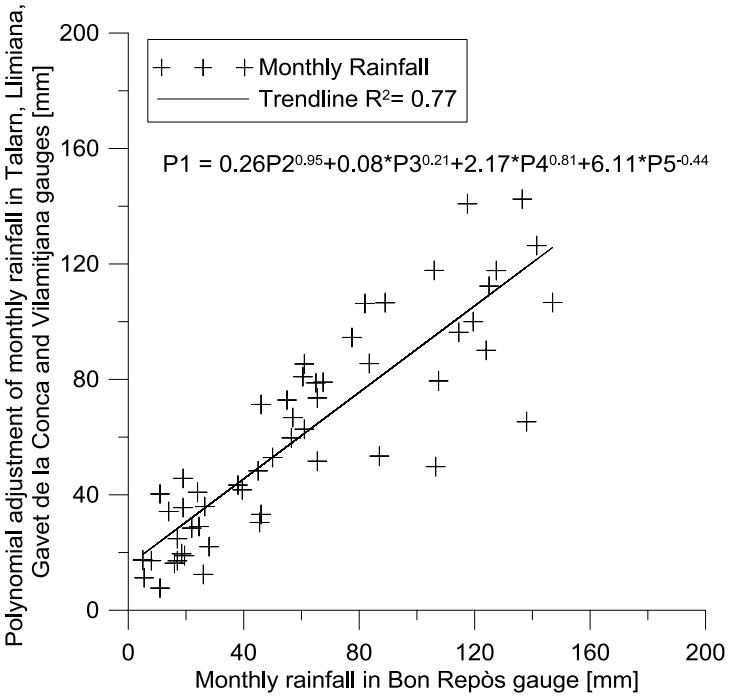

Figure 0-22: Comparison between monthly rainfall in the Bon Repòs gauge and its polynomial adjustment using the Talarn, Llimiana, Gavet de la conca and Vilamitjana gauges. Polynomial adjustment equation and coefficient of determination are shown. 1-Bon Repòs gauge; 2-Talarn gauge; 3-Llimiana gauge; 4-Gavet de la Conca gauge; 5-Vilamitjana gauge.

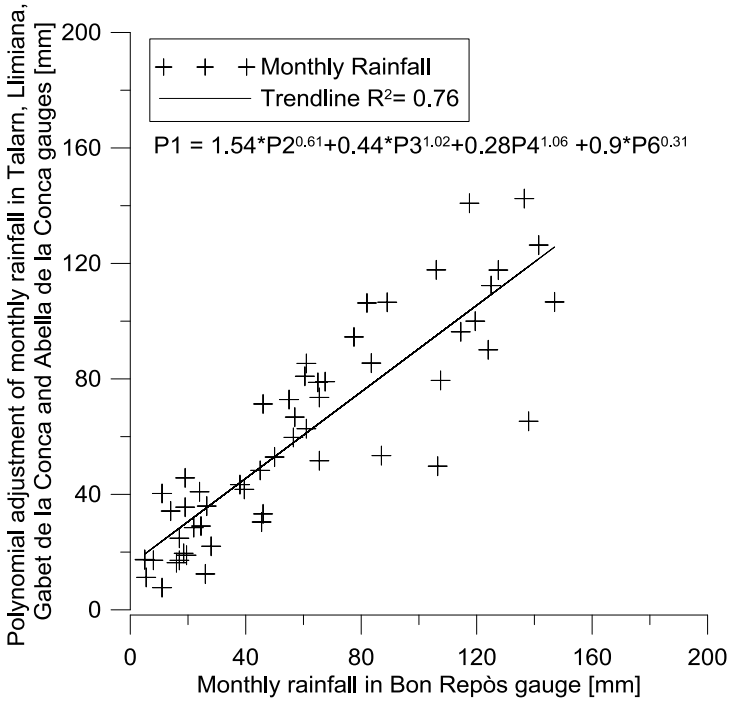

Figure 0-23: Comparison between monthly rainfall in the Bon Repòs gauge and its polynomial adjustment using the Talarn, Llimiana, Gavet de la conca and Abella de la Conca gauges. Polynomial adjustment equation and coefficient of determination are shown. 1-Bon Repòs gauge; 2-Talarn gauge; 3-Llimiana gauge; 4-Gavet de la Conca gauge; 6-Abella de la Conca gauge.

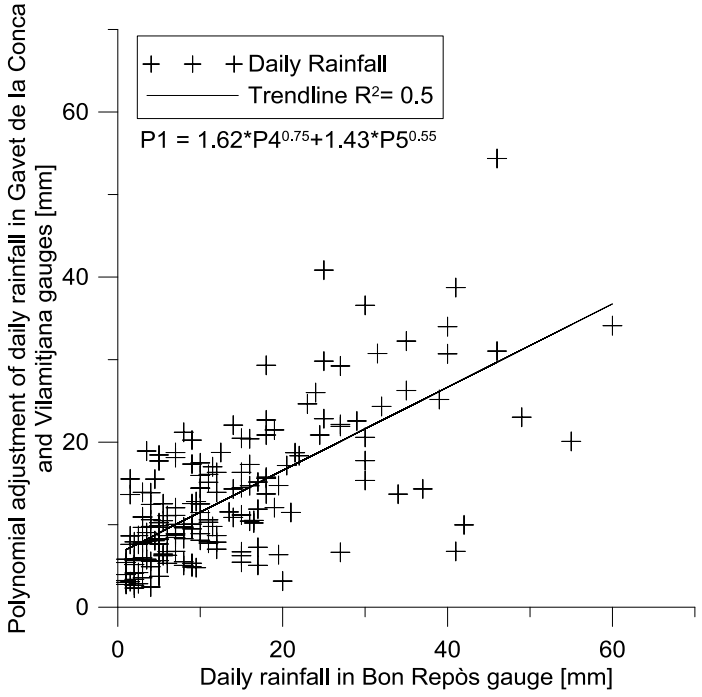

Figure 0-24: Comparison between daily rainfall in the Bon Repòs gauge and its polynomial adjustment using the Gavet de la conca and Vilamitjana gauges. Polynomial adjustment equation and coefficient of determination are shown. 1-Bon Repòs gauge; 4-Gavet de la Conca gauge; 5-Vilamitjana gauge.

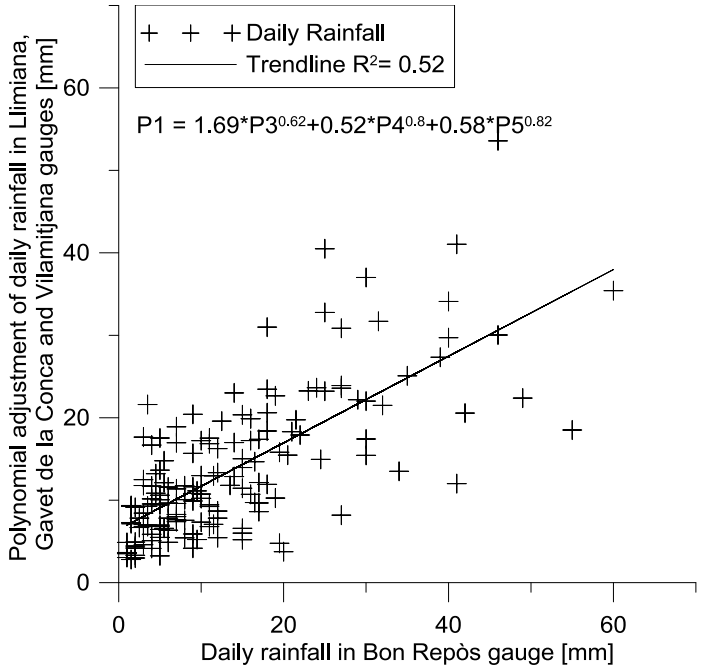

Figure 0-25: Comparison between daily rainfall in the Bon Repòs gauge and its polynomial adjustment using the Llimiana, Gavet de la Conca and Vilamitjana gauges. Polynomial adjustment equation and coefficient of determination are shown. 1-Bon Repòs gauge; 3-Llimiana gauge; 4-Gavet de la Conca gauge; 5-Vilamitjana gauge.

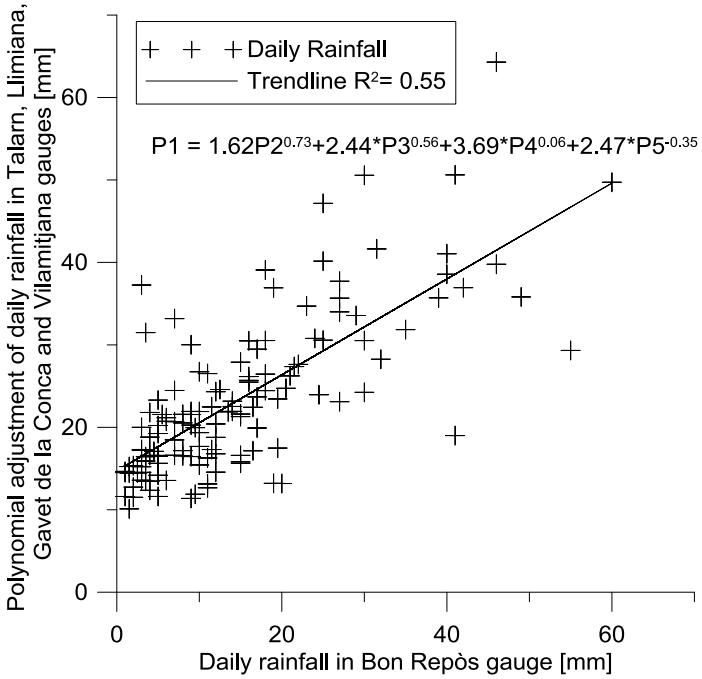

Figure 0-26: Comparison between daily rainfall in the Bon Repòs gauge and its polynomial adjustment using the Talarn, Llimiana, Gavet de la Conca and Vilamitjana gauges. Polynomial adjustment equation and coefficient of determination are shown. 1-Bon Repòs gauge; 2-Talarn gauge; 3-Llimiana gauge; 4-Gavet de la Conca gauge; 5-Vilamitjana gauge.

Annex 5: Accumulated rainfall

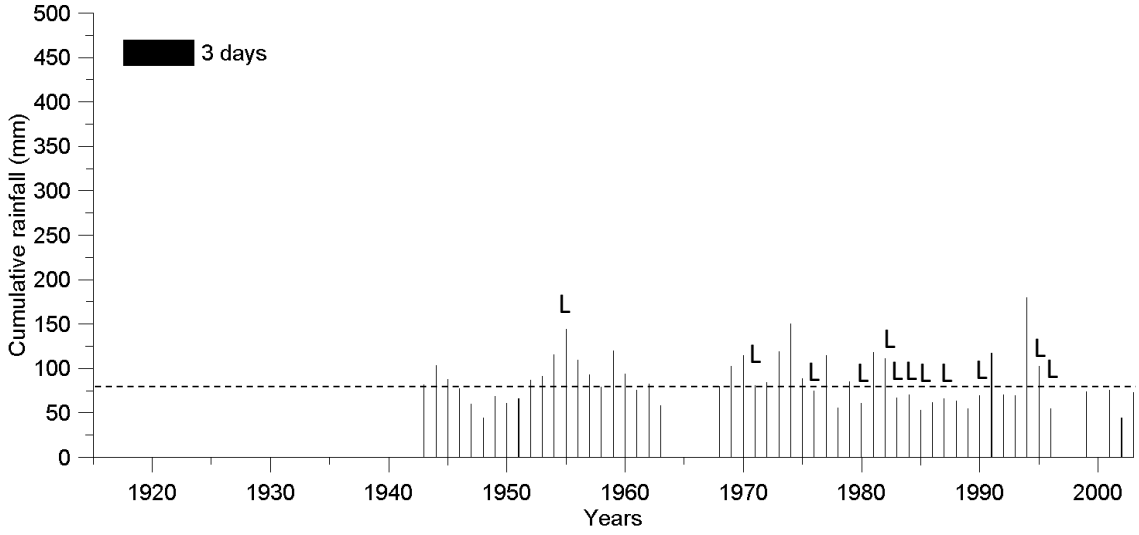

Figure 0-27: Accumulated rainfall and threshold (dashed line). 80 mm within 3 days. L: Landsliding event. The threshold is mostly reached during years with landslide reactivations, but some years with no failures identified present a higher amount of rainfall.

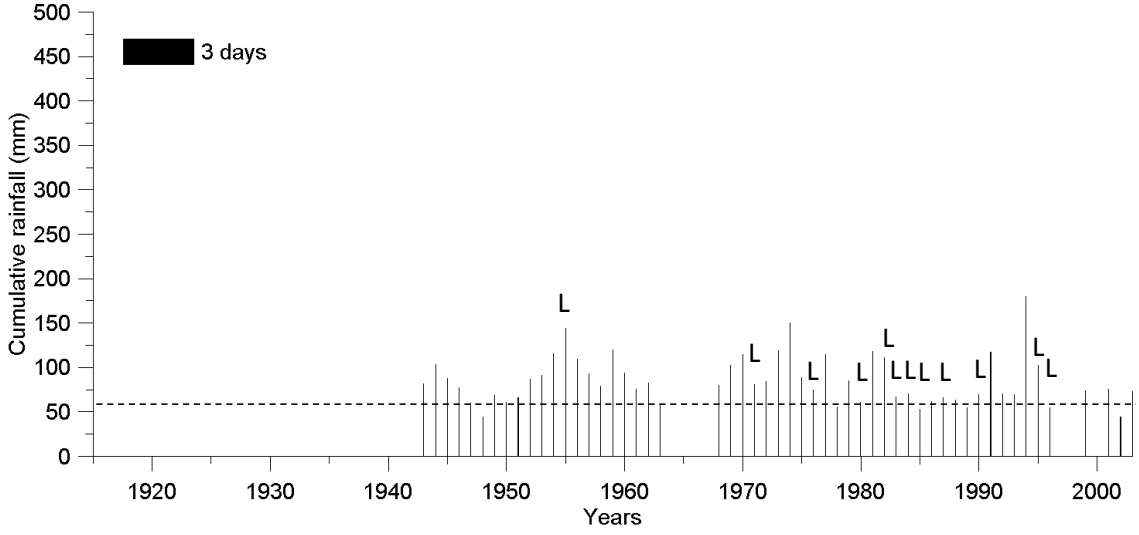

Figure 0-28: Accumulated rainfall and threshold (dashed line). 60 mm within 3 days. L: Landsliding event. The threshold is reached, mostly, during years with landslide reactivations, but some years with no failures identified present a higher amount of rainfall.

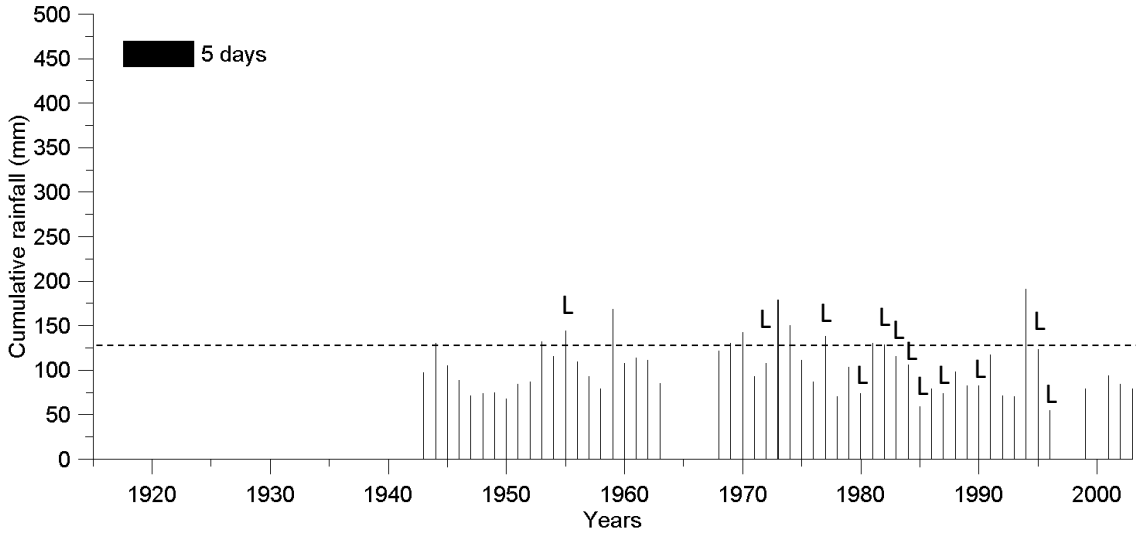

Figure 0-29: Accumulated rainfall and threshold (dashed line). 130 mm within 5 days. L: Landsliding event. The threshold is reached only during few years with landslide reactivations. Furthermore some years with no failures identified present a higher amount of rainfall.

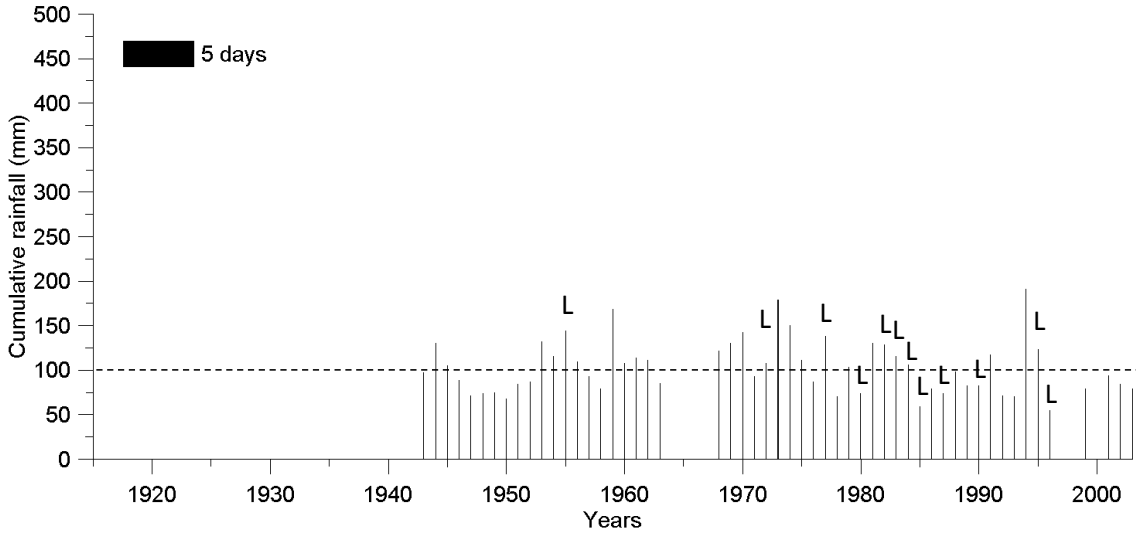

Figure 0-30: Accumulated rainfall and threshold (dashed line). 100 mm within 5 days. L: Landsliding event. The threshold is reached during some years with landslide reactivations, but also by some years with no failures identified.

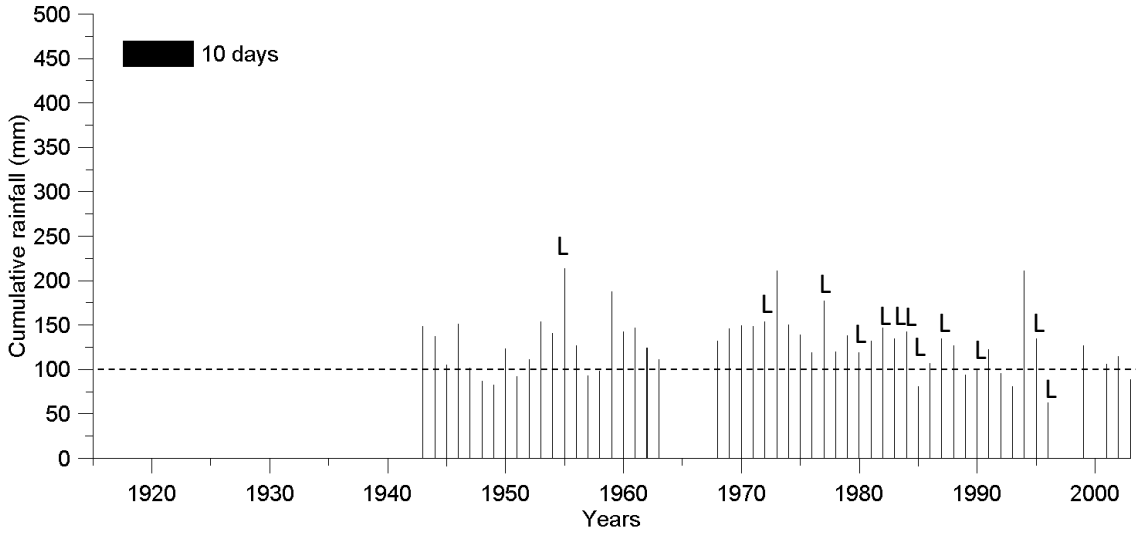

Figure 0-31: Accumulated rainfall and threshold (dashed line). 100 mm within 10 days. L: Landsliding event. The threshold is reached during almost all years with landslide reactivations, but also by some years with no failures identified.

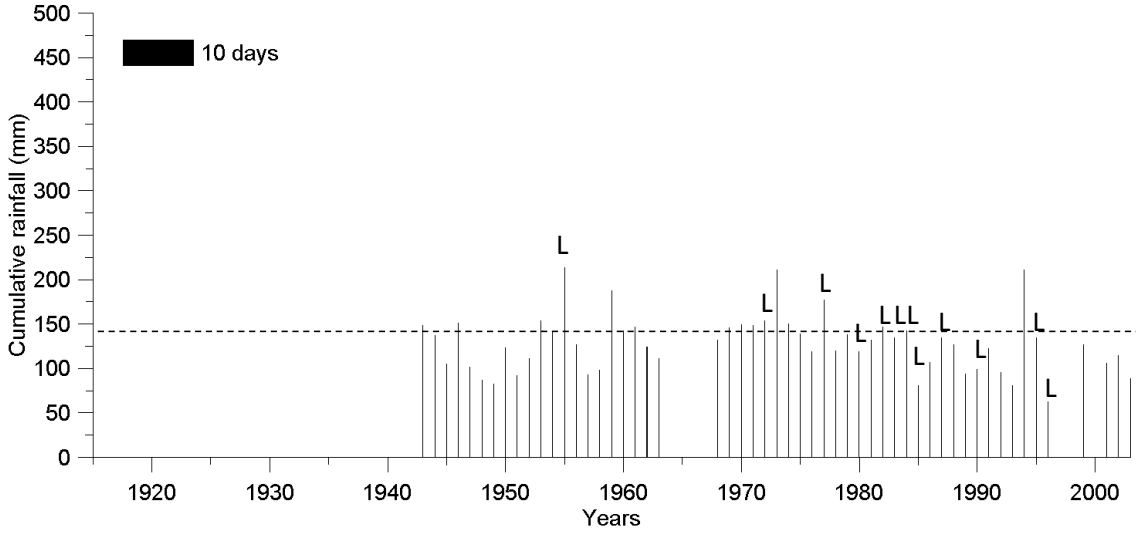

Figure 0-32: Accumulated rainfall and threshold (dashed line). 142 mm within 10 days. L: Landsliding event. The threshold is too much restrictive, being reached during a few years with landslide reactivations, but also by some years with no failures identified.

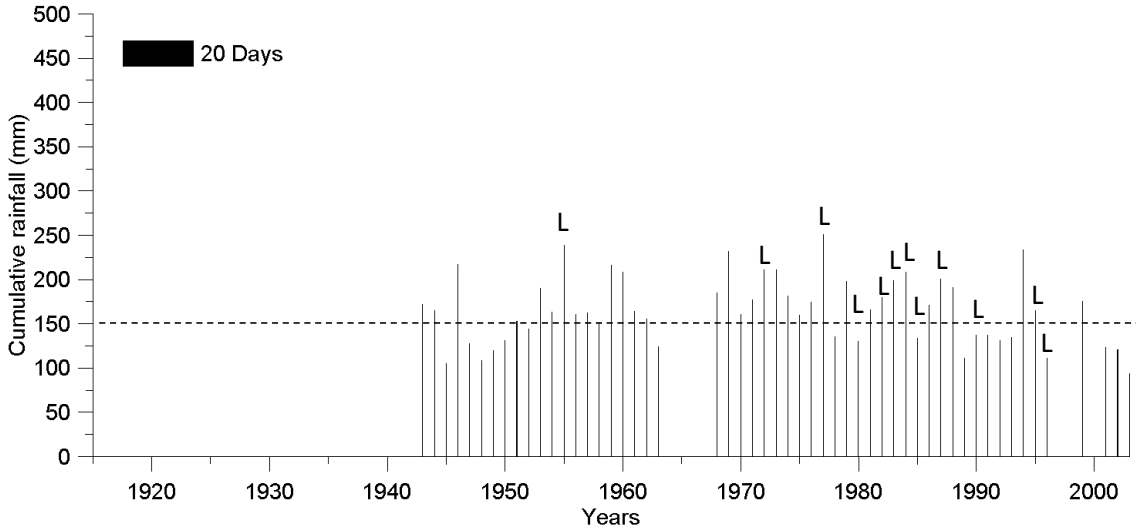

Figure 0-33: Accumulated rainfall and threshold (dashed line). 150 mm within 20 days. L: Landsliding event. Too many years with no failures identified present a higher amount of rainfall.

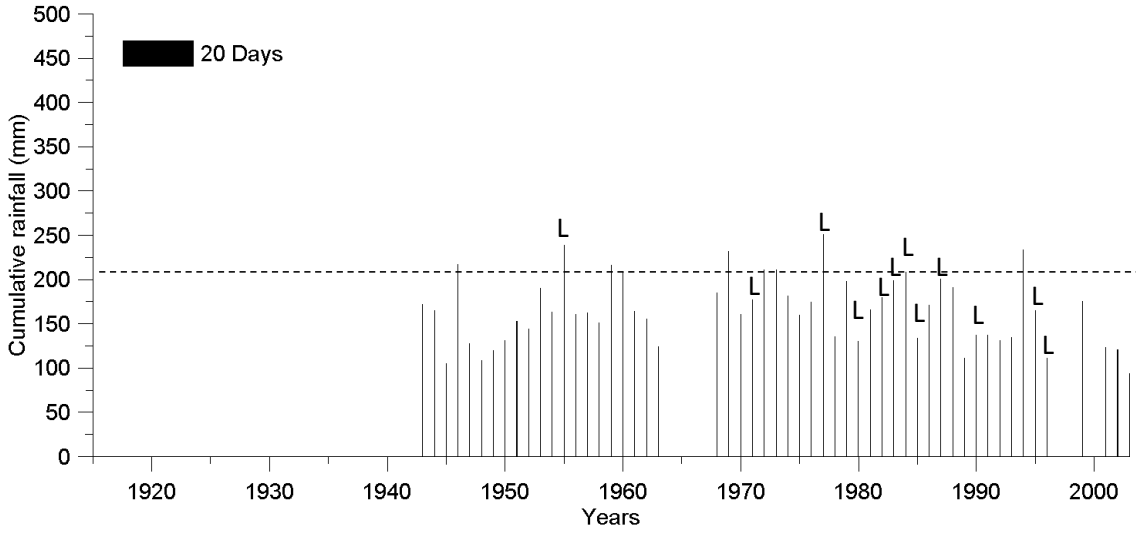

Figure 0-34: Accumulated rainfall and threshold (dashed line). 208 mm within 20 days. L: Landsliding event. Too much restrictive threshold, since it is reached by only a few years with landslide reactivations.

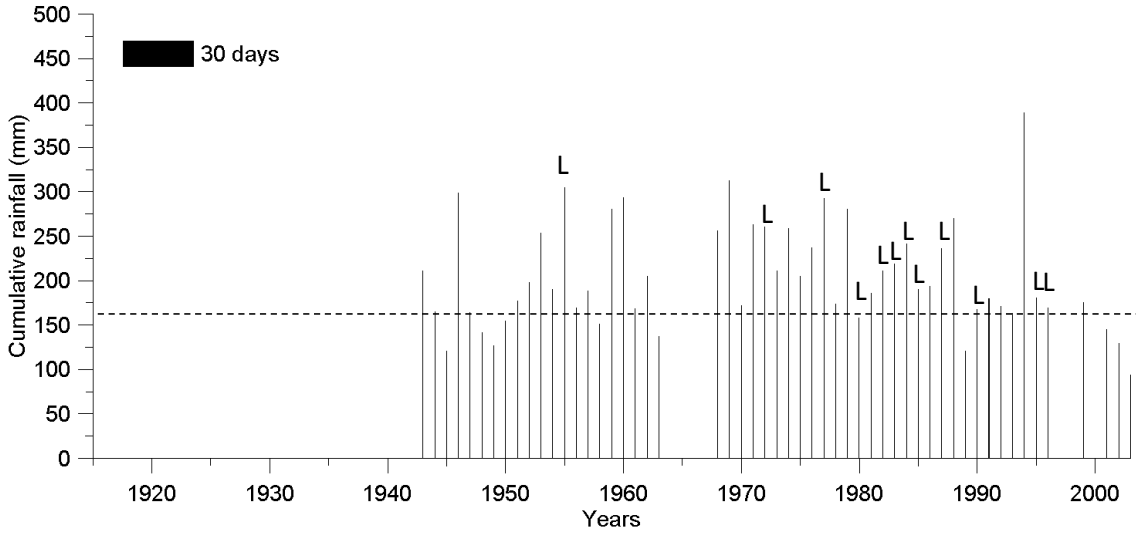

Figure 0-35: Accumulated rainfall and threshold (dashed line). 165 mm within 30 days. L: Landsliding event. The threshold is reached during all years with landslide reactivations as well as by some years with no failures identified.

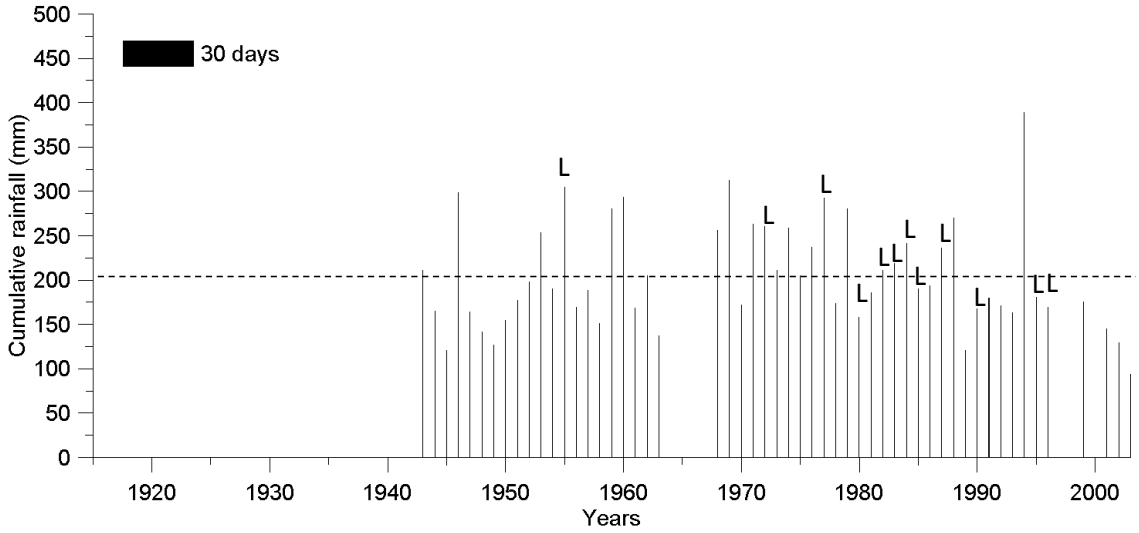

Figure 0-36: Accumulated rainfall and threshold (dashed line). 202 mm within 30 days. L: Landsliding event. The threshold is reached during some years with landslide reactivations, but some years with no failures identified present a higher amount of rainfall.

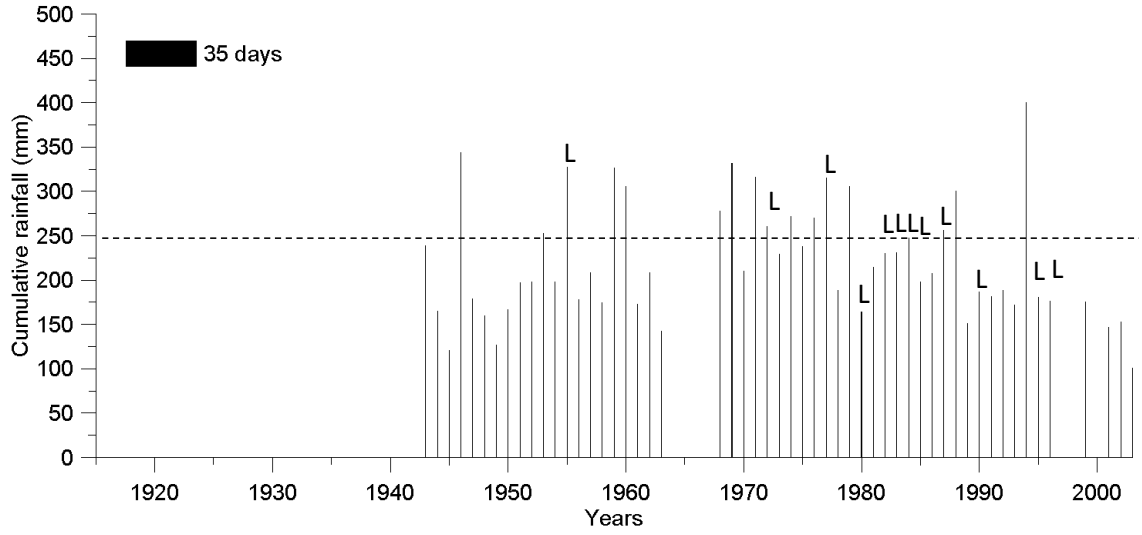

Figure 0-37: Accumulated rainfall and threshold (dashed line). 248 mm within 35 days. L: Landsliding event. The threshold is reached during some years with landslide reactivations. Furthermore, some years with no failures identified present a higher amount of rainfall.

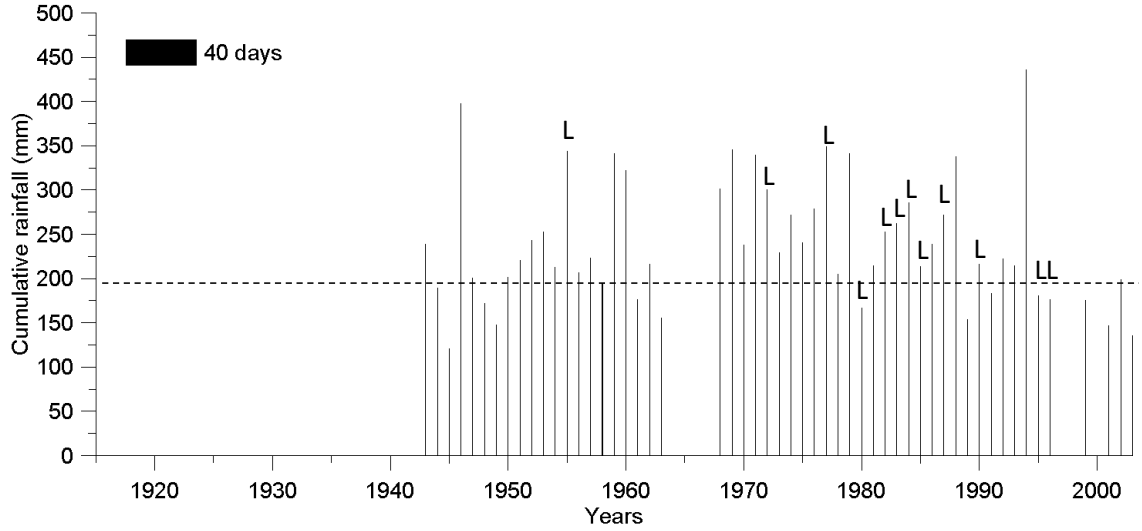

Figure 0-38: Accumulated rainfall and threshold (dashed line). 190 mm within 40 days. L: Landsliding event. The threshold is reached almost during all years with landslide reactivations, but also some years with no failures identified present a higher amount of rainfall.

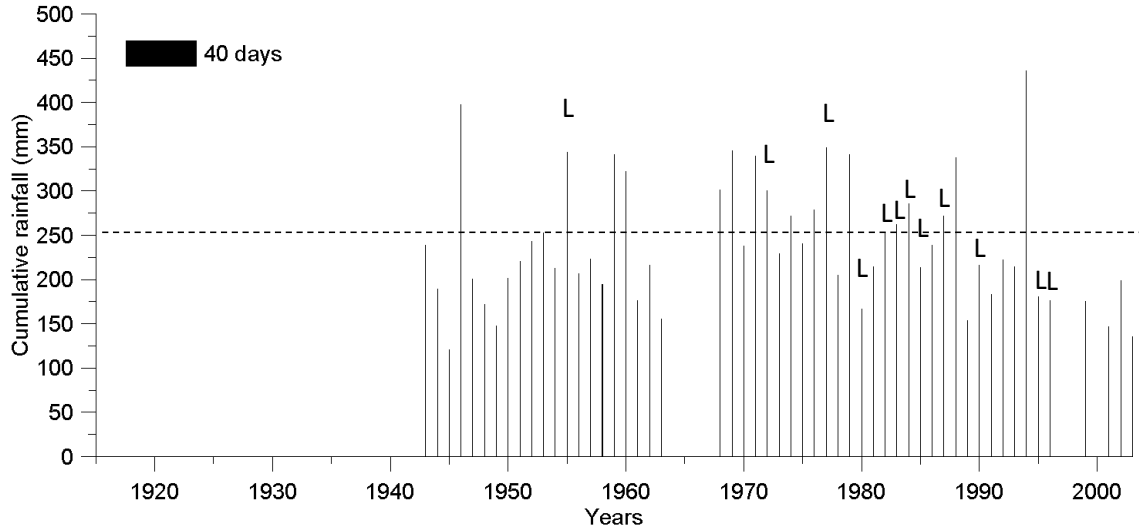

Figure 0-39: Accumulated rainfall and threshold (dashed line). 252 mm within 40 days. L: Landsliding event. The threshold is reached by some years with landslide reactivations, but also by some years with no failures identified.

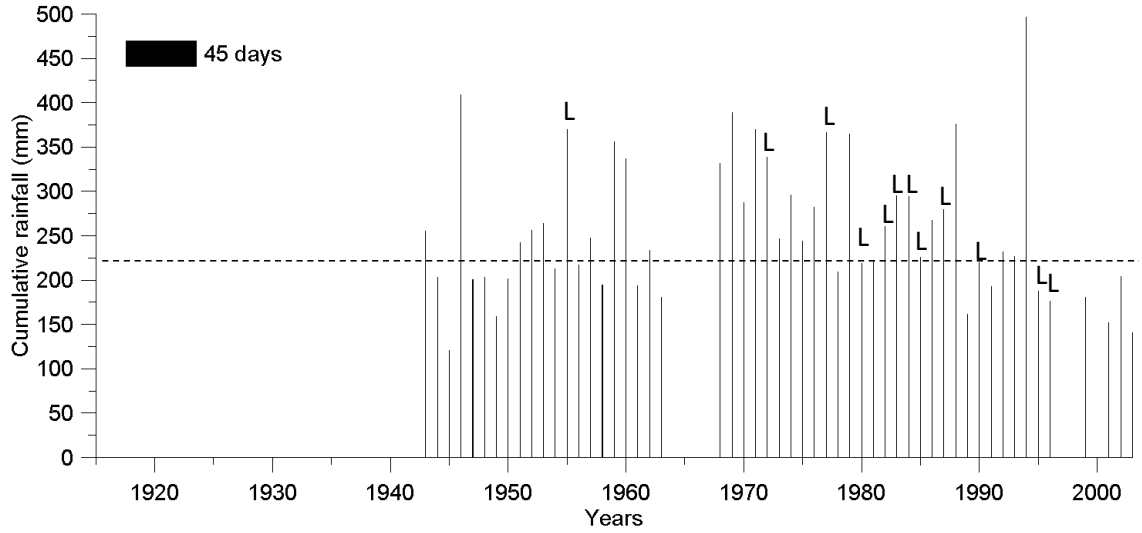

Figure 0-40: Accumulated rainfall and threshold (dashed line). 220 mm within 45 days. L: Landsliding event. The threshold is reached almost during all years with landslide reactivations, but also by some years with no failures identified.

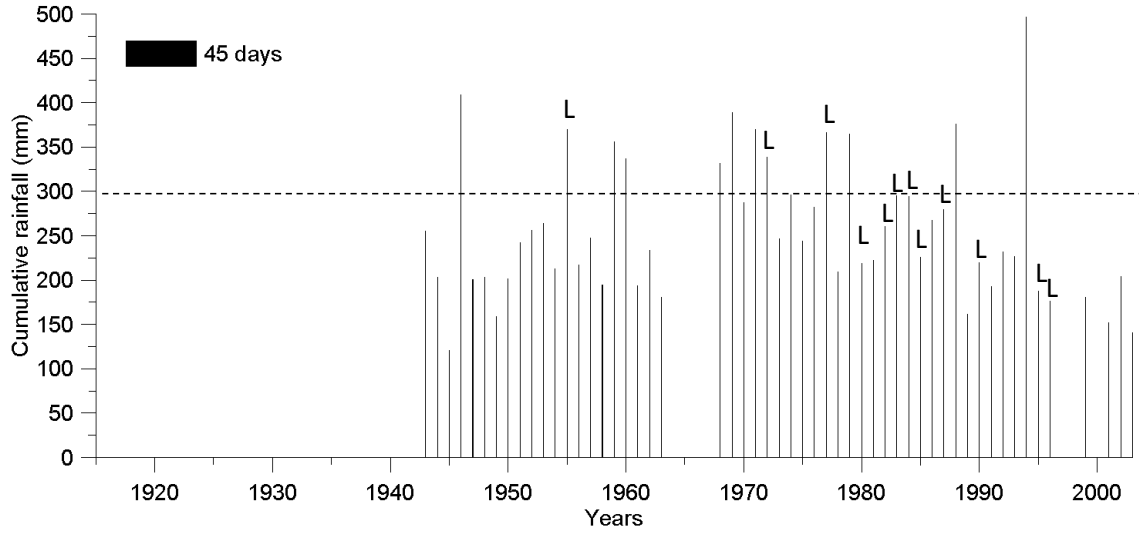

Figure 0-41: Accumulated rainfall and threshold (dashed line). 295 mm within 45 days. L: Landsliding event. The threshold is reached during a few years with landslide reactivations as well as by some years with no failures identified.

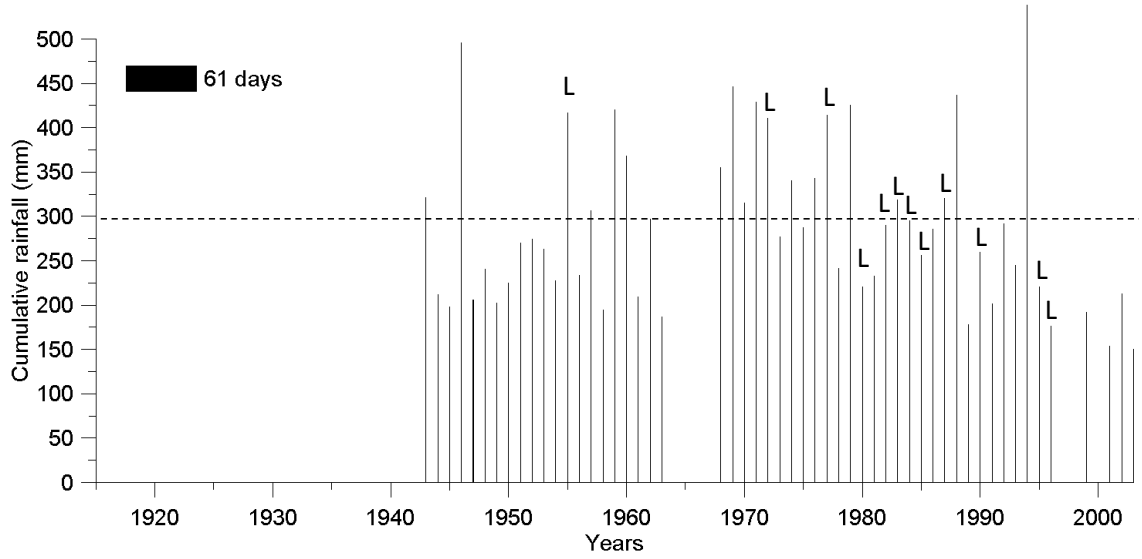

Figure 0-42: Accumulated rainfall and threshold (dashed line). 290 mm within 61 days. L: Landsliding event. The threshold is reached during a few years with landslide reactivations, but also by some years with no failures identified.

Annex 6: Antecedent rainfall

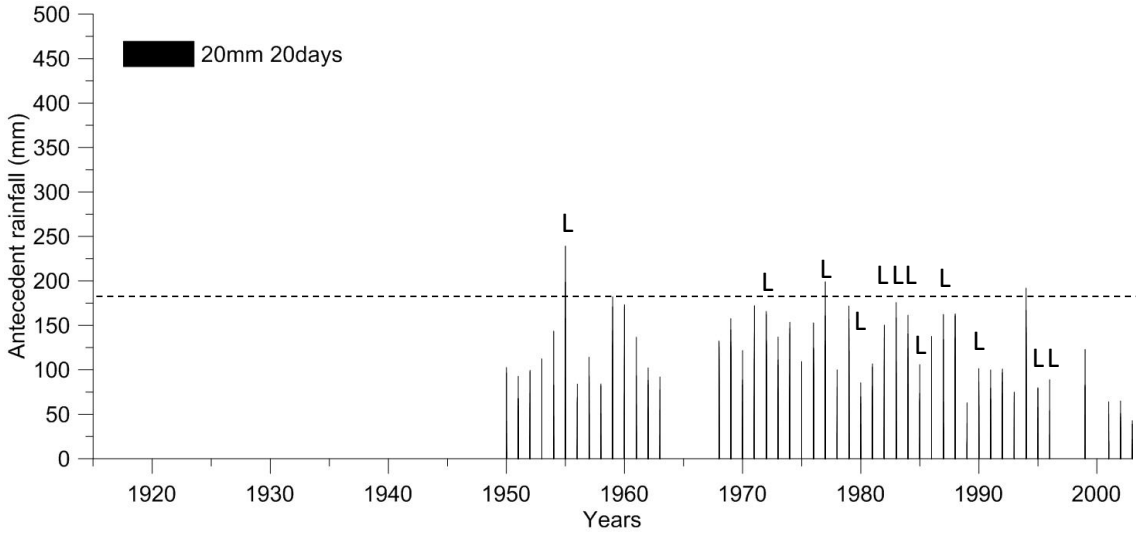

Figure 0-43: Antecedent rainfall and thresholds. Previous minimum triggering rainfall of 20 mm within 1 day followed by 180 mm of antecedent rainfall (dashed line) within 20 days. L: Landsliding event. Too much restrictive threshold, since it is reached by only two years with at least one reactivation identified and by one period without any failure detected.

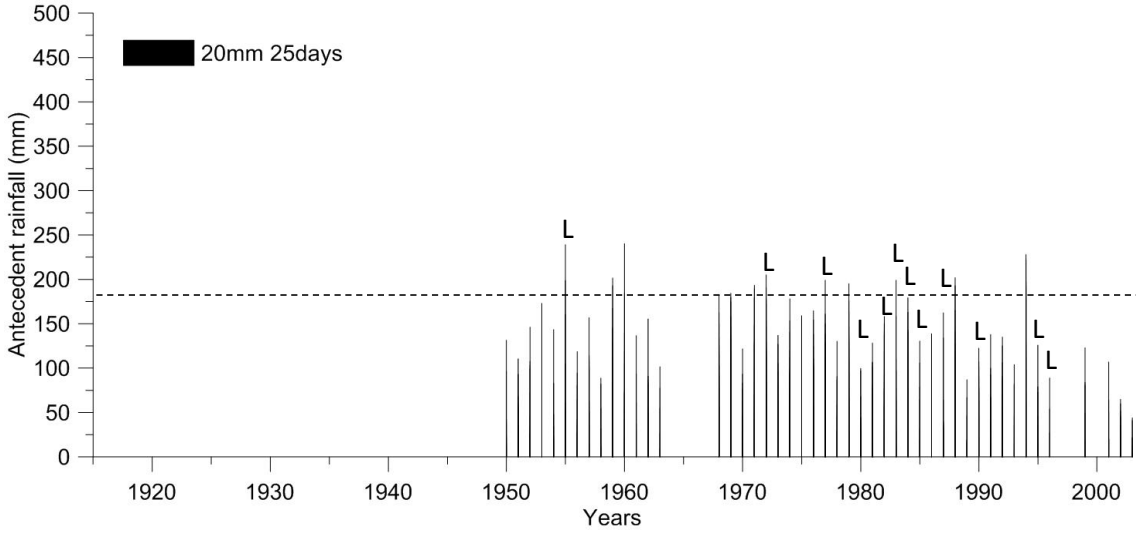

Figure 0-44: Antecedent rainfall and thresholds. Previous minimum triggering rainfall of 20 mm within 1 day followed by 180 mm of antecedent rainfall (dashed line) within 25 days. L: Landsliding event. The threshold is reached by some landsliding events, but also by some years with no failures identified.

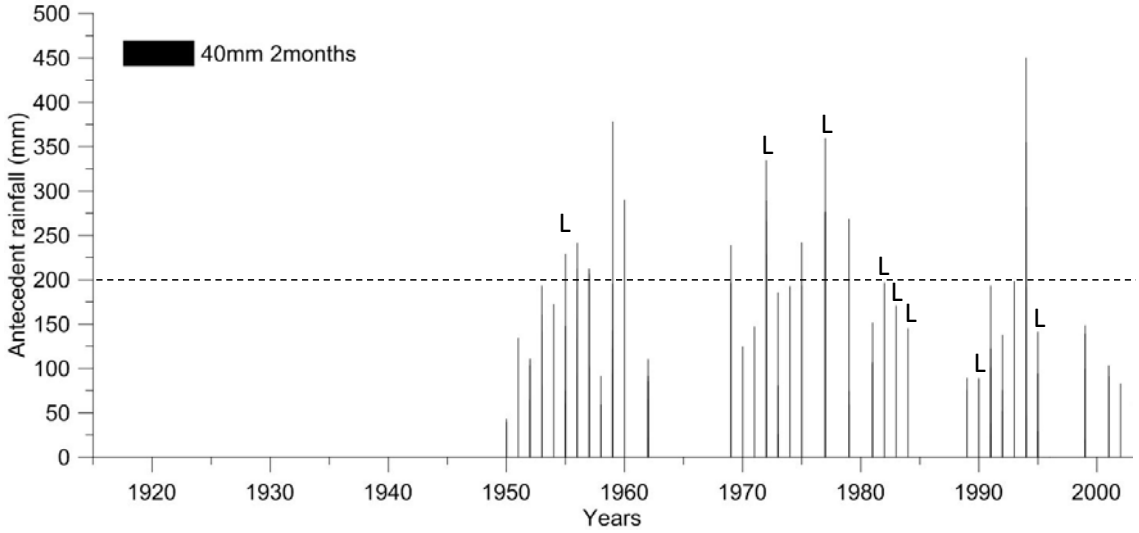

Figure 0-45: Antecedent rainfall and thresholds. Previous minimum triggering rainfall of 40 mm within 1 day followed by 200 mm of antecedent rainfall (dashed line) within 2 months. L: Landsliding event. It is not easy to find a proper threshold with such a combination as not a clear distinction exists between landsliding events and no landsliding events.

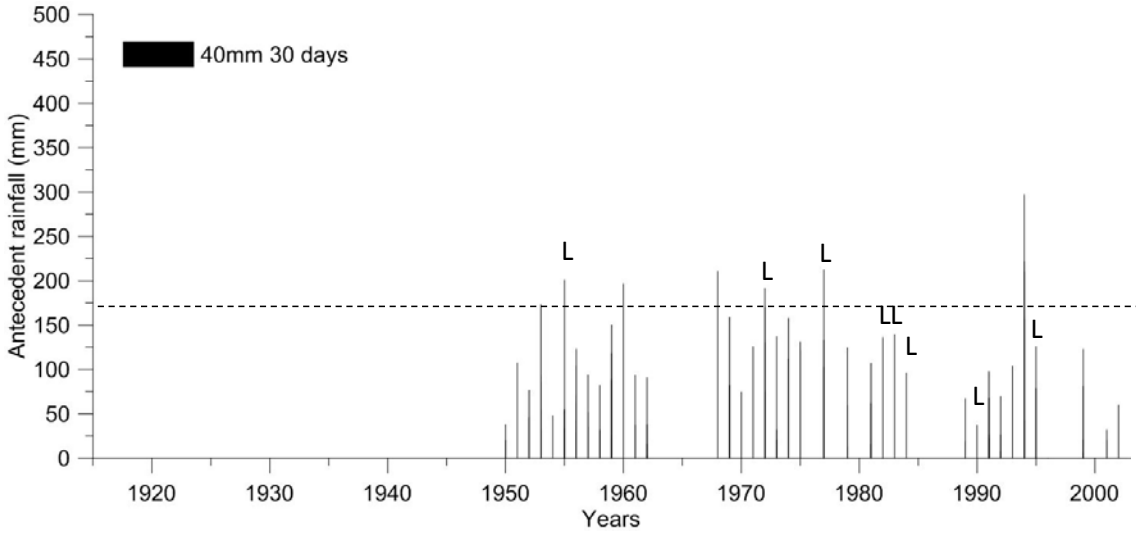

Figure 0-46: Antecedent rainfall and thresholds. Previous minimum triggering rainfall of 40 mm within 1 day followed by 170 mm of antecedent rainfall (dashed line) within 3 days. L: Landsliding event. The threshold is reached by a few years with at least one failure identified as well as by some years with no events detected.

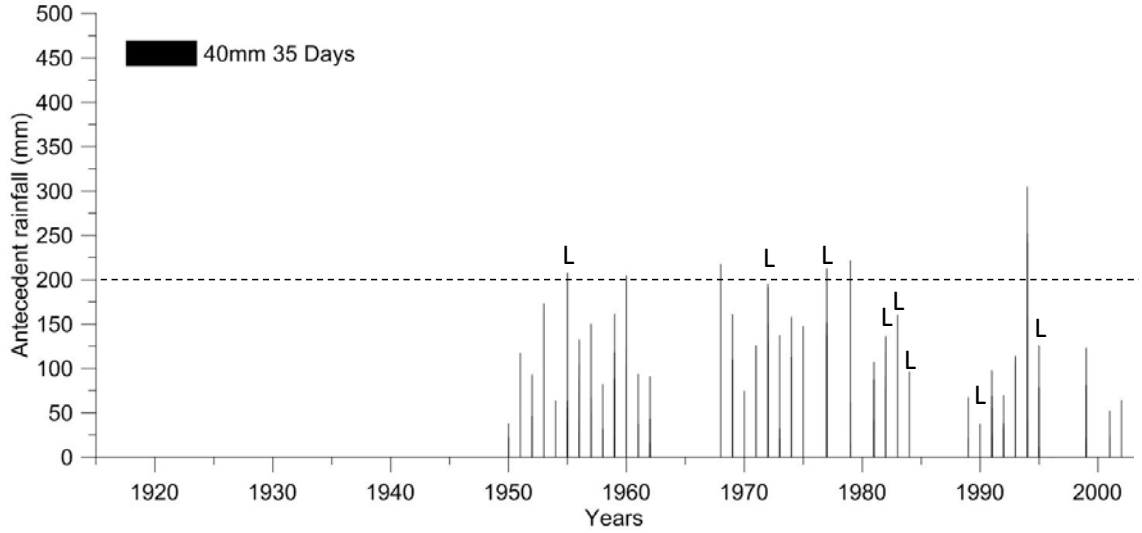

Figure 0-47: Antecedent rainfall and thresholds. Previous minimum triggering rainfall of 40 mm within 1 day followed by 200 mm of antecedent rainfall (dashed line) within 35 days. L: Landsliding event. Too much restrictive threshold since it is being reached by only some landsliding periods. Furthermore, some years with no failures identified present a higher amount of rainfall.

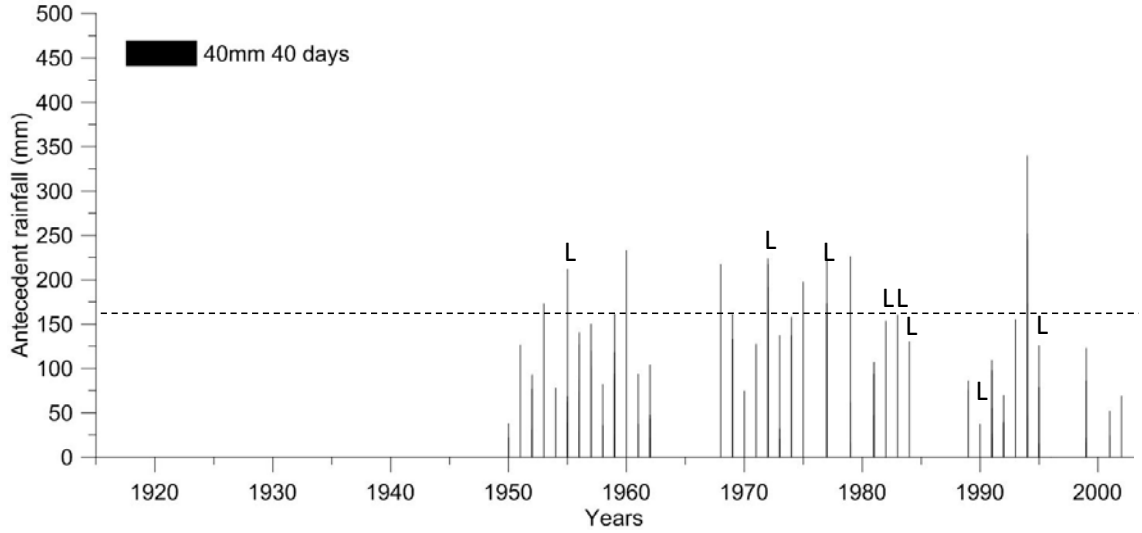

Figure 0-48: Antecedent rainfall and thresholds. Previous minimum triggering rainfall of 40 mm within 1 day followed by 170 mm of antecedent rainfall (dashed line) within 40 days. L: Landsliding event. The threshold is mostly reached during years with landslide reactivations, but some years with no failures identified present a higher amount of rainfall.

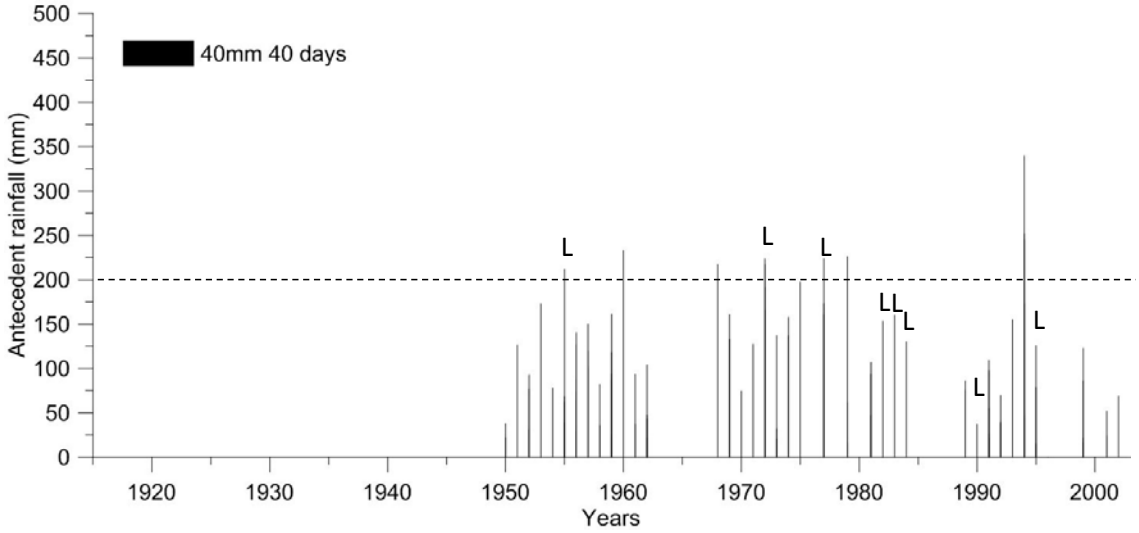

Figure 0-49: Antecedent rainfall and thresholds. Previous minimum triggering rainfall of 40 mm within 1 day followed by 200 mm of antecedent rainfall (dashed line) within 40 days. L: Landsliding event. The threshold is reached during some years with landslide reactivations as well as by some years with no failures identified.

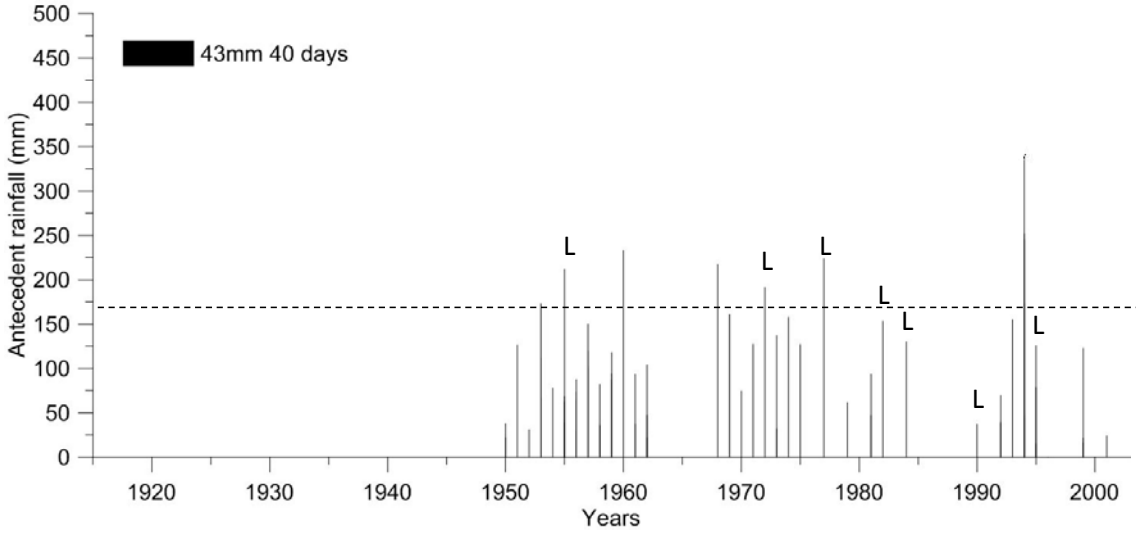

Figure 0-50: Antecedent rainfall and thresholds. Previous minimum triggering rainfall of 43 mm within 1 day followed by 170 mm of antecedent rainfall (dashed line) within 40 days. L: Landsliding event. The dendrological year 1989/1990 in which, at least, one failure has been identified, presents a very low antecedent rainfall. Hence, it is not an easy task to find a proper threshold.

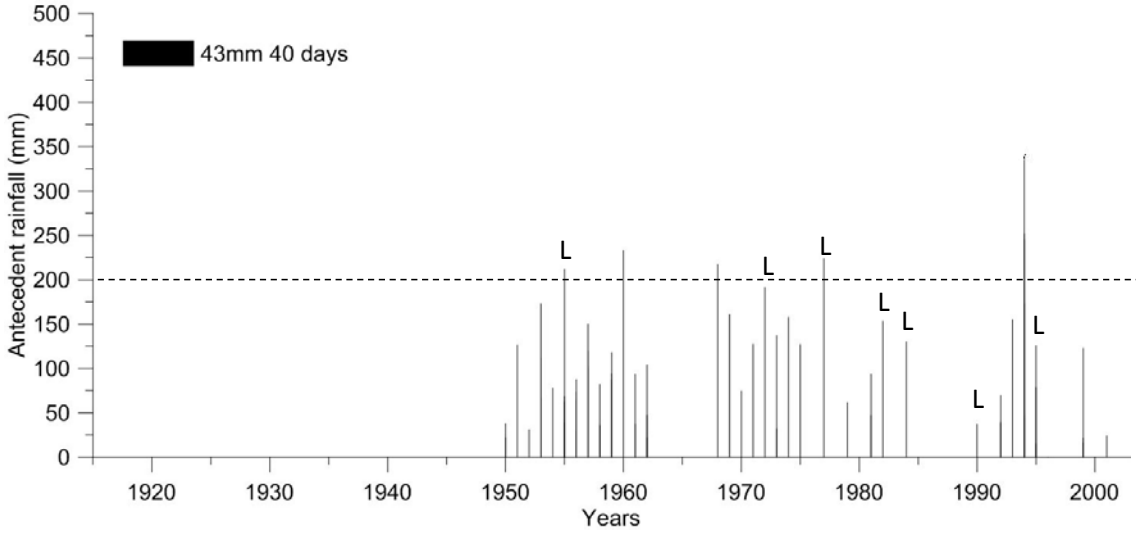

Figure 0-51: Antecedent rainfall and thresholds. Previous minimum triggering rainfall of 43 mm within 1 day followed by 200 mm of antecedent rainfall (dashed line) within 40 days. L: Landsliding event. Dendrological years 1989/1990 and 1994/1995 in which, at least, one failure has been identified, present a very low antecedent rainfall making it difficult to find a proper threshold.

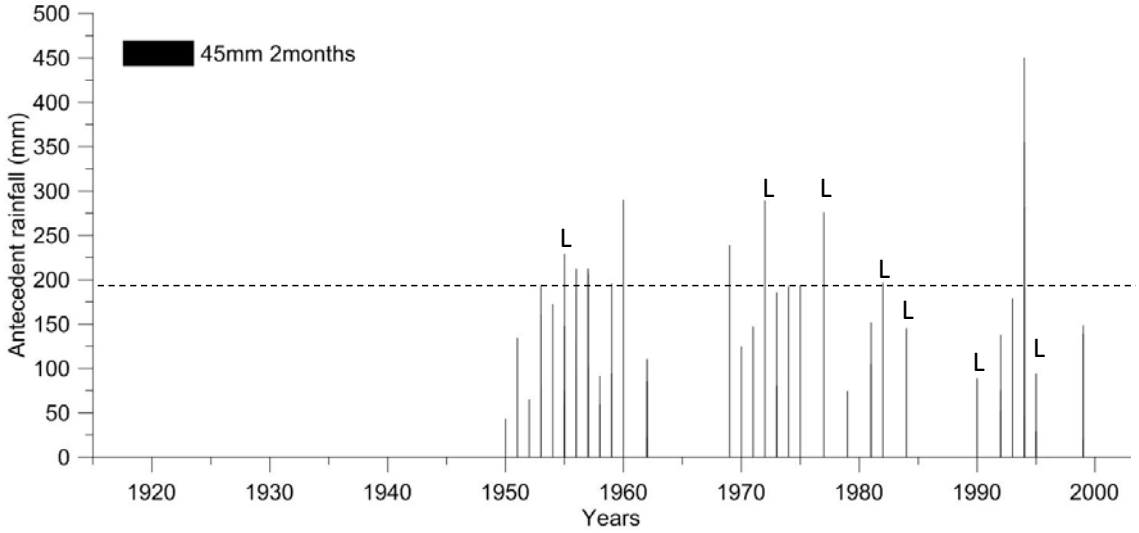

Figure 0-52: Antecedent rainfall and thresholds. Previous minimum triggering rainfall of 45 mm within 1 day followed by 191 mm of antecedent rainfall (dashed line) within 2 months. L: Landsliding event. The high amount of precipitation within dendrological years 1959/1960 and 1993/1994 in which no failures were identified does not allow to define a reliable threshold.

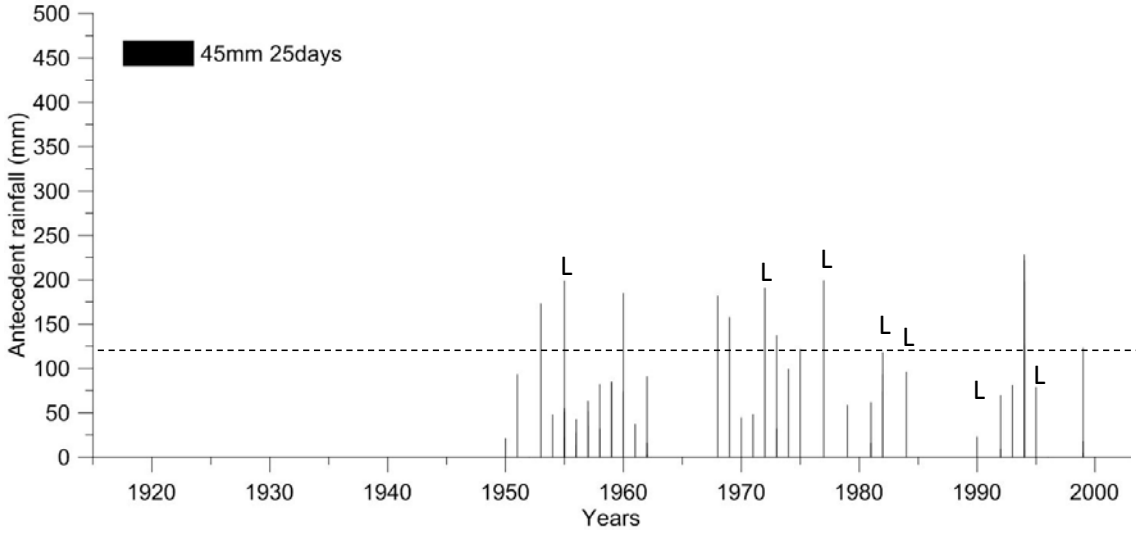

Figure 0-53: Antecedent rainfall and thresholds. Previous minimum triggering rainfall of 45 mm within 1 day followed by 120 mm of antecedent rainfall (dashed line) within 25 days. L: Landsliding event. Some years with no failures identified exceed the threshold.

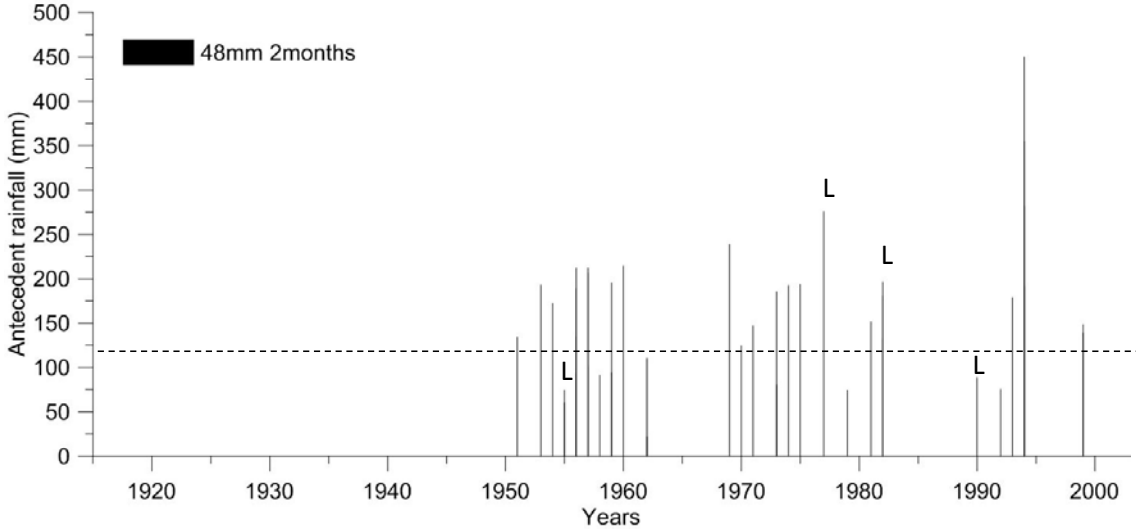

Figure 0-54: Antecedent rainfall and thresholds. Previous minimum triggering rainfall of 48 mm within 1 day followed by 121 mm of antecedent rainfall (dashed line) within 2 months. L: Landsliding event. 48 mm of minimum triggering daily rainfall seems to be a very restrictive threshold since only 4 dendrological years with, with at least, one failure identified exist.

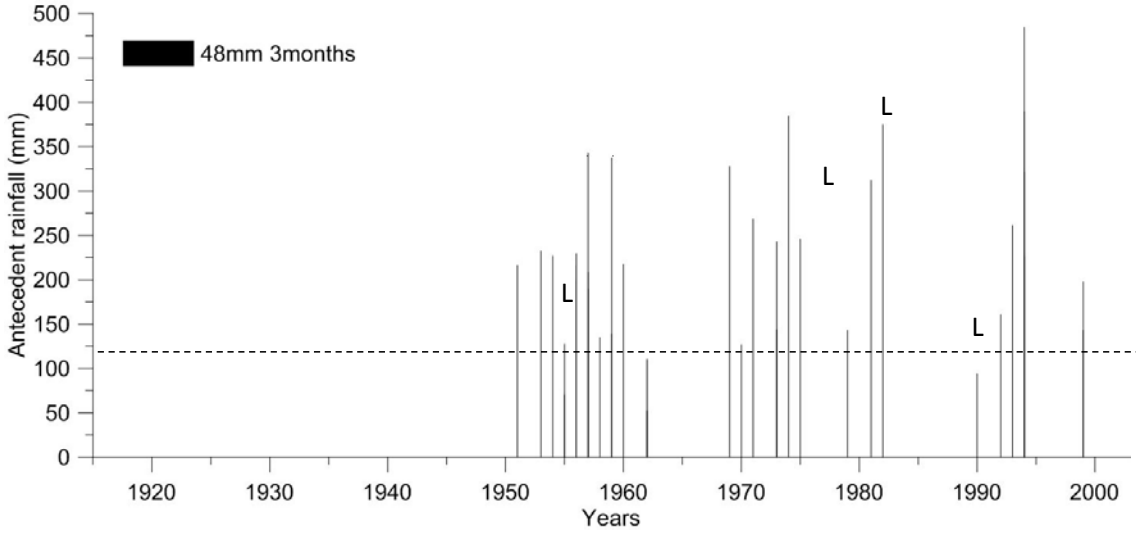

Figure 0-55: Antecedent rainfall and thresholds. Previous minimum triggering rainfall of 48 mm within 1 day followed by 121 mm of antecedent rainfall (dashed line) within 3 months. L: Landsliding event. As in the previous analysis, 48 mm of daily precipitation for landslide triggering, seems not to be very common.

Annex 7: First-time failures map

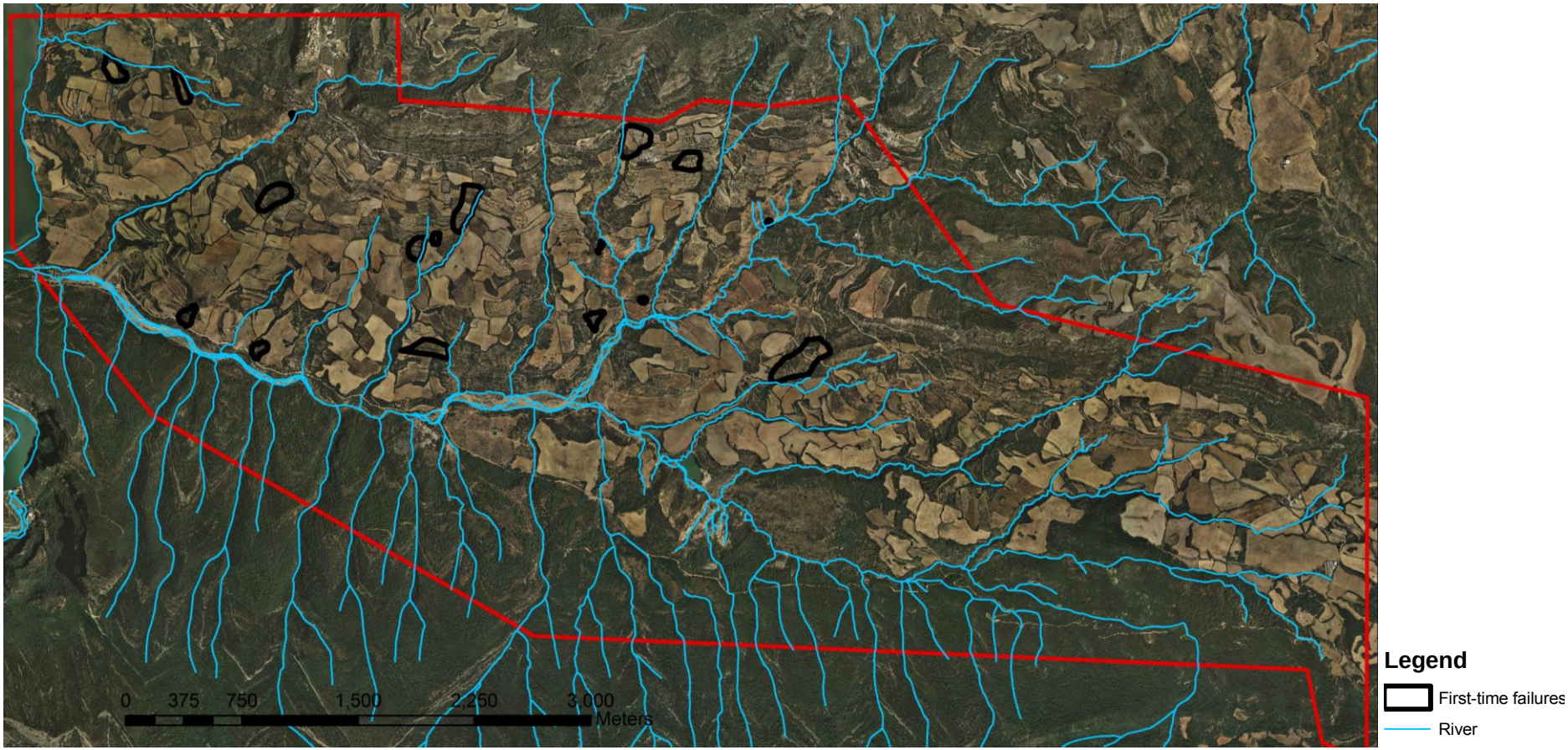

Figure 0-56: Inventoried first-time failures.

Annex 8: Susceptibility map

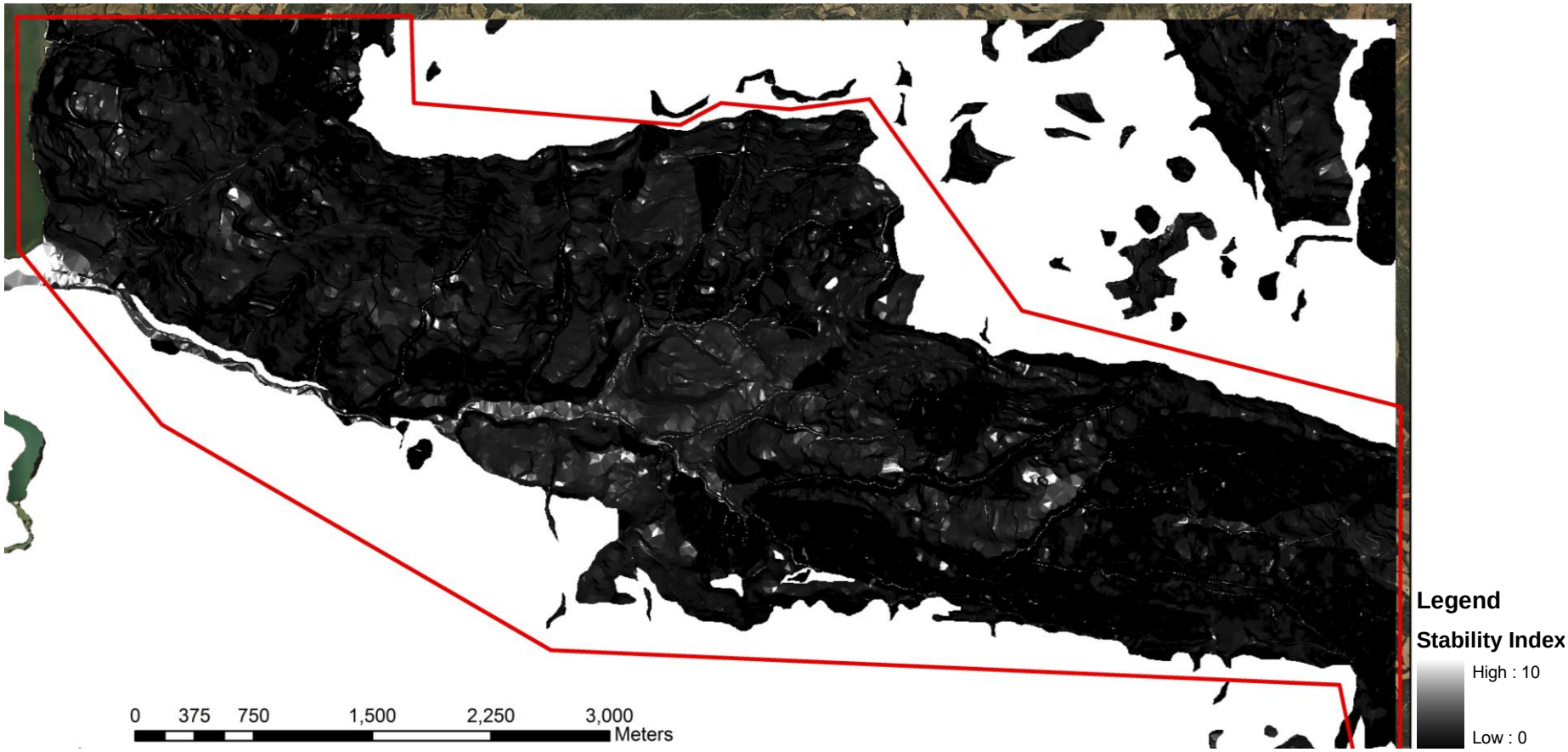

Figure 0-57: Map obtained directly from SINMAP.

Annex 9: Reclassified susceptibility map

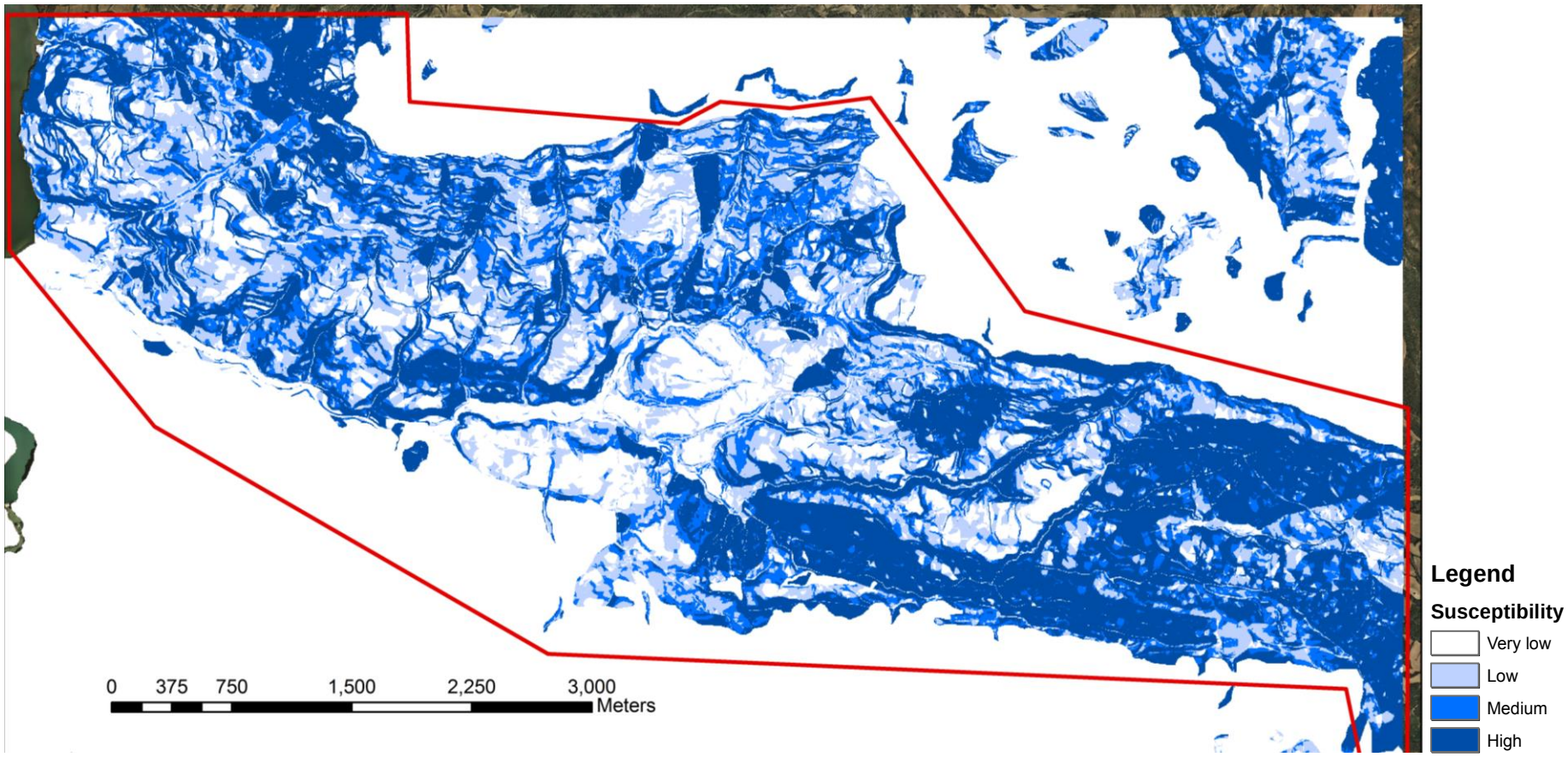

Figure 0-58: Map obtained from SINMAP and reclassified according to the four classes of susceptibility afore-mentioned.

Annex 10: Schematic pixel clustering methodology

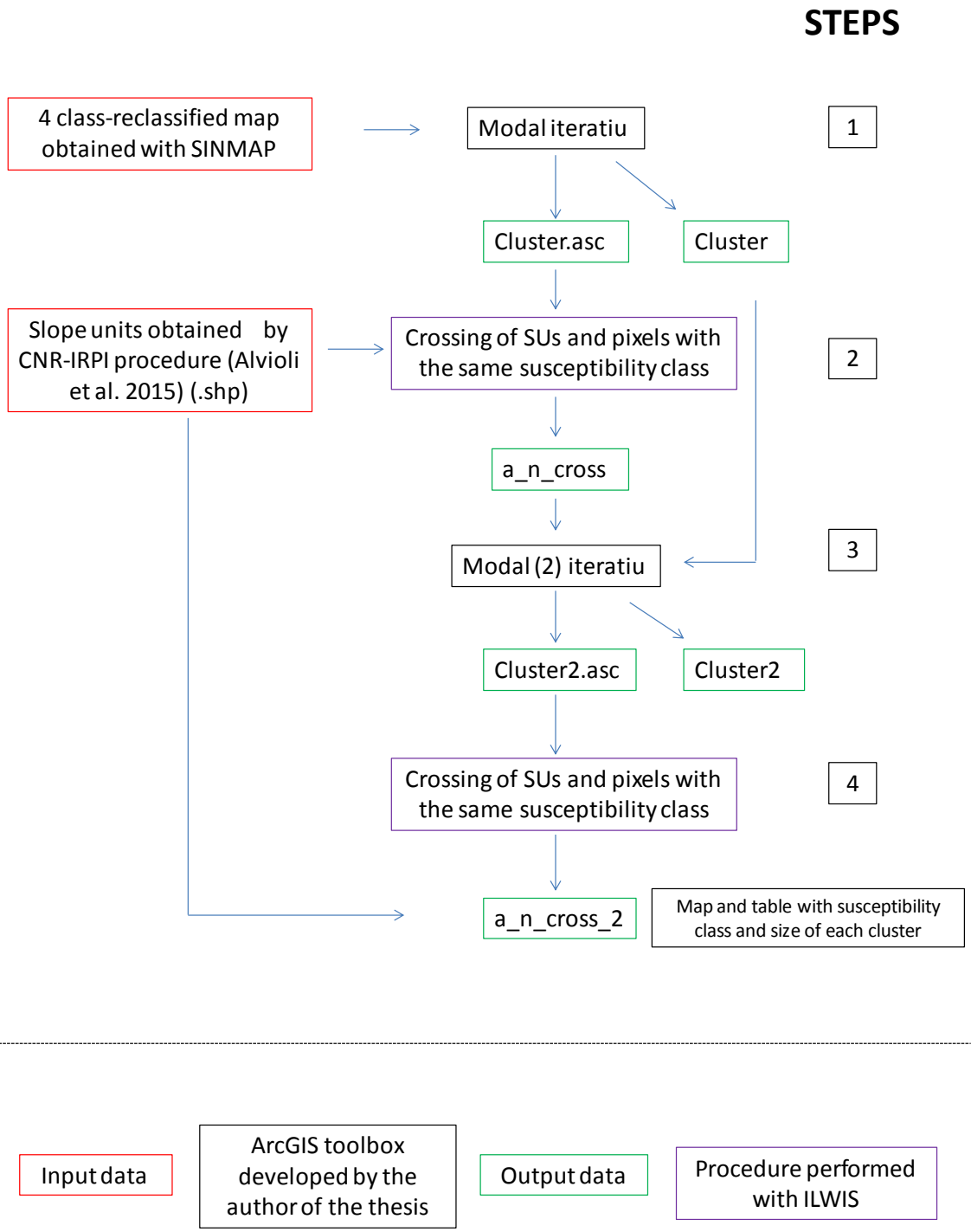

Figure 0-59: Steps to follow to perform the pixel clustering process from the reclassified susceptibility map obtained with SINMAP.

Annex 11: Hazard map obtained after pixel clustering by SU no. 28

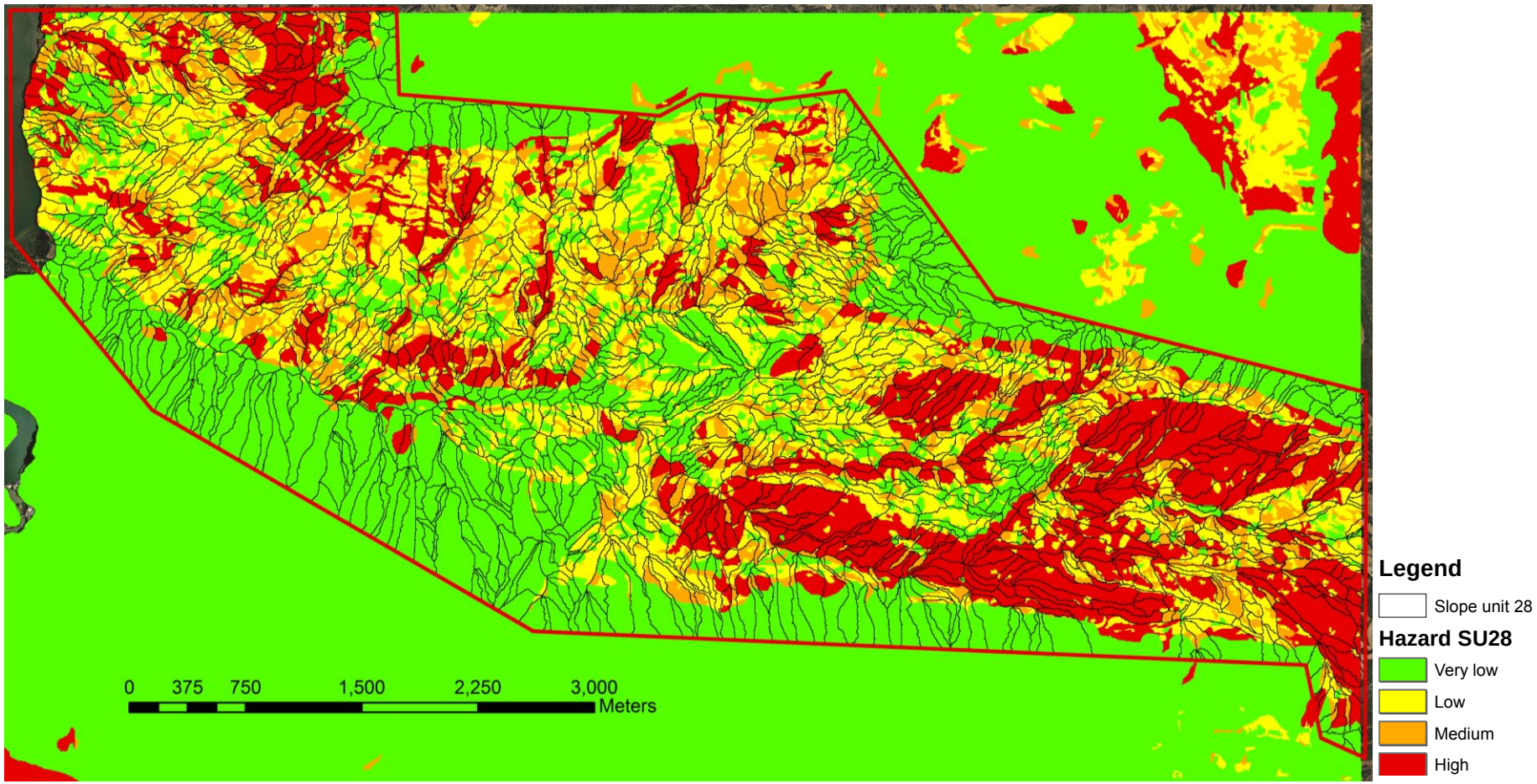

Figure 0-60: Landslide hazard map obtained with SINMAP and the application of the SU no. 28.

Annex 12: Hazard map obtained after pixel clustering by SU no. 35

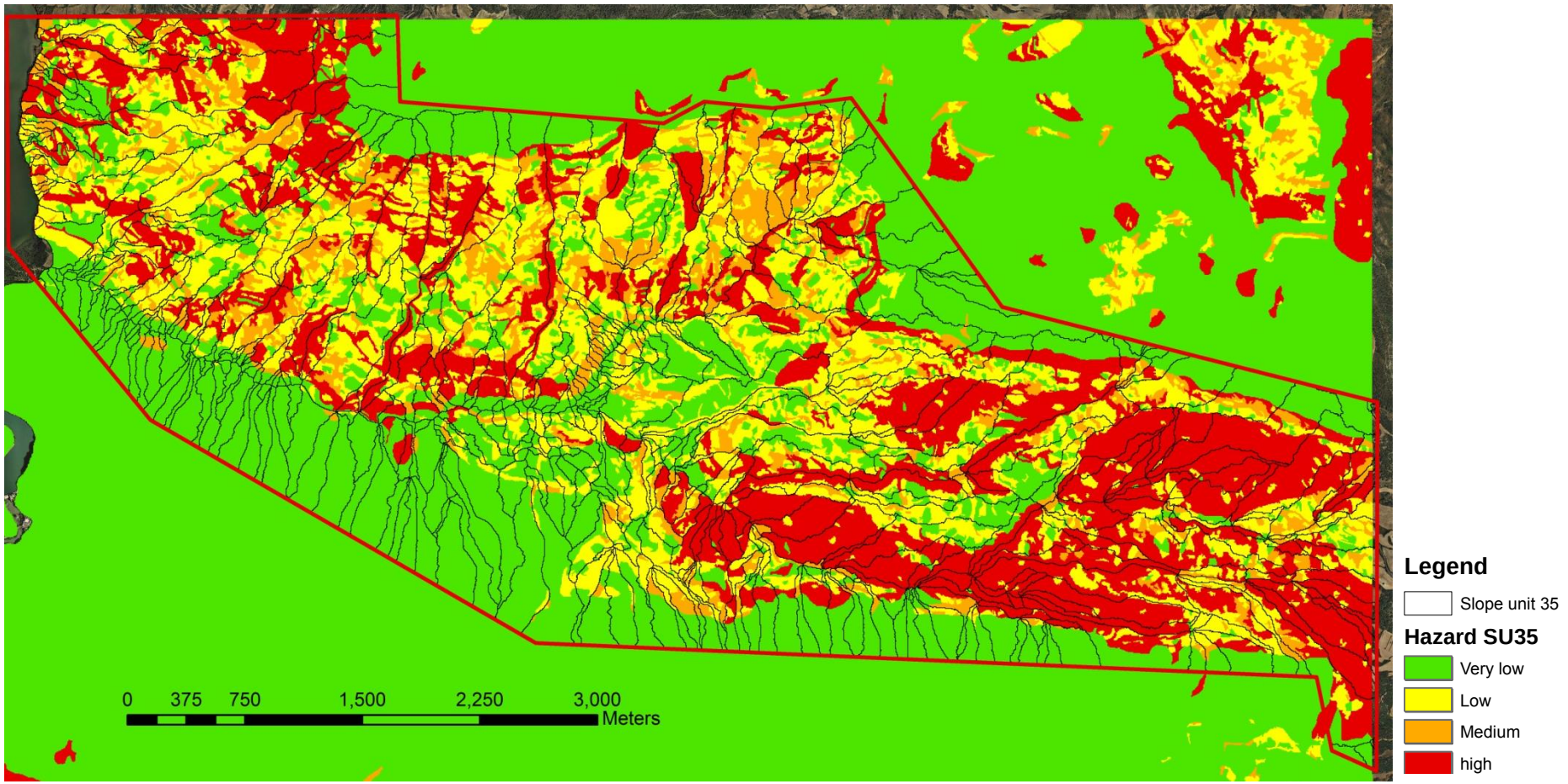

Figure 0-61: Landslide hazard map obtained with SINMAP and the application of the SU no. 35.

Annex 13: Hazard map obtained after pixel clustering by SU no. 40

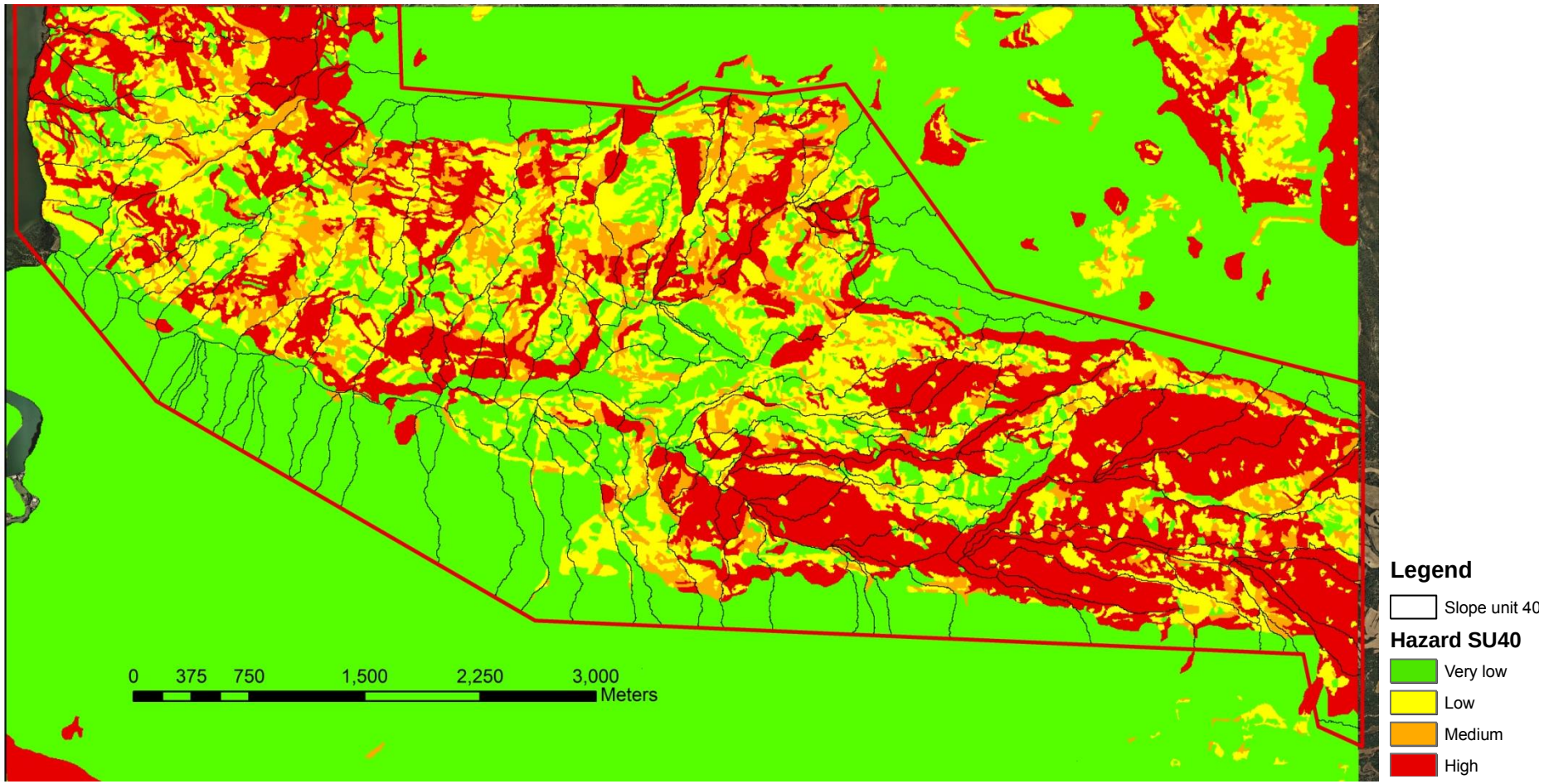

Figure 0-62: Landslide hazard map obtained with SINMAP and the application of the SU no. 40.

Annex 14: Hazard map obtained after pixel clustering by SU no. 42

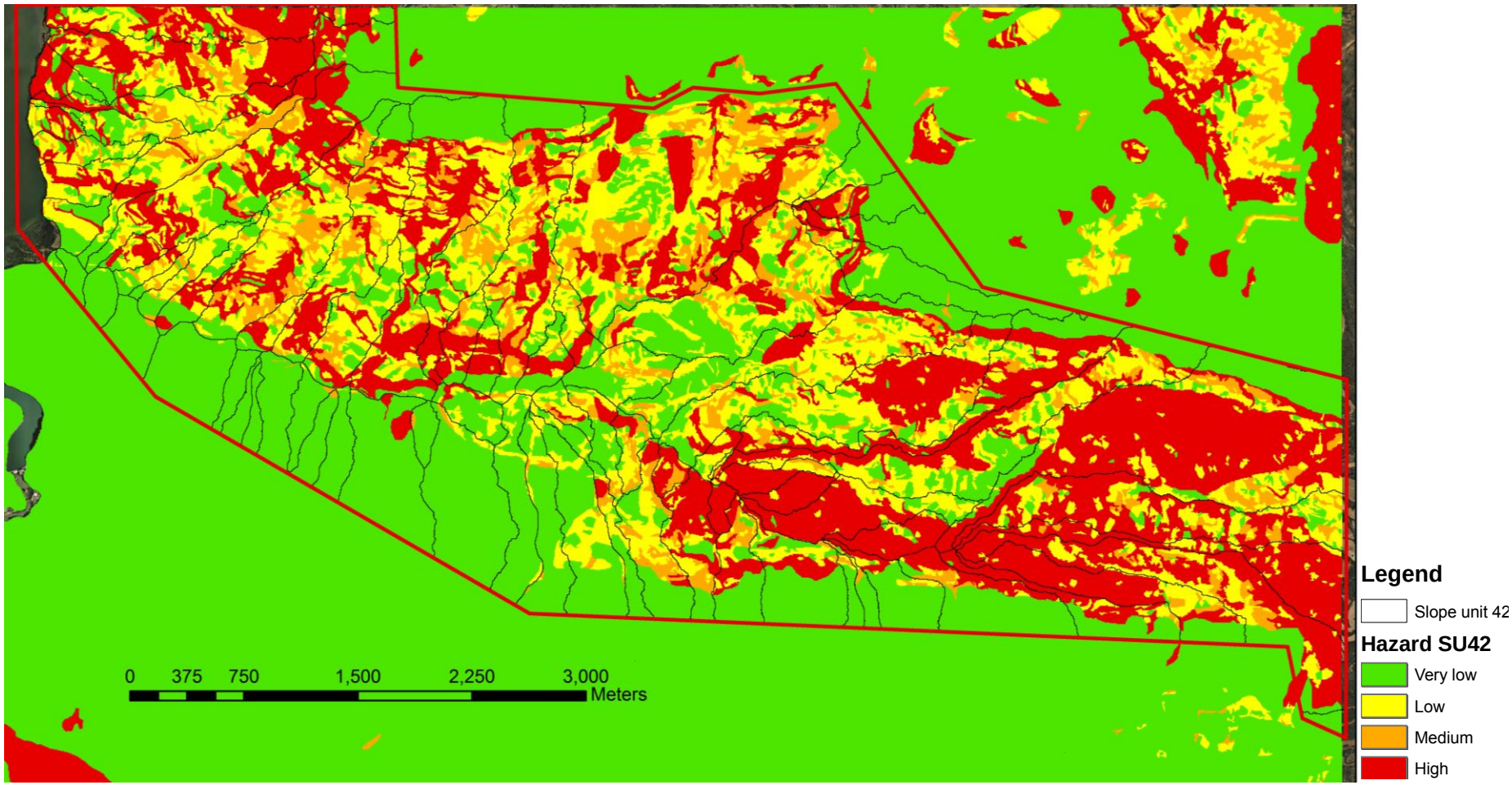

Figure 0-63: Landslide hazard map obtained with SINMAP and the application of the SU no. 42.

Annex 15: Sensitivity analysis for planar regression; normal vector definition for each point

Table 0- 2: Sensitivity analysis carried out to assess the best radius for the normal vector definition. 4 different search radiuses have been imposed. Opened: No values have been established. The minimum number of points to calculate a reliable planar regression is 5 (Garcia-Sellés et al. 2009, 2011).

Radius (m)	Coplanarity index (M)	Collinearity index (K)	Comments
0.2	Opened	Opened	Many points are removed, mostly in the western part of the point cloud were density is lower
0.25	Opened	Opened	Some points are lost in the western part where point density is lower. However, it does not belong to discontinuity planes of our interest
0.3	Opened	Opened	Just a few points are lost in the western part of the point cloud where the density is lower. Points located at the discontinuity boundaries and in small scar planes present very low M-values
0.35	Opened	Opened	No points are lost. Nevertheless, the coplanarity index in the boundaries and in small planes is really small

Table 0-3: Sensitivity analysis carried out to assess the collinearity and coplanarity indexes for the definition of the normal. 4 different M-values have been imposed. Results with different K-values (according to the literature) have been observed. Opened: No values have been established.

Radius (m)	Coplanarity index (M)	Collinearity index (K)	Comments
0.25	2.5	Opened	Very small value that leads to the generation of poor collinear planes such as small and eroded discontinuity surfaces. K-values below 1.2
0.25	3	Opened	Intermediate value. Generate high irregular surfaces. K-values below 1.2
0.25	3.5	Opened	Intermediate value recommended by García-Sellés et al. (2011) for irregular geometry surfaces (e.g. discontinuities of tectonic origin). K-values below 1.2
0.25	4	Opened	Very restrictive value that only keeps high collinear planes. Recommended value by Fernández (2005). K-values below 1.2

Annex 16: Sensitivity analysis for filter continuity; removal of isolated points

Table 0-4: Sensitivity analysis for filter continuity. It was carried out to assess the radius, the minimum number of points and the angular distance for set 1.

Radius (m)	Minimum number of points	Angular distance (º)	Comments
0.2	6	15	Too small radius. Small discontinuity planes are filtered
0.2	6	20	Too small radius. Small discontinuity planes are filtered
0.4	5	20	Much vegetation and very irregular surfaces are not filtered
0.4	6	15	Filtration of a reasonable amount of vegetation Small discontinuity planes are not eliminated
0.4	6	20	Filtration of a reasonable amount of vegetation Small discontinuity planes are not eliminated
0.4	6	30	Filtration of a reasonable amount of vegetation Small discontinuity planes are not eliminated
0.4	10	20	Vegetation but also small discontinuity planes are eliminated
0.4	10	30	Vegetation but also small discontinuity planes are eliminated
0.6	6	20	Much vegetation and very irregular surfaces not filtered

Table 0-5: Sensitivity analysis for filter continuity. It was carried out to assess the radius, the minimum number of points and the angular distance for set 2.

Radius (m)	Minimum number of points	Angular distance (º)	Comments
0.4	6	20	Much vegetation and very irregular surfaces not filtered
0.4	10	30	Much vegetation and very irregular surfaces not filtered
0.6	10	20	Much vegetation and very irregular surfaces not filtered
0.6	10	30	Much vegetation and very irregular surfaces not filtered
1	20	20	Much vegetation and very irregular surfaces not filtered
1	20	30	Vegetation but also discontinuity planes are eliminated
1	40	15	Vegetation but also discontinuity planes are eliminated
1	40	20	Filtration of a reasonable amount of vegetation. Small discontinuity planes are not eliminated.
1	40	30	Much vegetation and very irregular surfaces not filtered

Annex 17: Sensitivity analysis for the definition of discontinuity sets

Table 0-6: Sensitivity analysis for the definition of the discontinuity sets. It was carried out to assess the minimum spacing required to define planes belonging to set 1 for approach A.

Distance D (m)	Angular tolerance α (º)	Resulting spacing (m)	Comments
1	8.63	0.15	Over-segmentation
1	11.54	0.20	Over-segmentation
1	14.48	0.25	Well-fitted surfaces
1	17.45	0.3	Under-segmentation
1	20.48	0.35	Under-segmentation
1	23.6	0.4	Under-segmentation
1	26.74	0.45	Under-segmentation
1	30	0.5	Under-segmentation

Table 0-7: Sensitivity analysis for the definition of the discontinuity sets. It was carried out to assess the minimum spacing required to define planes belonging to set 1 for approach B.

Distance D (m)	Angular tolerance α (º)	Resulting spacing (m)	Comments
1	5	0.10	Over-segmentation
1		0.20	Over-segmentation
		0.3	Over-segmentation
1	24	0.4	Well-fitted in planes formed by more than 40 points
		0.5	Under-segmentation
1	30	0.6	Under-segmentation

Annex 18: Calculation of areas, lengths and spacings of discontinuity sets; application to the different scenarios

Zone 1

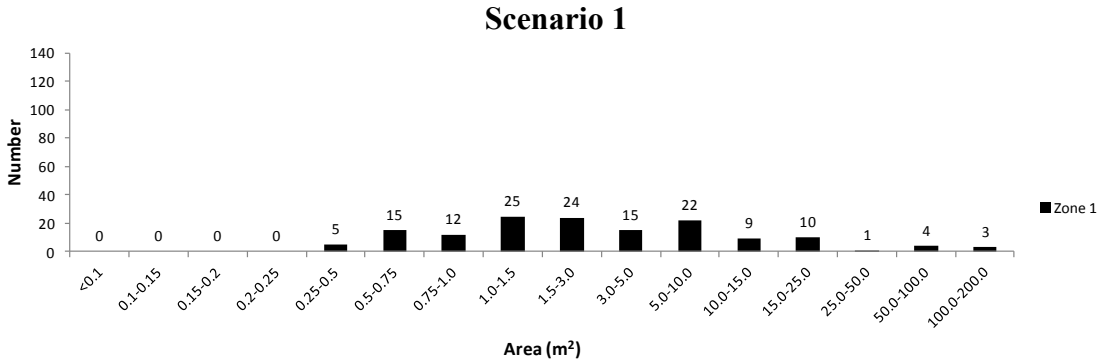

Figure 0-64: Discontinuity areas of set 1 defined in zone 1 for scenario 1. A total of 145 planes have been obtained.

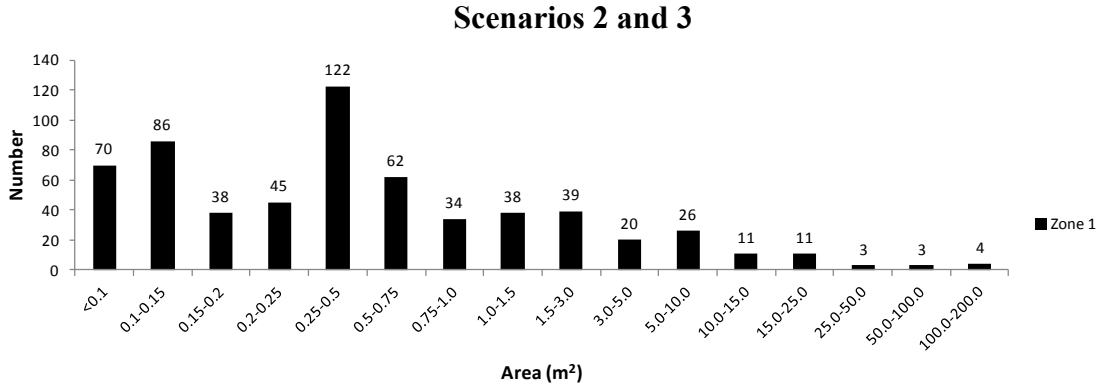

Figure 0-65: Discontinuity areas of set 1 defined in zone 1 for scenarios 2 and 3. A total of 612 planes have been obtained.

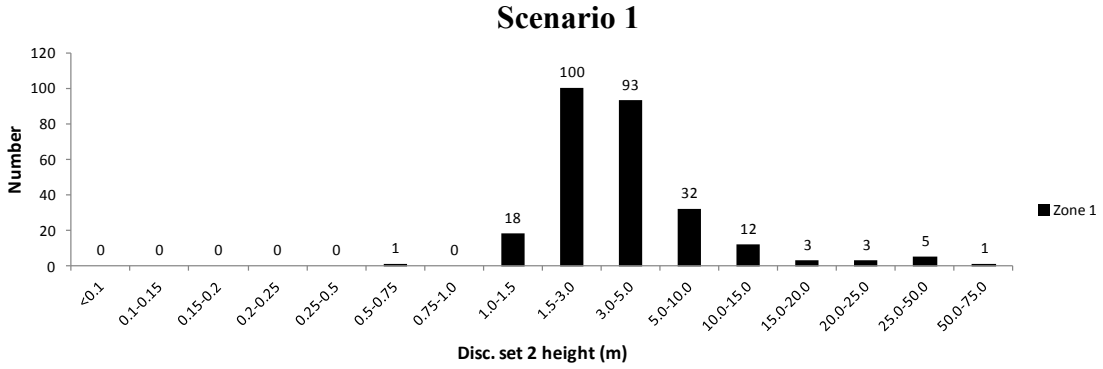

Figure 0-66: Discontinuity length of set 2. 268 planes belonging to zone 1 have been obtained. It has been used as an approximation of the rockfall scar height in scenario 1.

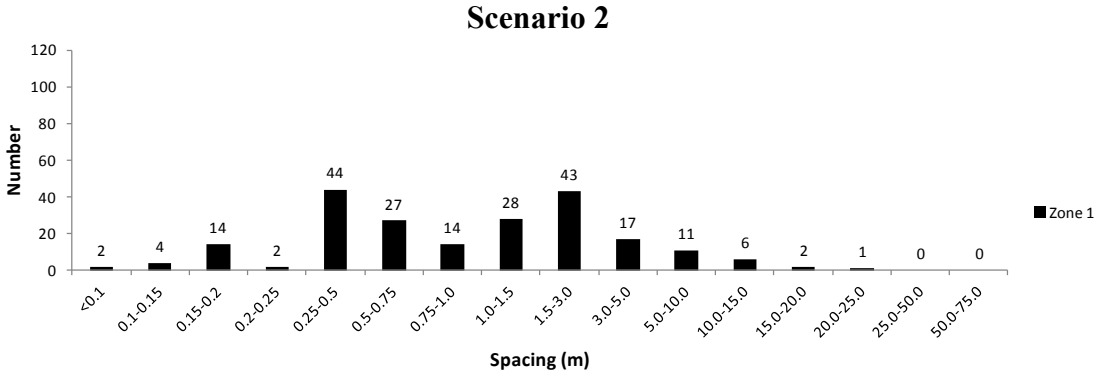

Figure 0-67: Spacings of set 1 measured between 215 consecutive discontinuities belonging to zone 1. It has been used as an approximation of the rockfall scar height in scenario 2.

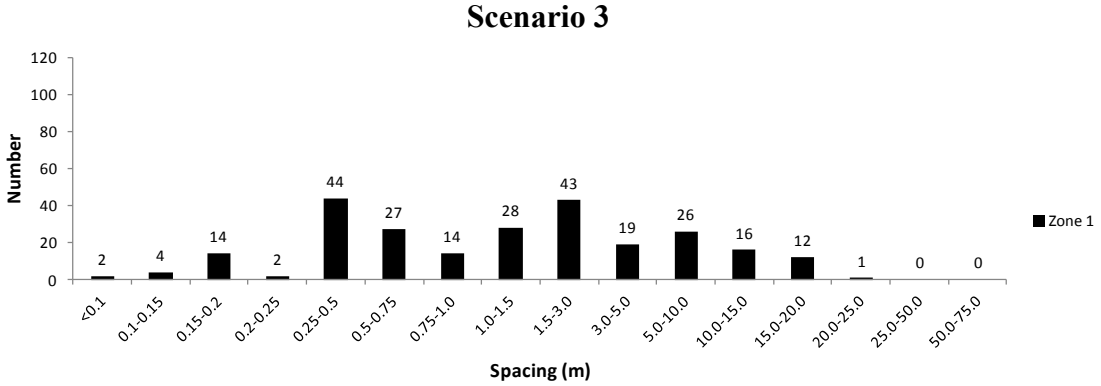

Figure 0-68: Spacing of set 1 measured between 252 discontinuities belonging to zone 1. It has been used as an approximation of the rockfall scar height in scenario 3.

Zone 2

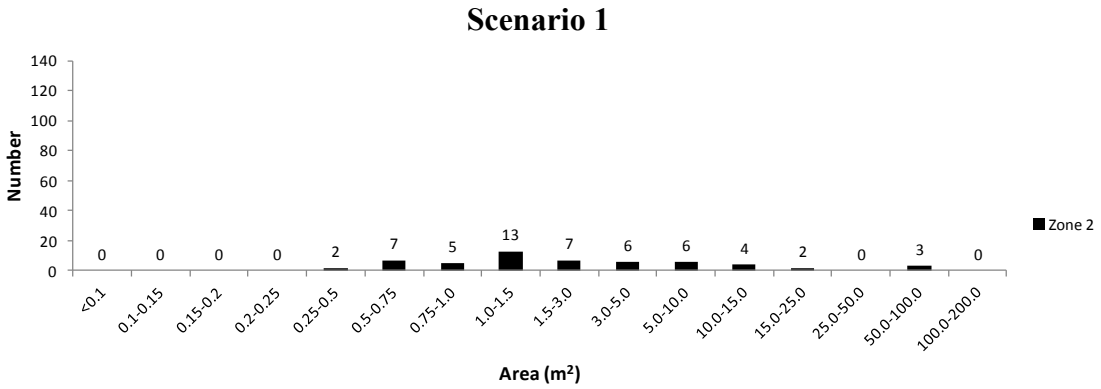

Figure 0-69: Discontinuity areas of set 1 defined in zone 2 for scenario 1. A total of 55 planes have been obtained.

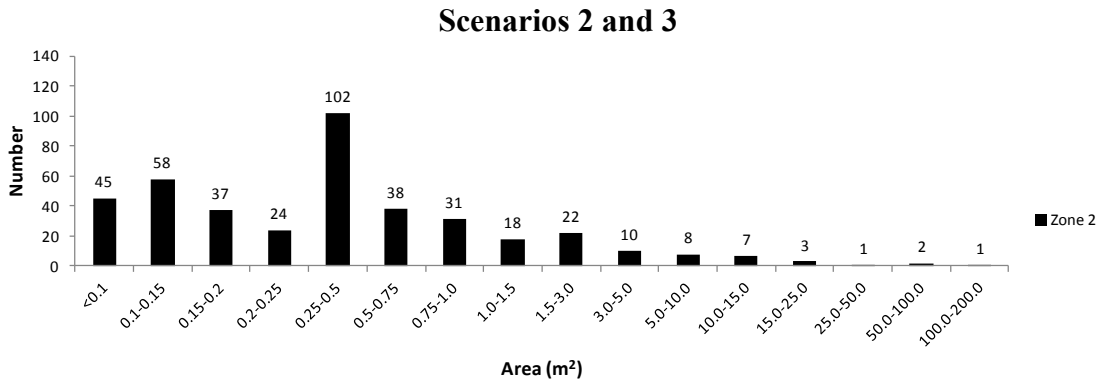

Figure 0-70: Discontinuity areas of set 1 defined in zone 2 for scenario 2 and 3. A total of 407 planes have been obtained.

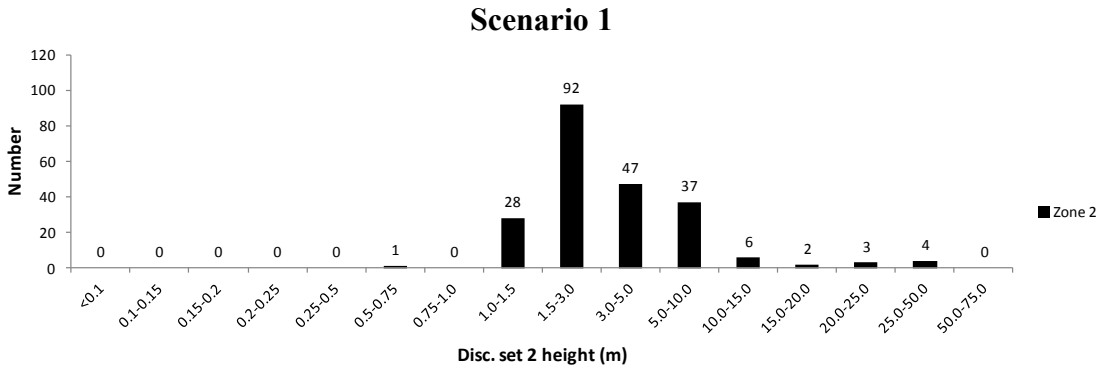

Figure 0-71: Discontinuity lengths of set 2. A total of 220 planes belonging to zone 2 have been obtained. It has been used as an approximation for the rockfall scar height in scenario 1.

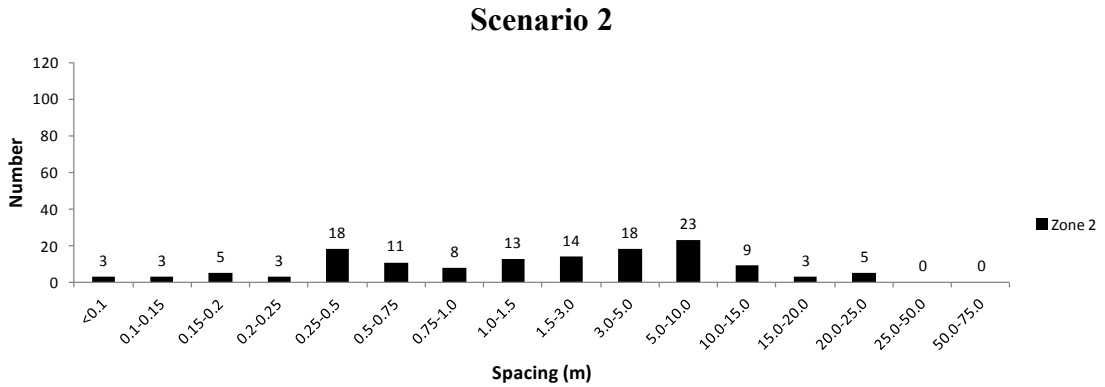

Figure 0-72: Spacing of set 1 measured between 136 consecutive discontinuities belonging to zone 2. It has been used as an approximation of the rockfall scar height in scenario 2.

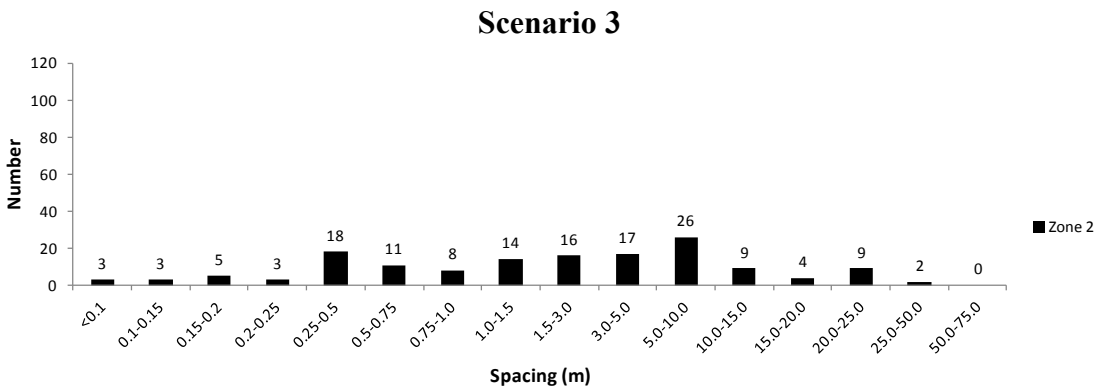

Figure 0-73: Spacing of set 1 measured between 148 discontinuities belonging to zone 2. It has been used as an approximation of the rockfall scar height in scenario 3.

Annex 19: DATING WITH IN SITU TERRESTRIAL COSMOGENIC ISOTOPES

1 Introduction

Although cosmic radiation was discovered in 1912 by Austrian physicist Victor Hess, it was in 1955 when Raymond Davis and Olivier A. Schaefer (Davis and Schaeffer, 1955) proposed the use of cosmogenic nuclides, formed within minerals in the earth surface, for geology purposes.
Further developments in nuclear methods have become crucial in geomorphology when concerning the study of sedimentation and erosion rates and surface exposure ages (Lal and Arnold, 1985; Phillips et al., 1986).
"In a search for an analogy to teach his geomorphology class about terrestrial cosmogenic nuclides (TCN) dating, professor Edward Evenson used the clever imagery of measuring the degree of redness on a person's skin to estimate the duration of exposure to sunlight" (Gosse and Phillips, 2001). The term terrestrial is used to refer to cosmogenic nuclides produced within rocks or minerals at the surface (or close). We differentiated them from those nuclides produced in the atmosphere (meteoric or atmospheric) whose production rates of nuclides are several orders of magnitude higher than at the Earth's surface (Dunai, 2010).
The method is based in the formation of radioactive nuclides within minerals by cosmic radiation exposition. Galactic cosmic rays (GCR) originates from outside the solar system, due to super nova explosions, which are estimated to have a return period of 50 years in our galaxy (Diehl et al., 2006). It consists of high-energy protons (87%), α-particles (12%) and heavier atomic nuclei (1%) (Dunai, 2010). Interaction of this primary cosmic-ray flux with nuclei of atoms in the atmosphere produces spallation reactions, which are the predominant nuclear reaction, creating a cascade of secondary radiation that penetrates through the atmosphere (nucleonic component). Most of the nucleonic cosmic-ray flux that reaches the surface of the earth consists of neutrons as they do not suffer ionization losses (Lal and Peters, 1967). On the other hand, collision of primary cosmic rays produces mesons as well (mesonic component). They are mostly pions which decay to muons (Eidelman et al., 2004). Finally, a third component named electromagnetic component also exists but it has a tiny contribution concerning geological applications (Figure 0-74).
Three main cosmogenic production mechanisms exist depending on the energy of neutrons and muons: A) Spallation is a high-incident energy process in which a neutron collides with a target nucleus (e.g. a calcium atom) and sputter off protons and neutrons from the target nucleus producing several lighter particles and leaving a lighter residual nucleus (e.g. ^{36}Cl). Such a reaction is produced forming an intranuclear cascade (Serber, 1947; Filges et al., 2001). As energy is lost, neutrons pass through the epithermal energy to become thermal neutrons (Phillips et al., 2001). When these neutrons are absorbed, by the nuclei of atoms they encounter, it results in the formation of B) thermal-neutron-produced cosmogenic nuclides The presence of radioactive elements such as uranium, thorium and samarium (α-particles source) within rocks can derive into thermal neutrons formation, as well, (Andrews and Kray, 1982) and the consequent production of cosmogenic nuclides. Finally, negative and fast muons of thermal energy can be captured by atom nucleids giving rise to the C) Muon absorption mechanism. Muons have a higher penetrating power in the subsurface than neutrons because of their poor interaction with matter (Dunai, 2010). Therefore, they are responsible for the main production

of cosmogenic nuclides at great depths.

Dating with in situ TCN is not an easy task as it requires a precise knowledge of local cosmogenic nuclides production rates which are affected by variations in the Earth's magnetic field, atmospheric depth, surrounding topography, surface coverage, sample thickness and sample orientation. These factors must be considered and corrections have to be carried out when estimating TCN production rates from different areas. Most widely used TCN are ^{3}He, ^{21}Ne, ^{14}C, ^{10}Be, ^{26}Al, and ^{36}Cl. In order to homogenise and uniform the use of TCN, two major networks in the US and Europe, respectively, were carried out: CRONUS-Earth (Cosmic-Ray Produced Nuclide Systematics) (NSF funded project) and CRONUS-EU (Stuart and Dunai, 2009).

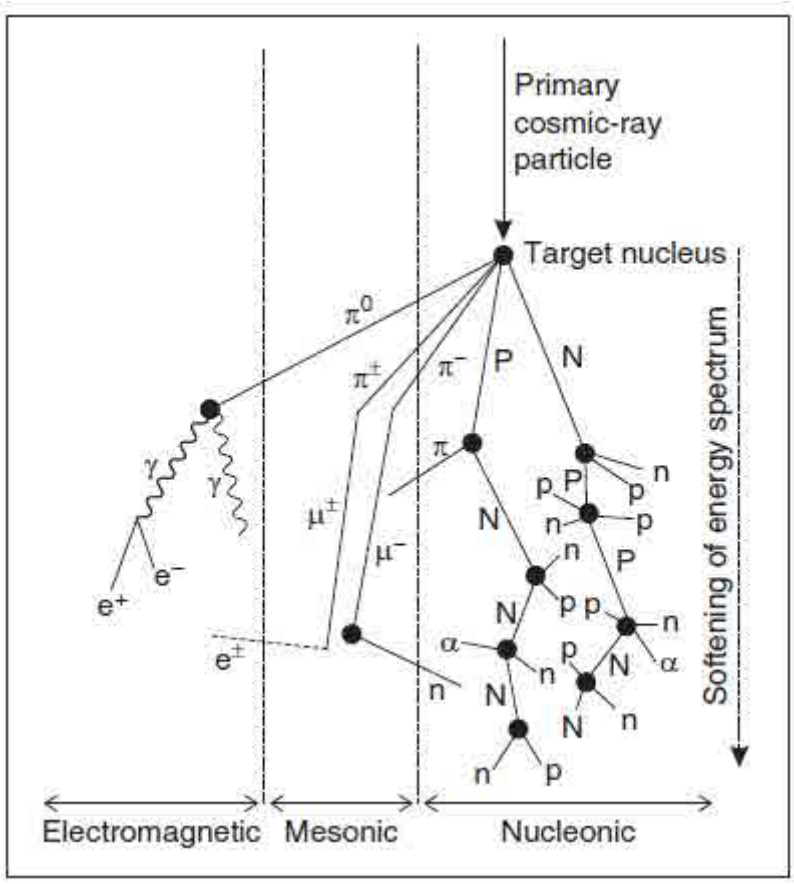

Figure 0-74: Cascade of secondary radiation produced by the interaction of primary cosmic-ray flux with nuclei of atoms in the atmosphere. P (proton), n (neutron), π (pion), μ (muon), α (alpha particles), $e^{\pm}$ (electron), γ (gamma-ray photon) (After Simpson and Fagot,1953).

2 Cosmogenic Isotopes Characteristics

8.2.1 Beryllium-10

^{10}Be is one of the most used cosmogenic isotopes for dating purposes due to its well constrained production rate, mostly on quartz, with a long half-life of 1.36±007Ma. In contrast, it exists, another cosmogenic radionuclide, ^{7}Be, which has a shortest half–life of 53 days to be used of dating purposes. ^{9}Be is the only stable nuclide.

^{10}Be is largely produced by spallation. Nucleonic production rates are generally too low to produce significant background concentrations except in Li, U and Th rich materials (Brown et

al., 1991). On the other hand, major problem when working with ^{10}Be is the high meteoric production, which is often much larger than the cosmogenic component (Brown et al., 1991; Klein et al., 1997; Kohl and Nishiizumi, 1992). Although several partial dissolution in HF must be done during the sample preparation, sometimes it is impossible to remove enough meteoric fraction as stated by Ivy-Ochs et al. (1998) who used pyroxene for ^{10}Be surface exposure dating. When working with calcite, clay-free material (e.g. well-crystallised material) is the best choice to avoid large amounts of atmospheric ^{10}Be (Merchel et al., 2008). It also can be found in olivine, magnetite and plagioclase.

8.2.2 Aluminium-26

Production of ^{26}Al, which has a half-life of 708±17ka, has been always tied with quartz and ^{10}Be production. Stable isotope ^{27}Al is very abundant; hence, the ^{26}Al/^{27}Al ratio is difficult to measure by Accelerator Mass Spectrometry (AMS). On the other hand, Merchel et al. (2010), measured ^{26}Al in calcite and quartz. Although the ^{26}Al production rate from calcite is much lower than from corresponding SiO_2, the ^{26}Al/^{27}Al ratio was in the same order due to the lower intrinsic ^{27}Al concentration. Moreover, working with an isotope produced mainly by spallation reduces the uncertainty of having several production pathways. It was also confirmed no influence by atmospheric ^{26}Al.

8.2.3 Chlorine-36

Two stable isotopes, ^{37}Cl and ^{35}Cl, exist with a natural ratio ^{37}Cl/^{35}Cl of 3.127. The half-life of ^{36}Cl is 301±2 ka (Holden, 1990).

Spallation of K, Ca, Ti and Fe, slow negative muon from K and Ca, and thermal and epithermal neutron capture by ^{35}Cl are the three main production pathways of ^{36}Cl. Hence, It will depend on the sample composition, mostly Ca, K and ^{35}Cl (75% of total chlorine in nature) (Schimmelpfennig et al., 2009), but also radiogenic elements such as U and Th. It means that several chemical analyses must be conducted to find out the percentage of the radiogenic and nucleogenic component contained in the sample. It could be a limitation in terms of low production rates. Furthermore, it needs to be established the contribution of each pathway to the ^{36}Cl production rate. For example, contribution of thermal neutrons is difficult to quantify due to the humidity, snow cover, surface geometry, and erosion.

Important differences in the estimation of production rates exist. Stone et al. (1996) calculated the ^{36}Cl production from calcium spallation, which was in excellent agreement with previous whole-rock calibration measurements at the same place. Braucher et al. (2011) determined the contribution of the muon-induced productions to the total production under natural conditions for ^{36}Cl, ^{10}Be and ^{26}Al concluding that parameters mostly used to quantify them, significantly overestimate muon-induced productions. Schimmelpfennig et al. (2009) evaluated the role of the mineralogy in the ^{36}Cl production and created an excel spreadsheet to calculate the exposure age of an uneroded or the exposure age or erosion rate of a sample from an eroding surface.

3 Calculation of production rates

The production rate of the nuclide of interest is the number of atoms produced per gram of target material per year [atoms/g/a]. As it is not possible to have available cosmogenic nuclides production rates everywhere, the most common procedure is to calculate them from well-dated places, scaled to sea level and high latitudes (SLHL).

According to Gosse and Phillips (2001) production rates can be determined by three general

methods: A) with geological calibration, from different rock surfaces with a known simple exposure history, B) experimentally by laboratory measurements of samples that have been exposed to secondary cosmic radiation at high latitudes for periods of years or placed into a nuclear accelerator beam line of particles which simulated such a secondary cosmic radiation. Finally, C) numerical simulation or processes involved in the nuclides production. Geological calibration is the most common process used to estimate it. These production rates are calculated and subsequently scaled to SLHL, in a horizontal and flat surface using different scaling factors. They also depend of the cosmogenic isotope, the production pathway and the target element. Discrepancies in different values can be attribute to the different scaling factors used but also to the different production ways when working with ^{36}Cl. Some of them are reported in Table 0-8.

Table 0-8: Production rates of several cosmogenic isotopes calibrated at sea level and high latitudes using various scaling methods that can be find in the literature.

Nuclide	Target	Production pathway	Rate (atom g^{-1} target element a^{-1})	Reference
^{36}Cl	K	Spallation	154	(Phillips et al., 1996)
^{36}Cl	Ca	Spallation	48.8	(Stone et al., 1996)
^{36}Cl	Ca	Spallation	66.8	(Phillips et al., 2000)
^{36}Cl	Ca	Total production	91.5	(Swanson and Caffee, 2001)
^{36}Cl	Ca	Spallation	57.5	(Licciardi et al., 2008)
^{36}Cl	Ca	Spallation	42	(Braucher et al., 2011)
^{36}Cl	Ca	Spallation	42.2	(Schimmelpfennig et al., 2011)
^{36}Cl	K	Spallation	124.9	(Schimmelpfennig et al., 2011)

4 Scaling and correction factors

Earth's magnetic field, atmospheric depth, topographic shielding, snow coverage, sample thickness, sample position and geometry contribute to vary the irradiation conditions and, therefore, the cosmogenic production rates. These differences must be taken into account and quantified.

The earth's magnetic field partly shields the surface from primary cosmic ray particles (Dunai, 2000). This cosmic ray flux is deflected being maximum at high latitudes and minimal in the magnetic equator. Furthermore, temporal variation in the earth's magnetic field has been observed and authors like Dunai (2000) and Dunai (2001) suggested methods to calculate the average paleo-inclination for young samples (less than 20000 years). Therefore, changes in the nuclide production rates are latitude dependant (Lal, 1991). On the other hand, cascade of secondary radiation is attenuated with atmospheric depth reducing the radionuclide production exponentially.

One of the most widely used scaling factors are the polynomials of Lal (1991). It is latitude, altitude dependant scaling factor for spallogenic and muogenic production. Several

discrepancies exists as Lal (1991) use elevation as a proxy of atmospheric depth assuming a standard atmosphere approximation (Vermeesch, 2007). It could entail great deviations in regions of persistent high or low pressure (e.g. Antarctica) (Stone, 2000). Instead, Stone (2000) used the air pressure and special Antarctic atmosphere. His scaling factor allows calculating muons production independently. Dunai (2000) worked directly with the atmospheric depth separating also the spallogenic pathway from the muonic one.
The existence of a surrounding relieve produces a decrease in the overall rate of production and a change in the effective attenuation length (Dunne et al., 1999). Cosmic ray flux intensity in a flat horizontal surface will be reduced by surrounding topography as indicated in Equation 0-1.

$$I(\phi) = I_{max} \sin^{2.3} \phi$$

Equation 0-1

Effective attenuation length can be defined from the weighted average of all penetration depths. A dipping surface has a shorter effective attenuation length, but an horizontal surface will have a longer effective attenuation length (Figure 1.1). Furthermore, when working with a sloping surface, the foreshortening effect, reduction of effective surface and topographically shielding of the slope above portion must be considered (Gosse and Phillips, 2001) (Figure 0-76). According to Dunne et al. (1999), for a large, vertical slope, such as a cliff face, the surface rate of production is half that for a horizontal surface with no obstructions. Several attempts have been done in order to create calculators for topographic scaling assessment. Some of them can be found in the work of Codilean (2006) called "Calculation of the cosmogenic nuclide production topographic shielding scaling factor for large areas using DEM's". Another geometric shielding calculator was created within the CRONUS-Earth project. It allows to asses the shielding due to the surrounding topography and the sample slope. Areas where snow cover could be present, TCN production rate must be corrected. It depends on temporal variation in depth. Typical corrections for 4 months of shielding by snow of different depths and densities are shown for spallogenic nuclide in Figure 0-77 (Gosse et al., 1995; Licciardi et al., 1999).

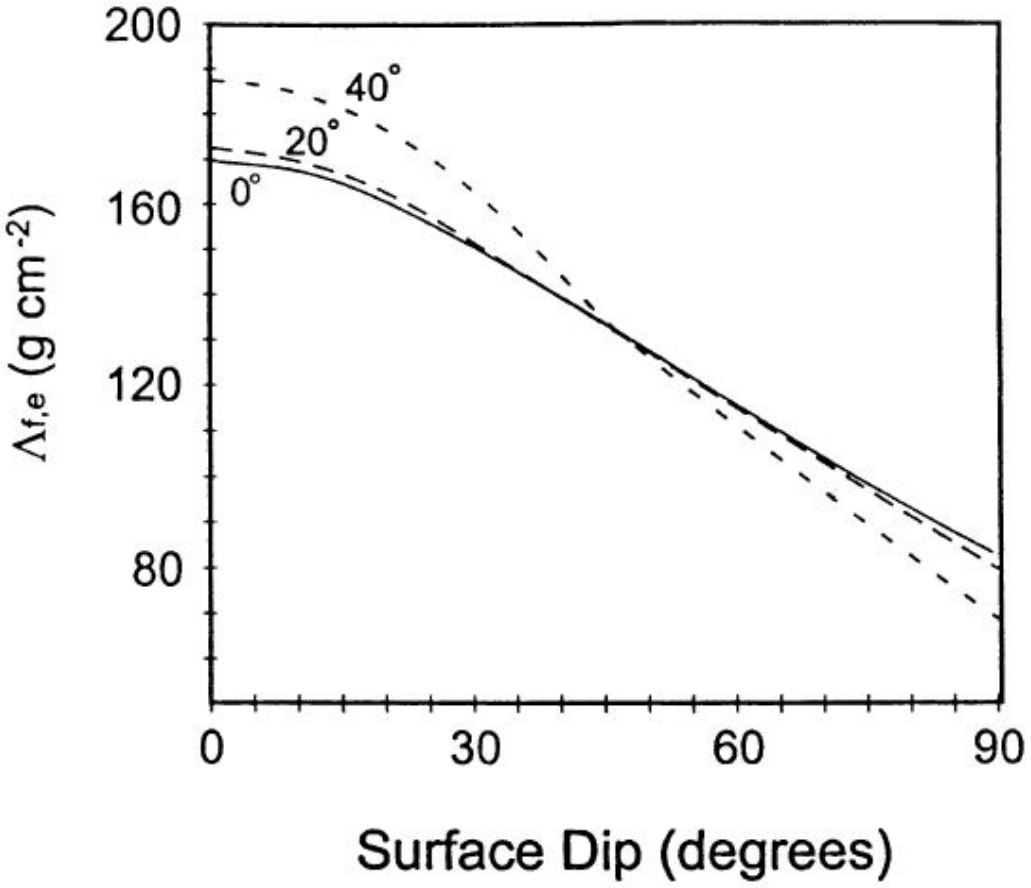

Figure 0-75 Effective attenuation length as function of surface dip and shielding topography (Gosse and Phillips, 2001).

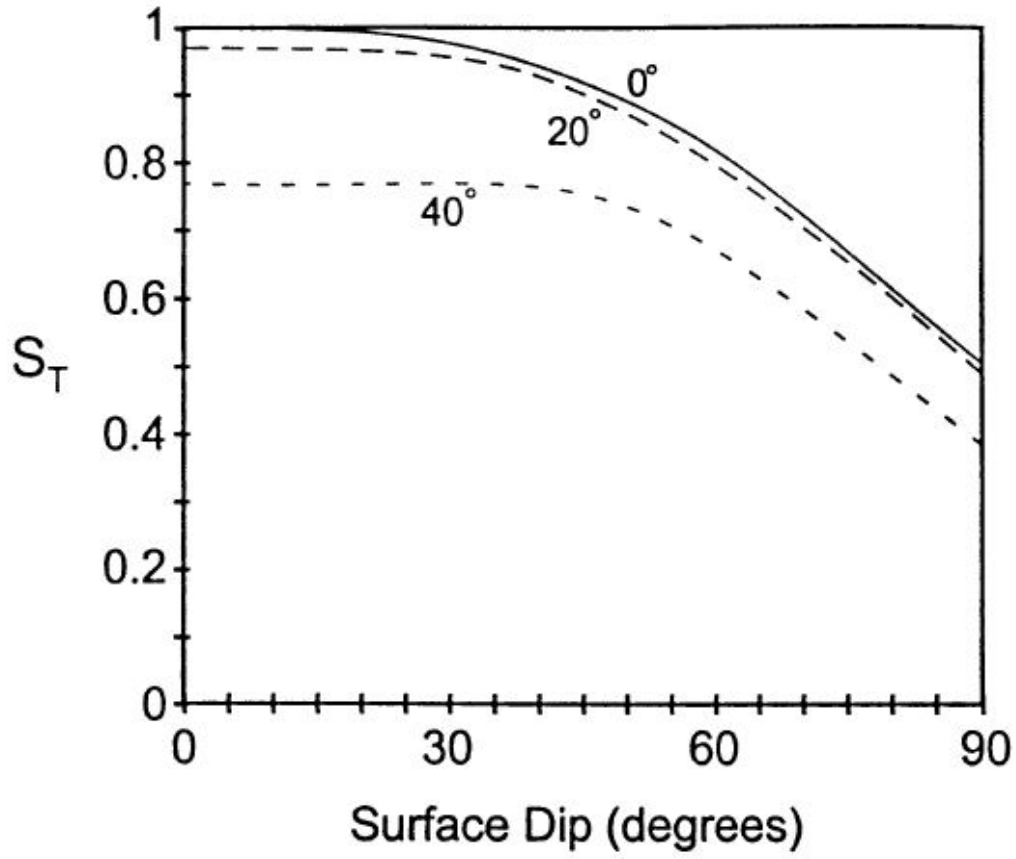

Figure 0-76: Total topographic scaling (S) as a function of surface dip angle and topographic shielding (Gosse and Phillips, 2001).

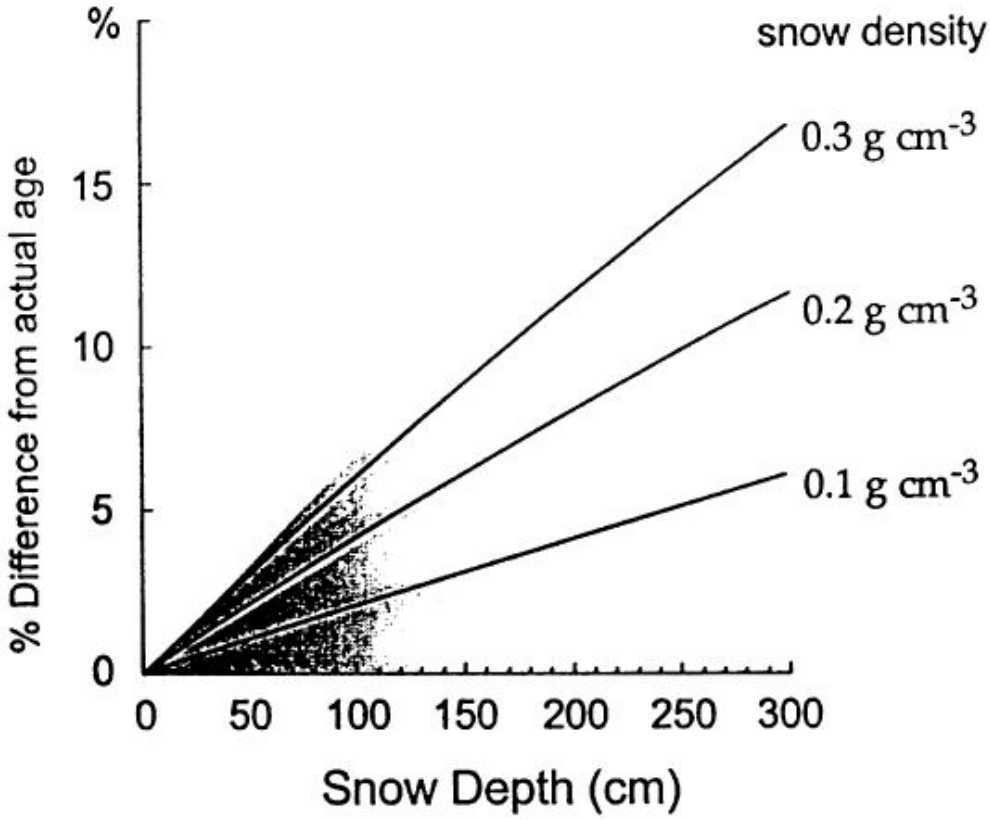

Figure 0-77: Effects of shielding by snow of common densities and thickness. Calculated for a spallogenic nuclide, assuming an otherwise simple exposure, with snow shielding instantaneously applied for 4 months each year. This is a multiplicative effect so the deviation can apply to any exposure age (Gosse and Phillips, 2001).

Sample thickness needs to be corrected as production rates are evaluated in the rock surface but samples collected in the field are of finite thickness with a production rate varying from the top. Gosse and Phillips (2001) obtained the correction factor integrating the production rate over the actual sample and divided it by the surface production:

$$Q_{i,m} = \frac{P_{i,m}}{P_{i,m}(0)} = \frac{\int_0^{Z_s} P_{i,m} dZ}{Z_s \, P_{i,m}(0)}$$

Equation 0-2

where $Q_{i,m}$ refers to the *i*th reaction producing the *m*th nuclide and Z_s is the thickness of the sample. However, such a procedure is only valid when the top of the sample is located in the surface. Schlagenhauf et al. (2010) recalculated the thickness factors as a function of depth. They are defined at the sample centre and allows to evaluated samplesm which are not located exactly in the surface. These scaling factors are used in Schimmelpfennig et al.(2009).
Finally, the production rate of some isotopes like ^{36}Cl is affected by the chemical sample composition (mainly Ca, K, Ti, Fe, H, Li, B, Sm, Gd and Cl) as these elmens affect the different production mechanisms. Furthermore, radiogenic elements as U and Th will also contribute to the production of ^{36}Cl since during its disintegration processes, fluxes of neutrons are generated

and can be captured by ^{35}Cl to produce ^{36}Cl. Therefore, its content in samples must be quantified.

5 Calculation of exposure age

A prerequisite for the application of the in situ nuclides for the study of erosional histories of surfaces is a knowledge of their production rates under different irradiation conditions: altitude, latitude, irradiation geometry and shielding (Lal, 1991). Given the different production paths, scaling, and correcting factors, the total production rate [atoms/g/a] of an uneroded rock sample of infinite thickness at mass depth z [g/cm2] is given by (Schimmelpfennig et al., 2009):

$$P_{total}(z) = S_{el,s}F_sQ_sP_s(z) + S_{el,\mu}F_\mu Q_\mu P_\mu(z) + S_{el,n}F_n\left(Q_{eth}P_{eth}(z) + Q_{th}P_{th}(z)\right) + P_r$$

Equation 0-3

Subscripts refer to the type of reaction: $_s$ for spallation, $_n$ for capture of low-energy neutrons and $_\mu$ for capture of slow negative muons, $_{eth}$ for epithermal neutron capture, $_{th}$ for thermal neutron capture and $_r$ for radiogenic production. $S_{el,s}$, $S_{el,n}$ and $S_{el,\mu}$ is the scaling factor for nucleonic production as a function of elevation and latitude. F_s, F_n, and F_μ correspond topographic shielding, snow shielding and geometry. Q factor refers to the sample thickness correction of a sample with a mass depth z. The total number of atoms of a specific isotope per grams of sample is

$$N_{total} = P_{total}(z)\left(1 - \exp^{-t\lambda}\right)/\lambda$$

Equation 0-4

Where t is the exposure time of the sample and λ is the decay constant of the isotope. Hence, the exposure time of a sample will be

$$t = (-\ln(1 - N_{total}\lambda/P_{total}(z)))/\lambda$$

Equation 0-5

6 Objective

The objective of this work is dating different limestone surfaces from a cliff in order to understand its temporal distribution. Such surfaces are scars resulting from rock detachments when having a rockfall. These scars do not appear randomly, but they belong to the discontinuity plains forming the massif. Being able to date each scar provides valuable information about the exact moment when the rockfall occurred. Furthermore, if some samples present a similar age it can be supposed that they belonged to the same surface at a certain time. It is a part of a bigger project consisting in assessing the rockfall frequency as a previous step to the evaluation of the rockfall hazard.

7 Procedure

Steps to carry out this work have been: A) Selection of the study area and sampling, B) Sample pre-treatment and previous analysis, C) Sample preparation for ^{36}Cl measurement by AMS D) Determination of chemical composition analysis of bulk rock and target fraction, E) Obtaining scaling and correction factors, F) accelerator mass spectrometry (AMS) measurements and G) calculation of exposure ages.

Selection of the study area and sampling

The area of study is located in the Montsec range, Spain (Northeastern Pyrenees) within the Montsec thrust, in the central part of the south Pyrenean Unit (Seguret, 1972). Developed during the Eocene Epoch (Soriano et al., 2006), it is oriented E-W with an extension about 40km. In the frontal part of the unit, where the slope is located, outcrop materials from the Upper-cretaceous (Caus et al., 1999). Such a cliff is made of limestones which are not very fractured (Figure 6-3). It is being affected by rockfalls since several scars from detached blocks can be recognized in the wall as well as fallen boulders at the bottom, mostly covered by vegetation. It is located at 1200m high with a Mediterranean continental climate.

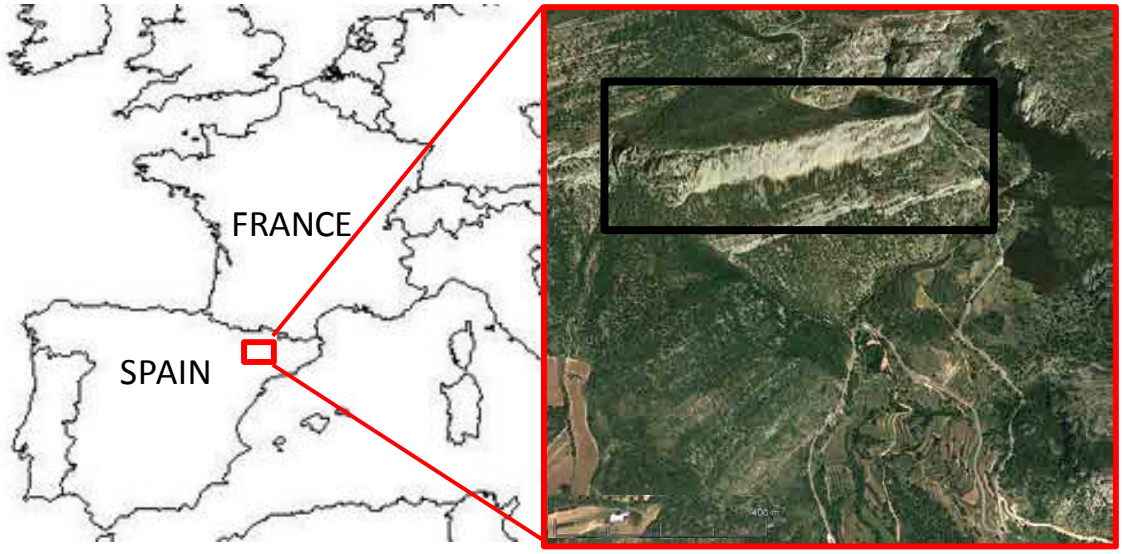

Figure 0-78: Area of sutdy.

The objective was to collect samples belonging to different scars from different periods of time. Criteria used to establish this first approach was based on the colour and relative position of scars. A first simply test was done adding a drop of HCl (10%) to the samples and observing its reaction to ensure that the carbonate component was sufficient to work with ^{36}Cl as not a lot of quartz was detected to work with ^{10}Be and the other isotopes did not seem to be appropriate.

When sampling, some aspects have been considered as stated in Gosse and Phillips (2001). Latitude, longitude and sample position (dip and dip direction) have been measured as well as the geometry to be extracted (slab). Nine samples from rock scars were collected considering it is an appropriate batch to be treated later (Figure 0-79, Figure 0-80, Figure 0-81, Figure 0-82, Figure 0-83, Figure 0-84, Figure 0-85, Figure 0-86, Figure 0-87 and Figure 0-88). In Table 0-9 some characteristics are shown.

Most of the samples are vertical or almost vertical (dip angle) because we are working in a cliff. They have an average dip direction angle of 161º (NESW oriented) and are located in an altitude about 1000 m. Coordinates are referenced according to the referencing system

ED50/UTM 31N.

Figure 0-79: Places from where samples were extracted. Labels indicate the sample number.

Figure 0-80: Position of sample 1 indicated with a black dot.

Figure 0-81: Position for sample 2 indicated with a black dot.

Figure 0-82: Position of sample 3 indicated with a black dot.

Figure 0-83: Position of sample 4 indicated with a black dot.

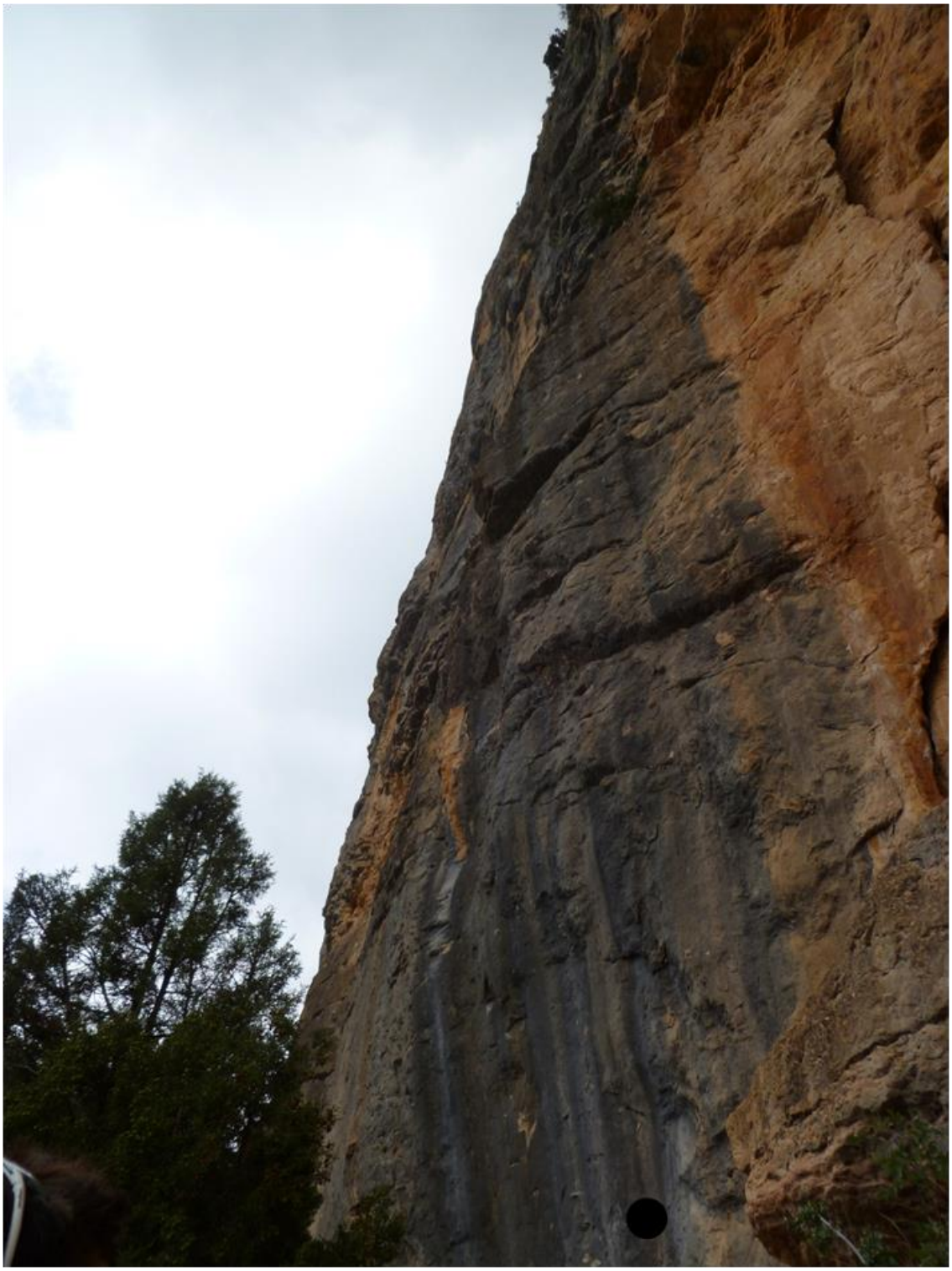

Figure 0-84: Position of sample 5 indicated with a black dot.

Figure 0-85: Position of sample 6 indicated with a black dot.

Figure 0-86: Position of sample 7 indicated with a black dot.

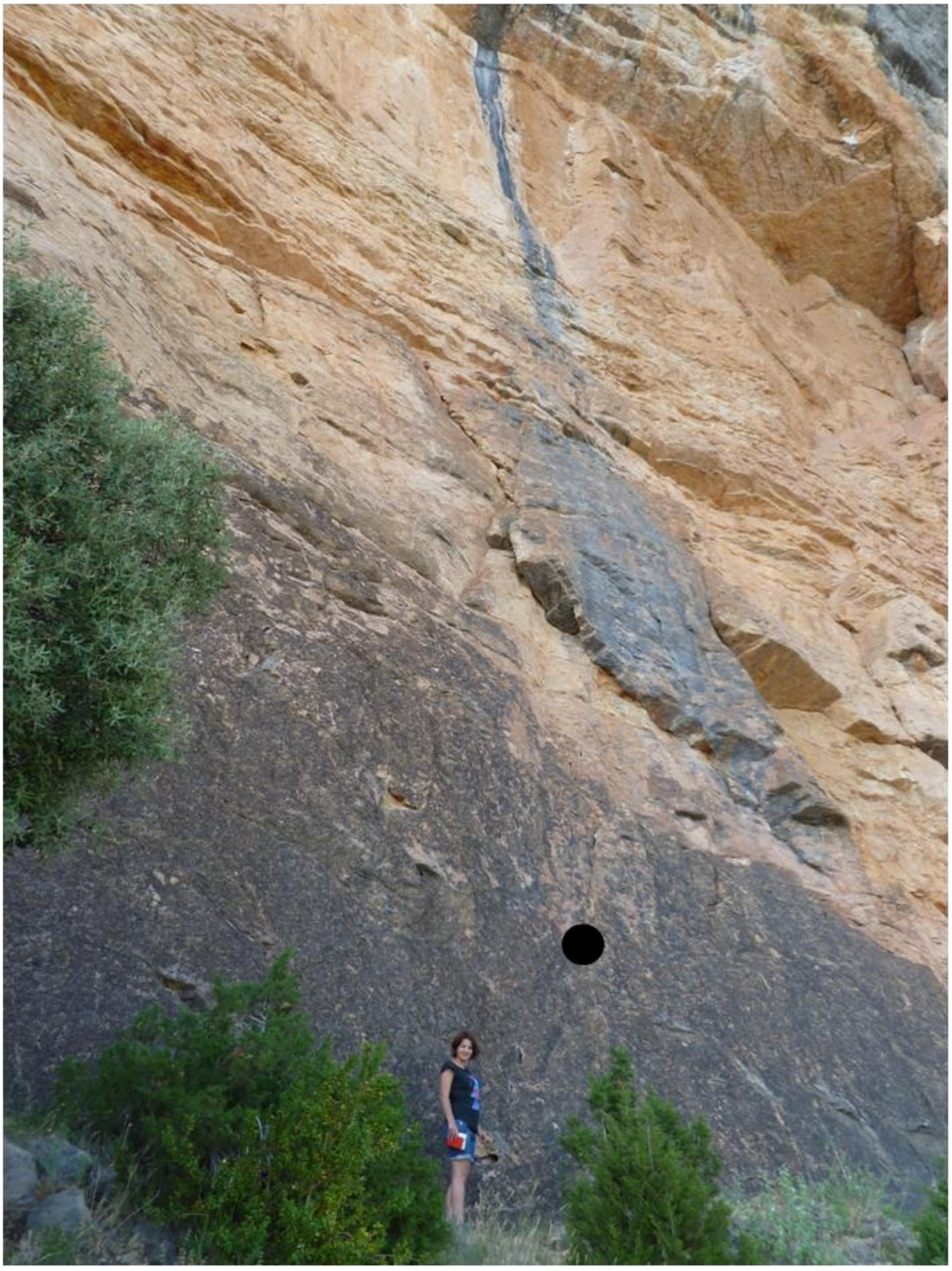

Figure 0-87: Position of sample 8 indicated with a black dot.

Figure 0-88: Position of sample 9 indicated with a black dot.

Table 0-9: Sample characteristics. X and Y coordinates according tot the referencing system ED50/UTM 31N

Sample	Dip Direction (º)	Dip angle(º)	X (m)	Y (m)	Z (m)	Lat (º)	Long (º)
1	130	70	337030	4654573	1025	42	1
2	120	65	337010	4654559	1025	42	1
3	170	69	336976	4654543	1050	42	1
4	135	90	336976	4654540	1025	42	1
5	140	85	336934	4654520	1025	42	1
6	170	90	336931	4654523	1050	42	1
7	250	75	336700	4654424	1075	42	1
8	160	73	336687	4654410	1100	42	1
9	170	79	336546	4654345	1075	42	1

Sample pre-treatment and previous analyses

This part of the work was carried out in the Geomar company lab. A calcimetry (according to the UNE 103-200-93) was performed to quantify the amount of calcium carbonate in each sample. It is a fast, cheap and easy analysis that provides a first approximation of material to be crushed as a minimum of 100 g of $CaCO_3$ are needed for each sample. Two portions of each rock surface were analysed. Information about calcite content in each sample is shown in Table 0-10. Most of samples present carbonate content higher than 80%. Hence, in most cases, 125 g of sample will be enough for ^{36}Cl extraction.

Table 0-10: Calcimetry results in each sample. Two analysis were applied in each rock surface. Samples contain an average amount of carbonate about 80%.

Sample	1a	1b	2a	2b	3a	3b	4a	4b	5a
calcite content (%)	87.9	88.9	84.3	84.7	81.8	79.6	82.3	82.7	78.4
Sample	5b	6a	6b	7a	7b	8a	8b	9a	9b
calcite content (%)	76.2	84.6	84.3	84.1	84.1	85.8	86	94.3	94.8

Thin sections of each sample were conducted to verify calcimetry results in the microscope (Figure 0-89). Most of the material is carbonate with some grains of quartz. A selective staining with Alizarin red was also conducted to differentiate between calcite ($CaCO_3$) and dolomite [$CaMg(CO_3)_2$]. Alizarin red dyes the calcium, in calcite, red but does not in the dolomite. It can be seen in Figure 0-90 as mostly of the dyed part of samples has become red due to the high content in calcite.

Therefore, it was assumed that calcimetry results were reliable and calcite amount was sufficient to work with ^{36}Cl.

First mm of samples were sawed to remove weathered or rusty surfaces noting the thickness of rock removed and the width (Figure 0-91) (Table 0-11). Finally, dry rock densities were measured using the Archimedes principle in the Technical University of Catalonia (UPC) lab (Table 0-11). Finally, rock samples were crushed to 250-1000 μm, as Dr. Merchel, from Helmholtz Zentrum Dresden Rossendorf (HZDR), indicated, first with a jaw crusher and then using a disc mill to reduce the grain size in the University of Barcelona facilities (UB). Afterwards, it was sieved until the desired grain size was achieved (250-1000 μm) (Figure 0-92). <80 μm fraction was collected for later chemical analysis as Dr. Padrós, from UB, suggested. The amount of each sample is shown in Table 0-12.

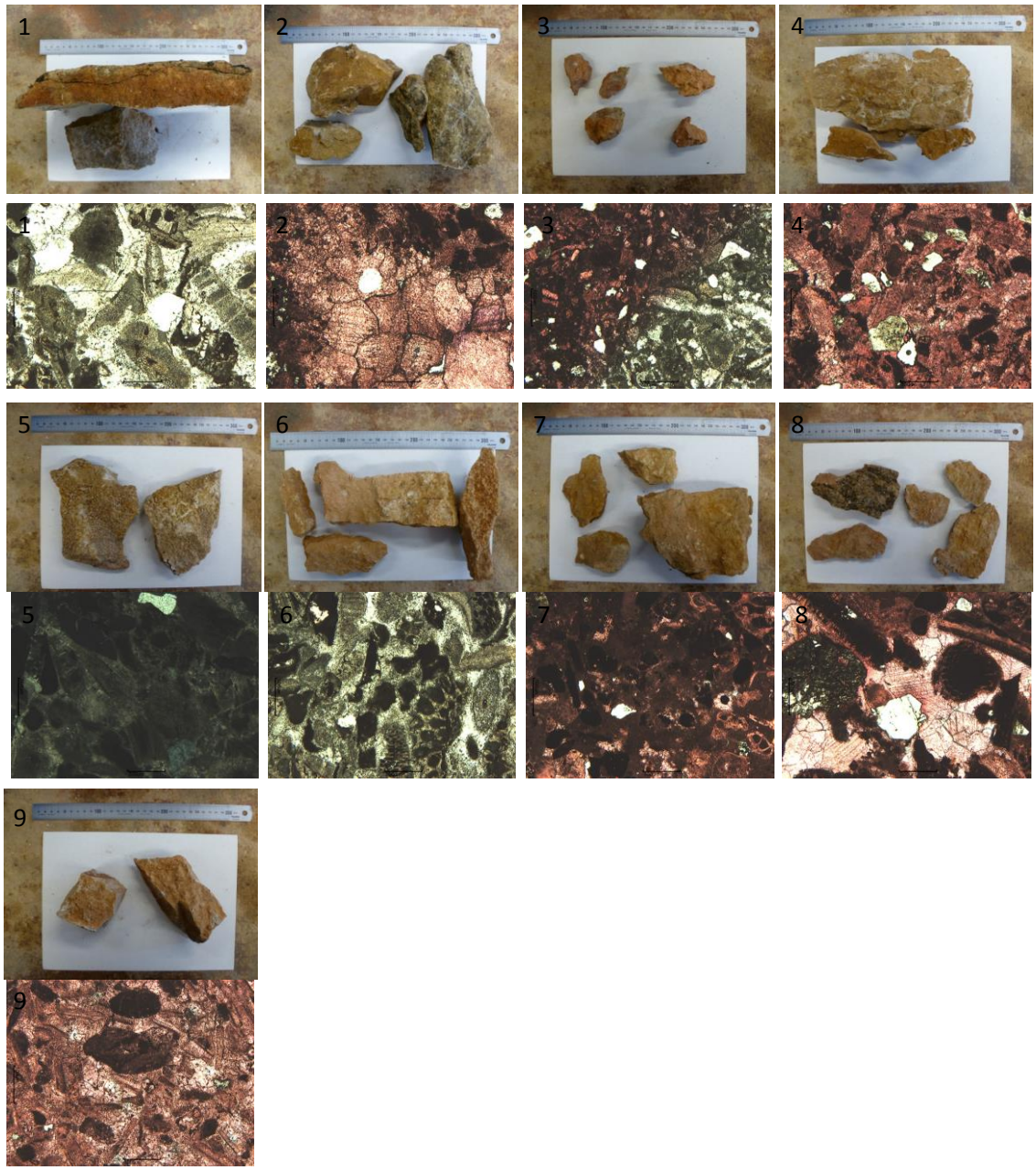

Figure 0-89: Labelled samples with their corresponding microscope view. In some samples, where the photo has been taken in the stained part, the high content in calcium carbonate is confirmed since the whole part has been coloured.

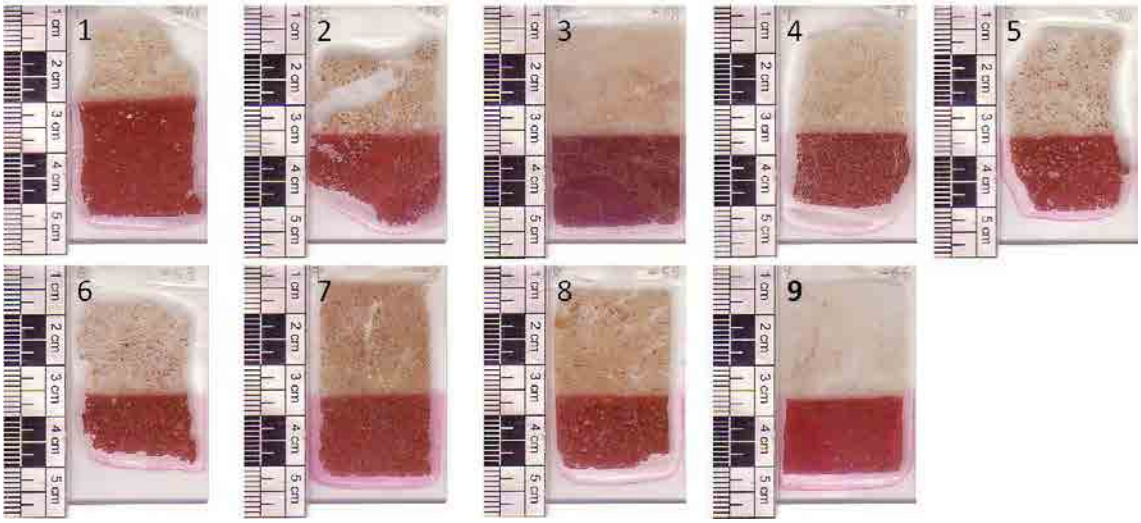

Figure 0-90: Coloured thin sections with Alizarin red due to their high content in calcite carbonate.

Figure 0-91: First millimetres of samples were sawn to eliminate rusty or weathered surfaces noting the thickness of soil removed.

Table 0-11: Density measurements, sample weight, rock removed and total sample thickness.

Sample	Sample weight [g]	Density [g/cm^3]	Rock removed [cm]	Sample thickness [cm]
1	24.09	2.61	0.8	1.85
2	24.07	2.55	0.55	2.75
3	30.8	2.63	0	2
4	22.76	2.57	0.25	2.5
5	17.51	2.56	0.25	1.45
6	23.63	2.58	1.05	3.4
7	37.44	2.63	0.6	2.8
8	21.81	2.63	0.1	1.6
9	18.28	2.63	0.6	3.25

Table 0-12: Samples's amount for ^{36}Cl analysis by AMS (250-1000 μm fraction) and bulk rock analysis (<80 μm fraction).

Sample	Weight (250-1000 μm fraction) [g]	Weight (<80 μm fraction) [cm]
1	207	20
2	186	23
3	142	19
4	189	23
5	168	19
6	190	17
7	179	14
8	185	11
9	211	28

Figure 0-92: Top-left: Jaw crusher used to reduce samples to an appropriate grain size to be introduced in the disc mill (top-right) to obtain the _nal grain size (250-1000 μm). Samples were stored in plastic (bottom) pots to be treated later.

Sample preparation for ^{36}Cl measurement by AMS

The applied chemistry has been carried out following the procedure described in Merchel et al. (2013). Basically, it is a variation of a procedure mainly developed at Rochester and Lawrence Livermore National Laboratory (LLNL), from works of Conrad et al. (1986) and Stone et al. (1996). Appropriate equipment and facilities as the ones of the Ion Beam Centre in HZDR, where this preparation has been conducted, are needed as well as experienced scientists as Dr. Silke Merchel.

A first pretest with 1 g of each crushed and sieved sample into 250-1000μm has been done to ensure the exact quantity of calcite in each sample. Previous analyses conducted in section "sample pre-treatment and previous analyses" have been extremely useful as a first estimation of calcite content concerning the suitability of the samples.

However, arrived at this point, more precise results are needed as exact amounts of material that will be used. Afterwards, two leaching processes with MilliQ water have been conducted to remove finer grains as clay and fine sand. A slow 10% dissolution of the acid-dissolve-particles

has been done. It removes atmospheric ^{36}Cl attacking the outside of each grain and reduces ^{nat}Cl (Merchel et al., 2008). A ^{35}Cl-enriched carrier ($^{35}Cl/^{37}Cl$=999) containing 1.5mg Cl has been added to each sample. Afterwards, a final dissolution of whole calcite is done. It must be very slow avoiding foam, since Cl could evaporate. Separation from residue and aliquot (for a later chemical composition analysis) is conducted. Such an aliquot will be analysed in order to know the content of Ca, Fe, K and Ti and correct its contribution to the ^{36}Cl production. First precipitation of AgCl is done by adding $AgNO_3$. Since ^{36}S is a ^{36}Cl isobar, which interfere in AMS measurements, it needs to be removed by adding $Ba(NO_3)_2$. $BaSO_4$ coprecipitates with $BaCO_3$ and it is eliminated. Finally, a second AgCl precipitation is done by adding $AgNO_3$ (Figure 0-93). Some data of the process can be found in Table 0-13. High content of sample loss during washing indicates poor sieving process, which should be improved if future studies exist.

Chemical composition analysis of bulk rock and target fraction

As it has been said before, production of ^{36}Cl also depends of different elements contained in rock samples. In order to quantify in a proper way its contribution is very important to know their concentration in each bulk rock sample but also in the target fraction. All the analyses were conducted in the "Technological and Scientific Centres" (CCIT) facilities using the <80 μm sample fraction. Major elements (Ca, K, Ti, Fe, Si, Na, Mg, Al, Mn and P) of bulk rocks were determined by X-Ray fluorescence (XRF) (Table 0-14). Water content must be estimated in each sample because rocks were quite dry, when they arrived in the lab. Cl content was determined by Ag titration obtaining 217 ppm. It was measured in one sample since its value does not affect considerably to the final result, particularly, when its concentration is low. Trace elements (Li, B, Sm, Gd, Th and U) from bulk rock were measured by ICP-MS (Table 0-15). Problems with boron evaporation prevented its determination. Carbon concentration was estimated using the calcination technique (Table 0-16). Major elements (Ca, K, Fe, Al, Ti) in aliquots obtained during the sample pre-treatment of ^{36}Cl were measured by ICP-OES (Table 0-17).

Table 0-13: Most relevant data of sample preparation process for Cl-36 analyisis by AMS.

Sample	Calcite content [%]	Initial sample weight [g]	Sample loss during washing [%]	^{35}Cl-carrier addition [10^{19} atoms]	Final AgCl [mg]
1	91	150.03	10	2.559	10.64
2	88	150	24	2.538	2.56
3	89	141.37	19	2.545	8.36
4	88	150.15	17	2.554	7.35
5	88	150	13	2.553	3.04
6	93	150.16	18	2.551	7.08
7	85	150.38	29	2.509	10.11
8	90	150.9	38	2.553	11.7
9	100	150.09	14	2.194	4.78

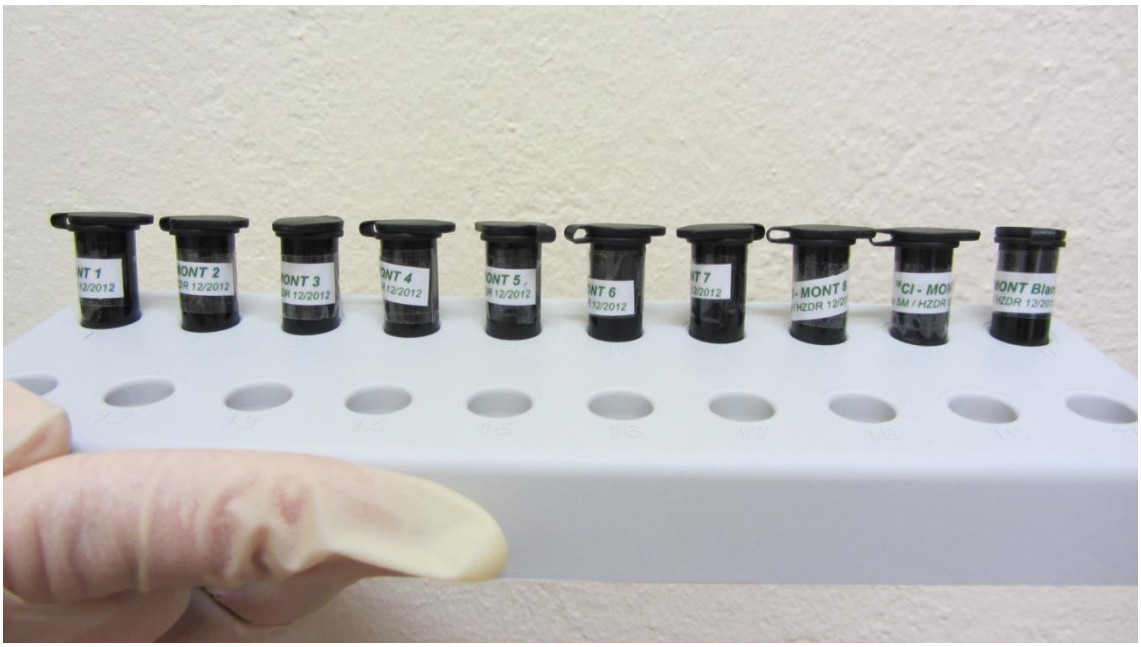

Figure 0-93: AgCl obtained from the second precipitation and ready to be measured by the AMS. It must be kept from light due to its photosensitivity.

Table 0-14: X-Ray Fluorescence analysis results for bulk rock.

Sample	Fe2O3 [%wt]	MnO [%wt]	TiO2 [%wt]	Cao [%wt]	K2O [%wt]	P2O5 [%wt]	SiO2 [%wt]	Al2O3 [%wt]	MgO [%wt]	Na2O [%wt]
1	2.76±0.25	0.06±0.002	0.04±0.0008	50.4±2.02	0.25±0.01	0.06±0.001	5.6±1.23	0.97±0.21	0.78±0.09	0.09±0.006
2	6.45±0.58	0.13±0.005	0.03±0.0006	48.24±1.93	0.3±0.01	0.1±0.001	5.05±1.11	1.08±0.24	0.51±0.06	0.03±0.002
3	2.35±0.21	0.04±0.002	0.11±0.002	45.48±1.82	0.74±0.03	0.05±0.001	11.08±2.44	2.62±0.58	1±0.12	0.04±0.003
4	5.42±0.49	0.11±0.004	0.02±0.0004	46.39±1.86	0.51±0.02	0.1±0.001	7.97±1.75	1.3±0.29	0.6±40.08	0.06±0.004
5	4.38±0.39	0.14±0.006	0.03±0.0006	48.54±1.94	0.28±0.01	0.09±0.001	6.9±1.52	0.91±0.2	0.49±0.06	0.02±0.001
6	4.06±0.37	0.1±0.004	0.03±0.0006	19.61±0.78	0.24±0.01	0.08±0.001	5.36±1.18	0.8±0.18	0.64±0.08	0.02±0.001
7	6.54±0.59	0.09±0.004	0.05±0.001	43.48±1.74	0.58±0.02	0.11±0.001	9.73±2.14	1.76±0.39	1.07±0.13	0.04±0.003
8	3.25±0.29	0.07±0.003	0.04±0.0008	48.96±1.96	0.35±0.01	0.08±0.001	5.91±1.3	1.2±0.26	0.86±0.1	0.04±0.003
9	0.56±0.05	0.02±0.001	0	54.65±2.19	0.07±0.003	0.02±0.0002	1.13±0.25	0.28±0.06	0.49±0.06	0.01±0.001

Scaling and correcting factors

Altitude and latitude scaling factors ($S_{el,s}$, $S_{el,\mu}$ and $S_{el,n}$) were calculated using the Excel add ins called CosmoCalc (Vermeesch, 2007) and the method of Stone (2000) (Table 0-18). Input data are Latitude (deg) and pressure (mbar) of each sample. Converting from altitude to latitude is also possible with CosmoCalc. Surrounding topography (S_T) was evaluated using the Geometric shielding calculator from the CRONUS-Earth project (Balco, 2006). Spatial disposition of each surface sample (Strike and Dip) is required as well as azimuth and angular elevation of points defining the horizon. These points have been selected so that horizon was perfectly described. They are represented by circles and labelled from A to E. Sample positions are represented with black triangles and labelled from 1 to 9 (Figure 0-94). Relative position between each topographic point and sample has been calculated (Table 0-24 in Annex: A10). Results are shown in Table 0-19.

Table 0-15: Trace elements mesured in bulk rock by ICP_MS.

Sample	B [µg/g]	Sm [µg/g]	Gd [µg/g]	Li [µg/g]	Th [µg/g]	U [µg/g]
1	-	1.7±0.17	1.8±0.09	3.6±0.18	1.9±0.19	0.5±0.03
2	-	1.6±0.16	1.7±0.09	5.4±0.27	2±0.2	0.6±0.03
3	-	1.6±0.16	1.5±0.08	14.5±0.73	3.3±0.33	1.5±0.08
4	-	1.9±0.19	2±0.1	10.7±0.53	2.8±0.28	0.7±0.03
5	-	1.7±0.17	1.8±0.1	6±0.3	1.8±0.18	0.5±0.03
6	-	1.5±0.15	1.6±0.08	3.9±0.19	1.7±0.17	0.5±0.03
7	-	1.9±0.19	2±0.1	6.6±0.33	2.8±0.28	0.8±0.04
8	-	1.5±0.15	1.6±0.08	5.3±0.26	1.9±0.19	0.5±0.03
9	-	0.5±0.05	0.5±0.03	1.8±0.09	0.5±0.05	0.6±0.03

Table 0-16: Calcination results.

Sample	Crucible [g]	Crucible+sample[g]	After calcinations [g]	%wt CO2
1	14.3316	15.3314	14.9366	39.5
2	13.1371	14.1374	13.7526	38.5
3	15.7946	16.7949	16.4271	36.8
4	46.4245	17.4248	17.0489	37.6
5	16.1942	17.1944	16.8084	38.6
6	16.1942	17.1944	16.8084	39.3
7	12.9841	13.9846	13.6242	36
8	18.1135	19.1137	18.796	37.8
9	17.5648	18.565	18.1378	42.7

Table 0-17: Major elements measured in the target fraction aliquots obtained during the sample pretreatment of ^{36}Cl by ICP_OES.

Sample	CaO [%wt]	K2O [%wt]	Fe2O3 [%wt]	Al2O3 [%wt]	TiO2 [%wt]
1	54.6 ± 1.09	0.12	0.13	<L.D.	<L.D.
2	56.01 ± 1.12	0.13	0.08	<L.D.	<L.D.
3	54.77 ± 1.1	0.13	0.46	<L.D.	<L.D.
4	55.34 ± 1.11	0.13	0.09	<L.D.	<L.D.
5	55.28 ± 1.11	0.13	0.13	<L.D.	<L.D.
6	55.01 ± 1.1	0.13	0.12	<L.D.	<L.D.

7	54.91 ± 1.1	0.15	0.22	<L.D.	<L.D.
8	54.97 ± 1.1	0.15	0.12	<L.D.	<L.D.
9	55.27 ± 1.11	0.13	0.11	<L.D.	<L.D.

L.D: Limit of determination

Table 0-18: Altitude and latitude scaling factors for each sample using the method of (Stone, 2000).

Sample	Sel_s	Sel_μ
1	2.29	1.54
2	2.29	1.54
3	2.34	1.55
4	2.29	1.54
5	2.29	1.54
6	2.34	1.55
7	2.38	1.57
8	2.43	1.59
9	2.38	1.57

Table 0-19: Geometric shielding results for each sample calculated using the shielding calculator of (Balco, 2006).

Sample	Strike [º]	Dip [º]	Geometric Shielding
1	40	70	0.486
2	30	65	0.481
3	80	69	0.488
4	45	90	0.452
5	50	85	0.483
6	80	90	0.442
7	160	75	0.307
8	70	73	0.491
9	80	79	0.479

As it was expected, scaling factors are lower than 0.5 because samples are located in a cliff, which reduces the surface rate production in 50% (Dunne et al., 1999) and surrounded by a mountainous relieve. Snow shielding (S_{Snow}) has not been considered since neither glacial deposits exist nor snow is common in that area. Time dependence of the magnetic field variations for young samples (<20000 years according to Dunai (2000)) has not been considered, since it would affect similarly to all samples. Effective fast neutron attenuation length (f,e) was calculated for each sample using equation 3.74 in Gosse and Phillips (2001) as its value depends of the surface dip (Figure 0-75). Results for each sample are shown in Table 0-20. As it was stated in section 1.4, dipping surfaces will have a shorter effective attenuation length because most of the particles will enter at oblique angles. On the contrary, more horizontal surfaces will have a longer e_ective attenuation length because fewer of the particles will be entering from oblique angles. Finally, corrections factors for sample thickness have been calculated according to Schlagenhauf et al. (2010) (Table 1.14).

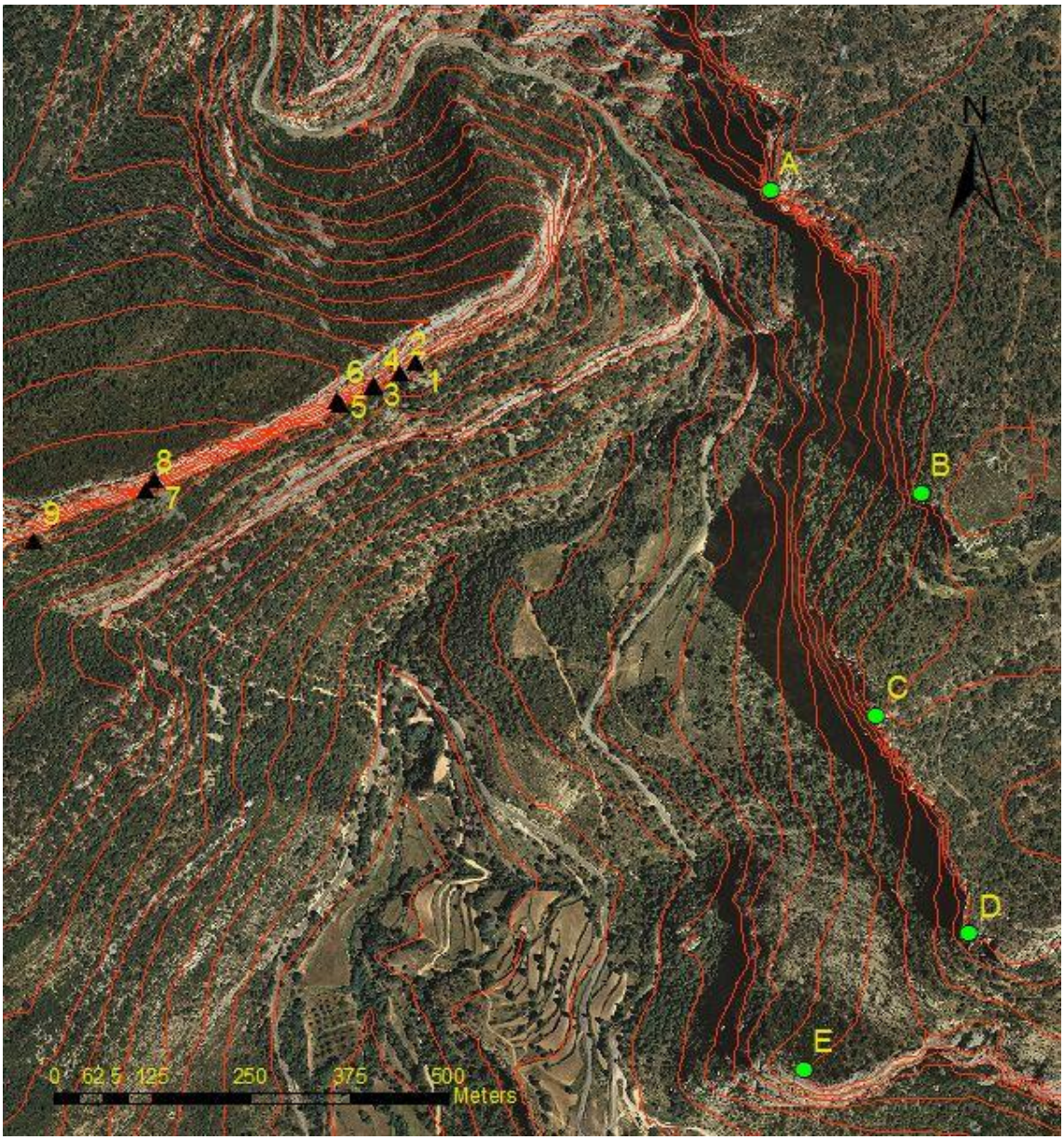

Figure 0-94: Area of study with circles representing the topographic points used to define the horizon. Sample positions in the cliff are represented with black triangles.

Table 0-20: Effective fast neutron attenuation length calculated for each sample with equation 3.74 in (Gosse and Phillips, 2001).

Sample	Dip angle [º]	Attenuation length [g/cm^2]
1	70	104
2	65	110
3	69	107
4	90	83
5	85	88
6	90	83
7	75	100
8	73	100
9	79	94

Table 0-21: Correction factors for sample thickness according to Schlagenhauf et al. (2010). Q_s refers to spallation, Q_{th} to thermal neutron absortion, Q_{eth} to epithermal neutron absorption and Q_μ to muon absorption.

Sample	Q_s	Q_{th}	Q_{eth}	Q_μ
1	1	0.999	0.998	1
2	1	0.997	0.995	1
3	1	0.998	0.997	1
4	1	0.998	0.996	1
5	1	0.999	0.998	1
6	1	0.996	0.994	1
7	1	0.997	0.995	1
8	1	0.999	0.998	1
9	1	0.996	0.994	1

AMS measurements

Measurements were conducted at Ion Beam Centre facilities, at HZDR (Dresden, Germany), using the AMS operating at 6 MV (Akhmadaliev et al., 2013) and the ion source developed by Pavetich et al.(2014). Data has been normalized to the SM-Cl-13 standard, which has been described in Merchel et al. (2011). Addition of a ^{35}Cl-enriched spike solution permitted the calculation of both ^{36}Cl and Cl concentrations. Blank correction was performed to ensure that no external contamination could affect the results by subtracting the blank ^{36}Cl calculated atoms from the ^{36}Cl calculated atoms of each sample. A natural ^{35}Cl/^{37}Cl ratio has supposed to be 3.127. ^{35}Cl/^{37}Cl and ^{36}Cl/^{35}Cl measured ratios, blank correction, and calculation of ^{nat}Cl and ^{36}Cl are shown in Table 0-22.

Calculation of exposure ages

The exposure age calculation has been done by means of the spreadsheet provided by Schimmelpfennig et al. (2009) and later modified by Braucher et al.(2011). He changed the rate for spallation (42 ± 2 ^{36}Cl atoms gCa^{-1} a^{-1}), but the main change was for muons production introducing a production rate for fast muons (0.982±0.233 ^{36}Cl atoms gCa^{-1} a^{-1}) and changing the production rate for slow muons (0.982±0.233 ^{36}Cl atoms gCa^{-1} a^{-1}) at sea level.

All data concerning the bulk rock and target fraction chemistry (Table 0-14, Table 0-15, Table 0-16 and Table 0-17), as well as scaling factors (Table 0-18), geometric shielding (Table 0-19), effective fast neutron production (Table 0-20), correcting factors for sample thickness (Table 0-21) and the amount of ^{36}Cl (Table 0-22) have been inserted into the spreadsheet.

On the other hand, the ^{36}Cl production by inheritance must be quantified and corrected. Inherited ^{36}Cl, which is produced at depth, can contribute significantly to the ^{36}Cl concentration and consequently affect the sample exposure age, mostly in shallow samples (<15m): As stated before, muons have a higher penetrating power in the subsurface than neutrons because of their poor interaction with matter (Dunai 2010) being the muon absorption mechanism responsible for the main production of cosmogenic nuclides at great depths. Furthermore, the concentration in U, Th and ^{nat}Cl also contributes to the generation of inherited ^{36}Cl. Therefore, the radiogenic production (U, Th and Cl) and the erosion rate mostly controls the production of ^{36}Cl inherited. In the literature, numerous denudation rates have been calculated in different places, for different lithologies and affected by different processes. In chapter 7 of this thesis, several tests have been performed and the most appropriated rockwall retreat rate has been 365mm/ka.

Table 0-22: $^{35}Cl/^{37}Cl$ and $^{36}Cl/^{35}Cl$ ratios of each sample (bulk rock) measured at the 6 MV AMS (Akhmadaliev et al., 2013) at DREAMS (Dresden, Germany) and calculation of blank correction by ^{36}Cl atoms, ^{nat}Cl, and ^{36}Cl.

Sample	Sample weight dissolved [g]	$^{35}Cl/^{37}Cl$	$^{36}Cl/^{35}Cl$ [10^{-14}]	Blank correction by ^{36}Cl atoms [%]	^{nat}Cl [µg/g] (blank corrected)	^{36}Cl [10^5 atoms/g] (blank corrected)
1	90.18	5.02 ± 0.022	46.41 ± 2.0	0.8	35.95 ± 0.16	3.45 ± 0.15
2	84.24	11.011 ± 0.091	45.05 ± 1.9	1.6	8.864 ± 0.073	1.86 ± 0.08
3	88.85	4.833 ± 0.024	6.7 ± 0.44	5.2	40.30 ± 0.20	0.514 ± 0.034
4	84.65	5.355 ± 0.034	32.21 ± 1.5	1.3	32.41 ± 0.21	2.3 ± 0.1
5	83.91	8.496 ± 0.098	72.04 ± 3.0	0.9	13.33 ± 0.15	3.43 ± 0.14
6	85.41	5.417 ± 0.025	16.73 ± 0.83	2.5	31.21 ± 0.15	1.149 ± 0.057
7	74.94	4.713 ± 0.021	27.85 ± 1.3	1.2	50.71 ± 0.23	2.73 ± 0.13
8	71.75	4.877 ± 0.022	44.49 ± 1.9	0.8	48.79 ± 0.22	4.36 ± 0.19
9	88.77	5.686 ± 0.027	28.82 ± 1.3	1.8	23.03 ± 0.11	1.55 ± 0.071
Blank	-	189.3 ± 1.2	0.9903 ± 0.19	-	-	-

8 Results

Measurements of each sample are shown in Table 0-22. The amount of material dissolved was 71-90g. Uncertainties for $^{35}Cl/^{37}Cl$ range from 0.4% to 1.2% being maximum in S5 and from 4.2% to 6.6% concerning $^{36}Cl/^{35}Cl$-ratios. 36Cl/35Cl rate present values from $6.7 \cdot 10^{-14}$ to $72.04 \cdot 10^{-14}$. The value for S3 is extremely low compared with the others. Such an anomaly can be observed in the corresponding blanks where corrections range from 0.8 to 2.5% except for S3 being 5.2%, thus, confirming its non consistency. ^{nat}Cl concentration values are 8.87-50.71 [μg/g] blank corrected being reduced an average of 26.8 μg per sample dissolution. ^{36}Cl blank-corrected values are 0.514-4.36 [10^5 atoms/g] being sample 3 extremely low compared with the others, as well.

In Table 0-23 exposure ages, sample depth and inherited ^{36}Cl of each sample are shown. Depth has been determined using a high resolution point cloud and by field observations (the procedure can be found in the annex of this chapter). It has been assumed that S1, S5, S7 and S8 belong to an old and continuous surface that exists at a certain time 0 (T_0). Therefore, they are located at a depth of 0 cm. Remaining samples have been located at depths between 611 and 730cm.

Exposure surface ages are in good agreement with previous assumption since presupposed older samples are in the range of 13.95-16.79 Ka. On the other hand, younger samples such as S6 and S9 present ages of 5.57 and 6.83 ka respectively. S4 has an intermediate age of 11.27 ka. Field work and cross section suggest that such a sample does not belong to T_0, but to a rockfall scar surface older than S6 and S9. S3 presents a very low exposure age as the result of afore-mentioned anomaly produced during the sample treatment since neither field work nor point cloud suggest it could belong to a much more recent rockfall scar.

Table 0-23: Depth, exposure age and inherited ^{36}Cl of each sample calculated according to the spreadsheet of Schimmelpfennig et al.(2009) and later modified by Braucher et al. (2011).

Sample	Sample depth (cm)	Calculated exposure ages [Ka]	Calculated exposure age uncertainty (%)	^{36}Cl from inheritance (%)
1	0	13.95± 1.45	10.7	17.3
2	670	8.77± 0.94	10.7	5.97
3	730	1.51± 0.21	13.7	27
4	664	11.27± 1.18	10.5	5.18
5	0	14.68± 1.59	10.8	15.3
6	697	5.57± 0.6	10.8	9.24
7	0	16.79± 1.82	10.8	15
8	0	15.97± 1.7	10.6	15.6
9	611	6.83± 0.73	10.6	8.1

Finally, inherited ^{36}Cl ranges from 5.97 % to 17.3% excepting for S3 that presents a value of 27%. Scars belonging to T_0 (S1, S5, S7 and S8) have a higher amount of ^{36}Cl by inheritance, as expected, but not excessive. Since erosion rate is a crucial parameter that controls the generation of inherited ^{36}Cl and it has been deduced from others works carried out in similar places close to

the area of study, a sensitivity analysis has been performed to ensure its reliability (chapter 7). Varying the denudation rate by 45%, the maximum deviation in the exposure ages is about 8%, being minimum than the exposure age uncertainties (Table 0-23).

9 Conclusions

9 samples from a calcareous cliff within the Montsec range have been date using TCN. Even the small depth at which samples were located, values of ^{36}Cl inherited (5.18%-17.3%) are not significantly high compared with other works (e.g. Merchel et al., 2013 and Merchel et al., 2014). It could be the consequence of the low amount of ^{nat}Cl (Table 0-22) and the erosion rate used. However, the sensitivity analysis carried out for the denudation rate in chapter 7 confirms the fairly influence of the ^{36}Cl inherited in the final results.

The oldest surface scars (S1, S5, S7 and S8) match with the more grayish and eroded ones as it was supposed. More reddish and with a high fresh appearance rockfall scars present the youngest exposure ages. It suggests thatS1, S5, S7 and S8 could be part of an old and continuous surface (T_0) that existed 15,400 years ago (average exposure ages) from which several blocks were dethatched exposing the current rockfall scars. Concerning S2, S4, S6 and S9), their exposure ages confirm that they belong to more recent rockfall scars (8,770, 11,270, 5,570 and 6.830 years respectively). Obtained S3 exposure age (1,510 years) seems to be erroneous due to its high difference compared with other samples as well as the high amount of ^{36}Cl inherited and the low value of cosmogenic ^{36}Cl (Table 0-22).

10 Annex: A

Table 0-24: Calculation of geometric shielding.

Sample	Strike [º]	Dip [º]	Topographic points	X (m)	Y (m)	Z (m)	Azimut between sampling and topographic point	Difference in height (m)	Distance (m)	Angular elevation (º)	Geometric shielding
1	40	70					60	-	-	90	0.486
			A	337479	4654789	1100	64.3085	75	495	8.6	
X (m)	Y (m)	Z (m)	B	337670	4654406	1125	104.625	100	659	8.6	
			C	337613	4654124	1100	127.603	75	731	5.9	
337030	4654573	1025	D	337730	4653846	1100	136.085	75	1007	4.3	
			E	337520	4653675	1000	111.382	0	1019	0	
							239	0	1	0	
							240	-	-	90	
2							60	-	-	90	0.481
			A	337479	4654789	1100	63.8757	75	516	8.3	
X (m)	Y (m)	Z (m)	B	337670	4654406	1125	103.052	100	675	8.4	
			C	337613	4654124	1100	125.807	75	741	5.8	
337010	4654559	1025	D	337030	4653846	1100	134.721	75	1012	4.2	
			E	337520	4653675	1000	150.02	0	1022	0	
							239	0	1	0	
							240	-	-	90	
3							60	-	-	90	0.488
			A	337479	4654789	1100	63.9376	50	558	5.1	
X (m)	Y (m)	Z (m)	B	337670	4654406	1125	101.167	75	708	6	
			C	337613	4654124	1100	123.337	50	762	3.8	
336976	4654543	1050	D	337730	4653846	1100	132.752	50	1028	2.8	
			E	337520	4653675	1000	147.925	0	1025	0	
							239	0	1	0	
							240	-	-	90	

4						60	-	-	90	0.452
			A	337479	4654789	1100	63.6624	75	558	7.7	
X (m)	Y (m)	Z (m)	B	337670	4654406	1125	100.929	100	708	8	
			C	337613	4654124	1100	123.148	75	762	5.6	
336976	4654540	1025	D	337730	4653846	1100	132.628	75	1028	4.2	
			E	337520	4654406	1100	147.836	0	1025	0	
							239	0	1	0	
							240	-	-	90	
5							60	-	-	90	0.483
			A	337479	4654789	1100	63.7293	75	607	7	
X (m)	Y (m)	Z (m)	B	337670	4654406	1125	98.8049	100	739	7.7	
			C	337613	4654124	1100	120.252	75	782	5.5	
336934	4654520	1025	D	337730	4653846	1100	130.257	75	1037	4.1	
			E	337520	4653675	1000	145.261	0	1024	0	
							239	0	1	0	
							240	-	-	90	
6							60	-	-	90	0.442
			A	337479	4654789	1100	64.1072	12.5	607	1.2	
X (m)	Y (m)	Z (m)	B	337670	4654406	1125	18.9968	50	739	3.9	
			C	337613	4654124	1100	40.3304	25	782	1.8	
336931	4654523	1075	D	337730	4653846	1100	50.2761	25	1037	1.4	
			E	337520	4653675	1000	65.2187	0	1024	0	
							239	0	1	0	
							240	-	-	90	
7							60	-	-	90	0.307
			A	337479	4654789	1100	64.8938	0	859	0	
X (m)	Y (m)	Z (m)	B	337670	4654406	1125	91.0631	25	970	1.5	
			C	337613	4654124	1100	108.19	0	958	0	
336700	4654424	1100	D	337730	4653846	1100	119.3	0	1178	0	
			E	337520	4653675	1000	132.41	0	1110	0	
							239	0	1	0	
							240	-	-	90	
8							60	-	-	90	0.491

			A	337479	4654789	1100	64.4265	12.5	870	0.8	
X (m)	Y (m)	Z (m)	B	337670	4654406	1125	90.2332	25	976	1.5	
			C	337613	4654124	1100	107.164	0	962	0	
336687	4654410	1100	D	337030	4653846	1100	118.403	0	1181	0	
			E	337520	4653675	1000	131.425	0	1109	0	
							239	0	1	0	
							240	-	-	90	
9							60	-	-	90	0.479
			A	337479	4654789	1100	64.5502	37.5	1035	2.1	
X (m)	Y (m)	Z (m)	B	337670	4654406	1125	86.8935	50	1126	2.5	
			C	337613	4654124	1100	101.702	25	1089	1.3	
336546	4654345	1075	D	337730	4653846	1100	112.854	25	1287	1.1	
			E	337520	4653675	1000	124.525	0	1183	0	
							239	0	1	0	
							240	-	-	90	

11 Annex: B

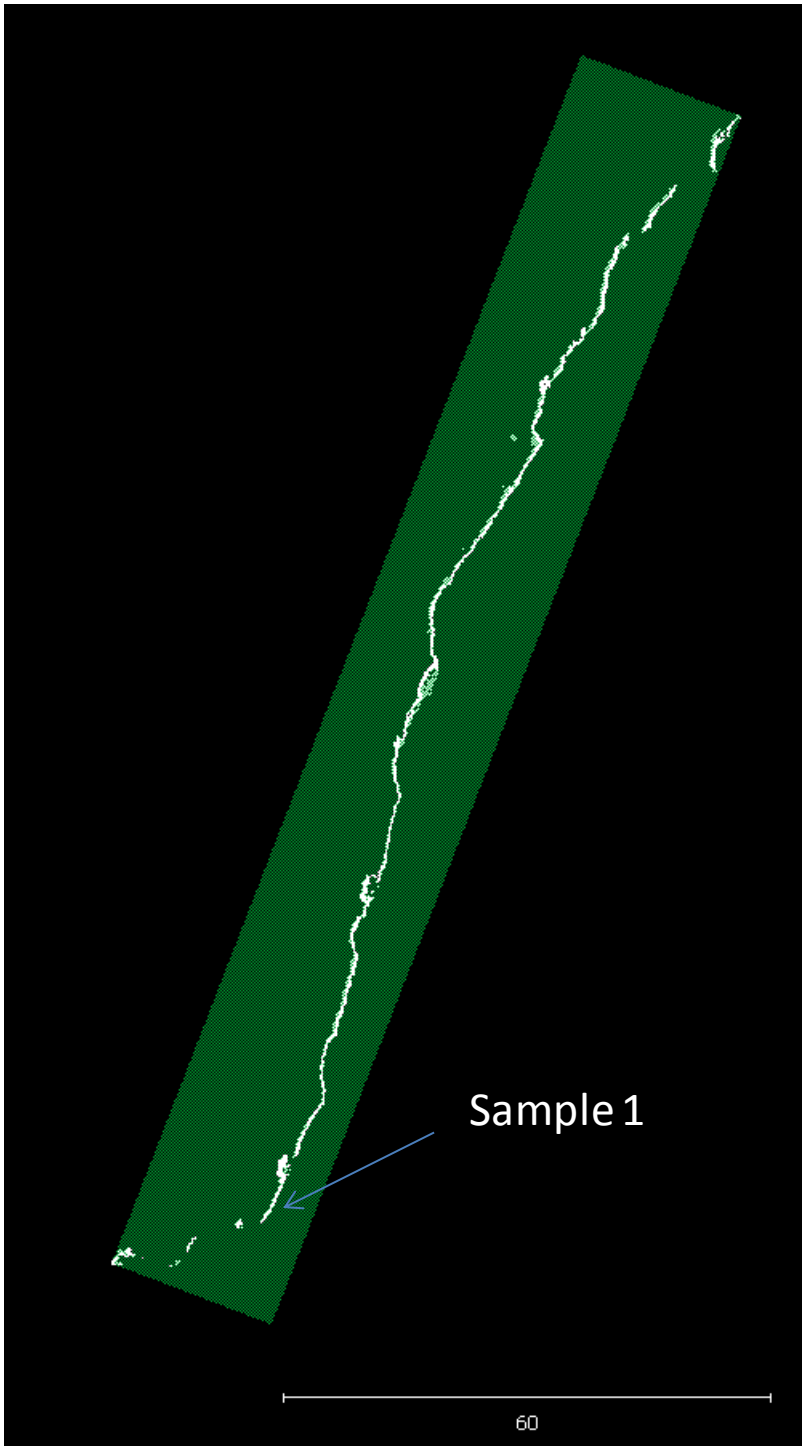

Figure 0-95: Cross section where sample 1 is located.

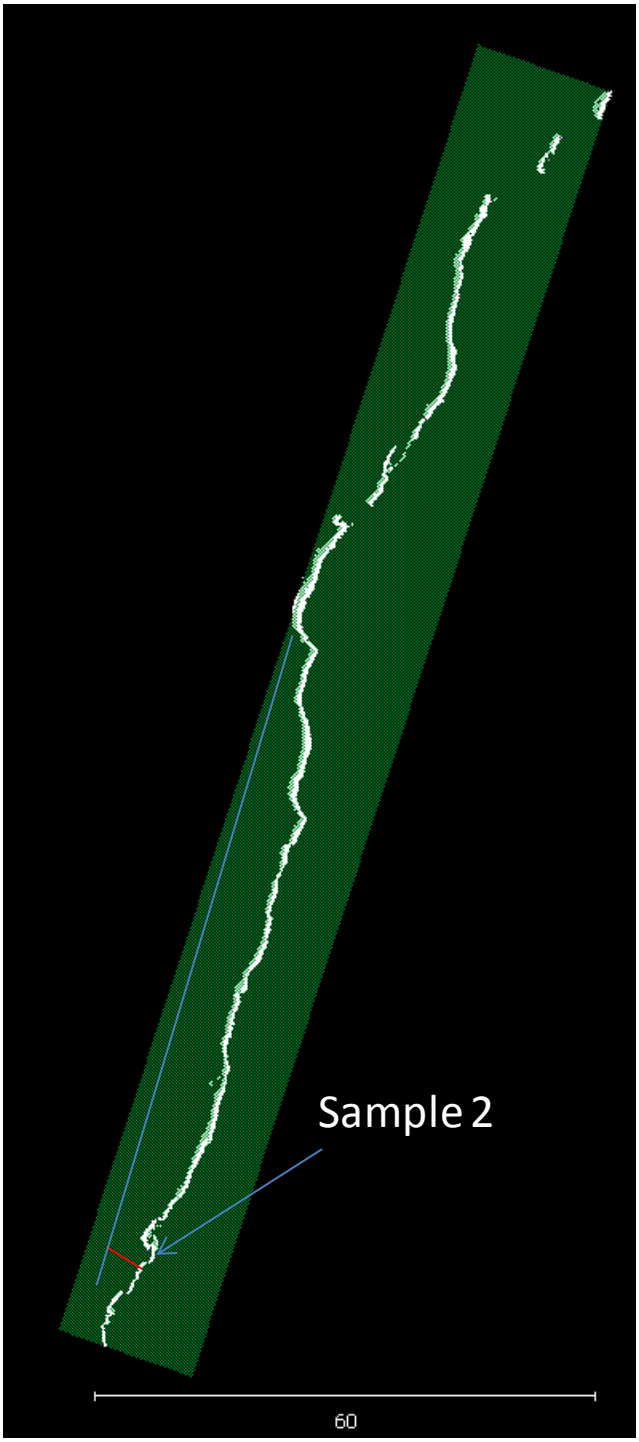

Figure 0-96: Cross section where sample 2 is located. Red line indicates the sample depth, i.e. the distance between the current surface (sample 2) and the approximated position of the slope face just before the exposition.

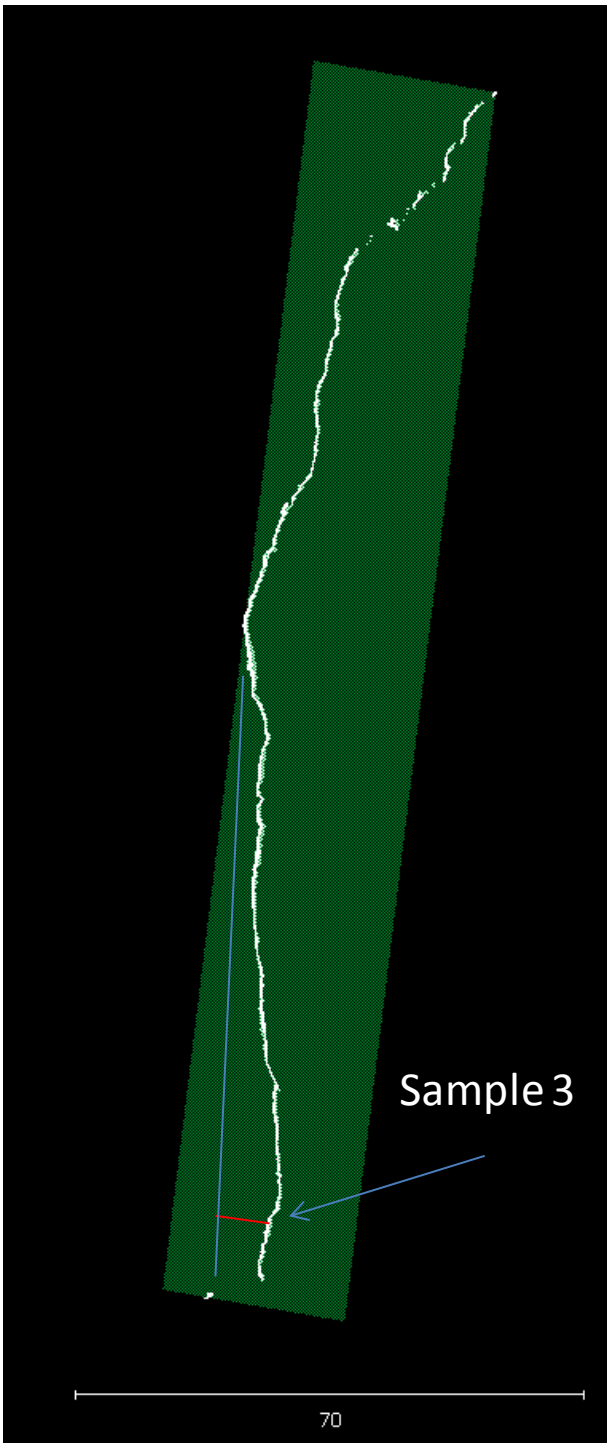

Figure 0-97: Cross section where sample 3 is located. Red line indicates the sample depth, i.e. the distance between the current surface (sample 3) and the approximated position of the slope face just before the exposition.

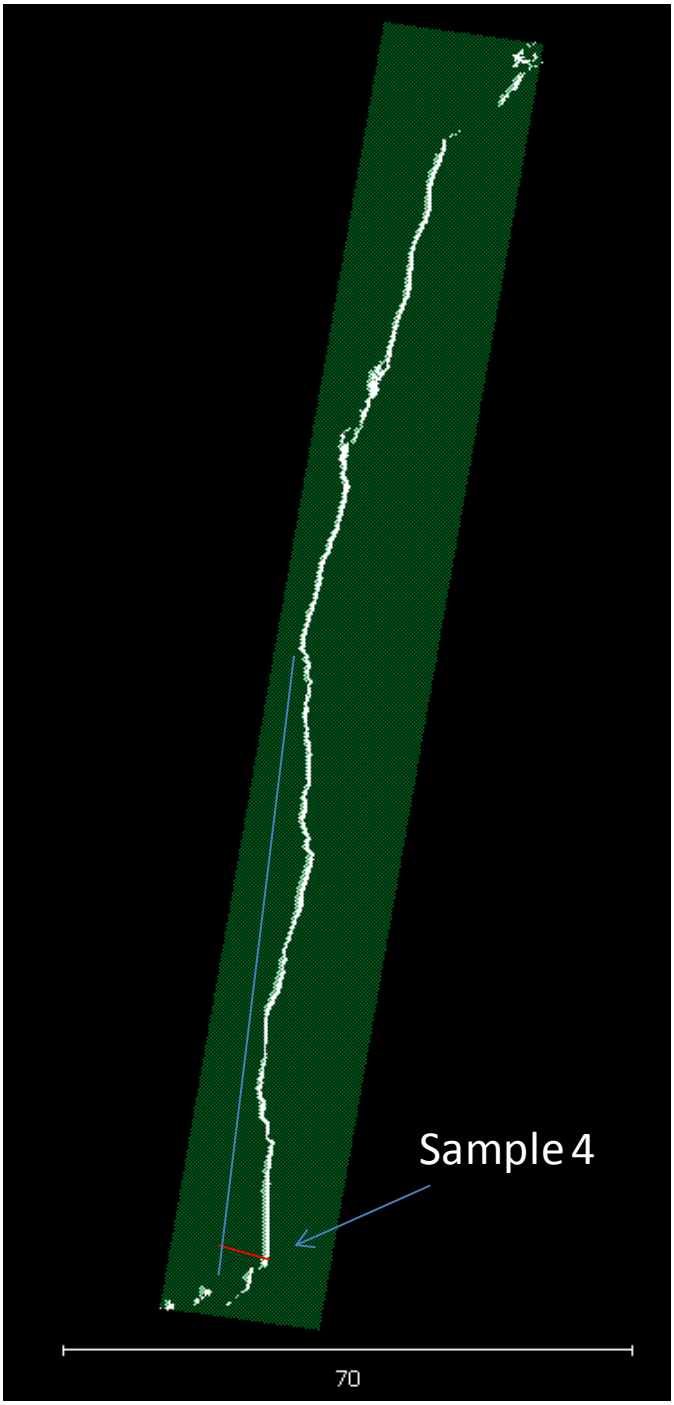

Figure 0-98: Cross section where sample 4 is located. Red line indicates the sample depth, i.e. the distance between the current surface (sample 4) and the approximated position of the slope face just before the exposition.

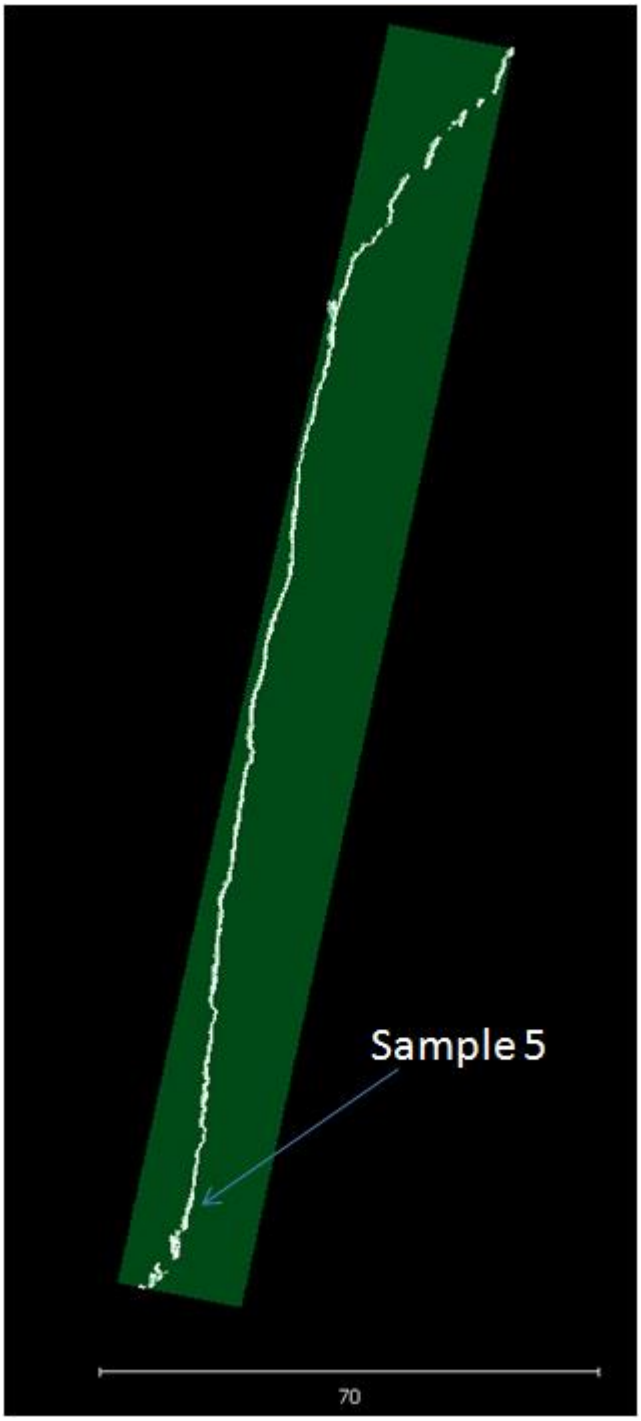

Figure 0-99: Cross section where sample 5 is located.

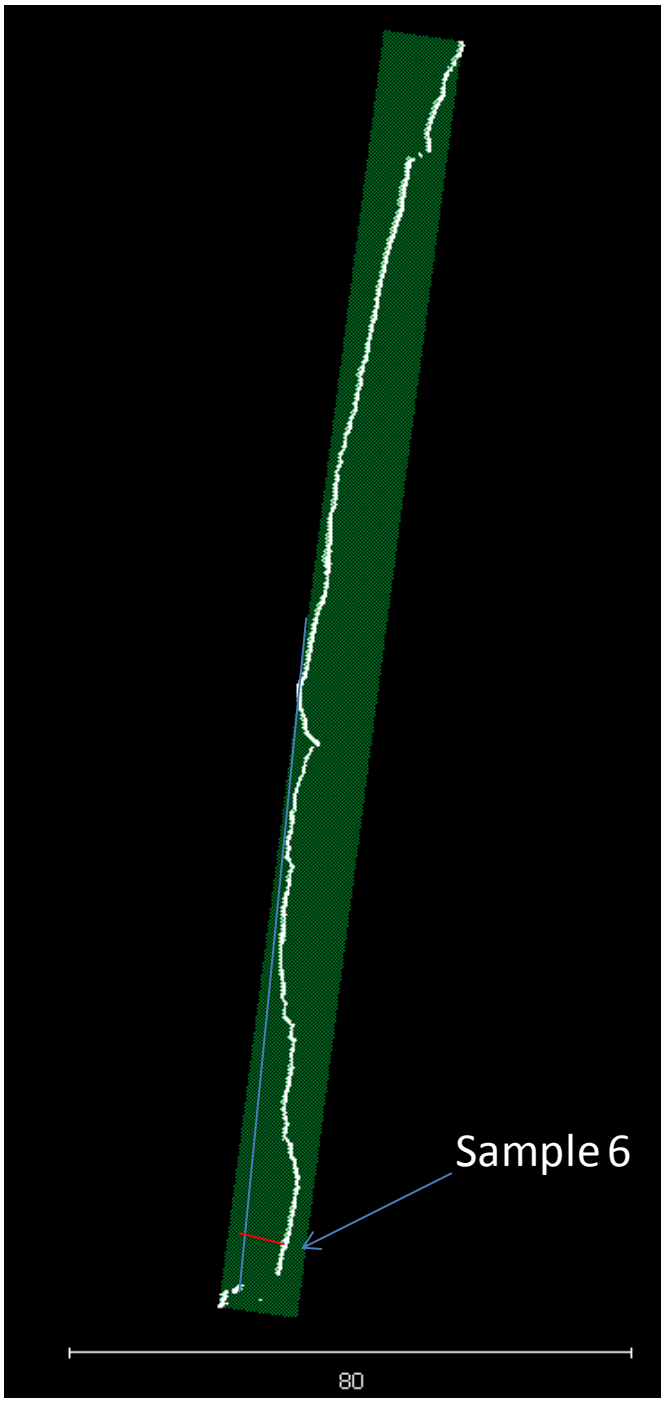

Figure 0-100: Cross section where sample 6 is located. Red line indicates the sample depth, i.e. the distance between the current surface (sample 6) and the approximated position of the slope face just before the exposition.

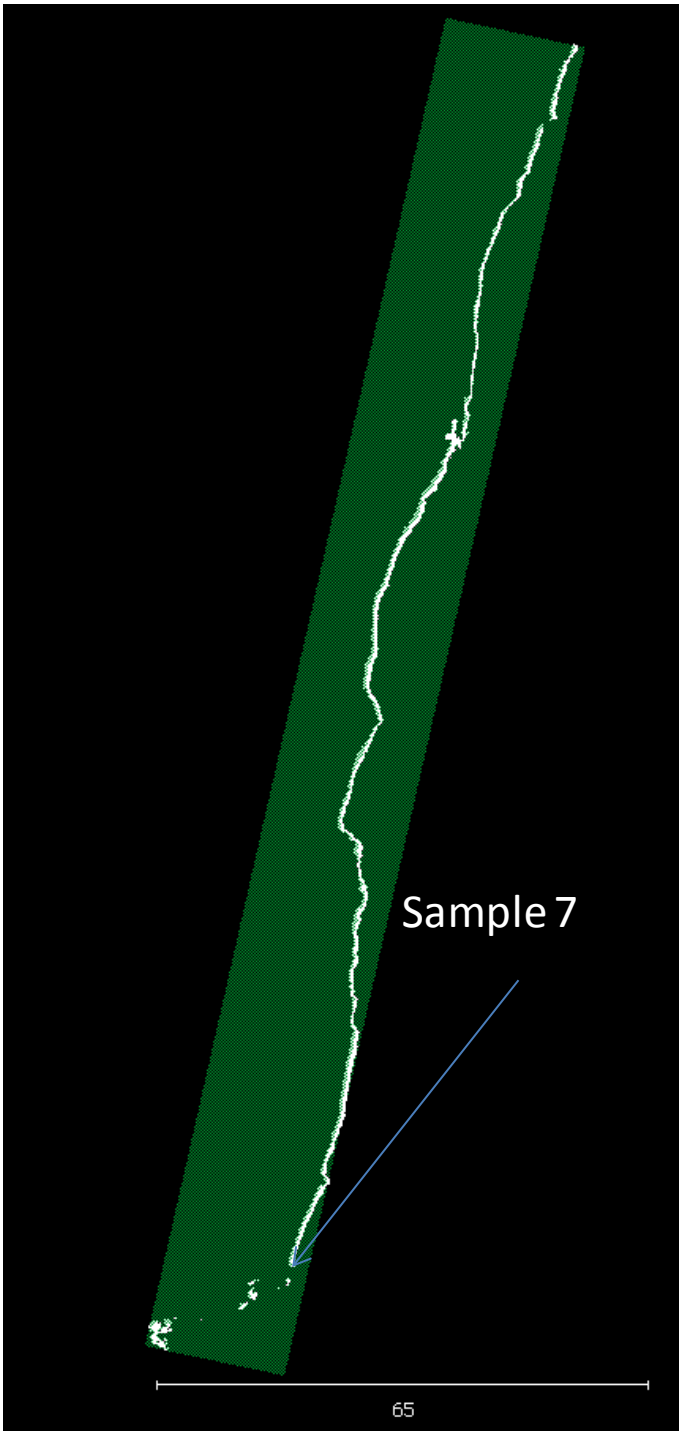

Figure 0-101: Cross section where sample 7 is located.

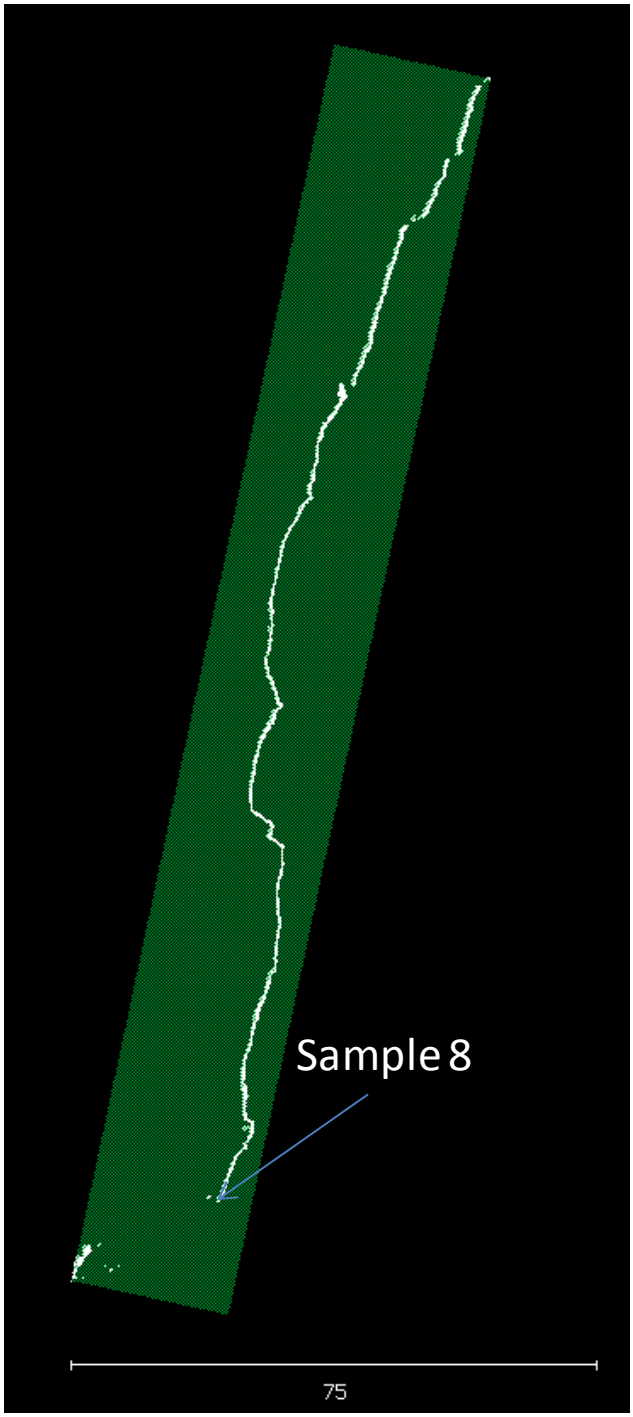

Figure 0-102: Cross section where sample 8 is located.

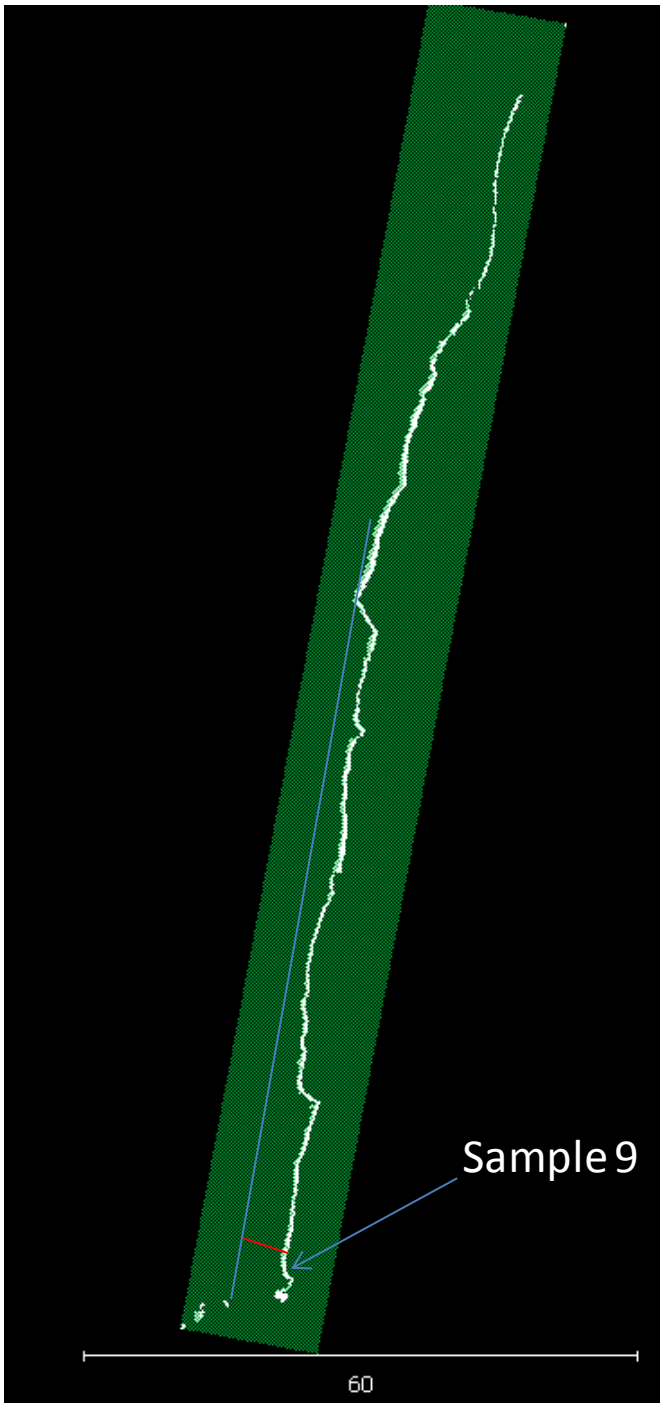

Figure 0-103: Cross section where sample 9 is located. Red line indicates the sample depth, i.e. the distance between the current surface (sample 9) and the approximated position of the slope face just before the exposition.